Integrated Photocatalytic-Biological Treatment of Pharmaceutical Wastewater and Catalyst Recovery

Thesis Submitted in Partial Fulfilment of the Requirements
for the Award of the Degree of

DOCTOR OF PHILOSOPHY

by

RAVI

Centre for the Environment
Indian Institute of Technology Guwahati
Assam-781039, INDIA

December 2025

To my parents, family, and loved one –

the pillars of my journey, the comfort in my struggles, and the inspiration behind my success

CENTRE FOR THE ENVIRONMENT
INDIAN INSTITUTE OF TECHNOLOGY GUWAHATI
GUWAHATI – 781039
ASSAM, INDIA

DECLARATION

I hereby declare that the work embodied in this thesis entitled **"Integrated Photocatalytic-Biological Treatment of Pharmaceutical Wastewater and Catalyst Recovery"** is the outcome of original investigations carried out by me at the Indian Institute of Technology Guwahati, Assam, INDIA – 781039, under the supervision of Prof. Animes Kumar Golder, Department of Chemical Engineering, IIT Guwahati. This thesis is submitted to Indian Institute of Technology Guwahati for the award of the degree of Doctor of Philosophy.

In accordance with standard academic practice, due acknowledgements have been made wherever the work presented is based on the contributions or findings of other researchers.

Ravi
Roll no.: 206152102
Centre for the Environment
Indian Institute of Technology Guwahati
Guwahati, Assam, INDIA

CENTRE FOR THE ENVIRONMENT
INDIAN INSTITUTE OF TECHNOLOGY GUWAHATI
GUWAHATI – 781039
ASSAM, INDIA

CERTIFICATE

This is to certify that the thesis entitled **"Integrated Photocatalytic-Biological Treatment of Pharmaceutical Wastewater and Catalyst Recovery"** submitted by Mr. Ravi to Indian Institute of Technology Guwahati, India, for the award of the degree of Doctor of Philosophy, has been carried out by him under my guidance and supervision.

We further certify that the work embodied in this thesis is an original contribution of the candidate and has not been submitted, either in part or in full, to any other university or institute for the award of any degree or diploma.

Animes Kumar Golder
(Thesis Supervisor)
Professor
Department of Chemical Engineering
Indian Institute of Technology Guwahati
Guwahati – 781039
Assam, INDIA

ACKNOWLEDGEMENT

It gives me great pleasure to acknowledge the invaluable contributions of several individuals and institutions who made this doctoral journey achievable.

First and foremost, I extend my heartfelt gratitude to **Prof. Animes Kumar Golder** for his constant encouragement, insightful guidance, and the generous liberty to pursue research independently. His constructive feedback and thought-provoking inputs at different stages of my work have been pivotal in shaping the quality and direction of this thesis.

I feel privileged to have received the support of my Doctoral Committee members, **Prof. Bishnupada Mandal** (Chairman), **Prof. Mahuya De**, and **Prof. Pranab Kumar Ghosh**, whose critical evaluation, valuable suggestions, and constant guidance were instrumental in refining my research and keeping me focused.

I would like to express my sincere gratitude to my thesis examiners, **Prof. Parag R. Gogate (ICT Mumbai, India)** and **Prof. Raja Ghosh (McMaster University, Canada)**, for their thorough evaluation of my thesis and for their insightful, constructive, and valuable comments, which significantly helped in improving the quality and clarity of this work.

I am also deeply thankful to the Viva-Voce Committee members, **Prof. Bishnupada Mandal (Chairman)**, **Prof. Parag R. Gogate**, **Prof. Chandan Das**, and **Prof. Partho S. G. Pattader**, for their time, careful assessment, and thoughtful questions during the viva-voce examination. Their critical feedback and encouragement greatly contributed to the refinement and finalization of my research.

I sincerely acknowledge the support of **Prof. Animes Kumar Golder**, Head, Centre for the Environment, IIT Guwahati, for providing essential facilities and a nurturing research environment. My appreciation also goes to the former Heads of the Centre, Prof. Utpal Bora and Prof. Mihir Kumar Purkait, as well as the faculty and staff members of the Centre for the Environment, and the Central Instrument Facility (CIF) at IIT Guwahati. The state-of-the-art instrumentation facilities at CIF played a vital role in carrying out this research. I am also thankful to the Centre staff for their timely technical help and consistent assistance.

I am thankful to Dr. Angana Sarkar, Associate Professor, NIT Rourkela and her team for providing the bacterial strains for biological degradation of the PhACs.

I am deeply thankful to my lab seniors, Dr. Paulomi Bose, Dr. Smruti Ranjan Dash, Dr. Anirban Chowdhury, Dr. Swagata Patra, Dr. Daisy Das, and Dr. Sourav Maity for generously sharing their experience and for their constant support in lab activities. I also extend my

gratitude to my lab mates and colleagues Dr. Chandra Bhan, Mr. Pramod Madhukar Gawal, Mr. Biswajit Bhattacharjya, Mr. Mrinal Kanti Dolai, Mr. Shuvam Bhowmick, Ms. Deblina Hota, Mr. Srijan Acharya, Dr. Anil Kumar, Mr. Bharat Bhushan Negi, Mr. Ajay Kumar Shakya, Ms. Gnana Sangeetha R, Mr. Joy Sriman Sarmah, Mr. Priyanuj Bania, Mr. Ayush Singh, and Mr. Suraj Kumar Yadav for their cooperation, encouragement, and for creating a positive and stimulating research atmosphere.

A special note of gratitude goes to my friends, Dr. Chandra Bhan, Dr. Sukhjeet Arora, Ms. Shilpa Nandi, and Mr. Sandeep Mudgal whose constant support, patience, and unwavering faith in me have been a true source of strength. Their encouragement and understanding gave me the determination to overcome challenges and bring this work to completion.

I would also like to express my heartfelt gratitude to all my sports partners and friends, specially, Dr. Rushikesh Fopase, Mr. Balasubramannyan S, Mr. Madhav Dwivedi, Dr. Angana Bhattacharya, Mr. Shubham Narwan, Mr. Mangal, and all others, whose companionship and encouragement provided me with balance and joy beyond academics. The time spent on the field not only refreshed my mind but also strengthened my determination during this journey.

This journey would not have been possible without the blessings, unconditional love, and continuous support of my family. I dedicate this accomplishment to my mother, **Smt. Sumitra Devi**, my father, **Shri Ajit Singh**, and other family members, whose sacrifices and blessings have been the foundation of my strength.

Above all, I bow in gratitude to the Almighty for granting me health, strength, and opportunities to accomplish this work. I remain eternally thankful to God for giving me the courage to rise whenever I faltered and for blessing me with a loving family, supportive mentors, and wonderful friends.

Ravi

Roll no.: 206152102

Centre for the Environment

Indian Institute of Technology Guwahati

Guwahati, Assam, INDIA

ABSTRACT

Over the past few decades, the escalating issue of water pollution has primarily originated from the direct discharge of industrial and municipal waste. The perilous ramifications of waste laden with pharmaceutically active compounds (PhACs) are particularly concerning, largely due to the rise of antibiotic-resistant microbes. This makes the implementation of effective treatment processes for mitigating PhAC pollution increasingly difficult. Photocatalysis has emerged as a promising, environmentally friendly approach for pollutant degradation, but its practical application remains limited due to challenges such as poor photocatalytic efficiency, incomplete mineralization, generation of intermediate products, and inefficient catalyst recovery. This doctoral study explores bio-based modifications of photocatalytic materials to enhance catalytic performance by lowering the bandgap, delaying electron-hole pairs recombination, and improving hydrophilicity. This doctoral study also introduces a novel integrated mechanism combining photocatalytic degradation, membrane-based photocatalyst recovery, and biological degradation of PhACs and their intermediates, providing valuable insights for researchers and industrialists.

Herein, Pt-, Au-, Pd-, and Ni-doped TiO_2 photocatalysts were synthesized via bio-based routes using vegetal extracts of *S. edule*, waste banana and pineapple peel, achieving substantial improvements in band structure and charge carrier dynamics. The bandgap reduces from 3.29 eV (bare-TiO_2) to 3.02 eV (Pt-doped TiO_2), 2.45 eV (Au-doped TiO_2), 2.41 eV (Pd-doped TiO_2), and 2.54 eV (Ni-doped TiO_2), which enhances the visible-light absorption notably. The theoretical bandgap determined using DFT analyses closely matches with the experimental results and confirms the insertion of Pd and Ni states between the valence and conduction bands in Pd-doped and Ni-doped TiO_2, respectively. PL and TRPL analyses confirm suppressed charge recombination, and water contact angle reveals hydrophilic nature of all the photocatalysts. The metal-doping created oxygen vacancies and Ti^{3+} defects. These characteristics collectively enhance the visible light driven photocatalytic activity. The introduction of oxygen vacancies and Ti^{3+} defects promote efficient charge transfer and delayed recombination, as confirmed by PL, TRPL, and PEC analyses. Significant improvements in photocurrent density were observed with Pd-doped TiO_2 showing the highest enhancement (>22-fold compared to bare-TiO_2), followed by Ni-doped (>11-fold), Pt-doped (~8-fold), and Au-doped (~4-fold) based on photo-electrochemical (PEC) measurements. Surface hydrophilicity of the doped photocatalysts further facilitates better charge carrier generation and interaction with pollutants. While XRD and XPS confirm lattice modifications,

oxygen defect states, and metal incorporation. These structural and electronic modifications collectively enhanced the visible light driven photocatalytic activity.

Pt-doped TiO_2 achieves ~85.5% ciprofloxacin (CIP) degradation under visible light, while Au-doped TiO_2 exhibits 94.6% chloroquine (CLQ) degradation with ~69.6% mineralization efficiency. Pd-doped TiO_2 outperforms both, achieving >98% degradation of amoxicillin (AMX) under artificial visible light within 180 min and ~96.7% under solar irradiation (in 60 min), with excellent reusability (>90% maintained after the 5^{th} cycle). Ni-doped TiO_2 shows 90.4% furazolidone (FZD) degradation with 22.3% quantum yield. Across all systems, photocatalytic degradation significantly reduces aquatic toxicity and neutralizes antimicrobial activity of residual compounds.

To ensure reusability and minimize secondary pollution, a pilot-scale cross-flow ultrafiltration (CF-UF) membrane system was employed for catalyst recovery. The CF-UF membrane exhibited excellent structural and functional properties, including hydrophilic inner surfaces, 7.8% crystallinity, and 2.95 MPa tensile strength. Nearly complete recovery of bare-TiO_2 and Pt-doped TiO_2 photocatalysts (>99%) with fluxes of 10-11 L m^{-2} h^{-1} and permeability ~95% was achieved with feed and backflushing processes. The recovered bare-TiO_2 and Pt-doped TiO_2 exhibited no significance difference in photocatalytic degradation of CIP. However, slight decrease in dark adsorption was observed. Additionally, >98.7% recovery of other metal-doped TiO_2 photocatalyst was achieved. Membrane fouling and flux recovery studies revealed excellent antifouling properties of the membrane with a maximum of 9.86±0.04% reversible fouling and a minimum of 98.78±0.20% flux recovery. The hydrodynamic diameters of both catalyst particles increased in the reject and backflush streams with right-tailed lognormal distribution.

Further, the membrane-based recovery system was coupled with integrated photocatalytic and biological degradation process for complete mineralization of PhACs with catalysts recovery. The integrated process consists of three units, (i) Photocatalytic degradation unit, (ii) Membrane separation unit, and (iii) Biological degradation unit. At an optimized dosage of 0.05 g L^{-1} with CPC reflectors, bare-TiO_2 achieved 94.9% diclofenac (DIC), 92.4% paracetamol (PM), and 85.5% sulfamethoxazole (SULF) removal, while Pt-doped TiO_2 and Au-doped TiO_2 achieved >99% CIP and CLQ degradation. *Pseudomonas spp.* PDC11 showed highest biological degradation of DIC at laboratory (56.98% degradation) and pilot-scale (47.46% degradation). In mixed PhAC-spiked distilled water (PDW), Au-doped TiO_2 achieved 96.09% photodegradation with 87.67% TOC removal, which were further increased to 99.35 and 91.54%, respectively, after biological degradation by *Pseudomonas spp.* PDC11.

Additionally, in spiked hospital wastewater (PHW), photocatalytic degradation was 94.21% with 64.61% TOC removal through progressive mineralization. *Pseudomonas spp.* PDC11 achieved an additional 5.3% degradation, increasing total PHW degradation to 99.51% with TOC and COD removals exceeding 80%. In all the photocatalytic degradation studies, >99% photocatalysts recovery was achieved.

Overall, the integrated pilot-scale process thus demonstrated high degradation efficiency, almost complete catalyst recovery, and effective detoxification, offering a scalable and sustainable solution for pharmaceutical wastewater treatment.

Keywords: Bio-based metal-doped TiO_2; Vegetal extracts; Reduced bandgap; Delayed recombination; Oxygen vacancies and Ti^{3+} defects; Photoelectrochemical analysis; Pharmaceutical active compounds; Photocatalytic degradation; Ecotoxicity assessment, Photocatalyst recovery and reusability; Crossflow ultrafiltration membrane; Integrated photocatalytic and biological degradation process; Hospital wastewater; Pilot-scale mineralization of PhACs

Table of Contents

List of Figure Captions

List of Table Captions

CHAPTER 1

Conceptual Framework, Literature Review, and Research Objectives

This chapter provides a comprehensive introduction to the environmental challenges associated with pharmaceutically active compound (PhACs) pollution and their remediation through advanced oxidation processes, with particular emphasis on photocatalysis using bio-based, metal-doped photocatalysts. It outlines the ecological risks posed by PhACs contamination and the limitations associated with conventional treatment technologies. A critical review of the literature is presented, covering photocatalyst synthesis, photocatalytic degradation mechanisms, and strategies for photocatalyst recovery following treatment, with emphasis on existing research gaps. The chapter concludes by defining the research objectives and outlining the conceptual framework of the present study.

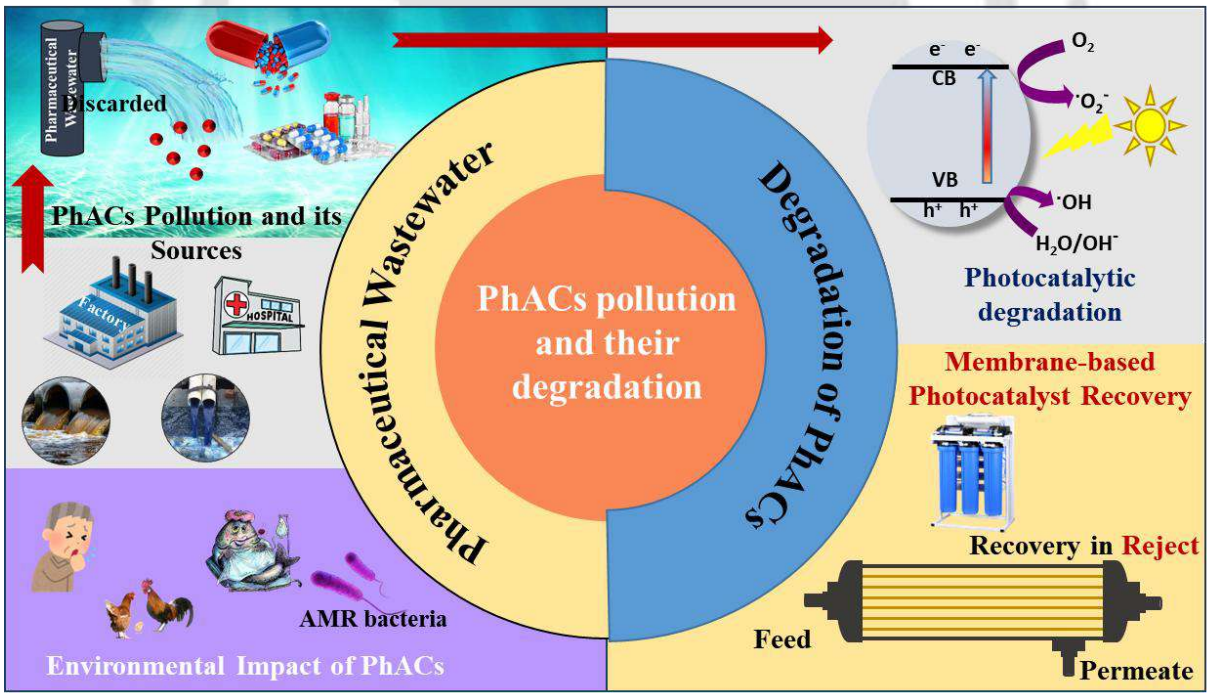


Contents lists available at ScienceDirect

Coordination Chemistry Reviews

journal homepage: www.elsevier.com/locate/ccr

ELSEVIER

Photocatalytic and biological degradation processes to mineralize pharmaceutically active compounds and catalyst recovery: A review

Ravi Ravi [a], Animes Kumar Golder [a,b,*]


Home > Sustainable Environment > Conference paper

Pharmaceutically Active Compounds' (PhACs) Threat: An Environmental Prospective

Conference paper | First Online: 15 March 2023

pp 51–66 | Cite this conference paper

Ravi Ravi & Animes Kumar Golder

Included in the following conference series: North-East Research Conclave

Sustainable Environment

(NERC 2022)

Intentionally Left Blank
Intentionally Left Blank

1.1 Introduction

Recently, there has been a significant surge in water pollution largely due to the unregulated discharge of emerging pollutants. The inadequacies of traditional treatment facilities have worsened the release of such contaminants into natural water sources. Key industries such as textiles, mining, pharmaceuticals, food production, and cement manufacturing significantly contribute to this growing problem (Ravi and Pandey, 2019). These industries release various pollutants, such as heavy metals, pesticides, dyes, fertilizers, pharmaceutically active compounds (PhACs), and microplastics (Patel et al., 2019). Pharmaceu

ticals, used to treat diseases in humans and animals, are being discharged directly and indirectly into water bodies. As the third-largest producer of PhACs globally, India has seen its pharmaceutical industry grow significantly, reaching USD 42 billion in 2021, with expectations to hit USD 65 billion by 2024 and USD 130 billion by 2030. Globally, the pharmaceutical market is expected to rise from USD 1423.5 billion in 2021 to USD 2363.3 billion by 2030, which would further worsen PhACs pollution (Fig. 1.1).

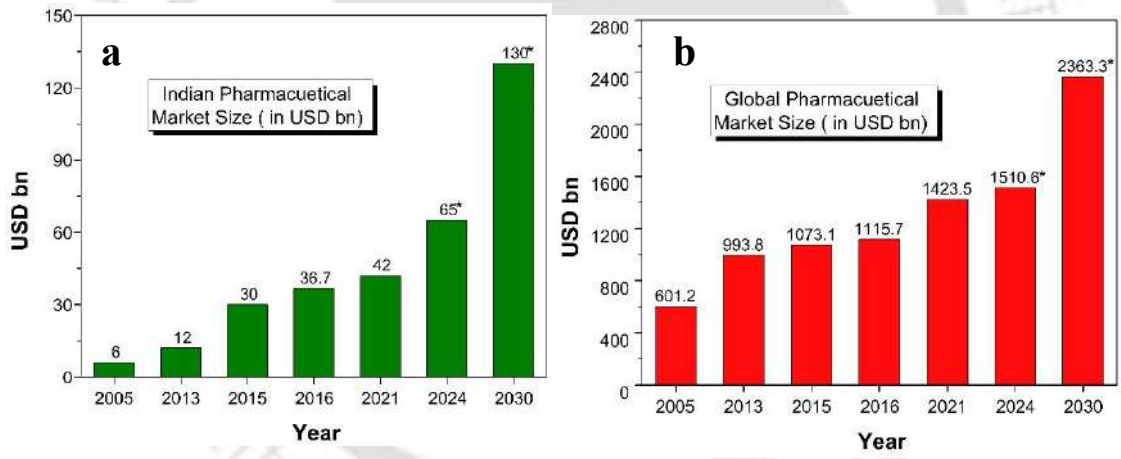

Figure 1.1: Pharmaceutical market revenue (in US$ billion) at (a) Indian and (b) Global scale. [* represents predicted values].

PhACs wastewater poses significant environmental and health risks even at very low concentrations (Akbari et al., 2021). The spectrum of PhACs encompasses antimicrobials, tranquilizers, diuretics, hormones, and various other drugs, which could cause severe health issues such as cardiovascular disorders, kidney problems, and poisoning while also harming aquatic organisms by reducing fertility and promoting antimicrobial-resistant microbes (Leigue et al., 2016; Fang et al., 2021; Munyai et al., 2021). These resistant microbes can be more lethal, emphasizing the urgent need for new antimicrobial drugs. Global antibiotic consumption

increased by 46% from 2000 to 2018, with India seeing at least a 48% rise (Browne et al., 2021). Additionally, 35 novel antibiotics were approved by the FDA from 2000 to 2020 for clinical use (Hori et al., 2022). The COVID-19 pandemic further accelerated the production of pharmaceuticals, increasing the global market by 8.47% in 2020. The presence of PhACs in natural water bodies and the influent and effluent of the pharmaceutical industries of India and other countries has been widely reported. A schematic illustration of the spreading of PhACs in natural waterbodies is given in Fig. 1.2. Industrial effluents, hospital wastes, and treatment plant effluents are the common point sources. In contrast, livestock waste, household effluent, and agricultural runoff are some non-point sources of PhACs pollution in natural water bodies.

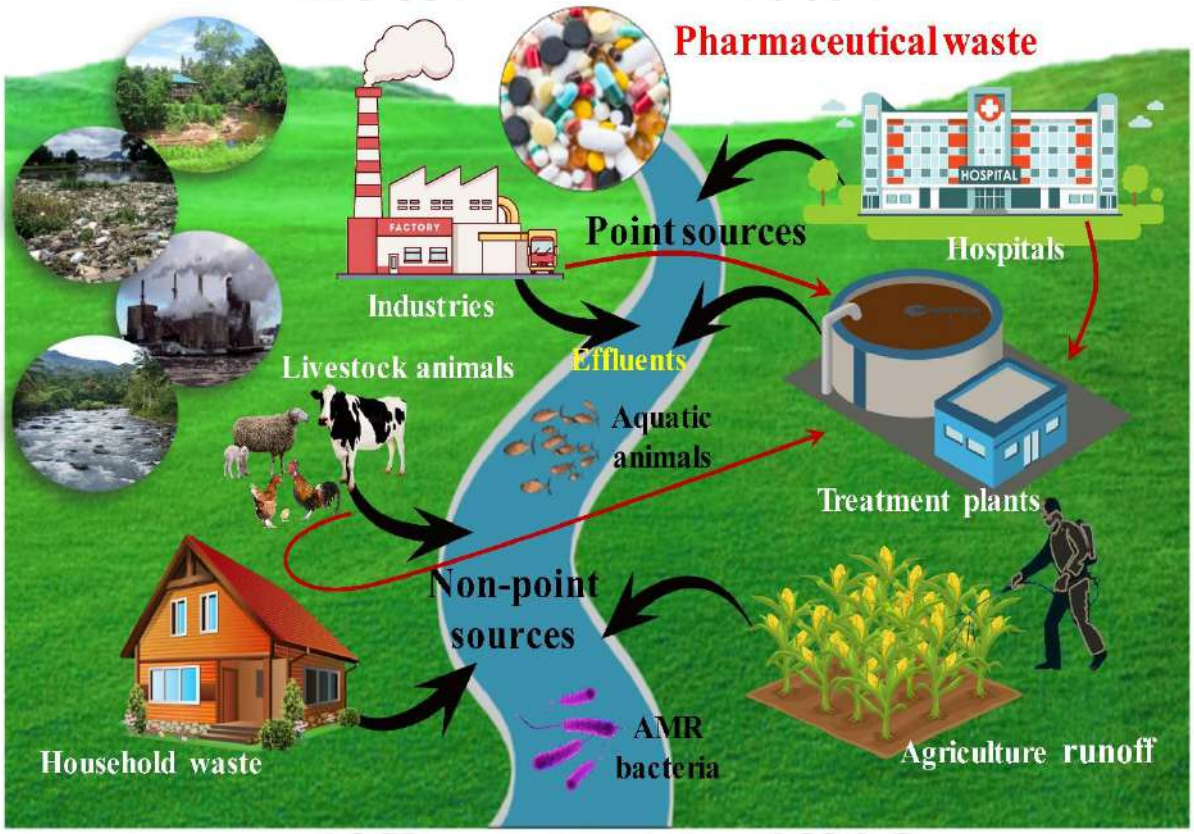

Figure 1.2: Graphical illustration of the spreading of PhACs from point and non-point sources to waterbodies.

Fick et al. (2010) reported the presence of various PhACs, especially antibiotics, in ponds, wells, and nearby lakes in Hyderabad, India (Fick et al., 2009). Additionally, PhACs pollution has also been reported in most rivers of India, namely, Yamuna, Brahmaputra, Vellar, Arkavathi, Cauvery, Thamiraparani, and their tributaries (Mutiyar et al., 2018; Vimalkumar et al., 2018; Kumar et al., 2019; Gopal et al., 2021). The effluent of the Mangalore and Udupi treatment plant (India) reported several PhACs (Subedi et al., 2017). This issue extends

globally, with the effluents of wastewater treatment plants in countries such as Italy, Spain, Canada, China, Bangladesh, Brazil, and Africa displaying the presence of PhACs, indicative of the inefficiencies of conventional treatment systems (Verlicchi et al., 2012; Guerra et al., 2014; Ma et al., 2017; Hossain et al., 2018). As a result, numerous antibiotic-resistant microbes, such as *A. hydrophila*, *E. facalis*, *S. pneumoniae*, *P. aeruginosa, E. coli*, *Pseudomonas* spp., *Acidovorax* spp., *Staphylococcus* spp., *Acinetobacter spp.*, *Chryseobacterium spp.,* etc., were reported to be developed in natural waterbodies and treatment plants (Kumar et al., 2021; Ali et al., 2021). Consequently, there is a pressing need for the treatment of effluents from pharmaceutical industries and hospitals before their release into the environment, as well as improvements to existing wastewater treatment plants to curb the spreading of PhACs in natural water bodies. However, treating PhACs wastewater is quite challenging due to lower concentration, interference of PhACs in the treatment process, high toxicity, complex chemical structure, etc.

The treatment processes, namely, adsorption, chemical treatment, membrane-based separation, microbial remediation, photocatalytic degradation, other advanced oxidation processes (AOPs), and electrochemical processes, have been employed to mitigate organic pollutant contamination. AOPs, such as ozonation, Fenton and photo-Fenton, sonolysis, photocatalysis, and electrochemical oxidation, are widely used to remove organic and inorganic contaminants from water and wastewater by generating highly reactive species, primarily hydroxyl radicals ($^{\bullet}OH$) and superoxide radicals ($^{\bullet}O_2^-$) (Chawla et al., 2024). Among these, heterogeneous photocatalytic degradation employs photocatalytically active materials to generate free radical species, making it particularly suitable for the remediation of PhACs under light energy due to its eco-friendly nature, pollutant mineralization capabilities, high efficiency, and ease of use (Zheng et al., 2024). The applications of heterogeneous photocatalysis extend beyond the degradation of organic waste; it also shows promise in hydrogen production, CO_2 reduction to value-added fuels, and energy storage. Recent studies have employed native photocatalysts, metal/non-metal-doped photocatalysts, and heterojunctions, such as metal-doped TiO_2, metal-doped ZnO, $CuWO_4/CuBi_2O_4$, MIL-101(Fe)/WO_3, oxygen-doped g-C_3N_4, Ag/Fe_2O_3, Sn/CdS, for photocatalytic degradation of PhACs under light energy (Yang et al., 2022; Chen et al., 2023; Kumar et al., 2023; Zheng et al., 2024). Incorporating metals or non-metals into native photocatalysts and fabricating heterojunctions or nanocomposites have been reported to enhance optical and chemical properties, significantly improving photocatalytic activity.

However, the recovery of photocatalysts after the degradation process limits their industrial application. Various methods have been reported to recover nanoparticles from their aqueous solutions, such as membrane separation, centrifugation, magnetic separation, chromatographic techniques, electrophoresis, etc. (Hanauer et al., 2007; Arcudi et al., 2016; Hassan et al., 2021). Among these membrane separation processes, ultrafiltration is the most suitable for recovering nano-scale photocatalysts. Dead-end membranes are not recommended for the recovery of photocatalysts due to the rapid clogging of pores and cake-layer formation. The cross-flow membranes facilitate the simultaneous separation of particles and de-clogging of pores. Therefore, cross-flow ultrafiltration membrane separation techniques could potentially recover the catalysts used for regeneration and reuse.

This chapter comprehensively reviews the global spread of PhACs, their risk to aquatic organisms, and the subsequent development of antimicrobial-resistant microbes, followed by the most suitable mitigation strategies. This includes an in-depth analysis of the photocatalytic degradation process, focusing on bio-based photocatalyst synthesis and modifications, the recovery of photocatalytic nanomaterials, and microbial remediation of PhACs. The review primarily covers publications from the last 10 years (2014-2024) and focuses on the specified topics. Keywords such as "PhACs in water bodies," "pharmaceutical waste in water bodies," "antimicrobial resistance microbes," "treatment of PhACs waste," "photocatalysis," "nanoparticle synthesis," "green synthesis of photocatalysts," "recovery of nanoparticles and photocatalysts," "nanoparticle separation process," and "effect of PhACs on treatment processes" were used to search databases including Google Scholar, Scopus, Science Direct, and Web of Science.

1.2 Ecological risk assessment

1.2.1 PhACs in the environment and their risk quotient (RQ)

The global presence of PhACs in water bodies is a major concern due to their high environmental risks, particularly to microbes and aquatic animals. Various case studies worldwide have reported the widespread occurrence of PhACs, predominantly antibiotics and analgesic drugs. The measured environmental concentrations (MEC) of PhACs in natural water bodies, including rivers, wells, and lakes, as well as in industrial effluents and wastewater treatment plants (WWTPs), are summarized in Table 1.1.

The ecotoxicological evaluation of PhACs in water bodies uses the risk quotient (RQ) analysis, which compares MEC to the predicted no-effect concentration (PNEC) for fish. The RQ is calculated using the following expression (Eq. 1.1):

$$RQ = \frac{MEC}{PNEC} \quad (1.1)$$

The impact of pollutants can be assessed based on their RQ values, categorized as follows:

(i) RQ < 0.1: low risk and minimal hazardous effects on aquatic animals.

(ii) 0.1 < RQ < 1.0: moderate risk and limited hazardous effects on aquatic animals.

(iii) RQ > 1.0: high risk and significant hazardous effects on aquatic animals, necessitating immediate mitigation action.

The PNEC values (in μg L^{-1}) for the PhACs were obtained and reported in Table 1.1 (Stuer-Lauridsen et al., 2000; Park and Choi, 2008; Chalew and Halden, 2009; Godoy et al., 2015; Giang et al., 2015; Schafhauser et al., 2018; Oldenkamp et al., 2019; Patel et al., 2019; Cardini et al., 2021; Ranjan et al., 2022; Almeida et al., 2023). Given that PNEC values for fish are generally higher than for macroinvertebrates and microorganisms, it is assumed that any pollutant posing hazardous effects on fish would likely have even more severe impacts on macroinvertebrates and microorganisms.

From Table 1.1, it is observed that antibiotics, specifically ciprofloxacin (CIP), norfloxacin (NOR), ofloxacin (OFL), and sulfamethoxazole (SMZ), were present in significantly high amounts in most water bodies. This was followed by non-steroidal anti-inflammatory drugs (NSAIDs) such as diclofenac (DIC), ibuprofen (IBU), and acetaminophen (APAP). Additionally, caffeine (CAF), a stimulant, was frequently found and is rapidly increasing in Brazilian water bodies. Sharma et al. (2019) investigated the presence of PhACs in groundwater and river water within the Ganges River Basin (India). In the pharmaceutical industrial area of Hyderabad, India, PhAC pollution in surface and groundwater poses a very high risk to aquatic animals and microbes, with hazardous RQ values for CIP, NOR, and cetirizine (CTZ) reaching 879, 5.8, and 5, respectively. Indian rivers like the Ganges, Brahmaputra, Arkavathi, Cauvery, Thamiraparani, Vellar, and Yamuna are moderately threatened by PhACs such as DIC, CAF, and APAP, each with an RQ value exceeding 0.1. Although other PhACs, including theophylline (THE), triclosan (TCS), triclocarban (TCC), aspirin (ASA), carbamazepine (CBZ), and IBU, have RQ values below 0.1, they still pose significant but limited risks to aquatic life.

Similarly, rivers in China, Bangladesh, and Brazil have reported PhAC pollution. Sewage and wastewater treatment plants (WWTPs) are largely ineffective in mitigating PhAC pollution. For instance, a sewage treatment plant in Karnataka, India, reported only a 39% reduction in SMZ. Other studies have found high concentrations of PhACs in the influent and effluent of WWTPs in Canada, the USA, and Italy, with RQ values greater than 0.1 for most PhACs. Some PhACs have very high RQ values, ranging from 1.1 to 23.2, highlighting the severity of PhAC pollution worldwide. The increasing concentration of PhACs demands regular monitoring of natural water bodies, industrial effluents, and WWTP effluents, as well as the implementation of effective treatment measures.

Table 1.1: Concentration of PhACs in various waterbodies worldwide, their predicted no-effect concentration (PNEC), and the risk quotient for fishes.

Source	PhACs	MEC (μg L^{-1})			PNEC (μg L^{-1})	Risk Quotient (RQ)	Ref.
Pharmaceutical industrial area Hyderabad (India)	–	Effluent	Lakes	Wells	–	–	(Fick et al., 2009)
	CIP[1]	14000	ND–6500	0.04–14	15.6	0.003–897	
	NOR[1]	25	≥ 60	ND–0.03	10.4	0–5.8	
	CTZ[5]	2100	≥ 5	≥ 0.9	423	0.002–5	
	OFL[1]	55	ND–11	ND–4.8	101	0–0.5	
Brahmaputra river, and its tributary (Bharalu river) (Assam, India)	APAP[2]	ND–6.0			38	0–0.16	(Kumar et al., 2019)
	THE[6]	ND–2.9			178	0–0.01	
	CAF[3]	0.04–22.7			87.5	0–0.26	
Arkavathi river and its tributaries (Bengaluru, India)	DIC[2]	0.008–1.1			9.7	0–0.11	(Gopal et al., 2021)
	TCS[1]	ND–1.8			115	0–0.02	
	IBU[2]	0.03–1.8			170	0–0.01	
Thamiraparani river (India)	TCC[1]	Water		Sediment	34.1	–	(Vimalkumar et al., 2018)
		0.003–0.02		ND–0.009		0–0.001	
Vellar river (India)		0.002–0.1		ND–0.004		0–0.003	
Cauvery river (India)		0.008–1.1		ND–0.003		0–0.03	
Yamuna river (Delhi, India)	ASA[2]	ND–1.3			61	0–0.02	(Mutiyar et al., 2018)
	IBU[2]	ND–2.3			170	0–0.01	
	APAP[2]	ND–1.6			63.7	0–0.003	
	CBZ[4]	ND–1.3			35.4	0–0.04	
Sewage treatment plants, Karnataka (India)		Influent		Effluent	–	–	(Subedi et al., 2017)
	APAP[2]	5.4–1.10		0.33–1.20	38	0.01–0.03	
	SMZ[1]	0.06–0.69		0.12–0.42	506	0–0.001	
	CIP[1]	ND–0.09			15.6	0–0.005	

Cauvery and its tributaries (India)	IBU[2]	ND–0.08	170	0–0.001	(Renganathan et al., 2021)
	DIC[2]	0.005–0.29	9.7	0–0.03	
	CBZ[4]	0.03–3.3	35.4	0–0.09	
	CAF[3]	0.02–0.44	87.5	0–0.01	
Beiyun river Basin (China)	ERY[1]	ND–1.3	1.0	0–1.3	(Ma et al., 2017)
	CAF[3]	0.03–2.7	87.5	0–0.01	
	APAP[2]	ND–3.6	38	0–0.09	
Brahmaputra river (Bangladesh)	MET[1]	0.001–0.01	50	0.0002	(Hossain et al., 2018)
	TMP[1]	ND–0.02	60	0.0003	
	SD[1]	ND–0.01	10	0.001	
Sinos river (Brazil)	CAF[3]	0.04–16.7	87.5	0.19	(Linden et al., 2015)
Beberibe river (Brazil)	DIC[2]	19–193	9.7	1.96–9.9	(Veras et al., 2019)
	APAP[2]	ND – 42	63.7	0.66	
		Influent / Effluent	–		
WWTPs (Canada)	SMZ[1]	0.06–3.1 / 0.03–1.8	38	0–0.08	(Guerra et al., 2014)
	CLA[1]	0.05–8 / 0.13–7	7.3	0.01–1.1	
	IBU[2]	2.5–45 / 0.02–47	170	0–0.28	
	APAP[2]	5.7–130 / 0.02–62	38	0–3.42	
WWTPs (Penn State USA)	APAP[2]	654.6 / 5.83	38	0.15–17.2	(Kibuye et al., 2019)
	SMZ[1]	25 / 68.3	506	0.05–0.14	
	OFL[1]	100.6 / 22.2	101	0.22–1.0	
	AMP[1]	283.1 / 26	12.2	2.13–23.2	
WWTPs (Italy)		Hospital / WWTPs	–		(Verlicchi et al., 2012)
	FRS[7]	5.3–18 / 0.08–0.47	154	0–0.11	
	OFL[1]	3.3–37 / 0.2–2.2	101	0.002–0.4	
	CIP[1]	1.4–26 / 0.3–3.7	15.6	0.02–1.7	
	NAP[1]	0.3–11 / 0.1–0.9	115.2	0.003–0.1	

**1: Antibiotics; 2: Analgesic/Non-steroidal anti-inflammatory drugs; 3: Stimulant; 4: anticonvulsants; 5: Antihistamine; 6: Xanthines; 7: Diuretic;*
**ND = Not detected; WWTPs: Wastewater treatment plants;*
#APAP: Acetaminophen; AMP: Ampicillin; ASA: Aspirin; CAF: Caffeine; CBZ: Carbamazepine; CLA: Clarithromycin; CTZ: Cetirizine; CIP: Ciprofloxacin; DIC: Diclofenac; ERY: Erythromycin; FRS: Furosemide; IBU: Ibuprofen; MET: Metronidazole; NAP: Naproxen; NOR: Norfloxacin; OFL: Ofloxacin; SD: Sulfadiazine; SMZ: Sulfamethoxazole; TCC: Triclocarban; TCS: Triclosan; THE: Theophylline; TMP: Trimethoprim;

1.2.2 Fate of antimicrobial-resistant bacteria (AMRB)

The presence of antibiotics or antimicrobial drugs in the environment could produce severe indirect impacts on humans and other animals, triggering the development of antimicrobial-resistant bacteria (AMRB). The persistent presence of antimicrobials in the environment affects the microbes, forcing them to evolve by developing some antimicrobial resistance mechanisms for survival. Penicillin (PEN) was the first antibiotic discovered by

Alexander Fleming in 1928 and used to treat several diseases. Introducing antibiotics in the health sector rapidly decreased the mortality rate. From the 1940s to the 1970s, about 160 more antimicrobial drugs and their derivatives were discovered. The extensive utilization of antimicrobials in health care, livestock, aquaculture, household, and agriculture sectors significantly triggers their environmental expansion due to high production and inappropriate waste management. As a result, the death associated with AMRB infection increases with time. The AMRB can have natural resistance and induced resistance against microbial agents. Natural resistance is regulated by their species and genomic characteristics, which always prompt an entire species. In contrast, induced resistance is regulated by extrinsic factors, including exposure to microbial agents, which could be induced by activation of the suppressed antimicrobial genes or mutation in their genome, leading to structural and chemical changes in their cell membrane characteristics (Almeida et al., 2023). Fig. 1.3 illustrates the development and spreading of AMRB in the environment. The continuous development of AMRB becomes very challenging due to the ineffectiveness of the present antimicrobial drugs. Consequently, administering high doses further increases PhACs pollution and poses possible health risks. It also triggers the need for new antimicrobial drugs to treat several diseases.

The stress of antimicrobial drugs on bacterial strains slows their metabolism and growth, which leads to a surge in mutation rate for survival. It is reported that the persistence of antimicrobial drugs in waterbodies is proportional to the mutation in bacterial strains. The mutation leads to physio-chemical changes in bacteria, further increasing their metabolic rate and growth in an antimicrobial-polluted environment (Akiba et al., 2015). Various case studies have reported the development of AMRB strains, especially in antimicrobial drug-contaminated waterbodies. Table 1.2 represents the bacterial strains resistant to numerous antimicrobial drugs. The over-utilization and improper management of the first discovered antibiotic, PEN, resulted in PEN-resistant bacteria throughout the globe.

Several ampicillin (AMP) and erythromycin (ERY) resistance bacteria, such as *A. hydrophila*, *E. facalis*, *S. pneumoniae*, and *P. aeruginosa* were observed in the municipal sewage water of Prayagraj (India), which is directly being discarded into the Ganga river. The presence of the *ermB* and *bla* genes in their genome could potentially enable their resistance to these antibiotics. The study showed that the *bla* gene-derived β-lactamase degrades AMP, while the *ermB* gene triggers methylation of 23S rRNA, inhibiting ERY binding and allowing bacterial survival (Kumar et al., 2021). Most of the isolated strains of the Ghaghara river (India) were resistant against AMX, AMP, CXM, CIP, ERY, and PEN with the presence of antimicrobial genes such as ant_3, blah, qnrS, tetM, and sul1 (Ravi et al., 2022).

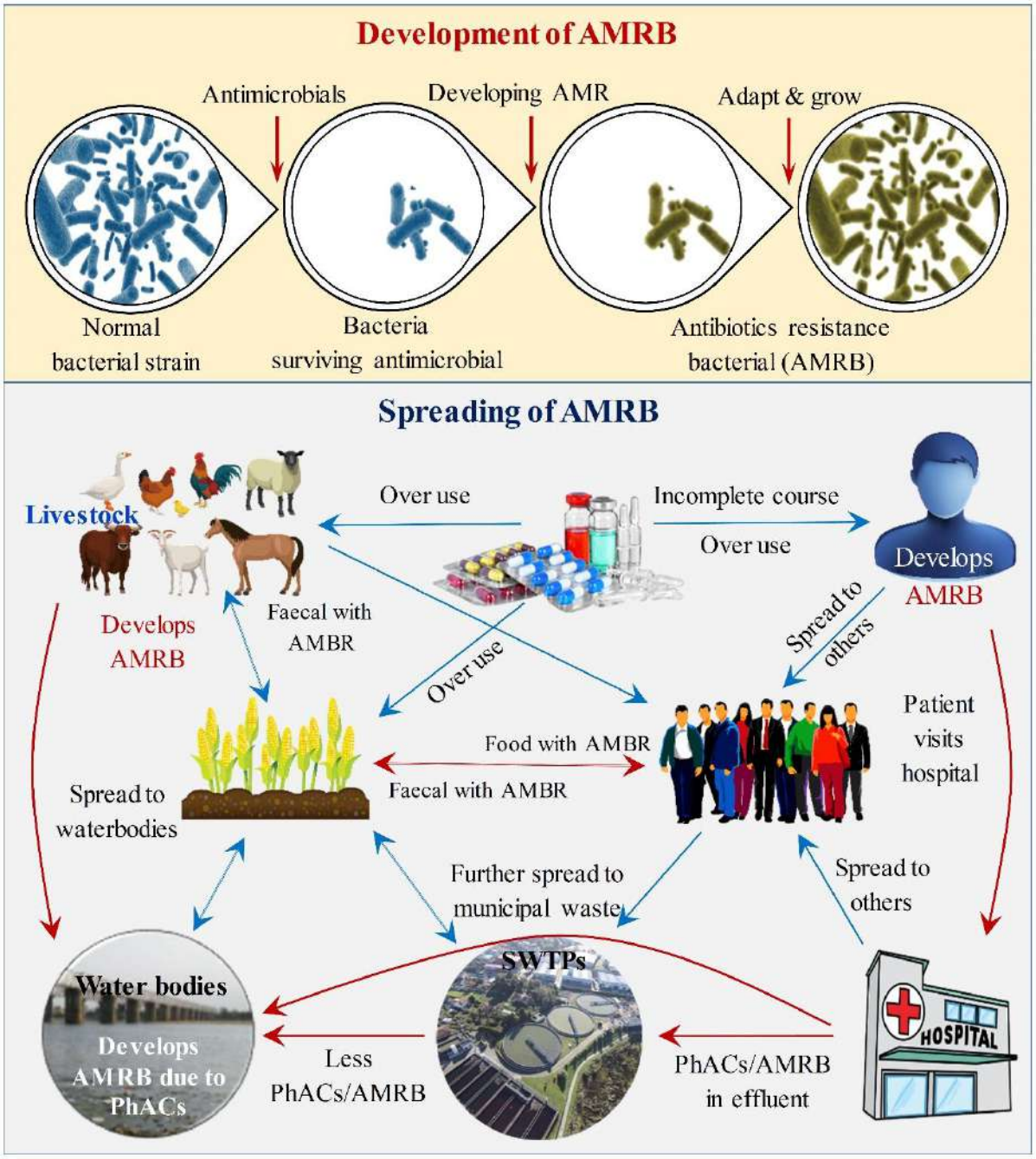

Figure 1.3: Schematic of the development and spread of antimicrobial-resistant bacteria (AMRB) in the environment.

The bacterial strains, especially *Bacillus* spp., *Pseudomonas* spp., and *Staphylococcus* spp. present in the effluent streams of pharmaceutical industries in Bangladesh were found resistant to penicillin. These strains were also resistant to other antibiotics such as AMX, CEX, CFX, CIP, CHL, CLOX, CTX, and SMZ (Mahmud et al., 2023). Additionally, ~60% of bacterial strains (out of 203) in the Meia Ponte river of Brazil showed antimicrobial properties against various broad-spectrum antibiotics. The bacterial strains isolated during the rainy

period showed significantly higher antimicrobial resistance (AMR) activity than that of dry-period isolates. The appropriate environmental factors and high use of antimicrobial drugs during the rainy season rather than the dry season provide suitable conditions for the development of the AMRB (Gomes et al., 2023). Similarly, the Karoon river of Iran also hosts several AMRB strains with higher potential during summer and spring than in autumn and winter (Besharati et al., 2018). Storteboom et al. (2010) isolated AMRB strains from anaerobic lagoons, WWTPs, and rivers. The bacterial strains isolated from anaerobic lagoons and WWTPs pose similar AMR profiles to pristine river strains. The water stagnation in lagoons and WWTPs increases the frequency of AMR development due to more persistent and significant concentrations of antimicrobial drugs (Storteboom et al., 2010). The WWTPs conventionally treat municipal waste, which contains numerous bacterial strains. A study identified the AMRB strains in Japan's influent and effluent WWTPs, indicating an inefficient treatment process. However, the count of all bacterial strains has decreased significantly (Honda et al., 2023).

According to statistics of 2022-23, India is the largest milk producer with ~26% global contribution. During the last 10 years, the overall milk production in India increased by ~60%. India stands in 3rd position in fish production with global production of ~7.6%, with over 75% increase in fish production over a decade. Additionally, India stands in 8th position in the production of poultry animals. The increase in the production of milk, fish, and poultry animals has increased the use of antibiotics, resulting in their contamination in waterbodies, animal products, and biomass. In West Bengal (India), subclinical mastitis cattle's milk was hosting about 48% tetracycline (TET) resistant bacterial strains such as *E. coli*, *Enterobacter* spp., Klebsiella spp., *Pseudomonas* spp., and *Proteus* spp. (Das et al., 2017). Detection of vancomycin (VAN) resistant *S. aureus* in bovine and caprine milk was also reported in West Bengal (India) (Bhattacharyya et al., 2016). A similar case was also observed in Brazil (6th largest producer of milk), *S. epidermidis* and coagulase-negative *staphylococci* (CoNS) bacterial strains isolated from bovine milk showed multidrug resistance against CEF, ERY, TET, MCN, and OXA (Santos et al., 2016).

Table 1.2: Presence of antimicrobial-resistant bacteria (AMRB) in various waterbodies worldwide and their resistance to antimicrobial drugs.

Sources	Microorganism	Resistant to PhACs	Ref.
Ganga river stretch (Rishikesh to Haridwar, India	*Aeromonas* spp.	AMP, AT, CIP, CTR, NX, PIT, VA	(Ali et al., 2021)
	Bacillus spp.	AT, CAZ, CD, COT, FO, IPM, NET, NX, TE	
	Corynebacterium spp.	AT, CAZ, CFS, IPM, PIT	
	Clostridium spp.	AT, C, CD, CTR, IPM, TE	
	Escherichia coli	AMP, AT, CAZ, CFS, CIP, COT, CTR, IPM, NET, NX	
	Enterococcus spp.	AT, CAZ, CFS, IPM, PIT, NET	
	Staphylococcus spp.	AMC, AMP, AT, CAZ, CIP, CTR, NX, PIT	
Kazipally lake (Telangana, India)	*E. coli*	CIP, SMZ	(Flach et al., 2015)
Municipal wastewater Prayagraj (India)	*A. hydrophila*	AMP	(Kumar et al., 2021)
	K. pneumoniae		
	P. aeruginosa		
	S. pneumoniae	ERY	
	E. faecalis		
WWTPs (south India)	*Escherichia coli*	AMP, CFZ, CIP, CTX, NAL	(Akiba et al., 2015)
Ghaghara river and its tributaries, India	*K. quasipneumoniae*	AMP, AMX, CIP, CXM, ERY, PEN	(Ravi et al., 2022)
	Bacillus spp.		
	E. coli		
Wastewater of pharmaceutical industries Dhaka and Gazipur districts, Bangladesh	*Bacillus* spp.	AMX, CEX, CFX, CIP, CHL, CLOX, CTX, PEN, SMZ	(Mahmud et al., 2023)
	Pseudomonas spp.	AMX, CEX, CFX, CHL, CLOX, CTX, PEN, SMZ	
	Staphylococcus spp.	AMX, CEX, CFX, CIP, CHL, CLOX, CTX, PEN, SMZ	
Pearl river China	*Enterobacteriaceae*	AMP, CIP, CHL, LEV, SMZ, TET, TMP	(Tao et al., 2010)
Meia Ponte River State of Goiás (Brazil)	*Bacillus* spp.	AMP, AMX, AZI, CFO, CFZ, CIP, CHL, ERY, MPM, PEN, RIF, SMZ, TET, VAN	(Gomes et al., 2023)
	Enterobacteriaceae		
	Pasteurellaceae		
	Staphylococcus spp.		
Wells water (Africa)	*Acidovorax* spp.	AMP	(Machado and Bordalo, 2014)
	Acinetobacter spp.	AMP, CHL	
	Chromobacterium spp.	AMC, AMX, GEN	
	Chryseobacterium spp.	AMC, AMP, CHL, DOX, GEN	
	Pseudomonas spp.	AMC, AMP, CHL, DOX	

	Ralstonia spp.	AMC, AMX, CHL, GEN	
	Xenophilus spp.	AMC, AMX, CHL, DOX	
Karoon river (Khuzestan, Iran)	*Klebsiella* spp.	CEX, CFO, CIP, ERY, GEN, PEN, SMZ, TET (Resistant strains in descending order)	(Besharati et al., 2018)
	P. aeruginosa		
	E. coli		
	Salmonella spp.		
	Enterobacter spp.		
Buffaloes milk (Bangalore, India)	*Coagulase-negative staphylococci (CoNS)*	AMX, CFO, MCN, PEN, CTX, CHL, GEN	(Preethirani et al., 2015)
	E. coli	AMP, AMX, CFO, CTX, MCN, OXA, PEN, STR	
	S. aurues	CFO, CTX, OXA, PEN, ENO	
Caprine milk	*S. aureus*	VAN	(Bhattacharyya et al., 2016)
Bovine milk			
Cattle milk (subclinical mastitis cattle)	*E. coli*	TET	(Das et al., 2017)
	Enterobacter spp.		
	Klebsiella spp.		
	Pseudomonas spp.		
Bovine milk (Brazil)	*Coagulase-negative staphylococci (CoNS)*	CEF, ERY, TET	(Santos et al., 2016)
	S. epidermidis	MCN, OXA	
O. mossambicus (Tilapia fish)	Aeromonadaceae	AMP, CTX, CIP, OXA	(Marathe et al., 2016)
	Bacillus spp.		
	Enterobacteriaceae		
Sea food (Blood clam, shrimp, surf clam, and squid) Malaysia	*V. parahaemolyticus*	AMP, CEF, CFZ, CIP, PEN, PIP	(Tan et al., 2020)
Chicken cecal samples (Nepal)	*E. coli*	CIP, CTX, AMP, CHL, GEN, TET, TMP-SMZ	(Koju et al., 2022)
Antibiotic free chicken meat (north India)	*E. coli*	AMP, COT, CTX, STR, TET	(Rawat et al., 2024)

#AMC: Amoxicillin-clavulanic acid; AMX: Amoxicillin; AZI: azithromycin; CEF: Cephalothin; CEX: Caphalexin; CFO: cefoxitin; CFX: Cefixime; CFZ: Cefazolin; CHL: Chloramphenicol; CLOX: Cloxacillin; COT: Co-trimoxazole; CTX: Cefotaxime; CXM: Cefuroxime; DOX: Doxycycline; ENO: Enrofloxacin; GEN: Gentamicin; LEV: Levofloxacin; MCN: Methicillin; MPM: Meropenem; NAL: Nalidixic acid; OXA: Oxacillin; PEN: Penicillin; PIP: Piperacillin; RIF: rifampicin; STR: streptomycin; TET: Tetracycline; VAN: vancomycin

The biomass of aquatic and poultry animals also poses AMRB strains, resulting in the further spreading of these strains in the food web. In a study, the gut of *O. mossambicus* (Tilapia) fish hosted several AMRB strains, such as *Aeromonadaceae*, *Bacillus* spp., and *Enterobacteriaceae*, which showed resistance against AMP, CTX, CIP, and OXA drugs (Marathe et al., 2016). Sea foods such as blood clam, shrimp, surf clam, and squid were found to be contaminated with multi-drug-resistant *Vibrio parahaemolyticus* in Malaysia (Tan et al.,

2020). *E. coli* strains isolated from chicken cecal were found to be resistant to multiple antibiotic drugs such as CIP, CTX, AMP, CHL, GEN, TET, and TMP-SMZ (Koju et al., 2022). Recently, antibiotic-free chicken meat has gained attention due to its cultivation under controlled conditions, such as food, supplements, and water, free from antimicrobial drugs and resistant microbes. In a recent study, the antibiotic-free chicken contained multi-antibiotic-resistant *E. coli* strains with significant resistance against AMP, COT, CTX, STR, and TET (Rawat et al., 2024). Conclusively, the presence of PhACs, especially antibiotics, in waterbodies and their extensive use in livestock results in the development of AMR bacterial strains. The expansion and utilization of other antimicrobial agents/materials, which are less prone to the development of AMRB, are required for an efficient AMRB mitigation process. Mitigating PhACs pollution, appropriate antibiotic utilization, and management could decrease the further spreading of AMRB.

1.3 Treatment methods

The spread of PhACs in water bodies is incessantly increasing due to their high production, utilization, and lack of proper monitoring. As a result, PhACs contaminate not only surface water but also groundwater, food products, aquatic life, and livestock. Therefore, the treatment of wastewater containing PhACs is urgently needed. Various separation and degradation methods, including adsorption, chemical treatment, membrane-based separation process, microbial remediation, photocatalytic degradation, and electrochemical processes, have been utilized to eliminate PhACs and other pollutants from the wastewater, as represented in Fig. 1.4 (Crini and Lichtfouse, 2019; Wu and Yin, 2020; Golder et al., 2021). Despite their effectiveness, each of these methods has its drawbacks and limitations, contributing to the complexity and challenges associated with achieving the complete degradation of pollutants.

Adsorption, involving the adherence of pollutants to a material surface, is a straightforward and widely employed process encompassing physical and chemical interactions to transfer pollutants from one medium to another (Golder et al., 2021). A schematic of adsorption-based removal of astrazon red dye using an eggshell/GO-embedded hydrogel is provided in Fig. 1.5a (Ahmed et al., 2023). It stands out as one of the most economically viable removal processes. However, the adsorption process has its limitations, including the hindrance of attachment for bulky compounds and a restriction to removing oppositely charged compounds (Chaari et al., 2019). This method is particularly effective for removing highly concentrated pollutants, but some amounts remain unadsorbed due to

establishing adsorption equilibrium. Moreover, the safe disposal of adsorbents containing pollutants and extracting adsorbed pollutants for other industrial applications pose significant challenges (Al-Ghouti et al., 2019).

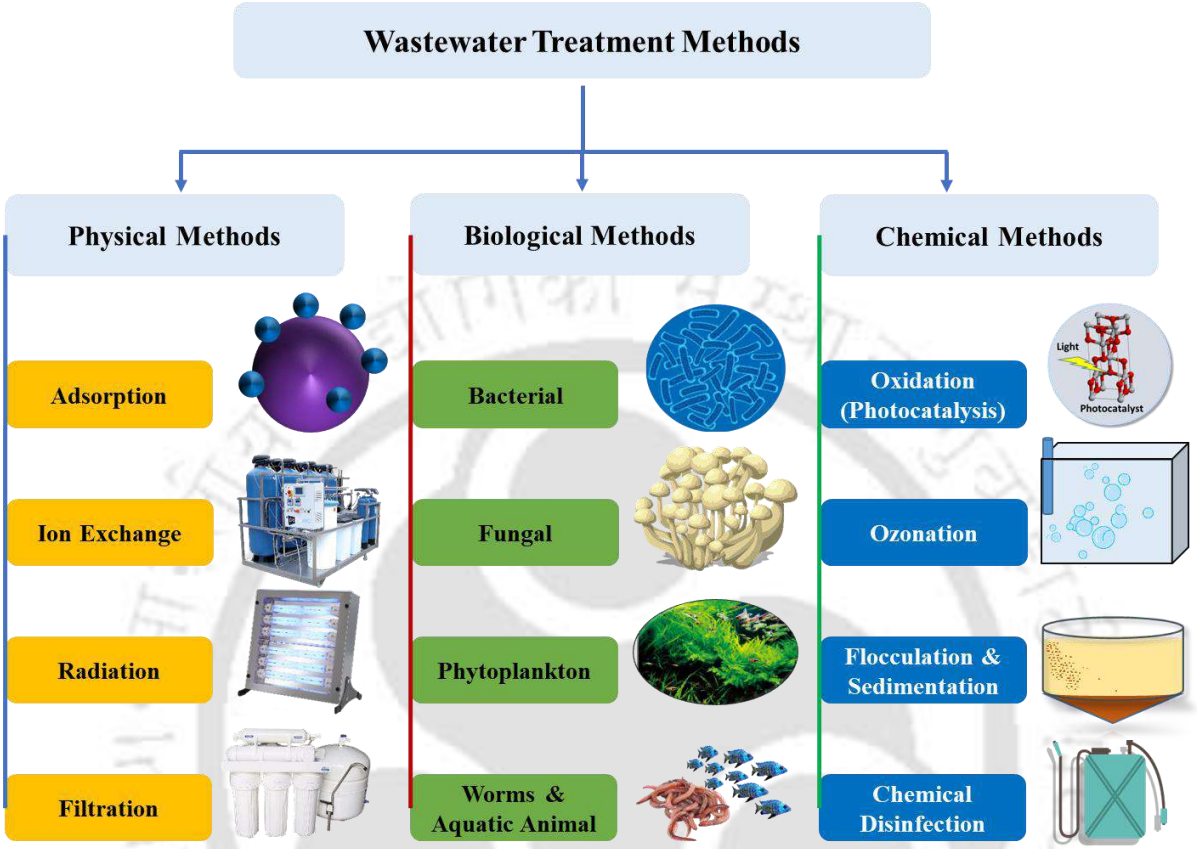

Figure 1.4: Typical methods used for treatment of wastewater.

Coagulation and flocculation processes are highly used to sediment fine solid pollutants by manipulating electrostatic charges. However, the generation of sludge and its safe disposal face complications in utilizing it to treat industrial effluents. However, these processes provide a valuable contribution to the effective pre-treatment of the effluents to expand better treatment efficiency (Al-Ghouti et al., 2019). Mohamad et al. (2021) utilized copperas and CaO-based coagulation/flocculation processes for palm oil mill effluent treatment, as depicted in Fig. 1.5b (Mohamad et al., 2021). The ion exchange system also removes the charged PhACs from their aqueous solution. Altunterim and Vergili (2020) utilized an ion exchange resin to remove clofibric acid under a magnetic field (Altunterim and Vergili, 2022). However, due to the high cost, releasing a high amount of saltwater in the regeneration process, and the requirement of charged (ionic form) pollutants are a few limitations of this technique.

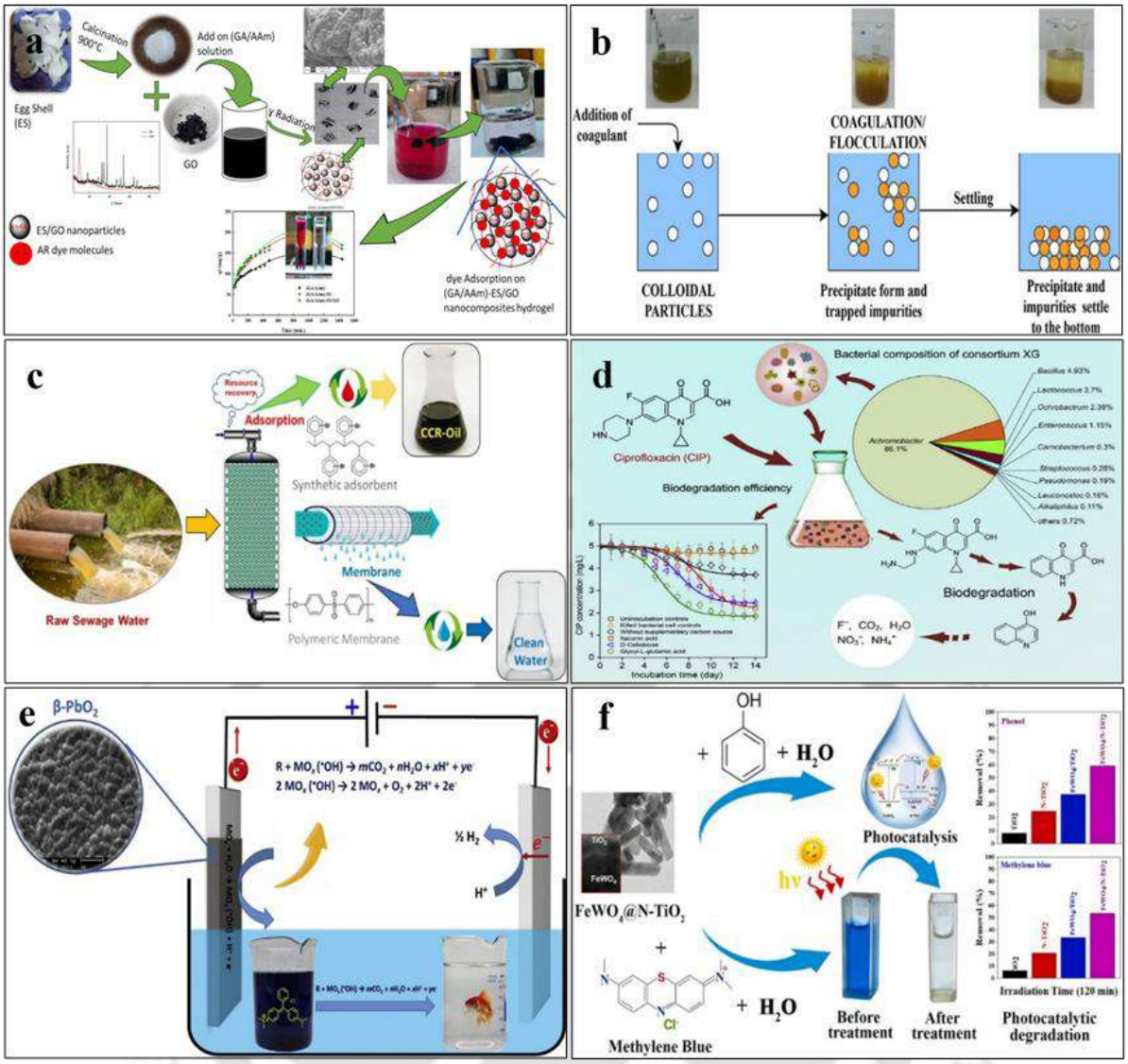

Figure 1.5: Schematic representation of (a) Adsorption of astrazon red dye using eggshell/GO-embed in hydrogel (Reprinted with permission from (Ahmed et al., 2023), Copyright©2023, Ahmed et al.), (b) Coagulation/flocculation of colloidal particles from palm oil mill effluent (Reprinted with permission from (Mohamad et al., 2021), Copyright 2021 Elsevier), (c) Membrane process for treatment of sewage wastewater (Reprinted with permission from (Shinde et al., 2021), Copyright 2020 Elsevier), (d) Microbial degradation of ciprofloxacin using microbial consortium (Reprinted with permission from (Feng et al., 2019), Copyright 2019 Elsevier), (e) Electrochemical degradation of malachite green using β-PbO_2 electrodes (Reprinted with permission from (Ansari and Nematollahi, 2018), Copyright 2018 Elsevier), and (f) Photocatalytic degradation of methylene blue and phenol using $FeWO_4$@N-TiO_2 nanocomposite (Reprinted with permission from (Chakraborty et al., 2024), Copyright 2024 Chakraborty et al., Elsevier).

The membrane-based separation process is widely used for the separation of pollutants and the purification of water for reuse. It is usually a size-selective process, which only allows passes of particles with a size of less than the pore cut-off value of the membrane. Fig. 1.5c illustrates a membrane-based sewage treatment for clean water regeneration and a carbon capture reactor (CCR)-oil recovery (Shinde et al., 2021). This process possesses the advantages of easy handling, high efficiency, and abundant availability of ready-made membranes. However, membrane separation techniques face limitations in removing PhACs due to their small size, resulting in high rejection rates and membrane fouling. The process is further hindered by concentration polarization, hydraulic resistance, and high maintenance costs, which collectively reduce the viability of membrane separation for eliminating pharmaceutical waste (Crini and Lichtfouse, 2019). Nevertheless, separating nanoparticles and photocatalysts using the membrane process provides valuable insight into their reusability, which is briefly covered in this review study.

Microbial degradation processes are extensively employed for the bioremediation of organic pollutants by microbes, specifically bacterial and fungi strains. Feng et al. (2019) studied microbial ciprofloxacin degradation using a bacterial consortium schematically represented in Fig. 1.5d (Feng et al., 2019). However, degradation of pharmaceutical waste, particularly antimicrobials, poses a significant challenge due to their antimicrobial effects on microbes, which hinder their growth. Also, properly managing microbial cultures before and after degradation and the generated biomass is highly challenging (Wu and Yin, 2020). The employment of microbial processes for the degradation of PhACs and surviving and generated by-products during the other degradation process could provide a valuable domain for the complete degradation of pharmaceutical waste.

Chemical-based treatment processes initially successfully utilized environmentally aggressive chemicals for rapid and efficient degradation of pollutants. Chemical oxidation processes are commonly used for degrading dyes, chelating heavy metals, pesticides, pharmaceuticals, food waste, textile waste, and microbial disinfection. However, their reliance on toxic chemicals and the generation of harmful by-products raises substantial concerns. Furthermore, the stabilization and neutralization of the resulting waste pose challenges regarding both expense and time consumption (Crini and Lichtfouse, 2019). Advanced oxidation processes (AOPs) are more efficient and eco-friendlier than basic chemical-based treatment processes. AOPs include electrocatalytic oxidation, H_2O_2-based oxidation, ozonation, photo-Fenton, photocatalysis, etc. The electrocatalytic oxidation process is highly effective for degrading an organic pollutant and chelating heavy metals. Fig. 1.5e presents an

electrocatalytic malachite green degradation using β-PbO_2 electrodes (Ansari and Nematollahi, 2018). However, this process is quite challenging and expensive, especially at a large scale. The H_2O_2-based oxidation and ozonation are faster in mineralizing the organic pollutants, but complete consumption of H_2O_2 and O_3 during the treatment process makes these processes expensive. Additionally, the photo-Fenton process involves Fe^{2+}, H_2O_2, and light energy to mineralize the pollutant. However, the requirement of acidic conditions and the generation of highly ionic treated water and ferrous sludge make this process the least interesting for industrial-scale applications (Giri and Golder, 2014).

Photocatalysis, a widely employed AOP, has the capability to mineralize pharmaceutical waste to CO_2 and water using photocatalytic materials under light energy, including UV, Visible, and IR light. A graphical representation of $FeWO_4$@N-TiO_2 photocatalyst degrading MB dye and phenol under visible light is shown in Fig. 1.5f (Chakraborty et al., 2024). Photocatalytic degradation offers the advantage of reducing the likelihood of generating antimicrobial-resistant microbes and minimizing harmful effects on flora and fauna. Photocatalytic nanomaterials have been employed extensively for various applications, particularly optics and electronics. These nanomaterials' specific physical, chemical, and optical characteristics make them well-suited for diverse applications (Ghosh et al., 2018). In the early stages, elements from group 3A-5A, particularly silicon-based materials, were recognized for their semiconductive properties, leading to their utilization in electronic devices. However, as other semiconductor materials emerged with overlapping and enhanced properties, their application spectrum expanded beyond electronic devices. Commonly employed photocatalysts include TiO_2, ZnO, CdS, Fe_2O_3, WO_3, Nb_2O_3, ZnS, SnO_2, CuO, NiO, metal and non-metal doped photocatalysts, heterojunctions, etc. These photocatalysts have specific physical, chemical, optical, and conductive characteristics (Jahdi et al., 2020; Ahmad et al., 2021; Arumugam et al., 2021; Elangovan et al., 2021; Fatimah et al., 2021; Sá et al., 2021). These materials are used in various applications such as photocatalysis, sensing, biofuel production, solar panels, electrochemical reduction, and more (Corro et al., 2017; Kumar et al., 2021). However, recovery and reusability of native and modified photocatalysts pose challenges, which augment the need for an efficient recovery system.

Inadequate mineralization of PhACs during the photocatalytic process may lead to the formation of several decent and harmful by-products, potentially increasing the toxicity of the generated waste. Therefore, a complete mineralization of organic pollutants is always desirable. Integrating other methods with the photocatalytic degradation process holds the potential to achieve the complete degradation of PhACs. The partial mineralization of PhACs

through photocatalysis could potentially lower their antimicrobial effect on microbes. Hence, utilization of microbial degradation after photocatalytic degradation could promise a complete mineralization of the PhACs. However, photocatalysts could interfere with the microbial degradation process. So, it is desired that the partially degraded PhACs wastewater must be free from any photocatalyst for microbial treatment. Additionally, recovery and reusability of photocatalysts are required to minimize the treatment cost.

1.4 Photocatalysis and photocatalysts

Advanced Oxidation Processes (AOPs) play a crucial role in degrading pollutants, and among them, photocatalysis is known for eco-friendliness and high efficiency for pollutant degradation (Tetteh et al., 2020). Photocatalysis involves the conversion of light into catalytic chemical reactions. In the presence of light energy, electrons from the valence band (VB) of photocatalysts are excited and move to the conduction band (CB). This transition creates free holes in the VB and free electrons in the CB. The resulting free electron-hole pairs then participate in chemical reactions, generating free radicals that can effectively degrade organic pollutants. The detailed reaction mechanism is illustrated in Fig. 1.6, and the associated equations are shown in Eqs. 1.2-1.9 (Pino et al., 2020).

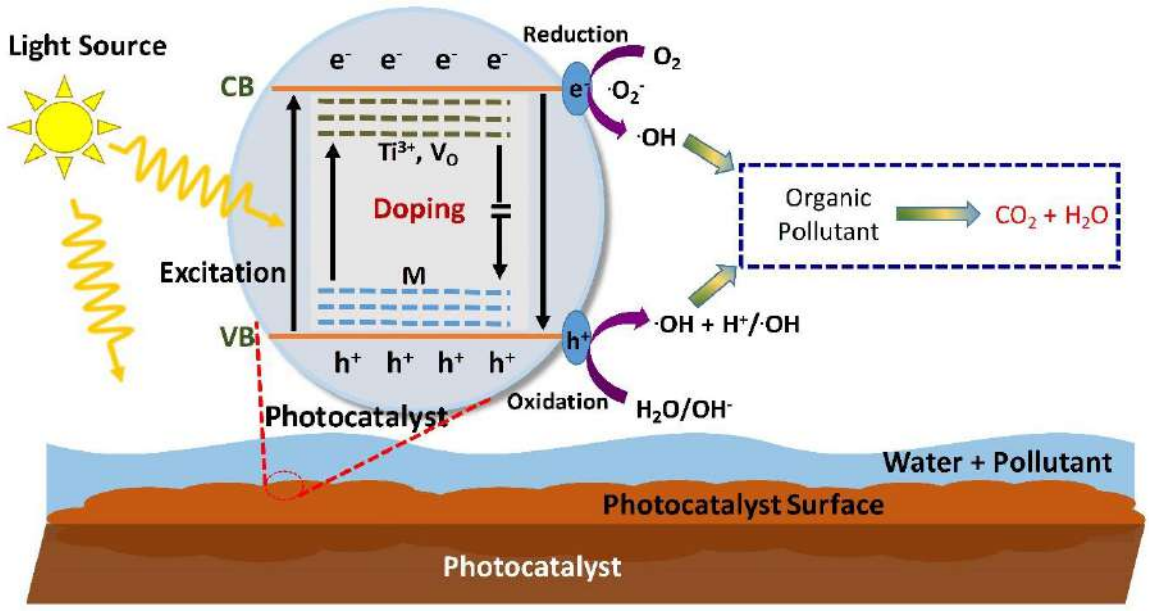

Figure 1.6: Mechanism of photocatalytic degradation of organic pollutants under light irradiation.

The overall photocatalysis process, driven by light energy, results in the degradation of organic pollutants into harmless by-products. This mechanism showcases the role of

photocatalysis in harnessing solar energy to drive oxidation-reduction reactions for environmental remediation.

Photo-excitation: $TiO_2 + h\upsilon \rightarrow e^- + h^+$ (1.2)

Charge-carrier trapping of electron: $e^-_{CB} + e^-_{TR}$ (1.3)

Charge-carrier trapping of hole: $h^+_{VB} + h^+_{TR}$ (1.4)

Electron-hole recombination: $e^-_{TR} + h^+_{VB}\,(h^+_{TR}) \rightarrow e^-_{CB} + \text{heat}$ (1.5)

Photo-excited e^- scavenging: $O_2(ads) + e^- \rightarrow O^{\bullet -}_2$ (1.6)

Oxidation of hydroxyls: $HO^- + h^+ \rightarrow HO^\bullet$ (1.7)

Photo-degradation by $HO^\bullet$: $R\text{-}H + HO^\bullet \rightarrow R'^\bullet + H_2O$ (1.8)

The overall photocatalysis reaction is:

Organic compound + H_2O/O_2 + Photocatalyst + $h\upsilon \longrightarrow CO_2 + H_2O$ (1.9)

Among the various photocatalysts developed, TiO_2 and ZnO are widely used materials in laboratory and industrial applications. These photocatalysts are preferred for their high chemical and mechanical stability, efficiency, non-toxic nature, cost-effectiveness, abundance, reusability, and eco-friendly characteristics (Xing et al., 2018; Rani et al., 2021). However, these photocatalysts did not gain versatile acceptability despite the aforementioned functional properties due to some precincts. The key challenges are their high bandgap and fast recombination of electron-hole pairs, which limits their photocatalytic efficiencies, particularly in visible light. Researchers have undertaken various methods to address these drawbacks and enhance the performance of these photocatalysts.

1.4.1 Limitations in photocatalysts

Various photocatalyst properties significantly impact the photocatalytic process, including its bandgap, active surface area, surface hydrophobicity/hydrophilicity, recombination rate, chemical and physical stability, particle size, and crystallinity. Moreover, factors such as pollutant concentration, pollutant characteristics, light energy, reaction media, and physiochemical parameters (such as pH, temperature, mixing, and reaction time) play crucial roles in regulating the photocatalytic process. Any variations in these reaction parameters can alter the photocatalytic process (Garcia et al., 2020; Nazim et al., 2021). Both native TiO_2 and ZnO exhibit limitations that hinder their widespread industrial adoption. The high bandgap of TiO_2 (3.22 eV) and ZnO (3.37 eV) restricts their utility in UV light, as the substantial energy required for electron excitation from the VB is typically provided by UV light. While the Earth receives approximately 5% UV light, it proves insufficient to sustain

robust photocatalytic activity (Chelli and Golder, 2018; Chelli et al., 2018; Gogoi et al., 2020). Hence, for effective photodegradation driven by visible or solar light, the photocatalyst's bandgap must fall within the visible range. Additionally, a high e^-/h^+ recombination rate and unfavorable hydrophobic surface of TiO_2 and ZnO decrease their photocatalytic efficiency due to short free radical generation time and inadequate surface interaction of pollutants (Xie et al., 2018; Zhang et al., 2019). The agglomeration of TiO_2 and ZnO photocatalysts poses an additional concern, reducing the active surface area and limiting light penetration (Li et al., 2010; Ali et al., 2021). Conclusively, these challenges collectively contribute to a decrease in the overall photocatalytic efficiency of these materials, hindering their widespread application on a larger scale with practical uses under visible or solar light irradiation. Therefore, overcoming these limitations is essential to achieve efficient and highly beneficial photodegradation with minimal power input.

1.4.2 Countermeasures

The efficiency of TiO_2 and ZnO under solar and visible light can be increased by lowering their bandgap, delaying recombination, and improving their surface properties (Nigussie et al., 2018; Ramírez et al., 2021). Numerous modification methods have been employed and reported to achieve these goals, including forming heterojunctions, metal and non-metal doping, fractionating anatase and rutile phases, and creating nanocomposites with other semiconductors (Xie et al., 2018). Furthermore, the photocatalytic activity of a photocatalyst can be enhanced through surface modification using organic materials and through the stabilization and immobilization of the photocatalyst on support structures. Among these approaches, most researchers have encouraged the doping of metals and non-metals in photocatalysts to overcome the limitations of native photocatalysts. However, thermal variability and optimization of dopant concentrations are major challenges with doping. It could favorably decrease the bandgap and delay recombination by inserting the impurities with minimal impact on other properties. These impurities could shift the discrete energy level of electrons to lower the bandgap energy (Cisneros et al., 2021).

Various noble (Pt, Pd, Ag, Au), transition (Fe, Se, Cu, Ni), and non-metals (B, N, Na, and P) are commonly used as dopants to synthesize doped TiO_2 and ZnO (Zhao et al., 2011; Rosario and Pereira, 2014; Cheng et al., 2020; Gogoi et al., 2020; Jahdi et al., 2020). While noble metals such as Pt, Pd, Au, and Ag are more expensive, they are preferred over base metals due to their enhanced stability and durability, providing heightened repeatability for photocatalytic degradation (Bumajdad and Madkour, 2014). Metal doping in TiO_2 and ZnO

shifts the Fermi level down to the CB, consequently lowering the bandgap. Additionally, metal dopants also trap excited free electrons, thereby delaying the recombination rate and promoting the generation of free radicals towards the VB. On the other hand, non-metal doping reduces the bandgap by introducing new energy levels towards the VB. However, non-metals do not function effectively as charge trappers or recombination centres, which helps minimize delays in charge carrier recombination. Introducing dopants into interstitial lattice sites also increases oxygen vacancies in the photocatalyst, directly enhancing photocatalytic activity by facilitating better charge transfer through free electrons. Each oxygen vacancy provides two free electrons that participate in catalytic activities. The type, concentration, and size of dopants, however, can influence photocatalytic efficiency. Some reported studies confirmed increased photocatalytic degradation efficiency of S-doped TiO_2, ZnO:Mo, and g-C_3N_4/ZnO:Mo photocatalyst with an increase in dopant concentration. However, at very high dopant concentration, degradation efficiency decreased due to increased bandgap and rapid recombination. (Helmy et al., 2021; Sudha et al., 2024). Furthermore, the doping method regulates electronic, structural, and surface properties, which are crucial for determining photocatalytic efficacy.

1.4.3 Synthesis methods

The fabrication of bare and metal-doped photocatalysts with specific properties is attainable by precisely controlling optimized parameters during synthesis. The physicochemical attributes of photocatalysts are significantly influenced by the chosen synthesis method. Any variation in synthesis parameters, such as pH, temperature, reaction time, reducing and capping agents, presence of other organic compounds, and surrounding environment, can drastically change their properties (Nazim et al., 2021). Various methods have been employed for the synthesis of photocatalytic nanomaterials, and based on the nature of the route used, photocatalytic nanomaterials synthesis methods can be classified into physical, chemical, and biological methods, as shown in Fig. 1.7 (Ijaz et al., 2020). Each method has its advantages and disadvantages, defining the suitability of a particular synthesis approach.

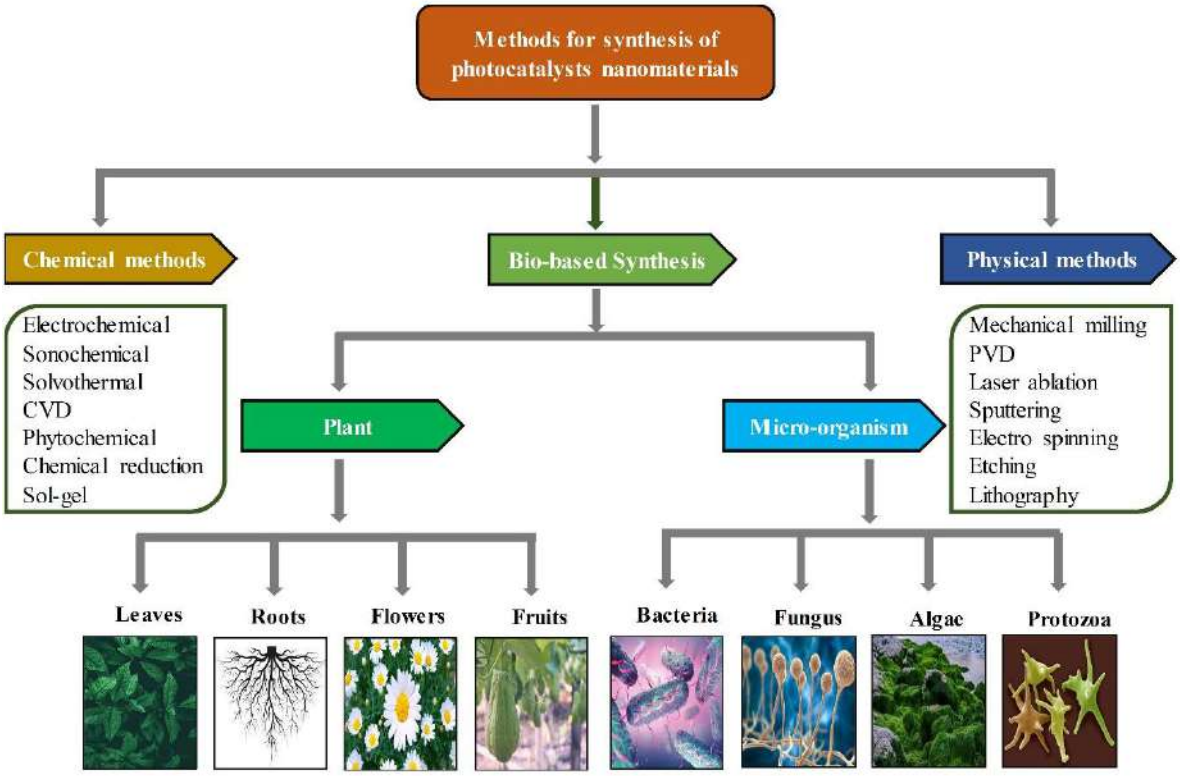

Figure 1.7: Graphical illustration of nanomaterials synthesis methods and expansion of bio-based methods.

1.4.3.1 Physical and chemical synthesis methods

Physical synthesis routes involve physical factors, i.e., electromagnetic radiation, plasma, electric power, heat, and mechanical force. Some commonly used physical methods are mechanical milling, arc discharge, physical vapour deposition, laser ablation, evaporation/condensation, and sputtering (Ijaz et al., 2020; Baig et al., 2021). Developing highly precise nanomaterials with desired properties is a significant outcome of physical methods. However, the requirements of advanced machinery, instruments, expensive techniques, and high power consumption are major concerns associated with physical techniques, limiting their widespread use (Golder et al., 2021).

Chemical methods have emerged as one of the most prominent approaches since the mid-20th century, involving various chemicals for synthesizing photocatalytic nanomaterials. Chemical methods and bio-mediated synthesis (using plant extracts, biomass, etc.) primarily operate on a bottom-up approach. However, a few chemical methods also rely on a top-down approach (Gawande et al., 2016). Chemical-based synthesis is a fast and straightforward method that yields photocatalysts with precise characteristics. Hoa et al. (2023) synthesized a chemical-based TiO_2/g-C_3N_4 photocatalyst, as illustrated in Fig. 1.8, for the degradation of MB

dye under visible light and exhibited about 98.5% degradation within 100 min (Hoa et al., 2023). Despite the effectiveness of various chemical agents for metal doping, their use poses environmental challenges due to the involvement of toxic chemicals and the generation of hazardous by-products (Zhang et al., 2020).

Figure 1.8: Schematic synthesis route of chemical-based TiO_2/g-C_3N_4 and photocatalytic degradation of MB dye (Reprinted with permission from (Hoa et al., 2023), Copyright 2023 Dang Thi Ngoc Hoa et al.).

1.4.3.2 Bio-based synthesis methods

Bio-based doping and synthesis of photocatalysts have emerged as effective and environmentally friendly methods, utilizing biologically active agents such as microorganisms (bacteria and fungi), enzymes, microbial metabolites, and plants (Bhan and Golder, 2023). The microbial synthesis route produces photocatalytic nanomaterials with more uniform shapes, smaller sizes, and reduced agglomeration. However, challenges remain in separating nanoparticles from the reaction medium, safe disposal of grown microbes, and effective doping of metals. Using plants and their derivatives as sources of reducing and capping agents is reported to be a highly suitable approach for metal doping. Plant extracts contain various compounds, such as amides, carotenoids, flavonoids, phytosterols, polyphenols, and vitamins. Various plant derivatives, especially those from vegetables and fruits, are rich sources of reducing agents like ascorbic acid, citric acid, and gallic acid (Bhan and Kumar Golder, 2023). Additionally, green tea extract, rich in catechins and their derivatives, is widely utilized in nanoparticle synthesis. Plant waste, including peels from citrus fruits and vegetables, plant

leaves, seeds, and debris, are also recognized as rich sources of reducing agents and other organic compounds, facilitating their use in nanomaterial synthesis.

Bio-derived agents' economic viability, ready availability, and efficacy underscore the growing importance of utilizing these materials in synthesizing doped photocatalysts (Dash et al., 2020). Beyond dopants, other defects, such as oxygen vacancies and Ti^{3+} defects, also enhance photocatalytic activity by reducing the bandgap, generating free electrons, and trapping excited electrons. Oxygen vacancies supply two free electrons toward the VB, while Ti^{3+} defects act as electron trappers toward the CB. However, the generation of oxygen deficiencies and Ti^{3+} defects poses significant challenges. Additionally, a hydrophilic surface facilitates the more effective generation of free radicals from surface water (H_2O). Bio-based methods could not only result in a lower bandgap and delayed recombination but also offer improved surface hydrophilicity, an abundance of oxygen vacancies, and Ti^{3+} defects due to the presence of various bio-analytes in plant extracts (Chelli et al., 2018).

Helmy et al. (2021) reported a decrease in the bandgap of TiO_2 from 3.22 to 2.58 eV, delayed recombination, and increased oxygen vacancies when using an extract from *M. parviflora* leaves to incorporate sulphur. A schematic of bio-based S-doped TiO_2 synthesis for the photodegradation of MO dye is shown in Fig. 1.9 (Helmy et al., 2021). In contrast, a chemical-based synthesis method only reduced the bandgap to 2.63 eV. Similar results were also reported for g-C_3N_4/ZnO:Mo, and CuO/Bi_2O_3 (Alsalmah, 2024; Sudha et al., 2024). These photocatalysts exhibited superior photocatalytic activity against organic pollutants under visible light irradiation compared to chemical-based photocatalysts. Plant extracts are widely utilized for synthesizing metal/non-metal-doped photocatalysts, and several studies have highlighted their ability to enhance electronic and physicochemical properties and photocatalytic activities, as summarized in Table 1.3.

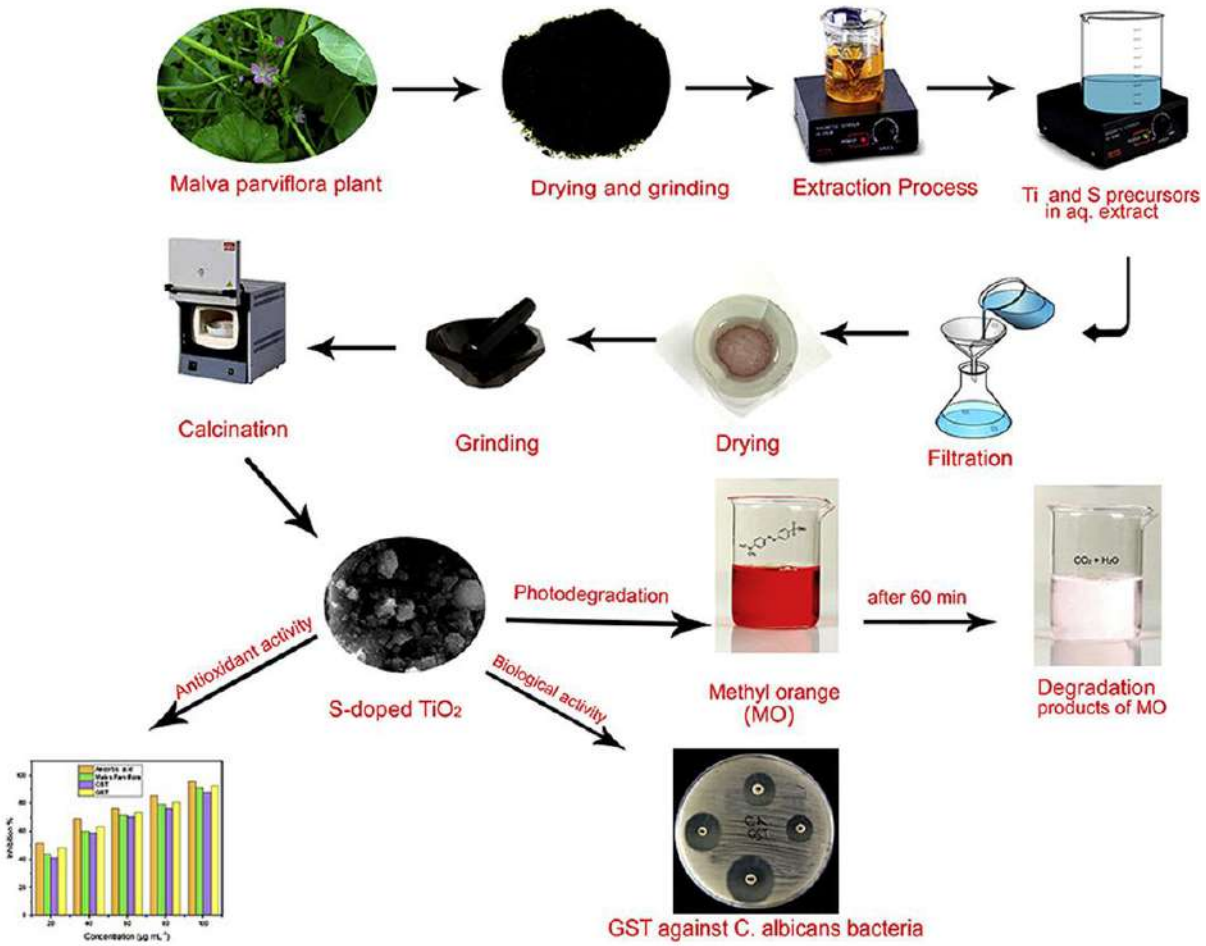

Figure 1.9: Graphical representation of the synthesis of bio-based S-doped TiO_2 for photocatalytic degradation of MO dye, antioxidant activity and antimicrobial activity (Reprinted with permission from (Helmy et al., 2021), Copyright 2021 Elsevier.

In Table 1.3, most of the reported studies on doped photocatalysts such as C-N/g-C_3N_4, Ag/ZnO, Mo/TiO_2, Ag/Fe_2O_3, Sn/CdS, rGO/TiO_2/Co_3O_4, etc., demonstrate a decrease in bandgap through bio-based doping processes, alongside significant improvements in electronic, physicochemical, and surface properties. Additionally, bio-based doping processes not only reduce the cytotoxicity of photocatalysts but also enhance seed germination. For instance, *M. citrifolia* synthesized surface functionalized g-C_3N_4/ZnO:Mo exhibited the lowest bandgap and improved photocatalytic activity, along with enhanced germination of *Vignaradiata* L. (mung bean) seeds (Sudha et al., 2024). Other bio-based photocatalysts, such as Nb/ZnO, Co/ZnO, Co/CeO_2, CuO/Bi_2O_3, and Mo/ZnO, also showed reduced particle size and increased surface area. Karthik et al. (2022) synthesized bio-based Cu-doped ZnO photocatalysts, where despite an increase in bandgap from 3.10 to 3.19 eV, the photocatalytic activity exhibited a remarkable improvement, rising from 26.5% (ZnO) to 92.2% (3% Cu-ZnO)

against IC dye. This enhancement was attributed to delayed recombination, oxygen vacancies, and other defects in Cu-doped ZnO (Karthik et al., 2022).

Table 1.3: Reported bio-based (vegetal extract) metal/non-metal doped photocatalysts and their comparison with bare and chemical-based photocatalysts in terms of their bandgap, physiochemical/electronic properties, and photocatalytic efficiency against organic contaminants such as dyes, and pharmaceuticals.

Photocatalyst	Origin of extract	Bandgap (eV)	Characteristics of bio-based over bare/chemical-based photocatalysts	Pollutant & Degradation (%)		Ref.
TiO_2	*M. parviflora* leaves	3.22	Delayed recombination and increased V_O	MO dye	-	(Helmy et al., 2021)
S/TiO_2		2.58			99	
	Chemical-based	2.63			98.1	
Pure g-C_3N_4	Pomegranate peel	2.98	Delayed recombination	TOL	56	(Tavakolain et al., 2023)
C-N/g-C_3N_4		2.34			91	
ZnO	*S. edule* fruit	3.13	Delayed recombination	DIP	12	(Chelli and Golder, 2018)
Ag/ZnO		2.85			79.5	
Bare TiO_2	*E. crassipes* plant	3.15	Delayed recombination and increased V_O	MB dye	-	(Zelekew et al., 2021)
Co/TiO_2		2.95			99.6	
ZnO	*S. grantii* leaves	3.10	Delayed recombination and increased V_O	IC dye	26.5	(Karthik et al., 2022)
Cu/ZnO		3.19			92.2	
TiO_2	*T. peruviana* fruit	3.20	Delayed recombination	MB dye	10.4	(Chelli et al., 2018)
Ag/TiO_2		2.30			98	
ZnO	*V. amygdalina* leaves	2.70	More uniform particles & higher surface area	TET	39.2	(Nguyen et al., 2022)
Nb-ZnO		2.25			93.2	
ZnO	*B. racemosa* Lam. leaves	3.20	Delayed recombination and increased V_O	AMP	81.2	(Mariappan et al., 2024)
Ni/ZnO		3.19			86.3	
Mn/ZnO		3.16			84.3	
Co/ZnO		3.06			88.0	
CeO_2	*S. persica* bark	3.93	Increased V_O & higher surface area	AO7	65.8	(Hamidian et al., 2021)
Co/CeO_2		3.37			86.3	
Fe oxides	R. officinalis leaves	2.50	Surface functionalization & high magnetization	MO dye	80.5	(Mirsadeghi et al., 2021)
Cu/Fe oxides		1.70			96.6	
Fe_2O_3	*Aloe Vera* leaves	2.01	Increased V_O and better thermal properties	MB dye	60.6	(A et al., 2020)
Ag/Fe_2O_3		1.93			88.2	
CdS	*O. sanctum* leaves	2.37	Delayed recombination	MB dye	69.8	(Mullamuri et al., 2021)
Pb/CdS		2.03			98.0	
Sn/CdS		2.04			97.8	
ZnO	*P. capillacea* biomass	3.19	Less particle size & surface functionalization	CIP	-	(Hassaan et al., 2024)
Co/ZnO		2.92			>99	
Fe_3O_4	*F. vulgare* seed	2.30	Surface functionalization	IMT	84.8	(Yousefi et al., 2021)
Au/Fe_3O_4		1.80			93	
ZnO	Chemical-based	3.22	Delayed recombination, Surface functionalization,	MO dye	68	(Sudha et al., 2024)
ZnO:Mo		3.47			81	
	M. citrifolia	3.43			85	

g-C_3N_4 /ZnO:Mo	Chemical-based	2.90	higher charge carrier density & higher seed germination rate		90	
	M. citrifolia	2.70			96	
Bi_2O_3	*C. limonum Risso* leaves	2.38	Delayed recombination, less particle size & surface functionalization	TB dye	55.4	(Alsalmah, 2024)
CuO/Bi_2O_3		2.27			85.5	
	Chemical-based	-			73.1	
ZnO	Chemical-based	3.25	Delayed recombination & less particle size	RhB dye	70.9	(Khalid et al., 2023)
	M. oleifera seeds	3.17			80.2	
Mo/ZnO		3.11			89.6	
TiO_2/Co_3O_4	*S. involucrata* leaves	2.86	Delayed recombination & surface functionalization	CV dye	~62	(Ranjith et al., 2019)
rGO /TiO_2/Co_3O_4		2.74			~78	
TiO_2	*A. muricata* L. leaves	3.34	Delayed recombination	MG dye	50.7	(Yulizar et al., 2023)
$YMnO_3$/TiO_2		2.38			95.3	

#AMP: Ampicillin; AO7: Acid Orange 7; CIP: Ciprofloxacin; CLQ: Chloroquine; CV: Crystal violet; DIP: Dipyrone; IC: Indigo carmine dye; MB: Methylene blue; MG: Malachite green dye; MO: Methyl orange; IMT: Imatinib; RB: Rose Bengal dye; Rh-B: Rhodamine B dye; TB: Trypan Blue dye; TET: Tetracycline; TOL: Toluene;

Conclusively, adopting a bio-based route for synthesizing metal (both noble and transition metals) doped photocatalysts has several advantages over chemical-based processes. The discussed literature survey highlights the effectiveness of the bio-based route in achieving a significant decrease in the bandgap, delayed recombination, improved surface hydrophilicity, and the creation of oxygen vacancies and Ti^{3+} defects. These factors collectively enhance the photodegradation efficiency of these materials, particularly under visible light. Notably, the case of Cu-doped ZnO demonstrated an increase in photodegradation efficiency without a decrease in the bandgap (Karthik et al., 2022), suggesting that delayed recombination and the presence of oxygen vacancies and Ti^{3+} defects play a substantial role in enhancing the photocatalytic efficacy of doped photocatalysts.

1.4.4 Literature review on photocatalytic degradation of PhACs

The presence of PhACs in natural water bodies poses a major threat to our ecosystem, with their proliferation increasing due to the inefficiency of conventional treatment systems. Various methods, including adsorption, chemical treatment, bio-remediation, ion exchangers, and photocatalysis, have been employed to treat PhACs in laboratory and industrial settings (Aronne et al., 2017; Jia et al., 2018; Ravi and Pandey, 2019). Among these, photocatalytic degradation stands out as the most widely used method owing to its high efficiency, eco-friendly nature, potential for mineralization, and ability to counter the inhibitory effects of PhACs. Various types of photocatalysts have been reported for the degradation of PhACs under both UV and visible light irradiation. The efficiency of photocatalytic degradation is highly

influenced by the reaction's physicochemical parameters, the photocatalyst's nature, the light source, the reaction time, and the formed intermediates (Kumar et al., 2021). Numerous native and modified photocatalysts, synthesized using both chemical and bio-based routes, have been employed to degrade PhACs. This section comprises a literature survey on the photocatalytic degradation of PhACs under UV and visible light irradiation by chemical-based and bio-based photocatalysts (Table 1.4), which includes photocatalysts used for PhACs degradation, their bandgap, light source, reaction time, and degradation efficiency (%).

In a study, 94.5% degradation of TET was achieved by flower-like Er^{3+}-Bi_2WO_6 nano-sheets having a lower bandgap of 2.35 eV and exhibiting delayed recombination and surface area of 67.1 m^2/g (Qiu et al., 2022). In another study, a hydrothermally synthesized KPCN/GO/$ZnFe_2O_4$ photocatalyst showed ~87% degradation of TET and 71% COD removal of wastewater within 60 min (Kumar et al., 2023). Patial et al. (2024) utilized NH_2-MIL-125/MnO_2 nanospheres for ornidazole (ORZ) degradation and observed 91.3% degradation efficiency under visible light irradiation (Patial et al., 2024). A Fenton-assisted degradation using α-Fe_2O_3/CdS/SiO_2 nanocomposite exhibited 99% TET degradation within 120 min, highlighting significant contributions from both the nanocomposites and H_2O_2 (Sharma et al., 2024). Zangeneh et al. (2018) explored the photocatalytic activity of metal and non-metal co-doped TiO_2 and revealed the highest efficiency of co-doped TiO_2 in the degradation of organic pollutants than mono-doped TiO_2 and bare TiO_2 (Zangeneh et al., 2018). Similar results were also observed with Ag-modified CeO_2@SnO_2 (Rani et al., 2024). This suggests that bi- or multi-metal co-doping could be effective against complex pollutants under visible light. The specifications of irradiated light, such as wavelength and intensity (power), also influence the photocatalytic degradation process. Yousefi et al. (2021) reported degradation of IMT and IMI drugs using Fe_3O_4-Au nanocomposite and observed superior degradation of both drugs (>90%) within 35 min under UV light irradiation, whereas under visible light it was decreased to <75% within 80 min (Yousefi et al., 2021). Solar light is widely reported as the most suitable source for photocatalytic degradation due to its high intensity, broad spectrum of light color, and UV light (~5%). For instance, F-Pd co-doped TiO_2 achieved ~97% degradation of SMZ under a solar simulator in 250 min, while under direct solar light, about 98.8% SMZ was degraded within just 70 min (Jahdi et al., 2020).

Table 1.4: Photocatalytic degradation of PhACs using various chemical-based and bio-based photocatalysts, including their bandgaps and photocatalytic experimental conditions.

PhACs	Photocatalyst	Band gap (eV)	Light source	Degradation (%)	Time (min)	Ref.
CIP	CeO_2/ZnO nanocomposites	2.9-3.2	200 W lamp (365 nm, UV)	60.0	60	(Wolski et al., 2021)
CIP	ZnO	3.7	Xe lamp (365 nm, UV)	50.0	60	(El-Kemary et al., 2010)
CIP	S, N-doped MgO	1.5-3.38	UVA-LED (365 nm)	~99.0	60	(Akbari et al., 2021)
CIP	N-TiO_2	2.74	500 W lamp (>420 nm)	97.5	180	(Xing et al., 2018)
CIP	CQDs/Bi_2WO_6	~2.75	300 W Xe lamp (>420 nm)	96	80	(Wu et al., 2020)
TET	KPCN/GO/$ZnFe_2O_4$	-	500 W halogen lamp (>400 nm)	87	60	(Kumar et al., 2023)
TET	BiOI/$CuInS_2$/ZnO heterojunction	-	500 W Xe lamp (>420 nm)	96.8	120	(Banyal et al., 2024)
TET	Fenton assisted Fe_2O_3/CdS/SiO_2	-	500 W Xe lamp (>420 nm)	~99	120	(Sharma et al., 2024)
TET	*Nb-doped ZnO	2.25	250 W lamp (>420 nm)	93.2	180	(Nguyen et al., 2022)
TET	Er^{3+}-Bi_2WO_6	2.35	500 W lamp (>420 nm)	94.6	60	(Qiu et al., 2022)
TET	$CuWO_4$/$CuBi_2O_4$	-	Visible light (>400 nm)	90.1	120	(Chen et al., 2023)
TET	rGO/g-C_3N_4/$FeTiO_3$	1.7	Direct sunlight	~90	90	(Priyadharsan et al., 2024)
TET	g-C_3N_4/MOF/CuO	0.81	500 W Xe lamp (>400 nm)	78.8	27	(Li et al., 2024)
OTC	$Zn_3In_2S_6$/Bi-MOF	-	Simulated sunlight	~87	60	(Wang et al., 2024)
PEN	TiO_2 (P25)	3.22	UV-A lamp (24 W, 365 nm)	56.7	150	(Berkani et al., 2022)
	ZnO	3.37		26.2		
SUL	Mo-doped BiOBr	2.13	300 W xenon lamp (>420 nm)	87.5	80	(Wu et al., 2022)
SSX	*CdS NPs	3.55	300 W UV light; 365 nm	68.0	120	(Munyai et al., 2021)
SMZ	F-Pd co-doped TiO_2	0.54	Solar simulator	97.0	250	(Jahdi et al., 2020)
			Solar light	98.8	70	
SMZ	WO_3-UiO-66@rGO	2.79	UV light (365 nm)	90.4	60	(Huong et al., 2024)
ORZ	NH_2-MIL-125/MnO_2	1.50	Visible light (>400 nm)	91.3	120	(Patial et al., 2024)
DIC	Cu-Al LDH.Bi_2O_3 -C	1.74	Visible light	83.0	50	(Kumari et al., 2021)
	Cu-Al LDH.Bi_2O_3 -S	1.76		65.0		
DIC	CdS@TiO_2	2.7	Visible light (400 W)	86.0	240	(Elangovan et al., 2021)
IBU	Ce-doped ZnO	3.31	UV light (125 W)	60.0	120	(Sá et al., 2021)
IBU	MOF-Fe_2O_3@TiO_2	2.94	UV-Visible light	91.0	240	

NAP			(25W, 365–700 nm)	~100	15	(Peña-Velasco et al., 2021)
Mixture				79.0	240	
CBZ	BiOBr	-	300 W lamp (>420 nm)	88.7	20	(Xu et al., 2022)
CBZ	BiOBr/N-CQDs	1.94	50 W lamp (475 nm)	99.6	15	(He et al., 2024)
CIP	Bi_2WO_6/Fe_3O_4/Biochar	~2.14	50 W lamp (475 nm)	96.8	30	(Wang et al., 2021)
OFL				99.9		
CIP	2D/1D Bi_2WO_6/Ta_3N_5	~1.93	300 W Xe lamp (>400 nm)	81.1	150	(Li et al., 2020)
TET				86.7	120	
CIP	Nb_2O_5-RGO/MoO_3	2.57	300 W lamp (>400 nm)	85.4	50	(Jones et al., 2022)
SSZ				88.2		
SMT	0D/2D CQDs/g-C_3N_4	2.86	16 LED light (395-500 nm)	97.3	50	(Di et al., 2020)
SMZ	*Au–ZnO–CSs	3.18	UV light (450 W)	78.0	120	(Bopape et al., 2024)
AMX	*$FeNi_3/SiO_2/TiO_2$	-	Solar light	96.0	90	(Alwared et al., 2023)
TET	*$NiFe_2O_4$	1.75	UV light	75.0	120	(Fatimah et al., 2023)
			Visible light	65.5		
OTC	*$CuFe_2O_4$/CuO-rGO	1.20	LED lamp	87.5	90	(Paghaleh et al., 2023)
APAP	*Bi_2O_3@CdS	2.00	Solar light	98.0	240	(Rani et al., 2023)
DIC				96.0		
MET	* SnO_2	3.56	Solar light	~42.5	300	(Rani et al., 2024)
TET				~44.5		
MET	*CeO_2	3.22		~53.0		
TET				~54.5		
MET	*Ag/CeO_2@SnO_2	2.20		94.0		
TET				96.0		
CIP	*BT-CL-PbO	2.90	Solar light	98.3	30	(Naeimi et al., 2022)
TCS	*LNRs/GCN-NRs	2.60	UV light (125 W)	99.9	90	(Venkatesan Savunthari et al., 2021)
DIP	*Ag/ZnO	2.85	Visible light	79.5	120	(Chelli and Golder, 2018)
TET	*Nb-ZnO	2.25	Visible light (250 W)	93.2	240	100
AMP	*Co/ZnO	3.06	Visible light	88.0	180 - 210	(Mariappan et al., 2024)
AMX				92.4		
TET				91.1		
IMT	*Fe_3O_4-Au	1.80	Visible light	72.8	80	(Yousefi et al., 2021)
			UV light	93.0	35	
IMI			Visible light	75.0	80	
			UV light	91.0	35	

**Indicated: photocatalyst was synthesized using bio-based synthesis route;*
#IMI: Imipenem; ORZ: Ornidazole; OTC: Oxytetracycline; SSX: Sulfisoxazole; SUL: Sulfanilamide; SMT: Sulfamethazine; SSZ: S*ulfasalazine*

Bismuth-based photocatalysts have been extensively employed for the photocatalytic degradation of organic pollutants. The photodegradation efficiency of these photocatalysts further can be enhanced through modifications using biochar, co-catalysts, and carbon quantum

dots (CQDs). For instance, Wang et al. (2021) synthesized a magnetic Bi_2WO_6/Fe_3O_4/biochar photocatalyst via the hydrothermal method. The incorporation of Fe_3O_4 reduces its bandgap from 2.74 to 2.20 eV with increasing magnetization and improved photocatalytic degradation of CIP and OFL. Additionally, biochar decoration on the magnetic Bi_2WO_6/Fe_3O_4 further reduce the bandgap to 2.14 eV, achieving 96.8% CIP and 99.9% OFL degradation within 30 min under visible light irradiation (Wang et al., 2021). In a study, nanofibers of a 2D/1D Bi_2WO_6/Ta_3N_5 Z-scheme heterojunction were synthesized via a solvothermal route, exhibiting 81.1 and 86.7% photodegradation of CIP and TET within 150 and 120 min (Li et al., 2020). In another study, decoration with CQDs over Bi_2WO_6 broadened the light absorption range and enhanced charge separation, increasing CIP photodegradation from 58 to 96% (Wu et al., 2020). Similarly, He et al. (2024) modified BiOBr with N-CQDs, reducing the bandgap from 2.46 to 1.94 eV, and observed an increase in CBZ photodegradation from 55.2 to 99.6% (He et al., 2024). Another study showed that CQD-modified g-C_3N_4 achieved 97.3% sulfamethazine (SMT) degradation, outperforming bare g-C_3N_4 (Di et al., 2020).

Ternary nanocomposites incorporating reduced graphene oxide (rGO) and metal-organic frameworks (MOFs) have demonstrated improved photocatalytic performance. For instance, a ternary WO_3-UiO-66@rGO nanocomposite was developed using 3D printing technology. The addition of rGO reduces the bandgap from 3.52 to 2.79 eV and increases the overall surface area, improving SMZ's photodegradation from 55.1 to 90.4% (Huong et al., 2024). He et al. (2024) synthesized a ternary rGO-modified $C_3N_4/FeTiO_3$ nanocomposite for TET photodegradation under direct solar light. This composite exhibited a lower bandgap of 1.7 eV, compared to its binary and pure forms and achieved superior photodegradation. In contrast, the binary and pure forms showed only 50-62% and 13-40% degradation (Priyadharsan et al., 2024). In another study, a ternary nanocomposite was created by wrapping honeycomb-like Nb_2O_5/rGO over MoO_3 nanorods, resulting in high photodegradation efficiencies of 85.4% for CIP and 88.2% for sulfasalazine (SSZ) within 50 min under visible light (Jones et al., 2022). Wang et al. (2024) developed a $Zn_3In_2S_6$/Bi-MOF S-scheme heterojunction, which degraded 87% oxytetracycline (OTC) within 60 min, compared to only 44-55% degradation by its pure counterparts (Wang et al., 2024). Similarly, g-C_3N_4/MOF-nanosheet/CuO ternary heterostructures showed improved TET photodegradation (78.8%) within 27 minutes, outperforming MOF (2%), g-C_3N_4 (42.8%), and CuO (22.2%) (Li et al., 2024). In nutshell, modifying binary photocatalysts with rGO and MOFs has been demonstrated to enhance photocatalytic degradation activity under visible light significantly.

TiO_2 (P25) and ZnO showed 56.71 and 26.21% degradation of penicillin G antibiotics due to high bandgap and rapid recombination rate. However, the degradation efficiency increased to 72.72% with adding persulfate sodium (PPS), which worked as an electron acceptor (Berkani et al., 2022). Banyal et al. (2021) reported that the heterojunction formation of BiOI/$CuInS_2$/ZnO enhanced TET photodegradation to 96.8% compared to 53.5% with ZnO alone (Banyal et al., 2024). Doped metal and Ti^{3+} defects work as natural electron acceptors in metal-doped TiO_2, which denied the use of additional electron acceptors for better photocatalytic degradation. The photocatalytic degradation process facilitates the generation of various by-products or intermediates before mineralizing into CO_2 and H_2O. The degradation of particular PhACs follows certain pathways involving plenty of chemical reactions. For example, photodegradation of other fluoroquinolone drugs (antibiotics), such as norfloxacin, ofloxacin, levofloxacin, etc., involves several chemical processes such as isomerization, hydroxylation of oxazole ring, hydrolysis, electrophilic substitution demethylation, dihydroxylation, decarboxylation, etc., (Czyrski et al., 2019; Yang et al., 2020).

In conclusion, various chemically and bio-based synthesized photocatalysts have been employed to degrade several PhACs under UV, visible, and solar light irradiations. Limited studies with bio-based metal/non-metal doping have explored their application for PhACs degradation. Furthermore, most studies have demonstrated excellent photodegradation efficiency under UV light irradiation, and some have shown reasonably good degradation under visible light, albeit with high power input (typically 350-500 W). The impact of high-power lights on the drug solution has not been thoroughly explored. Additionally, only a few studies have reported the degradation of PhACs under direct sunlight. The bio-based metal-doped photocatalysts can potentially degrade PhACs under visible light irradiation. However, further research is needed to explore the full potential of bio-based photocatalysts for the efficient and sustainable degradation of PhACs, especially under more environmentally relevant conditions, such as lower power input and direct solar light exposure.

Despite the various advantages of photocatalysis in environmental and industrial applications, its scalability is limited due to inefficient recovery and reusability, which require significant attention from researchers and scientists. Furthermore, many reported photocatalytic degradation processes do not completely degrade PhACs, potentially generating more toxic intermediates. Integrating photocatalytic processes with other methods, such as microbial or biological degradation, could facilitate the complete degradation of pollutants. Therefore, the upcoming sections will highlight strategies for the recovery of photocatalysts and will emphasize their potential integration with microbial or biological degradation

processes to achieve complete degradation of PhACs without losing photocatalysts and their efficiency.

1.5 Recovery of photocatalyst nanomaterials

1.5.1 Need of photocatalyst particles recovery

The precise size and high surface area of photocatalyst nanomaterials have fuelled their demand, transitioning from laboratory to industrial scale, with widespread applications in various fields such as wastewater treatment, sensing, drug delivery, enhanced oil recovery, antimicrobial activity, biomaterials, etc. (Peña-Velasco et al., 2021; Safat et al., 2021). The unique properties of photocatalysts contribute to their effectiveness in these processes, making them valuable candidates for addressing environmental and technological challenges. Despite having various beneficial properties, the recovery and reusability of nanoscale photocatalysts is quite challenging and a major concern due to the absence of a highly efficient separation system. Ensuring treated wastewater is free from photocatalyst material is crucial for further utilization. The persistence of photocatalyst materials in the environment could lead to elemental leaching and breakdown into their ionic forms. This, in turn, may contribute directly to metal pollution, potentially impacting aquatic life in contaminated water bodies (Du et al., 2011; Li et al., 2013). Previous studies have reported the breakdown of ZnO into Zn^{2+}, which can have detrimental effects on flora and fauna by interfering with their biochemical pathways (Liu et al., 2017; Vimercati et al., 2020). If not effectively removed, the persistent photocatalyst material could also pose challenges to other treatment processes, such as biological degradation, coagulation-flocculation, membrane separation, chemical treatment, electrochemical treatment, and adsorption (Honda et al., 2014; Alam et al., 2016; Leite et al., 2020). The potential interference from residual photocatalyst material underscores the importance of developing efficient methods to recover and separate nanoscale photocatalysts to ensure the effectiveness of subsequent treatment processes and prevent adverse environmental impacts.

Photocatalysts exhibit good antimicrobial activity, making them potentially useful for eradicating harmful microbes from wastewater. However, their presence during biological treatment processes can inhibit biological remediation by affecting or killing pollutant-degrading microbes (Leite et al., 2020). Many bacteria engaged in pollutant degradation form biofilms to entrap pollutants for better bioavailability. However, photocatalysts have been reported to deteriorate these biofilms, potentially reducing their degradation efficiency

(Pezzoni et al., 2020). In addition to inhibiting biological treatment, the intermediate by-products produced during the photocatalytic degradation process may interfere with coagulation-flocculation processes, reducing their removal efficiency (Honda et al., 2014). While effective for photocatalyst recovery, membrane separation is limited to specifically sized pollutants. Differently sized nano-photocatalysts may hinder membrane separation by clogging pores and forming cake layers (Alam et al., 2016).

Chemical treatment processes rely on specific chemical reactions to degrade pollutants, and introducing photocatalysts can interfere with these reactions by generating free radicals that affect the overall chemical treatment process (Hou et al., 2013). On the other hand, photocatalysts have been reported to enhance the degradation efficiency of electrochemical processes (Kumar et al., 2019). In electrochemical processes, photocatalysts generate free radicals under an electrical potential, contributing to the catalytic degradation of pollutants. Adsorption processes, a cost-effective and commonly used method for pollutant removal, rely on physical and chemical interactions on the adsorbent surface. Photocatalysts can alter the surface properties of the adsorbent, potentially reducing the mass transfer of pollutants to the adsorbent surface due to competitive inhibition (Nikpay, 2022). Additionally, photocatalysts can affect the analytical analysis of wastewater, such as UV-Vis spectrophotometry, sensing, biochemical oxygen demand (BOD), chemical oxygen demand (COD), turbidity analysis, etc. Therefore, it is essential to fully recover the photocatalyst from the treated water before considering its reuse or direct disposal into the environment (Baran et al., 2005). From an economic perspective, accepting any treatment system at an industrial scale depends on its cost-effectiveness. Photocatalytic degradation systems are highly effective and have the potential to be reusable for several cycles. Therefore, the complete recovery of the photocatalyst after the photocatalytic degradation process is crucial for its potential reusability. Various separation techniques have been employed for photocatalyst recovery at laboratory and pilot scales, each with its pros and cons, requiring careful consideration for implementation in photocatalyst recovery processes.

1.5.2 Different separation techniques

Physical separation of photocatalytic nanomaterials poses a challenging task, demanding precise separation techniques to minimize the loss of photocatalysts. Several traditional separation methods have been employed to separate nanomaterials from aqueous solutions. These include ultracentrifugation, fractional precipitation, ion-exchange chromatography, size exclusion chromatography, magnetic separation, electrophoresis, and

membrane separation (Hanauer et al., 2007; Arcudi et al., 2016; Hassan et al., 2021). Each of these separation techniques comes with its own merits and demerits, as given in Table 1.5.

Table 1.5: Advantages and disadvantages of different nanomaterial separation techniques.

Method	Advantages	Disadvantages	Sources
Centrifugation	Cheap and rapid method; High efficiency; Can easily separate NPs with different shapes and sizes	Cannot be used for very high volumes and separation of similar-sized NPs; Difficult to separate soft materials	(Kahnouji et al., 2019)
Chromatography	Analytical analysis can be performed along with separation; Precise and sensitive; Can be used for very small amounts of NPs	Expensive; Interaction of the NPs with the stationary phase; Aggregation of the NPs; clogging of channel	(Arcudi et al., 2016)
Magnetic Separation	Cost-effective; the rapid and simplest method	Limited to magnetic nanoparticles; Agglomeration of NPs during separation	(Hassan et al., 2021)
Electrophoresis	Economically feasible at a small scale, High resolution and sensitivity, can be used for the measurement of NPs size	Limited to small volume; need charged NPs; Need post-electrophoresis steps for purification	(Kim et al., 2013)
Membrane separation	Can be effectively used at a pilot scale; Size-selective removal; Suitable for thermolabile; cost-effective; Readymade devices are available commercially; Reduced preparation time	Clogging of the membrane (although backflow can clear it to an extent); Only concentrate the NPs; Regular maintenance is required	(Mehta et al., 2016)

A visual representation of various separation techniques is illustrated in Fig. 1.10. The choice of a particular separation method depends on factors such as the properties of photocatalyst nanomaterials, desired purity, and specific requirements of the application. Among all the recovery/separation processes (Table 1.5), the membrane separation process is most suitable for recovering used photocatalysts after photocatalytic degradation. However, the membrane process has some disadvantages of pore blocking, which needs regular maintenance and increases process costs. These issues could be resolved with modification of the membrane, improvement of membrane setup, and regulation of the experimental parameters.

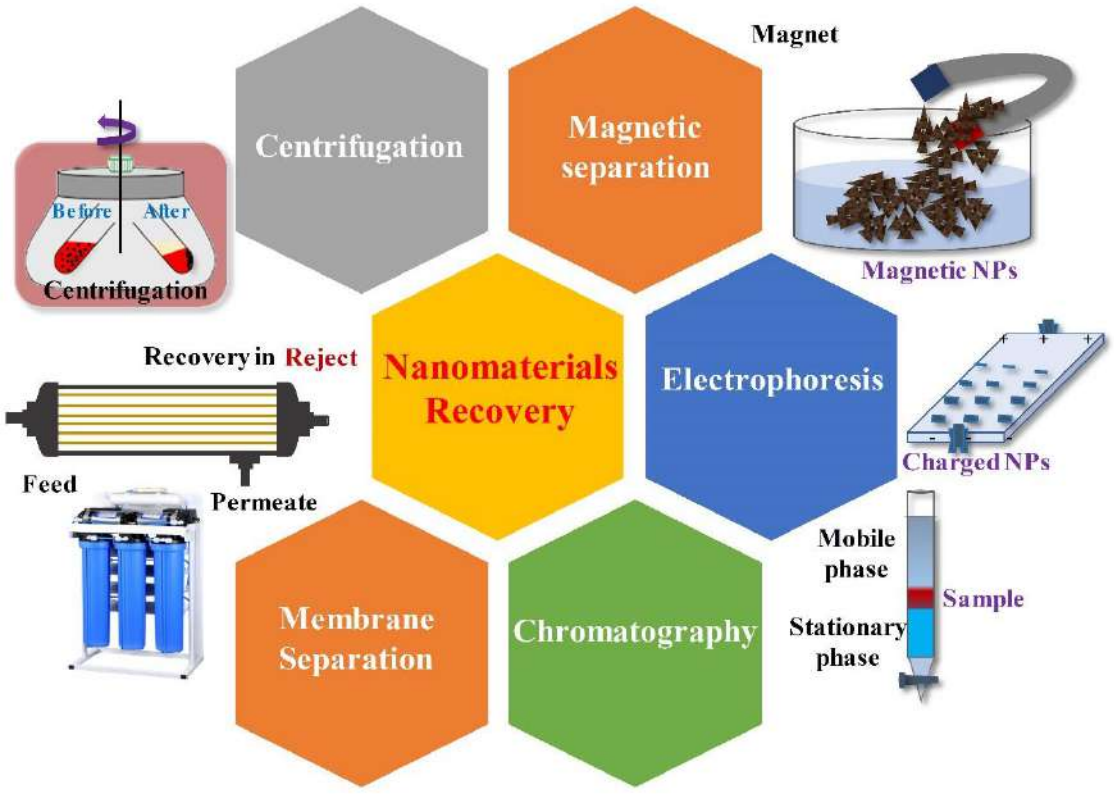

Figure 1.10: Schematic illustration of different techniques employed for the recovery of nanomaterials.

1.5.3 Membrane separation

1.5.3.1 Basic view of membrane separation

Membrane separation is a process that separates or removes specific substances from a heterogeneous mixture. In this process, the membrane allows the passage of specific materials based on their size, known as permeate, while rejecting other substances, known as retentant or reject (Qasem et al., 2021). In 1922, R. Zsigmondy invented the membrane-based filtration system (Peinador et al., 2020). However, it was not until the mid-1960s that membrane separation processes gained significant attention, particularly with the development of microfiltration and ultrafiltration membranes. Ultrafiltration membranes have been found to have various applications in various households and industries. The subsequent development of nanofiltration and reverse osmosis techniques further expanded the use of membrane-based separation techniques (Mehta et al., 2016). The membrane separation process has removed heavy metals, nanoparticles, debris, and microbes from municipal and industrial wastewater. On a household level, membrane separation is used to obtain drinking water by reducing its total dissolved solids (TDS) and removing other impurities. The membrane separation technique is usually a size-selective separation process that separates the particles based on

size. The porosity of the membrane allows the small-sized particles to pass across the membrane under applied pressure. In contrast, the large-sized particles either can make a cake over the membrane surface or come out as rejected (in the cross-flow membrane) (Mehta et al., 2016).

Dead-end filtration and cross-flow membranes are both utilized for separation. Still, the formation of a cake due to the settling of large particles can rapidly clog the membrane, particularly in dead-end filtration. Cross-flow membranes are more effective in reducing cake layer formation due to the tangent flow (Fig. 1.11). The efficiency of membrane separation is significantly influenced by operational and physicochemical parameters, including membrane porosity, transmembrane pressure, flow rate, pollutant concentration, membrane surface properties, solution pH, temperature, and ionic strength. Variations in these parameters can impact the flux, separation of pollutants, and cake layer thickness.

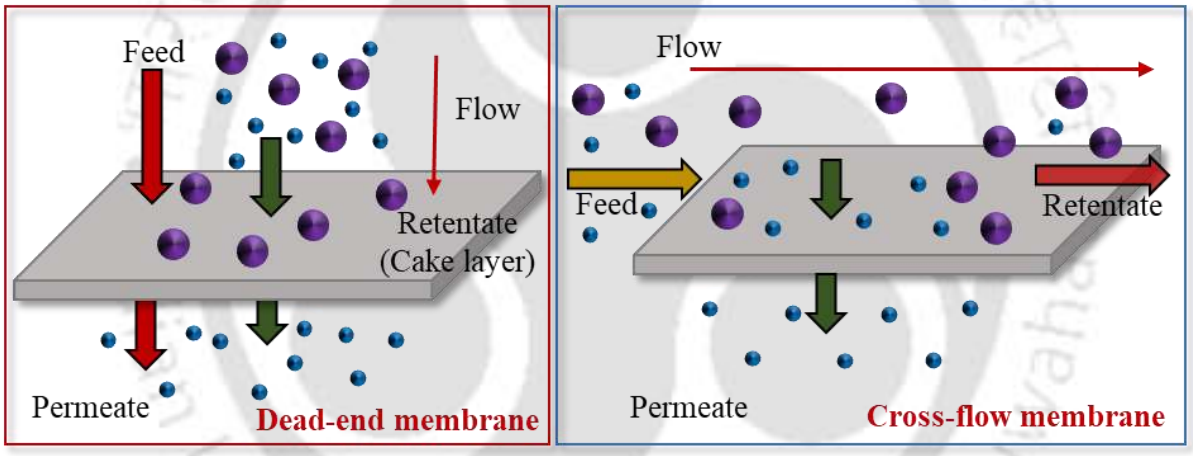

Figure 1.11: Graphical illustration of the operation of (a) dead-end membrane and (b) cross-flow membrane.

1.5.3.2 Literature survey of membrane separation

A literature summary on the utilization of the techniques mentioned above and various membranes for the recovery/separation of pollutants and nanoparticles is provided in Table 1.6. However, only a few studies were reported on the recovery of photocatalysts after the photocatalytic degradation process. Based on the pore size, the membrane techniques can be classified into microfiltration, ultrafiltration, nanofiltration, and reverse osmosis. Microfiltration (MF) is highly used to separate bacteria, debris, dead cell biomass, plant debris, etc., from contaminated water. Microfiltration effectively separates particles with sizes ranging from 0.1 to 10 µm. MF provides the highest flux among all membrane separation processes

and is employed in industries for the serial separation of large particles before ultra and nanofiltration processes. Despite its excellent flux at low pressure, MF membranes are limited to separating large particles (Yogarathinam et al., 2022).

Table 1.6: Literature summary on separation of utilization of different separation techniques for separation of nanoparticles.

Separation technique	Nanoparticle	Separation condition	Size (nm)	Sources
Centrifugation	Ag@Pt NPs	Speed: 14000 rpm; Time: 15 min	23.5	(Dash et al., 2020)
	Ag-doped ZnO	Speed: 4000 rpm; Time: 3 min	25-95	(Chelli and Golder, 2018)
	Ag NPs	Speed: 6000 rpm; Time: 2 h	25-235	(Kahnouji et al., 2019)
Chromatography	Au NPs	Detection: 560 nm; Retention time: 2.8 min	100	(Suthar et al., 2017)
	N/CNDs	Pressure: 150 psi	1.24-2.65	(Arcudi et al., 2016)
Magnetic separation	Li^{+}-Al^{3+}/Fe_3O_4	Time: 10 min	Ionic form	(Chen et al., 2020)
	Ag and Cu NPs by FeO	Time:30 min	9.23	(Hassan et al., 2021)
Electrophoresis	Au and AgNPs	Time:30 min; Potential: 150 V	20-40	(Hanauer et al., 2007)
	Au NPs	Time:30 min; Potential: 100 V	22	(Kim et al., 2013)
Membrane separation	Microplastics	Ceramic HF microporous membrane	<10	(Yogarathinam et al., 2022)
	ZnO NPs	UF membrane	20-100	(Mehta et al., 2016)
	Heavy metals		-	(Shi et al., 2022)
	Amino acids and small peptides	NF membrane	1-2	(Yu et al., 2022)
	NaCl	Ag/CNT coated RO membrane	-	(Zhao et al., 2021)

Ultrafiltration (UF) is a widely utilized membrane separation technique among various processes due to its suitability for recovering nanoparticles, viruses, large proteins, cell debris, and inner core components. UF membranes offer advantages such as high flux with low-pressure requirements (1-5 bar), efficient separation (>90%), a high permeate-to-reject ratio (up to 9:1), good retention of large particles, and a wide range of sizes for separation (10 – 1000 nm) (Li et al., 2018). Particles smaller than 100 nm present a challenge for separation

using traditional methods, making ultrafiltration (UF) membranes a significant advancement for pilot and industrial applications. Various studies have examined the efficiency of UF membranes for nanoparticle separation. Membrane clogging leads to a decrease in membrane flux and efficiency. However, the use of cross-flow UF membranes can address the clogging issue for an extended period by employing backflush techniques for membrane cleaning. The UF membrane has been utilized for efficient separation of bovine serum albumin (BSA, 92%), recovery of crude oil from waste (95%), removal of heavy metals (>91%), and recovery of ZnO (95-98%) (Mehta et al., 2016; G.N. and M., 2021; Peng et al., 2022; Shi et al., 2022).

The nanofiltration (NF) technique separates the particles within the 1-2 nm size range, including PhACs, small proteins, sugar, various salts, etc. Based on their application, two main types of NF membranes are aqueous NF and organic NF. Aqueous NF is suitable for hydrophilic particle separation, while organic NF separates hydrophobic compounds such as oil, fatty acids, and certain pharmaceuticals (Yu et al., 2022). Additionally, using NF membranes to remove salt and fatty acids instead of reverse osmosis membranes could provide better water flux with less reject volume. However, NF membranes may not be suitable for separating particles larger than 5 nm due to membrane clogging, lower volumetric flux, and higher-pressure requirements. On the other hand, reverse osmosis (RO) is a widely used process at the household and laboratory levels to generate drinking water and deionized water. In reverse osmosis, water moves across a semi-permeable membrane from an area of high concentration to an area of low concentration against the concentration gradient (Al-Abri et al., 2019). While reverse osmosis is commonly used on a smaller scale, its adoption at the industrial level has faced challenges due to the high volume of rejects, low volumetric flux, rapid fouling, and expensive maintenance.

Various separation techniques have been explored to recover nanoparticles and photocatalysts from untreated or treated wastewater. The cross-flow UF membrane, particularly the hollow fiber UF membrane, has been identified as highly efficient for separating nanoparticles, offering excellent permeate-to-reject ratios. UF membranes are known for providing better flux with less input power, are readily available in the market with different pore sizes, and exhibit high stability, making them resistant to PhACs and their by-products. Therefore, UF membranes are generally recommended to recover photocatalysts after the photocatalytic degradation.

1.6 Inferences from literature review, research gaps, and thesis objectives

In recent decades, industrial expansion has considerably intensified water pollution, posing serious risks to environmental and human health. Among the emerging contaminants, PhACs pose severe environmental and health threats due to their persistence, bioactivity, and ability to promote the development of antibiotic-resistant microorganisms and related health disorders. Therefore, an efficient and sustainable system is essential for treating PhACs wastewater. Photocatalysis has emerged as an eco-friendly and common degradation process. Numerous studies have demonstrated the photocatalytic activity of both chemically synthesized and bio-based photocatalysts under UV, visible, and solar irradiation. Recycling photocatalysts after photocatalytic degradation is also important to ensure material reusability and to reduce the risk of secondary water pollution. Among various separation methods described in Chapter 1, ultrafiltration membrane separation in particular is promising for efficiently recovering used photocatalysts. The key inferences from the literature can be summarized as follows:

- Antibiotics are among the most frequently detected and persistent pharmaceutical contaminants in wastewater, exhibiting high stability and low biodegradability. In addition, CLQ emerged as a widely consumed drug during the COVID-19 pandemic, leading to its increased presence in aquatic environments. Therefore, three different antibiotics such as CIP, FZD and AMX, along with CLQ were selected as model PhACs for degradation studies in this thesis.
- Photocatalyst limitations: Most studies utilize native, non-metal-doped, or transition metal-doped photocatalysts, primarily TiO_2 and ZnO, under UV or artificial visible light. However, their high bandgap energy and fast e^-/h^+ recombination restrict practical applications, underscoring the need for visible- and solar-light-responsive efficient doped photocatalysts.
- Noble metals such as Pt, Au, and Pd have been widely applied due to their stability, plasmonic activity, and recyclability. They improve photocatalytic efficiency by reducing charge recombination and narrowing the bandgap. Despite their cost, their stability and superior performance often justify their use. However, most reported doping techniques rely on chemically intensive and potentially hazardous methods. Therefore, noble metals such as Pt, Au, and Pd, were selected as model dopant for photocatalysts synthesis. Additionally, Ni-doping was included to provide a cost-effective alternative.

- Bio-based synthesis gap: Bio-mediated synthesis has been successfully explored for photocatalysts targeting dye degradation, its application to PhACs removal remains limited. Moreover, the incorporation of noble metals into photocatalysts via bio-based methods presents additional challenges and they are largely underexplored.
- Recovery methods: Conventional recovery approaches such as centrifugation, coagulation, chromatography, magnetic separation, and membrane filtration have been employed for nanoparticles recovery from contaminated water and their slurry/solutions. Nonetheless, recovery of photocatalysts from treated or partially treated wastewater has received limited attention.
- Limited to laboratory scale: Most investigations into photocatalyst recovery following degradation have been confined to laboratory-scale experiments with small reaction volumes (10–100 mL).
- Membrane system: Dead-end membrane systems are commonly used at laboratory scales for catalyst separation but they are prone to membrane fouling due to cake layer formation. As a solution, a cross-flow membrane configuration is proposed for efficient and scalable recovery of photocatalysts.
- Scale-up challenge: Most studies were conducted at lab scale (10-100 mL reactor), limiting the real-world application of photocatalysts. Additionally, most laboratory experiments employed batch reactors; therefore, continuous-flow systems for PhAC degradation remain largely unexplored. Pilot-scale studies are scanty, and it is imperative to validate the practical feasibility of the photocatalytic degradation process in a scaled-up reactor.

Therefore, the overall objectives of the study are summarized as:

- Development of visible light-driven noble metals (Pt, Au, Pd) and transition metal (Ni) doped TiO_2 photocatalysts via a bio-based route using plant bioanalytes **(Chapters 3–6)**
- Studies on the photocatalytic degradation of selected PhACs in a batch stirred photo-reactor **(Chapters 3–6)**
- Development of a zero-catalyst loss photocatalytic system for recycling of photocatalytic nanomaterials via membrane separation **(Chapter 7)**
- Development of a pilot-scale integrated treatment system for photocatalytic PhACs degradation, catalysts recovery, and biological degradation **(Chapter 8)**

1.7 Organization of the thesis

CHAPTER 1: Conceptual framework, literature review, and research objectives

This chapter lays the foundation of the study by introducing the background, significance, and current challenges related to PhACs pollution, which includes the global spread of PhACs in surface water, groundwater, domestic animals, and food sources, along with their risk for aquatic organisms. The subsequent risk of developing antimicrobial-resistant microbes is also emphasized, supported by a comprehensive literature survey that confirms their widespread presence. It presents a conceptual framework integrating the photocatalytic degradation approach using bio-based metal-doped photocatalysts along with photocatalyst recovery using a membrane system. The chapter critically reviews existing literature, identifies research gaps, and outlines the specific research objectives.

CHAPTER 2: Materials, experimental approaches and analytical techniques

This chapter outlines the materials used, preparation of vegetal extracts, and the synthesis of bio-based metal-doped TiO_2 photocatalysts, as detailed further in Chapters 3 to 6. It also describes the characterization techniques employed and the experimental setup utilized for the photocatalytic degradation of PhACs. Furthermore, the process of TiO_2 and Pt-doped TiO_2 recovery is described. A brief graphical representation of experimental processes described in Chapter 2 is illustrated in Fig. 2. The primary experimental steps and methodologies include (i) Preparation and quantification of vegetal extract, (ii) Bio-based synthesis of Pt-doped TiO_2, Au-doped TiO_2, Pd-doped TiO_2, and Ni-doped TiO_2 photocatalysts, (iii) Characterization of prepared photocatalysts, (iv) Photocatalytic degradation of PhACs using prepared metal-doped TiO_2 in a batch reactor at laboratory scale, and (v) Recovery of TiO_2 and Pt-doped TiO_2 through a membrane separation.

CHAPTER 3: A Bio-based process of Pt-doping onto TiO_2 for improved photocatalytic functionalities

This chapter presents the bio-based synthesis of Pt-doped TiO_2 using *S. edule* vegetal extract in a streamed autoclave. The study optimizes doping parameters to tune its structural and electronic properties. Comprehensive characterizations were performed to confirm enhanced photoelectrochemical and photocatalytic functionalities. The photocatalyst is evaluated for the degradation of ciprofloxacin (CIP) under visible light irradiation. The aquatic toxicity and antimicrobial activity of CIP before and after photodegradation were assessed.

CHAPTER 4: Bio-based Au-doped TiO_2 with dominant oxygen vacancies and Ti^{3+} defects for chloroquine photodegradation

Chapter 4 investigates on the bio-based synthesis of Au-doped TiO_2 using *S. edule* juice extract, emphasizing the reduced bandgap along with the formation of oxygen vacancies and Ti^{3+} defects. These intrinsic modifications are shown to enhance light absorption and charge separation efficiency. The prepared photocatalyst was utilized to degrade chloroquine under visible light irradiation. The degradation mechanism was also proposed, and the formed intermediates were analyzed for ecotoxicity assessment.

CHAPTER 5: Pd-doped TiO_2 with induced Ti^{3+} defects and oxygen vacancies for photocatalytic amoxicillin decomposition

This chapter investigates the effect of reduced bandgap, abundant Ti^{3+} defects, oxygen vacancies, and increased surface hydrophilicity on amoxicillin (AMX) photocatalytic degradation by using Pd-doped TiO_2 synthesized via a bio-based route utilizing banana peel extract. The density functional theory (DFT) calculations provide insight into its electronic structure and charge transfer behaviour. Additionally, the ecotoxicity assessment and antimicrobial activity of AMX and reaction intermediates were assessed.

CHAPTER 6: Bio-based synthesis of oxygen-deficient Ni-doped TiO_2 for photocatalytic degradation of furazolidone

In chapter 6, a bio-based Ni-doped TiO_2 photocatalyst was synthesized using waste pineapple peel extract by focusing on reduced bandgap, increased hydrophilicity, and abundant surface defects of Ti^{3+} and oxygen vacancies. The band structures and density of Ti, O, and Ni states were analyzed using DFT studies. The synthesized photocatalyst demonstrated superior photocatalytic degradation of furazolidone (FZD) than that of bare and chemical counterparts. The photodegradation process significantly reduced the aquatic toxicity and neutralized the antimicrobial activity.

CHAPTER 7: Efficient recovery of bare-TiO_2 and metal-doped TiO_2 using a pilot-scale cross-flow ultrafiltration system

In this chapter, the cross-flow ultrafiltration unit was employed for the recovery of TiO_2 and metal-doped TiO_2 photocatalysts. The operational parameters, such as pH, catalyst concentration, transmembrane pressure, and flow rate were optimized for recovery of catalysts. The recovery process was performed through forward flow and back-flush. Further, the

experimental and theoretical outputs of the recovery process were compared through modeling, and the recovered catalysts were characterized.

CHAPTER 8: Development of a pilot-scale integrated PhACs treatment system for photocatalytic degradation, catalysts recovery, and biological degradation

In the last chapter, a pilot-scale integrated photocatalytic and biological degradation reactor with an ultrafiltration membrane system was designed, fabricated, and installed at the rooftop of the Department of Chemical Engineering, IIT Guwahati, India. The integrated process possesses three different units: (i) Photocatalytic degradation unit: For photocatalytic degradation of PhACs under solar light, (ii) Membrane separation unit: For recovery of used photocatalysts using cross-flow ultrafiltration membrane, and (iii) Biological degradation unit: For microbial degradation of PhACs surviving the photocatalytic process and reaction intermediates.

The pilot-scale reactor was utilized for the photodegradation of synthetic PhACs wastewater containing individual PhACs and mixtures of various PhACs using bare-TiO_2, Pt-doped TiO_2, and Au-doped TiO_2 catalysts. Further, the hospital wastewater was collected and spiked with a mixture of five different PhACs. The spiked hospital wastewater was degraded in the integrated reactor with a reaction volume of 10 L. The degradation efficiency of all the photocatalysts was superior in the pilot-scale reactor than in the laboratory-scale reactor. The used photocatalysts were recovered by membrane filtration.

CHAPTER 9: Conclusions and future scopes of study

This chapter presents the key conclusions drawn from the study. The chapter also outlines limitations and proposes future research directions for sustainable applications for wastewater treatment.

References

A, S., Thamer, A., K, R., A, P., V, R., K, M., Murad, A., P, M., 2020. Facile one pot microwave-assisted green synthesis of Fe_2O_3/Ag nanocomposites by phytoreduction: Potential application as sunlight-driven photocatalyst, antibacterial and anticancer agent. J. Photochem. Photobiol. B Biol. 207, 111885. https://doi.org/10.1016/j.jphotobiol.2020.111885

Ahmad, W., Singh, A., Jaiswal, K.K., Gupta, P., 2021. Green synthesis of photocatalytic TiO_2

nanoparticles for potential application in photochemical degradation of ornidazole. J. Inorg. Organomet. Polym. Mater. 31(2), 614–623. https://doi.org/10.1007/s10904-020-01703-6

Ahmed, N.A., Elshahawy, M.F., Mohammed, R.D., Mahmoud, G.A., 2023. Removal of astrazon red dye from wastewater using eggshell/graphene oxide embed in (gum acacia/acrylamide) hydrogel nanocomposites synthesized by gamma irradiation. J. Inorg. Organomet. Polym. Mater. 33(4), 1561–1574. https://doi.org/10.1007/s10904-023-02775-w

Akbari, S., Moussavi, G., Giannakis, S., 2021. Efficient photocatalytic degradation of ciprofloxacin under UVA-LED, using S,N-doped MgO nanoparticles: Synthesis, parametrization and mechanistic interpretation. J. Mol. Liq. 324, 114831. https://doi.org/10.1016/j.molliq.2020.114831

Akiba, M., Senba, H., Otagiri, H., Prabhasankar, V.P., Taniyasu, S., Yamashita, N., Lee, K. ichi, Yamamoto, T., Tsutsui, T., Ian Joshua, D., Balakrishna, K., Bairy, I., Iwata, T., Kusumoto, M., Kannan, K., Guruge, K.S., 2015. Impact of wastewater from different sources on the prevalence of antimicrobial-resistant *Escherichia coli* in sewage treatment plants in South India. Ecotoxicol. Environ. Saf. 115, 21–27. https://doi.org/10.1016/j.ecoenv.2015.02.018

Al-Abri, M., Al-Ghafri, B., Bora, T., Dobretsov, S., Dutta, J., Castelletto, S., Rosa, L., Boretti, A., 2019. Chlorination disadvantages and alternative routes for biofouling control in reverse osmosis desalination. npj Clean Water. 2, 2 https://doi.org/10.1038/s41545-018-0024-8

Al-Ghouti, M.A., Da'ana, D., Abu-Dieyeh, M., Khraisheh, M., 2019. Adsorptive removal of mercury from water by adsorbents derived from date pits. Sci. Rep. 9, 1535. https://doi.org/10.1038/s41598-019-51594-y

Alam, J., Alhoshan, M., Dass, L.A., Shukla, A.K., Muthumareeswaran, M.R., Hussain, M., Aldwayyan, A.S., 2016. Atomic layer deposition of TiO_2 film on a polyethersulfone membrane: separation applications. J. Polym. Res. 23, 78. https://doi.org/10.1007/s10965-016-1063-9

Ali, M.M., Haque, M.J., Kabir, M.H., Kaiyum, M.A., Rahman, M.S., 2021. Nano synthesis of ZnO–TiO_2 composites by sol-gel method and evaluation of their antibacterial, optical and photocatalytic activities. Results Mater. 11, 100199. https://doi.org/10.1016/j.rinma.2021.100199

Ali, S., Babali, Singh, S., Singh, R., Tyagi, M., Pandey, R.P., 2021. Influence of multidrug

resistance bacteria in river Ganges in the stretch of Rishikesh to Haridwar. Environ. Challenges 3, 100068. https://doi.org/10.1016/j.envc.2021.100068

Almeida, A., De Mello-Sampayo, C., Lopes, A., Carvalho da Silva, R., Viana, P., Meisel, L., 2023. Predicted Environmental risk assessment of antimicrobials with increased consumption in portugal during the covid-19 pandemic; the groundwork for the forthcoming water quality survey. Antibiotics 12(4), 652. https://doi.org/10.3390/antibiotics12040652

Alsalmah, H.A., 2024. Green synthesis of copper doped bismuth oxide: A novel inorganic material for photocatalytic mineralization of Trypan blue dye. Inorg. Chem. Commun. 163, 112270. https://doi.org/10.1016/j.inoche.2024.112270

Altunterim, R., Vergili, I., 2022. Clofibric acid removal by ion exchange using a magnetic ion exchange resin: equilibrium, kinetics, reusability and characterisation. Int. J. Environ. Anal. Chem. 102(3), 643–662. https://doi.org/10.1080/03067319.2020.1799998

Alwared, A.I., Sulaiman, F.A., Raad, H., Al-Musawi, T.J., Mohammed, N.A., 2023. Ability of $FeNi_3/SiO_2/TiO_2$ nanocomposite to degrade amoxicillin in wastewater samples in solar light-driven processes. South African J. Bot. 153, 331–339. https://doi.org/10.1016/j.sajb.2022.12.031

Ansari, A., Nematollahi, D., 2018. A comprehensive study on the electrocatalytic degradation, electrochemical behavior and degradation mechanism of malachite green using electrodeposited nanostructured B-PbO_2 electrodes. Water Res. 144, 215–227. https://doi.org/10.1016/j.watres.2018.07.056

Arcudi, F., Dordevic, L., Prato, M., 2016. Synthesis, separation, and characterization of small and highly fluorescent nitrogen-doped carbon nanodots. Angew. Chemie - Int. Ed. 55(16), 4234–4238. https://doi.org/10.1002/anie.201510158

Aronne, A., Fantauzzi, M., Imparato, C., Atzei, D., De Stefano, L., D'Errico, G., Sannino, F., Rea, I., Pirozzi, D., Elsener, B., Pernice, P., Rossi, A., 2017. Electronic properties of TiO_2-based materials characterized by high Ti^{3+} self-doping and low recombination rate of electron-hole pairs. RSC Adv. 7, 54803–54814. https://doi.org/10.1039/c6ra27111a

Arumugam, J., Thambidurai, S., Suresh, S., Selvapandiyan, M., Kandasamy, M., Pugazhenthiran, N., Karthick Kumar, S., Muneeswaran, T., Quero, F., 2021. Green synthesis of zinc oxide nanoparticles using *Ficus carica* leaf extract and their bactericidal and photocatalytic performance evaluation. Chem. Phys. Lett. 783, 139040. https://doi.org/10.1016/j.cplett.2021.139040

Asnaashari Kahnouji, Y., Mosaddegh, E., Bolorizadeh, M.A., 2019. Detailed analysis of size-

separation of silver nanoparticles by density gradient centrifugation method. Mater. Sci. Eng. C 103, 109817. https://doi.org/10.1016/j.msec.2019.109817

Ayadi Hassan, S., Gorji, V., Ghadam, P., 2021. The efficient magnetic separation of the four biogenic nanoparticles from aqueous media by the unmodified iron oxide nanoparticles. Int. J. Environ. Sci. Technol. 18(6), 1343–1356. https://doi.org/10.1007/s13762-020-03113-0

Baig, N., Kammakakam, I., Falath, W., Kammakakam, I., 2021. Nanomaterials: A review of synthesis methods, properties, recent progress, and challenges. Mater. Adv. 2(6), 1821–1871. https://doi.org/10.1039/d0ma00807a

Banyal, R., sudhaik, A., kumar, R., Sonu, Raizada, P., Ahamad, T., Kaya, S., Maslov, M.M., Chaudhary, V., Hussain, C.M., Singh, P., 2024. Construction of novel BiOI/$CuInS_2$/ZnO Dual S-scheme charge transfer pathway for efficient antibiotic degradation. J. Phys. Chem. Solids 195, 112132. https://doi.org/10.1016/j.jpcs.2024.112132

Baran, W., Makowski, A., Wardas, W., 2005. The separation of catalyst after photocatalytic reactions conducted in the presence of TiO_2/$FeCl_3$/UV. Chemosphere 59(8), 1135–1141. https://doi.org/10.1016/j.chemosphere.2004.10.059

Berkani, M., Smaali, A., Kadmi, Y., Almomani, F., Vasseghian, Y., Lakhdari, N., Alyane, M., 2022. Photocatalytic degradation of Penicillin G in aqueous solutions: Kinetic, degradation pathway, and microbioassays assessment. J. Hazard. Mater. 421, 126719. https://doi.org/10.1016/j.jhazmat.2021.126719

Besharati, S., Motamedi, H., Zallaghi, R., 2018. A survey on microbial quality and antibiotic resistance in Karoon River, Khuzestan, Iran. Appl. Water Sci. 8, 146. https://doi.org/10.1007/s13201-018-0786-7

Bhan, C., Golder, A.K., 2023. Utilizing bioinspired AgNPs as an antibacterial agent to enhance ceramic membrane performance. J. Environ. Chem. Eng. 11(3), 110283. https://doi.org/10.1016/j.jece.2023.110283

Bhan, C., Kumar Golder, A., 2023. Bio-based hierarchical vertically aligned 2D ZnO nanostructures for ultra selective electrochemical sensing of p-Chloroaniline. Chem. Eng. J. 475, 146122. https://doi.org/10.1016/j.cej.2023.146122

Bhattacharyya, D., Banerjee, J., Bandyopadhyay, Samiran, Mondal, B., Nanda, P.K., Samanta, I., Mahanti, A., Das, A.K., Das, G., Dandapat, P., Bandyopadhyay, Subhasish, 2016. First report on vancomycin-resistant *staphylococcus aureus* in bovine and caprine milk. Microb. Drug Resist. 22(6), 454–461. https://doi.org/10.1089/mdr.2015.0330

Bopape, D.A., Motaung, D.E., Hintsho-Mbita, N.C., 2024. Biosynthesis of gold- and silver-

incorporated carbon-based zinc oxide nanocomposites for the photodegradation of textile dyes and various pharmaceuticals. Textiles 4(1), 8. https://doi.org/10.3390/textiles4010008

Browne, A.J., Chipeta, M.G., Haines-Woodhouse, G., Kumaran, E.P.A., Hamadani, B.H.K., Zaraa, S., Henry, N.J., Deshpande, A., Reiner, R.C., Day, N.P.J., Lopez, A.D., Dunachie, S., Moore, C.E., Stergachis, A., Hay, S.I., Dolecek, C., 2021. Global antibiotic consumption and usage in humans, 2000–18: a spatial modelling study. Lancet Planet. Heal. 5(7), e893–e903. https://doi.org/10.1016/S2542-5196(21)00280-1

Bumajdad, A., Madkour, M., 2014. Understanding the superior photocatalytic activity of noble metals modified titania under UV and visible light irradiation. Phys. Chem. Chem. Phys. 16(16), 7146–7158. https://doi.org/10.1039/c3cp54411g

Cardini, A., Pellegrino, E., Ercoli, L., 2021. Predicted and measured concentration of pharmaceuticals in surface water of areas with increasing anthropic pressure: A case study in the coastal area of central Italy. Water (Switzerland) 13(20), 2807. https://doi.org/10.3390/w13202807

Chaari, I., Fakhfakh, E., Medhioub, M., Jamoussi, F., 2019. Comparative study on adsorption of cationic and anionic dyes by smectite rich natural clays. J. Mol. Struct. 1179, 393–402. https://doi.org/10.1016/j.molstruc.2018.11.039

Chakraborty, A.K., Akter, S., Ganguli, S., Haque, M.A., Nur, A.S.M., Sabur, M.A., 2024. Design of $FeWO_4$@N-TiO_2 nanocomposite and its enhanced photocatalytic activity in decomposing methylene blue and phenol under visible light. Environ. Technol. Innov. 33, 103536. https://doi.org/10.1016/j.eti.2024.103536

Chalew, T.E.A., Halden, R.U., 2009. Environmental exposure of aquatic and terrestrial biota to triclosan and triclocarban. J. Am. Water Resour. Assoc. 45(1), 4–13. https://doi.org/10.1111/j.1752-1688.2008.00284.x

Chawla, A., Sudhaik, A., Sonu, Kumar, R., Raizada, P., Khan, A.A.P., Ahamad, T., Nguyen, V.H., Selvasembian, R., Kaushik, A., Singh, P., 2024. Recent advances in synthesis methods and surface structure manipulating strategies of copper selenide (CuSe) nanoparticles for photocatalytic environmental and energy applications, J. Environ. Chem. Eng. 12(4), 113125. https://doi.org/10.1016/j.jece.2024.113125

Chelli, V.R., Chakraborty, S., Golder, A.K., 2018. Ag-doping on TiO_2 using plant-based glycosidic compounds for high photonic efficiency degradative oxidation under visible light. J. Mol. Liq. 271, 566–575. https://doi.org/10.1016/j.molliq.2018.08.140

Chelli, V.R., Golder, A.K., 2018. Ag-doping on ZnO support mediated by bio-analytes rich in

ascorbic acid for photocatalytic degradation of dipyrone drug. Chemosphere 208, 149–158. https://doi.org/10.1016/j.chemosphere.2018.05.158

Chen, J., Lin, S., Yu, J., 2020. Quantitative effects of Fe_3O_4 nanoparticle content on Li^+ adsorption and magnetic recovery performances of magnetic lithium-aluminum layered double hydroxides in ultrahigh Mg/Li ratio brines. J. Hazard. Mater. 388, 122101. https://doi.org/10.1016/j.jhazmat.2020.122101

Chen, W., Zhang, W.J., Wang, K., Chang, L., Yan, R.Q., Xiong, X., Huang, G.B., Han, D.M., 2023. Oxygen vacancy-mediated $CuWO_4/CuBi_2O_4$ Samples with efficient charge transfer for enhanced catalytic activity toward photodegradation of pharmacologically active compounds. Langmuir 39(48), 17164–17178. https://doi.org/10.1021/acs.langmuir.3c02408

Cheng, G., Liu, X., Song, X., Chen, X., Dai, W., Yuan, R., Fu, X., 2020. Visible-light-driven deep oxidation of NO over Fe doped TiO_2 catalyst: Synergic effect of Fe and oxygen vacancies. Appl. Catal. B Environ. 277, 119196. https://doi.org/10.1016/j.apcatb.2020.119196

Cisneros, S., Chen, S., Diemant, T., Bansmann, J., Abdel-Mageed, A.M., Goepel, M., Olesen, S.E., Welter, E.S., Parlinska-Wojtan, M., Gläser, R., Chorkendorff, I., Behm, R.J., 2021. Effects of SiO_2-doping on high-surface-area Ru/TiO_2 catalysts for the selective CO methanation. Appl. Catal. B Environ. 282, 119483. https://doi.org/10.1016/j.apcatb.2020.119483

Corro, G., Sánchez, N., Pal, U., Cebada, S., Fierro, J.L.G., 2017. Solar-irradiation driven biodiesel production using Cr/SiO_2 photocatalyst exploiting cooperative interaction between Cr^{6+} and Cr^{3+} moieties. Appl. Catal. B Environ. 203, 321–331. https://doi.org/10.1016/j.apcatb.2016.10.005

Crini, G., Lichtfouse, E., 2019. Advantages and disadvantages of techniques used for wastewater treatment. Environ. Chem. Lett. 17(1), 145–173. https://doi.org/10.1007/s10311-018-0785-9

Czyrski, A., Anusiak, K., Teżyk, A., 2019. The degradation of levofloxacin in infusions exposed to daylight with an identification of a degradation product with HPLC-MS. Sci. Rep. 9, 16272. https://doi.org/10.1038/s41598-019-40201-9

Das, A., Guha, C., Biswas, U., Jana, P.S., Chatterjee, A., Samanta, I., 2017. Detection of emerging antibiotic resistance in bacteria isolated from subclinical mastitis in cattle in West Bengal. Vet. World 10(5), 517–520. https://doi.org/10.14202/vetworld.2017.517-520

Dash, S.R., Bag, S.S., Golder, A.K., 2020. Synthesis of highly structured spherical Ag@Pt core-shell NPs using bio-analytes for electrocatalytic Pb(II) sensing. Sensors Actuators, B Chem. 314, 128062. https://doi.org/10.1016/j.snb.2020.128062

Di, G., Zhu, Z., Dai, Q., Zhang, H., Shen, X., Qiu, Y., Huang, Y., Yu, J., Yin, D., Küppers, S., 2020. Wavelength-dependent effects of carbon quantum dots on the photocatalytic activity of g-C_3N_4 enabled by LEDs. Chem. Eng. J. 379, 122296. https://doi.org/10.1016/j.cej.2019.122296

Du, W., Sun, Y., Ji, R., Zhu, J., Wu, J., Guo, H., 2011. TiO_2 and ZnO nanoparticles negatively affect wheat growth and soil enzyme activities in agricultural soil. J. Environ. Monit. 13, 611–619. https://doi.org/10.1039/c0em00611d

El-Kemary, M., El-Shamy, H., El-Mehasseb, I., 2010. Photocatalytic degradation of ciprofloxacin drug in water using ZnO nanoparticles. J. Lumin. 130, 2243–2247. https://doi.org/10.1016/j.jlumin.2010.07.013

Elangovan, M., Bharathaiyengar, S.M., PonnanEttiyappan, J., 2021. Photocatalytic degradation of diclofenac using TiO_2-CdS heterojunction catalysts under visible light irradiation. Environ. Sci. Pollut. Res. 28(15), 18186–18200. https://doi.org/10.1007/s11356-020-11538-w

Fang, H., Oberoi, A.S., He, Z., Khanal, S.K., Lu, H., 2021. Ciprofloxacin-degrading Paraclostridium sp. isolated from sulfate-reducing bacteria-enriched sludge: Optimization and mechanism. Water Res. 191, 116808. https://doi.org/10.1016/j.watres.2021.116808

Fatimah, I., Purwiandono, G., Hidayat, H., Sagadevan, S., Ghazali, S.A.I.S.M., Oh, W.C., Doong, R.A., 2021. Flower-like SnO_2 nanoparticle biofabrication using pometia pinnata leaf extract and study on its photocatalytic and antibacterial activities. Nanomaterials 11(11), 3012. https://doi.org/10.3390/nano11113012

Fatimah, I., Yanti, I., Hana Afiyah Putri, F., Herianto, D., Sagadevan, S., Tamyiz, M., Doong, R. an, 2023. Phyto-mediated hydrothermal synthesis of $NiFe_2O_4$ as photocatalyst in tetracycline photodegradation. Environ. Nanotechnology, Monit. Manag. 20, 100879. https://doi.org/10.1016/j.enmm.2023.100879

Feng, N.X., Yu, J., Xiang, L., Yu, L.Y., Zhao, H.M., Mo, C.H., Li, Y.W., Cai, Q.Y., Wong, M.H., Li, Q.X., 2019. Co-metabolic degradation of the antibiotic ciprofloxacin by the enriched bacterial consortium XG and its bacterial community composition. Sci. Total Environ. 665, 1104–1112. https://doi.org/10.1016/j.scitotenv.2019.01.322

Fernandes dos Santos, F., Mendonça, L.C., Reis, D.R. de L., Guimarães, A. de S., Lange, C.C.,

Ribeiro, J.B., Machado, M.A., Brito, M.A.V.P., 2016. Presence of mecA-positive multidrug-resistant *Staphylococcus epidermidis* in bovine milk samples in Brazil. J. Dairy Sci. 99(2), 1222–1228. https://doi.org/10.3168/jds.2015-9931

Fick, J., Söderström, H., Lindberg, R.H., Phan, C., Tysklind, M., Larsson, D.G.J., 2009. Contamination of surface, ground, and drinking water from pharmaceutical production. Environ. Toxicol. Chem. 28(12), 2522–2532. https://doi.org/10.1897/09-073.1

Flach, C.F., Johnning, A., Nilsson, I., Smalla, K., Kristiansson, E., Larsson, D.G.J., 2015. Isolation of novel IncA/C and IncN fluoroquinolone resistance plasmids from an antibiotic-polluted lake. J. Antimicrob. Chemother. 70(10), 2669–2676. https://doi.org/10.1093/jac/dkv167

G.N., M., M., H.K., 2021. Performance studies of GO/PF127 incorporated Polyetherimide Ultrafiltration membranes for the rejection of oil from oil wastewater. Chem. Eng. Res. Des. 168, 217–225. https://doi.org/10.1016/j.cherd.2021.01.019

Garcia, B.B., Lourinho, G., Romano, P., Brito, P.S.D., 2020. Photocatalytic degradation of swine wastewater on aqueous TiO_2 suspensions: optimization and modeling via Box-Behnken design. Heliyon 6(7), e03293. https://doi.org/10.1016/j.heliyon.2020.e03293

Gawande, M.B., Goswami, A., Felpin, F.X., Asefa, T., Huang, X., Silva, R., Zou, X., Zboril, R., Varma, R.S., 2016. Cu and Cu-Based Nanoparticles: Synthesis and Applications in Catalysis. Chem. Rev. 116(5), 3722–3811. https://doi.org/10.1021/acs.chemrev.5b00482

Ghosh, P., Chelli, V.R., Giri, A.S., Golder, A.K., 2018. Steroid glycosides as potential analytes for Cu-doping on TiO_2 for photocatalytic water treatment. Environ. Prog. Sustain. Energy 37(1), 315–323. https://doi.org/10.1002/ep.12879

Giri, A.S., Golder, A.K., 2014. Fenton, photo-fenton, H_2O_2 Photolysis, and TiO_2 Photocatalysis for Dipyrone Oxidation: Drug Removal, Mineralization, Biodegradability, and Degradation Mechanism. Ind. Eng. Chem. Res. 53(23), 9673–9684. https://doi.org/10.1021/ie402279q

Godoy, A.A., Kummrow, F., Pamplin, P.A.Z., 2015. Ecotoxicological evaluation of propranolol hydrochloride and losartan potassium to *Lemna minor L.* (1753) individually and in binary mixtures. Ecotoxicology 24(7), 1128–1140. https://doi.org/10.1007/s10646-015-1455-3

Gogoi, D., Namdeo, A., Golder, A.K., Peela, N.R., 2020. Ag-doped TiO_2 photocatalysts with effective charge transfer for highly efficient hydrogen production through water splitting. Int. J. Hydrogen Energy 45(4), 2729–2744. https://doi.org/10.1016/j.ijhydene.2019.11.127

Golder, A.K., Chauhan, S., Ravi, R., 2021. Synthesis of low-cost bentonite/Duranta erecta's fruit powder imbedded alginate beads and its application in surfactant removal. Environ. Sci. Pollut. Res. 28(50), 58945–58957. https://doi.org/10.1007/s11356-021-14306-6

Gomes, R.P., Oliveira, T.R., Rodrigues, A.B., Ferreira, L.M., Vieira, J.D.G., Carneiro, L.C., 2023. Occurrence of antibiotic resistance genes, antibiotics-resistant and multi-resistant bacteria and their correlations in one river in central-western Brazil. Water (Switzerland) 15(4), 762. https://doi.org/10.3390/w15040747

Gopal, C.M., Bhat, K., Ramaswamy, B.R., Kumar, V., Singhal, R.K., Basu, H., Udayashankar, H.N., Vasantharaju, S.G., Praveenkumarreddy, Y., Shailesh, Lino, Y., Balakrishna, K., 2021. Seasonal occurrence and risk assessment of pharmaceutical and personal care products in Bengaluru rivers and lakes, India. J. Environ. Chem. Eng. 9(6), 106189. https://doi.org/10.1016/j.jece.2021.105610

Guerra, P., Kim, M., Shah, A., Alaee, M., Smyth, S.A., 2014. Occurrence and fate of antibiotic, analgesic/anti-inflammatory, and antifungal compounds in five wastewater treatment processes. Sci. Total Environ. 473–474, 235-243. https://doi.org/10.1016/j.scitotenv.2013.12.008

Hamidian, K., Najafidoust, A., Miri, A., Sarani, M., 2021. Photocatalytic performance on degradation of Acid Orange 7 dye using biosynthesized un-doped and Co doped CeO_2 nanoparticles. Mater. Res. Bull. 138, 111206. https://doi.org/10.1016/j.materresbull.2021.111206

Hanauer, M., Pierrat, S., Zins, I., Lotz, A., Sönnichsen, C., 2007. Separation of nanoparticles by gel electrophoresis according to size and shape. Nano Lett. 7(9), 2881–2885. https://doi.org/10.1021/nl071615y

Hassaan, M.A., Meky, A.I., Fetouh, H.A., Ismail, A.M., El Nemr, A., 2024. Central composite design and mechanism of antibiotic ciprofloxacin photodegradation under visible light by green hydrothermal synthesized cobalt-doped zinc oxide nanoparticles. Sci. Rep. 14(1), 9144. https://doi.org/10.1038/s41598-024-58961-4

He, J., Wang, Y., Xie, X., Qi, K., Yuan, Y., Dong, W., Wang, Z., 2024. N-CQDs modified BiOBr with different nitrogen configurations synthesized from different precursors for efficient photocatalytic degradation of carbamazepine. Sep. Purif. Technol. 335, 126124. https://doi.org/10.1016/j.seppur.2023.126124

Helmy, E.T., Abouellef, E.M., Soliman, U.A., Pan, J.H., 2021. Novel green synthesis of S-doped TiO_2 nanoparticles using Malva parviflora plant extract and their photocatalytic, antimicrobial and antioxidant activities under sunlight illumination. Chemosphere 271,

129524. https://doi.org/10.1016/j.chemosphere.2020.129524

Hoa, D.T.N., Tu, N.T.T., Thinh, H.Q.A., Van Thanh Son, L., Son, L.V.T., Quyen, N.D.V., Son, L.L., Tuyen, T.N., Thong, P.L.M., Diem, L.H., Khieu, D.Q., 2023. TiO_2/g-$_3N_4$ Visible-light-driven photocatalyst for methylene blue decomposition. 1–15, 9967890. J. Nanomater. 2023. https://doi.org/10.1155/2023/9967890

Honda, R., Matsuura, N., Sorn, S., Asakura, S., Morinaga, Y., Van Huy, T., Sabar, M.A., Masakke, Y., Hara-Yamamura, H., Watanabe, T., 2023. Transition of antimicrobial resistome in wastewater treatment plants: impact of process configuration, geographical location and season. npj Clean Water 6, 1–12. https://doi.org/10.1038/s41545-023-00261-x

Honda, R.J., Keene, V., Daniels, L., Walker, S.L., 2014. Removal of TiO_2 nanoparticles during primary water treatment: Role of coagulant type, dose, and nanoparticle concentration. Environ. Eng. Sci. 31(3), 127–134. https://doi.org/10.1089/ees.2013.0269

Hori, T., Owusu, Y.B., Sun, D., 2022. US FDA-Approved Antibiotics During the 21st Century, in: Encyclopedia of Infection and Immunity. https://doi.org/10.1016/B978-0-12-818731-9.00144-0

Hossain, A., Nakamichi, S., Habibullah-Al-Mamun, M., Tani, K., Masunaga, S., Matsuda, H., 2018. Occurrence and ecological risk of pharmaceuticals in river surface water of Bangladesh. Environ. Res. 165, 258–266. https://doi.org/10.1016/j.envres.2018.04.030

Hou, L., Xia, J., Li, K., Chen, J., Wu, X., Li, X., 2013. Removal of ZnO nanoparticles in simulated wastewater treatment processes and its effects on COD and NH_4^+-N reduction. Water Sci. Technol. 67(2), 254–260. https://doi.org/10.2166/wst.2012.530

Huong, V.T., Duc, B. Van, An, N.T., Anh, T.T.P., Aminabhavi, T.M., Vasseghian, Y., Joo, S.W., 2024. 3D-Printed WO_3-UiO-66@reduced graphene oxide nanocomposites for photocatalytic degradation of sulfamethoxazole. Chem. Eng. J. 483, 149277. https://doi.org/10.1016/j.cej.2024.149277

Ijaz, I., Gilani, E., Nazir, A., Bukhari, A., 2020. Detail review on chemical, physical and green synthesis, classification, characterizations and applications of nanoparticles. Green Chem. Lett. Rev. 13(3), 223–254. https://doi.org/10.1080/17518253.2020.1802517

Jahdi, M., Mishra, S.B., Nxumalo, E.N., Mhlanga, S.D., Mishra, A.K., 2020. Smart pathways for the photocatalytic degradation of sulfamethoxazole drug using F-Pd co-doped TiO_2 nanocomposites. Appl. Catal. B Environ. 267, 118716. https://doi.org/10.1016/j.apcatb.2020.118716

Jia, Y., Khanal, S.K., Shu, H., Zhang, H., Chen, G.H., Lu, H., 2018. Ciprofloxacin degradation

in anaerobic sulfate-reducing bacteria (SRB) sludge system: Mechanism and pathways. Water Res. 136, 64–74. https://doi.org/10.1016/j.watres.2018.02.057

Jones, B.M.F., Mamba, G., Maruthamani, D., Muthuraj, V., 2022. Honeycomb Nb_2O_5/RGO wrapped on MoO_3 nanorods for visible light-driven degradation of sulfasalazine and ciprofloxacin in water. Colloids Surfaces A Physicochem. Eng. Asp. 653, 129836. https://doi.org/10.1016/j.colsurfa.2022.129836

Karthik, K. V., Raghu, A. V., Reddy, K.R., Ravishankar, R., Sangeeta, M., Shetti, N.P., Reddy, C.V., 2022. Green synthesis of Cu-doped ZnO nanoparticles and its application for the photocatalytic degradation of hazardous organic pollutants. Chemosphere 287, 132081. https://doi.org/10.1016/j.chemosphere.2021.132081

Khalid, N.R., Sabir, M., Ali, F., Tahir, M.B., Javid, M.A., Niaz, N.A., Ahmed, R., Rafique, M., Imran, M., Assiri, M.A., 2023. Green synthesis and characterizations of bi-functional Mo-doped ZnO nanostructures for antimicrobial and photocatalytic applications. Mater. Chem. Phys. 296, 127306. https://doi.org/10.1016/j.matchemphys.2023.127306

Kibuye, F.A., Gall, H.E., Elkin, K.R., Ayers, B., Veith, T.L., Miller, M., Jacob, S., Hayden, K.R., Watson, J.E., Elliott, H.A., 2019. Fate of pharmaceuticals in a spray-irrigation system: From wastewater to groundwater. Sci. Total Environ. 654, 514–523. https://doi.org/10.1016/j.scitotenv.2018.10.442

Kim, J.Y., Kim, H.B., Jang, D.J., 2013. Electrophoretic separation of gold nanoparticles according to bifunctional molecules-induced charge and size. Electrophoresis 34(10), 1495–1502. https://doi.org/10.1002/elps.201200492

Koju, P., Shrestha, R., Shrestha, Abha, Tamrakar, S., Rai, A., Shrestha, P., Madhup, S.K., Katuwal, N., Shrestha, Archana, Shrestha, Akina, Shrestha, S., K.C, S., Karki, P., Tamang, P., Thekkur, P., Shakya Shrestha, S., 2022. Antimicrobial Resistance in *E. coli* isolated from chicken cecum samples and factors contributing to antimicrobial resistance in Nepal. Trop. Med. Infect. Dis. 7(9), 249. https://doi.org/10.3390/tropicalmed7090249

Kumar, A., Kumar, Abhishek, Prasad, K.S., 2021. Antibiotic-resistant bacteria in municipal sewage water joining river Ganga, at Prayagraj (India). Gene Reports 23, 101175. https://doi.org/10.1016/j.genrep.2021.101175

Kumar, M., Negi, K., Umar, A., Chauhan, M.S., 2021. Photocatalytic and fluorescent chemical sensing applications of La-doped ZnO nanoparticles. Chem. Pap. 75(9), 4703–4714. https://doi.org/10.1007/s11696-020-01388-8

Kumar, M., Ram, B., Honda, R., Poopipattana, C., Canh, V.D., Chaminda, T., Furumai, H., 2019. Concurrence of antibiotic resistant bacteria (ARB), viruses, pharmaceuticals and

personal care products (PPCPs) in ambient waters of Guwahati, India: Urban vulnerability and resilience perspective. Sci. Total Environ. 693, 133640. https://doi.org/10.1016/j.scitotenv.2019.133640

Kumar, N., Bhadwal, A.S., Mizaikoff, B., Singh, S., Kranz, C., 2019. Electrochemical detection and photocatalytic performance of MoS_2/TiO_2 nanocomposite against pharmaceutical contaminant: Paracetamol. Sens. Bio-Sensing Res. 24, 10028. https://doi.org/10.1016/j.sbsr.2019.100288

Kumar, R., Sudhaik, A., Sonu, Raizada, P., Nguyen, V.H., Van Le, Q., Ahamad, T., Thakur, S., Hussain, C.M., Singh, P., 2023. Integrating K and P co-doped g-C_3N_4 with $ZnFe_2O_4$ and graphene oxide for S-scheme-based enhanced adsorption coupled photocatalytic real wastewater treatment. Chemosphere 337, 139267. https://doi.org/10.1016/j.chemosphere.2023.139267

Kumari, P., Das, R.K., Pal, B., 2021. Enhanced photocatalytic degradation of eco-toxic pharmaceutical waste diclofenac sodium by anion loaded Cu-Al LDH·Bi_2O_3 composites. J. Taiwan Inst. Chem. Eng. 129, 104172. https://doi.org/10.1016/j.jtice.2021.07.023

Leigue, L., Montiani-Ferreira, F., Moore, B.A., 2016. Antimicrobial susceptibility and minimal inhibitory concentration of *Pseudomonas aeruginosa* isolated from septic ocular surface disease in different animal species. 6(3), 215–220. https://doi.org/10.4314/ovj.v6i3.9

Leite, R.S., Santos, A.M.C., Severo, L.L., Duarte Neto, J.F., Castellano, L.R.C., Neves, G.A., Lira, H.L., Menezes, R.R., 2020. Photocatalytic degradation of dyes and microorganism inactivation using solution blow spun silver-modified titania fibers. Ceram. Int. 46(9), 14065–14075. https://doi.org/10.1016/j.ceramint.2020.02.132

Li, G., Lv, L., Fan, H., Ma, J., Li, Y., Wan, Y., Zhao, X.S., 2010. Effect of the agglomeration of TiO_2 nanoparticles on their photocatalytic performance in the aqueous phase. J. Colloid Interface Sci. 348(1), 342–347. https://doi.org/10.1016/j.jcis.2010.04.045

Li, M., Lin, D., Zhu, L., 2013. Effects of water chemistry on the dissolution of ZnO nanoparticles and their toxicity to Escherichia coli. Environ. Pollut. 173, 97–102. https://doi.org/10.1016/j.envpol.2012.10.026

Li, S., Chen, J., Hu, S., Wang, H., Jiang, W., Chen, X., 2020. Facile construction of novel Bi_2WO_6/Ta_3N_5 Z-scheme heterojunction nanofibers for efficient degradation of harmful pharmaceutical pollutants. Chem. Eng. J. 402, 126165. https://doi.org/10.1016/j.cej.2020.126165

Li, X., Jiang, L., Li, H., 2018. Application of ultrafiltration technology in water treatment. IOP Conf. Ser. Earth Environ. Sci. 186(3), 012009. https://doi.org/10.1088/1755-

1315/186/3/012009

Li, X., Wang, S., Ye, D., Wen, W., Li, H., Ma, Z., Li, G., Fu, W., Fu, M., 2024. g-C_3N_4/metal-organic framework nanosheet/CuO heterostructure for the visible photocatalytic degradation of tetracycline. ACS Appl. Nano Mater. 7(1), 1104–1116. https://doi.org/10.1021/acsanm.3c04508

Linden, R., Antunes, M. V., Heinzelmann, L.S., Fleck, J.D., Staggemeier, R., Fabres, R.B., Vecchia, A.D., Nascimento, C.A., Spilki, F.R., 2015. Caffeine as an indicator of human fecal contamination in the Sinos River: A preliminary study. Brazilian J. Biol. 75(2), 427–431. https://doi.org/10.1590/1519-6984.0513

Liu, J., Kang, Y., Yin, S., Song, B., Wei, L., Chen, L., Shao, L., 2017. Zinc oxide nanoparticles induce toxic responses in human neuroblastoma SHSY5Y cells in a size-dependent manner. Int. J. Nanomedicine 12, 8085–8099. https://doi.org/10.2147/IJN.S149070

Ma, R., Wang, B., Yin, L., Zhang, Y., Deng, S., Huang, J., Wang, Y., Yu, G., 2017. Characterization of pharmaceutically active compounds in Beijing, China: Occurrence pattern, spatiotemporal distribution and its environmental implication. J. Hazard. Mater. 323, 147–155. https://doi.org/10.1016/j.jhazmat.2016.05.030

Machado, A., Bordalo, A.A., 2014. Prevalence of antibiotic resistance in bacteria isolated from drinking well water available in Guinea-Bissau (West Africa). Ecotoxicol. Environ. Saf. 106, 26–31. https://doi.org/10.1016/j.ecoenv.2014.04.037

Mahmud, M.S., Hosen, M.A., Hossion, M.I., Sadik Sabuj, M.S., Rumi, N.A., Hossain, M.K., Dauelbait, M., Nafidi, H.A., Dawoud, T.M., Ibrahim, M., Bourhia, M., 2023. Isolation, identification, and characterization of resistant bacteria to antibiotics from pharmaceutical effluent and study of their antibiotic resistance. Front. Microbiol. 14, 1307291. https://doi.org/10.3389/fmicb.2023.1307291

Marathe, N.P., Gaikwad, S.S., Vaishampayan, A.A., Rasane, M.H., Shouche, Y.S., Gade, W.N., 2016. Mossambicus tilapia (*Oreochromis mossambicus*) collected from water bodies impacted by urban waste carries extended-spectrum beta-lactamases and integron-bearing gut bacteria. J. Biosci. 41(4), 527–536. https://doi.org/10.1007/s12038-016-9620-2

Mariappan, A., Harikrishnan, L., Eswaran, J., Arumugham, N., Balasubramaniam, Y., Daniel, S., Kanthapazham, R., 2024. Green synthesis of metal-doped ZnO nanoparticles using *Bauhinia racemosa lam.* extract and evaluation of their photocatalysis and biomedical applications. ACS Appl. Bio Mater. 7(6), 2519–2532. https://doi.org/10.1021/acsabm.4c00132

Mehta, N., Basu, S., Kumar, A., 2016. Separation of zinc oxide nanoparticles in water stream by membrane filtration. J. Water Reuse Desalin. 6(2), 219–228. https://doi.org/10.2166/wrd.2015.069

Mirsadeghi, S., Zandavar, H., Rajabi, H.R., Sajadiasl, F., Ganjali, M.R., Pourmortazavi, S.M., 2021. Superior degradation of organic pollutants and H_2O_2 generation ability on environmentally-sound constructed Fe_3O_4-Cu nanocomposite. J. Mater. Res. Technol. 14, 2393–2406. https://doi.org/10.1016/j.jmrt.2021.07.007

Mohamad, N.A., Hamzah, S., Che Harun, M.H., Ali, A., Rasit, N., Awang, M., Rahman, W.R.W.A., Azmi, A.A.A.R., Abu Habib, A.A., Amri Zahid, M.S., Fahmi Mustofa, A.A., Latfi, S.A., Aripin, S.M., Saad, R., 2021. Integration of copperas and calcium hydroxide as a chemical coagulant and coagulant aid for efficient treatment of palm oil mill effluent. Chemosphere 281, 130873. https://doi.org/10.1016/j.chemosphere.2021.130873

Mullamuri, B., Sai Sriram Mosali, V., Maseed, H., Majety, S.S., Chandu, B., 2021. Photocatalytic activity of heavy metal doped Cds nanoparticles synthesized by using *Ocimum sanctum* leaf extract. Biointerface Res. Appl. Chem. 11(5), 12547–12559. https://doi.org/10.33263/BRIAC115.1254712559

Munyai, S., Tetana, Z.N., Mathipa, M.M., Ntsendwana, B., Hintsho-Mbita, N.C., 2021. Green synthesis of cadmium sulphide nanoparticles for the photodegradation of Malachite green dye, Sulfisoxazole and removal of bacteria. Optik (Stuttg). 247, 167851. https://doi.org/10.1016/j.ijleo.2021.167851

Mutiyar, P.K., Gupta, S.K., Mittal, A.K., 2018. Fate of pharmaceutical active compounds (PhACs) from River Yamuna, India: An ecotoxicological risk assessment approach. Ecotoxicol. Environ. Saf. 150, 297–304. https://doi.org/10.1016/j.ecoenv.2017.12.041

Naeimi, A., Honarmand, M., Ali Chaji, M., Khosravi, S., 2022. Green synthesis of bentonite/cellulose@lead oxide bio-nanocomposite with assistance of *Pistacia atlantica* extract for efficient photocatalytic degradation of ciprofloxacin. Adv. Powder Technol. 33, 103441. https://doi.org/10.1016/j.apt.2022.103441

Nazim, M., Khan, A.A.P., Asiri, A.M., Kim, J.H., 2021. Exploring rapid photocatalytic degradation of organic pollutants with porous CuO nanosheets: Synthesis, dye removal, and kinetic studies at room temperature. ACS Omega 6(2), 1217–1227. https://doi.org/10.1021/acsomega.0c04747

Nguyen Dang Giang, C., Sebesvari, Z., Renaud, F., Rosendahl, I., Hoang Minh, Q., Amelung, W., 2015. Occurrence and dissipation of the antibiotics sulfamethoxazole, sulfadiazine, trimethoprim, and enrofloxacin in the Mekong Delta, Vietnam. PLoS One 10(7),

e0131855. https://doi.org/10.1371/journal.pone.0131855

Nguyen, T.H.A., Le, V.T., Doan, V.D., Tran, A.V., Nguyen, V.C., Nguyen, A.T., Vasseghian, Y., 2022. Green synthesis of Nb-doped ZnO nanocomposite for photocatalytic degradation of tetracycline antibiotic under visible light. Mater. Lett. 308, 131129. https://doi.org/10.1016/j.matlet.2021.131129

Nigussie, G.Y., Tesfamariam, G.M., Tegegne, B.M., Weldemichel, Y.A., Gebreab, T.W., Gebrehiwot, D.G., Gebremichel, G.E., 2018. Antibacterial activity of Ag-Doped TiO_2 and Ag-Doped ZnO nanoparticles. Int. J. Photoenergy 2018, 5927485. https://doi.org/10.1155/2018/5927485

Nikpay, M., 2022. Wastewater fines influence the adsorption behavior of pollutants onto microplastics. J. Polym. Environ. 30(3), 1054–1063. https://doi.org/10.1007/s10924-021-02243-x

Oldenkamp, R., Beusen, A.H.W., Huijbregts, M.A.J., 2019. Aquatic risks from human pharmaceuticals - modelling temporal trends of carbamazepine and ciprofloxacin at the global scale. Environ. Res. Lett. 14(3), 034017. https://doi.org/10.1088/1748-9326/ab0071

Paghaleh, E.S., Dashtian, K., Seyf, J.Y., Seidi, F., Kolvari, E., 2023. Green synthesis of stable $CuFe_2O_4$/CuO-rGO heterostructure photocatalyst using basil seeds as chemo-reactors for improved oxytetracycline degradation. J. Environ. Chem. Eng. 11, 110676. https://doi.org/10.1016/j.jece.2023.110676

Park, S., Choi, K., 2008. Hazard assessment of commonly used agricultural antibiotics on aquatic ecosystems. Ecotoxicology 17(5), 526–538. https://doi.org/10.1007/s10646-008-0209-x

Patel, M., Kumar, R., Kishor, K., Mlsna, T., Pittman, C.U., Mohan, D., 2019. Pharmaceuticals of emerging concern in aquatic systems: Chemistry, occurrence, effects, and removal methods. Chem. Rev. 119(2), 3510–3673. https://doi.org/10.1021/acs.chemrev.8b00299

Patial, S., Kumar, R., Sudhaik, A., Sonu, Thakur, S., Kumar, N., Ahamad, T., Kaya, S., Hussain, C.M., Singh, P., Raizada, P., 2024. A novel NH_2-MIL-125/dandelion-like MnO_2 nanosphere composite with a rapid interfacial electron transfer pathway for photocatalytic degradation of ornidazole. Solid State Sci. 153, 107576. https://doi.org/10.1016/j.solidstatesciences.2024.107576

Peinador, R.I., Kaabouch, M., Aim, R. Ben, Calvo, J.I., 2020. Non-destructive characterization of industrial membrane cartridges by using liquid–liquid displacement porosimetry (LLDP). Membranes (Basel). 10(12), 369. https://doi.org/10.3390/membranes10120369

Peña-Velasco, G., Hinojosa-Reyes, L., Morán-Quintanilla, G.A., Hernández-Ramírez, A., Villanueva-Rodríguez, M., Guzmán-Mar, J.L., 2021. Synthesis of heterostructured catalyst coupling MOF derived Fe_2O_3 with TiO_2 for enhanced photocatalytic activity in anti-inflammatory drugs mixture degradation. Ceram. Int. 47(16), 22902–22912. https://doi.org/10.1016/j.ceramint.2021.05.185

Peng, G., Yaoqin, W., Changmei, S., Chunnuan, J., Ying, Z., Rongjun, Q., Ying, W., 2022. Preparation and properties of PVC-based ultrafiltration membrane reinforced by in-situ synthesized p-aramid nanoparticles. J. Memb. Sci. 642, 119993. https://doi.org/10.1016/j.memsci.2021.119993

Pezzoni, M., Catalano, P.N., Delgado, D.C., Pizarro, R.A., Bellino, M.G., Costa, C.S., 2020. Antibiofilm effect of mesoporous titania coatings on *Pseudomonas aeruginosa* biofilms. J. Photochem. Photobiol. B Biol. 203, 111762. https://doi.org/10.1016/j.jphotobiol.2019.111762

Pino, E., Calderón, C., Herrera, F., Cifuentes, G., Arteaga, G., 2020. Photocatalytic degradation of aqueous rhodamine 6G using supported tio_2 catalysts. a model for the removal of organic contaminants from aqueous samples. Front. Chem. 8, 365. https://doi.org/10.3389/fchem.2020.00365

Preethirani, P.L., Isloor, S., Sundareshan, S., Nuthanalakshmi, V., Deepthikiran, K., Sinha, A.Y., Rathnamma, D., Prabhu, K.N., Sharada, R., Mukkur, T.K., Hegde, N.R., 2015. Isolation, biochemical and molecular identification, and in-vitro antimicrobial resistance patterns of bacteria isolated from bubaline subclinical mastitis in South India. PLoS One 10(12), e0142717. https://doi.org/10.1371/journal.pone.0142717

Priyadharsan, A., Kamaraj, C., Ranjith, R., Sivakumar, S., Dewiani, R.Y., Muqoyyanah, Thammasak, R., Periyasami, G., Murni, H., 2024. Synthesis of multifunctional rGO/g-C_3N_4/$FeTiO_3$ ternary nanocomposites for photocatalyst, antibacterial, and ecotoxicity assessment of zebrafish embryo model. J. Alloys Compd. 1007, 176256. https://doi.org/10.1016/j.jallcom.2024.176256

Qasem, N.A.A., Mohammed, R.H., Lawal, D.U., 2021. Removal of heavy metal ions from wastewater: a comprehensive and critical review. npj Clean Water. 4(1), 36. https://doi.org/10.1038/s41545-021-00127-0

Qiu, Y., Lu, J., Yan, Y., Niu, J., 2022. Enhanced visible-light-driven photocatalytic degradation of tetracycline by 16% Er^{3+}-Bi_2WO_6 photocatalyst. J. Hazard. Mater. 422, 126920. https://doi.org/10.1016/j.jhazmat.2021.126920

Ramírez, A.E., Montero-Muñoz, M., López, L.L., Ramos-Ibarra, J.E., Coaquira, J.A.H.,

Heinrichs, B., Páez, C.A., 2021. Significantly enhancement of sunlight photocatalytic performance of ZnO by doping with transition metal oxides. Sci. Rep. 11, 1893. https://doi.org/10.1038/s41598-020-78568-9

Rani, M., Choudhary, S., Shukla, G., Shanker, U., 2024. Highly efficient photo-adsorptive degradation of tetracycline and metronidazole antibiotics by green synthesized Ag doped CeO_2@SnO_2 nanocomposites. Environ. Nanotechnology, Monit. Manag. 21, 100935. https://doi.org/10.1016/j.enmm.2024.100935

Rani, M., Keshu, Shanker, U., 2021. Sunlight-induced photocatalytic degradation of organic pollutants by biosynthesized hetrometallic oxides nanoparticles. Environ. Sci. Pollut. Res. 28(28), 37374–37389. https://doi.org/10.1007/s11356-021-15003-0

Rani, M., Meenu, Shanker, U., 2023. Efficient cleanup of emerging contaminants by green biosynthesized Z-scheme-type Bi_2O_3@CdS nanocomposite with improved photoactivity. Nanotechnol. Environ. Eng. 8, 283. https://doi.org/10.1007/s41204-022-00283-9

Ranjan, N., Singh, P.K., Maurya, N.S., 2022. Pharmaceuticals in water as emerging pollutants for river health: A critical review under Indian conditions. Ecotoxicol. Environ. Saf. 238, 114220. https://doi.org/10.1016/j.ecoenv.2022.114220

Ranjith, R., Renganathan, V., Chen, S.M., Selvan, N.S., Rajam, P.S., 2019. Green synthesis of reduced graphene oxide supported TiO_2/Co_3O_4 nanocomposite for photocatalytic degradation of methylene blue and crystal violet. Ceram. Int. 45(9), 12926–12933. https://doi.org/10.1016/j.ceramint.2019.03.219

Ravi, N.K., Pal, A.K., Soni, R., Tripathi, P., Singhal, A., Jha, P.K., Tripathi, V., 2022. Assessment of antibiotic resistance profile of bacteria isolated from Ghaghara River, India. Water Supply 22(7), 6551–6563. https://doi.org/10.2166/ws.2022.365

Ravi, Pandey, L.M., 2019. Enhanced adsorption capacity of designed bentonite and alginate beads for the effective removal of methylene blue. Appl. Clay Sci. 169, 48–58. https://doi.org/10.1016/j.clay.2018.12.019

Ravi, R., Bhan, C., Golder, A.K., 2025. Bio-analytic synthesis of Cu-doped TiO_2 for photocatalytic degradation of ciprofloxacin under visible light. Opt. Mater. (Amst). 159, 116577. https://doi.org/10.1016/j.optmat.2024.116577

Rawat, N., Anjali, Shreyata, Sabu, B., Bandyopadhyay, A., Rajagopal, R., 2024. Assessment of antibiotic resistance in chicken meat labelled as antibiotic-free: A focus on Escherichia coli and horizontally transmissible antibiotic resistance genes. LWT 194, 115751. https://doi.org/10.1016/j.lwt.2024.115751

Renganathan, J., S, I.U.H., Ramakrishnan, K., Ravichandran, M.K., Philip, L., 2021. Spatio-

temporal distribution of pharmaceutically active compounds in the River Cauvery and its tributaries, South India. Sci. Total Environ. 800, 149340. https://doi.org/10.1016/j.scitotenv.2021.149340

Rosario, A. V., Pereira, E.C., 2014. The role of Pt addition on the photocatalytic activity of TiO_2 nanoparticles: The limit between doping and metallization. Appl. Catal. B Environ. 144, 77–85. https://doi.org/10.1016/j.apcatb.2013.07.029

Sá, A.S., Feitosa, R.P., Honório, L., Peña-Garcia, R., Almeida, L.C., Dias, J.S., Brazuna, L.P., Tabuti, T.G., Triboni, E.R., Osajima, J.A., da Silva-Filho, E.C., 2021. A brief photocatalytic study of zno containing cerium towards ibuprofen degradation. Materials (Basel). 14(19), 5891. https://doi.org/10.3390/ma14195891

Safat, S., Buazar, F., Albukhaty, S., Matroodi, S., 2021. Enhanced sunlight photocatalytic activity and biosafety of marine-driven synthesized cerium oxide nanoparticles. Sci. Rep. 11, 16415. https://doi.org/10.1038/s41598-021-94327-w

Schafhauser, B.H., Kristofco, L.A., de Oliveira, C.M.R., Brooks, B.W., 2018. Global review and analysis of erythromycin in the environment: Occurrence, bioaccumulation and antibiotic resistance hazards. Environ. Pollut. 238, 944–957. https://doi.org/10.1016/j.envpol.2018.03.052

Sharma, K., Sudhaik, A., Sonu, Kumar, R., Nguyen, V.H., Le, Q. Van, Ahamad, T., Thakur, S., Kaya, S., Nguyen, L.H., Raizada, P., Singh, P., 2024. Advanced photo-Fenton assisted degradation of tetracycline antibiotics using α-Fe_2O_3/CdS/SiO_2 based S-scheme photocatalyst. J. Water Process Eng. 59, 105011. https://doi.org/10.1016/j.jwpe.2024.105011

Shi, D., Zeng, F., Gong, T., Li, J., Shao, S., 2022. Iron amended gravity-driven membrane (IGDM) system for heavy-metal-containing groundwater treatment. J. Memb. Sci. 643, 120067. https://doi.org/10.1016/j.memsci.2021.120067

Shinde, P.A., Ukarde, T.M., Gogate, P.R., Pawar, H.S., 2021. An integrated approach of adsorption and membrane separation for treatment of sewage water and resource recovery. J. Water Process Eng. 40, 101795. https://doi.org/10.1016/j.jwpe.2020.101795

Storteboom, H., Arabi, M., Davis, J.G., Crimi, B., Pruden, A., 2010. Tracking antibiotic resistance genes in the south platte river basin using molecular signatures of urban, agricultural, and pristine sources. Environ. Sci. Technol. 44(14), 4930–4936. https://doi.org/10.1021/es101657s

Stuer-Lauridsen, F., Birkved, M., Hansen, L.P., Holten Lützhøft, H.C., Halling-Sørensen, B., 2000. Environmental risk assessment of human pharmaceuticals in Denmark after normal

therapeutic use. Chemosphere 40(7), 783–793. https://doi.org/10.1016/S0045-6535(99)00453-1

Subedi, B., Balakrishna, K., Joshua, D.I., Kannan, K., 2017. Mass loading and removal of pharmaceuticals and personal care products including psychoactives, antihypertensives, and antibiotics in two sewage treatment plants in southern India. Chemosphere 167, 429–437. https://doi.org/10.1016/j.chemosphere.2016.10.026

Sudha, A., Manimehan, I., Shalini, R., Varshini, M., Ravichandran, K., Ayyanar, M., Praseetha, P.K., Saravanakkumar, D., 2024. Assessment of de-toxicity of treated dye solution via seed germination test: Photocatalytic treatment by Morinda citrifolia leaf extract mediated ZnO:Mo/g-C_3N_4 nanocomposite. Mater. Sci. Semicond. Process. 178, 108437. https://doi.org/10.1016/j.mssp.2024.108437

Suthar, J.K., Rokade, R., Pratinidi, A., Kambadkar, R., Ravindran, S., 2017. Purification of Nanoparticles by Liquid Chromatography for Biomedical and Engineering Applications. Am. J. Anal. Chem. 8(10), 541–554. https://doi.org/10.4236/ajac.2017.810044

Tan, C.W., Rukayadi, Y., Hasan, H., Thung, T.Y., Lee, E., Rollon, W.D., Hara, H., Kayali, A.Y., Nishibuchi, M., Radu, S., 2020. Prevalence and antibiotic resistance patterns of *Vibrio parahaemolyticus* isolated from different types of seafood in Selangor, Malaysia. Saudi J. Biol. Sci. 27, 1602–1608. https://doi.org/10.1016/j.sjbs.2020.01.002

Tao, R., Ying, G.G., Su, H.C., Zhou, H.W., Sidhu, J.P.S., 2010. Detection of antibiotic resistance and tetracycline resistance genes in *Enterobacteriaceae* isolated from the Pearl rivers in South China. Environ. Pollut. 158, 1441–1446. https://doi.org/10.1016/j.envpol.2010.03.004

Tavakolain, M., Jafari, M., Ebrahimian, M.R., Rahimpour, M.R., Hosseini-Sarvari, M., 2023. Sustainable and green synthesis of C- and N-doped nanoporous g-C_3N_4: powerful sunlight-responsive photocatalysts for aerobic oxidation of toluene. React. Chem. Eng. 8, 1914–1922. https://doi.org/10.1039/d2re00587e

Tetteh, E.K., Rathilal, S., Naidoo, D.B., 2020. Photocatalytic degradation of oily waste and phenol from a local South Africa oil refinery wastewater using response methodology. Sci. Rep. 10, 8850. https://doi.org/10.1038/s41598-020-65480-5

Venkatesan Savunthari, K., Arunagiri, D., Shanmugam, S., Ganesan, S., Arasu, M.V., Al-Dhabi, N.A., Chi, N.T.L., Ponnusamy, V.K., 2021. Green synthesis of lignin nanorods/g-C_3N_4 nanocomposite materials for efficient photocatalytic degradation of triclosan in environmental water. Chemosphere 272, 129801. https://doi.org/10.1016/j.chemosphere.2021.129801

Veras, T.B., Luiz Ribeiro de Paiva, A., Duarte, M.M.M.B., Napoleão, D.C., da Silva Pereira Cabral, J.J., 2019. Analysis of the presence of anti-inflammatories drugs in surface water: A case study in Beberibe river - PE, Brazil. Chemosphere 222, 623–631. https://doi.org/10.1016/j.chemosphere.2019.01.167

Verlicchi, P., Al Aukidy, M., Galletti, A., Petrovic, M., Barceló, D., 2012. Hospital effluent: Investigation of the concentrations and distribution of pharmaceuticals and environmental risk assessment. Sci. Total Environ. 430, 109–118. https://doi.org/10.1016/j.scitotenv.2012.04.055

Vimalkumar, K., Arun, E., Krishna-Kumar, S., Poopal, R.K., Nikhil, N.P., Subramanian, A., Babu-Rajendran, R., 2018. Occurrence of triclocarban and benzotriazole ultraviolet stabilizers in water, sediment, and fish from Indian rivers. Sci. Total Environ. 625, 1252–1264. https://doi.org/10.1016/j.scitotenv.2018.01.042

Vimercati, L., Cavone, D., Caputi, A., De Maria, L., Tria, M., Prato, E., Ferri, G.M., 2020. Nanoparticles: An experimental study of zinc nanoparticles toxicity on marine crustaceans. general overview on the health implications in Humans. Front. Public Heal. 8, 192. https://doi.org/10.3389/fpubh.2020.00192

Wang, J., Gao, M., Xu, M., Chu, Q., Gong, Y., Meng, M., Cui, H., Feng, Y., 2024. Construction of multi-functional S-Vacancy-$Zn_3In_2S_6$/Bi-MOF S-scheme heterojunction containing interfacial chemical bonds for the efficient photocatalytic production of H_2O_2 and excellent photocatalytic degradation of OTC and TC. Colloids Surfaces A Physicochem. Eng. Asp. 702(2), 135169. https://doi.org/10.1016/j.colsurfa.2024.135169

Wang, Zirun, Cai, X., Xie, X., Li, S., Zhang, X., Wang, Zhaowei, 2021. Visible-LED-light-driven photocatalytic degradation of ofloxacin and ciprofloxacin by magnetic biochar modified flower-like Bi_2WO_6: The synergistic effects, mechanism insights and degradation pathways. Sci. Total Environ. 764, 142879. https://doi.org/10.1016/j.scitotenv.2020.142879

Wolski, L., Grzelak, K., Muńko, M., Frankowski, M., Grzyb, T., Nowaczyk, G., 2021. Insight into photocatalytic degradation of ciprofloxacin over CeO_2/ZnO nanocomposites: Unravelling the synergy between the metal oxides and analysis of reaction pathways. Appl. Surf. Sci. 563, 150338. https://doi.org/10.1016/j.apsusc.2021.150338

Wu, G., Yin, Q., 2020. Microbial niche nexus sustaining biological wastewater treatment. npj Clean Water 3, 33. https://doi.org/10.1038/s41545-020-00080-4

Wu, K., Song, S., Wu, H., Guo, J., Zhang, L., 2020. Carbon quantum dots modified Bi_2WO_6 nanoflowers for enhancing photocatalytic activity: An experimental and DFT study.

Micro Nano Lett. 15, 0702. https://doi.org/10.1049/mnl.2019.0702

Wu, Y., Ji, H., Liu, Q., Sun, Z., Li, P., Ding, P., Guo, M., Yi, X., Xu, W., Wang, C.C., Gao, S., Wang, Q., Liu, W., Chen, S., 2022. Visible light photocatalytic degradation of sulfanilamide enhanced by Mo doping of BiOBr nanoflowers. J. Hazard. Mater. 424, 127563. https://doi.org/10.1016/j.jhazmat.2021.127563

Xie, W., Li, R., Xu, Q., 2018. Enhanced photocatalytic activity of Se-doped TiO_2 under visible light irradiation. Sci. Rep. 8, 1–10. https://doi.org/10.1038/s41598-018-27135-4

Xing, X., Du, Z., Zhuang, J., Wang, D., 2018. Removal of ciprofloxacin from water by nitrogen doped TiO_2 immobilized on glass spheres: Rapid screening of degradation products. J. Photochem. Photobiol. A Chem. 359, 23-32. https://doi.org/10.1016/j.jphotochem.2018.03.026

Xu, S., Gao, X., Xu, W., Jin, P., Kuang, Y., 2022. Efficient photocatalytic degradation of commercial pharmaceutical contaminants of carbamazepine using BiOBr nanosheets under visible-light irradiation. Mater. Sci. Semicond. Process. 137, 106207. https://doi.org/10.1016/j.mssp.2021.106207

Yang, Chuanxi, Wang, X., Zhang, L., Dong, W., Yang, Cheng, Shi, X., Fan, Y., Wang, Y., Lv, H., Wang, W., Zhao, Y., 2020. Investigation of kinetics and mechanism for the degradation of antibiotic norfloxacin in wastewater by UV/H_2O_2. J. Taiwan Inst. Chem. Eng. 115, 117-127. https://doi.org/10.1016/j.jtice.2020.09.036

Yang, H., Zhao, Z.C., Yang, Y.P., Zhang, Z., Chen, W., Yan, R.Q., Jin, Y., Zhang, J., 2022. Defective WO_3 nanoplates controllably decorated with MIL-101(Fe) nanoparticles to efficiently remove tetracycline hydrochloride by S-scheme mechanism. Sep. Purif. Technol. 300, 121846. https://doi.org/10.1016/j.seppur.2022.121846

Yogarathinam, L.T., Usman, J., Othman, M.H.D., Ismail, A.F., Goh, P.S., Gangasalam, A., Adam, M.R., 2022. Low-cost silica based ceramic supported thin film composite hollow fiber membrane from guinea corn husk ash for efficient removal of microplastic from aqueous solution. J. Hazard. Mater. 424, 127298. https://doi.org/10.1016/j.jhazmat.2021.127298

Yousefi, M., Zandavar, H., Pourmortazavi, S.M., Rajabi, H.R., Sajadiasl, F., Ganjali, M.R., Mirsadeghi, S., 2021. UV and visible-assisted photocatalytic degradation of pharmaceutical pollutants in the presence of rational designed biogenic Fe_3O_4-Au nanocomposite. Environ. Sci. Pollut. Res. 28, 33344-33354. https://doi.org/10.1007/s11356-021-12932-8

Yu, W.H., Qiu, Z.L., Wang, J.R., Shen, Y.J., Han, J., Fang, L.F., Zhu, B.K., 2022. Novel

nanofiltration membrane prepared by amphiphilic random copolymer nanoparticles packing for high-efficiency biomolecules separation. Chem. Eng. J. 430, 132914. https://doi.org/10.1016/j.cej.2021.132914

Yulizar, Y., Abdullah, I., Surya, R.M., Alifa, N.L., 2023. Green synthesis of novel $YMnO_3$-doped TiO_2 for enhanced visible-light- driven photocatalytic degradation of malachite green. J. Environ. Manage. 342, 118139. https://doi.org/10.1016/j.jenvman.2023.118139

Zangeneh, H., Zinatizadeh, A.A., Feyzi, M., Zinadini, S., Bahnemann, D.W., 2018. Application of a novel triple metal-nonmetal doped TiO_2 (K-B-N-TiO_2) for photocatalytic degradation of Linear Alkyl Benzene (LAB) industrial wastewater under visible light. Mater. Sci. Semicond. Process. 75, 193–205. https://doi.org/10.1016/j.mssp.2017.11.040

Zelekew, O.A., Aragaw, S.G., Sabir, F.K., Andoshe, D.M., Duma, A.D., Kuo, D.H., Chen, X., Desissa, T.D., Tesfamariam, B.B., Feyisa, G.B., Abdullah, H., Bekele, E.T., Aga, F.G., 2021. Green synthesis of Co-doped ZnO via the accumulation of cobalt ion onto Eichhornia crassipes plant tissue and the photocatalytic degradation efficiency under visible light. Mater. Res. Express 8(2), 025010. https://doi.org/10.1088/2053-1591/abe2d6

Zhang, D., Ma, X.L., Gu, Y., Huang, H., Zhang, G.W., 2020. Green synthesis of metallic nanoparticles and their potential applications to treat cancer. Front. Chem. 8, 799. https://doi.org/10.3389/fchem.2020.00799

Zhang, Y., Apostoluk, A., Theron, C., Cornier, T., Canut, B., Daniele, S., Masenelli, B., 2019. Doping of ZnO inorganic-organic nanohybrids with metal elements. Sci. Rep. 9, 11959. https://doi.org/10.1038/s41598-019-48497-3

Zhao, A., Zhang, N., Li, Q., Zhou, L., Deng, H., Li, Zhenghua, Wang, Y., Lv, E., Li, Zhen, Qiao, M., Wang, J., 2021. Incorporation of silver-embedded carbon nanotubes coated with tannic acid into polyamide reverse osmosis membranes toward high permeability, antifouling, and antibacterial properties. ACS Sustain. Chem. Eng. 9(34), 11388–11402. https://doi.org/10.1021/acssuschemeng.1c03313

Zhao, Y., Liu, J., Shi, L., Yuan, S., Fang, J., Wang, Z., Zhang, M., 2011. Solvothermal preparation of Sn^{4+} doped anatase TiO_2 nanocrystals from peroxo-metal-complex and their photocatalytic activity. Appl. Catal. B Environ. 103(3–4), 436–443. https://doi.org/10.1016/j.apcatb.2011.02.007

Zheng, C.J., Zhang, R.C., Xu, K., Zhang, J., Wang, K., Chen, W., Huang, G.B., Yin, H., 2024. Protonated g-C_3N_4/oxygen-doped g-C_3N_4 S-scheme homojunction fabricated by

electrostatic self-assembly for photocatalytic hydrogen evolution and tetracycline hydrochloride degradation. Carbon N. Y. 226, 119153. https://doi.org/10.1016/j.carbon.2024.119153

CHAPTER 2

Materials, Experimental Approaches and Analytical Techniques

This chapter provides a detailed overview of the materials, experimental protocols, and analytical techniques adopted in the study. It includes the preparation of vegetal extracts from S. edule, pineapple, and banana peel for the bio-based synthesis of metal-doped TiO_2 photocatalysts, which includes noble (Pt, Au, Pd) and transition (Ni) metals. Further, the prepared photocatalysts were characterized using various analytical techniques to study their structural, morphological, optical, and photoelectrochemical properties. The procedure for photocatalytic degradation of PhACs such as ciprofloxacin, chloroquine, amoxicillin, and furazolidone, under visible light irradiation, is also explained. Furthermore, insights on aquatic toxicity and antimicrobial activity assessment of PhACs before and after photocatalytic degradation are provided.

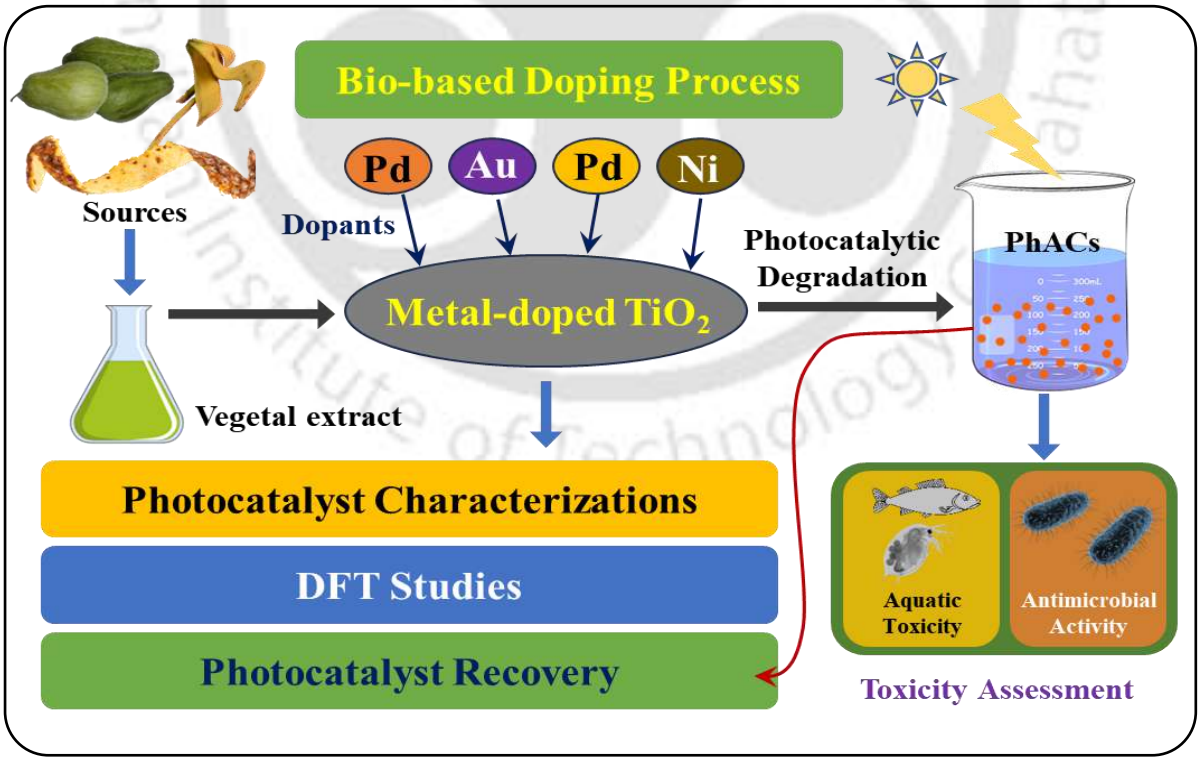

Intentionally Left Blank
Intentionally Left Blank

2.1 Chemicals

The details of all the chemicals utilized during the doctoral work are provided in Table 2.1. All the chemicals were utilized without any further purifications, and de-ionized (DI, Millipore, USA) water (resistance 18.2 ohm at room temperature) was used to prepare all reagents and solutions.

Table 2.1: Details of the chemicals utilized during the doctoral work.

Chemical	Purity (%)	CAS No.	Make
P-25 TiO_2 nano-powder	≥99.5	13463–67–7	Sigma Aldrich, Bangalore, India
Chloroplatinic acid solution (8% w/w)	~100	16941–12–1	
Gold(III) chloride hydrate	99.995	27988–77–8	
Ciprofloxacin	≥98	85721–33–1	
Chloroquine diphosphate salt	≥98	50–63–5	
Amoxicillin	≥95.0-102.0	26787-78-0	
Furazolidone	≥98	67-45-8	
Fluorine-doped tin oxide (FTO) glass	-	735159	
2,6-dichloroindophenol sodium salt hydrate	-	1082681-24-0	
Palladium (II) chloride anhydrous	≥98	7647-10-1	Merck, Mumbai, India
Nickel (II) sulfate heptahydrate	≥99	10101-98-1	
Hydrochloric acid	~37	7647-01-0	
Sodium hydroxide	≥98	1310–73–2	
Ascorbic Acid	~99	50-81-7	
Gallic Acid	≥98	5995-86-8	
Ethanol	99.9	64-17-5	
Acetonitrile	99.9	75–05–8	Finar, Gujrat, India
Nafion® D-521 dispersion, 5% w/w	-	31175-20-9	Alfa Aesar, Massachusetts, USA
Folin-Ciocalteu reagent	-	39520	SRL Pvt. Ltd. Mumbai, India
Sodium carbonate	99.9	497-19-8	
Barium sulphate extrapure	98	7727-43-7	

2.2 Vegetal extract preparation

2.2.1 Preparation and quantification of *S. edule* extract

A fresh *S. edule* was purchased, rinsed with DI water, and then chopped into small pieces. A quantity of 150 g chopped fruit was added to 200 mL of DI water, followed by incubation at 90 ºC overnight (Chelli and Golder, 2018). Further, the vegetal extract was separated with the help of a sieve and centrifuged at 5000 rpm for 5 min, followed by further clarification through a 2 µm filter paper. Furthermore, the ascorbic acid equivalent (AAE, mg L^{-1}) of the vegetal extract was quantified according to the method used by Senguttuvan at el. (2014) (Senguttuvan et al., 2014). To quantify AAE, 0.2 mL of vegetal extract was mixed with 1.8 mL of 50 µM 2,6-dichloroindophenol sodium salt hydrate, followed by an incubation for 30 min. The absorbance was measured at 592 nm (λ_{max}) in a UV-Vis spectrophotometer. Furthermore, 0-50 mg L^{-1} ascorbic acid was used instead of bio-extract, and the absorbance values were linearly fitted to obtain the calibration equation. The ascorbic acid content in bio-extract was calculated using the calibration equation, y = -0.00701x + 0.37186 (expressed as AAE, mg L^{-1}), as given in Fig. 2.1a. The negative slope could be due to scavenging of 2,6-dichloroindophenol sodium by ascorbic acid, resulting in progressively lower absorbance with increase in ascorbic acid concentration. The non-zero intercept arises from the absorbance of the reagent blank. The AAE of the vegetal extract was found to be 15 mg L^{-1}. Further, the prepared vegetal extract was used to synthesize Pt-doped TiO_2 photocatalyst.

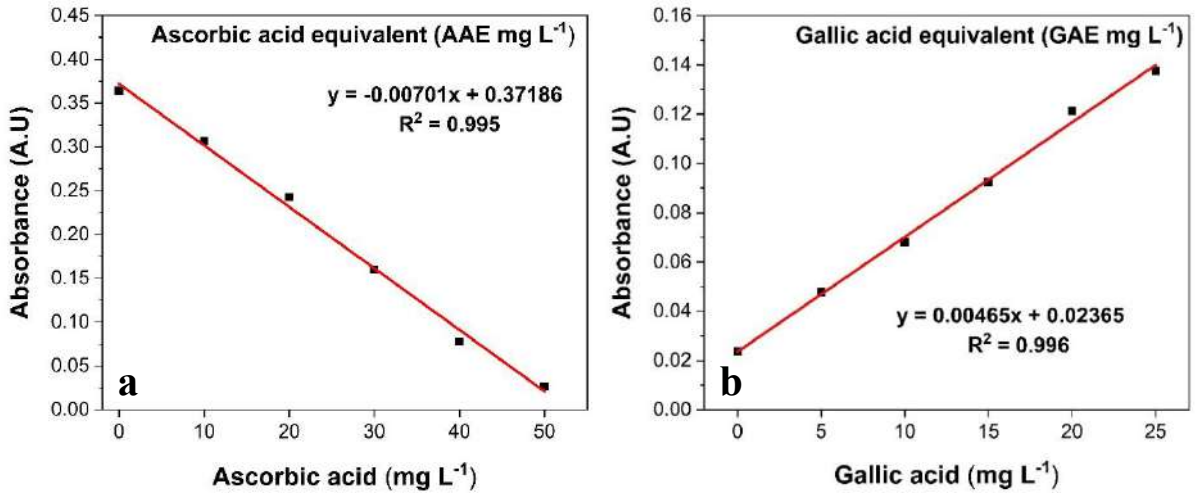

Figure 2.1: Calibration curve of (a) ascorbic acid and (b) gallic acid.

2.2.2 Preparation and quantification of *S. edule* juice

To prepare *S. edule* juice, fresh fruit was thoroughly rinsed with DI water, and the outer peel was removed. Further, 50 g of the fruit flesh was added to 100 mL of DI water and ground

using a mixer grinder. The resulting viscous solution was first sieved to remove coarse particulates, then centrifuged at 5000 rpm for 5 min, and filtered through a 0.2 µm membrane filter. The AAE of the extract was quantified following the procedure described in Section 2.2.1 of Chapter 2, and the AAE concentration was found to be ~12.0 mg L^{-1}. The prepared vegetal extract was utilized for the bio-based synthesis of Au-doped TiO_2.

2.2.3 Preparation and quantification of waste banana peel extract

Waste banana (*Musa acuminata Colla*) peels were collected from Amingaon market, Kamrup, Guwahati, Assam, India, and washed with DI water. Further, 50 g of chopped peels were added to 100 mL DI water and incubated at 90±2 ºC for 12 h. The resulting supernatant was filtered through a 0.2 µm filter paper. The AAE was quantified by following the procedure given in section 2.2.1 of chapter 2, and the AAE was found to be ~12.5 mg L^{-1}. Further, the prepared vegetal extract was utilized to synthesize bio-based Pd-doped TiO_2.

2.2.4 Preparation and quantification of waste pineapple peel extract

Waste pineapple (*Ananas comosus*) peels were collected and washed with de-ionized water. Subsequently, 50 g of chopped peels were dispersed in 100 mL DI water and incubated at 90±2 ºC for 12 h. The resulting supernatant was filtered through a 0.2 µm filter paper. The gallic acid equivalent (GAE mg L^{-1}) of vegetal extract was quantified using the Folin-Ciocalteu method as reported by (Deng et al., 2013). For this, 1 mL of vegetal extract was added to 5 mL of Folin-Ciocalteu reagent (1:10 diluted), followed by the addition of 4 mL of sodium carbonate solution, and kept for 2h in complete darkness. Further, absorbance was measured at 760 nm using a UV-Vis spectrophotometer. The calibration curve was obtained using different commercial gallic acid concentrations (0-25 mg L^{-1}) instead of vegetal extract. The gallic acid content in the vegetal extract was calculated using the obtained calibration equation, $y = 0.00465x + 0.02365$ (Fig. 2.1b). The non-zero intercept arises from the absorbance of the reagent blank. The GAE of pineapple peel extract was found to be 8.1 mg L^{-1} and utilized for the synthesis of Ni-doped TiO_2 photocatalysts.

2.3 Bio-based synthesis of photocatalysts

2.3.1 Synthesis of Pt-doped TiO_2 photocatalyst

An eco-friendly and bioinspired synthesis approach has been used for the preparation of Pt-doped TiO_2 by using ascorbic acid-rich *S. edule* vegetal extract in a fully automatic

pressure cooker-based autoclave (Fig. 2.2). For this, 0.5-2.5% (w/w) chloroplatinic acid solution (precursor of Pt(IV) ions) was loaded on 1% TiO_2 solution (50 mL) at various pH ranging from 5 to 11 and mixed at 300 rpm on a magnetic stirrer for 30 min followed by the collection of $Pt(IV)_{0\text{-}2.43}/TiO_2$ by centrifugation at 7000 rpm for 5 min. The residual Pt(IV) concentration after Pt(IV) adsorption on TiO_2 and the leached-out Pt(IV)/Pt, if any, during the doping test, was analysed by using atomic absorption spectroscopy (AAS). The dopant (Pt) content in TiO_2 ($Pt_{0\text{-}2.43}/TiO_2$) was determined by subtracting the residual Pt(IV) and Pt(IV)/Pt during adsorption and doping tests from the initial amount of Pt(IV) (0.5-2.5% w/w).

$Pt(IV)_{0\text{-}2.43}/TiO_2$ was then added in 20% (v/v) vegetal extract (15 mg L^{-1} AAE) at pH 9 in an autoclave at 121 °C for 20 min. The steam-based autoclave technique was adopted because it is easy to handle, simple, and rapid to synthesize material with desired properties. After incubation, the resultant solution was kept for 2 h and centrifuged at 7000 rpm for 5 min. The obtained pellet was washed twice with 50% (v/v) ethanol, followed by washing with DI water for 4-5 cycles to eliminate the organic part, and the pellet was kept at 90 °C for drying. The dried pellet was ground and stored in the dark for characterization and photocatalytic testing. Additionally, the doping pH (5 to 11) and Pt loading (0.49–2.43%) were optimized to obtain Pt-doped TiO_2 with the desired functional properties. Furthermore, Pt doping onto TiO_2 (Pt 1.47% w/w) was carried out using ascorbic acid [$Pt_{1.47}/TiO_2$(Chem)], and its functionality was tested and compared to bio-based $Pt_{1.47}/TiO_2$(bio).

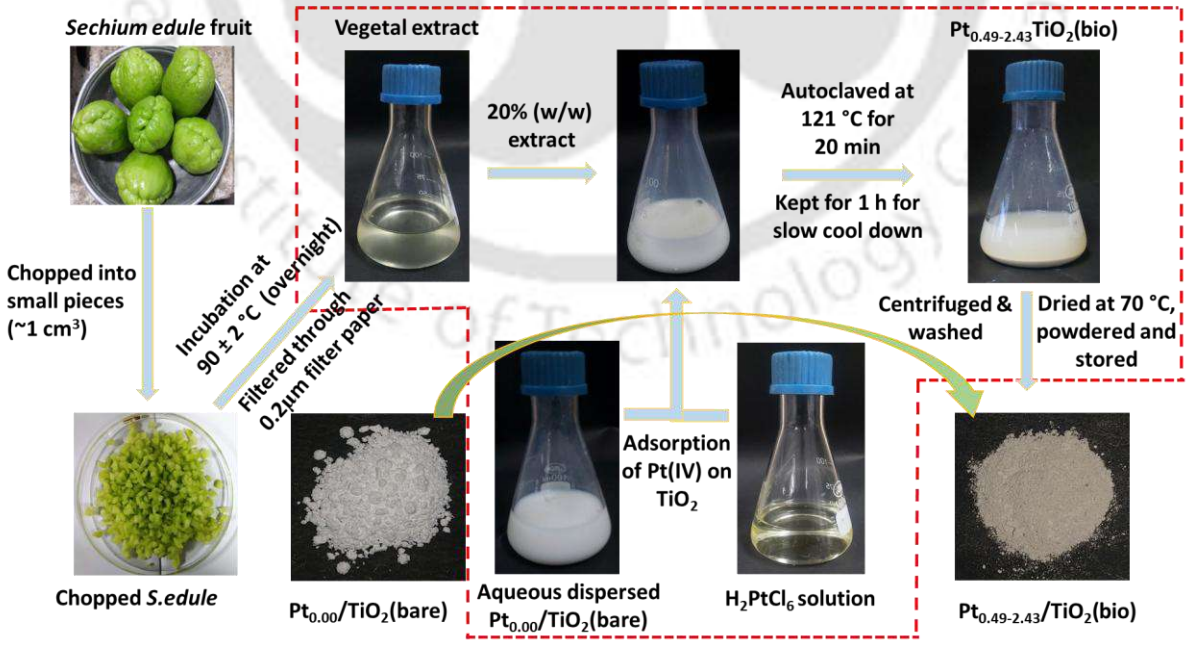

Figure 2.2: Graphical representation of the synthesis of Pt-doped TiO_2 using *S. edule* vegetal extract.

Pt nanoparticles (PtNPs) were also synthesized and characterized to investigate the photocatalytic degradation performance of individual PtNPs compared to Pt-doped TiO_2. The synthesis of PtNPs was carried out with 0.0147% Pt(VI) (w/v), which was equivalent to 1.47% (w/w) Pt-doping in TiO_2, following a similar method as illustrated in Fig. 2.2, simply eliminating TiO_2 from the experimental procedure. To minimize the impact of environmental factors on Pt-doping onto TiO_2, 20% (v/v) vegetal extract of *S. edule* #1 (AAE, 15 mg L^{-1}) and *S. edule* #2 (AAE, 3 mg L^{-1}), 100% (v/v) vegetal extract of *S. edule* #2 and ascorbic acid (15 mg L^{-1}) were used separately for synthesis of $Pt_{1.47}/TiO_2$ at pH 9 in a steamed autoclave for 20 min at 121°C.

2.3.2 Synthesis of Au-doped TiO_2 photocatalyst

Fig. 2.3 illustrates the synthesis of Au-doped TiO_2 using *S. edule* juice, which is a rich source of ascorbic acid. Prior to Au-doping, Au(III) (0-1.5% w/w) was adsorbed on the TiO_2 surface. For this, 1 g of TiO_2 was dispersed in 100 mL Au(III) solution at pH 3-11 and at a temperature of 25 °C with continuous stirring at 300 rpm. The resulting particles are denoted as Au(III)/TiO_2. For doping, Au(III)/TiO_2 was dispersed in 10-50% (v/v) vegetal extract (ascorbic acid equivalent (AAE) 12 mg L^{-1}) for each batch of experiment. It was then incubated in a steam autoclave for 20 min at 121 °C and 15 psi pressure at a natural pH of 5.5. The resulting particles were washed with 100 mL of 50% ethanol several times to remove the organic impurities adhering to them. Particles were recuperated by centrifugation at 7000 rpm for 5 min. After the final wash, the particles obtained were dried at 60 °C. Dry particles were calcined at 400 °C for 2 h and stored for further use. Au-doping onto TiO_2 (denoted as Au_x/TiO_2(bio), x = 0, 0.25, 0.50, 0.75, 1.00, 1.23, 1.45 % w/w) was conducted at variant dopant concentrations at the optimal concentration of vegetal extract (20% v/v). It corresponds to 0, 5, 10, 15, 20, 24.6, and 29 mg of adsorbed Au(III) onto 1 g TiO_2, respectively.

Similarly, $Au_{1.00}/TiO_2$(chem) was synthesized using 20% (v/v) commercial ascorbic acid (12 mg L^{-1}), which is equal to the AAE of the vegetal extract. The pristine AuNPs were also synthesized under the same conditions using 20 mg (equivalent to 1% w/w) of Au(III) precursor with 100 mL reaction volume without TiO_2. All the resulting photocatalysts were further investigated for their characteristics and photocatalytic activity for CLQ decomposition. To minimize the effect of environmental factors on Au-doping onto TiO_2, two different types of *S. edule* fruits were employed for Au-doping: *S. edule*@T (tendered with a mass of ~270 g each) and *S. edule*@M (fully matured with a mass of ~125 g each). Further, 20% (v/v) vegetal extract of *S. edule*@T (AAE, 12 mg L^{-1}) and *S. edule*@M (AAE, 4.82 mg L^{-1}), 50% (v/v)

vegetal extract of *S. edule*@M (to keep equal final ascorbic content as *S. edule*@T) and ascorbic acid (12 mg L^{-1}) were used separately for the synthesis of $Au_{1.00}/TiO_2$(bio).

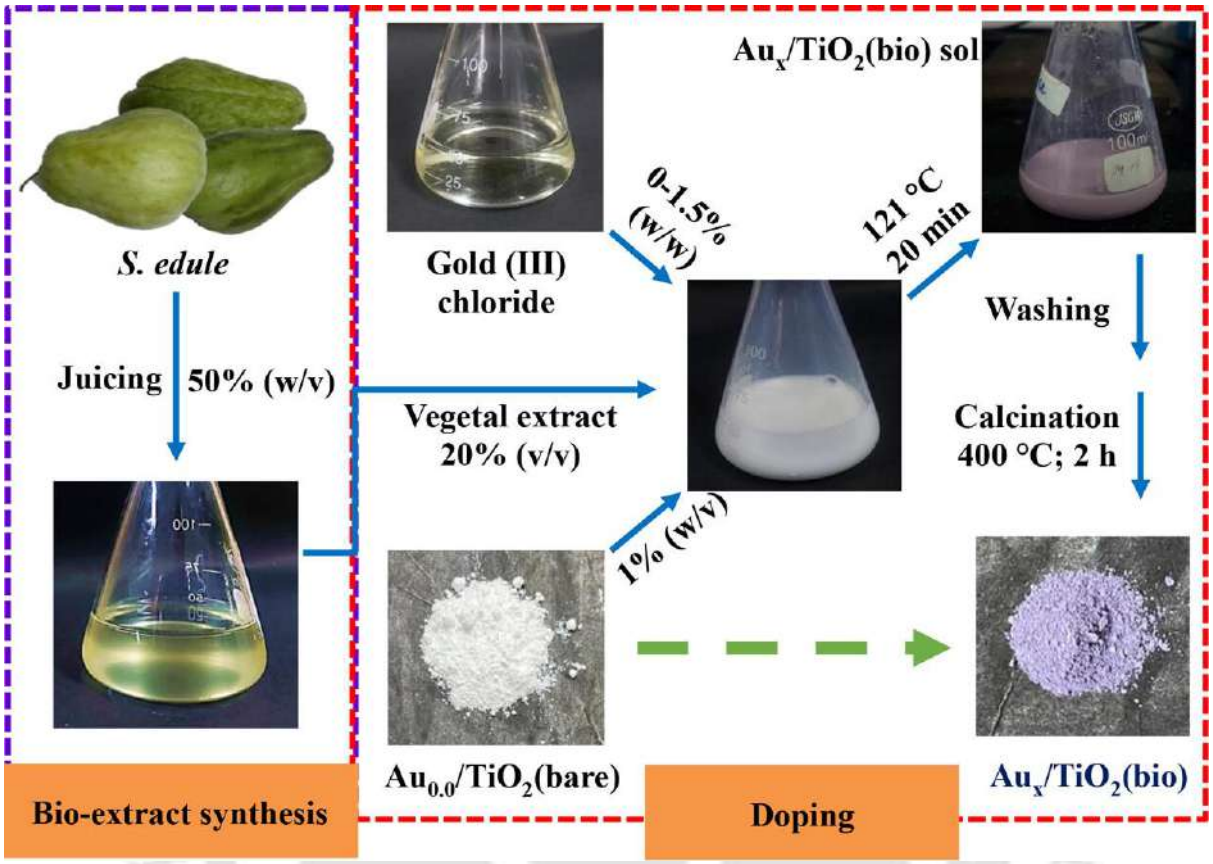

Figure 2.3: Illustration of green synthesis methodology of Au-doped TiO_2 using *S. edule* vegetal extract.

2.3.3 Synthesis of Pd-doped TiO_2 photocatalyst

Fig. 2.4 illustrates the preparation of the banana peel's vegetable extract and the synthesis of Pd-doped TiO_2. The synthesis of Pd-doped TiO_2 was completed in a dual-step process, including loading Pd(II) over the TiO_2 surface and doping in the TiO_2 lattice using vegetal extract. First, 1 % TiO_2 (w/v) was dispersed in $PdCl_2$ solution (1 % w/w) and kept at continuous stirring for 30 min at various pH conditions (pH 3 to 11), followed by centrifugation at 8000 rpm for 10 min. Further, the supernatant was analyzed for Pd traces through inductively coupled mass spectrometry (ICPMS). The loading process was also performed with different Pd(II) concentrations (0.25 to 1.50 % (w/w)). Further, the pellet was added to DI water followed by adding vegetal extract (10-50 % v/v) with a fixed ascorbic acid equivalent of 12.5 mg L^{-1} for keeping the final concentration of TiO_2 to 1 % (w/v) and incubated in a closed chamber microwave synthesizer (Discover, CEM corporation, NC, USA) at 100 W power, 90-

120 °C temperature, and for 2.5-10 min followed by washing with 50 % ethanol for 5 cycles of centrifugation (at 7500 rpm for 5 min) to remove the vegetal extract's debris and dried at 60 °C before storing it for further characterization and photocatalytic application.

To normalize the effect of environmental factors, vegetal extracts of two different types of banana peels: BP@Y (yellow banana peel) and BP@G (green banana peel) were used to synthesize the Pd-doped TiO_2. For this, 20% (v/v) vegetal extract of BP@Y (AAE, 12.5 mg L^{-1}) and BP@G (AAE, 9.7 mg L^{-1}), and 25.8% (v/v) vegetal extract of BP@G (to keep equal final ascorbic acid content as BP@Y) and commercial ascorbic acid (12.5 mg L^{-1}) were used separately for the synthesis of $Pd_{1.00}/TiO_2$(chem).

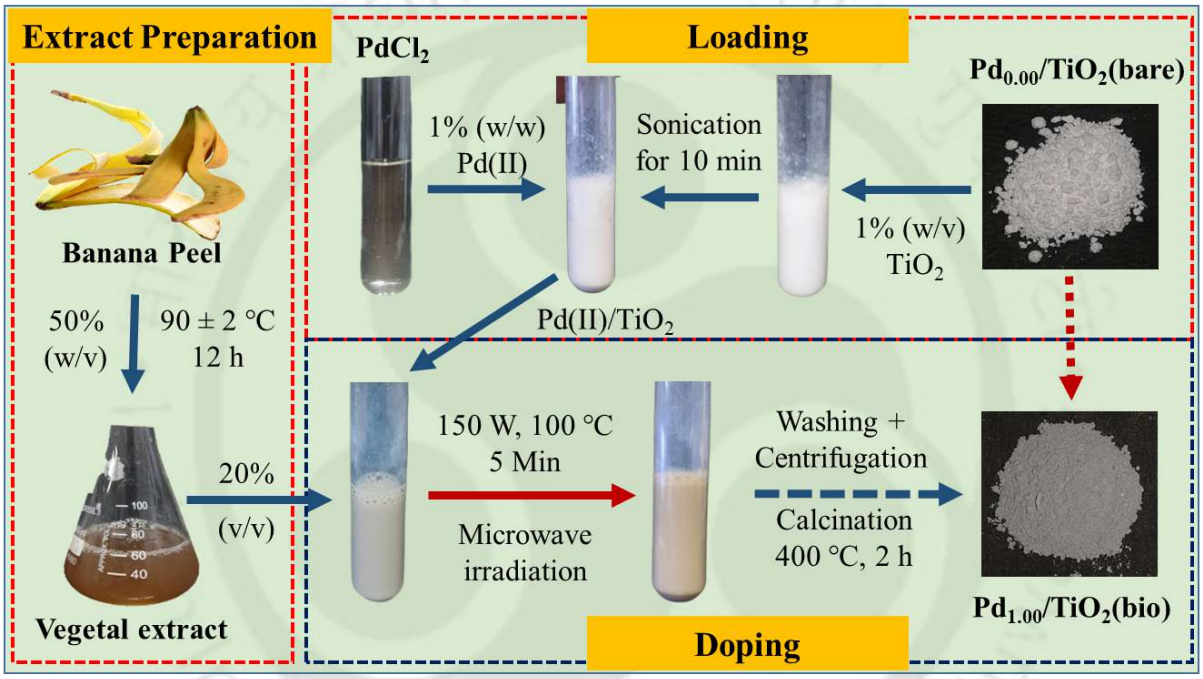

Figure 2.4: Graphical illustration of banana peel extract preparation and its utilization for Pd-doped TiO_2 synthesis.

2.3.4 Synthesis of Ni-doped TiO_2 photocatalyst

The preparation of Ni-doped TiO_2 involves a two-step process, which includes the adsorption of Ni(II) on the TiO_2 surface, followed by the doping of Ni into TiO_2 using vegetal extract at a natural pH of 4.8 (Fig. 2.5). The reaction parameters were adapted from Mustafa et al. (2022) with necessary modifications (Mustafa et al., 2022). The adsorption of 5% (at%) onto 1 g of TiO_2 powder was performed under varying pH conditions ranging from 3 to 11, with a reaction time of 30 min and a reaction volume of 100 mL. Subsequently, the adsorption of 0-9% (at%) Ni(II) was exerted at the optimized pH of 7. The Ni(II) adsorbed TiO_2 (denoted

as Ni(II)/TiO_2) was centrifuged at 7500 rpm for 5 min, and the resulting pellets of 5% (at%) Ni(II) were separately dispersed in 10-50% vegetal extract (with 8.1 mg L^{-1} GAE) to initiate the doping process. Furthermore, an optimized 20% vegetal extract concentration was used for 0-9% (at%) Ni(II) adsorbed TiO_2 (denoted as Ni_x/TiO_2(bio), where x = 0, 0.99, 2.93, 4.80, 6.64, and 8.42% representing the actual percentage of adsorbed Ni(II). The doping process was performed at 70±2 ºC and 300 rpm, stirring for 2 h, and the subsequent solution was centrifuged at 7500 rpm for 5 min. The pellet was washed with DI water and 50% ethanol 4-5 times to remove the free Ni nanoparticles and residuals of vegetal extract. The pellet was dried at 60±2 ºC for 12 h, followed by calcination at 400±10 ºC for 2 h, and the prepared Ni-doped TiO_2 was stored for characterization and photocatalytic degradation studies.

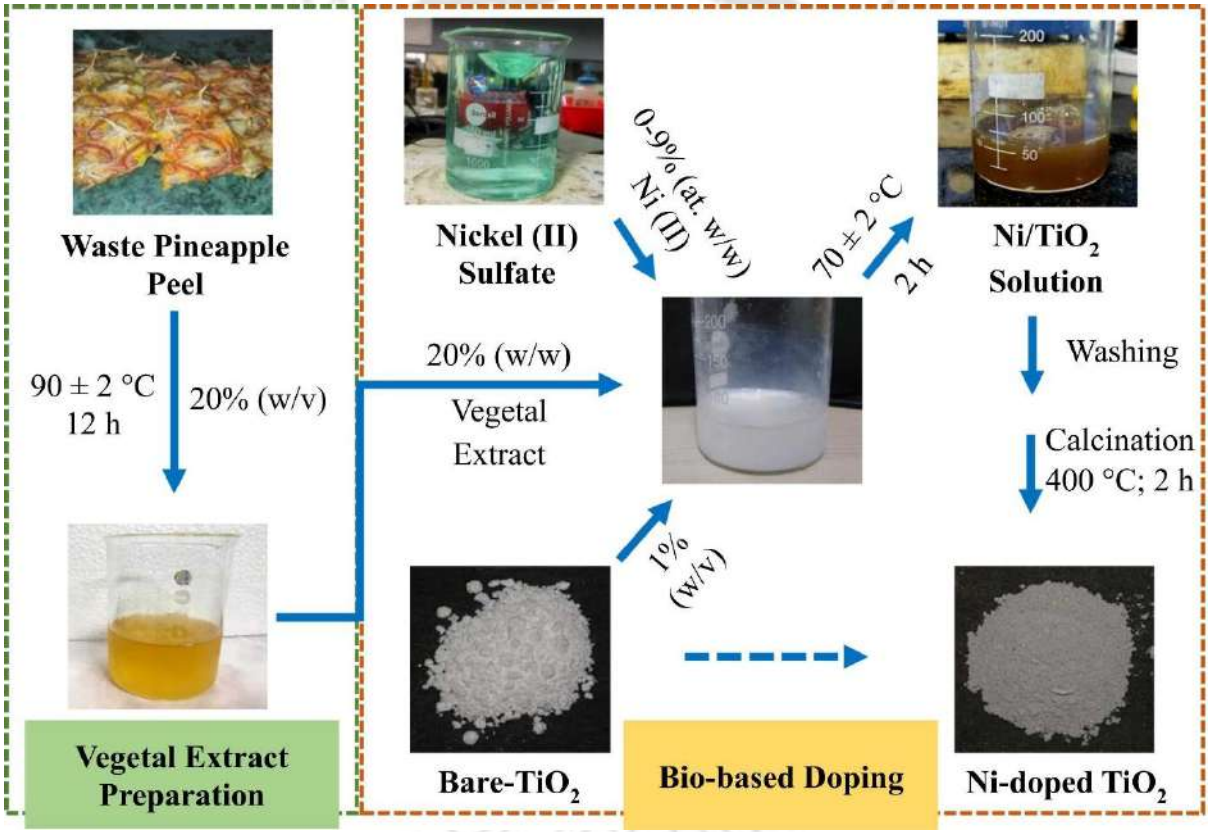

Figure 2.5: Schematic representation of waste pineapple vegetal extract preparation and bio-based synthesis of Ni-doped TiO_2.

The effect of environmental factors on Ni reduction efficiency of vegetal extract prepared from different variety of pineapple peels, such as dark-yellow pineapple peel (PP@DY) and greenish-yellow pineapple peel (PP@GY), was evaluated. For this, 20% (v/v) vegetal extract of PP@DY (GAE, 8.1 mg L^{-1}) and PP@GY (GAE, 5.8 mg L^{-1}), and 28% (v/v) vegetal extract of PP@GY (to keep equal final gallic acid content as PP@DY) were utilized to synthesize

$Ni_{4.80}/TiO_2$(bio). Additionally, synthesis of chemically synthesized Ni-doped TiO_2 (denoted as $Ni_{4.80}/TiO_2$(chem)) was carried out using commercial gallic acid (8.1 mg L^{-1}) by keeping other conditions similar to the bio-based synthesis of Ni-doped TiO_2.

2.4 Characterizations of prepared photocatalysts

2.4.1 Atomic absorption spectroscopy (AAS) analysis

Atomic absorption spectroscopy (AAS; Spectra AA 220 FS, Varian, Netherlands) was employed to quantitatively determine the residual concentration of Pt, Au, and Ni ions in the supernatant after adsorption onto TiO_2. The analysis was conducted following centrifugation to remove solid metal-adsorbed TiO_2 particles, ensuring only unadsorbed dissolved metal ions remained in the solution. The instrument utilized a metal-specific hollow cathode lamp and operated under flame mode to accurately detect a specific wavelength (Hill and Fisher, 2016). The measured concentration of metal ions in the supernatant was then subtracted from the initial concentration to calculate the amount of metal ion adsorbed onto the TiO_2 surface (Chelli and Golder, 2018). Furthermore, an AAS analysis was performed after the doping process. These adsorption values were used to determine the loading and doping efficiency of metal ions on the catalyst, which is critical for understanding the interaction between the metal ions and TiO_2 matrix, and determining the actual concentration of metal ions present in the doped photocatalysts.

2.4.2 Inductively coupled plasma mass spectrometry (ICP-MS) analysis

The quantification of Pd(II) ions was performed through ICP-MS (7850 ICPMS, Agilent Technologies, California, USA) analysis (Prasanna et al., 2019). Prior to analysis, the supernatant solutions after loading and doping of Pd onto TiO_2 were obtained after centrifugation to separate the solid catalyst particles. The calculation and further analysis of Pd concentration into TiO_2 were performed as described in “Section 2.4.1 of Chapter 2”.

2.4.3 UV–Vis diffuse reflectance spectroscopy (DRS)

UV–Vis diffuse reflectance spectroscopy (DRS) was employed to investigate the optical absorption properties and bandgaps of the synthesized photocatalysts. The measurements were carried out using a spectrophotometer (UV-2600, Shimadzu, Singapore), with high wavelength a (±0.1 nm) and photometric (±0.001 absorbance units) accuracies. The diffuse reflectance data were converted using the Kubelka–Munk function, F(R), as shown in

Eq. (2.1), where R is the reflectance of the sample. The transformed data were then used to construct Tauc's plots based on the direct bandgap transition model using Eq. (2.2), where F(R)hν is plotted against photon energy (hν), and the tangent line down to the x-axis was extrapolated to determine the optical bandgap (E_g). The bandgap analysis was used as a key parameter for optimization of synthesis conditions, including vegetal extract concentration and metal dopant concentration (Wu et al., 2014; Gao et al., 2021).

$$F(R) = \frac{(1-R)^2}{2R} \quad (2.1)$$

$$F(R)h\nu = B\,(h\nu - E_g)^2 \quad (2.2)$$

$$E_{CB} = E_{VB} - E_g \quad (2.3)$$

Additionally, the positions of the conduction band (E_{CB}) and valence band (E_{VB}) were estimated using Eq. (2.3), which considers the relationship between the bandgap and the valence band maximum. These energy values are critical for evaluating the photocatalytic efficiency of the materials, as the position of the band edges governs the redox potential and the capacity to generate reactive species under visible light (Ravi et al., 2025a).

2.4.4 X-ray diffraction (XRD) analysis

X-ray diffraction (XRD) analysis was conducted to determine the crystalline structure, phase composition, and microstructural properties of the synthesized photocatalysts. The analysis was carried out using a Rigaku SmartLab diffractometer (Tokyo, Japan), equipped with a Cu Kα radiation source (λ = 0.154 nm). The diffraction patterns were recorded in the 2θ range of 20 – 80° at a scanning speed of two measurements per second, maintaining an angular accuracy of ±0.02°. The acquired diffraction peaks were used to calculate the average crystallite size (d), lattice strain (ε), and dislocation density (δ) using the Debye–Scherrer equation and related relations (Eqs. 2.4 – 2.7).

$$d = \frac{k\lambda}{\beta\cos\theta_B} \quad (2.5)$$

$$\varepsilon = \frac{\beta}{4\mathrm{Tan}\theta_B} \quad (2.6)$$

$$\delta = \frac{1}{d^2} \quad (2.7)$$

$$\text{Rutile} = \frac{1}{\left(1+\frac{I_A}{\alpha \times I_R}\right)\times 100}\ \% \quad (2.8)$$

Here, d is estimated based on the FWHM of the XRD peaks (β) and Bragg's angle (θ_B). Lattice strain (ε) was evaluated to understand the internal stress and structural distortion, while

dislocation density (δ) offered insight into crystallographic defects and imperfections. Furthermore, the phase composition, specifically the relative proportion of anatase and rutile phases, was determined using Eq. 2.8, where I_A and I_R denote the peak intensities of anatase and rutile phases, respectively. The constants k (0.94) and α (1.265) correspond to the Scherrer constant and anatase-to-rutile scattering coefficient ratio (Ismail et al., 2021).

2.4.5 X-ray Photoelectron Spectroscopy (XPS)

To investigate the elemental composition, oxidation states, and electronic structure of the synthesized catalysts, X-ray photoelectron spectroscopy (XPS) was performed using a Thermo Fisher Scientific ESCALAB 250Xi spectrometer (Massachusetts, USA). The analysis was carried out with an Al Kα radiation source (photon energy = 1486.6 eV), operated under ultra-high vacuum conditions (base pressure ~1.69×10^{-7} Pa), and provided a high binding energy resolution of ±0.1 eV. The XPS survey and high-resolution spectra allowed precise identification of core-level peaks associated with Ti, O, C, and dopant elements (Pt, Au, Pd, and Ni). The C 1s peak at 284.8 eV was used as a reference to calibrate all binding energies, ensuring accuracy in chemical state assignment (Velasquez-Tamayo et al., 2023). Further, the obtained XPS parameters were used to determine the composition of each state in bare and metal-doped photocatalysts. In addition to the surface chemistry, valence band XPS (VB-XPS) was employed to determine the position of the valence band maximum (E_{VB}), which was further used to determine the position of the CB band using Eq. 2.3.

2.4.6 Field emission transmission electron microscopy (FETEM) analysis

Field emission transmission electron microscopy (FETEM, model 2100 F, JEOL, Peabody, MA, USA) was utilized to investigate the detailed morphological and structural features of the synthesized photocatalysts. This instrument with a spatial resolution of 0.1 nm was used to capture particle shape, particle size distribution, and internal lattice fringes of the nanoparticles. High-resolution TEM (HRTEM) images were observed to reveal the lattice fringes, indicating the crystalline nature of the materials. The average particle sizes and particle size distribution were determined by analysing the multiple particles of bare-TiO_2 and metal-doped TiO_2 photocatalysts. Additionally, the selected area electron diffraction (SAED) patterns were also performed to analyze diffraction rings of the crystalline planes, confirming the mono/polycrystalline nature of the photocatalysts (Liu et al., 2021).

2.4.7 Energy dispersive X-ray spectroscopy (EDX) analysis

The elemental composition and distribution of the synthesized photocatalysts were analyzed using energy dispersive X-ray spectroscopy (EDX) coupled with FESEM (Sigma, Zeiss, Oberkochen, Germany). This technique provided qualitative and semi-quantitative elemental analyses of elements such as titanium (Ti), oxygen (O), and metal dopants (Pt, Au, Pd, Ni) and presence of any residual elements from the vegetal extract-derived synthesis (Bhan and Kumar Golder, 2023). The elemental mapping was performed to visualize the spatial distribution of these elements on the catalyst surface.

2.4.8 Water contact angle measurement (surface wettability)

The surface wettability of the synthesized bare and metal-doped photocatalysts was evaluated using a contact angle goniometer (Model: HO-IAD-CAM-01, Holmarc Opto-Mechatronics, Kochi, India). This technique measures the angle formed between a liquid droplet and the solid surface, providing critical insight into the hydrophilic or hydrophobic nature of the material. The water contact angle was measured over a photocatalyst powder-coated glass slide. For coating, the photocatalyst was first dispersed in DI water (1 mg/mL) and sonicated for 30 min. Further, 1 mL photocatalyst suspension was spread on the cover glass (No. 1 English Glass, 22 × 40 mm, blue star, Mumbai, India) and kept at 60 °C for 12 h for complete drying. For contact angle measurement, a sessile drop method was employed, where a deionized water droplet (typically ~2 µL) was placed gently onto the flat surface of the catalyst-coated substrate. The contact angle was then measured at room temperature using a high-resolution camera and image analysis software integrated into the system. The lower contact angle values (typically <90°) indicated hydrophilic behavior, which is favorable for photocatalytic applications as it enhances the generation of reactive species from surface water and also improves the interaction between the catalyst surface and aqueous-phase pollutants (Li et al., 2022). In contrast, higher contact angles suggest a more hydrophobic surface, which may hinder photocatalytic efficiency (Mimouni et al., 2020).

2.4.9 Electron paramagnetic resonance (EPR) spectroscopy

The EPR analysis was performed to investigate the presence of paramagnetic defects, particularly oxygen vacancies and Ti^{3+} states, in the synthesized photocatalysts, which play a vital role in enhancing photocatalytic performance by acting as charge carrier traps and extending charge separation lifetime (Wang et al., 2024). The measurements were performed using an X-band EPR spectrometer (Model: JES-FA200, JEOL, Peabody, MA, USA) operating

at room temperature. The spectra were recorded in the magnetic field range of ~300–360 mT with a modulation frequency of 100 kHz and microwave power optimized to avoid signal saturation.

2.4.10 Photoluminescence (PL) and time-resolved photoluminescence (TRPL) analysis

Photoluminescence (PL) spectroscopy was conducted to evaluate the recombination behavior of photoinduced charge carriers in the synthesized photocatalysts. PL spectra were recorded using a spectrofluorometer (Fluoromax-4, Horiba Jobin Yvon, Kyoto, Japan) at an excitation wavelength of 320 nm. This technique is crucial for understanding the optical properties of the material and qualitatively estimating the recombination rate of photogenerated electrons and holes. A higher PL intensity typically signifies rapid recombination, whereas a quenched PL signal indicates improved charge separation efficiency (Baruah et al., 2022).

Time-resolved photoluminescence (TRPL) measurements were also performed using a fluorimeter (Lifespec II, Edinburgh Instruments, Livingston, UK) to gain deeper insights into the carrier dynamics. The TRPL analysis was carried out at an excitation wavelength of 320 nm and an emission wavelength of 396 nm to monitor the decay behavior of charge carriers. The decay lifetime provides quantitative information on the carrier recombination kinetics. Prolonged carrier lifetimes in the photocatalysts support better photocatalytic activity due to generating more free radicals from free electron and hole pairs (Gogoi et al., 2021).

2.5 Photoelectrochemical analysis

The photoelectrochemical characterization of bare and metal-doped TiO_2 was performed in a Potentiostat/Galvanostat (AUTOLAB 302N, Metrohm Autolab B.V., Utrecht, Netherlands) where the working (photocatalyst coated FTO 1.5 cm×2 cm), counter (Pt wire, diameter: 1 mm) and reference (Ag/AgCl, 3M KCl) electrodes were used in a three-electrode assembly with 0.5M Na_2SO_4 electrolyte solution (Fig. 2.6). The working electrode was prepared by spin coating of photocatalysts (bare-TiO_2 and metal-doped TiO_2) on FTO substrate in a spin coater (SpinNXG-P1, Apex Instruments, Kolkata, India). The FTO substrate was consecutively washed in acetone, ethanol, and water by sonication for 15 min, followed by drying at 80 °C for 2 h. Simultaneously, 2% (w/v) photocatalyst was dispersed in 200 µL nafion and isopropanol (1:2 v/v) solution and sonicated for 2 h before the coating. A homogeneous deposition of catalysts was performed at 1500 rpm for 15 s and dried at room temperature for

24 h (Gogoi et al., 2020). A detailed graphical representation of catalyst deposition on FTO is given in Fig. 2.6.

The chronoamperometry was conducted with continuous on/off cycles of light illumination with an interval of 20 s, to analyze the effect of metal doping and light irradiation on photocurrent density. Furthermore, electrochemical impedance spectroscopy (EIS) was performed under and without light illumination to measure the charge transfer resistance of the bare and metal-doped TiO_2 (Senobari and Nezamzadeh-Ejhieh, 2020).

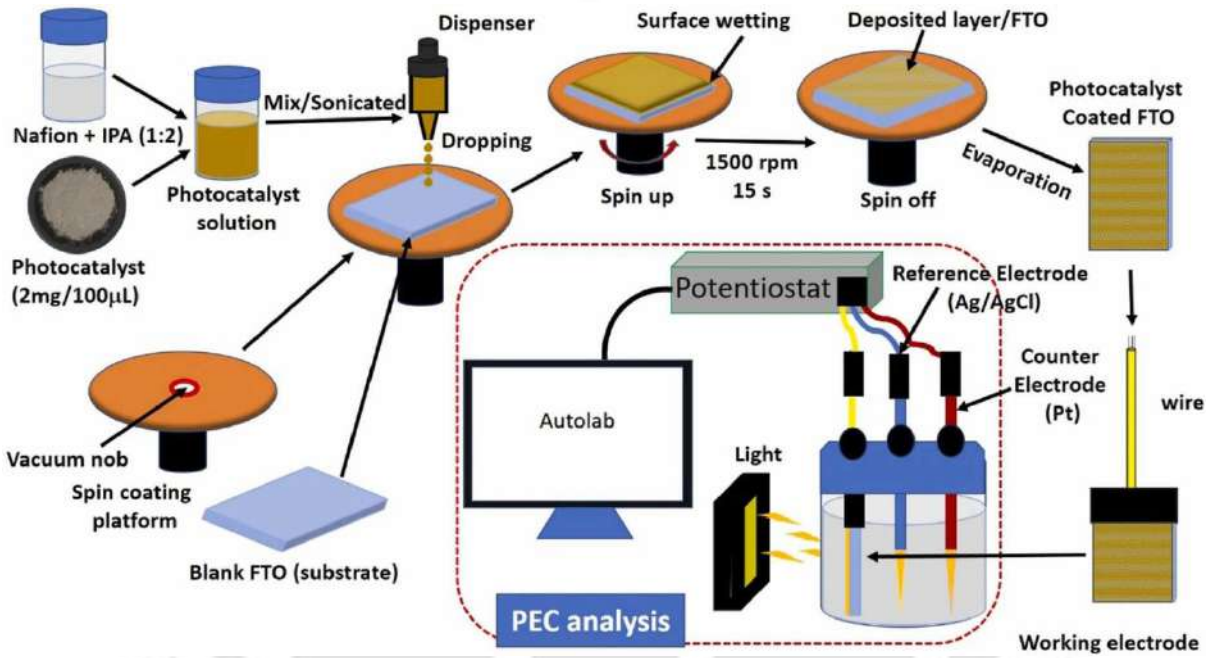

Figure 2.6: Schematic representation of the preparation of the working electrode by spin coating for photoelectrochemical (PEC) analysis.

2.6 Theoretical analysis using Density function theory (DFT)

The electronic structure and projected density of state (PDOS) of bare and metal-doped TiO_2 (Pd and Ni) with oxygen vacancies (OVs) were investigated using density functional theory (DFT)-based calculations using the Quantum ESPRESSO package. The crystallographic information file of TiO_2 (anatase phase) with I41/amd space group and tetragonal geometry (material id: mp-390) was used to obtain the lattice parameter of TiO_2, followed by Rietveld refinement of XRD data. The prominence of anatase TiO_2 (101) in both samples was evidenced by XRD and FETEM analysis.

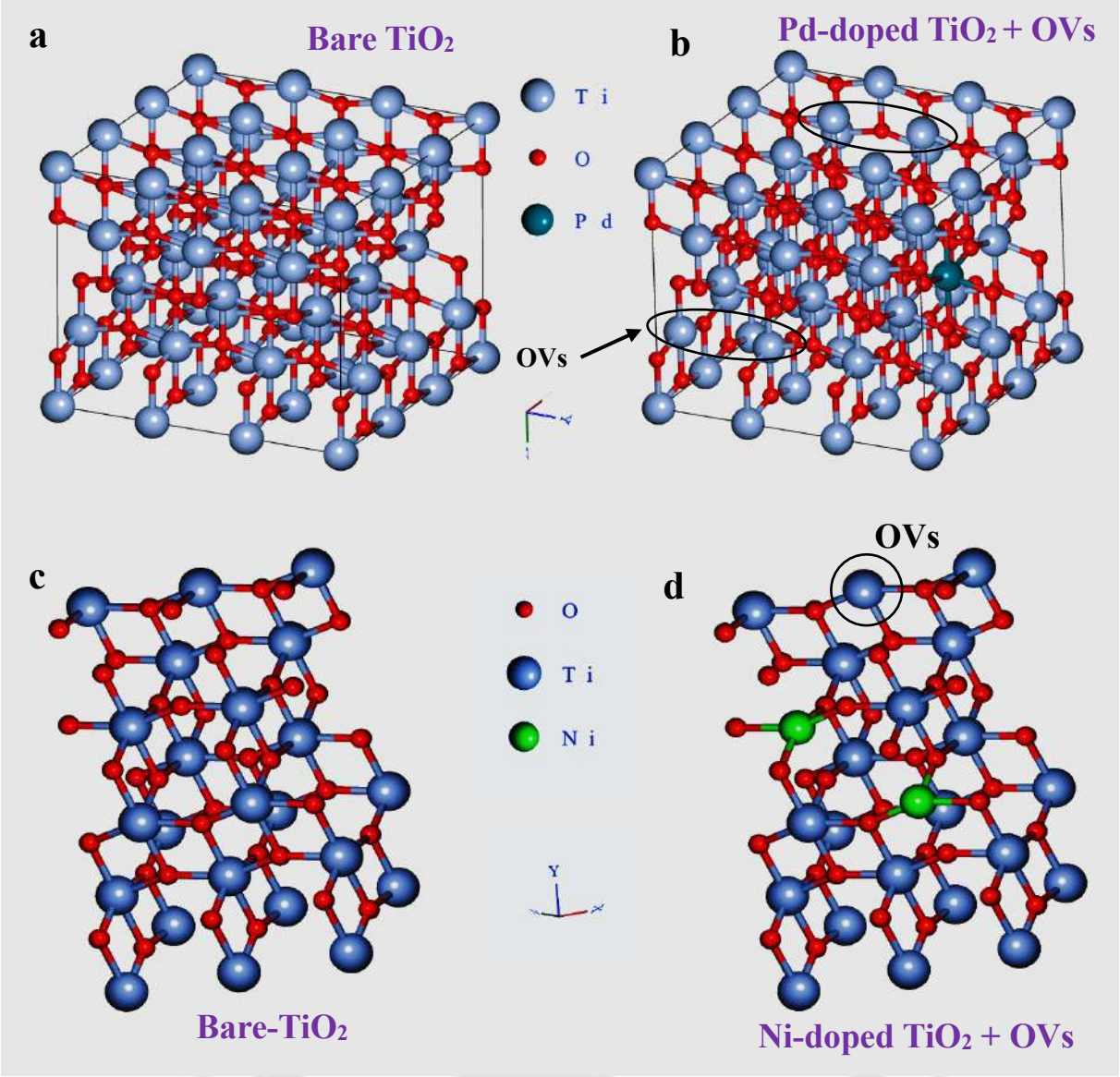

Figure 2.7: Supercell (3×3×1) model of anatase TiO_2 (101) of (a) bare TiO_2 (having 36 Ti and 72 O atoms) and (b) Pd-doped TiO_2 (having 35 Ti, 70 O, and 1 Pd atoms). Anatase TiO_2 (101) supercell (2×2×1) model of (c) bare TiO_2 (with 16 Ti and 32 O atoms) and (d) Ni-doped TiO_2 (with 14 Ti, 31 O, and 2 Ni atoms).

For DFT studies of Pd-doped TiO_2, a supercell with 108 atoms (36 Ti and 72 O atoms) was modulated with (101) Miller index and scaling of 3×3×1 (Fig. 2.7a). The supercell of Pd-doped TiO_2 was created by replacing one Ti atom with one Pd atom and incorporating 2 OVs to evaluate the synergistic effect of dual modification (35 Ti, 70 O, and 1 Pd atoms). This incorporation of Pd and oxygen vacancies in the TiO_2 lattice was performed according to the concentration of doped Pd, and the composition of Ti^{3+} obtained through XPS analysis. The

conversion of two atoms from Ti^{4+} to Ti^{3+} generates one oxygen vacancy (Fig. 2.7b) (Singh et al., 2023).

For DFT calculations, the Perdew-Burke-Ernzerhof (PBE) generalized gradient approximation (GGA) was used to describe the exchange-correlation function. The k-point mess and plane-wave cut-off (PWC) were optimized by ensuring the difference between two successive self-consistent energies was $<10^{-4}$ Ry. The optimization and relaxation of anatase (101) TiO_2 structure were performed at optimized PWC and k-points mesh with Fermi-Dirac smearing. To accurately capture the localized nature of the Ti, O, and Pd electrons, the DFT + U approach was employed by applying the Hubbard (U) corrections of 2.0, 6.0, and 5.0 eV on the Ti, O, and Pd orbitals, respectively (Sirajuddeen et al., 2020).

For DFT studies of Ni-doped TiO_2, a supercell of anatase TiO_2 (101) with 16 Ti and 32 O atoms was constructed with a scaling of 2×2×1 and a slab model with a Miller index of 101 (Fig. 2.7c). For the Ni-doped TiO_2 model (Fig. 2.7d), two Ti atoms were substituted with two Ni atoms to keep the Ni concentration similar to the experimental doped Ni concentration. An oxygen vacancy was created in a constructed 48 atoms supercell, according to the proportion of Ti^{3+} defects observed through XPS analysis. An optimized plane-wave energy cutoff of 70 Ry (952.7 eV) and a k-points mesh of 4×4×2 with Fermi-Dirac smearing were selected to optimize the structure. According to reported studies on DFT calculations, U values of 2.0 eV and 6.0 eV were assigned to Ti and O orbitals, respectively, while an additional U value of 4.5 eV was inserted in the Ni orbital of Ni-doped TiO_2 [38,39].

Additionally, the formation energy (E_f) of Pd-doped TiO_2 and Ni-doped TiO_2 with the OVs model was calculated from the total energy of bare ($E_{T(bare)}$) and Pd-doped TiO_2 ($E_{T(bio)}$) as given in Eq. 2.9 to test its stability (Zhang et al., 2014). Here, μ and n are the chemical potential of a specific element and the number of atoms, respectively.

$$E_f = E_{T(doped)} - E_{T(bare)} - n_{Ti}\mu_{Ti} - n_O\mu_O - n_{Ni}\mu_{Ni} \quad (2.9)$$

2.7 Photocatalytic degradation of PhACs

2.7.1 Experimental procedure

The photocatalytic activity of prepared catalysts was evaluated by degrading PhACs using 50 W visible light with an average intensity of 5×10^4 lm m^{-2} in a batch reactor, as illustrated in Fig. 2.8. The photocatalytic degradation of PhACs was carried out at different pH values, from 3 to 8 with photocatalyst with lowest bandgap. Further, variants of catalysts with different dopant concentrations were employed for PhACs degradation at optimized pH. In

each experiment, 0.05% (w/v) catalyst was dispersed in DI water by sonication for 30 min and then it was mixed with PhAC solution at a constant stirring speed of 300 rpm, with a reaction volume of 100 mL and PhACs concentration of 5 mg L^{-1}. Subsequently, a surface adsorption process was conducted for 30 min under dark conditions to establish the adsorption-desorption equilibrium. Further, the visible light was irradiated, and the sample was collected at 30 min intervals to analyze the residual concentration of PhACs. The photocatalytic degradation process was performed at room temperature with continuous stirring at 300 rpm on a magnetic stirrer. The collected sample was centrifuged at 7000 rpm for 5 min, and the supernatant was filtered through 0.2 µm filter paper before quantified through HPLC analysis. All the experiments were performed in triplicate to ensure reproducibility, and the reported values represent the average of independent experiments with standard deviations.

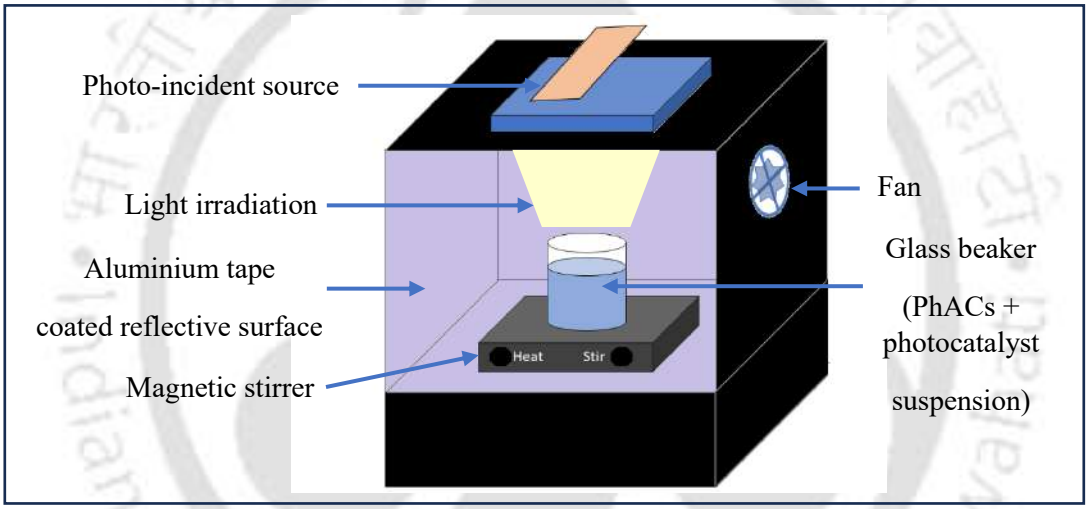

Figure 2.8: Schematic of laboratory-scale batch photocatalytic reactor for degradation of PhACs by synthesized photocatalysts.

High-performance liquid chromatography analysis (HPLC) was employed to quantify the remaining concentration of PhACs. This analysis was conducted through (HPLC, 1260 Infinity II, Agilent Technologies, California, USA) using a C18 column (UMISil C18(3), Thermo Scientific, Waltham, USA, 5 µm, 250 mm × 4.6 mm, SN: 20009091) with a retention time accuracy of ±0.1 min. The detection was accomplished at different wavelengths of 277 nm (CIP, retention time (RT): 3.844 min), 343 nm (CLQ, RT: 2.274 min), 276 nm (AMX, RT: 2.368 min), and 367 nm (FZD, RT: 7.510-8.626 min) using a mobile phase of acetonitrile and water (90:10 v/v) with a constant flow rate of 0.7 mL per min.

Furthermore, the PhAC and photodegradation PhAC samples were analyzed using liquid chromatography and mass spectroscopy (LC-MS, 6410 Triple Quadrupole LC/MS,

Agilent Technologies, California, USA) to identify PhACs and any intermediates that formed during the degradation process. The obtained mass spectra were subsequently used to study the reaction mechanism of PhACs degradation. The degradation mechanism was sketched by using ChemDraw Ultra 12.0 software.

PhAC degradation (%) and quantum yield (QY, %) for the photodegradation process were determined using Eqs. 2.10 and 2.11. Subsequently, the obtained data were fitted into a first-order kinetic model to calculate the rate constant of PhAC degradation (Eq. 2.12) (Shidpour, 2015; Wang et al., 2019).

$$\text{Degradation (\%)} = \left(\frac{C_o - C_t}{C_o}\right) \times 100 \quad (2.10)$$

$$\text{QY (\%)} = \frac{DV_0C_0N_ahc}{Pt\lambda_m} \times 100 \quad (2.11)$$

$$C_t = C_o e^{-k_1 t} \quad (2.12)$$

Where C_0 is the initial PhAC concentration (mg L^{-1}), and C_t represents PhAC concentration (mg L^{-1}) at any time t. D, V_0, N_a, h, c, P, and λ_m represent degradation fraction ($D=1-(C_t/C_0)$), reaction volume (L), Avogadro number, Plank constant, speed of light (m s^{-1}), and power (W) and wavelength of light, respectively.

2.7.2 Total organic carbon (TOC) and chemical oxygen demand (COD) analyses

For TOC and COD determination, the photodegraded sample was centrifuged at 7000 rpm and filtered through 0.2 µm filter paper. The total organic carbon (TOC) was determined in a torch TOC combustion analyzer (Teledyne Tekmar, Ohio, USA) and TOC removal (%) was calculated using Eq. 2.13.

COD was analyzed using the standard closed reflux titrimetric method. Briefly, 2 mL of sample was transferred into COD digestion tubes containing potassium dichromate digestion reagent in concentrated sulfuric acid with silver sulfate as a catalyst and mercuric sulfate as a chloride masking agent. The tubes were sealed and digested at 150 °C for 2 h in a COD incubator (DRB200, HACH OTT Pvt. Ltd., New Delhi, India), followed by cooling to room temperature. The digested samples were titrated against standardized 0.1 N ferrous ammonium sulfate (FAS) using ferroin as the indicator, where the colour change from blue-green to reddish brown indicated the endpoint. A reagent blank was run in parallel. COD was determined using Eq. 2.14 and COD removal (%) was calculated using Eq. 2.15 (Dhanjai et al., 2019). The TOC and COD measurements of hospital wastewater was performed after filtration of hospital wastewater through 0.2 µm filter paper.

$$\text{TOC removal (\%)} = \left(\frac{\text{TOC}_o - \text{TOC}_f}{\text{TOC}_o}\right) \times 100 \quad (2.13)$$

$$\text{COD (mg L}^{-1}) = \frac{(A - B) \times N \times 8000}{V} \times 100 \quad (2.14)$$

$$\text{COD removal (\%)} = \left(\frac{\text{COD}_o - \text{COD}_f}{\text{COD}_o}\right) \times 100 \quad (2.15)$$

Where TOC_o and TOC_f are the TOC of PhACs before and after photocatalytic degradation. A and B are the titrant volumes (mL) for blank and sample, respectively, N is the normality of FAS, and V is the sample volume (mL). COD_o and COD_f are the COD of PhACs before and after photocatalytic degradation.

2.7.3 Reusability and stability

The reusability of metal-doped TiO_2 photocatalysts was evaluated by photocatalytic degradation of 5 mg L^{-1} PhACs for 4-5 consecutive cycles at the optimized pH. After each photocatalytic degradation cycle, the used photocatalyst was recovered through centrifugation at 7000 rpm for 5 min. Further, the recovered catalyst was dispersed in DI water, followed by sonication for 15 min to remove surface adsorbed FZD and any intermediates formed during the photocatalytic process. It was again centrifuged and used for the next photocatalytic degradation cycle. This process of photocatalyst recovery was repeated for multiple cycles.

The stability of used photocatalysts was analyzed using XRD and XPS analysis after the first cycle of photodegradation. After 1st cycle of photocatalytic degradation, the used catalyst was recovered using centrifugation at 7000 rpm for 5 min, followed by dispersion in DI water through sonication for 15 min and again centrifuged before drying at 60 °C for 24 h. XRD patterns and XPS spectra of the used photocatalysts were compared with the fresh photocatalysts to assess their structural and chemical stability.

2.8 Aquatic toxicity and antimicrobial activity assessment

The toxicity of PhACs and their photodegradation products was evaluated using the Toxicity Estimation Software Tool (TEST, version 5.1, U.S. EPA), complemented by quantitative structure-activity relationship (QSAR) models. The assessment targeted key toxicity endpoints, including acute aquatic toxicity against *Daphnia magna* and *fathead minnow* (Wen et al., 2023; Han et al., 2024). The toxicity profiles of the degradation products were compared with that of the parent PhAC to determine any increase or decrease in overall toxicity post-photodegradation. Additionally, the antimicrobial efficacy of PhAC before and after photocatalytic degradation was examined against *Escherichia coli* (Gram-negative) and

Staphylococcus aureus (Gram-positive) (Das et al., 2018). The well-diffusion method was employed, wherein 100 µL of freshly prepared bacterial cultures (optical density = 1) were inoculated onto Muller-Hinton agar plates. Subsequently, 100 µL of fresh and photodegraded PhAC solutions were introduced into wells (7.5 mm diameter), followed by incubation at 25 °C for 16 h.

2.9 Membrane-based recovery of photocatalysts

2.9.1 Experimental set-up

A cross-flow ultrafiltration (CF-UF) membrane setup was utilized to recover TiO_2 and Pt-doped TiO_2 nano-photocatalysts. Fig. 2.9 shows the schematic representation of the membrane separation system setup, which encompasses both filtration and backflush loops. The setup includes a CF-UF membrane with a nominal pore size of 75 kDa (0.01 µm) and an area of 2 m^2, sourced from Technorbital Advance Material Pvt. Ltd., Kanpur, India. In addition, the arrangement features four stainless steel (SS316 L) tanks with lids, each with a working volume of 10 L. These tanks were used for feed storage, permeate collection, reject collection, and a backflush reservoir. The feed tank is also equipped with 2 pH probe and an impeller, which is driven by a BLDC motor (RQ-129/D, Remi Sales & Engineering Ltd., Mumbai, India) for proper mixing and dispersion of photocatalyst particles within the solution.

During the experiment, a peristaltic pump (EPP 50 V and EPP 201 V, Electrolab, Mumbai, India), denoted as PP_1, with an adjustable cross-flow velocity (CFV) of 0.01-0.14 m s^{-1} (flow rate of 12–100 L h^{-1}) was used as a feed pump for the separation of photocatalysts through CF-UF. CFV was calculated by dividing the feed flow rate by the cross-sectional area of the membrane (Chen et al., 2018). The transmembrane pressure was regulated by adjusting the value V_2 with simultaneous monitoring through a pressure gauge (P). Thus, this setup provided flexibility in adapting to various operating conditions to separate a wide range of particles. The permeate was accumulated in the permeate collection tank in the separation loop. At the same time, the reject stream was directed either to the reject collection tank (via open value V_4) or back to the feed tank (via open value V_6), facilitating the potential reusability of materials. The backflush technique was employed to effectively dislodge trapped particles from both the membrane surface and its pores to enhance the recovery of catalyst particles. The backflushing process utilized double distilled (DI) water and was carried out through the membrane module using a diaphragm pump, PP_2 (B.N.Q.S. DP-125-300W, Ningbo Qiangsheng Electric Motor Co. Ltd., Yuyao, China), operating at a flow velocity of 0.14 m s^{-1}

(flow rate of 100 L h^{-1}). During the forward separation process, valve V_5 remained closed, and values V_1, V_2, V_3, and V_4/V_6 remained open. However, during the backflush procedure, valves V_1 and V_3 were closed, and valves V_2, V_5, and V_4/V_6 were kept open.

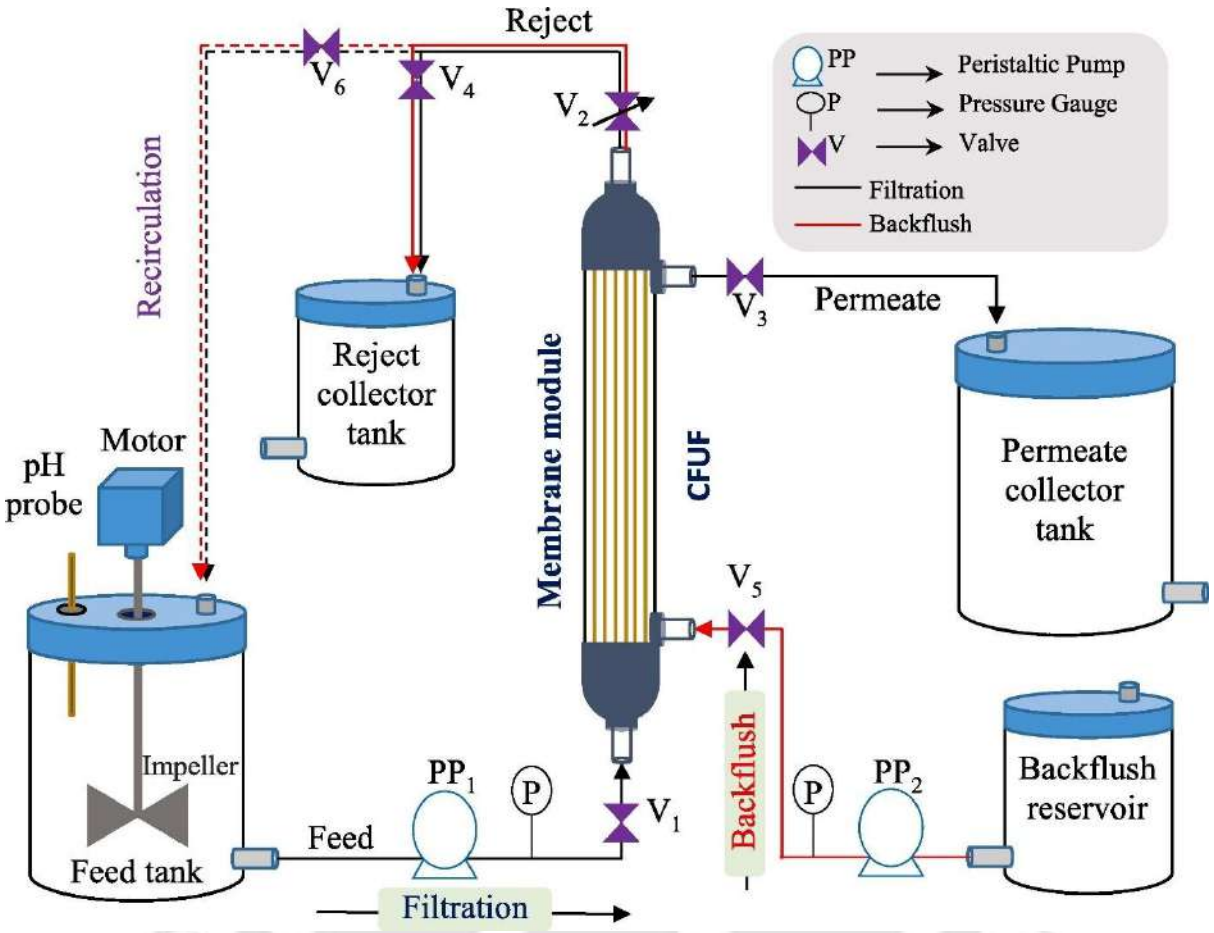

Figure 2.9: Schematic of cross-flow ultrafiltration (CF-UF) membrane setup.

2.9.2 Characterizations of membrane and membrane process

2.9.2.1 Field emission scanning electron microscopy (FESEM) analysis

Field emission scanning electron microscopy (FESEM; Sigma, Zeiss, Oberkochen, Germany) was employed to examine the surface morphology and structural features of the membrane. For FESEM analysis, the membrane was sliced horizontally to obtain a cross-sectional view. To perform the inter/outer surface analysis, a tubular section of the fresh membrane was unplugged and longitudinally sliced. Then, it was flattened by positioning it between two clean glass slides by applying a 19.6 N weight force. This technique enabled the detailed visualization of surface architecture, diameter, and thickness of the nanospikes or surface protrusions, which are crucial for understanding the membrane's surface characteristics (Jaya, 2020; Ravi et al., 2025b). The pore size, shape, and density were quantitatively assessed

to evaluate porosity and interconnectivity, which directly influence membrane permeability and separation performance.

2.9.2.2 Fourier transform infrared (FTIR) spectroscopy analysis

FTIR spectroscopy was conducted to identify the surface functional groups and chemical bonding characteristics of the membrane materials. The analysis was performed using FTIR spectrometer (IRAffinity-1, Shimadzu, Tokyo, Japan) equipped with an attenuated total reflectance (ATR) accessory, allowing for direct surface analysis without the need for extensive sample preparation. The spectral data were collected in the 400–4000 cm^{-1} range at a resolution of 4 cm^{-1}. This enabled the detection of various vibrational modes associated with functional groups such as hydroxyl (–OH), carbonyl (C=O), amine (–NH), and other groups originating from the polymer backbone (Golder et al., 2021; Bhan and Golder, 2023). FTIR spectra provided insights into the chemical interactions between the incorporated components and the polymer matrix, which is crucial for understanding the physicochemical properties, surface reactivity, and interaction of the membrane with photocatalyst.

2.9.2.3 Tensile strength measurement

The mechanical strength of the membrane spikes was evaluated by measuring their tensile strength using a 5 kN electro-mechanical Universal Testing Machine (UTM, Z005TNProline, ZwickRoell, Chennai, India). Rectangular membrane specimens were clamped and subjected to a uniaxial tensile force under controlled conditions until breakage occurred. The test was conducted at a constant crosshead speed, and the applied force along with the corresponding elongation was recorded to generate stress-strain curves. The key mechanical parameters such as ultimate tensile strength, elongation at break, and Young's modulus were determined from the curves. This analysis provides critical insight into the structural integrity, flexibility, and suitability of the membrane for practical water treatment operations, especially under varying pressure or flow conditions (Kotsilkova et al., 2018).

2.9.2.4 Hydrodynamic diameter and zeta potential

The particle size distribution of fresh and recovered catalysts was determined using the dynamic light scattering (DLS) technique with a Litesizer™ 500 particle size analyzer (Anton Paar, Virginia, USA). This technique measures the hydrodynamic diameter of nanoparticles in suspension by analysing fluctuations in light scattering due to Brownian motion, providing

insights into their colloidal stability and aggregation behavior in aqueous media. To assess the surface charge of membrane materials, membrane spikes were dried at 50 °C and finely ground using a mortar and pestle to obtain a homogeneous powder. The crushed sample was then dispersed in deionized water, and its zeta potential was measured using the same instrument. Zeta potential values of the membrane help to understand the electrostatic and dispersion behaviours of materials, which are critical parameters for predicting their interactions with photocatalytic materials (Ravi and Pandey, 2019; Berg and Ulbricht, 2020).

2.9.2.5 Dynamic viscosity measurement

The dynamic viscosity of the catalyst solution was measured using a precision-controlled rheometer (Physica MCR 301, Anton Paar, Virginia, USA). The measurements were carried out at a constant shear rate of 10 s^{-1} and a fixed gap of 0.2 mm between the parallel plates. This analysis provides crucial information regarding the flow behavior and internal resistance of the catalyst suspension, which influences its dispersion stability, mass transfer characteristics, and overall performance in photocatalytic and membrane applications (Yan et al., 2021).

2.9.3 Permeability (%) and rejection studies

The pure water flux (PWF), rejection (%), and TiO_2 recovery (%) were determined using our CF-UF membrane setup at 25 °C with a cross-flow velocity (CFV) of 0.032-0.105 m s^{-1} (feed flow rate of 22.5-75 L h^{-1}) and a backflush transmembrane flow velocity (TMFV) of 0.140 m s^{-1} (flow rate of 100 L h^{-1}). To prevent particle agglomeration, both TiO_2 and Pt/TiO_2 were dispersed in DI water through sonication for 30 min before initiating the recovery process. Recovery of TiO_2 was performed at various pH conditions, and the optimized pH was subsequently employed to recover various concentrations of both catalysts (10-250 mg L^{-1}). However, the recovery of Pt/TiO_2 was performed at a fixed CFV of 0.032 m s^{-1} (flow rate of 22.5 L h^{-1}), which was optimized in the case of TiO_2 recovery. The recovered catalyst after the CF-UF test was sonicated for 30 min, followed by measuring its turbidity using a portable turbidity meter (Eutech TN-100, Thermo Scientific, Massachusetts, U.S). The concentration of catalysts in the recovered solution was calculated by employing a standard curve that related turbidity (NTU) to catalyst concentration ranging from 10-200 mg L^{-1}.

The permeability (%) indicates the fraction of feed volume that successfully passes through the membrane as permeate during the recovery process (Eq. 2.16). The permeate water flux and rejection rate (%) were computed using Eqs. 2.17 and 2.18 respectively. Additionally,

the catalyst recovery (%) (Eq. 2.19) was calculated based on the concentration of the catalysts in the reject and backflush streams. The total filtration resistance (R_t) was calculated using Eq. 2.20 (Peng et al., 2022).

$$\text{Permeability (\%)} = \frac{V_p}{V_f} \times 100 \quad (2.16)$$

$$J = \frac{V}{A \times t} \quad (2.17)$$

$$R\% = \frac{C_f - C_p}{C_f} \times 100 \quad (2.18)$$

$$\text{Recovery (\%)} = \frac{(V_f.\ C_f) - (V_b.\ C_b + V_r.\ C_r)}{V_f.\ C_f} \times 100 \quad (2.19)$$

$$J = \frac{TMP}{\mu_w . R_t} \quad (2.20)$$

Where J is the flux (L $m^{-2}.h^{-1}$), A is the nominal area of the membrane, V is the volume of permeate water, and t is the permeation time in h. C_f, C_p, C_b, and C_r are the concentrations (mg L^{-1}) of photocatalysts in the feed, permeate, backflush, and reject streams, respectively. While V_f, V_p, V_b, and V_r represent feed, permeate, backflush, and reject streams volume, respectively. μ_w (kg m^{-2} s) and R_t (m^{-1}) are the dynamic viscosity of water and total filtration resistance, respectively. Total filtration resistance is the sum of membrane resistance (R_m) and cake layer resistance (R_c). The membrane resistance is calculated using PWF, while the total filtration resistance at a particular catalyst's concentration was calculated using the permeate flux obtained during the catalyst's recovery.

2.9.4 Flux recovery

Flux recovery studies were conducted over 5 consecutive cycles of TiO_2 separation. In this process, 50 mg L^{-1} TiO_2 solution was filtered at pH 5, using a CFV of 0.032 (flow rate of 22.5 L h^{-1}) and 0.063 m s^{-1} (flow rate of 45 L h^{-1}) and a transmembrane pressure (TMP) of 0.75 and 1.05 kg cm^{-2}, followed by filtration of DI water to measure PWF. Furthermore, the membrane was subjected to backflushing at a constant TMFV of 0.140 m s^{-1} (flow rate of 100 L h^{-1}), followed by the measurement of PWF once again. Fouling (F) and flux recovery (F_r) were calculated using the Eqs. 2.21 and 2.22, as given below (Peng et al., 2022).

$$F\ (\%) = \frac{F_{BF} - F_{AF}}{F_B} \times 100 \quad (2.21)$$

$$F_r\ (\%) = \frac{F_{AB}}{F_B} \times 100 \quad (2.22)$$

Where F_{BF}, $F_{AF,}$ and F_{AB} are the PWF before filtration, after filtration, and after backflushing, respectively.

2.9.5 Resistance-in-series (RIS) model

The resistance-in-series (RIS) model was employed to theoretically calculate membrane separation parameters in ultrafiltration. The expressions for Darcy's law-based RIS model for the computation of theoretical flux are presented in Eqs. 2.23-2.27 (Mulder, 1991).

$$J = \frac{1}{A}\frac{dV}{dt} \quad (2.23)$$

$$J = \frac{TMP}{\mu_w (R_m + R_c)} \quad (2.24)$$

$$J = \frac{TMP}{\mu_w \left(R_m + \frac{r_c c_f V}{c_c A}\right)} \quad (2.25)$$

$$R_c = \frac{r_c c_f V}{c_c A} \quad (2.26)$$

$$r_c = \frac{\frac{TMP}{\mu_w J} - R_m}{m} \quad (2.27)$$

Where, J (L m^{-2} h^{-1}) is water (permeate) flux. V, A, μ_w, $R_{m,}$ and R_c are the permeate volume, membrane area, dynamic viscosity of water, membrane resistance, and cake resistance, respectively. In the case of complete solute (catalyst) rejection, the theoretical R_c was calculated using Eq. 2.26, where r_c, c_f, and c_c represent the specific cake resistance, solute concentration in the feed and cake layer, respectively. The r_c was calculated using Eq. 2.27, where m is cake mass per unit membrane area (kg m^{-2}), which was obtained from mass balance of TiO_2 concentration in feed and reject streams (McCarthy et al., 2002).

References

Baruah, M., Ezung, S.L., Sharma, S., Bora Sinha, U., Sinha, D., 2022. Synthesis and characterization of Ni-doped TiO_2 activated carbon nanocomposite for the photocatalytic degradation of anthracene. Inorg. Chem. Commun. 144, 109905. https://doi.org/10.1016/j.inoche.2022.109905

Berg, T. van den, Ulbricht, M., 2020. Polymer nanocomposite ultrafiltration membranes: The influence of polymeric additive, dispersion quality and particle modification on the integration of zinc oxide nanoparticles into polyvinylidene difluoride membranes. Membranes (Basel). 10(9), 197. https://doi.org/10.3390/membranes10090197

Bhan, C., Golder, A.K., 2023. Utilizing bioinspired AgNPs as an antibacterial agent to enhance ceramic membrane performance. J. Environ. Chem. Eng. 11, 110283.

https://doi.org/10.1016/j.jece.2023.110283

Bhan, C., Kumar Golder, A., 2023. Bio-based hierarchical vertically aligned 2D ZnO nanostructures for ultra selective electrochemical sensing of p-Chloroaniline. Chem. Eng. J. 475, 146122. https://doi.org/10.1016/j.cej.2023.146122

Chelli, V.R., Golder, A.K., 2018. Ag-doping on ZnO support mediated by bio-analytes rich in ascorbic acid for photocatalytic degradation of dipyrone drug. Chemosphere 208, 149–158. https://doi.org/10.1016/j.chemosphere.2018.05.158

Chen, Z., Xiao, T., Hu, D., Xu, J., Li, X., Jia, F., Wang, H., Gu, F., Su, H., Zhang, Y., 2018. The performance and membrane fouling rate of a pilot-scale anaerobic membrane bioreactor for treating antibiotic solvent wastewater under different cross flow velocity. Water Res. 135, 180–190. https://doi.org/10.1016/j.watres.2018.02.027

Das, S., Ghosh, S., Misra, A.J., Tamhankar, A.J., Mishra, A., Lundborg, C.S., Tripathy, S.K., 2018. Sunlight assisted photocatalytic degradation of ciprofloxacin in water using fe doped zno nanoparticles for potential public health applications. Int. J. Environ. Res. Public Health 15(11), 2440. https://doi.org/10.3390/ijerph15112440

Deng, G.F., Lin, X., Xu, X.R., Gao, L.L., Xie, J.F., Li, H. Bin, 2013. Antioxidant capacities and total phenolic contents of 56 vegetables. J. Funct. Foods 5(1), 260–266. https://doi.org/10.1016/j.jff.2012.10.015

Dhanjai, Sinha, A., Zhao, H., Chen, J., Mugo, S.M., 2019. Water analysis | determination of chemical oxygen demand, in: Encyclopedia of Analytical Science. https://doi.org/10.1016/B978-0-12-409547-2.14517-2

Gao, P., Zhang, Z., Feng, L., Liu, Y., Du, Z., Zhang, L., 2021. Novel Ti_3C_2/Bi@BiOI nanosheets with gradient oxygen vacancies for the enhancement of spatial charge separation and photocatalytic performance: The roles of reactive oxygen and iodine species. Chem. Eng. J. 426, 130764. https://doi.org/10.1016/j.cej.2021.130764

Gogoi, D., Namdeo, A., Golder, A.K., Peela, N.R., 2020. Ag-doped TiO_2 photocatalysts with effective charge transfer for highly efficient hydrogen production through water splitting. Int. J. Hydrogen Energy 45(4), 2729–2744. https://doi.org/10.1016/j.ijhydene.2019.11.127

Gogoi, D., Shah, A.K., Rambabu, P., Qureshi, M., Golder, A.K., Peela, N.R., 2021. Step-Scheme Heterojunction between CdS Nanowires and Facet-Selective Assembly of MnOx-$BiVO_4$ for an Efficient Visible-Light-Driven Overall Water Splitting. ACS Appl. Mater. Interfaces 13, 45475–45487. https://doi.org/10.1021/acsami.1c11740

Golder, A.K., Chauhan, S., Ravi, R., 2021. Synthesis of low-cost bentonite/*Duranta erecta*'s

fruit powder imbedded alginate beads and its application in surfactant removal. Environ. Sci. Pollut. Res. 28, 58945–58957. https://doi.org/10.1007/s11356-021-14306-6

Han, M., Wang, S., Yu, X., Zhang, Y., Li, M., Yi, Z., Gao, H., Yang, H., Fang, L., Syed, A., 2024. Enhanced Photocatalytic Activity of O-deficient Modified $CuAl_2O_4/MoS_2$ Composite Photocatalysts in Wastewater Treatment Applications. Adv. Sustain. Syst. 8, 2300478. https://doi.org/10.1002/adsu.202300478

Hill, S.J., Fisher, A.S., 2016. Atomic absorption, methods and instrumentation, in: Encyclopedia of Spectroscopy and Spectrometry. https://doi.org/10.1016/B978-0-12-803224-4.00099-6

Ismail, M.A., Hedhili, M.N., Anjum, D.H., Singaravelu, V., Chung, S.H., 2021. Synthesis and characterization of iron-doped TiO_2 nanoparticles using ferrocene from flame spray pyrolysis. Catalysts 11(4), 438. https://doi.org/10.3390/catal11040438

Jaya, R.P., 2020. Porous concrete pavement containing nanosilica from black rice husk ash, in: New Materials in Civil Engineering. https://doi.org/10.1016/B978-0-12-818961-0.00014-4

Kotsilkova, R., Borovanska, I., Todorov, P., Ivanov, E., Menseidov, D., Chakraborty, S., Bhattacharjee, C., 2018. Tensile and Surface Mechanical Properties of Polyethersulphone (PES) and Polyvinylidene Fluoride (PVDF) Membranes. J. Theor. Appl. Mech. 48(1), 37–50. https://doi.org/10.2478/jtam-2018-0018

Li, H., Wang, L., Pi, X., Ma, M., Jiang, X., Ji, S., Jiang, F., Luo, L., 2022. Effect of the wettability of $Ag_2MoO_4/BiVO_4$ {010} composite on the photocatalytic degradation for 17α-ethinyl estradiol. J. Alloys Compd. 899, 163295. https://doi.org/10.1016/j.jallcom.2021.163295

Liu, G., Liang, W., Xue, X., Rosei, F., Wang, Y., 2021. Atomic Identification of Interfaces in Individual Core@shell Quantum Dots. Adv. Sci. 8(21), 2102784. https://doi.org/10.1002/advs.202102784

McCarthy, A.A., Walsh, P.K., Foley, G., 2002. Experimental techniques for quantifying the cake mass, the cake and membrane resistances and the specific cake resistance during crossflow filtration of microbial suspensions. J. Memb. Sci. 201(1–2), 31–45. https://doi.org/10.1016/S0376-7388(01)00691-3

Mimouni, R., Askri, B., Larbi, T., Amlouk, M., Meftah, A., 2020. Photocatalytic degradation and photo-generated hydrophilicity of Methylene Blue over $ZnO/ZnCr_2O_4$ nanocomposite under stimulated UV light irradiation. Inorg. Chem. Commun. 121, 107889. https://doi.org/10.1016/j.inoche.2020.107889

Mulder, M., 1991. Basic principles of membrane technology. https://doi.org/10.1524/zpch.1998.203.part_1_2.263

Mustafa, S.M., Barzinjy, A.A., Hamad, A.H., Hamad, S.M., 2022. Green synthesis of Ni doped ZnO nanoparticles using dandelion leaf extract and its solar cell applications. Ceram. Int. 48(15), 21747–21757. https://doi.org/10.1016/j.ceramint.2022.05.202

Peng, G., Yaoqin, W., Changmei, S., Chunnuan, J., Ying, Z., Rongjun, Q., Ying, W., 2022. Preparation and properties of PVC-based ultrafiltration membrane reinforced by in-situ synthesized p-aramid nanoparticles. J. Memb. Sci. 642, 119993. https://doi.org/10.1016/j.memsci.2021.119993

Prasanna, S.R.V.S., Pandey, S., Balaji, K., Rana, S., 2019. Metal Oxide Based Nanomaterials and Their Polymer Nanocomposites, in: Nanomaterials and Polymer Nanocomposites: Raw Materials to Applications. https://doi.org/10.1016/B978-0-12-814615-6.00004-7

Ravi, Pandey, L.M., 2019. Enhanced adsorption capacity of designed bentonite and alginate beads for the effective removal of methylene blue. Appl. Clay Sci. 169, 1–10. https://doi.org/10.1016/j.clay.2018.12.019

Ravi, R., Bhan, C., Golder, A.K., 2025a. Bio-analytic synthesis of Cu-doped TiO_2 for photocatalytic degradation of ciprofloxacin under visible light. Opt. Mater. (Amst). 159, 116577. https://doi.org/10.1016/j.optmat.2024.116577

Ravi, R., Singh, A., Golder, A.K., 2025b. Electrifying CQDs-doped PANI-embedded membrane for enhanced self-cleaning targeting wastewater treatment. J. Chem. Technol. Biotechnol. https://doi.org/10.1002/jctb.70017

Senguttuvan, J., Paulsamy, S., Karthika, K., 2014. Phytochemical analysis and evaluation of leaf and root parts of the medicinal herb, Hypochaeris radicata L. for in vitro antioxidant activities. Asian Pac. J. Trop. Biomed. 4(5), 359–367. https://doi.org/10.12980/APJTB.4.2014C1030

Senobari, S., Nezamzadeh-Ejhieh, A., 2020. A novel ternary nano-composite with a high photocatalyitic activity: Characterization, effect of calcination temperature and designing the experiments. J. Photochem. Photobiol. A Chem. 394, 112455. https://doi.org/10.1016/j.jphotochem.2020.112455

Shidpour, R., 2015. A Power-Law Relationship between Characteristics of Light Source and Quantum Yield in Photocatalytic Systems. J. Phys. Chem. C 119(28), 16279–16287. https://doi.org/10.1021/acs.jpcc.5b02318

Singh, K., Harish, S., Hayakawa, Y., Shimomura, M., 2023. Experimental and theoretical study of oxygen vacancy induced La-doped mesoporous TiO_2 for enhanced thermal stability.

AIP Adv. 13(3), 035317. https://doi.org/10.1063/5.0138159

Sirajuddeen, M.M.S., Sundareswari, M., Mohamed, I.R., Elavarasi, S.B., Lone, I.N., Teli, N. ahmed, Rahmathulla, S.S., Hussain, M.S., 2020. A DFT+U study to report magnetic phase transition, electronic properties and half metallic ferromagnetism in palladium oxide using Hubbard method. Mater. Chem. Phys. 241, 122263. https://doi.org/10.1016/j.matchemphys.2019.122263

Velasquez-Tamayo, J.P., Torres-Ceron, D.A., Amaya-Roncancio, S., Santacruz, S.I., Acosta-Medina, C.D., Restrepo-Parra, E., 2023. Use of nickel-electroplating wastewater to synthesize Ni-doped TiO_2 and $NiTiO_3$ coatings by plasma electrolytic oxidation to treat hexavalent chromium in real electroplating wastewater. Chem. Eng. J. 477, 147080. https://doi.org/10.1016/j.cej.2023.147080

Wang, K., Xu, L., Li, K., Liu, L., Zhang, Y., Wang, J., 2019. Development of polyaniline conductive membrane for electrically enhanced membrane fouling mitigation. J. Memb. Sci. 570–571, 371–379. https://doi.org/10.1016/j.memsci.2018.10.050

Wang, Y., Qiu, C., Xie, Y., Wang, L., Ding, J., Zhang, J., Wan, H., Guan, G., 2024. Intentionally Introducing Oxygen Vacancies and Ti^{3+} Defects on the Surface of $Bi_4Ti_3O_{12}$ Nanosheets for Promoting the Photoreduction of CO_2 to CH3OH. ACS Appl. Nano Mater. 7(3), 2761–2772. https://doi.org/10.1021/acsanm.3c05346

Wen, L., Liu, P., Zhou, Z., Wang, K., Zhou, Y., 2023. Biosafety Photooxidation Strategy of Levofloxacin Driven by Manganese-doped Indium Zinc Sulfide. Chem. - An Asian J. 18(1), e202300161, 2–8. https://doi.org/10.1002/asia.202300161

Wu, P., Wang, J., Zhao, J., Guo, L., Osterloh, F.E., 2014. Structure defects in g-C_3N_4 limit visible light driven hydrogen evolution and photovoltage. J. Mater. Chem. A 2(48), 20338–20344. https://doi.org/10.1039/c4ta04100c

Yan, X., Wang, G., Ma, C., Li, J., Cheng, S., Yang, C., Chen, L., 2021. Effects of pollutants in alkali/surfactant/polymer (ASP) flooding oilfield wastewater on membrane fouling in direct contact membrane distillation by response surface methodology. Chemosphere 282, 131130. https://doi.org/10.1016/j.chemosphere.2021.131130

Zhang, H., Yu, X., McLeod, J.A., Sun, X., 2014. First-principles study of Cu-doping and oxygen vacancy effects on TiO_2 for water splitting. Chem. Phys. Lett. 612, 106–110. https://doi.org/10.1016/j.cplett.2014.08.003

CHAPTER 3

A Bio-based Process of Pt-doping onto TiO_2 for Improved Photocatalytic Functionalities

This chapter presents the bio-based synthesis of Pt-doped TiO_2 using S. edule vegetal extract in a streamed autoclave. The study optimizes doping parameters to tune its structural and electronic properties. Comprehensive characterizations were performed to confirm the enhanced photoelectrochemical and photocatalytic performance. The photocatalyst is evaluated for the degradation of CIP under visible light irradiation, demonstrating improved activity and stability after Pt-doping. The aquatic toxicity and antimicrobial activity of CIP before and after photodegradation were assessed.

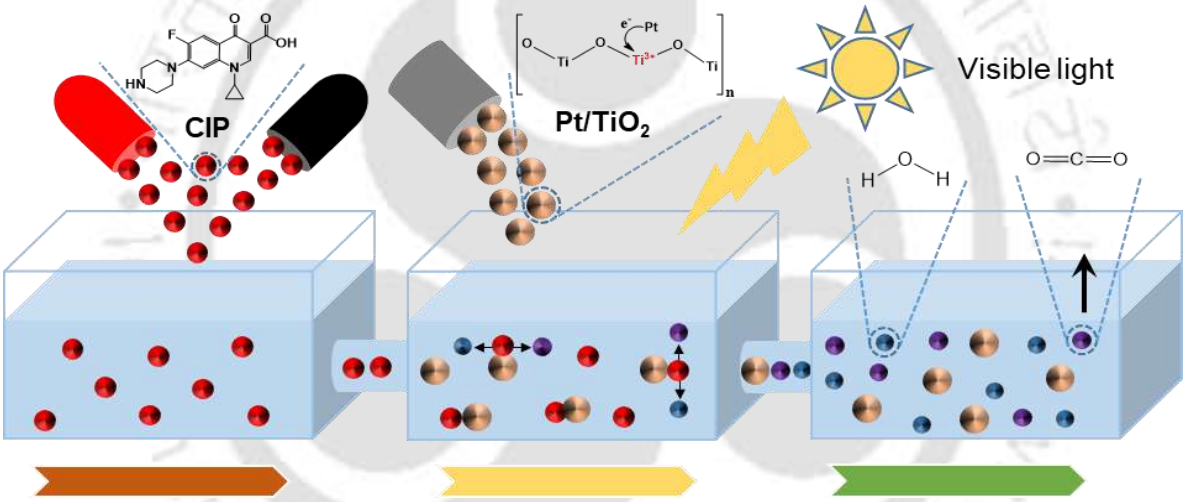

Chapter highlights

- A new bio-based-steamed autoclaving method developed to synthesize Pt-doped TiO_2
- Pt-doping took place as Pt(IV)→Pt(II)→Pt(0) with 90% Pt(0) abundance
- Bandgap of optimal $Pt_{1.47}/TiO_2$(bio) of 3.02 eV with improved functionality
- 2-fold increase in Ciprofloxacin degradation and quantum yield under visible light
- Photocatalytic degradation in three different pathways with 17 intermediates

Intentionally Left Blank
Intentionally Left Blank

3.1 Background and executive motivation

In the last few decades, rapid industrialization and its impacts have augmented the risk of incongruous living conditions. Despite odd environmental conditions, improved health care facilities have been key factors for the blooming population by decreasing the mortality rate. As a result, pharmaceutical waste production has been increased, and it causes serious health consequences across the globe. Direct disposal of pharmaceutical waste from industries, hospitals, and day-care centres drastically affects the habitat conditions of aquatic and terrestrial organisms (Wolski et al., 2021). Ciprofloxacin (CIP) is a fluoroquinolone antibiotic that is highly administered against various bacterial infections. Quinolone antibiotics in pharmaceutical waste and wastewater could stimulate persistent pollution, which could cause poisoning, allergic reactions, vomiting, nausea, heart disorders, bronchial asthma, and other harmful effects on living organisms. Persistence of low concentrations of antibiotics (<5 mg L^{-1}, lower than the MIC value of CIP) in the environment can trigger the resistance capability of the microbes, which ingeminate the need for the finest treatment for their elimination from the environment (Duo et al., 2019; Tamaddon et al., 2020). Hence, before discarding, the effluents of industries should be effectively treated to reduce the pollutant concentration below the critical level.

The methods, like adsorption, bio-mediated degradation, chemical treatments, photocatalysis, membrane separation, etc., are in place to treat industrial waste and wastewater, although each of these methods has specific advantages and disadvantages (Xing et al., 2018; Ravi and Pandey, 2019; Nandi et al., 2020; Bhan and Golder, 2023). Photocatalysis is one of the most effective tools for the degradation of pharmaceutical waste and wastewater, and it could mineralize the pharmaceutically active compounds (PhACs) to subdue the effects of microbial resistance and harmfulness on flora and fauna. Photocatalyst accelerates free radical-mediated decontamination in the presence of UV/visible/solar irradiation (Silva et al., 2016). TiO_2 and ZnO are widely used photocatalysts due to their easy availability, eco-friendly nature, cost-effectiveness, low toxicity, and high chemical stability. The high bandgap energy (E_g) and rate of recombination of electron-hole pairs are a few limitations of TiO_2, which decrease its photocatalytic efficiency in visible and solar light (Khan et al., 2019). High E_g of TiO_2 (3.22 eV) limits its application in solar/visible light due to the requirement of high energy for excitation of the electron, which can be provided by ultraviolet (UV) light. However, the Earth receives only 5% UV light, which is not efficient for adequate photocatalytic activity. The methods to reduce the E_g include forming heterojunctions, metal doping, fractionating anatase

and rutile phases, and forming composites with other semiconductors (Chelli and Golder, 2018; Khan et al., 2019).

Doping is considered the most acceptable technique to decrease the E_g by inserting the impurities into the crystal structure of semiconducting materials, which ultimately shifts the discrete energy level of electrons to lower the bandgap energy. Noble and transition metals are widely used as dopants for various applications (Chelli and Golder, 2018; Ghosh et al., 2018; Wolski et al., 2021). Pt, Pd, Au, and Ag are expensive, but they are preferred over base metals because of more stability and durability, which provide high activity for prolonged photocatalytic functionality (Bumajdad and Madkour, 2014). Various chemical routes have been practiced for metal ions doping for a long while, but the use of aggressive agents triggers a tremendous onslaught on the environment by producing hazardous by-products (Chelli et al., 2018; Bhan and Golder, 2023). Conversely, bio-mediated doping is an effective and eco-friendly technique where plants and their derivatives are employed as a source of reducing and capping agents. The economic status, easy availability, and effectiveness in metal doping demand the need for bio-derived agents to synthesize visible-light active photocatalysts. Additionally, plant extracts are reported to be effective for the controlled synthesis of nanoparticles (NPs) with the desired shape, dimensions, and dispersity over biological materials and extracts (microbes, microbial extract, enzymes, etc.) (Chelli et al., 2018; Bhan and Golder, 2023). Bio-based doping of Ag into TiO_2 was performed by using *T. peruviana* to degrade the MB dye. Ag doping on ZnO was achieved in the presence of analytes found in *S. edule* and tested for the degradation of the dipyrone drug. Bio-based bimetallic Zn and Cu were doped in TiO_2 to mineralize Congo red dye. Although bio-based doping of metal ions with positive reduction potential is quite challenging, it could improve the functionality of noble metal-doped photocatalysts for various applications. *S. edule* (chayote squash) is a copious source of ascorbic acid, which works as both reducing and capping agent (Chowdhury et al., 2021). The potential of these natural resources for the functionalization of TiO_2 by using a metal with high reduction potential, namely, Pt, for photocatalytic decomposition of the PhACs is a new direction of environmental research.

In this study, we have introduced an autoclave-based bio-based doping system for the functionalization of TiO_2 using Pt to decompose ciprofloxacin (CIP) under visible light. Ascorbic acid was extracted from *S. edule* to synthesize Pt-doped TiO_2. A succession of Pt-doped TiO_2 ($Pt_{0.49\text{-}2.43}/TiO_2$(bio)) was synthesized after optimization of various physiochemical parameters for efficient loading and doping of Pt. The bandgap energy was used as a critical factor for analyzing optimal Pt-doping. Further, bare-TiO_2 and Pt-doped TiO_2 ($Pt_{0.49\text{-}}$

$_{2.43}/TiO_2$(bio)) were characterized to investigate physiochemical variations, stability, doping mechanisms, and enhanced photocatalytic efficiency. The degradation of CIP molecules from their aqueous solution was performed under 50 W visible light (λ_{max} = 450 nm). Furthermore, the degradation reactions were investigated, and the mechanism of the reactions was proposed by analyzing the fragments of CIP molecules that originated during the photocatalytic reaction.

3.2 Results and discussion

3.2.1 UV–Vis diffuse reflectance spectra (UV-Vis DRS) and bandgap

Figs. 3.1a and 3.1b show the optimization results of Pt(IV) adsorption at pH 5-11 and $Pt(IV)_{0.00\text{-}2.43}$. The adsorption of Pt(IV) was almost equal at pH 5 and 7. The neutral pH was selected for further investigations as the Pt(IV) precursor did not cause a noteworthy alteration of the solution pH. The Pt(IV) adsorption ($Pt(IV)/TiO_2$, mg g^{-1}) was found to increase with an increase in Pt(IV) concentration, ranging up to 2.5% (w/w) studied in this work. However, the percentage Pt(IV) adsorption was about ~98%, irrespective of the initial Pt(IV) concentration.

The adsorbed Pt(IV) was then doped into TiO_2 at different pH levels and concentrations of vegetal extract. The bandgap of $Pt_{1.47}/TiO_2$(bio) was decreased with the increase in pH from 5 to 9 (Fig. 3.1c). The pH value >9 caused an increase in bandgap because of a lowering in Pt(IV) reduction due to the conversion of ascorbic acid to dehydroascorbic acid (DHA). The abundant bio-analytes with the increased vegetal extract concentration to 20 from 10% caused a decrease in the bandgap of $Pt_{1.47}/TiO_2$(bio) (Fig. 3.1d). The adsorbed Pt(IV) ions might have been entirely capped at a higher vegetal extract concentration (>20%). Large undoped PtNPs could also be formed by the Ostwald ripening effect, which is driven by a faster reduction rate of Pt(IV) ion. As a result, an increase in bandgap was noted. The bandgap at various pH and vegetal extract concentrations is listed in Table 3.1. The traces of Pt(IV)/Pt, if any, after the doping test in the used vegetal extract were undetectable. It confirms that Pt(IV) ions did not leach out during the doping experiment.

The bandgap of $Pt_{0.00}/TiO_2$(bare) and $Pt_{0.49\text{-}2.43}/TiO_2$(bio) at pH 9 with 20% vegetal extract is presented in Fig. 3.1e. The results confirmed the decrease in the bandgap of $Pt_{0.00}/TiO_2$(bare) from 3.29 to 3.02 eV in $Pt_{1.47}/TiO_2$(bio) at pH 9 with 20% vegetal extract concentration. The bandgap energy of $Pt_{0.00}/TiO_2$(bare) was observed to be decreased with an increase in the Pt concentration. Still, at a higher Pt concentration (Pt>1.5% w/w), the bandgap energy increased further, which might be attributed to the Burstein–Moss effect due to an increase in the electron carrier.

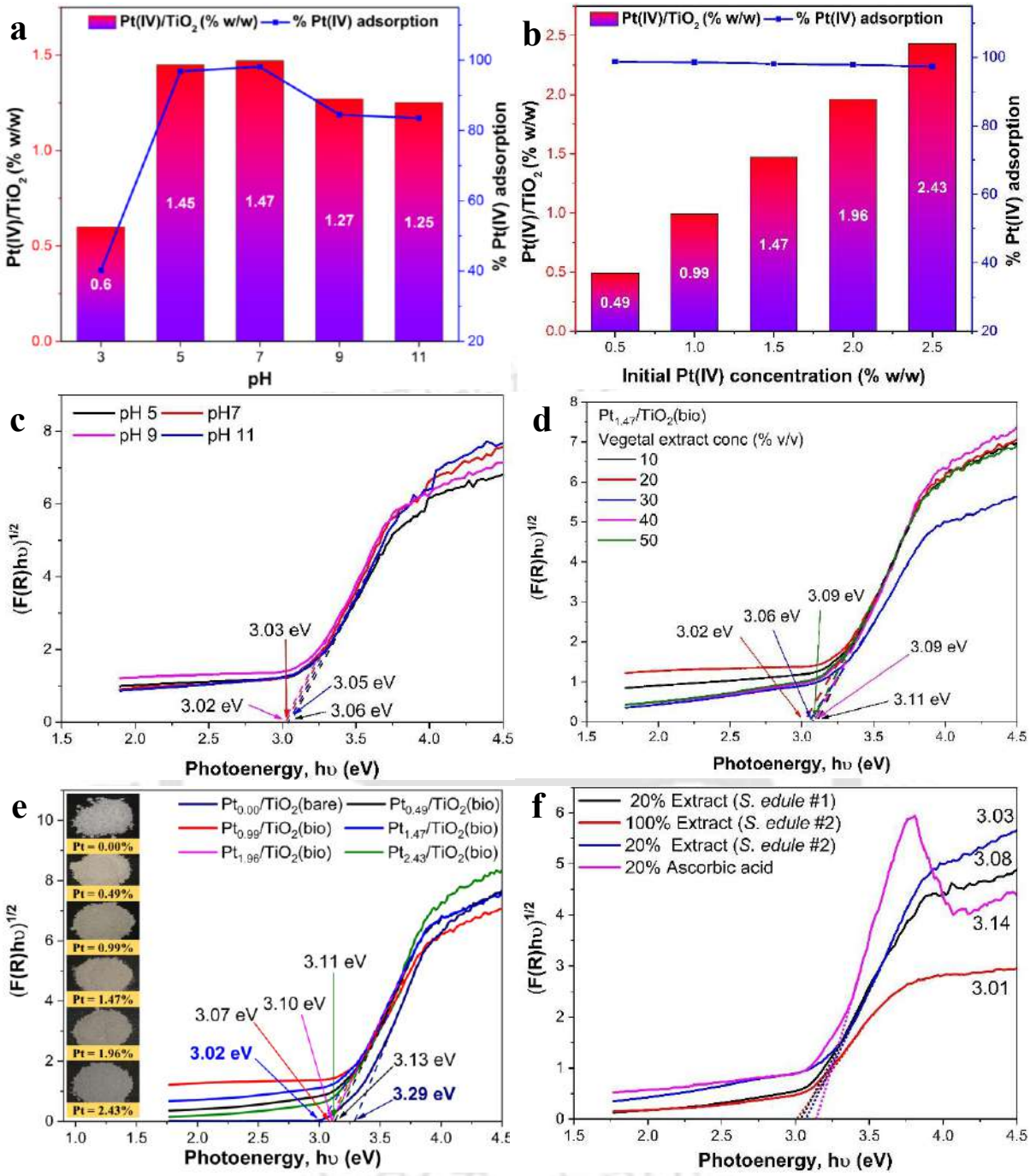

Figure 3.1: Adsorption of (a) 1.5% (w/w) Pt(IV) on Degussa P-25 TiO_2 at various pH (3-11) and (b) 0.5-2.5% (w/w) Pt(IV) at optimized pH 7; Tauc's plot (Kubelka-Munk function) for optical band gap of (c) $Pt_{1.47}/TiO_2$(bio) synthesized at various pH (5-11) (d) $Pt_{1.47}/TiO_2$(bio) synthesized using various vegetal-extract concentrations (10-50), (e) $Pt_{0.00}/TiO_2$(bare) and $Pt_{0.49\text{-}2.43}/TiO_2$(bio), and (f) $Pt_{1.47}/TiO_2$(bio) synthesized using different maturity of *S. edule* fruit extract and commercial ascorbic acid in a steamed autoclave for 20 min at 121°C.

The absorption edge is shifted to a high energy level due to a high electron carrier, which increases the density of electrons in the lower conduction band. The electron coming from the valence band needs more energy to jump to the upper valence band (Gahlawat et al., 2019). Similar kinds of results were also observed by Cervantes-Juárez et al. (2020) and Gahlawat et al. (2019) (Gahlawat et al., 2019; Cervantes-Juárez et al., 2020). $Pt_{1.47}/TiO_2$(chem) (Fig. 3.1f) could only reduce the bandgap to 3.14 eV. Further, the modified photocatalysts were more hydrophilic in nature with a high surface area in the case of the bio-based process.

Table 3.1: Optical band gap of $Pt_{1.47}/TiO_2$(bio) synthesized at various pH (5-11), using various vegetal extract concentrations (10-50% v/v) and different concentrations of Pt ($Pt_{0.00}/TiO_2$(bare) and $Pt_{0.49\text{-}2.43}/TiO_2$(bio)).

Catalyst	Doping pH	Vegetal extract (%, v/v)	Bandgap energy (eV)
$Pt_{1.47}/TiO_2$(bio)	5	20	3.06
	7		3.05
	9		**3.02**
	11		3.06
	9	10	3.11
		30	3.06
		40	3.09
		50	3.09
$Pt_{0.00}/TiO_2$(bare)		20	3.29
$Pt_{0.49}/TiO_2$(bio)			3.13
$Pt_{0.99}/TiO_2$(bio)			3.07
$Pt_{1.96}/TiO_2$(bio)			3.10
$Pt_{2.43}/TiO_2$(bio)			3.11
$Pt_{1.47}/TiO_2$(chem)	9	20 (Ascorbic acid)	3.14

3.2.2 X-ray diffraction (XRD) analysis

The X-ray diffraction patterns of $Pt_{0.00}/TiO_2$(bare) and $Pt_{0.49\text{-}2.43}/TiO_2$(bio) are shown in Fig. 3.2. It confirms the presence of both anatase and rutile phases in bare and doped TiO_2. The peak positions at 2θ = 25.24 (101), 36.91 (103), 37.76 (004), 38.51 (112), 47.98 (200), 53.88 (105), 55.01 (211), 62.62 (204), 68.92 (116), 70.28 (220), and 75.01° (215) correspond to the anatase phase (JCPDS, file No. 21-1272). On the other hand, the peak positions at 2θ = 27.34 (101), 36.01 (101), 41.18 (111), 44.04 (210), 54.27 (211), 56.56 (220), and 64.01° (310) confirms the rutile phase (JCPDS, file No. 21-1276). A peak shift was observed at 2θ = 48.20° in all $Pt_{0.49\text{-}2.43}/TiO_2$(bio), which attributes to the presence of the Pt (200), and a small

merged peak at 2θ = 70.55° with TiO_2 (anatase) is representing Pt (220) (JCPDS, file No. 01-085-5673) (He et al., 2019). However, the peak intensity was too low because of the very low concentration of Pt.

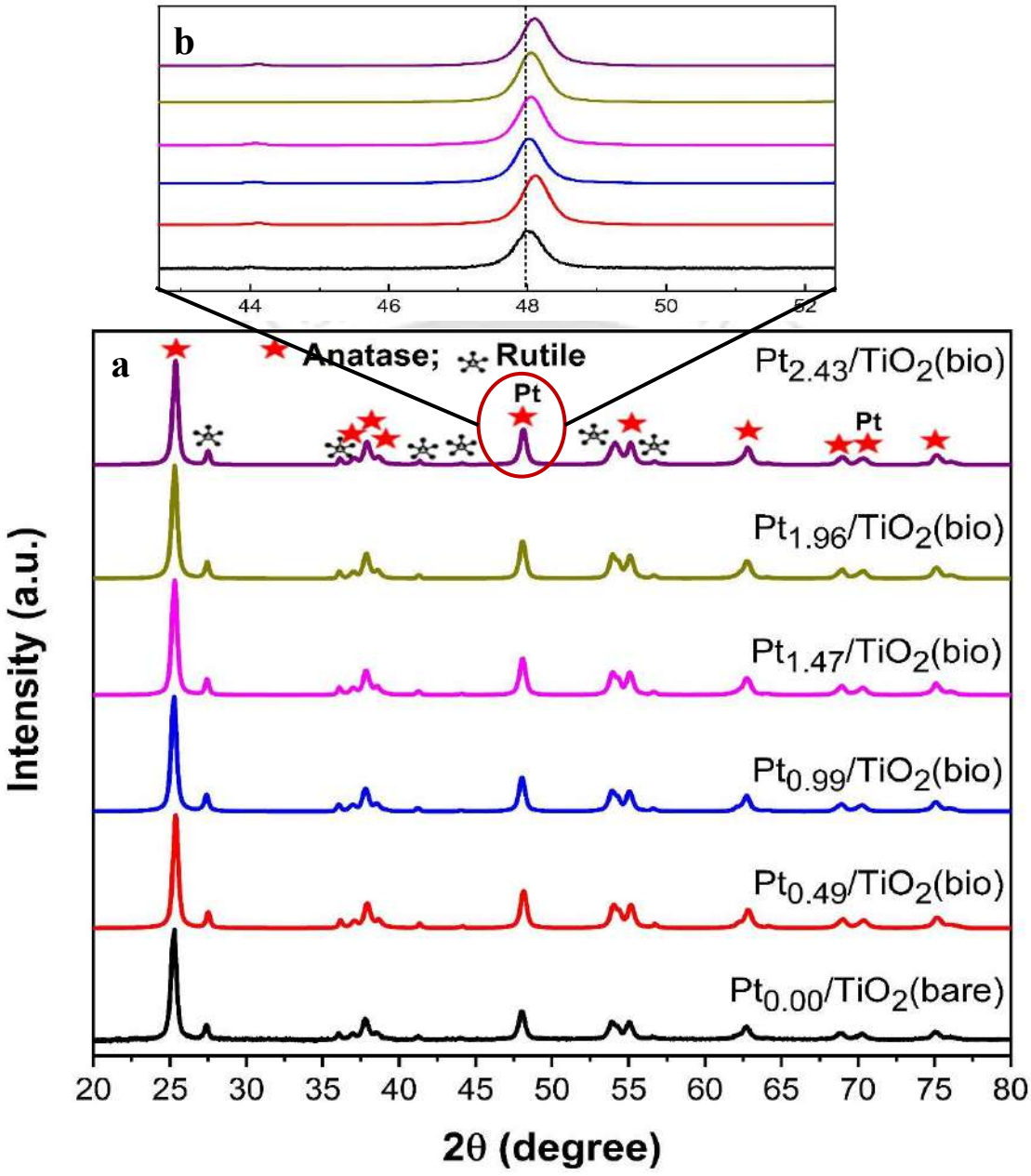

Figure 3.2: (a) XRD patterns, and (b) Magnified XRD patterns, showing peak shifting in $Pt_{0.00}/TiO_2$(bare) and $Pt_{0.49\text{-}2.43}/TiO_2$(bio). Here, "red star symbol" represents the anatase phase and "black star symbol" represents the rutile phase of TiO_2.

The obtained XRD parameters are summarized in Table 3.2. The results confirm the presence of anatase and rutile phases at 4:1 in bare-TiO_2. Only a slight increase in the rutile phase fraction (1.96-2.43% only) was noted with Pt doping, which might be attributed to the

co-existence of Pt within the lattice of TiO_2. A similar kind of anatase to rutile phase transformation was also observed due to iron and cobalt doping (Ismail et al., 2021). The increase in the crystallite size owing to Pt doping is attributed to filling the vacant sites and interstitial or substantial doping.

The defect in the lattices of particles was also measured in terms of lattice strain. $Pt_{0.49-2.43}/TiO_2$(bio) lattice developed a tensile strain with doping of Pt, originated due to the correction of deformations and replacement of Ti atoms (215 pm) with Pt atoms (175 pm) (Elzbieciak and Marciniak, 2018). The decrease in lattice strain reduces the free energy of the system and enhances the diffusivity of reaction species (free radicals), which ultimately could increase its photocatalytic efficiency (Li et al., 2019). The decrease in dislocations with doping of Pt caused an increase in the compressive strength of the TiO_2 lattice structure (Komaraiah et al., 2020).

Table 3.2: XRD parameters of $Pt_{0.00}/TiO_2$(bare) and $Pt_{0.49-2.43}/TiO_2$(bio).

Sample	Crystallite size (nm)	Anatase (%)	Rutile (%)	Lattice strain (ε)	Dislocation densities (Lines/nm^2)
$Pt_{0.00}/TiO_2$(bare)	20.59	80	20	8.05×10^{-3}	2.36×10^{-3}
$Pt_{0.49}/TiO_2$(bio)	21.00	79.69	20.31	7.88×10^{-3}	2.27×10^{-3}
$Pt_{0.99}/TiO_2$(bio)	21.20	79.46	20.54	7.82×10^{-3}	2.23×10^{-3}
$Pt_{1.47}/TiO_2$(bio)	21.65	79.40	20.60	7.62×10^{-3}	2.13×10^{-3}
$Pt_{1.96}/TiO_2$(bio)	21.02	79.77	20.23	7.87×10^{-3}	2.26×10^{-3}
$Pt_{2.43}/TiO_2$(bio)	21.05	79.49	20.51	7.84×10^{-3}	2.25×10^{-3}

3.2.3 X-ray photoelectron spectroscopic (XPS) analysis

Figs. 3.3a-e illustrates the high-resolution spectra of Ti2p, O1s, and Pt4f in $Pt_{0.00}/TiO_2$(bare), and $Pt_{1.47}/TiO_2$(bio), and the obtained relative elemental and configuration state composition are tabulated in Table 3.3. The XPS survey scan of $Pt_{0.00}/TiO_2$(bare), and $Pt_{1.47}/TiO_2$(bio) (Fig. 3.3f) confirms the presence of Ti2p, O1s, and C1s peaks in all the photocatalyst specimens. C1s peak attributed to carbon belongs to the adventitious and bioanalyses' carbon species. $Pt_{1.47}/TiO_2$(bio) showed an extra peak corresponding to the Pt4f state in the presence of Pt in $Pt_{1.47}/TiO_2$(bio). Fig. 3.3a represents the high-resolution XPS spectra of Ti2p of $Pt_{0.00}/TiO_2$(bare), showing two peaks at 464.7 (14.4%) and 458.9 eV (31.2%) corresponding to $Ti_{1/2}$ 2p and $Ti_{3/2}$, respectively, which ascribe to the Ti^{4+} state (Zhang et al., 2022).

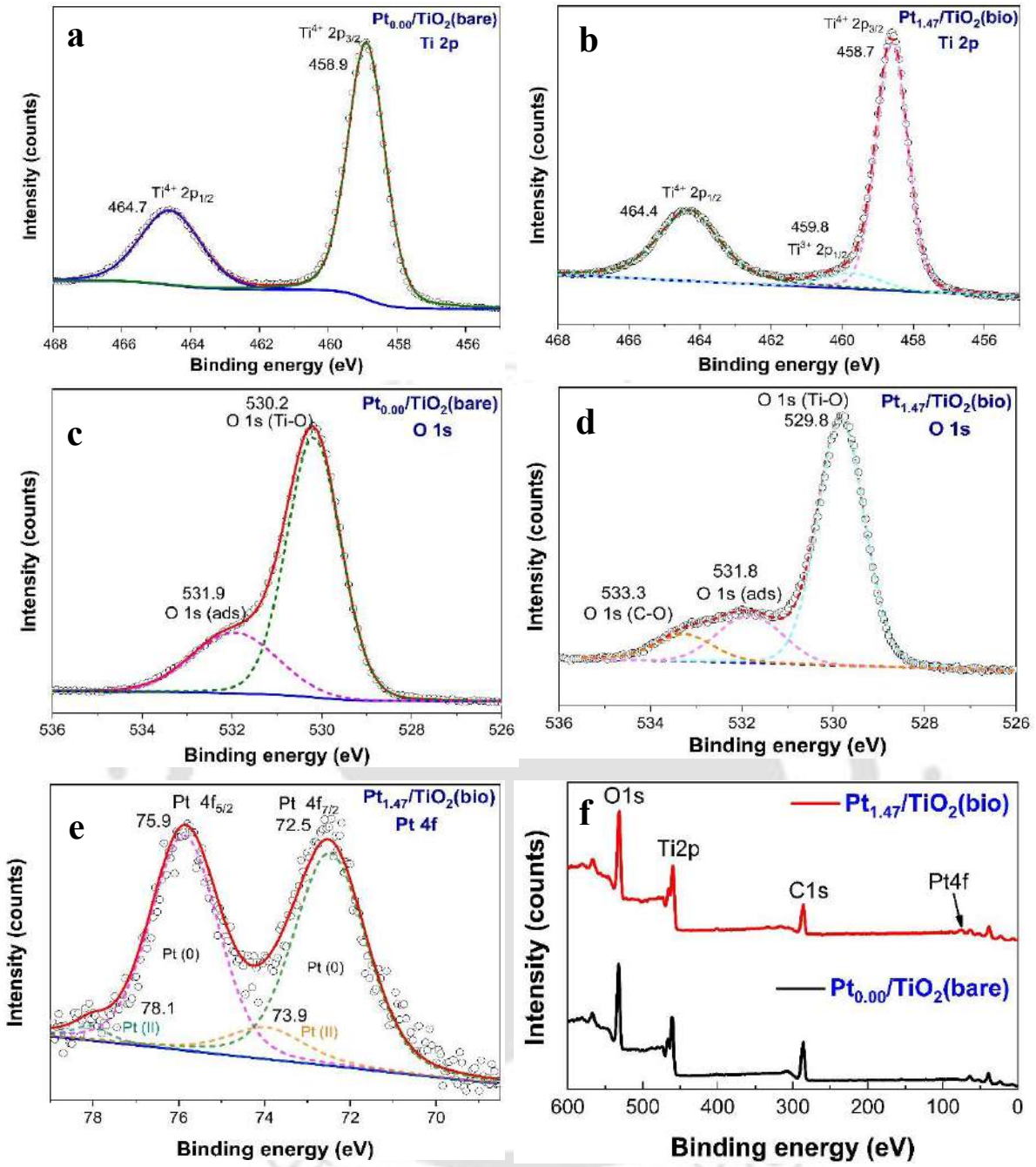

Figure 3.3: (a) XPS spectra of Ti2p of (a) $Pt_{0.00}/TiO_2$(bare), and (b) $Pt_{1.47}/TiO_2$(bio); O1s of (c) $Pt_{0.00}/TiO_2$(bare), and (d) $Pt_{1.47}/TiO_2$(bio); (e) Pt4f of $Pt_{1.47}/TiO_2$(bio) and (f) XPS survey spectra of $Pt_{0.00}/TiO_2$(bare), and $Pt_{1.47}/TiO_2$(bio).

Further, Fig. 3.3b shows the Ti2p spectra of $Pt_{1.47}/TiO_2$(bio) containing two sets of characteristic peak pairs where the dominant peak pair was located at 464.4 eV (19.2%) and 458.7 eV (28.9%) because of Ti^{4+}, and a new weak peak appeared at 459.8 eV (3.2%) attribute to the presence of Ti^{3+} state after doping of Pt (Xie et al., 2018). The reduction of Ti(IV) to the Ti(III) state could increase the oxygen vacancy (OVs) in $Pt_{1.47}/TiO_2$(bio). The red shifting (0.2-

0.3 eV) in the peaks (Ti2p) after doping indicates the impact of Pt on the Ti2p state, which might be the replacement of Ti^{4+} by Pt ion in the crystal lattice (Cheng et al., 2020). A decrease in the binding energy increases the electron density. Therefore, the reduction in bandgap energy from 3.29 to 3.02 eV might have resulted from introducing the electron donor states, i.e., Ti^{3+} and OVs.

Fig. 3.3c represents the high-resolution O1s spectra of $Pt_{0.00}/TiO_2$(bare) with two peaks at 530.2 (40.2%) and 531.9 eV (14.2%), which demonstrate the lattice (O_L) and surface adsorbed oxygen (O_{ads}, mainly hydroxide form), respectively. As shown in Fig. 3.3d, two similar peak shifts were observed at 531.8 (8.3%, O_{ads}) and 529.8 eV (33.6%, O_L), and an additional peak was detected at 533.3 eV (5.0%), which could be ascribed to the C-O group of vegetal extract constituents adsorbed during the doping test (Wang et al., 2020). The decrease in the peaks binding energies (0.2 - 0.3 eV) could cause an increase in electron density, which decreases the bandgap energy and rate of recombination (Xie et al., 2018). Hence, an increase in surface adsorbed oxygen positively impacts the rate of free radical formation for enhanced photocatalytic degradation.

Table 3.3: Relative elemental and configuration state composition of $Pt_{0.00}/TiO_2$(bare), and $Pt_{1.47}/TiO_2$(bio), analyzed through XPS.

Element	Chemical state	Sample (% area)	
		$Pt_{0.00}/TiO_2$(bare)	**$Pt_{1.47}/TiO_2$(bio)**
Ti	Ti^{4+} 2p	48.3	48.1
	Ti^{3+} 2p	-	3.2
	Ti 2P (Total)	48.3	51.3
O	O_L 1s	40.4	33.5
	O_a 1s	11.3	8.3
	O(C-O) 1s	-	5.0
	O 1s (Total)	51.7	46.8
Pt	Pt^0 4f	-	1.7
	Pt^{2+} 4f	-	0.2
	Pt 4f (Total)	-	1.9

3.2.4 FETEM and EDX analysis

The size and shape of $Pt_{0.00}/TiO_2$(bare) and $Pt_{1.47}/TiO_2$(bio) were determined using HRTEM micrographs. The morphologies, SAED pattern, and size distribution of TiO_2 before and after doping are shown in Fig. 3.4.

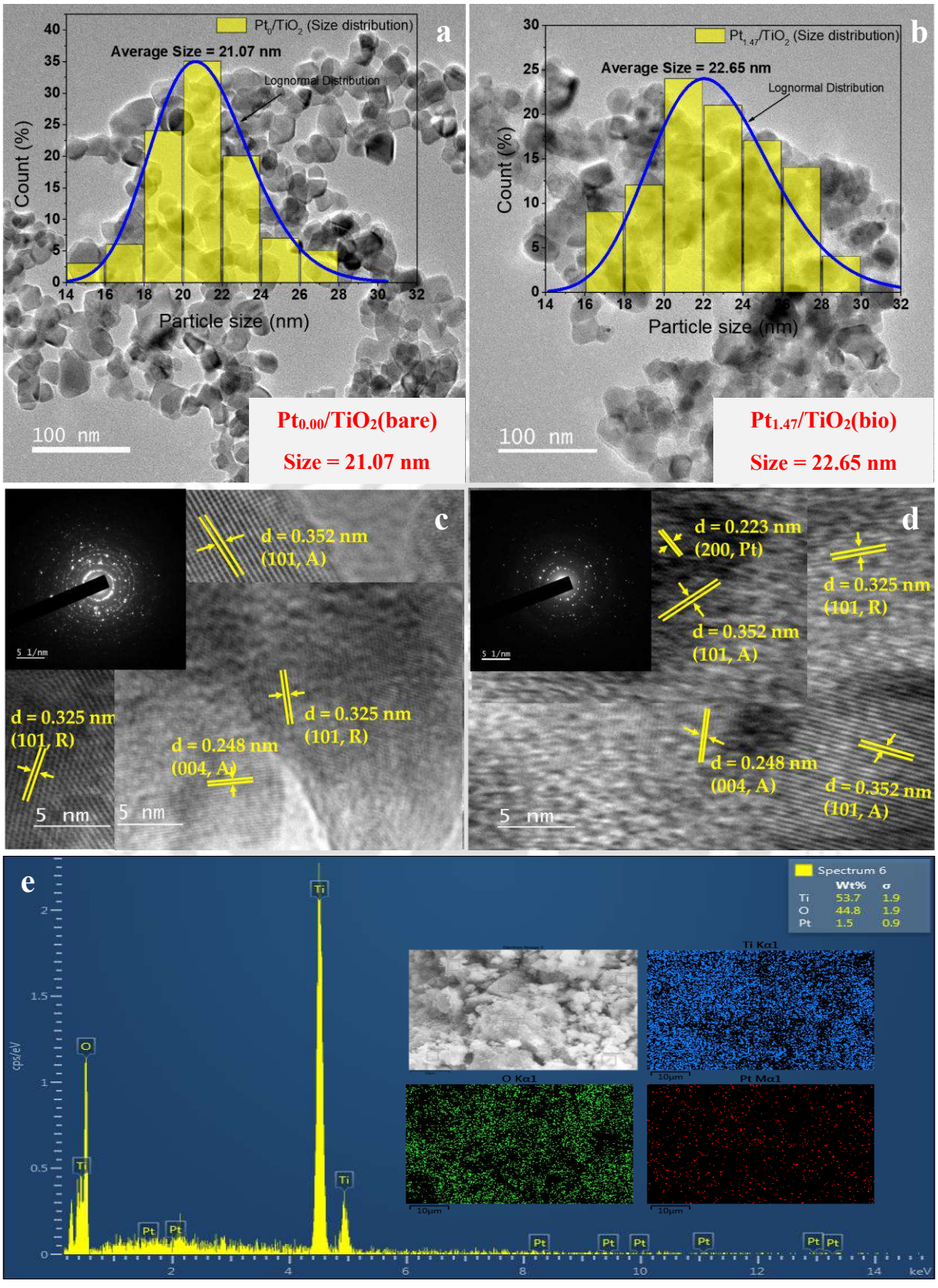

Figure 3.4: FETEM micrograph and particle size distribution of (a) $Pt_{0.00}/TiO_2$(bare), and (b) $Pt_{1.47}/TiO_2$(bio), HRTEM micrograph and SAED patterns of (c) $Pt_{0.00}/TiO_2$(bare), and (d) $Pt_{1.47}/TiO_2$(bio), and (e) EDX spectra and elemental mappings of Ti, O, and Pt in $Pt_{1.47}/TiO_2$(bio).

TEM micrographs confirm that both $Pt_{0.00}/TiO_2$(bio) and $Pt_{1.47}/TiO_2$(bio) particles are nearly spherical in shape with an average size of 21.07 nm (Fig. 3.4a) and 22.65 nm (Fig. 3.4b), respectively. An increase in particle size caused a decrease in lattice strain. The increase in particle size with Pt doping is due to the combined effect of (i) Pt incorporation into interstitial sites of TiO_2 and (ii) formation of PtNPs on the TiO_2 surface (Boiko et al., 2021). Compared to $Pt_{0.00}/TiO_2$(bare), small nanodots were observed in the FETEM image of $Pt_{1.47}/TiO_2$(bio) due to tiny PtNPs formed on TiO_2.

The lattice fringes with d-spacings of 0.352, 0.325, and 0.248 nm belong to the anatase, rutile, and anatase phase of TiO_2, respectively (Fig. 3.4c). The d spacings of 0.352, 0.325, 0.248, and 0.23 nm correspond to the anatase phase (101), rutile phase (101), and anatase phase (004) of TiO_2, and PtNPs (200), respectively (Fig. 3.4d) (Pugazhenthiran et al., 2018). The obtained interplanar spacing is in close agreement with the XRD patterns. Further, HRTEM images and SAED pattern (insets of Figs. 3.4c and 3.4d) demonstrate the distinctive electron diffraction rings because of the polycrystalline nature of $Pt_{0.00}/TiO_2$(bare) and $Pt_{1.47}/TiO_2$(bio) (Komaraiah et al., 2020).

The elemental analysis of $Pt_{1.47}/TiO_2$(bio) was also performed, and the spectra along with their elemental mapping are shown in Fig. 3.4e. A uniform distribution of Pt onto TiO_2 and Ti and O could provide more sites for catalytic applications.

3.2.5 Thermogravimetric analysis (TGA)

Thermogravimetric spectra of mass degradation of $Pt_{0.00}/TiO_2$(bare) and $Pt_{1.47}/TiO_2$(bio) with temperature are shown in Fig. 3.5a. Like $Pt_{0.00}/TiO_2$(bare), $Pt_{1.47}/TiO_2$(bio) also retained its stability till 800°C. A mass loss of ~2% was observed up to 200°C due to evaporation of the water present in $Pt_{0.00}/TiO_2$(bare) and $Pt_{1.47}/TiO_2$(bio). The mass was almost invariant for $Pt_{0.00}/TiO_2$(bare) at >200°C because of the absence of impurities and/or any phase transformation (Mahlambi et al., 2012). $Pt_{1.47}/TiO_2$(bio) lost 3.9% of its mass at 200-400°C. It is attributed to the degradation of organic compounds adsorbed on $Pt_{1.47}/TiO_2$(bio) from vegetal extract, which acted as reducing and capping agents (Chelli et al., 2018). Further, a minor mass loss of ~1% was observed for $Pt_{1.47}/TiO_2$(bio) at 400-800°C, which might be attributed to an irreversible phase transition of anatase to rutile due to oxygen vacancies originating from doping (Mahlambi et al., 2012).

3.2.6 BET surface area analysis

N_2 adsorption-desorption isotherms and pore size distributions of $Pt_{0.00}/TiO_2$(bare) and $Pt_{1.47}/TiO_2$(bio) are shown in Fig. 3.5b. Both the specimens followed a typical IV isotherm, which implies the proximity of pores in both nanoparticles, and the hysteresis loop is indicative of pore condensation at high pressure and mesoporous nature (Pugazhenthiran et al., 2018). The surface area, average pore size, and pore volume of $Pt_{1.47}/TiO_2$(bio) were found to be 53.8 $m^2\ g^{-1}$, 34.5 nm, and 0.5 cc g^{-1}, respectively (Fig. 3.5b). For $Pt_{0.00}/TiO_2$(bare), it was 60.7 $m^2\ g^{-1}$, 18.1 nm, and 0.3 cc g^{-1}, respectively. The results confirm a decrease in BET surface area and an increase in pore size and pore volume in $Pt_{1.47}/TiO_2$(bio), which is in line with the increase in particle size. In fact, the formation of tiny PtNPs could have filled some of the pores. So, a reduction in surface area was observed.

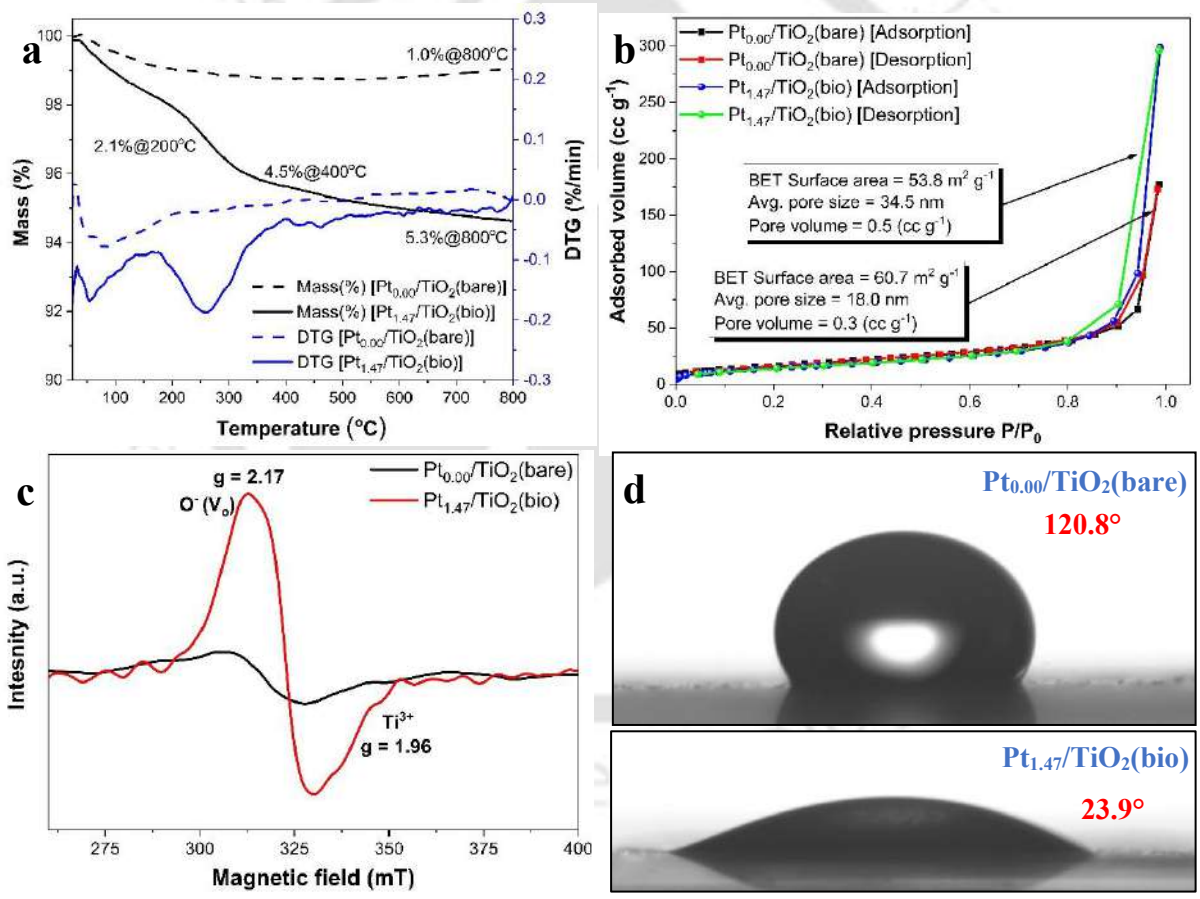

Figure 3.5: (a) TGA analysis, (b) N_2 adsorption-desorption isotherm curves, (c) EPR spectra, and (d) Water contact angle of $Pt_{0.00}/TiO_2$(bare), and $Pt_{1.47}/TiO_2$(bio).

3.2.7 Electron paramagnetic resonance (EPR) analysis

Fig. 3.5c shows the EPR spectra of $Pt_{0.00}/TiO_2$(bare), and $Pt_{1.47}/TiO_2$(bio). The EPR peak with a g-value of 2.17 at 310 mT and a low-intensity peak with a g-value of 1.96 at 337

mT imply the formation of superoxide radicals. A strong EPR intensity at a g-value of 2.17 in $Pt_{1.47}/TiO_2$(bio) indicates abundant oxygen vacancy, and a weak EPR signal at a g-value of 1.96 could be because of the presence of Ti^{3+} defects to Pt doping (Komaraiah et al., 2020). Oxygen vacancy increases H_2O adsorption, which in turn participates in free radical formation. Ti^{3+} defects also could trap the electrons, reducing h^+/e^- recombination for an enhanced photocatalytic activity (Gogoi et al., 2020).

3.2.8 Hydrophilicity analysis

The surface wettability of $Pt_{0.00}/TiO_2$(bare) and $Pt_{1.47}/TiO_2$(bio) was studied by measuring the water contact angle on photocatalyst-coated cover glass. For coating, the photocatalyst was first dispersed in DI water (1 mg mL^{-1}) and sonicated for 30 min. Further, 1 mL photocatalyst suspension was spread on the cover glass (No. 1 English Glass, 22 × 40 mm, BLUE STAR, Mumbai, INDIA) and kept at 60°C for 12 h. The water drop formation and the corresponding contact angle are illustrated in Fig. 3.5d. $Pt_{0.00}/TiO_2$(bare) is hydrophobic in nature (120.8°), and Pt doping made it hydrophilic with a water contact angle of 23.9° in $Pt_{1.47}/TiO_2$(bio). Hydrophilic particles could adsorb more -OH groups owing to high affinity toward surface water, which could improve the photocatalytic activity. The adsorption of contaminants may turn $Pt_{0.49\text{-}2.43}/TiO_2$(bio) particles less hydrophilic, but it could be regained with the decomposition of contaminants (Mimouni et al., 2020).

3.2.9 Photoluminescence (PL) and time-resolved photoluminescence (TRPL)

The charge separation, e^-/h^+ recombination, and trapping efficiency of $Pt_{0.00}/TiO_2$(bare) and $Pt_{1.47}/TiO_2$(bio) are investigated by PL spectroscopy. Fig. 3.6a illustrates the excitation-emission spectra of $Pt_{0.00}/TiO_2$(bare) and $Pt_{1.47}/TiO_2$(bio), which were recorded at 320 nm excitation wavelength. The results confirmed the PL spectra with similar emission peaks at 396, 438, 449, 468, 480, 492, 524, and 562 nm for both specimens. The major peak at 396 nm determines the recombination of the e^-/h^+ pairs, and the peaks from 438 to 562 nm represent localized states of the valence band of TiO_2 (Gogoi et al., 2020). No new emission peak was found in $Pt_{1.47}/TiO_2$(bio). There was a significant decrease in photoluminescence intensity because of the retardation of e^-/h^+ recombination due to Pt doping. Hence, delayed recombination and lower E_g will facilitate the enhanced photocatalytic activity of $Pt_{1.47}/TiO_2$(bio) (Ismael, 2019).

The lifetimes of charge carriers in $Pt_{0.00}/TiO_2$(bare) and $Pt_{1.47}/TiO_2$(bio) were analyzed using TRPL spectra. TRPL analyses were performed at 320 nm excitation and 396 nm emission

wavelength with 1000 counts. The normalized data were fitted with a biphasic exponential function, and the obtained parameters are shown in Fig. 3.6b. The lifetime of charge carriers' parameters values τ_1, τ_2, A_1, and A_2 were found to be 0.74 ns, 8.73 ns, 0.96, and 0.04, respectively, for $Pt_{1.47}/TiO_2$(bio). The same were found to be 0.56 ns, 5.05 ns, 0.97, and 0.3 for $Pt_{0.00}/TiO_2$(bare). The decay rate constant of $Pt_{1.47}/TiO_2$(bio) was higher than that of $Pt_{0.00}/TiO_2$(bare). It confirms retardation in the recombination of the charge carriers. τ_1 decay constant represents the PL of free excitation states, while the τ_2 decay rate constant corresponds to PL due to Shockley-Read-Hall (SRH) recombination of h^+ and trapped e^- where e^- transits through a new localized state (Zhou et al., 2020).

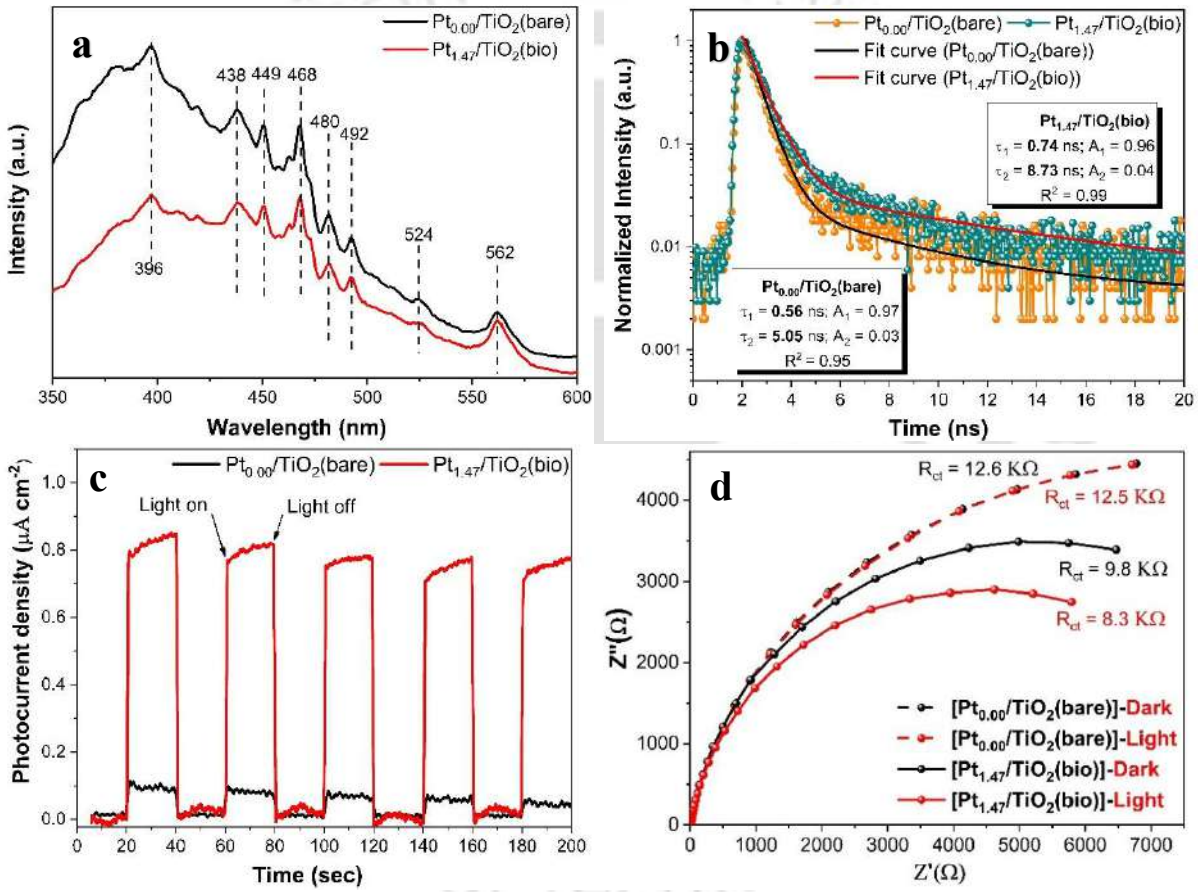

Figure 3.6: (a) Photoluminescence (PL) spectra, and (b) Time resolved photoluminescence (TRPL) of $Pt_{0.00}/TiO_2$(bare), and $Pt_{1.47}/TiO_2$(bio); (c) Chronoamperometric transient photocurrent response, and (d) Nyquist's plot for EIS analysis, in presence and absence of light, of $Pt_{0.00}/TiO_2$(bare), and $Pt_{1.47}/TiO_2$(bio).

3.2.10 Photoelectrochemical (PEC) characteristics

The photosensitivity of the photocatalysts was investigated by chronoamperometric measurements with several on/off light cycles at 20 s intervals (Fig. 3.6c). A sharp increase in

the current density was observed with $Pt_{1.47}/TiO_2$(bio) (maximum CD 0.85 μA cm^{-2}) over $Pt_{0.00}/TiO_2$(bio) (maximum CD 0.11 μA cm^{-2}). The obtained results with $Pt_{1.47}/TiO_2$(bio) confirm (i) a better charge separation due to e^- excitation and promotion from the valence band to the conduction band, (ii) delayed recombination, and (iii) interfacial charge transfer, which is supported by PL and TRPL analyses (Kumar et al., 2020). Bubble formation at the electrode surface due to the release of dissolved gases and produced H_2 gas could mask a part of the electrode surface, decreasing its active surface area. Therefore, a slow electron transfer, deterioration of the photocatalyst layer, and bubble formation are a few common reasons for the decrease in the photocurrent density in both $Pt_{0.00}/TiO_2$(bare) and $Pt_{1.47}/TiO_2$(bio) with prolonged irradiation time (Cheng et al., 2020).

Fig. 3.6d shows Nyquist's plot representing the fitted data of electrochemical impedance spectra (EIS) recorded with $Pt_{0.00}/TiO_2$(bare) and $Pt_{1.47}/TiO_2$(bio) with and without visible light irradiation. The charge transfer resistance (R_{ct}) of $Pt_{1.47}/TiO_2$(bio) was 9.8 and 8.3 KΩ in dark and light, respectively. R_{ct} was slightly higher for $Pt_{0.00}/TiO_2$(bare), which was 12.6 and 12.5 KΩ, in dark and light, respectively. The decrease in the charge transfer resistance indicates better charge separation, fast electron movement, and delayed recombination due to Pt doping. The decrease in R_{ct} for $Pt_{1.47}/TiO_2$(bio) was more under irradiation, which supports the generation of more accessible electrons in the conduction band for $Pt_{1.47}/TiO_2$(bio) (Krishnapriya et al., 2021).

3.2.11 Photocatalytic degradation of CIP

The degradation efficiency at different time intervals and non-linear first-order kinetic model fitting at various pH and dopant concentrations are shown in Figs. 3.7a and 3.7b. The degradation efficiency, k_1, QY, and $t_{1/2}$ are tabulated in Table 3.4. The QY and degradation efficiency at various pH levels using $Pt_{1.47}/TiO_2$(bio) and various Pt-doped TiO_2 photocatalysts at the optimal pH 5 are depicted in Figs. 3.7c and 3.7d, respectively. The maximum CIP degradation of 85.50±0.94% was achieved at pH 5 with $Pt_{1.47}/TiO_2$(bio) within 180 min of irradiation with a photocatalyst dose of 1 g L^{-1} and an initial CIP concentration of 5 mg L^{-1}. The degradation efficiency and k_1 were found to increase from 71.40±2.63 to 85.50±0.94% and 0.0062 to 0.0148 min^{-1} in 180 min, respectively, with an increase in pH from 3 to 5, but they decreased further with an increase in pH>5. Likewise, the half-life of CIP degradation decreased from 112.61 to 46.76 min with an increase in pH from 3 to 5, and it further increased to 75.80 min with a further increase in pH till 8. Adsorption of CIP was more at higher pH in

the dark, which might be attributed to the enhancement in the ionic interaction between photocatalyst and CIP molecules at higher pH (Ravi and Pandey, 2019). An increase in photocatalytic efficiency and k_1 (55.97±1.61 to 85.50±0.94% and 0.0046 to 0.0148 min^{-1}, respectively, at pH 5 in 180 min) was observed with an increase in dopant concentration from 0 to 1.47% (w/w). However, a further increase in Pt concentration resulted in a decline in the photocatalytic efficiency to 76.80±1.59% with k_1 of 0.0098 min^{-1} in 180 min, which might be due to decreased radicals' generation because of high bandgap energy (Chelli and Golder, 2018). The maximum QY of 21.05±0.23% was obtained by $Pt_{1.47}/TiO_2$(bio).

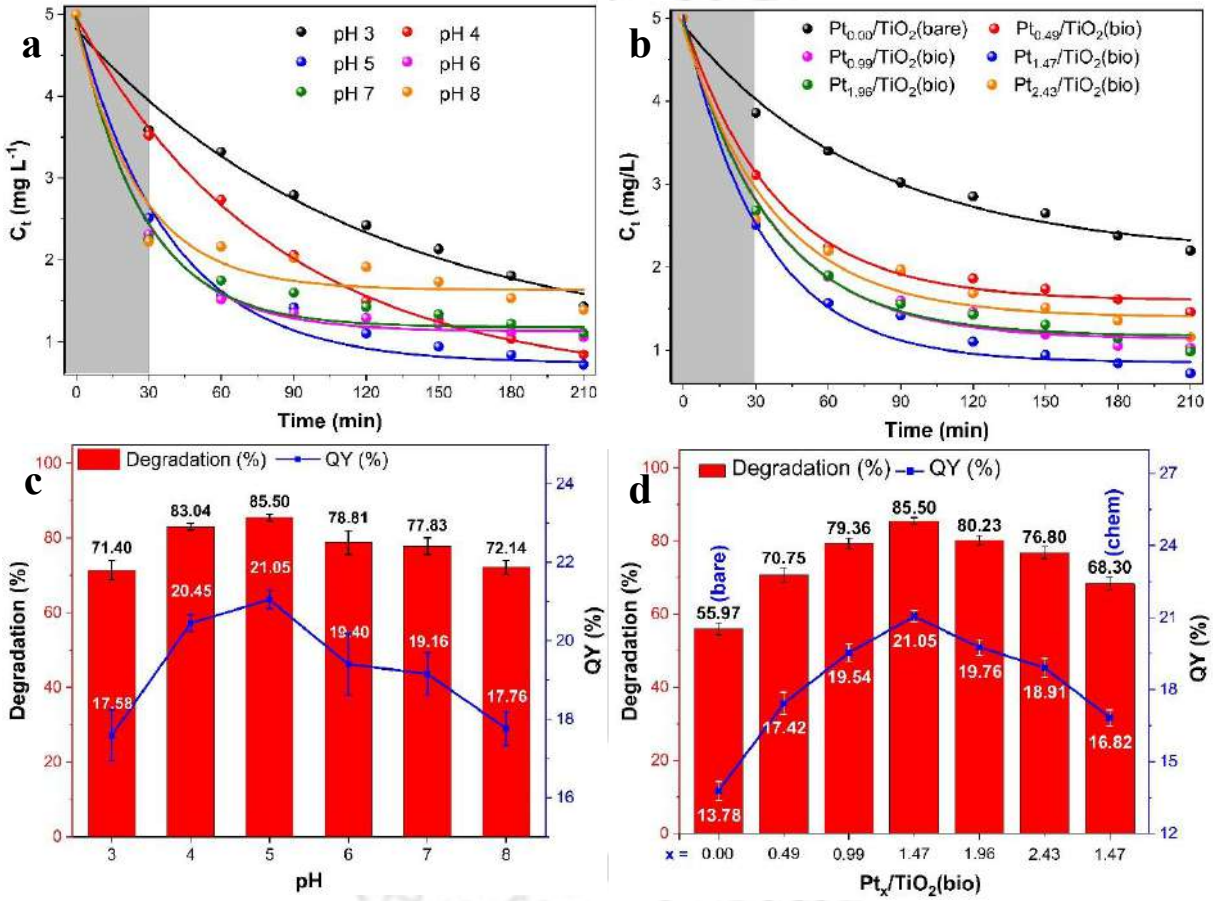

Figure 3.7: (a) CIP decay (symbols: experimental and line: non-linear first-order kinetic model fitted) at different pH using $Pt_{1.47}/TiO_2$(bio), (b) CIP decay (symbols: experimental and line: non-linear first-order kinetic model fitted) using different photocatalysts at pH 5, (c) CIP degradation efficiency and QY at different pH using $Pt_{1.47}/TiO_2$(bio), and (d) CIP degradation efficiency and QY using different photocatalysts at pH 5.

Table 3.4: CIP degradation efficiency (%), rate constant (min^{-1}), half-life (min) and QY (%) of CIP photocatalytic degradation of 100 mL CIP (5 mg L^{-1}) using $Pt_{1.47}/TiO_2$(bio) (1 g L^{-1}) at various pH (3-8) and $Pt_{0\text{-}2.43}/TiO_2$(bio) (1 g L^{-1}) at optimized pH 5 under 50W visible light (450 nm) for 180 min with continuous stirring at 300 rpm.

Catalysts	pH	CIP degradation (%)	k_1 (min^{-1})	Half-life (min)	QY (%)
$Pt_{0.00}/TiO_2$(bare)	5	55.97 ± 1.61	0.46 x 10^{-2}	151.02	13.78 ± 0.40
$Pt_{0.49}/TiO_2$(bio)		70.75 ± 1.90	0.85 x 10^{-2}	81.45	17.42 ± 0.47
$Pt_{0.99}/TiO_2$(bio)		79.36 ± 1.47	1.19 x 10^{-2}	58.20	19.54 ± 0.36
$Pt_{1.47}/TiO_2$(bio)		85.50 ± 0.94	1.48 x 10^{-2}	46.76	21.05 ± 0.23
$Pt_{1.96}/TiO_2$(bio)		80.23 ± 1.34	1.18 x 10^{-2}	58.95	19.76 ± 0.33
$Pt_{2.43}/TiO_2$(bio)		76.80 ± 1.59	0.98 x 10^{-2}	70.47	18.91 ± 0.39
$Pt_{1.47}/TiO_2$(bio)	3	71.40 ± 2.63	0.62 x 10^{-2}	112.61	17.58 ± 0.65
	4	83.04 ± 0.88	0.96 x 10^{-2}	72.27	20.45 ± 0.22
	6	78.81 ± 3.22	1.39 x 10^{-2}	49.90	19.40 ± 0.79
	7	77.83 ± 2.19	1.22 x 10^{-2}	56.67	19.16 ± 0.54
	8	72.14 ± 1.79	0.91 x 10^{-2}	75.80	17.76 ± 0.44
$Pt_{1.47}/TiO_2$(chem)	5	68.30 ± 2.21	-	-	16.82 ± 0.54

Table 3.5: Photocatalytic degradation of CIP by various chemically synthesized photocatalysts and their comparison with $Pt_{1.47}/TiO_2$(bio) (present study).

Photocatalyst	Light source	Initial CIP concentration (mg L^{-1})	Catalyst dose (g L^{-1})	Reaction time (min)	CIP degradation (%)	Reference
CeO_2/ZnO nanocomposites	200 W Hg-Xe lamp (365 nm, UV)	15	0.25	60	60	(Wolski et al., 2021)
$CuFe_2O_4$@methyl cellulose	UV-C light	3	0.67	90	80.8	(Tamaddon et al., 2020)
Fe_3O_4/Bi_2WO_6 nanocomposites	300W Visible light (> 400 nm)	15	1	120	65	(Song et al., 2020)
Au/TiO_2	Visible light (Solar Spectra)	5	1.3	180	49	(Martins et al., 2020)
$MoS_2/NiSe_2$	Photo-electrocatalysis (100 W Xe lamp)	5	0.5	120	78	(Yusuf et al., 2024)
Ag_2MoO_4	UV light (365 nm)	20	5	40	98	(Kumar et al., 2016)
Ce−doped BiOCl nanosheets	500 W Xe lamp (>420 nm)	10	1	30	90	(Duo et al., 2019)
N-TiO_2	500 W Xe lamp (>420 nm)	20	3	180	97.5	(Xing et al., 2018)
TiO_2	UVA light (365 nm)	0.3	1	45	85	(Silva et al., 2016)
ZnO		0.3	1	45	63	
$Pt_{1.47}/TiO_2$(bio)	50 W visible light	5	1	180	85.5 ± 0.94	**Present study**

CIP degradation of 4.1% was observed under visible light irradiation alone without any photocatalyst. $Pt_{0.00}/TiO_2$(bare), and PtNPs showed 22.77 and 31.6% CIP adsorption under dark conditions against 55.97 and 35.34% photocatalytic efficiency of CIP degradation within 180 min, respectively. Further, the photocatalytic degradation of CIP was also performed using $Pt_{1.47}/TiO_2$(chem) (0.1%, w/v) at pH 5. $Pt_{1.47}/TiO_2$(bio) and $Pt_{1.47}/TiO_2$(chem) could adsorb 49.72±2.38% and 29.85±1.97% CIP under dark conditions against 85.50±0.94 and 68.30±2.21% CIP degradation within 180 min, respectively. It implies that $Pt_{1.47}/TiO_2$(bio) exhibited a better mineralization efficiency than $Pt_{1.47}/TiO_2$(chem). The photocatalytic efficiency of $Pt_{1.47}/TiO_2$(bio) degrading CIP was compared with earlier reports. The present work showed clear superiority over many earlier studies (Table 3.5).

3.2.12 CIP degradation mechanism

LC-MS spectra acquired via positive EIS mode $[M+H]^+$ before and after CIP decomposition are illustrated in Fig. 3.7. The LC spectra of CIP before and after photodegradation showed two peaks (Figs. 3.7a and 3.7b). Two major peaks were observed in the case of pure CIP at the retention times of 1.960–2.466 and 2.608–3.182 min. It represents CIP molecule with m/z of 332.3 (Fig. 3.7a) and CIP–HCl (chlorinated) with m/z of 340.4 (Fig. 3.7b) (Wang et al., 2017). Similarly, two peaks were also noted after CIP decomposition at the retention time of 1.945–2.213 and 2.601–3.033 min (Figs. 3.7c and 3.7d).

The obtained MS spectra were utilized to predict the CIP photodegradation mechanism, and the proposed CIP degradation mechanism is illustrated in Fig. 3.9. Several intermediate products (P1-P17) were identified in mass spectra with CIP decomposition mainly in three different pathways. The chlorinated CIP (P1, m/z = 340.4) was produced by simultaneous addition of Cl on the quinolone ring and cleavage of the piperazine ring (dealkylation) (Wang et al., 2017). P2 (m/z=306.1) is formed by partial cleavage of the piperazine ring with a loss of ethane (Pathway #I). Chlorinated CIP could also be cleaved to P2 by releasing Cl via dechlorination, and P2 is defluorinated to P3 (m/z=301.3) by substituting F with an -OH group. The piperazine chain ($C_2H_5N_2$) is cleaved from P3 and transformed to P4 (m/z =245.1). It is degraded to P5 (m/z = 201.1) intermediate with the release of formic acid, which is anticipated to degrade further, forming CO_2 (decarboxylation). P5 intermediate loses the cyclopropane to form P6 (m/z =160.1) (Xu et al., 2019).

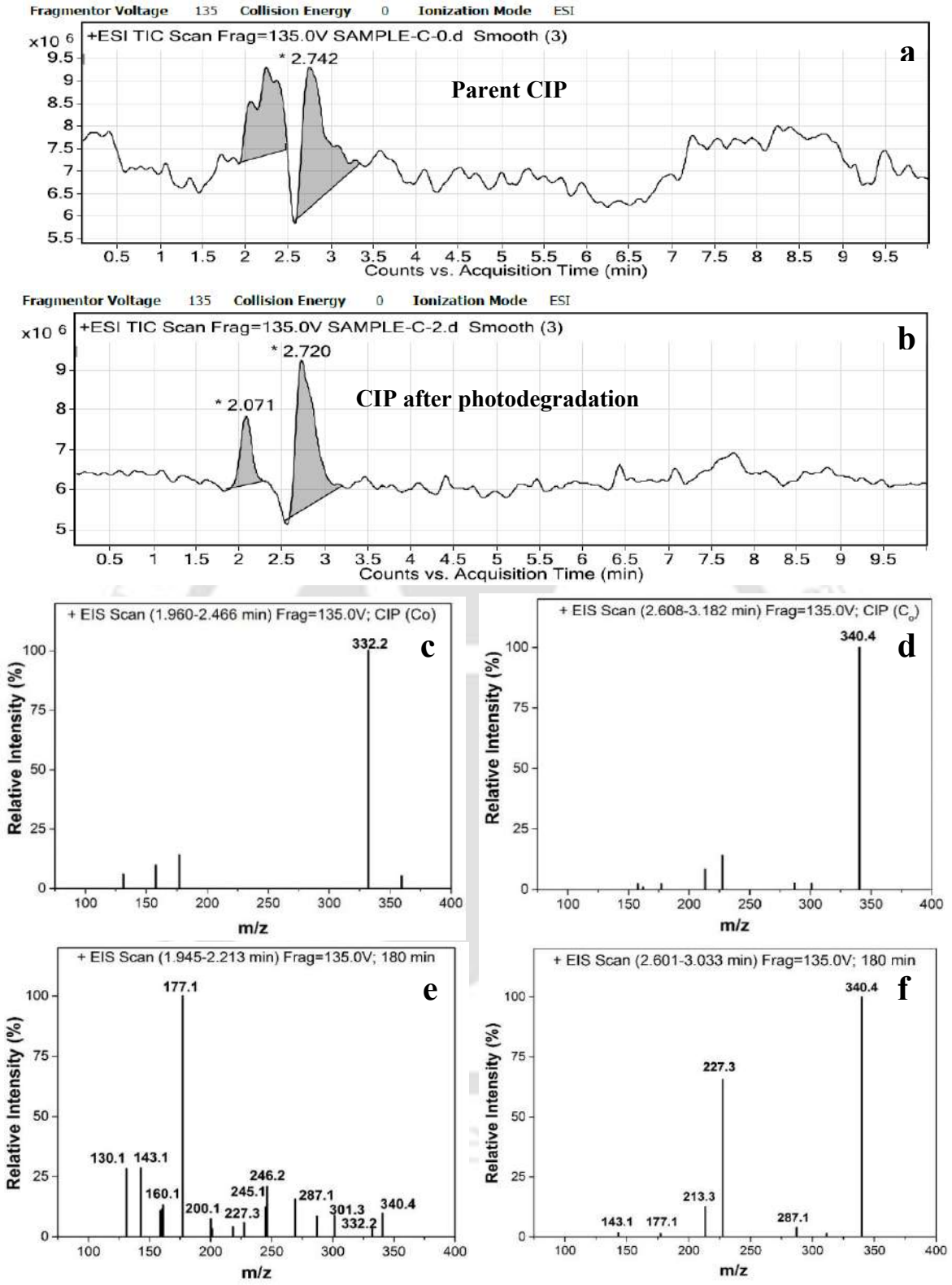

Figure 3.8: LC-MS analysis: Chromatograms of CIP (a) before and (b) after photocatalytic degradation using $Pt_{1.47}/TiO_2$(bio), captured via positive EIS mode $[M + H]^+$. MS spectra of CIP (c and d) before and (e and f) after photocatalytic degradation.

Pathway #II involves the formation of 7 intermediates, which is initiated with the degradation of CIP to P7 (m/z =287.1) by direct decarboxylation reaction, which results in the production of CO_2. Further, the cleavage of the piperazine ring (dealkylation) of the P7 molecule results in the formation of P8 (m/z =246.2) with a loss of dimethylamine (C_2H_7N). Chlorinated CIP (P1) could also be degraded to P8 by releasing CO_2 and ammonia. P8 is decomposed further to P9 (m/z =227.3) through defluorination. P9 is gradually degraded to P10 (m/z =213.3) and P11 (m/z =200.1) via cleavage of the piperazine side chain with a net loss of CH_4 in each step. The quinolone ring of P11 is oxidized to form P12 (m/z = 159.1), and the cleavage of its cyclopropane ring could also lead to the formation of P16 with the release of ammonia (NH_3) (Xu et al., 2020).

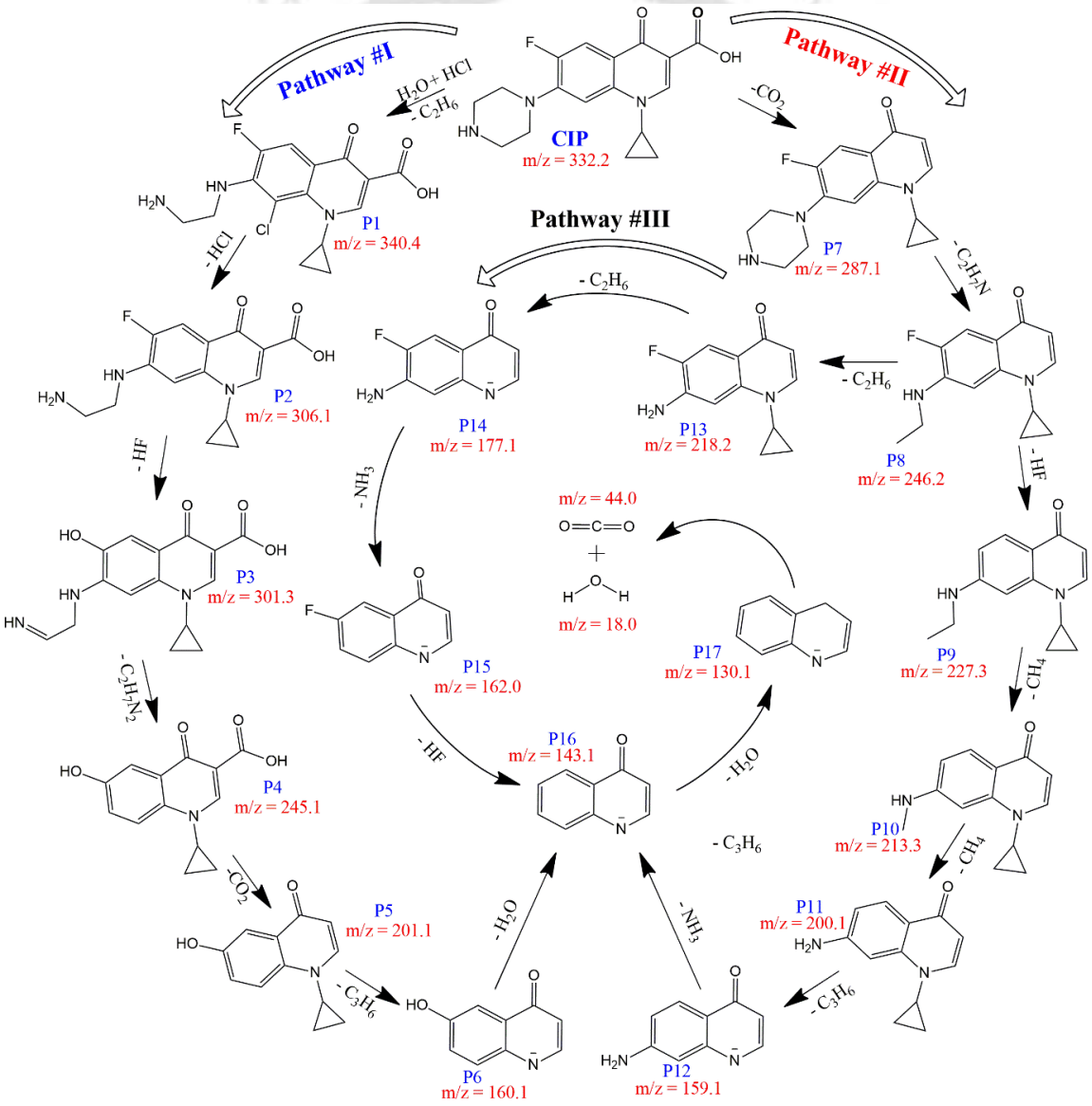

Figure 3.9: Proposed mechanism of CIP degradation by $Pt_{1.47}/TiO_2$(bio) at pH 5 for 180 min of reaction under visible light irradiation.

In Pathway #III, the P8 molecule is degraded to P13 (m/z = 218.2) with ethane (C2H6) formation. Further, an abundant intermediate, P14 (m/z =177.1) is originates with the cleavage of the cyclopropane ring followed by degradation of P14 to P15 (m/z =162.0) by a deamination process via phenolic or benzene diazonium ring intermediates. Defluorination of P15 results in the formation of P16 (m/z =143.1), yielding hydrogen fluoride. P16 intermediate could also be originated through dehydration of the quinolone ring of P6. In fact, P16 could be formed through multiple degradation pathways, and the intermediate product, P17 (m/z =130.1), is formed upon its dehydration (Wolski et al., 2021).

The mass error is found to be only 0.0 to 0.9 mol/g for the intermediates identified in the mass spectra and proposed mechanism. However, 11 out of 17 intermediates did not show any difference in the mass number.

3.2.13 Reusability and stability analysis

Fig. 3.10a shows the photocatalytic degradation of CIP up to 5 cycles. An insignificant decrease in CIP degradation efficiency from 85.5±0.94 to 83.09±2.84% was observed up to the 3rd cycle. The degradation efficiency was decreased to 80.75±1.68 and 75.09±1.58% in the 4th and 5th cycles, respectively. Further, CIP adsorption on the used photocatalyst ($Pt_{1.47}/TiO_2$(bio)/used) in dark conditions (for 30 min) before illuminating it for the photocatalytic reaction was found to decrease gradually from one cycle to the next cycle of its reuse. CIP pre-adsorption was decreased by about 56% in the 5th cycle. However, a reduction in the degradation efficiency of CIP was found to be around 10.4%. Adsorption of CIP molecules, if any, and intermediate products might have debarred some of the active sites of $Pt_{1.47}/TiO_2$(bio)/used of further photo-reactions.

Fig. 3.10b represents the XPS survey scan of $Pt_{1.47}/TiO_2$(bio)/used, which confirms the presence of Ti2p, O1s, Pt 4f, and C1s peaks after the photocatalytic reaction, which indicates that $Pt_{1.47}/TiO_2$(bio) retained its electronic and surface chemical stability even after the CIP degradation test. Additionally, Fig. 3.10c illustrates the XRD pattern of $Pt_{1.47}/TiO_2$(bio) and $Pt_{1.47}/TiO_2$(bio)/used and its confirms that there is no significant change in the lattice structure of $Pt_{1.47}/TiO_2$(bio)/used (Bharti et al., 2016).

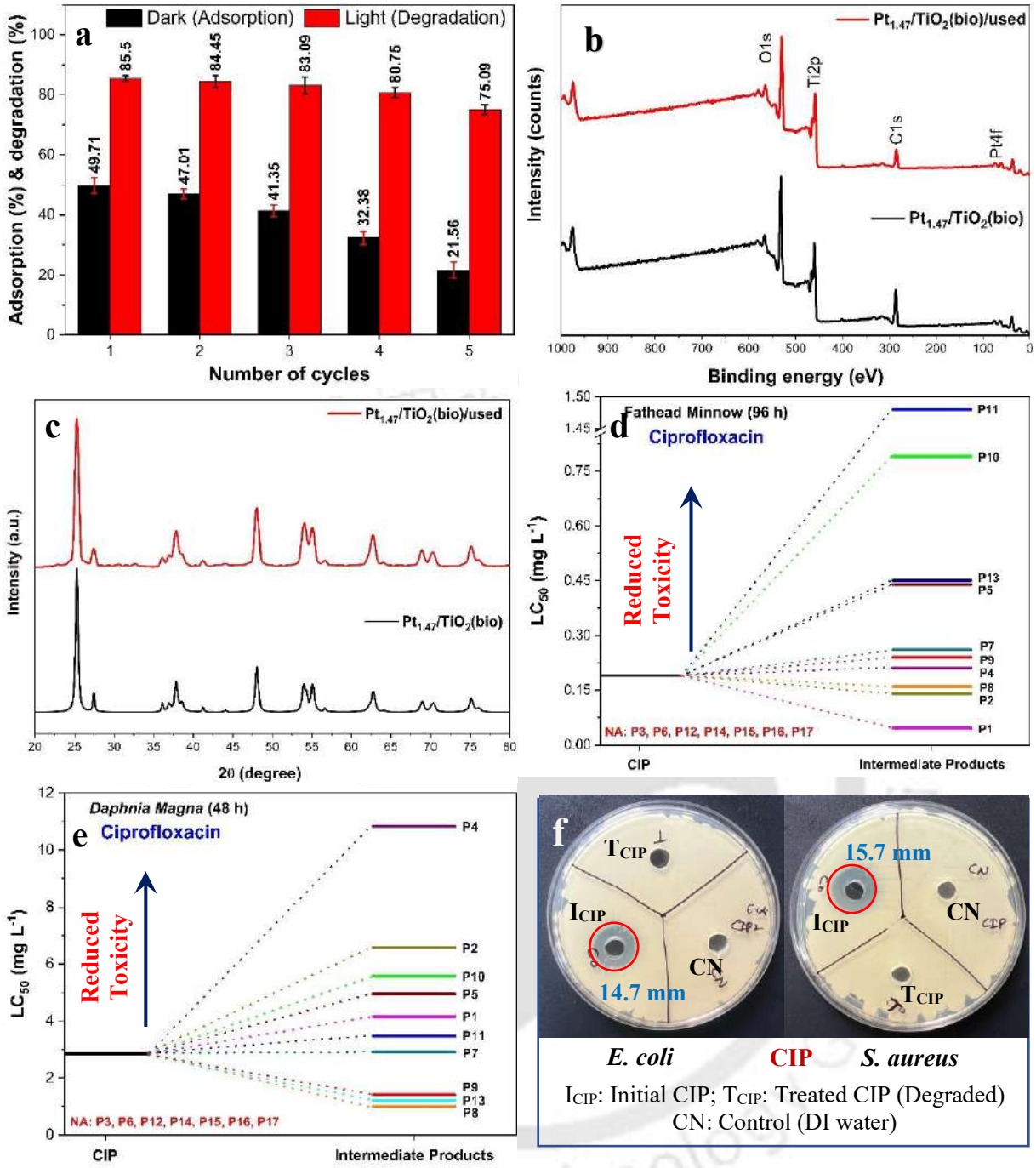

Figure 3.10: (a) CIP degradation (%) and its pre-adsorption (%) before light illumination for 5 consecutive cycles, (b) XPS survey spectra, and (c) XRD spectra of $Pt_{1.47}/TiO_2$(bio) and $Pt_{1.47}/TiO_2$(bio)/used. Aquatic toxicity of CIP and intermediate products against (d) Fathead minnow, and (e) *Daphnia magna*. (f) Antimicrobial activity of CIP before and after photodegradation against *E. coli* and *S. aureus*.

3.2.14 Aquatic toxicity assessment and antimicrobial activity

The photocatalytic degradation of CIP took place in three different routes with the formation of 17 different intermediates, as illustrated in Fig. 3.9. The lethal concentration 50 (LC_{50}) values for fathead minnow (96 h) are presented in Fig. 3.10c. The untreated CIP exhibited an LC_{50} of 0.19 mg L^{-1}, signifying high toxicity to aquatic organisms. Several degradation products, including P4, P9, P7, P5, P13, P10, and P11, showed increased LC_{50} values, indicating reduced toxicity following photocatalytic degradation (Jiang et al., 2022). However, P1, P2, and P8 products retained similar or slightly lower LC_{50} values than the parent compound. For *Daphnia magna*, CIP exhibited an LC_{50} of 2.84 mg L^{-1}, suggesting moderate toxic effects on freshwater invertebrates (Fig. 3.10d) (Cai et al., 2019). The LC_{50} values for degradation products such as P7, P11, P1, P5, P10, P2, and P4 were found to be higher (2.91-10.83 mg L^{-1}) than that of CIP, indicating effective detoxification through photocatalytic degradation. However, P8, P13, and P9 products exhibited marginally reduced LC_{50} values (Su et al., 2022). Notably, the LC_{50} values of some degradation products (P3, P6, P12, P14, P15, P16, and P17) could not be determined, likely due to the unavailability of structural predictions in the TEST software (Wen et al., 2023). These findings suggest that the photocatalytically treated CIP solution poses a significantly lower ecological risk than the untreated solution.

The parent CIP exhibited significant antibacterial activity against both bacterial strains, with a zone of inhibition of 14.7 mm against *E. coli* and 15.7 mm against *S. aureus* (Fig. 3.10f). Notably, the degraded solutions (after photocatalytic degradation for 180 min) of CIP did not show any antimicrobial activity, indicating that the degradation process effectively neutralized their antibacterial properties (Tolouietabar et al., 2020). Similarly, the blank samples (sterile DI water) exhibited no inhibition. The absence of antimicrobial activity of treated solutions provides valuable insights into the effectiveness of post-photocatalytic integration of biological degradation for the complete degradation of remaining intermediate products.

3.3 Major findings

In this study, we have successfully synthesized a visible-light-driven Pt-doped TiO_2 via a bio-based and steamed autoclaving method using the analytes present in *S. edule* vegetal extract. The functionality of a variant of Pt-doped TiO_2 was evaluated for photocatalytic degradation of Ciprofloxacin (CIP), an antibiotic drug, under 50W visible light. The bandgap of TiO_2 was decreased from 3.29 to 3.02 eV with 1.47% (w/w) Pt doping in Degussa P-25 TiO_2 ($Pt_{1.47}/TiO_2$(bio)) at pH 9 with 20% vegetal extract. Pt was incorporated into the TiO_2 lattice via

a two-step mechanism of Pt(IV) reduction as Pt(IV)→Pt(II)→Pt(0) (91%), which is well supported by the X-ray photoelectron spectroscopic analyses of pristine materials ($Pt_{0.00}/TiO_2$(bare) and PtNPs). For doped photocatalysts, a better charge separation, delayed recombination of free e^-/h^+ pairs, reduction of Ti(IV) to Ti(III), enriched oxygen vacancies, and improved hydrophilicity and surface adsorption of CIP were observed. After doping, the lattice strain was also decreased, and the dislocation density and particle size (21.07 to 22.65 nm) were increased. Under visible-light irradiation, the photocurrent density increased 8-fold in the case of $Pt_{1.47}/TiO_2$(bio) over $Pt_{0.00}/TiO_2$(bare). CIP degradation and quantum yield using $Pt_{1.47}/TiO_2$(bio) were increased by ~2-fold (55.97 ± 1.61 to 85.50 ± 0.94%, and 13.78 ± 0.40 to 21.05 ± 0.23%, respectively) under 50W visible light for 180 min reaction time. A decrease of CIP degradation by ~10.4% was noted in the 5th cycle of its reuse. CIP degradation mainly occurred in three different pathways, and 17 intermediate products were identified after 180 min of photoreaction.

Variant electron donor bio-analytes induced more defects in Pt-doped TiO_2, resulting in a narrow bandgap, high surface area, and hydrophilicity compared to chemically synthesized $Pt_{1.47}/TiO_2$(bio). In a nutshell, bio-based and steamed autoclaving is a novel and effective technique for synthesizing visible-light-driven photocatalysts for the degradation of emerging pollutants and is worthy of further investigation.

Despite the significant enhancement in photocatalytic activity achieved through Pt-doping, the relatively high bandgap energy (3.02 eV, light absorption edge of 410 nm) and the high cost of the Pt precursor present notable limitations. Au is less expensive than Pt and more readily reducible using bio-analytes, making it suitable for bio-based synthesis while targeting a lower bandgap (Chapter 4).

References

Batalović, K., Bundaleski, N., Radaković, J., Abazović, N., Mitrić, M., Silva, R.A., Savić, M., Belošević-Čavor, J., Rakočević, Z., Rangel, C.M., 2017. Modification of N-doped TiO_2 photocatalysts using noble metals (Pt, Pd) - A combined XPS and DFT study. Phys. Chem. Chem. Phys. 19. https://doi.org/10.1039/c7cp00188f

Bhan, C., Golder, A.K., 2023. Utilizing bioinspired AgNPs as an antibacterial agent to enhance ceramic membrane performance. J. Environ. Chem. Eng. 11, 110283. https://doi.org/10.1016/j.jece.2023.110283

Bharti, B., Kumar, S., Lee, H.N., Kumar, R., 2016. Formation of oxygen vacancies and Ti^{3+} state in TiO_2 thin film and enhanced optical properties by air plasma treatment. Sci. Rep.

6. https://doi.org/10.1038/srep32355

Boiko, V., Dai, Z., Markowska, M., Leonelli, C., Mortalò, C., Armetta, F., Ursi, F., Nasillo, G., Saladino, M.L., Hreniak, D., 2021. Particle size-related limitations of persistent phosphors based on the doped $Y_3Al_2Ga_3O_{12}$ system. Sci. Rep. 11. https://doi.org/10.1038/s41598-020-80335-9

Bumajdad, A., Madkour, M., 2014. Understanding the superior photocatalytic activity of noble metals modified titania under UV and visible light irradiation. Phys. Chem. Chem. Phys. https://doi.org/10.1039/c3cp54411g

Cai, Z., Hao, X., Sun, X., Du, P., Liu, W., Fu, J., 2019. Highly active WO_3@anatase-SiO_2 aerogel for solar-light-driven phenanthrene degradation: Mechanism insight and toxicity assessment. Water Res. 162. https://doi.org/10.1016/j.watres.2019.06.017

Cervantes-Juárez, E., Meza-Rocha, A.N., Carmona-Téllez, S., Palomino-Ovando, M., Zelaya-Angel, O., Zayas, M.E., Soriano-Romero, O., Salazar-Kuri, U., Lozada-Morales, R., 2020. Burstein Moss effect in CdO–V_2O_5–P_2O: Er^{3+} glasses, and the Yb^{3+} concentration effect on up conversion and downshifting emissions. J. Alloys Compd. 834. https://doi.org/10.1016/j.jallcom.2020.154966

Chelli, V.R., Chakraborty, S., Golder, A.K., 2018. Ag-doping on TiO_2 using plant-based glycosidic compounds for high photonic efficiency degradative oxidation under visible light. J. Mol. Liq. 271. https://doi.org/10.1016/j.molliq.2018.08.140

Chelli, V.R., Golder, A.K., 2018. Ag-doping on ZnO support mediated by bio-analytes rich in ascorbic acid for photocatalytic degradation of dipyrone drug. Chemosphere 208, 149–158. https://doi.org/10.1016/j.chemosphere.2018.05.158

Cheng, G., Liu, X., Song, X., Chen, X., Dai, W., Yuan, R., Fu, X., 2020. Visible-light-driven deep oxidation of NO over Fe doped TiO_2 catalyst: Synergic effect of Fe and oxygen vacancies. Appl. Catal. B Environ. 277. https://doi.org/10.1016/j.apcatb.2020.119196

Chowdhury, A., Peela, N.R., Golder, A.K., 2021. Synthesis of Cu_2O NPs using bioanalytes present in *Sechium edule*: Mechanistic insights and application in electrocatalytic CO_2 reduction to formate. J. CO_2 Util. 51. https://doi.org/10.1016/j.jcou.2021.101622

Duo, F., Zhang, M., Zhou, J., Wang, C., Chu, L., Su, X., 2019. Fast photocatalytic degradation of ciprofloxacin over Ce^{3+}/Ce^{4+}-induced BiOCl nanosheets and antibacterial activity elimination. Mater. Res. Express 6. https://doi.org/10.1088/2053-1591/ab51c2

Elzbieciak, K., Marciniak, L., 2018. The Impact of Cr^{3+} Doping on Temperature Sensitivity Modulation in Cr^{3+} Doped and Cr^{3+}, Nd^{3+} Co-doped $Y_3Al_5O_{12}$, $Y_3Al_2Ga_3O_{12}$, and $Y_3Ga_5O_{12}$ Nanothermometers. Front. Chem. 6.

https://doi.org/10.3389/fchem.2018.00424

Gahlawat, S., Singh, J., Yadav, A.K., Ingole, P.P., 2019. Exploring Burstein-Moss type effects in nickel doped hematite dendrite nanostructures for enhanced photo-electrochemical water splitting. Phys. Chem. Chem. Phys. 21, 20463–20477. https://doi.org/10.1039/c9cp04132j

Ghosh, P., Chelli, V.R., Giri, A.S., Golder, A.K., 2018. Steroid glycosides as potential analytes for Cu-doping on TiO_2 for photocatalytic water treatment. Environ. Prog. Sustain. Energy 37. https://doi.org/10.1002/ep.12879

Gogoi, D., Namdeo, A., Golder, A.K., Peela, N.R., 2020. Ag-doped TiO_2 photocatalysts with effective charge transfer for highly efficient hydrogen production through water splitting. Int. J. Hydrogen Energy 45. https://doi.org/10.1016/j.ijhydene.2019.11.127

He, J., Du, Y. en, Bai, Y., An, J., Cai, X., Chen, Y., Wang, P., Yang, X., Feng, Q., 2019. Facile formation of anatase/rutile TiO_2 nanocomposites with enhanced photocatalytic activity. Molecules 24. https://doi.org/10.3390/molecules24162996

Hu, Y., Song, X., Jiang, S., Wei, C., 2015. Enhanced photocatalytic activity of Pt-doped TiO_2 for NOx oxidation both under UV and visible light irradiation: A synergistic effect of lattice Pt^{4+} and surface PtO. Chem. Eng. J. 274. https://doi.org/10.1016/j.cej.2015.03.135

Ismael, M., 2019. Highly effective ruthenium-doped TiO_2 nanoparticles photocatalyst for visible-light-driven photocatalytic hydrogen production. New J. Chem. 43. https://doi.org/10.1039/c9nj02226k

Ismail, M.A., Hedhili, M.N., Anjum, D.H., Singaravelu, V., Chung, S.H., 2021. Synthesis and characterization of iron-doped TiO_2 nanoparticles using ferrocene from flame spray pyrolysis. Catalysts 11. https://doi.org/10.3390/catal11040438

Jiang, W., Li, J., Jiang, Y., Zhou, S., Liu, B., Zhou, T., Liu, C., Che, G., 2022. A 3D porphyrinic metal-organic framework with fsc topology for efficient visible-light-driven photocatalytic degradation. Polyhedron 226. https://doi.org/10.1016/j.poly.2022.116091

Khan, S.A., Arshad, Z., Shahid, S., Arshad, I., Rizwan, K., Sher, M., Fatima, U., 2019. Synthesis of TiO_2/Graphene oxide nanocomposites for their enhanced photocatalytic activity against methylene blue dye and ciprofloxacin. Compos. Part B Eng. 175. https://doi.org/10.1016/j.compositesb.2019.107120

Komaraiah, D., Radha, E., Sivakumar, J., Ramana Reddy, M. V., Sayanna, R., 2020. Photoluminescence and photocatalytic activity of spin coated Ag^+ doped anatase TiO_2 thin films. Opt. Mater. (Amst). 108. https://doi.org/10.1016/j.optmat.2020.110401

Krishnapriya, R., Nizamudeen, C., Saini, B., Mozumder, M.S., Sharma, R.K., Mourad, A.H.I.,

2021. MOF-derived Co^{2+}-doped TiO_2 nanoparticles as photoanodes for dye-sensitized solar cells. Sci. Rep. 11. https://doi.org/10.1038/s41598-021-95844-4

Kumar, J.V., Karthik, R., Chen, S.M., Muthuraj, V., Karuppiah, C., 2016. Fabrication of potato-like silver molybdate microstructures for photocatalytic degradation of chronic toxicity ciprofloxacin and highly selective electrochemical detection of H_2O_2. Sci. Rep. 6. https://doi.org/10.1038/srep34149

Kumar, M.P., Jagannathan, R., Ravichandran, S., 2020. Photoelectrochemical System for Unassisted High-Efficiency Water-Splitting Reactions Using N-Doped TiO_2 Nanotubes. Energy and Fuels 34. https://doi.org/10.1021/acs.energyfuels.0c00634

Li, R., Li, W., Liu, M., He, Q., Wang, Y., Zhan, Q., Wang, T., 2019. Structural, Morphological, Optical and Electrical Properties of Cu-Doped PbS Nanofilms. ES Mater. Manuf. 4. https://doi.org/10.30919/esmm5f217

Mahlambi, M.M., Mishra, A.K., Mishra, S.B., Krause, R.W., Mamba, B.B., Raichur, A.M., 2012. Comparison of rhodamine B degradation under UV irradiation by two phases of titania nano-photocatalyst, in: Journal of Thermal Analysis and Calorimetry. https://doi.org/10.1007/s10973-011-1852-7

Martins, P., Kappert, S., Nga Le, H., Sebastian, V., Kühn, K., Alves, M., Pereira, L., Cuniberti, G., Melle-Franco, M. and Lanceros-Méndez, S., 2020. Enhanced photocatalytic activity of Au/TiO_2 nanoparticles against ciprofloxacin. Catalysts, 10(2), 234. https://doi.org/10.3390/catal10020234

Mimouni, R., Askri, B., Larbi, T., Amlouk, M., Meftah, A., 2020. Photocatalytic degradation and photo-generated hydrophilicity of Methylene Blue over ZnO/$ZnCr_2O_4$ nanocomposite under stimulated UV light irradiation. Inorg. Chem. Commun. https://doi.org/10.1016/j.inoche.2020.107889

Nandi, S., Das, S., Singh, S., Verma, R., 2020. Phytotoxicity and Effect on Allium Cepa of the Permeate Obtained After the Physico-Biological Treatment of Congo Red By Physico-Biological Treatment 20, 3378–3384.

Pugazhenthiran, N., Mangalaraja, R. V., Sathishkumar, P., Murugesan, S., Muneeswaran, T., Pandiyarajan, T., Naveenraj, S., Contreras, D., Anandan, S., 2018. Green synthesis of porous Au-Nx-TiO_2 nanospheres for solar light induced photocatalytic degradation of diazo and triazo dyes and their eco-toxic effects. New J. Chem. 42. https://doi.org/10.1039/c8nj04554b

Ravi, Pandey, L.M., 2019. Enhanced adsorption capacity of designed bentonite and alginate beads for the effective removal of methylene blue. Appl. Clay Sci. 169.

https://doi.org/10.1016/j.clay.2018.12.019

Silva, A.R., Martins, P.M., Teixeira, S., Carabineiro, S.A.C., Kuehn, K., Cuniberti, G., Alves, M.M., Lanceros-Mendez, S., Pereira, L., 2016. Ciprofloxacin wastewater treated by UVA photocatalysis: Contribution of irradiated TiO_2 and ZnO nanoparticles on the final toxicity as assessed by Vibrio fischeri. RSC Adv. 6. https://doi.org/10.1039/c6ra19202e

Song, S.Y., Chen, H.D., Li, C.X., Shi, D.S., Ying, Y., Han, Y.B., Xu, J.C., Hong, B., Jin, H.X., Jin, D.F., Peng, X.L., Ge, H.L., Wang, X.Q., 2020. Magnetic Bi_2WO_6 nanocomposites: Synthesis, magnetic response and their visible-light-driven photocatalytic performance for ciprofloxacin. Chem. Phys. 530. https://doi.org/10.1016/j.chemphys.2019.110614

Su, Q., Li, J., Yuan, H., Wang, B., Wang, Y., Li, Y., Xing, Y., 2022. Visible-light-driven photocatalytic degradation of ofloxacin by g-C_3N_4/NH_2-MIL-88B(Fe) heterostructure: Mechanisms, DFT calculation, degradation pathway and toxicity evolution. Chem. Eng. J. 427. https://doi.org/10.1016/j.cej.2021.131594

Tamaddon, F., Nasiri, A., Yazdanpanah, G., 2020. Photocatalytic degradation of ciprofloxacin using $CuFe_2O_4$@methyl cellulose based magnetic nanobiocomposite. MethodsX 7. https://doi.org/10.1016/j.mex.2019.12.005

Tolouietabar, H., Hatamnia, A.A., Sahraei, R., Soheyli, E., 2020. Biologically green synthesis of high-quality silver nanoparticles using scrophularia striata boiss plant extract and verifying their antibacterial activities. J. Nanostructures 10. https://doi.org/10.22052/JNS.2020.01.006

Wang, H., Hu, C., Liu, L., Xing, X., 2017. Interaction of ciprofloxacin chlorination products with bacteria in drinking water distribution systems. J. Hazard. Mater. 339. https://doi.org/10.1016/j.jhazmat.2017.06.033

Wang, Q., Xie, D., Chen, J., Liu, G., Yu, M., 2020. Superhydrophobic paper fabricated via nanostructured titanium dioxide-functionalized wood cellulose fibers. J. Mater. Sci. 55. https://doi.org/10.1007/s10853-020-04489-7

Wen, L., Liu, P., Zhou, Z., Wang, K., Zhou, Y., 2023. Biosafety Photooxidation Strategy of Levofloxacin Driven by Manganese-Doped Indium Zinc Sulfide. Chem. - An Asian J. 18, 2–8. https://doi.org/10.1002/asia.202300161

Wolski, L., Grzelak, K., Muńko, M., Frankowski, M., Grzyb, T., Nowaczyk, G., 2021. Insight into photocatalytic degradation of ciprofloxacin over CeO_2/ZnO nanocomposites: Unravelling the synergy between the metal oxides and analysis of reaction pathways. Appl. Surf. Sci. 563. https://doi.org/10.1016/j.apsusc.2021.150338

Xie, W., Li, R., Xu, Q., 2018. Enhanced photocatalytic activity of Se-doped TiO_2 under visible

light irradiation. Sci. Rep. 8, 1–10. https://doi.org/10.1038/s41598-018-27135-4

Xing, X., Du, Z., Zhuang, J., Wang, D., 2018. Removal of ciprofloxacin from water by nitrogen doped TiO_2 immobilized on glass spheres: Rapid screening of degradation products. J. Photochem. Photobiol. A Chem. 359. https://doi.org/10.1016/j.jphotochem.2018.03.026

Xu, D., Feng, H., Dong, Y., Wang, Q., Zhang, G., Lv, L., Ren, Z., Wang, P., 2020. Enhanced Molecular Oxygen Activation on (001) Facets of Zn-Doped BiOCl Nanosheets for Ciprofloxacin Degradation. Adv. Mater. Interfaces 7. https://doi.org/10.1002/admi.202000548

Xu, L., Chen, W.Q., Ke, S.Q., Zhu, M., Qiu, W.H., Liu, N., Namuangruk, S., Maitarad, P., Impeng, S., Tang, L., 2019. Efficient photocatalytic reactions of Cr(vi) reduction and ciprofloxacin and RhB oxidation with Sn(ii)-doped BiOBr. Catal. Sci. Technol. 9. https://doi.org/10.1039/c9cy01405e

Yusuf, T.L., Olatunde, O.C., Masekela, D., Modibane, K.D., Onwudiwe, D.C. and Makgato, S., 2024. Charge redistribution in $Nise_2/Mos_2$ n–n heterojunction towards the photoelectrocatalytic degradation of ciprofloxacin. ChemElectroChem, 11(16), e202400309. https://doi.org/10.1002/celc.202400309

Zhang, J., Zhang, L., Wang, W., Yu, J., 2022. In Situ Irradiated X-ray Photoelectron Spectroscopy Investigation on Electron Transfer Mechanism in S-Scheme Photocatalyst. J. Phys. Chem. Lett. https://doi.org/10.1021/acs.jpclett.2c02125

Zhou, Y., Ding, Q., Wang, Y., Ouyang, X., Liu, L., Li, J., Wang, B., 2020. Carrier transfer and capture kinetics of the $TiO_2/Ag_2V_4O_{11}$ photocatalyst. Nanomaterials 10. https://doi.org/10.3390/nano10050828

CHAPTER 4

Bio-based Au-doped TiO_2 with Dominant Oxygen Vacancies and Ti^{3+} Defects for Chloroquine Photodegradation

This chapter explores the bio-based synthesis of Au-doped TiO_2 using S. edule juice extract, emphasizing the reduced bandgap along with the formation of oxygen vacancies and Ti^{3+} defects. These intrinsic modifications are shown to enhance light absorption and charge separation efficiency. The detailed characterization confirms the structural and electronic alterations due to Au-doping. The prepared photocatalyst was utilized to degrade chloroquine under visible light irradiation. The degradation mechanism was also proposed, and the formed intermediates were analyzed for ecotoxicity assessment.

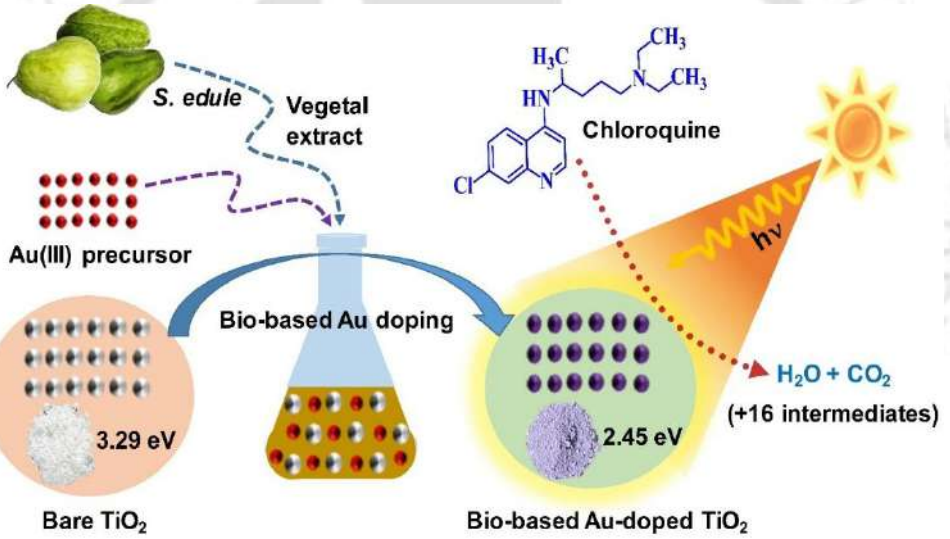

Chapter highlights

- Bio-based process using vegetal analytes could successfully dope 95% Au onto TiO_2
- Au-doping notably increased oxygen-vacancies and Ti^{3+} defects over chemical route
- Lower bandgap (2.45 eV), delayed recombination and hydrophilicity (16.8°) achieved
- Chloroquine degradation of 94.6% following 1st order reaction with 16 intermediates

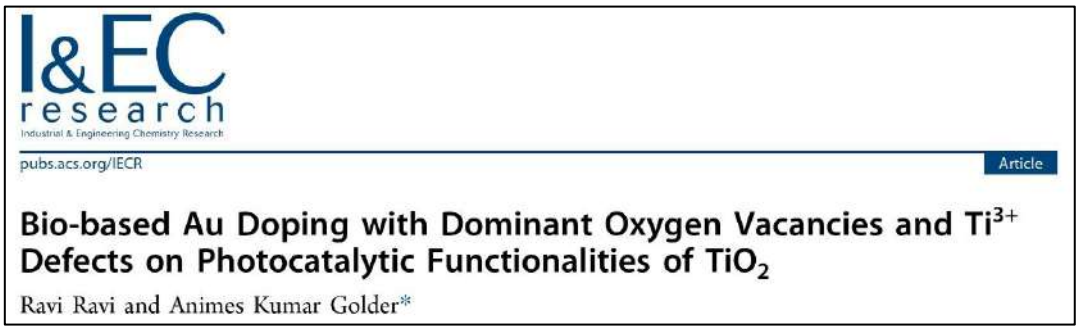

Intentionally Left Blank
Intentionally Left Blank

4.1 Background and executive motivation

The continuous release and accretion of pharmaceutically active compounds (PhACs) in water bodies have become a global threat due to their persistency and hazardous impact even at very low concentrations. Chloroquine (CLQ) is an antimalarial drug primarily used to treat malaria, rheumatoid arthritis, amoebic liver abscess, and lupus erythematosus (Lei et al., 2020). Synthetic CLQ is an alternative to the natural antimalarial drug quinine, developed by Hans Andersag in the 1940s. Recently, CLQ has been largely administered for prophylaxis of Zika virus and emergency treatment of Covid-19 (Baildya et al., 2021). The contamination of CLQ in waterbodies has increased since the Covid-19 pandemic. In fact, prolonged consumption of CLQ could cause hypertension, gender identity disorder, hypokalaemia, arrhythmias, heart-related disorders, and kidney problem (Maxwell et al., 2015; Ramesh et al., 2018). Additionally, the development of CLQ-resistant parasites is also a major concern. Therefore, CLQ must be removed from industrial and hospital effluents to prevent its harmful impacts.

The presence of CLQ is not only detected in surface water but also in groundwater. One of the reasons is that the conventional wastewater treatment plants (WWTPs) are ineffective for the elimination of CLQ. Thus, CLQ surviving the treatment spreads in natural waterbodies (da Silva et al., 2021). In general, CLQ is difficult to eliminate in conventional treatment methods, namely, bioremediation, adsorption, and chlorination due to complex molecular structure (Derikvandi and Nezamzadeh-Ejhieh, 2017). While, photocatalysis is merited with non-selective mineralization of a wide range of emerging pollutants. Highly reactive free radical species formed in this process could rapidly transform the contaminant into H_2O and CO_2, and valuable chemicals (occasionally) (Zhang et al., 2023). Photocatalysts with narrower bandgap, better change separation (delayed recombination), and hydrophilic surface could impart an efficient visible light-driven degradation (Ramírez et al., 2021). However, a narrow light-absorption range of native photocatalysts such as TiO_2, limits its use only in UV light, and the rapid recombination of electron and hole pairs (e^-/h^+) decreases the photocatalytic efficiency of TiO_2. Therefore, development of effective modification strategies of TiO_2 to enable its photocatalytic functionality under visible light is a key research area of many environmental scientists.

Many strategies, namely, doping of metals and non-metals, type-II and Z-scheme heterojunctions, and nanocomposite formation, are practiced to widen spectral absorptivity, delay recombination and enhance hydrophilicity of photocatalysts (Ravi and Pandey, 2019; Cheng et al., 2020; Jahdi et al., 2020; Tao et al., 2023). In particular, doping of metals is

considered to be the most promising approach as it could easily decrease the bandgap and recombination rate by inserting new energy levels and charge-trapping sites for enhanced photocatalytic activity (Cisneros et al., 2021). The charge trapping sites formed help to diffuse highly energetic electron from conduction band (CB) into network structure of metal dopant, which eventually delay e^-/h^+ recombination. Au is a potential dopant due to its high stability and non-reactivity and also it could insertion new energy levels by equivalent substitution of Ti (atomic radius 0.147 nm) with Au (atomic radius of 0.147 nm) (Shi et al., 2017; Cheng et al., 2020). Few studies reported on Au-doping onto TiO_2 using toxic chemicals of environmental concerns (Yi et al., 2021; Gayathri et al., 2023). The bio-based methods are eco-friendly and environmentally benign. It could improve the surface properties and increase the defects in metal-doped photocatalysts to enhance their activity. Chelli and Golder (2018) doped Ag onto ZnO using *Sechium edule* extract, and the resulting catalysts exhibited remarkable efficiency of dipyrone drug decomposition (Chelli and Golder, 2018). Therefore, Au-doping into TiO_2 could improve its photocatalytic functionalities under visible light by reducing the bandgap and e^-/h^+ recombination with induced oxygen vacancies. Furthermore, the use of vegetal extract could turn the catalyst surface more hydrophilic (Mimouni et al., 2020). Therefore, development of Au-doped TiO_2 at natural pH in an environmentally benign route is a prudent research direction.

This study aims towards the development of a bio-based Au-doping strategy onto TiO_2 by utilizing the vegetal analytes present in *S. edule* extract. The developed photocatalysts were thoroughly characterized to gain insights into the doping mechanism and assess the variations in their optical and chemical characteristics. The photocatalytic functionality of Au-doped TiO_2 was evaluated by studying the CLQ degradation under various operating conditions and catalysts types using 50W visible light. The refractory nature of CLQ and reaction intermediates was examined by determining total organic carbon content and the intermediates surviving the photocatalytic reaction.

4.2 Results and discussion

4.2.1 Optimization of synthesis parameters and determination of band potential

The synthesis of Au-doped TiO_2 photocatalysts involves two steps: (i) surface adsorption of Au(II) onto TiO_2 and (ii) Au-doping onto TiO_2. The results describing the adsorption of Au(III) (%) onto TiO_2 at various pH levels (3-11) and concentrations of Au(III) (0.25-1.5 w/w%) are presented in Figs. 4.1a and 4.1b. The findings suggest that pH 7 displayed

the highest surface adsorption of 99.51%. The concentration of adsorbed Au(III) (mg g^{-1}) was more as the initial concentration of Au(III) was increased. However, the percentage of adsorption was decreased due to the short fall of binding sites as more Au(III) ions were present (Ravi and Pandey, 2019). Fig. 4.1c and Table 4.1 show the bandgap of $Au_{1.00}/TiO_2$(bio) at different vegetal extract concentrations (10-50%, v/v). The photocatalyst with the lowest bandgap was considered for CLQ degradation study. The results showed that the photocatalyst synthesized using 20% (v/v) vegetal extract exhibited the lowest bandgap of 2.45 eV. Therefore, it was selected for the synthesis of $Au_{0.25\text{-}1.45}/TiO_2$(bio). However, the bandgap was increased at higher vegetal extract concentrations (30-50%, v/v) due to the Ostwald ripening effect, which involves the rapid reduction of Au(III) forming larger AuNPs. Additionally, $Au_{1.00}/TiO_2$(bio) was also synthesized using the vegetal extract prepared using tendered(T) and fully matured (M) *S. edule* fruit of different maturity and size. *S. edule*@T and *S. edule*@M (used as 50% v/v) based $Au_{1.00}/TiO_2$(bio) show almost equal bandgap of 2.46 and 2.47 eV, respectively. *S. edule*@M (used as 20% (v/v)) synthesized $Au_{1.00}/TiO_2$(bio) has a higher bandgap of 2.76 eV (Fig. 4.1d). $Au_{1.00}/TiO_2$(chem) showed a bandgap of 2.73 eV. Hence, the bio-analytes including the ascorbic acid content in the vegetal extract had an enormous effect on Au-doping in TiO_2.

Fig. 4.1e illustrate the absorption band edge and bandgap of $Au_{0.00}/TiO_2$(bare) and $Au_{0.25\text{-}1.45}/TiO_2$(bio). The findings confirmed that the bandgap was reduced from 3.29 to 2.45 eV, which resulting in shifting of adsorption edge from ultraviolet (377 nm) to visible light range (507 nm) with doping of optimized 1% (w/w) Au ($Au_{1.00}/TiO_2$(bio)). The bandgap was decreased as the Au concentration was increased up to 1% (w/w). However, the bandgap was more at higher Au concentrations (1.23-1.45% w/w). This unexpected increase in bandgap could potentially be attributed to the Burstein–Moss effect. It suggests that at a higher dopant concentration, the lower layer of CB becomes highly e^- dense. This, in turn, causes the shifting of the adsorption edge to the upper layers of CB (high energy level). It is resulted as an increased bandgap of $Au_{1.23\text{-}1.45}/TiO_2$(bio) (Zhu et al., 2016).

The maximal VB values of $Au_{0.00}/TiO_2$(bare) and $Au_{1.00}/TiO_2$(bio) photocatalysts were found to be -0.75 and -0.66 eV, respectively (Fig. 2f). The inset of Fig. 2f depicts the energy level diagram. The minimal CB values of $Au_{0.00}/TiO_2$(bare) and $Au_{1.00}/TiO_2$(bio) were calculated as 2.54 and 1.79 eV, respectively. A shifting of VB and CB after Au-doping was observed, which could be attributed to a synergetic effect from introduction of new energy levels of Au, increased oxygen vacancies (OVs), and presence of Ti^{3+} defects in $Au_{1.00}/TiO_2$(bio) which is confirmed from XPS analysis included later on (Gao et al., 2021).

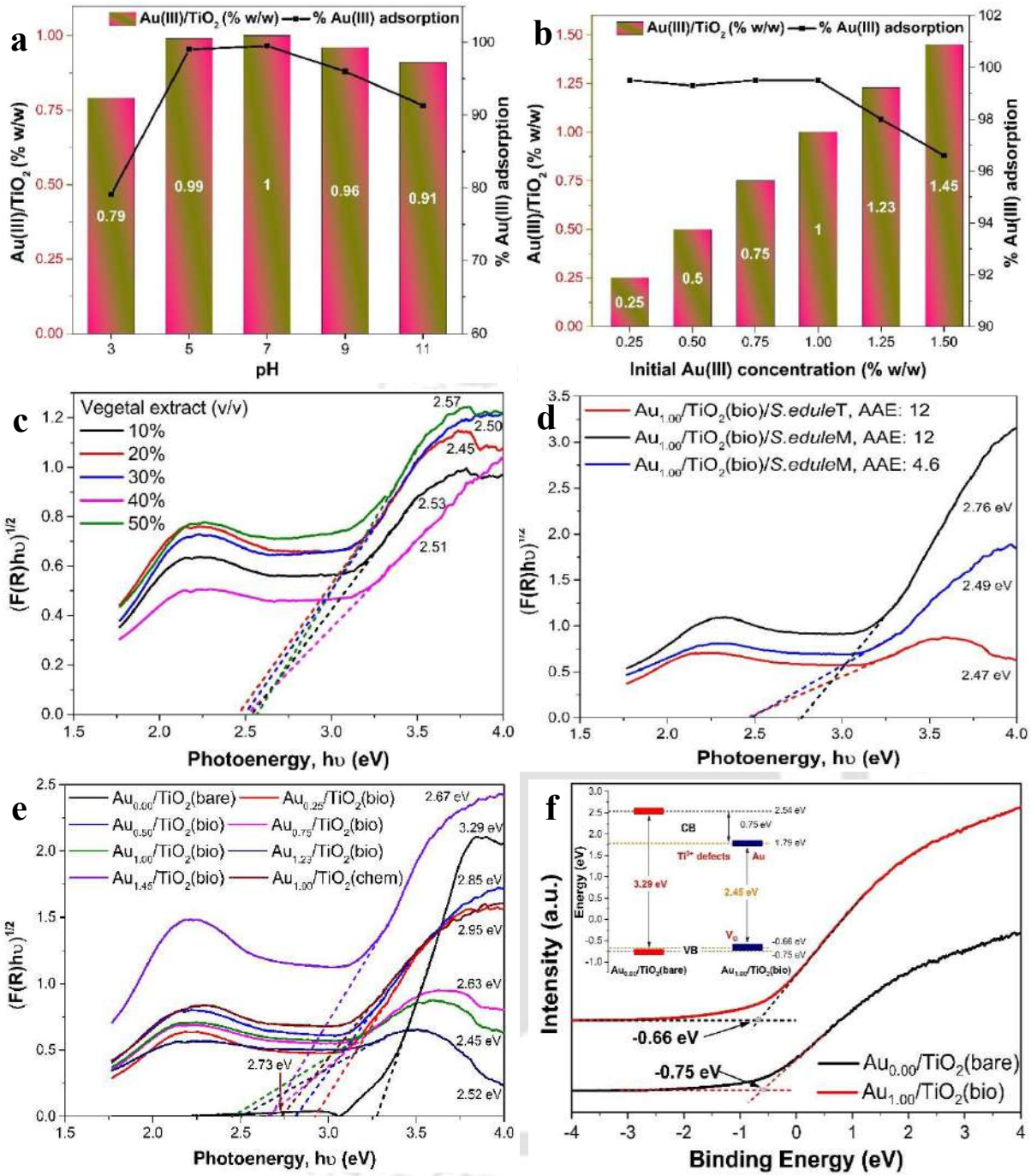

Figure 4.1: Adsorption of (a) 1.0% (w/w) Au(III) on Degussa P-25 TiO_2 at various pH (3-11) and (b) 0.25-1.5% (w/w) Au(III) at optimized pH 7; Tauc's plot (Kubelka-Munk function) for optical band gap of (c) $Au_{1.00}/TiO_2$(bio) synthesized at using various vegetal-extract (juice) concentrations (10-50%), (d) $Au_{1.00}/TiO_2$(bio) synthesized using different maturity of *S. edule* fruit extract (juice) and (e) $Au_{0.00}/TiO_2$(bare) and $Au_{0.25\text{-}1.45}/TiO_2$(bio) photocatalysts. (f) XPS valence band spectra, and energy level diagram (inset) of $Au_{0.00}/TiO_2$(bare) and $Au_{1.00}/TiO_2$(bio). Here, VB is the valence band maxima and CB is the conduction band minima.

Table 4.1: Optical bandgap of $Au_{0\text{-}1.45}/TiO_2$(bio) synthesized using 20% bio-extract and at various bio-extract concentrations (10-50% v/v) in synthesizing $Au_{1.00}/TiO_2$(bio) by steamed autoclaving at 121°C for 20 min.

Catalyst	Vegetal extract concentration (%) of 12 mg L^{-1} AAE*	Bandgap energy (eV)
$Au_{1.00}/TiO_2$(bio)	10	2.53
	20	**2.45**
	30	2.50
	40	2.51
	50	2.57
$Au_{0.00}/TiO_2$(bare)	20	3.29
$Au_{0.25}/TiO_2$(bio)		2.95
$Au_{0.50}/TiO_2$(bio)		2.85
$Au_{0.75}/TiO_2$(bio)		2.63
$Au_{1.23}/TiO_2$(bio)		2.52
$Au_{1.45}/TiO_2$(bio)		2.67
$Au_{1.00}/TiO_2$(chem)	20 (12 mg L^{-1} Ascorbic acid)	2.73

4.2.2 X-ray diffraction (XRD) analysis

Fig. 4.2 shows the XRD patterns of $Au_{0.00}/TiO_2$(bare) and $Au_{0.25\text{-}1.45}/TiO_2$(bio). The diffraction patterns confirmed the presence of both the anatase phase (corresponding to JCPDS file No. 01-021-1272) and the rutile phase (corresponding to JCPDS file No. 01-21-1276) of TiO_2 (Fig. 4.2a). In fact, the peaks at 2θ = 36.08 (101), 37.83 (004), 41.27 (111), and 62.70° (204) were observed to be shifted with Au-doping (Figs. 4.2a and 4.2b). The peak shifting phenomena could be attributed to the incorporation of Au into the TiO_2 lattice and merging of diffraction peaks originating from both AuNPs (JCPDS file No. 01-71-4614) and TiO_2 (Jahdi et al., 2020). The peak shifting was prominent with increasing concentration of Au dopant. More AuNPs was formed and adhered on the surface of TiO_2 at a higher concentration of Au(III) due to the Ostwald ripening effect which in turn, could reduce the net Au-doping into the lattice. It results a decrease in the peak shift.

The crystallite size of $Au_{0.25\text{-}1.45}/TiO_2$(bio) was increased with an increase in Au concentration (Table 4.2), which could be due to filling of lattice voids in TiO_2 with AuNPs (Valian et al., 2023). A decrease in lattice strain and dislocation density was observed with Au-doping. It is indicative of increased tensile strain and compressive strength of $Au_{0.25\text{-}1.45}/TiO_2$(bio). It in turn could improve the photocatalytic activity by accelerating the diffusivity of free radicals to the photocatalyst surface (Li et al., 2019; Bhan and Kumar Golder, 2023).

The decrease in interplanar distance may be caused by the replacement of large Ti^{4+} (ionic radius 215 nm) by smaller Au^{3+} (ionic radius 0.166 nm) and generation of oxygen vacancies (Irfan et al., 2017).

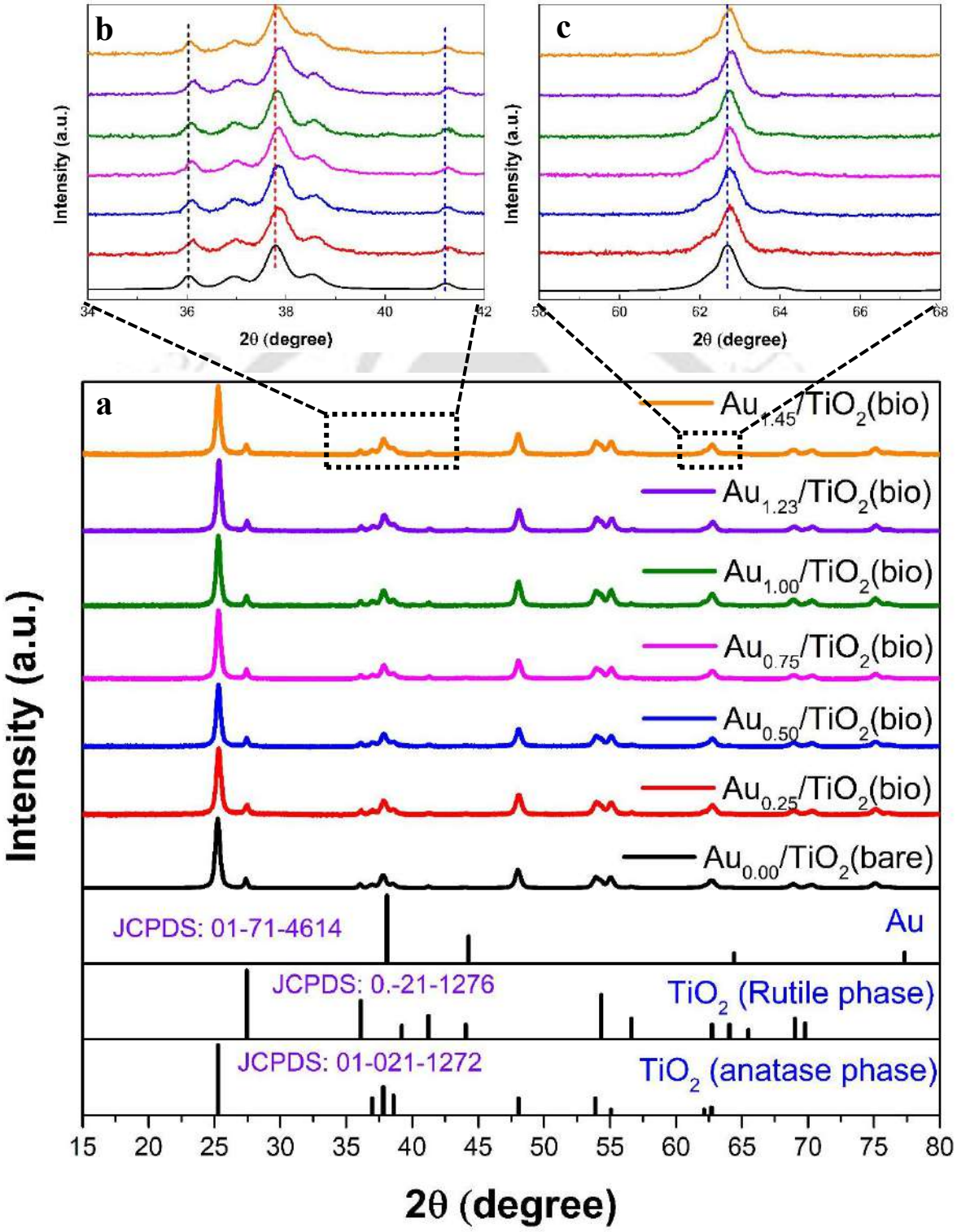

Figure 4.2: (a) XRD patterns, and (b) Magnified XRD patterns, showing peak shifting in $Au_{0.00}/TiO_2$(bare) and $Au_{0.25\text{-}1.45}/TiO_2$(bio).

Table 4.2: XRD parameters of $Au_{0.00}/TiO_2$(bare) and $Au_{0.49\text{-}2.43}/TiO_2$(bio).

Sample	Crystallite size (nm)	Anatase (%)	Rutile (%)	Lattice strain (ε)	Dislocation densities (Lines/nm²)
$Au_{0.00}/TiO_2$(bare)	20.53	80	20	8.05×10^{-3}	2.36×10^{-3}
$Au_{0.25}/TiO_2$(bio)	20.96	79.41	20.59	7.88×10^{-3}	2.28×10^{-3}
$Au_{0.50}/TiO_2$(bio)	22.33	79.34	20.66	7.39×10^{-3}	2.00×10^{-3}
$Au_{0.75}/TiO_2$(bio)	22.54	79.27	20.73	7.34×10^{-3}	1.97×10^{-3}
$Au_{1.00}/TiO_2$(bio)	22.59	78.83	21.17	7.31×10^{-3}	1.96×10^{-3}
$Au_{1.23}/TiO_2$(bio)	22.56	78.86	21.14	7.32×10^{-3}	1.96×10^{-3}
$Au_{1.45}/TiO_2$(bio)	22.33	78.91	21.09	7.41×10^{-3}	2.01×10^{-3}

4.2.3 X-ray photoelectron spectroscopic (XPS) analysis

Fig. 4.3 shows the high-resolution spectra of Ti2p (Figs. 4.3a and 4.3b), O1s (Figs. 4.3c and 4.3d), and Au4f (Fig. 4.3e) and XPS survey spectra (Fig. 4.3f) of $Au_{0.00}/TiO_2$(bare) and $Au_{1.00}/TiO_2$(bio). The composition of all the chemical states is provided in Table 3.4. The Ti2p spectra exhibited two characteristic peaks of Ti^{4+} at 466.2 ($Ti_{1/2}$) and 460.4 eV ($Ti_{3/2}$) in $Au_{0.00}/TiO_2$(bare) and at 465.9 ($Ti_{1/2}$) and 460.2 eV ($Ti_{3/2}$) in $Au_{1.00}/TiO_2$(bio) (Zhang et al., 2022). An additional peak of Ti^{3+} ($Ti_{1/2}$ 2p) at 461.9 eV was observed in $Au_{1.00}/TiO_2$(bio). The Ti^{3+} defects could be produced due to charge compensation of Ti^{4+} by free electrons generated through oxygen vacancies (Xie et al., 2018; Wu et al., 2023). A red shifting of 0.2-0.3 eV in the Ti2p peak position for $Au_{1.00}/TiO_2$(bio) could be of increased electron density due to the generation of oxygen vacancies and replacement of Ti^{4+} by Au(0) and Ti^{3+} (Cheng et al., 2020).

The O1s spectra of $Au_{1.00}/TiO_2$(bio) (Fig. 4d) exhibited the characteristic peak of lattice oxygen (O_L) at 531.4 eV and a small peak of surface oxygen (O_{ads}, mainly OH^-) at 533.0 eV. These peaks are in close accordance with O1s peaks of $Au_{0.00}/TiO_2$(bare) (Fig. 4c) (Cheng et al., 2020). However, a red shift of 0.3 eV in O1s spectra of $Au_{1.00}/TiO_2$(bio) was observed. Compared to $Au_{0.0}/TiO_2$(bare), a new peak was detected in $Au_{1.00}/TiO_2$(bio) at 534.3 eV, because of C-O group of surface adsorbed bio-analytes from the vegetal extract (Wang et al., 2020)vv. The high-resolution spectra of Au4f (Fig. 4e) showed two characteristic peaks of Au(0)(~95%) at 88.5 and 84.8 eV and Au(I) (~5%) at 90.6 and 86.7 eV in $Au_{1.00}/TiO_2$(bio) (Lanza et al., 2022). No Au4f peak was existed in $Au_{0.00}/TiO_2$(bare). Therefore, it can be inferred that Au-doping took place in two steps. Au(III) is first reduced to Au(I), which is then reduced to Au(0) and incorporated into the lattice of TiO_2. Au(I) is mainly present over the surface of TiO_2. It could enhance the photocatalytic activity of $Au_{1.00}/TiO_2$(bio) by acting as a co-catalyst (Guo et al., 2022).

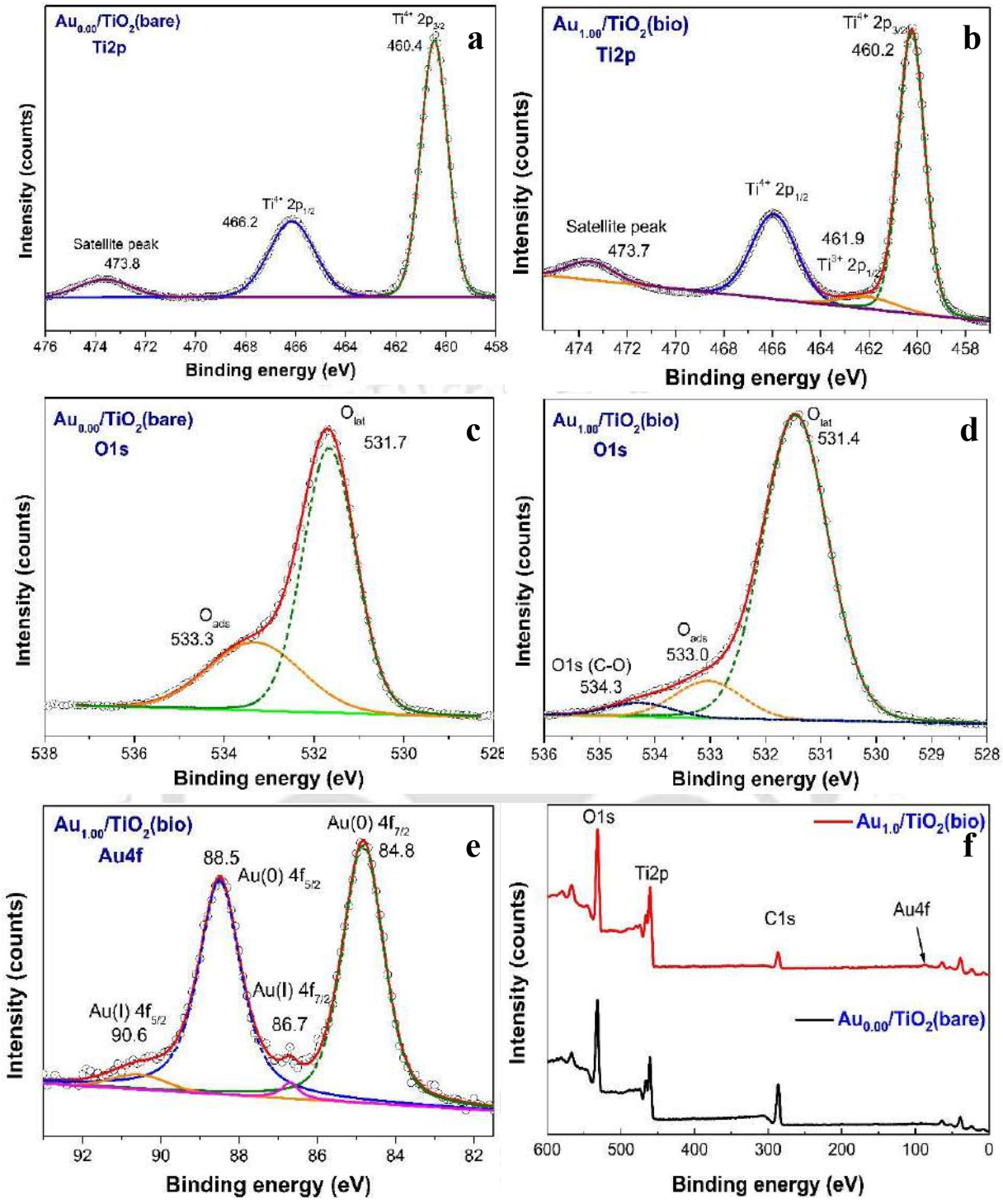

Figure 4.3: (a) XPS spectra of Ti2p of (a) $Au_{0.00}/TiO_2$(bare), and (b) $Au_{1.00}/TiO_2$(bio); O1s of (c) $Au_{0.00}/TiO_2$(bare), and (d) $Au_{1.00}/TiO_2$(bio); (e) Au4f of $Au_{1.00}/TiO_2$(bio) and (f) XPS survey spectra of $Au_{0.00}/TiO_2$(bare), and $Au_{1.00}/TiO_2$(bio).

Table 4.3: Relative elemental and configuration state composition of $Au_{0.00}/TiO_2$(bare), and $Au_{1.00}/TiO_2$(bio), analyzed through XPS.

Element	Chemical state	Sample (% area)	
		$Au_{0.00}/TiO_2$(bare)	**$Au_{1.00}/TiO_2$(bio)**
Ti	Ti^{4+} 2p	48.3	44.5
	Ti^{3+} 2p	-	3.4
	Ti 2P (Total)	48.3	47.9
O	O_L 1s	40.4	39.8
	O_a 1s	11.3	6.6
	O(C-O) 1s	-	4.7
	O 1s (Total)	51.7	51.1
Au	Au(0) 4f	-	0.953
	Au(I) 4f	-	0.045
	Au 4f (Total)	-	~1.0

4.2.4 FETEM and EDX analysis

FETEM images and particle size distribution curves of $Au_{0.00}/TiO_2$(bare) and $Au_{1.00}/TiO_2$(bio) are shown in Figs. 4.4a and 4.4b. It is seen that $Au_{0.00}/TiO_2$(bare) and $Au_{1.00}/TiO_2$(bio) particles are shaped spherical with an average particle size of 21.21 and 23.15 nm, respectively. Au nano-dots adhered on TiO_2 surface (size 5.4±1.3 nm) and incorporated into TiO_2 lattice caused an increase in particle size. The lattice fringe with the d-spacing of 0.352 (101) corresponding to TiO_2 was observed in the HRTEM images (Figs. 4.4c and 4.4d). An additional lattice fringe with the d-spacing of 0.237 nm (111) (Fig. 5d) owes to AuNPs in $Au_{1.00}/TiO_2$(bio). These findings are in close agreement to XRD analysis. The distinctive electron diffraction rings in SAED patterns infers to polycrystalline nature of both photocatalysts (insets of Figs. 4.4c and 4.4d) (Manuputty et al., 2019). The elemental composition and image mapping confirm the presence of Ti, O and Au in $Au_{1.00}/TiO_2$(bio) (Fig. 4.4e). It is clearly evident from the mapped image that Au was uniformly doped, provide better charge transfer and enhanced photocatalytic activity.

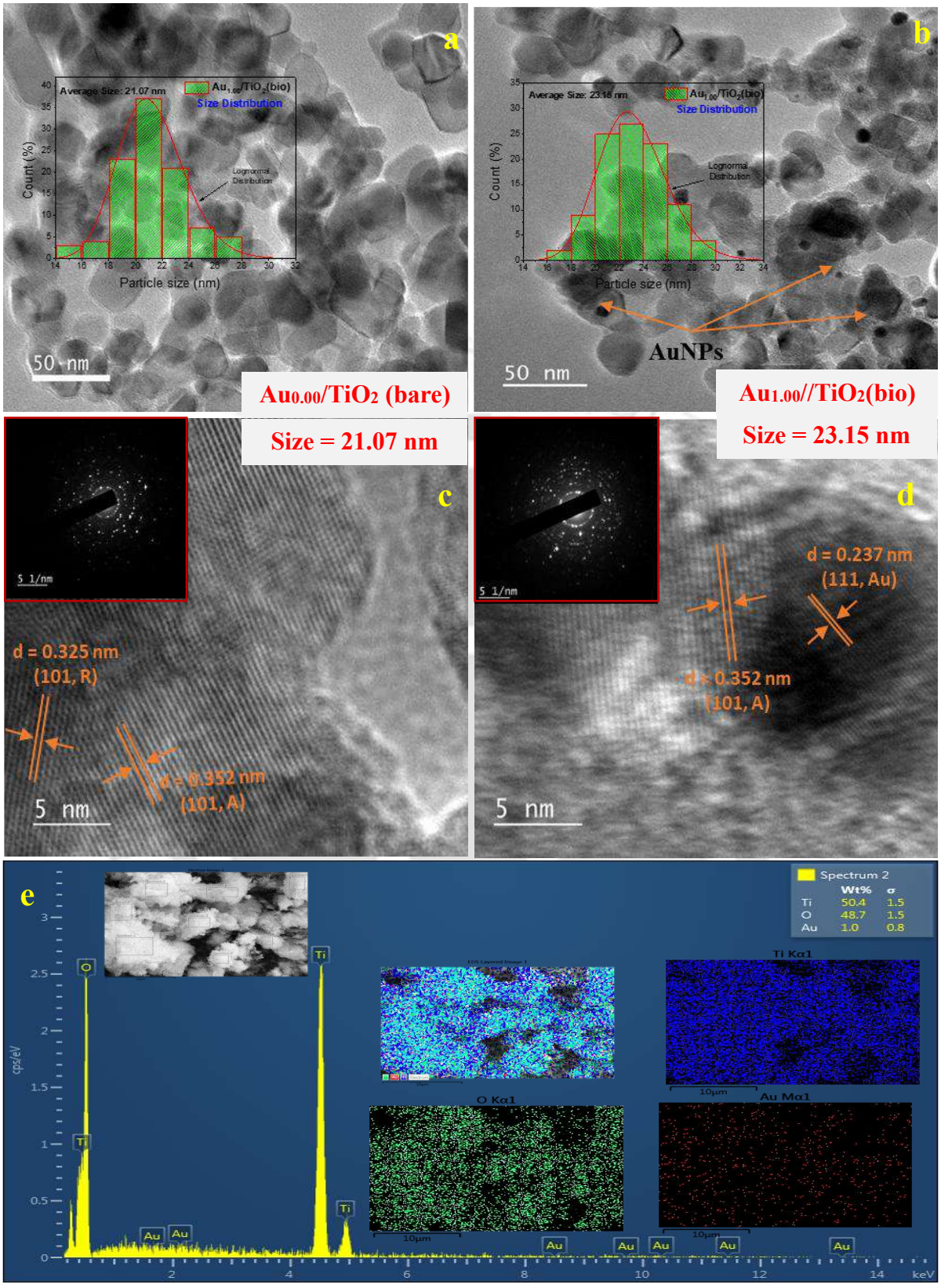

Figure 4.4: FETEM micrograph and particle size distribution of (a) $Au_{0.00}/TiO_2$(bare), and (b) $Au_{1.00}/TiO_2$(bio), HRTEM micrograph and SAED patterns of (c) $Au_{0.00}/TiO_2$(bare), and (d) $Au_{1.00}/TiO_2$(bio), and (e) EDX spectra and elemental mappings of Ti, O, and Au in $Au_{1.00}/TiO_2$(bio).

4.2.5 Thermogravimetric analysis (TGA)

Fig. 4.5a illustrates the TGA spectra of $Au_{0.00}/TiO_2$(bare) and $Au_{1.00}/TiO_2$(bio). In both specimens, a mass loss of barely 1% was observed from 50 to 200°C. It ascribes to water evaporation (Bhan and Golder, 2023). For doped particles, a mass loss of ~1.3% from 200 to 475°C might be of decomposition of trace impurities and bio-analytes adsorbed on TiO_2. A tiny mass gain in both photocatalysts at >475 °C, could of buoyancy effect (Nasrollahzadeh et al., 2019). The buoyancy effect occurs due to lower buoyant lift (force) in less dense air at high temperature, resulting in apparent weight gain.

4.2.6 BET surface area analysis

Fig. 4.5b illustrates the N_2 adsorption-desorption isotherm curves and BET parameters of $Au_{0.00}/TiO_2$(bare) and $Au_{1.00}/TiO_2$(bio). The observed hysteresis loops indicate that both catalysts exhibit a type IV isotherm pattern, signifying their mesoporous nature (Chelli and Golder, 2018). The introduction of Au doping reduced the BET surface area of $Au_{0.00}/TiO_2$(bare) from 60.73 to 51.06 $m^2\ g^{-1}$ in $Au_{1.00}/TiO_2$(bio). Additionally, the pore volume and average pore size of $Au_{1.00}/TiO_2$(bio) were determined to be 0.46 cc g^{-1} and 35.83 nm, respectively. In contrast, for $Au_{0.00}/TiO_2$(bare), it was 0.27 cc g^{-1} and 18.04 nm, respectively. The introduction of AuNPs into TiO_2 pores resulted in a reduction of the surface area and an expansion of both the overall pore volume and pore size of $Au_{1.00}/TiO_2$(bio) particles (Li et al., 2022).

4.2.7 Electron paramagnetic resonance (EPR) analysis

Fig. 4.5c represents the EPR spectra of $Au_{0.00}/TiO_2$(bare) and $Au_{1.00}/TiO_2$(bio). Two EPR peaks were detected at g-values of 2.005 and 1.990 in $Au_{1.00}/TiO_2$(bio). Trapped electrons owing to oxygen vacancies could generate a high-intensity peak at the g-value of 2.005, while Ti^{3+} defects are associated with an indistinct peak at 1.990 (Komaraiah et al., 2020). The low-intensity EPR signals (inset of Fig. 4.5c) is because of negligible OVs and Ti^{3+} sites in $Au_{0.00}/TiO_2$(bare). OVs and Ti^{3+} could trap the electron resulting a delayed recombination. Oxygen vacancies also stimulate the interaction of H_2O with the photocatalyst surface, which in turn could boost the photocatalytic activity of $Au_{1.00}/TiO_2$(bio) (Aronne et al., 2017).

4.2.8 Hydrophilicity analysis

After Au-doping, hydrophobic $Au_{0.00}/TiO_2$(bare) became highly hydrophilic, as the water contact angle decreased from 120.8 to 16.9° (Fig. 4.5d). The hydrophilicity could be

more due to the surface adsorption of functional groups from vegetal extract, as supported by XPS analysis. In fact, $Au_{1.00}/TiO_2$(chem) was found to be less hydrophilic (water contact angle 36.3°) compared to $Au_{1.00}/TiO_2$(bio) (Fig. 4.5d). The hydrophilic photocatalysts exhibit a better photocatalytic activity due to the generation of more free radicals from stimulated H_2O surrounding the photocatalysts and an improved availability of hydrophilic contaminants to catalyst's surface (Mimouni et al., 2020).

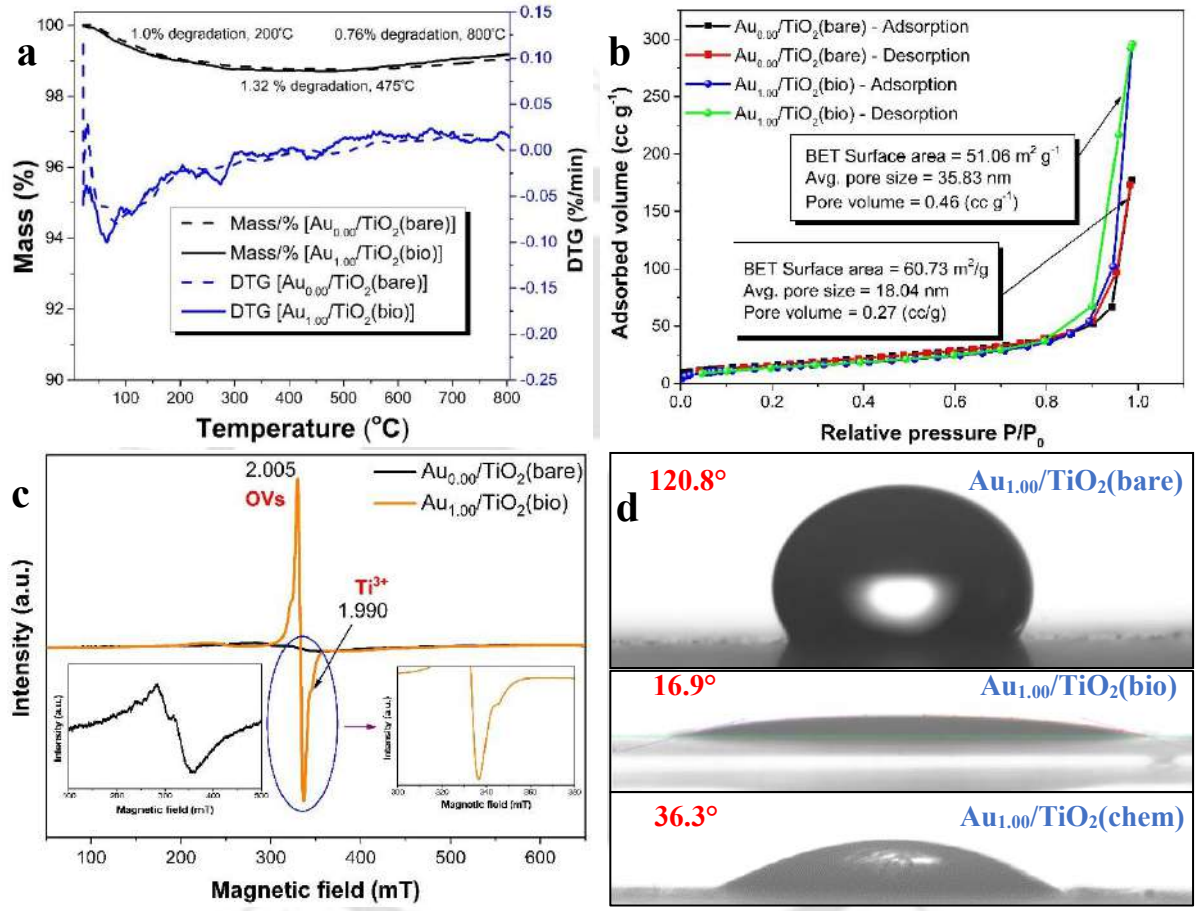

Figure 4.5: (a) TGA analysis, (b) N_2 adsorption-desorption isotherm curves, and (c) EPR spectra of $Au_{0.00}/TiO_2$(bare), and $Au_{1.00}/TiO_2$(bio). (d) Water contact angle of $Au_{0.00}/TiO_2$(bare), $Au_{1.00}/TiO_2$(bio), and $Au_{1.00}/TiO_2$(chem).

4.2.9 Charge trapping and recombination

The photoluminescence (PL) spectra of $Au_{0.00}/TiO_2$(bare) and $Au_{1.00}/TiO_2$(bio) are shown in Fig. 4.6a. In $Au_{0.00}/TiO_2$(bare), a sharp peak was observed at 396 nm, which implies to the recombination of e^-/h^+ charge carriers. The presence of a shoulder peak at the same position (396 nm) in $Au_{1.00}/TiO_2$(bio) is indicative of the decrease in charge carriers' recombination due to Au-doping (Cheng et al., 2020). Numerous emission peaks, i.e., at 438

and 562 (localized state of VB), 449 (free excitons), and 468 nm (shallow traps near CB, Ti^{3+}), were observed in both photocatalysts (Gogoi et al., 2020). The delayed recombination of hole-pairs at free excitons and shallow traps is related to the presence of more oxygen vacancies and Ti^{3+} state in $Au_{1.00}/TiO_2$(bio) than $Au_{0.00}/TiO_2$(bare) (Xue et al., 2019). Fig. 4.6b shows the time-resolved PL (TRPL) spectra. A significant increase in the lifetime of free e^-/h^+ pairs was noted. Compared to $Au_{0.00}/TiO_2$(bare), τ_2 of $Au_{1.00}/TiO_2$(bio) was increased from 5.01 to 12.84 ns, which implies to delayed Shockley-Read-Hall (SRH) recombination of holes with trapped electrons. A small increment in τ_1 of $Au_{1.00}/TiO_2$(bio) epitomized the PL of free excitons (Zhou et al., 2020).

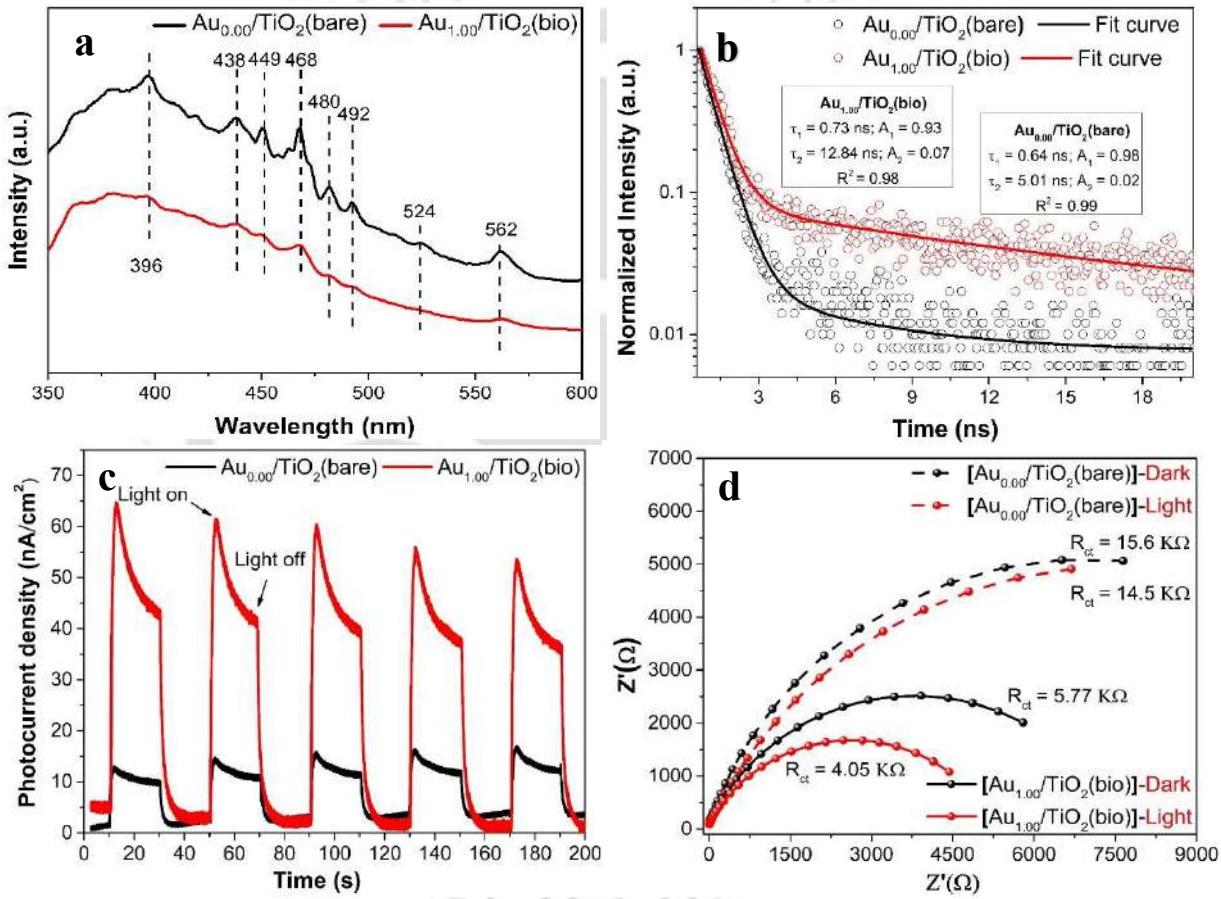

Figure 4.6: (a) Photoluminescence (PL) spectra, and (b) Time resolved photoluminescence (TRPL) of $Au_{0.00}/TiO_2$(bare), and $Au_{1.00}/TiO_2$(bio); (c) Chronoamperometric transient photocurrent response, and (d) Nyquist's plot for EIS analysis, in presence and absence of light, of $Au_{0.00}/TiO_2$(bare), and $Au_{1.00}/TiO_2$(bio).

4.2.10 Photoelectrochemical (PEC) characteristics

The transient photocurrent was measured by analysing the chronoamperometric response of prepared catalysts for several cycles at 20 s intervals in the presence and absence

of light irradiation. Fig. 4.6c shows the current density profile with on/off light cycles. In the presence of light (50W visible light), $Au_{1.00}/TiO_2$(bio) exhibited ~4 folds higher current density of 64.70 nA cm^{-2} than $Au_{0.00}/TiO_2$(bare) (16.98 nA cm^{-2}). The unsaturated photocurrent during each illuminated cycle indicates the presence of electron traps in $Au_{1.00}/TiO_2$(bio) (Wang et al., 2016). Additionally, coated $Au_{1.00}/TiO_2$(bio) leached from FTO surface with progression of the light on/off cycles, which gradually decreased the photocurrent density of $Au_{1.00}/TiO_2$(bio) in presence and absence of light. The charge transfer resistance (R_{ct}) was calculated through Nyquist's plot (Fig. 4.6d) of the fitted electrochemical impedance spectra (EIS). A smaller arc radius in the fitted Nyquist's plot signifies lower charge transfer resistance and better charge transfer efficiency of $Au_{1.00}/TiO_2$(bio) (Senobari and Nezamzadeh-Ejhieh, 2020). In the dark, R_{ct} of $Au_{0.00}/TiO_2$(bare) and $Au_{1.00}/TiO_2$(bio) were found to be 15.60, and 5.77 KΩ, respectively. $Au_{1.00}/TiO_2$(bio) exhibited a lower R_{ct} of 4.05 KΩ than $Au_{0.00}/TiO_2$(bare) with R_{ct} of 14.5 KΩ under light irradiation. The increased photocurrent density and decreased R_{ct} are indicative of improved charge separation and interfacial charge transfer, and delayed recombination in the case of $Au_{1.00}/TiO_2$(bio) (Kumar et al., 2020).

4.2.11 Photocatalytic degradation of CLQ

The efficiency of developed catalysts was evaluated by photodegradation of CLQ under 50W visible light. Figs. 4.7a and 4.7b illustrate the fitted non-linear first-order kinetic models. Figs. 4.7c and 4.7d show the CLQ degradation (%) and QY (%) at various pH and dopant concentrations. Table 4.4 shows the values of rate constant (k_1), CLQ degradation (%), QY (%), and TOC removal (%) under various test conditions. The photocatalytic degradation process is significantly affected by the solution's pH, as it governs the generation of free radicals and change of surface properties of catalysts. In dark condition, the adsorption of CLQ on $Au_{1.00}/TiO_2$(bio) surface was increased with solution pH. This phenomenon can be attributed to the transition of the catalyst's surface to a negative charge at higher pH, facilitating attraction of cationic CLQ molecules (Irfan et al., 2017; Farsi and Nezamzadeh-Ejhieh, 2022). The optimally doped $Au_{1.00}/TiO_2$(bio) exhibited the highest CLQ degradation of 94.59 ± 1.23 % at pH 7 with the maximum k_1 and QY of 2.19×10^{-2} min^{-1} and 23.29±0.30%, respectively. $Au_{0.00}/TiO_2$(bare) showed the lowest with CLQ degradation, k_1 and QY of 64.29 ±2.02%, 0.83×10^{-2} min^{-1}, and 15.83±0.50%. The surface adsorption of CLQ was increased with Au-doping (15.23±2.41% →45.99±0.57%), which could be of the fact that the hydrophilic $Au_{1.00}/TiO_2$(bio) particles could attract more CLQ molecules towards its surface than

hydrophobic $Au_{0.00}/TiO_2$(bare). Further, a fast photo-degradation of CLQ was observed during initial 60 min, which was gradually decreased due to the interference caused by intermediate compounds. Only 2.72% photolysis of CLQ was observed in light. Additionally, pristine AuNPs showed 31.97% CLQ degradation along with 29.34% surface adsorption. Whereas, CLQ photo-degradation of 80.48±1.14% was found by $Au_{1.00}/TiO_2$(chem) which is notably lower than that of $Au_{1.00}/TiO_2$(bio).

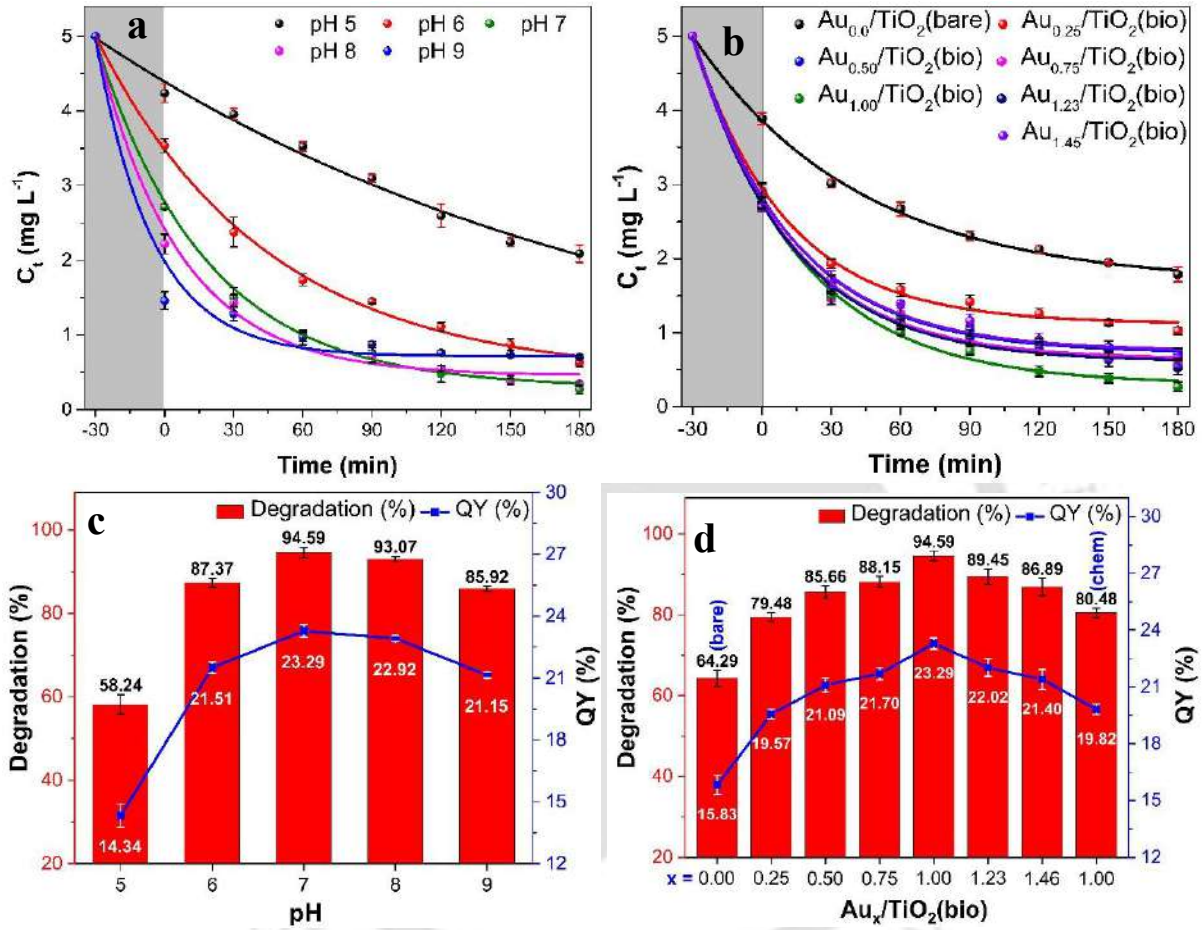

Figure 4.7: (a) CLQ decay (symbols: experimental and line: non-linear first-order kinetic model fitted) at different pH using $Au_{1.00}/TiO_2$(bio), (b) CIP decay (symbols: experimental and line: non-linear first-order kinetic model fitted) using different photocatalysts at pH 5, (c) CLQ degradation efficiency and QY at different pH using $Au_{1.00}/TiO_2$(bio), and (d) CLQ degradation efficiency and QY using different photocatalysts at pH 5. Photocatalytic reaction with CLQ concentration of 5 mg L^{-1} (100 mL solution), 1 g L^{-1} photocatalyst dose under 50 W visible light (450 nm) for 180 min with continuous stirring at 300 rpm.

Table 4.4: CLQ degradation efficiency (%), rate constant (min^{-1}), QY (%), and TOC removal (%) of photocatalytic degradation of 100 mL CLQ (5 mg L^{-1}) using $Au_{1.00}/TiO_2$(bio) (0.5 g L^{-1}) at various pH (5-9) and $Au_{0\text{-}1.45}/TiO_2$(bio) (0.5 g L^{-1}) at optimized pH 7 under 50W visible light (450 nm) for 180 min with continuous stirring at 300 rpm.

Catalysts	pH	CLQ degradation (%)	k_1 (min^{-1})	QY (%)	(%) TOC removal
$Au_{1.00}/TiO_2$(bio)	5	58.24 ± 2.31	0.74 x 10^{-2}	14.34 ± 0.57	21.98
	6	87.37 ± 1.09	1.62 x 10^{-2}	21.51 ± 0.27	39.86
	7	**94.59 ± 1.23**	2.19 x 10^{-2}	**23.29 ± 0.30**	**69.57**
	8	93.07 ± 0.59	2.07 x 10^{-2}	22.92 ± 0.15	59.18
	9	85.92 ± 0.57	1.95 x 10^{-2}	21.15 ± 0.14	44.2
$Au_{0.00}/TiO_2$(bare)	7	64.29 ± 2.02	0.83 x 10^{-2}	15.83 ± 0.50	37.44
$Au_{0.25}/TiO_2$(bio)		79.47 ± 1.02	1.05 x 10^{-2}	19.57 ± 0.25	43.72
$Au_{0.50}/TiO_2$(bio)		85.66 ± 1.52	1.81 x 10^{-2}	21.09 ± 0.37	50.97
$Au_{0.75}/TiO_2$(bio)		88.15 ± 1.36	1.95 x 10^{-2}	21.70 ± 0.34	58.7
$Au_{1.23}/TiO_2$(bio)		89.44 ± 1.86	2.00 x 10^{-2}	22.02 ± 0.46	62.32
$Au_{1.45}/TiO_2$(bio)		86.90 ± 2.16	1.60 x 10^{-2}	21.40 ± 0.53	62.08
$Au_{1.00}/TiO_2$(chem)	7	80.48 ± 1.14	1.47 x 10^{-2}	19.82 ± 0.28	45.17

Table 4.5: Photocatalytic Degradation of CLQ by Chemically Synthesized Photocatalysts and its Comparison with $Au_{1.00}/TiO_2$(bio) (Present Study).

Photocatalyst	Light source	Initial CLQ concentration (mg L^{-1})	Catalyst dose (g L^{-1})	Reaction time (min)	CLQ degradation (%)	Ref.
ZnO supported clinoptilolite zeolite	UV A lamp	10	2	180	96	(da Silva et al., 2021)
Nano ZnO	UV light (400 W)	20	0.1	60	65	(Cisneros et al., 2021)
PDINH/MIL-88A(Fe)	Visible light (> 400 nm)	10	0.4	30	53.3	(Tao et al., 2023)
$Gd_2Ti_2O_7$/N-GQD nanocomposite	Visible light 300 W xenon lamp	10	1	90	75.9	(Zhang et al., 2018)
$Au_{0.00}/TiO_2$(bare)	50 W visible light	5	0.5	180	64.3	**Present study**
$Au_{1.00}/TiO_2$(bio)					94.6	
$Au_{1.00}/TiO_2$(chem)					80.48	

It is seen that the $Au_{1.00}/TiO_2$(bio) attained the highest TOC removal of 69.57% (Table 4.4), which is in close line with CLQ degradation (%) trend. Whereas, $Au_{0.00}/TiO_2$(bare) and $Au_{1.00}/TiO_2$(chem) showed 37.44 and 45.17% TOC removal, respectively (Table S5 of the Supporting Information). A lower TOC removal (%) than CLQ degradation (%) supports the fact that mineralization is a slower process along with the formation of refractory intermediates (Ahmad et al., 2020). Table 4.5 demonstrates a comparison between the photocatalytic efficiencies of $Au_{1.00}/TiO_2$(bio) and previous studies. Only a very few studies reported on CLQ photocatalytic degradation either using UV light or high-intensity visible light sources. Bio-based Au-doped TiO_2 outperformed most of the previous studies under low-intensity visible light conditions.

4.2.12 LC-MS analysis and CLQ photodegradation mechanism

Figs. 4.8a-4.8d show the LC chromatogram and mass spectra of CLQ and intermediates formed during its degradation. A sharp peak at the retention time of 2.541 min and a mass number of 320.1 (Figs. 4.8a and 4.8c) represent the CLQ molecules. After CLQ degradation, the peak intensity was decreased, and multiple spikes appeared in the mass spectra (Figs. 4.8b and 4.8d). Fig. 4.9 depicts possible mechanistic pathways of CLQ degradation by $Au_{1.00}/TiO_2$(bio). CLQ was degraded in two different pathways involving formation 16 intermediates. In this Chapter, the intermediate products are denoted as F (fragment) to avoid any confusion with Chapter 3, where the formed intermediates were denoted with P (intermediate products).

In pathway #I, CLQ degradation is initiated with the formation of F1 through ·OH free radical attack, which is subsequently followed by a dehydration reaction forming F2. Alkylation and demethylation of F2 upon $OH^{\cdot}$ attack yielded F3 with the release of ethane and methanol, which is further dehydrated to F4. Concurrently, amine dealkylation of CLQ originated F4 and underwent an alkylation reaction yielding F5, which is further amine dealkylated to F6 (Ahmad et al., 2016). Deamination and dechlorination of F6 led to the formation of two sub-products, F7(I) and F7(II), respectively. The aromatic dihydropyridine ring of F7(I) was cleaved forming chlorobenzene (F8), followed by the generation of benzene (F9) with the release of HCl.

Pathway #2 involves the formation of F10 through the loss of chloride ions from the quinoline ring of CLQ, which is gradually degraded to F11 and F12 by dealkylation and deamination. F13 intermediate is formed through both demethylation of F7(II) and amine dealkylation of F12, which is further transformed into the most common intermediate, benzene

(F9), via quinoline formation (F14) (Ahmad et al., 2016). Finally, benzene (F9) underwent a ring-opening process to yield muconic dialdehyde (F15), which is ultimately mineralized to CO_2 and H_2O (Yi et al., 2021).

Comparing the m/z values of intermediates obtained from the mass spectra and the predicted compounds, only 3 out of 16 intermediates exhibited any mass error of 0.1-0.2% mol g^{-1}.

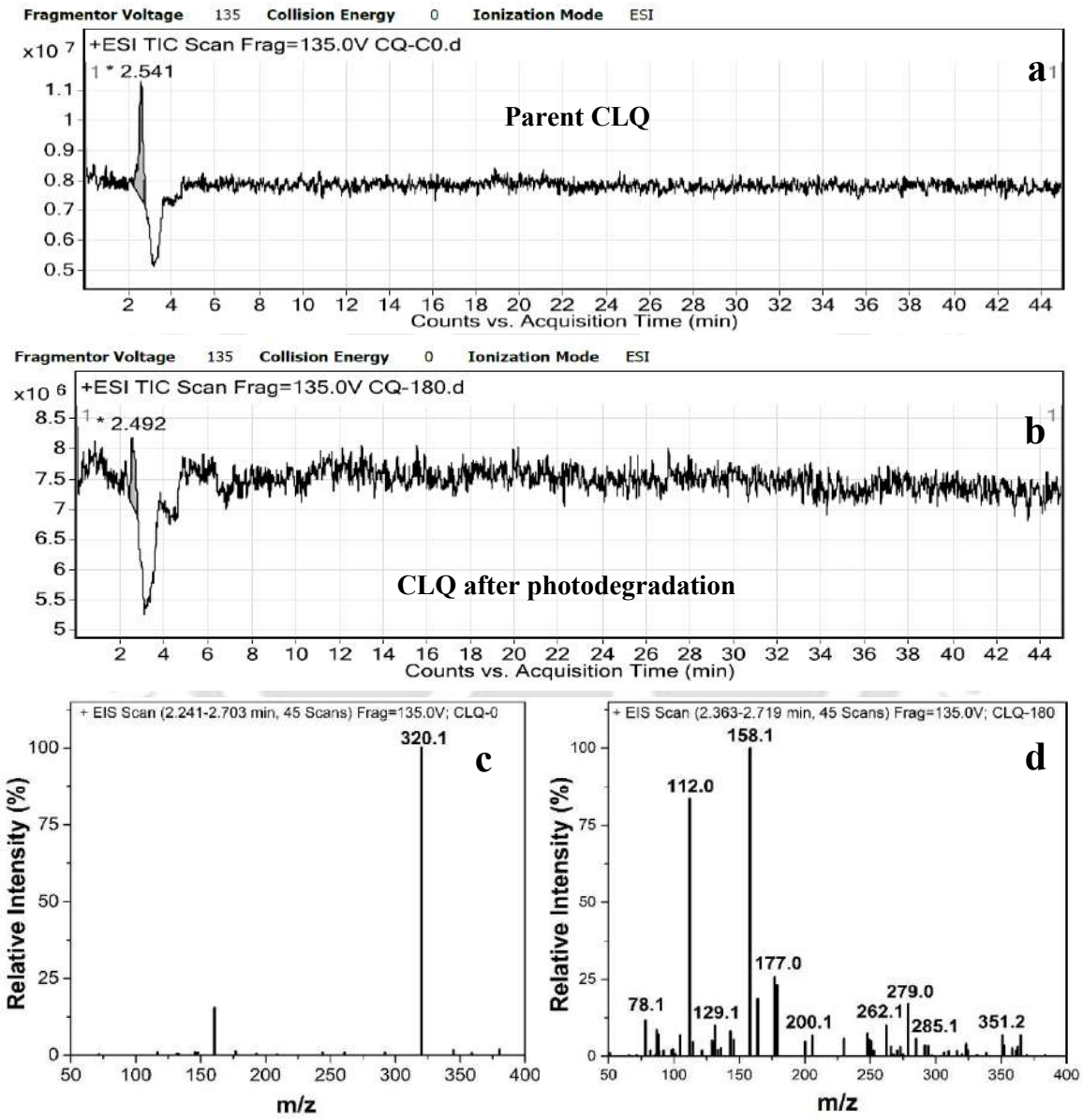

Figure 4.8: LC-MS analysis: Chromatograms of CLQ (a) before and (b) after photocatalytic degradation using $Au_{1.00}/TiO_2$(bio), captured via positive EIS mode $[M + H]^+$. MS spectra of CLQ (c) before and (d) after photocatalytic degradation.

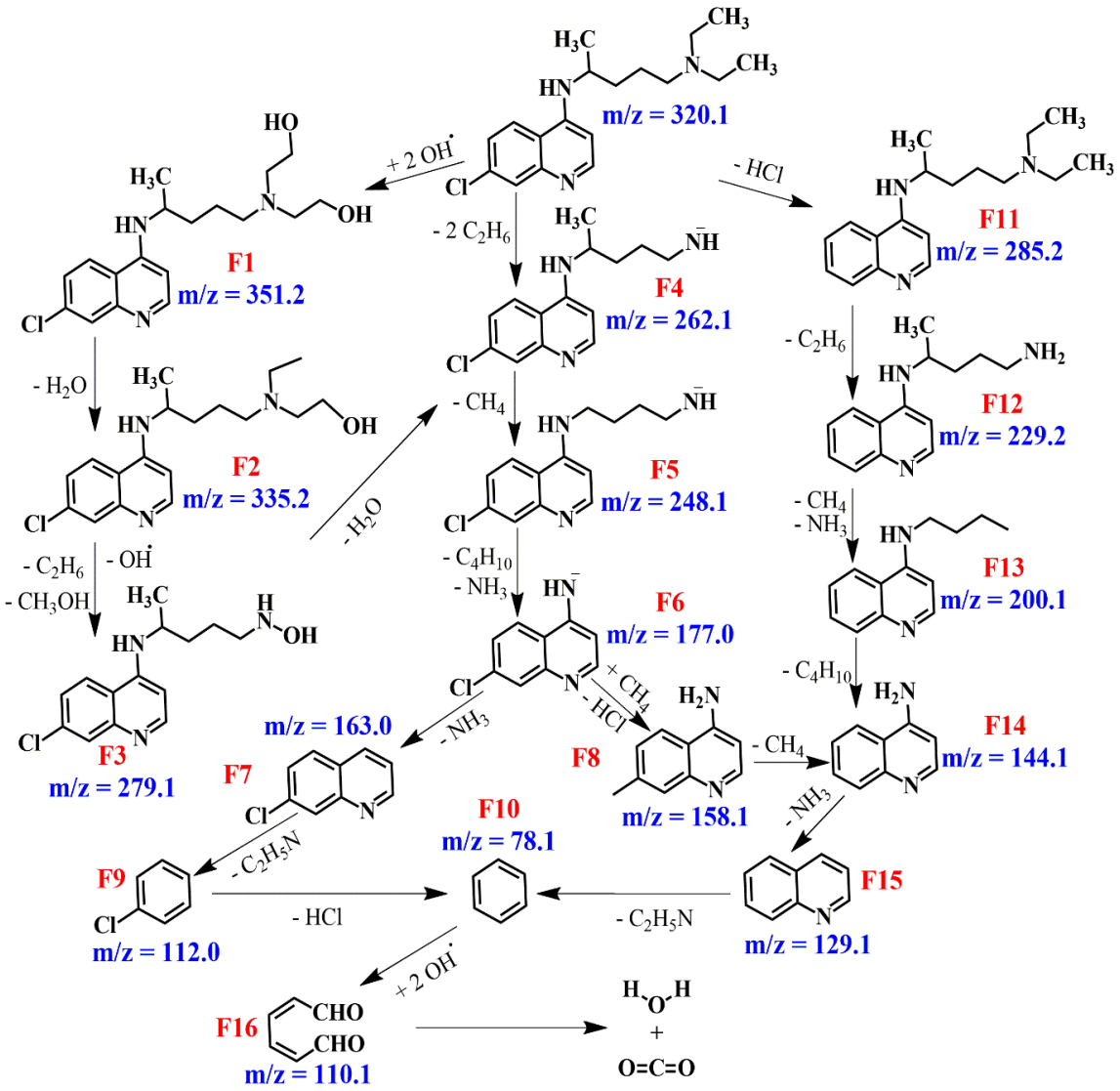

Figure 4.9: Proposed mechanism of CLQ degradation by $Au_{1.00}/TiO_2$(bio) at pH 7 for 180 min of reaction under visible light irradiation.

4.2.13 Reusability and stability analysis

The reusability of $Au_{1.00}/TiO_2$(bio) was assessed over 5 consecutive cycles by monitoring the surface adsorption (in dark for 30 min) and photodegradation of CLQ (in light for 180 min). After each cycle, the used photocatalyst was centrifuged at 7000 rpm for 5 min followed by sonication for 10 min to remove any CLQ and intermediates adhered to the surface. Fig. 4.10a shows the surface adsorption (%) and CLQ degradation (%) for each cycle. More than 90% CLQ degradation was observed up to the 3rd cycle. However, the CLQ degradation was decreased by 8.84 and 16.41% during the 4th and 5th cycles. It implies that CLQ and intermediate products remained adsorbed on the catalyst surface might have masked some of

it's of active sites. As a result, CLQ surface adsorption in the dark was decreased from 45.67 (±1.02) to 19.63 (±1.45) % with the progression of degradation cycles (1st to 5th).

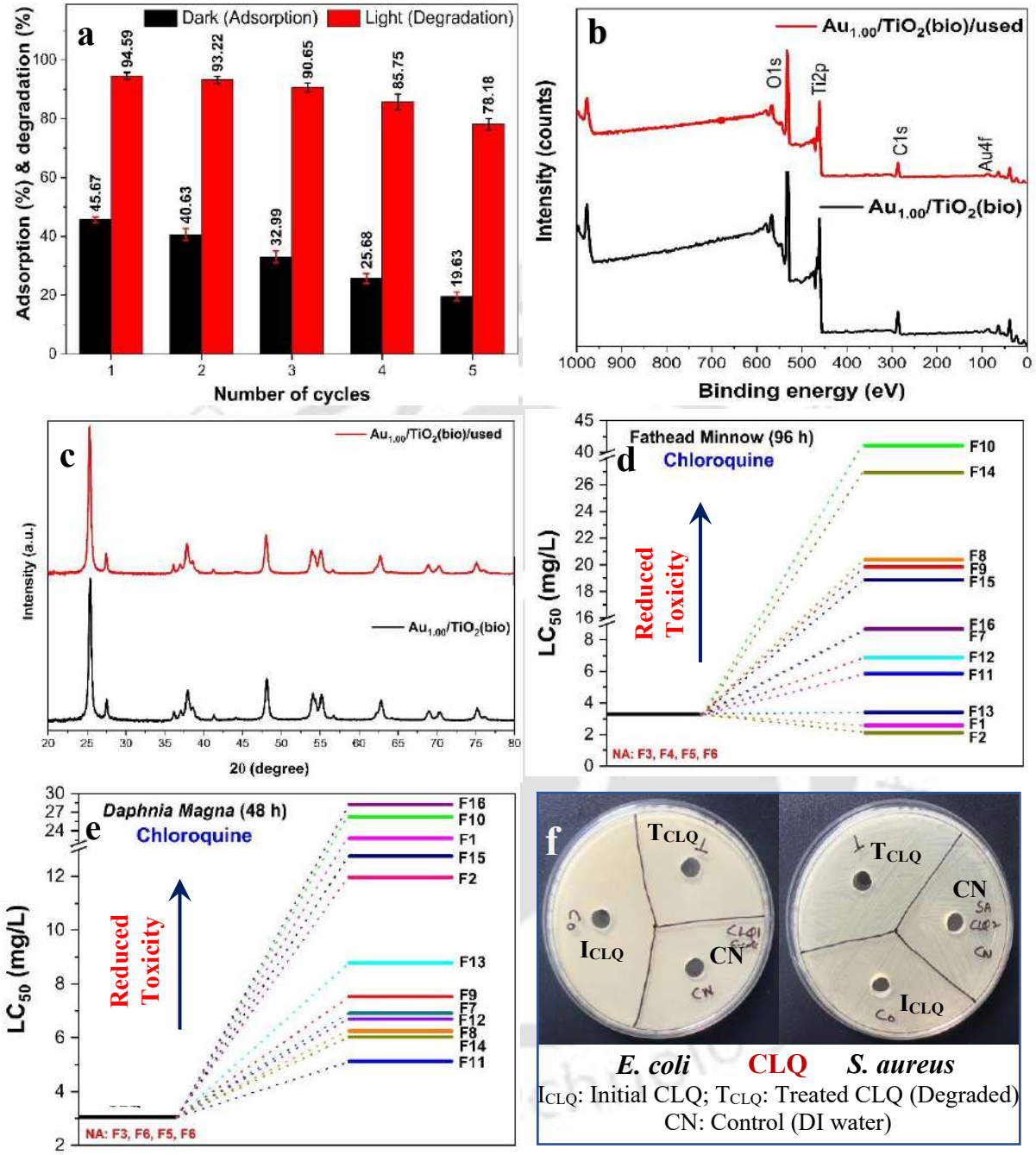

Figure 4.10: (a) CLQ degradation (%) and its pre-adsorption (%) before light illumination for 5 consecutive cycles, (b) XPS survey spectra, and (c) XRD spectra of $Au_{1.00}/TiO_2$(bio) and $Au_{1.00}/TiO_2$(bio)/used. Aquatic toxicity of CLQ and intermediate products against (d) Fathead minnow, and (e) *Daphnia magna*. (f) Antimicrobial activity of CLQ before and after photodegradation against *E. coli* and *S. aureus*.

The XPS and XRD analyses were conducted to assess the chemical and structural stability of $Au_{1.00}/TiO_2$(bio) after the 1st photocatalytic degradation cycle ($Au_{1.00}/TiO_2$(bio)/used). Figs. 10b-9c depict the XPS survey spectra, indicating presence of Ti2P, O1s, and Au4f states in used photocatalyst. The persistent XRD spectra (4.10c) of $Au_{1.00}/TiO_2$(bio) before and after the photocatalytic degradation process confirmed its structural and chemical stability after photocatalytic degradation.

4.2.14 Aquatic toxicity assessment and antimicrobial activity

The photocatalytic breakdown of CLQ took place through three distinct pathways, forming 16 different fragments, as shown in Fig. 4.9. The untreated CLQ exhibited an LC_{50} of 3.29 mg L^{-1}, indicating considerable toxicity toward aquatic life (Fig. 4.10d). The reaction fragments, such as F13, F11, F12, and F7, demonstrated increased LC_{50} values ranging from 3.40 to 8.69, which owns moderate toxicity. While F16, F15, F9, F8, F14, and F10 fragments were not toxic but lie in harmful categories with lower LC_{50} values (18.89-41.05 mg L^{-1}), demonstrating a substantial decline in the toxicity post-photocatalytic treatment (Truong et al., 2022). Additionally, fragments like F1 and F2 retained comparable toxicity levels to the parent compound. For *Daphnia magna*, CLQ exhibited an LC_{50} of 3.05 mg L^{-1}, denoting moderate toxicity toward freshwater crustaceans (Fig. 4.10e). The LC_{50} values of degradation fragments (F11, F14, F8, F12, F7, F9, and F13) were observed to be within the range of 5.12-8.78 mg L^{-1}, while F2, F15, F1, F10 and F16 fragments considered as harmful with lower $LC5_0$ values (11.96-28.24 mg L^{-1}), suggesting a detoxification effect due to the photocatalytic process (Zhou et al., 2023). The LC_{50} values of the remaining fragments could not be assessed. It is worth noting that no fragment exhibited a higher LC_{50} value than the CLQ. The findings suggest that the treated CLQ solution presents a lower ecological threat than CLQ molecules.

The parent CLQ and photodegraded CLQ did not showed any zone of inhibition (Fig. 4.10f), indicating lack of antimicrobial activity of 5 mg L^{-1} CLQ against both *E. coli* and *S. aureus* strains.

4.3 Major findings

This study has come out with an excellent visible-active Au-doped TiO_2 photocatalyst synthesized in a bio-based route using the phytochemicals present in *S. edule* vegetal extract coupled with steamed autoclaving. Au-doping merited TiO_2 to exhibit a narrow bandgap, delayed recombination, and highly hydrophilic nature due to the synergetic effect of newly

introduced electron traps and oxygen vacancies. The bandgap of $Au_{0.00}/TiO_2$(bare) was reduced from 3.29 to 2.45 eV at the optimal 1% (w/w) dopant concentration ($Au_{1.00}/TiO_2$(bio)). Au(III) was successfully doped with a relative abundance of 95% Au(0) and 5% Au(I). Au-doping resulted higher dislocation density (1.96×10^{-3} lines/nm^2) and particle size (21.21 to 23.15 nm), and decreased lattice strain (7.31×10^{-3}). Under visible-light illumination, R_{ct} of $Au_{0.00}/TiO_2$(bare) and $Au_{1.00}/TiO_2$(bio) were decreased by 1.08 and 1.43 folds, respectively, compared to that of under dark condition. $Au_{1.00}/TiO_2$(bio) displayed ~4 folds higher current density of 64.70 nA cm^{-2} than $Au_{0.00}/TiO_2$(bare). $Au_{1.00}/TiO_2$(bio) could degrade 94.59±1.23% CLQ against 69.57% mineralization efficiency, which is remarkably higher than, $Au_{0.00}/TiO_2$(bare) and $Au_{1.00}/TiO_2$(chem). $Au_{1.00}/TiO_2$(bio) could retain 90% of its CLQ degradation efficiency up to the 3rd cycle, and undergone a steady fall thereafter. As many as 16 intermediate products survived the photo-degradation, and the proposed routes showed their formation leading to mineralization with no mass error for 13 intermediates. Additionally, the photocatalytic degradation process significantly reduced the aquatic toxicity of CLQ. Therefore, this work could contribute insightful details in understanding the reaction and materials chemistry of phytochemical-based metal doping to synthesize visible-light driven photocatalysts for enhanced functionalities.

Au-doping could reduce the bandgap to 2.45 eV (absorption edge of 506 nm), enhancing visible light harvesting compared to Pt-doping. However, the improvement in photocurrent density was relatively modest (4-fold vs. 8-fold for Pt), and >16% drop in the photocatalytic activity after the 5th reuse cycle was observed. To overcome these challenges, Pd-doping emerges as a promising alternative (Chapter 5), offering enhanced photocatalytic performance while being more cost-effective and abundant compared to noble metals like Pt and Au.

References

Ahmad, I., Ahmed, S., Anwar, Z., Sheraz, M.A., Sikorski, M., 2016. Photostability and Photostabilization of Drugs and Drug Products. Int. J. Photoenergy. https://doi.org/10.1155/2016/8135608

Ahmad, M., Aziz, A.R.A., Mazari, S.A., Baloch, A.G., Nizamuddin, S., 2020. Photocatalytic degradation of methyl orange from wastewater using a newly developed Fe-Cu-Zn-ZSM-5 catalyst. Environ. Sci. Pollut. Res. 27. https://doi.org/10.1007/s11356-020-08940-9

Aronne, A., Fantauzzi, M., Imparato, C., Atzei, D., De Stefano, L., D'Errico, G., Sannino, F.,

Rea, I., Pirozzi, D., Elsener, B., Pernice, P., Rossi, A., 2017. Electronic properties of TiO_2-based materials characterized by high Ti^{3+} self-doping and low recombination rate of electron-hole pairs. RSC Adv. 7. https://doi.org/10.1039/c6ra27111a

Baildya, N., Ghosh, N.N., Chattopadhyay, A.P., 2021. Inhibitory capacity of chloroquine against SARS-COV-2 by effective binding with angiotensin converting enzyme-2 receptor: An insight from molecular docking and MD-simulation studies. J. Mol. Struct. 1230. https://doi.org/10.1016/j.molstruc.2021.129891

Bhan, C., Golder, A.K., 2023. Utilizing bioinspired AgNPs as an antibacterial agent to enhance ceramic membrane performance. J. Environ. Chem. Eng. 11, 110283. https://doi.org/10.1016/j.jece.2023.110283

Bhan, C., Kumar Golder, A., 2023. Bio-based hierarchical vertically aligned 2D ZnO nanostructures for ultra selective electrochemical sensing of p-Chloroaniline. Chem. Eng. J. 475. https://doi.org/10.1016/j.cej.2023.146122

Chelli, V.R., Golder, A.K., 2018. Ag-doping on ZnO support mediated by bio-analytes rich in ascorbic acid for photocatalytic degradation of dipyrone drug. Chemosphere 208, 149–158. https://doi.org/10.1016/j.chemosphere.2018.05.158

Cheng, G., Liu, X., Song, X., Chen, X., Dai, W., Yuan, R., Fu, X., 2020. Visible-light-driven deep oxidation of NO over Fe doped TiO_2 catalyst: Synergic effect of Fe and oxygen vacancies. Appl. Catal. B Environ. 277. https://doi.org/10.1016/j.apcatb.2020.119196

Cisneros, S., Chen, S., Diemant, T., Bansmann, J., Abdel-Mageed, A.M., Goepel, M., Olesen, S.E., Welter, E.S., Parlinska-Wojtan, M., Gläser, R., Chorkendorff, I., Behm, R.J., 2021. Effects of SiO_2-doping on high-surface-area Ru/TiO_2 catalysts for the selective CO methanation. Appl. Catal. B Environ. 282. https://doi.org/10.1016/j.apcatb.2020.119483

da Silva, P.L., Nippes, R.P., Macruz, P.D., Hegeto, F.L., Olsen Scaliante, M.H.N., 2021. Photocatalytic degradation of hydroxychloroquine using ZnO supported on clinoptilolite zeolite. Water Sci. Technol. 84. https://doi.org/10.2166/wst.2021.265

Derikvandi, H., Nezamzadeh-Ejhieh, A., 2017. Increased photocatalytic activity of NiO and ZnO in photodegradation of a model drug aqueous solution: Effect of coupling, supporting, particles size and calcination temperature. J. Hazard. Mater. 321. https://doi.org/10.1016/j.jhazmat.2016.09.056

Farsi, M., Nezamzadeh-Ejhieh, A., 2022. A coupled Cobalt(II) oxide-Silver Tungstate nano-photocatalyst: Moderate characterization and evaluation of the photocatalysis kinetics towards methylene blue in aqueous solution. Polyhedron 219. https://doi.org/10.1016/j.poly.2022.115823

Gao, P., Zhang, Z., Feng, L., Liu, Y., Du, Z., Zhang, L., 2021. Novel Ti_3C_2/Bi@BiOI nanosheets with gradient oxygen vacancies for the enhancement of spatial charge separation and photocatalytic performance: The roles of reactive oxygen and iodine species. Chem. Eng. J. 426. https://doi.org/10.1016/j.cej.2021.130764

Gayathri, P.V., Nair, D., Gopinath, G., Pilla, D., Joseph, S., 2023. Solar Photocatalysis for the Decontamination of Water from Emerging Pharmaceutical Pollutant Chloroquine Using Nano ZnO as the Catalyst. Water. Air. Soil Pollut. 234. https://doi.org/10.1007/s11270-023-06148-4

Gogoi, D., Namdeo, A., Golder, A.K., Peela, N.R., 2020. Ag-doped TiO_2 photocatalysts with effective charge transfer for highly efficient hydrogen production through water splitting. Int. J. Hydrogen Energy 45. https://doi.org/10.1016/j.ijhydene.2019.11.127

Guo, Z., Dai, F., Yin, H., Zhang, M., Xing, J., Wang, L., 2022. The dual role of Au nanoparticles in the surface plasmon resonance enhanced photocatalyst Au/g-C_3N_4. Colloids Interface Sci. Commun. 48. https://doi.org/10.1016/j.colcom.2022.100615

Irfan, S., Li, L., Saleemi, A.S., Nan, C.W., 2017. Enhanced photocatalytic activity of La^{3+} and Se^{4+} co-doped bismuth ferrite nanostructures. J. Mater. Chem. A 5. https://doi.org/10.1039/c7ta01847a

Jahdi, M., Mishra, S.B., Nxumalo, E.N., Mhlanga, S.D., Mishra, A.K., 2020. Smart pathways for the photocatalytic degradation of sulfamethoxazole drug using F-Pd co-doped TiO_2 nanocomposites. Appl. Catal. B Environ. 267. https://doi.org/10.1016/j.apcatb.2020.118716

Komaraiah, D., Radha, E., Sivakumar, J., Ramana Reddy, M. V., Sayanna, R., 2020. Photoluminescence and photocatalytic activity of spin coated Ag^+ doped anatase TiO_2 thin films. Opt. Mater. (Amst). 108. https://doi.org/10.1016/j.optmat.2020.110401

Kumar, M.P., Jagannathan, R., Ravichandran, S., 2020. Photoelectrochemical System for Unassisted High-Efficiency Water-Splitting Reactions Using N-Doped TiO_2 Nanotubes. Energy and Fuels 34. https://doi.org/10.1021/acs.energyfuels.0c00634

Lanza, G., Martinez Jimenez, M.J., Alvarez, F., Perez-Taborda, J.A., Avila, A., 2022. Valence State Tuning of Gold Nanoparticles in the Dewetting Process: An X-ray Photoelectron Spectroscopy Study. ACS Omega 7. https://doi.org/10.1021/acsomega.2c04259

Lei, Z.N., Wu, Z.X., Dong, S., Yang, D.H., Zhang, L., Ke, Z., Zou, C., Chen, Z.S., 2020. Chloroquine and hydroxychloroquine in the treatment of malaria and repurposing in treating COVID-19. Pharmacol. Ther. https://doi.org/10.1016/j.pharmthera.2020.107672

Li, Q., Zhao, J., Shang, H., Ma, Z., Cao, H., Zhou, Y., Li, G., Zhang, D., Li, H., 2022. Singlet

Oxygen and Mobile Hydroxyl Radicals Co-operating on Gas-Solid Catalytic Reaction Interfaces for Deeply Oxidizing NOx. Environ. Sci. Technol. 56. https://doi.org/10.1021/acs.est.2c00622

Li, R., Li, W., Liu, M., He, Q., Wang, Y., Zhan, Q., Wang, T., 2019. Structural, Morphological, Optical and Electrical Properties of Cu-Doped PbS Nanofilms. ES Mater. Manuf. 4. https://doi.org/10.30919/esmm5f217

Manuputty, M.Y., Dreyer, J.A.H., Sheng, Y., Bringley, E.J., Botero, M.L., Akroyd, J., Kraft, M., 2019. Polymorphism of nanocrystalline TiO_2 prepared in a stagnation flame: Formation of the TiO_2-II phase. Chem. Sci. 10. https://doi.org/10.1039/c8sc02969e

Maxwell, N.M., Nevin, R.L., Stahl, S., Block, J., Shugarts, S., Wu, A.H.B., Dominy, S., Solano-Blanco, M.A., Kappelman-Culver, S., Lee-Messer, C., Maldonado, J., Maxwell, A.J., 2015. Prolonged neuropsychiatric effects following management of chloroquine intoxication with psychotropic polypharmacy. Clin. Case Reports 3. https://doi.org/10.1002/ccr3.238

Mimouni, R., Askri, B., Larbi, T., Amlouk, M., Meftah, A., 2020. Photocatalytic degradation and photo-generated hydrophilicity of Methylene Blue over $ZnO/ZnCr_2O_4$ nanocomposite under stimulated UV light irradiation. Inorg. Chem. Commun. https://doi.org/10.1016/j.inoche.2020.107889

Nasrollahzadeh, M., Atarod, M., Sajjadi, M., Sajadi, S.M., Issaabadi, Z., 2019. Plant-Mediated Green Synthesis of Nanostructures: Mechanisms, Characterization, and Applications, in: Interface Science and Technology. https://doi.org/10.1016/B978-0-12-813586-0.00006-7

Ramesh, M., Anitha, S., Poopal, R.K., Shobana, C., 2018. Evaluation of acute and sublethal effects of chloroquine ($C_{18}H_{26}CIN_3$) on certain enzymological and histopathological biomarker responses of a freshwater fish Cyprinus carpio. Toxicol. Reports 5. https://doi.org/10.1016/j.toxrep.2017.11.006

Ramírez, A.E., Montero-Muñoz, M., López, L.L., Ramos-Ibarra, J.E., Coaquira, J.A.H., Heinrichs, B., Páez, C.A., 2021. Significantly enhancement of sunlight photocatalytic performance of ZnO by doping with transition metal oxides. Sci. Rep. 11. https://doi.org/10.1038/s41598-020-78568-9

Ravi, Pandey, L.M., 2019. Enhanced adsorption capacity of designed bentonite and alginate beads for the effective removal of methylene blue. Appl. Clay Sci. 169. https://doi.org/10.1016/j.clay.2018.12.019

Senobari, S., Nezamzadeh-Ejhieh, A., 2020. A novel ternary nano-composite with a high

photocatalyitic activity: Characterization, effect of calcination temperature and designing the experiments. J. Photochem. Photobiol. A Chem. 394. https://doi.org/10.1016/j.jphotochem.2020.112455

Shi, J.L., Zhao, X.J., Zhang, L.Y., Xue, X.L., Guo, Z.X., Gao, Y.F., Li, S.F., 2017. An oxidized magnetic Au single atom on doped TiO_2(110) becomes a high performance CO oxidation catalyst due to the charge effect. J. Mater. Chem. A 5. https://doi.org/10.1039/c7ta05483a

Tao, Y., Ma, Z., Wang, W., Zhang, C., Fu, L., Zhu, Q., Li, Y., Li, G., Zhang, D., 2023. Nickel Phosphide Clusters Sensitized TiO_2 Nanotube Arrays as Highly Efficient Photoanode for Photoelectrocatalytic Urea Oxidation. Adv. Funct. Mater. 33. https://doi.org/10.1002/adfm.202211169

Truong, H.B., Huy, B.T., Ray, S.K., Gyawali, G., Lee, Y.I., Cho, J., Hur, J., 2022. Magnetic visible-light activated photocatalyst $ZnFe_2O_4$/$BiVO_4$/g-C_3N_4 for decomposition of antibiotic lomefloxacin: Photocatalytic mechanism, degradation pathway, and toxicity assessment. Chemosphere 299. https://doi.org/10.1016/j.chemosphere.2022.134320

Valian, M., Soofivand, F., Khoobi, A., Yousif, Q.A., Salavati-Niasari, M., 2023. A green approach: Eco-friendly synthesis of $Gd_2Ti_2O_7$/N-GQD nanocomposite and photo-degradation and electrochemical measurement of hydroxychloroquine as a perdurable drug. Arab. J. Chem. 16. https://doi.org/10.1016/j.arabjc.2022.104401

Wang, D.Y., Li, C.H., Li, S.S., Kuo, T.R., Tsai, C.M., Chen, T.R., Wang, Y.C., Chen, C.W., Chen, C.C., 2016. Iron Pyrite/Titanium Dioxide Photoanode for Extended Near Infrared Light Harvesting in a Photoelectrochemical Cell. Sci. Rep. 6. https://doi.org/10.1038/srep20397

Wang, Q., Xie, D., Chen, J., Liu, G., Yu, M., 2020. Superhydrophobic paper fabricated via nanostructured titanium dioxide-functionalized wood cellulose fibers. J. Mater. Sci. 55. https://doi.org/10.1007/s10853-020-04489-7

Wu, J., Tao, Y., Zhang, C., Zhu, Q., Zhang, D., Li, G., 2023. Activation of chloride by oxygen vacancies-enriched TiO_2 photoanode for efficient photoelectrochemical treatment of persistent organic pollutants and simultaneous H_2 generation. J. Hazard. Mater. 443. https://doi.org/10.1016/j.jhazmat.2022.130363

Xie, W., Li, R., Xu, Q., 2018. Enhanced photocatalytic activity of Se-doped TiO_2 under visible light irradiation. Sci. Rep. 8, 1–10. https://doi.org/10.1038/s41598-018-27135-4

Xue, J., Fujitsuka, M., Majima, T., 2019. Shallow Trap State-Induced Efficient Electron Transfer at the Interface of Heterojunction Photocatalysts: The Crucial Role of Vacancy Defects. ACS Appl. Mater. Interfaces 11. https://doi.org/10.1021/acsami.9b14128

Yi, X.H., Ji, H., Wang, C.C., Li, Y., Li, Y.H., Zhao, C., Wang, A., Fu, H., Wang, P., Zhao, X., Liu, W., 2021. Photocatalysis-activated SR-AOP over PDINH/MIL-88A(Fe) composites for boosted chloroquine phosphate degradation: Performance, mechanism, pathway and DFT calculations. Appl. Catal. B Environ. 293. https://doi.org/10.1016/j.apcatb.2021.120229

Zhang, J., Zhang, L., Wang, W., Yu, J., 2022. In Situ Irradiated X-ray Photoelectron Spectroscopy Investigation on Electron Transfer Mechanism in S-Scheme Photocatalyst. J. Phys. Chem. Lett. https://doi.org/10.1021/acs.jpclett.2c02125

Zhang, M., Zhang, Y., Ye, L., Yu, Z., Liu, R., Qiao, Y., Sun, L., Cui, J., Lu, X., 2023. In situ fabrication Ti_3C_2Fx MXene/$CdIn_2S_4$ Schottky junction for photocatalytic oxidation of HMF to DFF under visible light. Appl. Catal. B Environ. 330. https://doi.org/10.1016/j.apcatb.2023.122635

Zhang, Y., Zhao, L., Yang, Y., Sun, P., 2018. Degradation of the antibiotic ornidazole in aqueous solution by using nanoscale zero-valent iron particles: Kinetics, mechanism, and degradation pathway. RSC Adv. 8. https://doi.org/10.1039/c8ra04079f

Zhou, T., Shi, J., Li, G., Liu, B., Hu, B., Che, G., Liu, C., Wang, L., Yan, L., 2023. Advancing n-π* electron transition of carbon nitride via distorted structure and nitrogen heterocycle for efficient photodegradation: Performance, mechanism and toxicity insight. J. Colloid Interface Sci. 632. https://doi.org/10.1016/j.jcis.2022.11.073

Zhou, Y., Ding, Q., Wang, Y., Ouyang, X., Liu, L., Li, J., Wang, B., 2020. Carrier transfer and capture kinetics of the $TiO_2/Ag_2V_4O_{11}$ photocatalyst. Nanomaterials 10. https://doi.org/10.3390/nano10050828

Zhu, Q., Lu, J., Wang, Y., Qin, F., Shi, Z., Xu, C., 2016. Burstein-Moss Effect Behind Au Surface Plasmon Enhanced Intrinsic Emission of ZnO Microdisks. Sci. Rep. 6. https://doi.org/10.1038/srep36194

CHAPTER 5

Pd-doped TiO_2 with Induced Ti^{3+} Defects and Oxygen Vacancies for Photocatalytic Amoxicillin Decomposition

This chapter investigates the role of reduced bandgap, abundant Ti^{3+} defects, oxygen vacancies, and increased surface hydrophilicity on the AMX photocatalytic degradation efficiency of Pd-doped TiO_2 synthesized via a bio-based route utilizing banana peel extract. The density functional theory (DFT) simulations provide insight into electronic structure modifications and charge transfer behavior. Experimental results demonstrate improved photocatalytic performance under visible and solar irradiation. Additionally, the ecotoxicity assessment and antimicrobial activity of parent and degraded AMX samples were performed to evaluate the environmental safety.

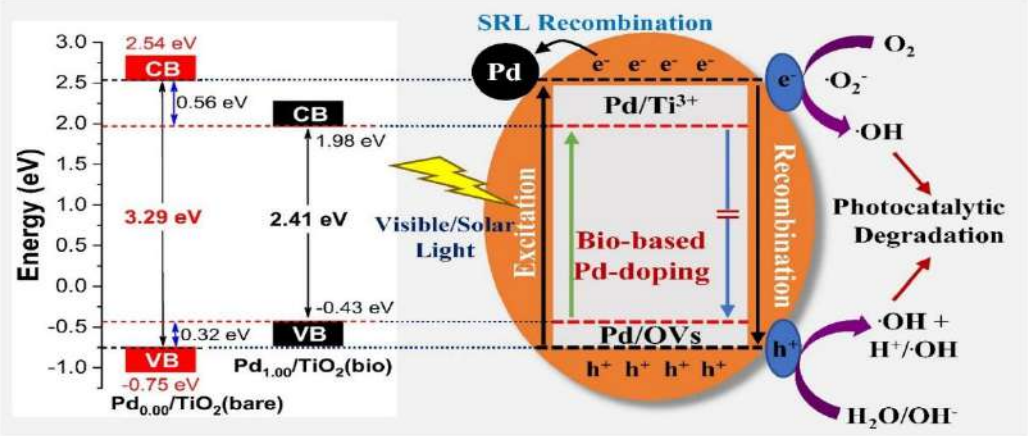

Chapter highlights

- Microwave-assisted bio-based Pd-doping onto TiO_2 for narrow bandgap
- O-vacancy and Ti^{3+} defects enhanced visible-light-driven photocatalytic activity
- DFT revealed mid-gap states and matched experimental bandgap narrowing trends
- Amoxicillin degradation of 98.9 and 96.7 % under artificial and solar light


Contents lists available at ScienceDirect
Chemical Engineering Science
journal homepage: www.elsevier.com/locate/ces
ELSEVIER
CHEMICAL ENGINEERING SCIENCE

Pd-doped TiO_2 with induced Ti^{3+} defects and oxygen vacancies for photocatalytic Amoxicillin Decomposition: DFT studies and Ecotoxicity assessment

Ravi Ravi [a], Animes Kumar Golder [a,b,*]

5.1 Background and executive motivation

The global expansion of pharmaceutically active compounds (PhACs) in natural water-bodies has severely threatened our ecosystem, posing toxic impacts on aquatic and terrestrial animals. Recent case studies have revealed the widespread presence of pharmaceuticals, especially antibiotics, in water bodies, affecting both natural environments and wastewater treatment plants (WWTPs) (Verma and Haritash, 2020; Bhan et al., 2025b; Kaur and Chadha, 2025). Prolonged exposure to antibiotics can not only harm animal health but also trigger the development of antibiotic-resistant microbes (Mmelesi et al., 2022). Amoxicillin (AMX) is an antibiotic that interact with penicillin-binding proteins (PBPs) and inhibits bacterial cell wall formation process. It is widely used to treat tonsillitis, sinusitis, pneumonia, and several infections such as nose, skin, urinary tract, throat, bronchitis, etc. However, AMX could have several side effects, including face swelling, breathing disorders, itching, wheezing, skin blister, rash, vomiting, headache, temporary teeth discoloration, etc. (Gillies et al., 2015). It has been reported to cause hemorrhagic colitis (severe diarrhea) in humans, leading to intestine damage (Report, 2024). Improper management of AMX has resulted in its presence in natural waterbodies worldwide, contributing to AMX resistant bacteria. The presence of AMX resistance bacteria such as Coagulase-negative *staphylococci*, *Xenophilus spp.*, *Ralstonia spp.*, *Bacillus spp.*, *K. quasipneumoniae*, *Pseudomonas spp.*, *Staphylococcus spp*., etc. have been reported in several waterbodies across the world, i.e., Karoon river (Iran), Wells water (Africa), Ghaghara River (India), and pharmaceutical industrial waste (Bangladesh). To prevent the generation of AMX-resistant microbes and mitigate toxic health impacts, AMX-containing effluents must be treated before being discharged into water bodies.

Various treatment methods, such as adsorption, photocatalysis, chemical-based degradation, biological degradation, ion exchangers, and membrane filtration, have been utilized for wastewater treatment (Nandi et al., 2020; Beshkar et al., 2022; Bhan and Golder, 2025). However, treating antimicrobial active organic contaminants that exist in very low concentrations is quite challenging. The advanced oxidation process, especially heterogeneous photocatalysis, has been widely reported to mitigate organic contaminants using light energy [12]. Therefore, the photocatalysis process could be highly efficient for mitigating the threat of PhACs. TiO_2 is a highly eco-friendly, efficient, and abundant photocatalyst extensively utilized in wastewater treatment, CO_2 reduction, electrochemical sensing, H_2 generation, drug delivery, and green energy production (Gawal and Golder, 2024; Kannadhasan et al., 2025; Vu et al., 2025). Despite its potential applications at the laboratory scale, its upscaling is hindered by its

high bandgap (>3.20 eV) and rapid recombination of free (e^-/h^+, limiting its efficient use under UV light. Solar light reaching the Earth contains only 5 % UV light, while visible light accounts for about 50 % of total sunlight. However, several countermeasures have been implemented to modify TiO_2, including non-metal and metal-doping, forming heterojunctions and generating Ti^{3+} defects/oxygen vacancies (Zhou et al., 2023). These modifications improve visible-light-driven activity by narrowing the bandgap and delaying recombination rate.

Metal doping in TiO_2 can improve the mentioned characteristics and noble metals such as gold (Au), silver (Ag), platinum (Pt), and palladium (Pd) have the potential to induce the photocatalytic activity of TiO_2 when introduced as dopants into its lattice sites (Javaid et al., 2013; Vu et al., 2025). Pd, in particular, could be an efficient dopant due to its inert nature, high conductivity, and stability. Pd^{2+}, with an atomic radius of 0.137 nm, can easily replace Ti^{4+} (atomic size of 147 nm), creating structural defects in the lattice structure of TiO_2, consequently enhancing its activity (Javaid et al., 2013). Several chemical-based methods have been employed to synthesized the metal-doped photocatalysts. However, the use of extensive chemicals and the potential generation of toxic byproducts are major concerns with these methods. Recently, bio-based synthesis methods adopted for synthesizing metal-doped photocatalysts, utilizing plant-based vegetal extracts as reducing and capping agents (Bhan and Golder, 2023; Kumar and Das, 2023). Additionally, the presence of a variety of bio-analytes in vegetal extracts can generate different types of defects. Bio-based photocatalysts have lower bandgaps than their chemical-based counterparts and exhibit better charge transfer, more oxygen and Ti^{3+} defects, and higher hydrophilicity due to surface functionalization, which collectively improve their photocatalytic efficiency.

Therefore, employing a bio-based method for Pd doping onto TiO_2 could be a highly eco-friendly and effective research direction for the efficient degradation of amoxicillin (AMX) under visible light. In this Chapter, we have synthesized a bio-based Pd-doped TiO_2 using banana peel extract as a reducing and capping agent source. The synthesis was performed in a closed chamber microwave synthesizer to ensure rapid and uniform volumetric heating that promotes fast nucleation, better dopant incorporation, and improved photocatalyst crystallinity (Dash et al., 2020). The prepared bio-based catalysts were characterized to analyze their structural, chemical, physical, and optical properties. The theoretical investigation of their band structure and projected density of states (PDOS) was also evaluated through density functional theory (DFT) analysis (Bhan and Golder, 2025). The photocatalytic activity of bare and Pd-doped TiO_2 was examined through AMX photodegradation, and the photodegradation mechanism was also proposed. Additionally, the toxicity assessment of photodegraded AMX

solution, including formed byproducts, was performed using a toxicity estimation software tool (TEST) with several endpoints and evaluating antimicrobial activity against both *E. coli* and *S. aureus* bacterial strains.

5.2 Results and discussion

5.2.1 Band structure

The adsorption of Pd(II) onto TiO_2 was performed at varying pH (3–11) and Pd precursor concentrations (0 – 1.5%, w/w), as shown in Fig. 5.1. Pd(II) adsorption increased with pH, achieving almost complete adsorption (~100%, 1.0%, w/w) at pH ≥ 7, indicating favorable electrostatic and surface interactions between Pd(II) species and the TiO_2 surface in neutral and basic conditions (Sheraz et al., 2024). Furthermore, at the optimized pH 7, a linear increase in Pd(II) adsorption was observed with rising precursor concentration. However, a marginal decline in adsorption efficiency at higher concentrations (1.25 and 1.50%, w/w) could result from saturation of available adsorption sites on the TiO_2 surface (Syeda et al., 2025).

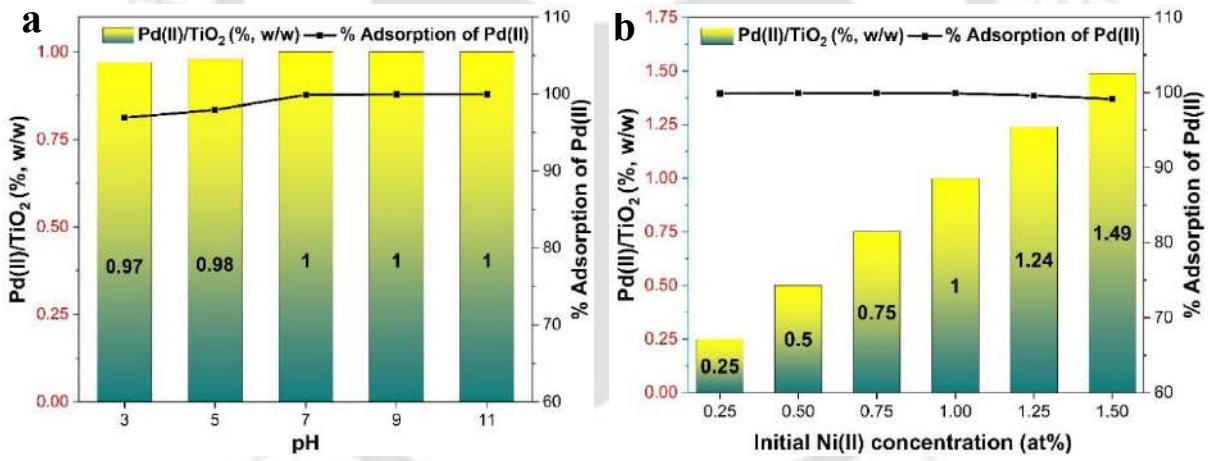

Figure 5.1: (a) Pd(II) adsorption (initial concentration 1.0% w/w Pd(II)) on TiO_2 at various pH (3-11) and (b) Pd(II) adsorption at various initial Pd(II) concentrations at optimized pH 7 with a continuous stirring at 300 rpm for 30 min.

The bandgaps of bio-based (1%, w/w) Pd-doped TiO_2 ($Pd_{1.00}/TiO_2$(bio)) synthesized at different reaction temperatures and times are shown in Figs. 5.2a and 5.2b, respectively, and Table 5.1. A noticeable decrease in bandgap from 2.49 to 2.41 eV was observed with increasing temperature from 90 to 100 °C. However, at 110 and 120 °C, the bandgap slightly increased (2.45 and 2.58 eV), potentially due to the decomposition of the vegetal extract's reducing agents, limiting effective Pd incorporation (de Lima Marsiglia et al., 2023). Similarly,

prolonging the reaction time from 2.5 to 5 min reduced the bandgap from 2.47 to 2.41 eV. In contrast, a further extension to 7.5 and 10 min did not result in any significant changes, suggesting saturation of doping kinetics (Yazdani et al., 2021). Fig. 3c presents the influence of vegetal extract concentration on the bandgap of $Pd_{1.00}/TiO_2$(bio). An initial increase in extract content from 10 to 20% (v/v) led to a decrease in the bandgap from 2.48 to 2.41 eV. However, its further increase resulted as slightly increase in the bandgap (2.43-2.50 eV). This could be attributed to the excessive presence of organic compounds, which facilitated a higher reduction rate of Pd(II), resulting in the formation of large Pd particles instead of interstitial insertion of Pd(II) in the TiO_2 lattice (Kim et al., 2016).

The bandgaps of bare-TiO_2 ($Pd_{0.00}/TiO_2$(bare)) and (0.25 – 1.49%, w/w) Pd-doped TiO_2 ($Pd_{0.25\text{-}1.49}/TiO_2$(bio)) are shown in Fig. 5.2d. A substantial bandgap narrowing from 3.29 to 2.41 eV was observed with increasing Pd concentration up to 1.00 % (w/w), could be due to the introduction of localized Pd(II) states in lattice of TiO_2. However, further increase in Pd loading (1.24 and 1.49 %, w/w) caused a slight increase in the bandgap, likely resulting from the Burstein-Moss effect, wherein elevated electron density populates the lower conduction band (CB) states and enforced the excited electrons to move in upper CB (Zarhri et al., 2022). Moreover, the formation of surface-bound Pd nanoparticles at higher precursor concentrations may also limit effective lattice doping, contributing to the observed bandgap shift. The light absorption edge of bare-TiO_2 was observed around 377 nm, which was shifted to longer wavelengths, up to 515 nm for $Pd_{1.00}/TiO_2$(bio), corroborating enhanced visible-light harvesting capability upon Pd-doping. VB-XPS spectra and energy level diagram (Figs. 5.2e) further demonstrated that $Pd_{1.00}/TiO_2$(bio) exhibited an upward shift in the VB position from –0.75 to –0.43 eV, and a corresponding CB downshift from 2.54 to 1.98 eV. These band edge modifications facilitate improved charge carrier separation and extended light absorption, ultimately enhancing the photocatalytic redox potential under visible-light irradiation (Kannadhasan et al., 2025).

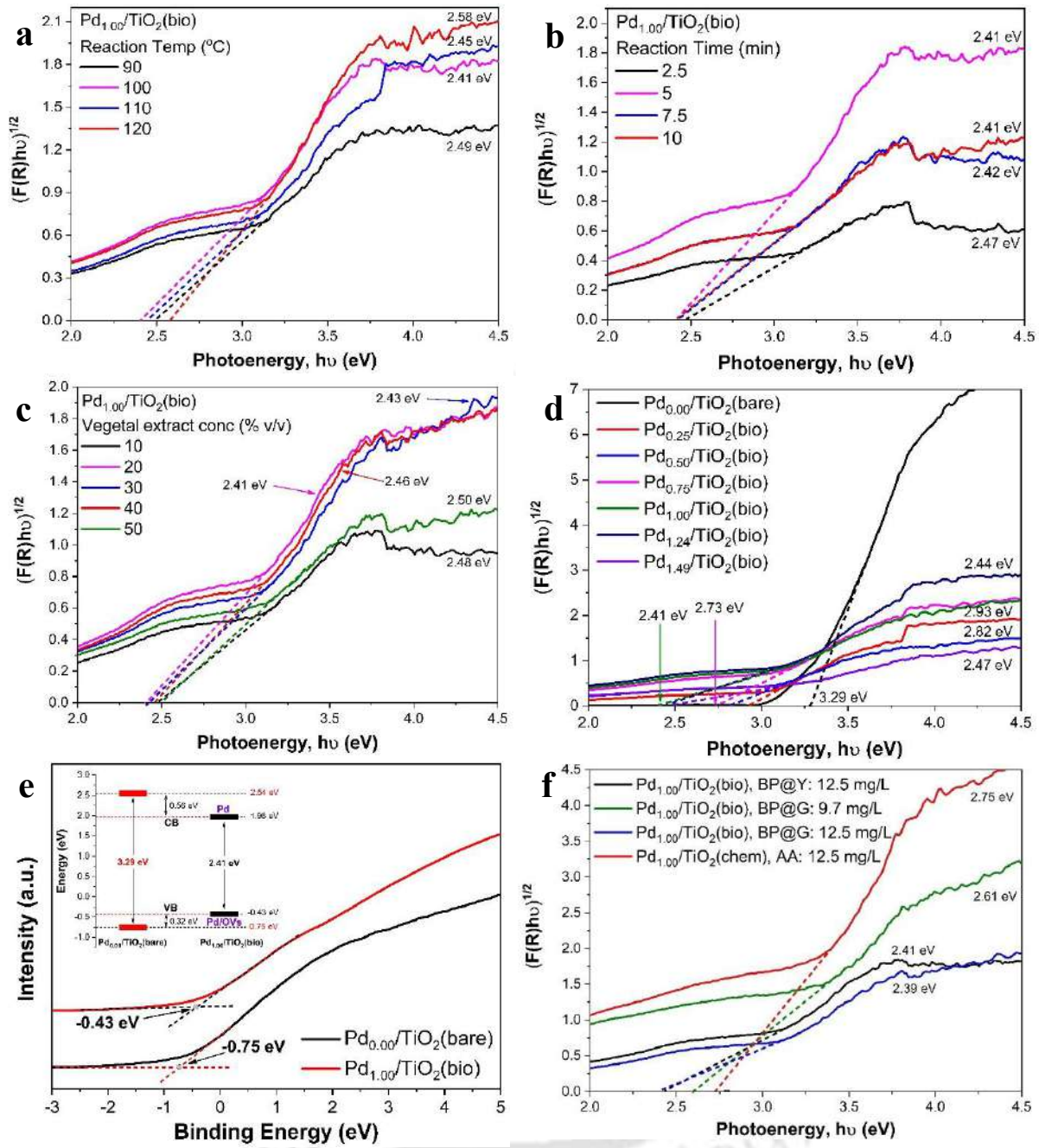

Figure 5.2: Optical bandgap (fitted Tau's plot) of $Pd_{1.00}/TiO_2$(bio) synthesized at different (a) Reaction temperature (90 – 120 °C), (b) Reaction time (2.5 – 10 min), and (c) Vegetal extract concentration (10 – 50% (v/v)); (d) Optical bandgap (fitted Tau's plot) of $Pd_{0.00}/TiO_2$(bare) and $Pd_{0.25\text{-}1.49}/TiO_2$(bio); (e) Valence band - X-ray photoelectron spectroscopy (VP-XPS) spectra, and energy levels (CB and VB) diagram (inset) of $Pd_{0.00}/TiO_2$(bare) and $Pd_{1.00}/TiO_2$(bio), and (f) Optical bandgap of $Pd_{1.00}/TiO_2$(bio) synthesized using different maturity waste banana peel vegetal extract.

Table 5.1: Optical bandgaps of $Pd_{1.00}/TiO_2$(bio) synthesized at different reaction temperature (90 – 120 °C), reaction time (2.5 – 10 min), and vegetal extract concentration (10-50% v/v); and optical bandgaps of $Pd_{0.00}/TiO_2$(bare) and $Pd_{0.25\text{-}1.49}/TiO_2$(bio) at optimized reaction conditions.

Catalyst	Reaction temp. (°C)	Reaction time (min)	Vegetal extract conc. (% v/v)	Precursor conc. (%, w/w)	Bandgap energy (eV)
$Pd_{1.00}/TiO_2$(bio)	90	**5**	**20**	1.00	2.49
	100				**2.41**
	110				2.45
	120				2.58
	100	2.5			2.47
		7.5			2.42
		10			2.41
		5	10		2.48
			30		2.43
			40		2.46
			50		2.50
$Pd_{0.00}/TiO_2$(bare)	-	-	-	-	3.29
$Pd_{0.25}/TiO_2$(bio)	100	5	20	0.25	2.93
$Pd_{0.50}/TiO_2$(bio)				0.5	2.82
$Pd_{0.75}/TiO_2$(bio)				0.75	2.73
$Pd_{1.24}/TiO_2$(bio)				1.25	2.44
$Pd_{1.47}/TiO_2$(bio)				1.50	2.47
$Pd_{1.00}/TiO_2$(chem)			Ascorbic acid (12.5 mg L^{-1}); 20%	1.00	2.75

The bandgap analysis was performed to investigate the influence of different vegetal extracts, varying in ascorbic acid content, on the Pd-doping effectiveness of TiO_2, using the 20% (v/v) yellow banana peel extract (BP@Y, AAE: 12.5 mg L^{-1}) and 20 and 25.8% (v/v) green banana peel extract (BP@G, AAE: 9.7 mg L^{-1}). BP@Y (20%, v/v)-based photocatalyst showed ~2.41 eV bandgap, while BP@G (20% v/v) extract showed a higher bandgap of 2.61 eV (Fig. 5.2f). Pd-doped TiO_2 synthesized with BP@G extract (25.8%) adjusted to match the AAE of BP@Y (12.5 mg L^{-1}) also resulted in a similar bandgap of 2.39 eV, suggesting that the ascorbic acid content in the extract significantly governs the extent of Pd-doping and band structure modification. In contrast, $Pd_{1.00}/TiO_2$ synthesized with commercial ascorbic acid

$Pd_{1.00}/TiO_2$(chem) shown higher bandgap of 2.75 eV, underscoring the superior doping efficiency and bandgap modulation offered by natural bio-extracts compared to chemical agents.

The photoluminescence (PL) spectra (Fig. 5.3a) reveal that $Pd_{1.00}/TiO_2$(bio) exhibits significantly lower emission intensity compared to $Pd_{0.00}/TiO_2$(bare), indicating reduced recombination of photogenerated electron-hole pairs and enhanced charge separation efficiency. The peaks at 360 and 396 nm correspond to the near-band-edge emission of TiO_2, originating from intrinsic band-to-band electron-hole recombination (Baruah et al., 2022). The noticeable suppression of these peaks in $Pd_{1.00}/TiO_2$(bio) indicates inhibited direct recombination, possibly due to the formation of Pd states between VB and CB. Peaks at 419, 439, 451, and 468 nm are associated with shallow trap states related to deeper lattice defects, such as interstitial Ti^{3+} or oxygen vacancies (Gogoi et al., 2020). Additionally, emissions at 482 and 493 nm are attributed to self-trapped excitons and recombination involving surface states. The reduced intensity of these peaks in $Pd_{1.00}/TiO_2$(bio) suggests fewer recombination events through these channels, facilitating improved charge carrier mobility and lifetime. The broad emissions at 524 and 562 nm are related to surface-adsorbed species and recombination via hydroxyl groups or residual organics. The bio-mediated synthesis route capped the surface with organic ligands, thereby passivating these surface states and further lowering recombination-related emissions (Chelli et al., 2018). These findings directly correlate with improved photocatalytic performance, as the enhanced charge carrier dynamics promote more efficient generation of reactive species essential for pollutant degradation.

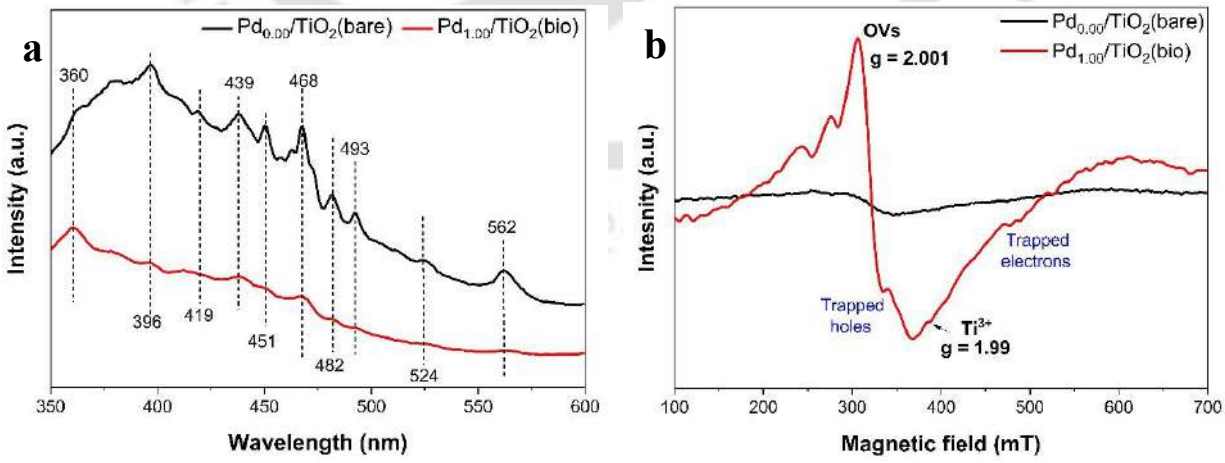

Figure 5.3: (a) PL spectra (excitation wavelength 320 nm) and (b) EPR spectra showing Ti^{3+} defects and oxygen vacancies (OVs) (temp.: 25 °C, amplitude: 5 and field modulation: 1) of $Pd_{0.00}/TiO_2$(bare) and $Pd_{1.00}/TiO_2$(bio).

The EPR spectra (Fig. 5.3b) demonstrate enhanced signal intensity for $Pd_{1.00}/TiO_2$(bio) compared to $Pd_{0.00}/TiO_2$(bare), suggesting an increased presence of unpaired electrons and defect sites. The prominent signal at g = 2.001 corresponds to oxygen vacancies (OVs), which act as electron traps and aid in suppressing electron-hole recombination. The signal around g = 1.99 attributed to Ti^{3+} species confirms the partial reduction of Ti^{4+} and indicates the formation of defect states that enhance charge separation by working as an electron trap (Komaraiah et al., 2020). Additionally, signals for trapped holes and electrons further support the existence of surface and lattice defects facilitating prolonged charge carrier periods. The bio-mediated Pd doping induces more oxygen vacancies and Ti^{3+} centers, which promote better charge carrier dynamics and directly contribute to the superior photocatalytic performance of $Pd_{1.00}/TiO_2$(bio) by enhancing the generation of reactive oxygen species for pollutant degradation.

5.2.2 Structural and morphological analysis

The X-ray diffraction (XRD) patterns of $Pd_{0.00}/TiO_2$(bare) and $Pd_{0.25\text{-}1.49}/TiO_2$(bio) are shown in Fig. 5.4a. The diffraction peaks observed at 2θ = 25.24, 36.92, 37.74, 38.48, 47.97, 53.84, 62.61, 68.89, 70.28, and 74.99° are attributed to the (101), (103), (004), (112), (200), (105), (211), (204), (116), (220), and (215) planes of the anatase phase (JCPDS No. 21-1272), respectively. Additionally, weak peaks corresponding to the rutile phase appear at 2θ = 27.38, 36.00, 41.24, 54.93, and 56.58° indexed to (101), (101), (111), (211), and (220) planes, respectively (JCPDS No. 21-1276) (Baruah et al., 2022). The anatase and rutile phases may promote interfacial charge transfer between both phases and facilitate better photocatalytic activity. No new peak corresponding to Pd phases was observed in $Pd_{0.25\text{-}1.49}/TiO_2$(bio) due to a very low concentration of Pd. However, a slight peak shifting was observed at 2θ = 25.24 and 62.61° (Figs. 5.4b and 5.4c), reflecting interstitial incorporation of Pd into the TiO_2 lattice (Heryanto et al., 2024). Additionally, the bio-based Pd-doping led to a slight increase in the rutile phase from 20 to 21.62%, indicating slight phase transfer during the doping process.

The $Pd_{0.00}/TiO_2$(bare) exhibited a crystallite size of 20.59 nm, which progressively increased with Pd concentration, reaching a maximum of 21.65 nm in $Pd_{1.24}/TiO_2$ could be due to the incorporation of Pd into TiO_2 lattice (Table 5.2) (Valian et al., 2023). This increase in crystallite size is accompanied by a decrease in the lattice strain from 8.05×10^{-3} to 7.64×10^{-3} and dislocation density from 2.38×10^{-3} to 2.13×10^{-3} lines nm^{-2}). However, these parameters were slightly increased in $Pd_{1.49}/TiO_2$. The decreased lattice strain and dislocation density are

known to enhance photocatalytic activity by providing more active surface sites and facilitating better charge transport (Bhan and Golder, 2025).

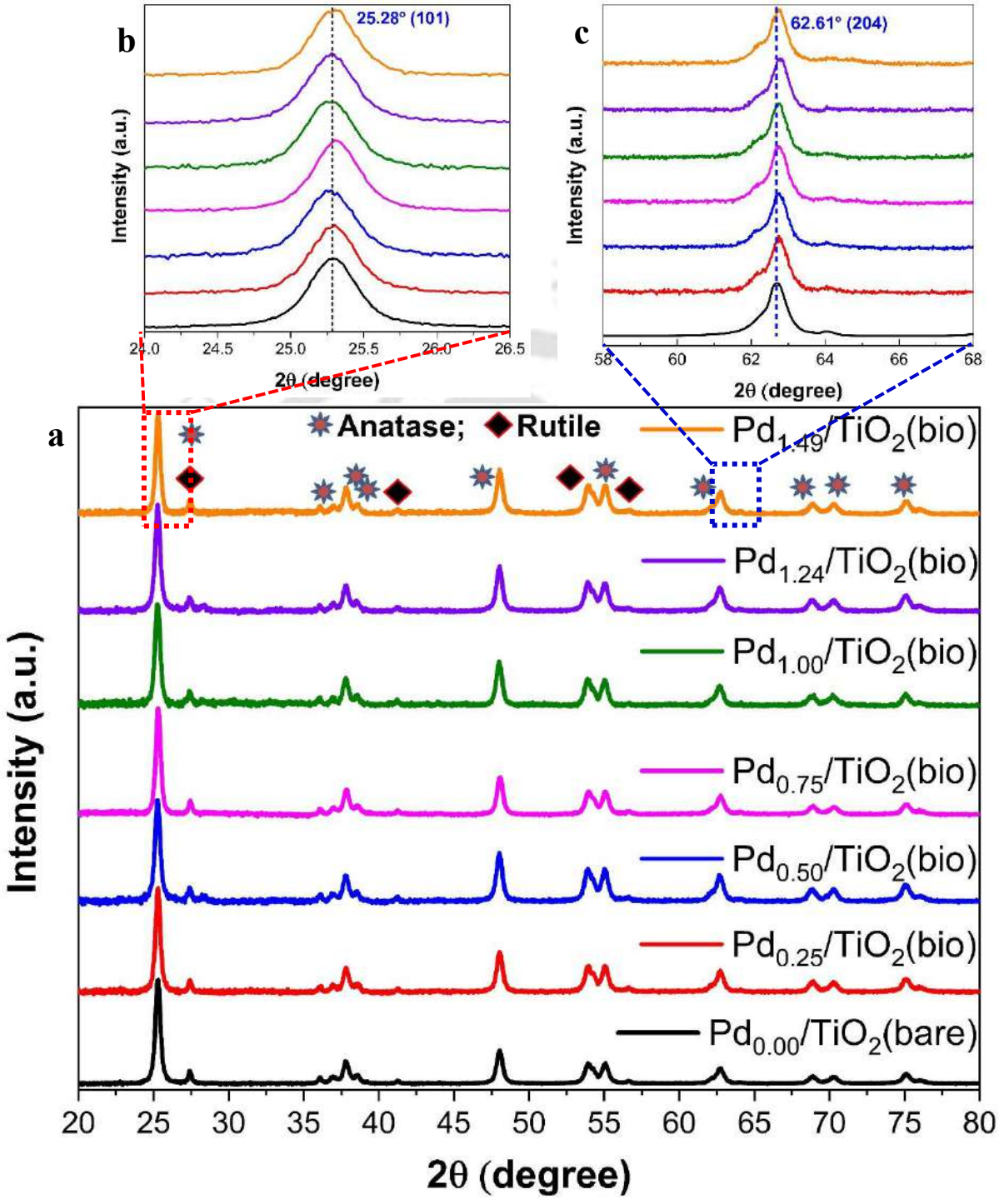

Figure 5.4: (a) X-ray diffraction (XRD) patterns $Pd_{0.00}/TiO_2$(bare) and $Pd_{0.25\text{-}1.49}/TiO_2$(bio). The red/blue star symbol representing anatase phase and black-red square showing rutile phase of TiO_2; (b) and (c) Magnified XRD patterns highlighting peak shifting in TiO_2 after Pd-doping.

Table 5.2: XRD parameters of $Pd_{0.00}/TiO_2$(bare) and $Pd_{0.25\text{-}1.49}/TiO_2$(bio).

Sample	Crystallite size (nm)	Anatase (%)	Rutile (%)	Lattice strain (ε)	Dislocation densities (Lines/nm^2)
$Pd_{0.00}/TiO_2$(bare)	20.59	80	20	8.05×10^{-3}	2.36×10^{-3}
$Pd_{0.25}/TiO_2$(bio)	20.96	79.47	20.53	7.88×10^{-3}	2.28×10^{-3}
$Pd_{0.50}/TiO_2$(bio)	21.26	79.53	21.47	7.78×10^{-3}	2.21×10^{-3}
$Pd_{0.75}/TiO_2$(bio)	21.38	79.39	21.59	7.74×10^{-3}	2.19×10^{-3}
$Pd_{1.00}/TiO_2$(bio)	21.58	79.47	21.53	7.67×10^{-3}	2.15×10^{-3}
$Pd_{1.24}/TiO_2$(bio)	21.65	79.38	21.62	7.64×10^{-3}	2.13×10^{-3}
$Pd_{1.49}/TiO_2$(bio)	21.62	79.46	21.54	7.65×10^{-3}	2.14×10^{-3}

Fig. 5.5 demonstrates the FETEM images, HRTEM, SAED pattern and particle size distribution of $Pd_{0.00}/TiO_2$(bare) and $Pd_{1.00}/TiO_2$(bio). The spherical-shaped $Pd_{0.00}/TiO_2$(bare) exhibits an average particle size of 21.07±2.51 nm (Fig. 5.5a), whereas Pd doping increases the particle size to 22.03±3.48 nm (Fig. 5.5b) in $Pd_{1.00}/TiO_2$(bio) without any change in the morphology. This slight increase in the particle size is likely due to the surface adsorption of Pd species and enlargement of TiO_2 crystals, which is well supported by XRD analysis (Liza et al., 2024). The HRTEM images (Figs. 5.5c and 5.5d) confirm the crystalline nature of both samples, displaying lattice fringes corresponding to the (101) plane of anatase (d = 0.352 nm) and rutile (d = 0.325 nm) phases. The presence of both phases in both samples is typical for mixed-phase TiO_2, which is favorable for enhancing charge separation due to interfacial heterojunctions. The SAED patterns (Figs. 5.5e and 5.5f) further validate the polycrystalline nature of both samples with clear ring patterns (Bhan et al., 2025a). The presence of well-defined crystalline domains and preserved mixed-phase structure supports efficient photoinduced charge carrier transport, corroborating the superior photocatalytic activity.

5.2.3 Elemental and chemical states analysis

The elemental composition and spatial distribution of the $Pd_{1.00}/TiO_2$(bio) are shown in Fig. 5.5g, which showed clear signatures of Pd with Ti and O elements, confirming its successful incorporation. Elemental mapping revealed a well-dispersed distribution of Pd throughout the sample, with no detectable clustering or phase separation. The homogeneity of Pd ensures maximum exposure of active sites, thereby contributing to enhanced photocatalytic performance compared to the bare TiO_2 (Veerakumar et al., 2024).

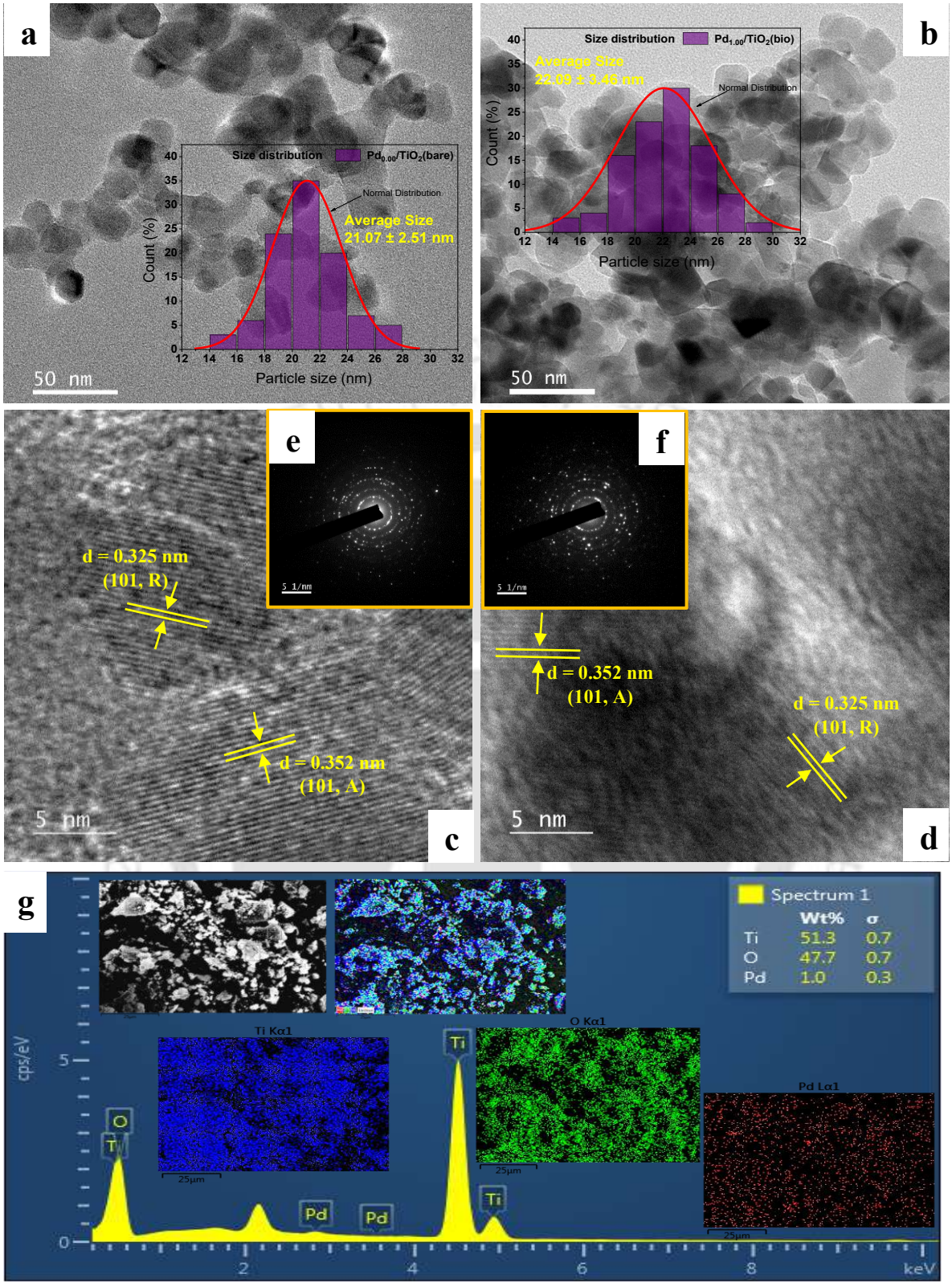

Figure 5.5: FETEM images showing morphology of (a) $Pd_{0.00}/TiO_2$(bare) and (b) $Pd_{1.00}/TiO_2$(bio) with insets illustrate the particle size distribution. (c and d) HRTEM images, and (e and f) SAED patterns of $Pd_{0.00}/TiO_2$(bare) and (d) $Pd_{1.00}/TiO_2$(bio). (g) EDX spectra and elemental mapping of $Pd_{1.00}/TiO_2$(bio).

The high-resolution spectra (Figs. 5.6a-5.6e) and survey spectra (Fig. 5.6f) of $Pd_{0.00}/TiO_2$(bare) and $Pd_{1.00}/TiO_2$(bio) exhibited characteristic peaks of Pd, Ti, and O with slight shifting in binding energies and changes in peak intensities, which confirmed strong interaction between Pd species and the TiO_2 surface. The composition (%) of each chemical species in $Pd_{0.00}/TiO_2$(bare) and $Pd_{1.00}/TiO_2$(bio) is provided in the Table 5.3. The Ti 2p spectra of $Pd_{0.00}/TiO_2$(bare) (Fig. 5.6a) display two prominent peaks centered at 460.4 eV and 466.2 eV, corresponding to Ti $2p_{3/2}$ and Ti $2p_{3/2}$, respectively, confirming the presence of Ti^{4+} oxidation state. Notably, in the $Pd_{1.00}/TiO_2$(bio) spectra (Fig. 5.6b), the corresponding Ti 2p peaks exhibit a slight red shifting (1.8–1.9 eV) with the appearance of a new peak at 460.1 eV, representing Ti^{3+} defects formed to electron redistribution and charge compensation due to formation of oxygen vacancies (Qahtan et al., 2024). The results indicate strong electronic interactions between Pd species and the TiO_2 lattice, facilitating charge transfer and enhancing photocatalytic efficiency. In O 1s spectra (Fig. 5.6c) of $Pd_{0.00}/TiO_2$(bare), the dominant peak at 531.7 eV corresponds to lattice oxygen (Ti–O–Ti). The higher binding energy peak at 533.3 eV is attributed to surface hydroxyl groups (El-Sawaf et al., 2024). In $Pd_{1.00}/TiO_2$(bio), a red shifting was observed in lattice and surface hydroxyl group peaks (Fig. 5.6d), confirming the establishment of high electron density (Cheng et al., 2020). The emergence of additional components associated with chemisorbed oxygen species (532.8 eV), mainly from vegetal extract, was also observed. These surface hydroxyls, high electron density, and active oxygen species are known to play a critical role in the photocatalytic degradation of pollutants by promoting hydroxyl radical generation.

The high-resolution Pd 3d spectrum of $Pd_{1.00}/TiO_2$(bio) (Fig. 5.6e) reveals the presence of two peaks at 335.1 eV and 340.4 eV, assigned to Pd^0 $3d_{5/2}$ and $3d_{3/2}$, respectively. In contrast, the other two peaks were observed at 336.8 eV and 341.7 eV, corresponding to Pd^{2+} $3d_{5/2}$ and $3d_{3/2}$ (Guerrero-Ortega et al., 2019). The coexistence of Pd^0 (~81 %) and Pd^{2+} (~20 %) suggests a partial reduction of Pd precursors by the vegetal extract. Pd^{2+} incorporation into interstitial sites contributes to bandgap narrowing by introducing intermediate energy levels within the TiO_2 band structure. Additionally, the presence of metallic Pd^0 could act as an electron trap, thereby suppressing charge recombination (Gonçalves et al., 2023). The synergistic presence of Pd^0 and Pd^{2+} facilitates improved charge carrier separation, enhanced light absorption, and increased active surface sites, collectively contributing to superior photocatalytic performance compared to bare TiO_2.

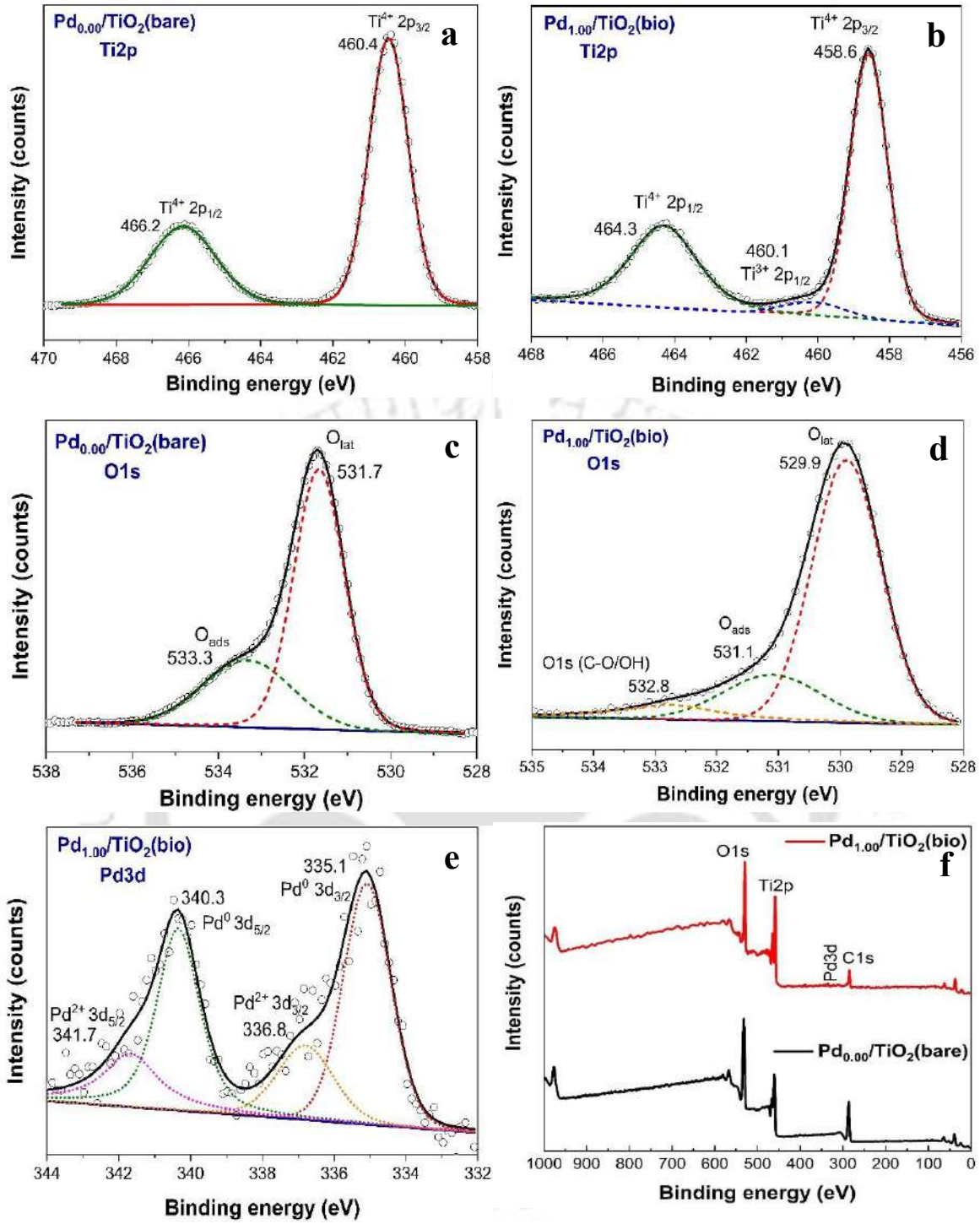

Figure 5.6: XPS spectra of Ti2p of (a) $Pd_{0.00}/TiO_2$(bare), and (b) $Pd_{1.00}/TiO_2$(bio); O1s of (c) $Pd_{0.00}/TiO_2$(bare), and (d) $Pd_{1.00}/TiO_2$(bio); and (e) Pd3d of $Pd_{1.00}/TiO_2$(bio) and (f) XPS survey spectra of $Pd_{0.00}/TiO_2$(bare), and $Pd_{1.00}/TiO_2$(bio).

Table 5.3: Relative elemental and configuration state composition of $Pd_{0.00}/TiO_2$(bare), and $Pd_{1.00}/TiO_2$(bio), analyzed through XPS.

Element	State	Sample (% area)	
		$Pd_{0.00}/TiO_2$(bare)	
Ti	Ti^{4+} 2p	48.2	Ti
	Ti^{3+} 2p	-	3.4
	Ti 2p (Total)	48.2	47.9
O	O_L 1s	40.4	O
	O_a 1s	11.4	6.6
	O(C-O) 1s	-	4.7
	O 1s (Total)	51.8	51.1
Pd	Pd(0) 3d	-	Pd
	Pd(II) 3d	-	0.045
	Pd 3d (Total)	-	~1.0

5.2.4 Other physical characteristics

The water contact angle measurements (Fig. 5.7a) reveal a substantial difference in surface wettability between $Pd_{0.00}/TiO_2$(bare) and $Pd_{1.00}/TiO_2$(bio). The bare TiO_2 sample exhibits a higher contact angle (120.8°), indicating a strongly hydrophobic surface. In contrast, the bio-synthesized Pd-doped TiO_2 demonstrates a markedly reduced contact angle of 37.5°, confirming enhanced hydrophilicity. This significant shift can be attributed to the synergistic effect of Pd incorporation and bio-mediated synthesis, which introduces surface defects, oxygen vacancies, and polar functional groups, facilitating better interaction with surface water. Improved wettability enhances the availability of surface-adsorbed hydroxyl groups, which are critical for generating reactive oxidative species during photocatalysis (Mekhemer et al., 2024).

The N_2 adsorption-desorption isotherms (Fig. 5.7b) revealed distinctive Type-IV isotherms with H3-type hysteresis loops, indicative of mesoporous structures of $Pd_{0.00}/TiO_2$(bare) and $Pd_{1.00}/TiO_2$(bio) (Li et al., 2022). The bio-based Pd-doped TiO_2 demonstrates a BET surface area of 52.68 m^2/g, compared to 60.73 m^2/g for the bare counterpart. Moreover, the average pore diameter increased from 18.04 to 34.57 nm, while the pore volume also increased from 0.27 to 0.46 cc/g. These changes in the BET parameters could

be due to the filling of the pores by Pd nanoparticles, which could provide better charge distribution throughout the catalysts for enhanced photocatalytic activity (Saqib et al., 2023).

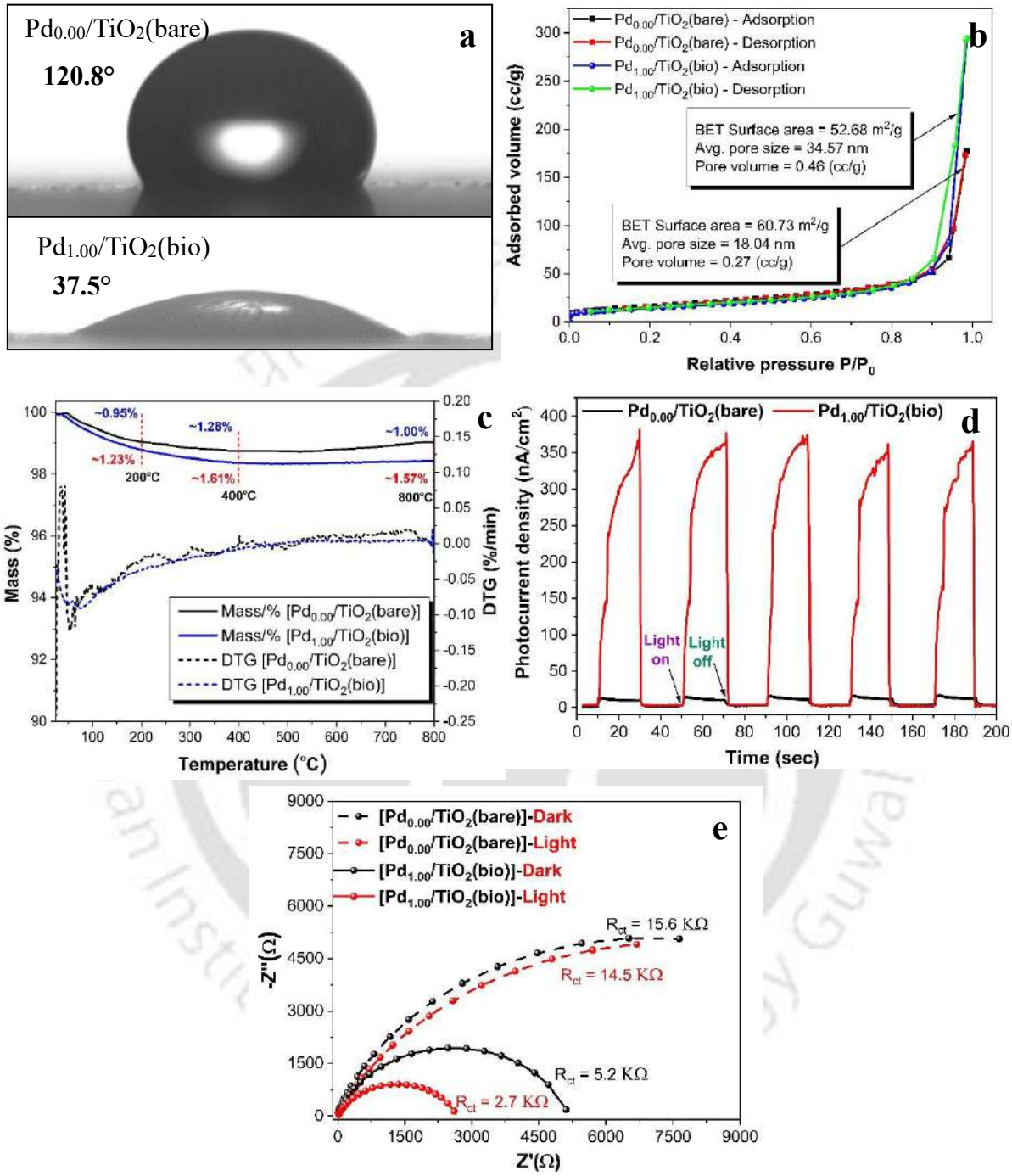

Figure 5.7: (a) Water contact angle, and (b) N_2 adsorption-desorption isotherm plots and BET parameters, and TGA profile (c) of $Pd_{0.00}/TiO_2$(bare) and $Pd_{1.00}/TiO_2$(bio); (d) Photocurrent at 20s intervals of light on/off cycles, and (e) Nyquist's plot (EIS) of $Pd_{0.00}/TiO_2$(bare) and $Pd_{1.00}/TiO_2$(bio) in presence/absence of light irradiation.

Thermogravimetric analysis (TGA) outlines of $Pd_{0.00}/TiO_2$(bare) and $Pd_{1.00}/TiO_2$(bio) are illustrated in Fig. 5.7c. The bare catalyst exhibits a mass loss of ~1.28 %, with distinct stages at 200 °C (~0.95 % loss), 400 °C (~1.28 % loss), and up to 800 °C (~1.00 % loss). In contrast, the bio-synthesized catalyst shows slightly higher total mass loss of ~1.61 %, with weight reductions at 200 °C (~1.23 %), 400 °C (~1.61 %), and a slight increase in the mass (%) thereafter, with ~1.57 % mass loss at 800 °C. The initial weight loss is attributed to physiosorbed water and volatile organics, while subsequent losses are likely due to the decomposition of organic moieties introduced during bio-based synthesis (Bhan and Golder, 2023). However, a slight increase in the weight (mass %) after 400 °C could be due to the buoyancy effect at high temperatures by exerting an upward force on the sample because of a decrease in the gas density (Nasrollahzadeh et al., 2019). Notably, both samples remain thermally stable up to 800 °C, affirming their suitability for high-temperature photocatalytic applications. Additionally, the slightly greater mass loss in the bio-sample is consistent with residual bio-organic compounds but does not compromise its structural integrity.

5.2.5 Photoelectrochemical analysis

The transient photocurrent response and EIS analyses of $Pd_{0.00}/TiO_2$(bare) and $Pd_{1.00}/TiO_2$(bio) under dark and light conditions were illustrated in Figs. 5.7d and 5.7e. Under light irradiation, $Pd_{1.00}/TiO_2$(bio) exhibited a significantly higher photocurrent density (~375 nA cm^{-2}) compared to bare $Pd_{1.00}/TiO_2$(bio) (~17 nA cm^{-2}) (Fig. 5.7d), indicating that Pd doping significantly enhances the separation and mobility of photogenerated charge carriers. The periodically stable photocurrent response further confirms the robustness and repeatability of the photoactivity under light on/off cycles. The gradual slow rise in photocurrent density in each cycle of light irradiation observed in the $Pd_{1.00}/TiO_2$(bio), attributed to trapping state filling, gradual accumulation of charge carries at the electrode-electrolyte interface, and improved interfacial charge transfer over time under steady-state illumination (Hu et al., 2014; Long et al., 2014). The photocurrent response was negligible in the dark for both bare and Pd-doping TiO_2, confirming that the photoresponse is solely light-driven.

The Nyquist plots fitting the electrochemical impedance spectra (EIS) (Fig. 5.7e) revealed that the charge transfer resistance (R_{ct}) of $Pd_{0.00}/TiO_2$(bare) decreased from 15.6 to 14.5 kΩ under light irradiation, showing the modest reduction indicates limited photoactivity. In contrast, $Pd_{1.00}/TiO_2$(bio) showed a significantly lower R_{ct} of 5.2 kΩ in the dark, which further dropped to 2.7 kΩ under light irradiation. This noteworthy reduction under light irradiation highlights the superior charge transfer efficiency of $Pd_{1.00}/TiO_2$(bio), attributable to

the Pd-induced formation of Schottky junctions and shallow trap states that facilitate fast electron migration and hinder recombination, leading to visible-light-driven improved photocatalytic activity (Ayaz et al., 2024).

5.2.6 DFT analysis

Fig. 5.8 illustrates the self-consistent energies at different k-points mesh and plane-wave energy cut-offs. The results confirmed PWC optimization at 70 Ry PWC and k-points mesh of 3×3×3. The structural optimization of bare-TiO_2 revealed a stable anatase phase with regular Ti-O bond lengths and a clean bandgap characteristic. Upon Pd doping and introducing an oxygen vacancy, the lattice underwent slight distortion near the defect site, indicating successful substitution and defect formation.

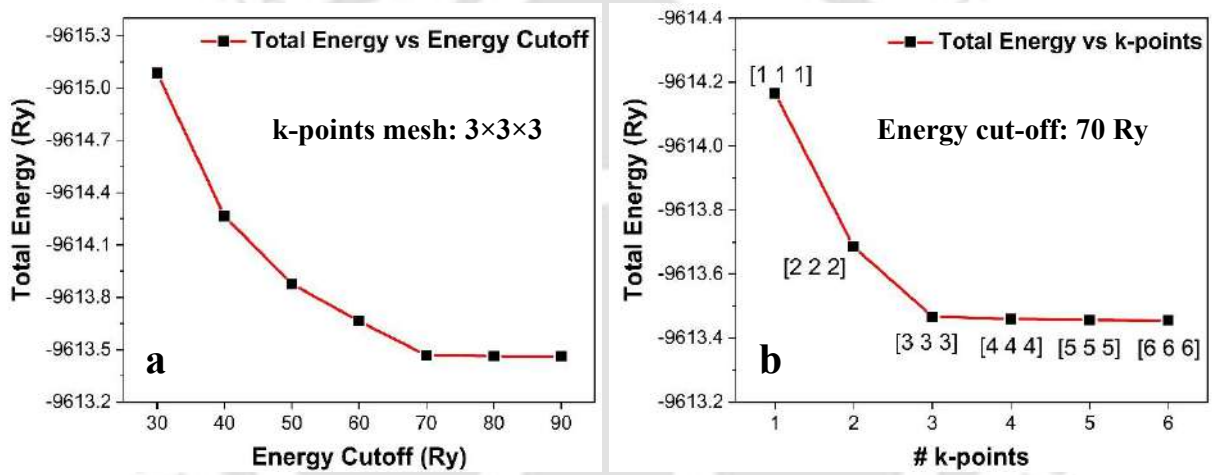

Figure 5.8: Self-consistent energy calculations: (a) Optimization of plane-wave energy cut-off (energy cutoff vs. total energy) and (b) k-points mesh (#k-point vs total energy).

Table 5.4: Comparison of calculated and experimental bandgaps of bare TiO_2 and Pd-doped TiO_2. The theoretical bandgaps were calculated with and without Hubbard parameters.

Photocatalyst	Method	Hubbard parameter (eV)	Cal. Bandgap (eV)	Experimental bandgap (eV)	Difference (%)
Bare TiO_2	GGA-PBE	-	2.06	3.29	-37.4
	GGA-PBE+U	U (Ti) = 2.0	3.26		-0.9
		U (O) = 6.0			
Pd-doped TiO_2	GGA-PBE	-	0.28/0.98	2.41	-88.4/-59.3
	GGA-PBE+U	U (Ti) = 2.0	2.37		+1.7
		U (O) = 6.0			
		U (Pd) = 5.0			

"-" sign indicates lower calculated bandgap; **"+"** sign indicates higher cal. bandgap than exp. data.

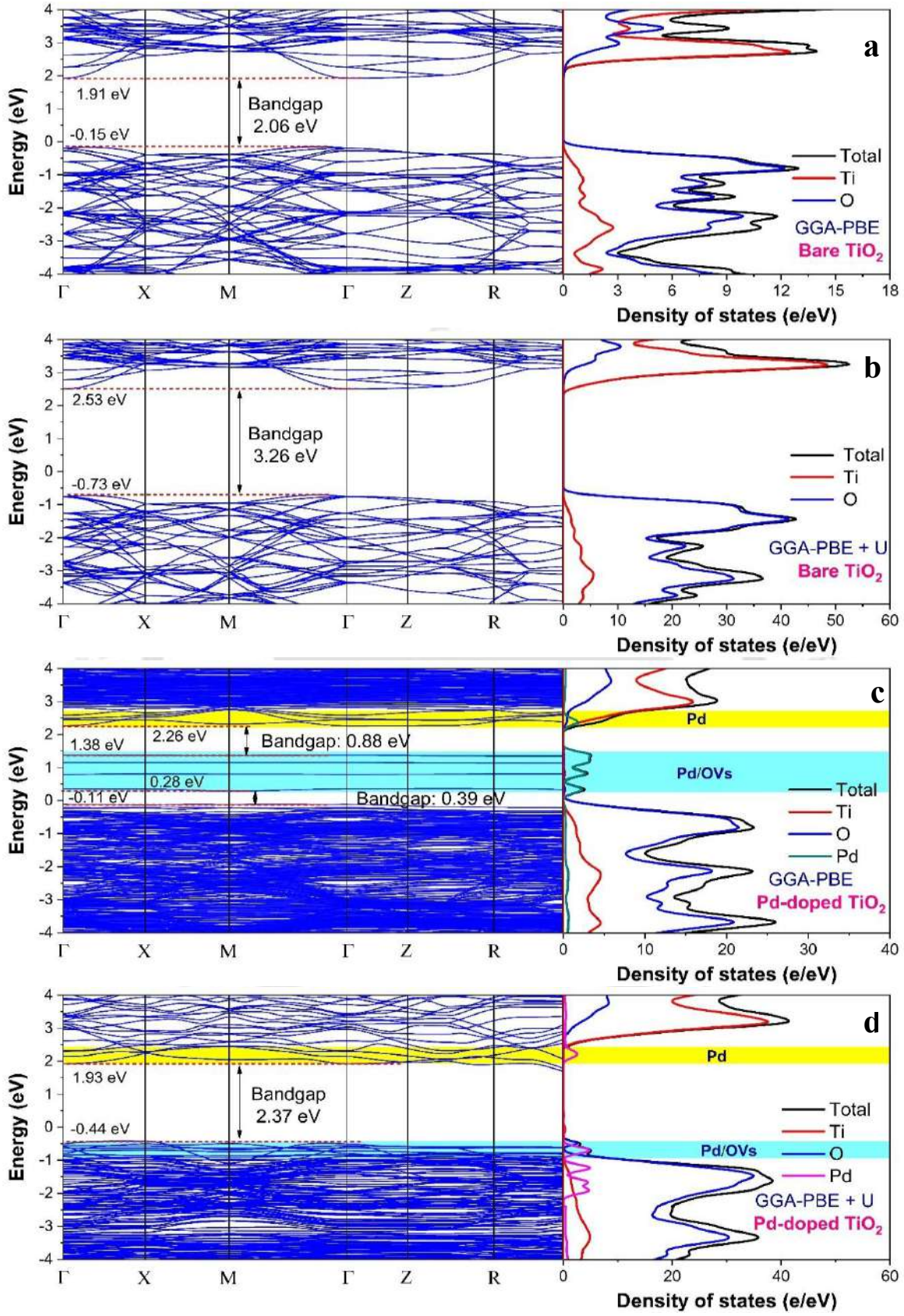

Figure 5.9: Band structure profile and PDOS plot of bare TiO_2 acquired using (a) GGA-PBE and (b) GGA-PBE+U method. Band structure profile and PDOS plot of Pd-doped TiO_2 with oxygen vacancies procured through (c) GGA-PBE and (d) GGA-PBE+U method.

The calculation methods utilized, the theoretical bandgaps obtained, and their comparison with experimental bandgaps are tabulated in Table 5.4. The band structure and PDOS of bare-TiO_2 and Pd-doped TiO_2 with OVs are shown in Fig. 5.9. The bare-TiO_2 band structure of calculated using the standard GGA-PBE functional showed a significantly underestimated bandgap of approximately 2.06 eV, consistent with known limitations of GGA (Fig. 5.9a). However, after applying the Hubbard U correction to the Ti and O orbitals, the bandgap increased to ~3.26 eV with position of VB at -0.73 eV and CB at 2.53 eV, aligning closely with the experimental values for bare-TiO_2 (bandgap = 3.29 eV, VB = -0.75 eV, and CB = 2.54 eV) (Fig. 5.9b). The PDOS analysis showed that the VB was primarily composed of O states, while the CB was dominated by Ti orbitals (Alarab et al., 2021).

For the Pd-doped TiO_2 system with OVs, the band structure under GGA-PBE exhibited pronounced impurity states within the bandgap. Specifically, a Pd-induced impurity level emerged between 1.38 and 2.26 eV, significantly narrowing the effective bandgap to approximately 0.88 eV (Fig. 5.9c). Additionally, the Pd/OV-related defect state, attributed to the formation of Ti^{3+} species, appeared near the Fermi level with an even smaller bandgap of 0.39 eV between -0.11 (VB) and 0.28 eV (CB). These mid-gap states benefit visible-light absorption but may act as recombination centers if overly populated (Rega et al., 2024). When the Hubbard correction was applied, the bandgap of the Pd-doped system increased to 2.37 eV with VB at -0.44 eV and CB at 1.93 eV. Yet, the defect-induced states persisted within the bandgap, albeit with modified energy levels (Fig. 5.9d). The theoretical bandgap and position of VB/CB align closely with the experimental band structure (bandgap = 2.41 eV, VB = -0.43 eV, and CB = 1.98 eV). The PDOS confirmed the hybridization between Pd orbitals and Ti/O states, supporting the formation of localized states that facilitate visible-light activity. The calculated E_f value (-252.3 Ry) was negative, supporting its thermodynamic feasibility and signifying the stability of the proposed Pd-doped TiO_2 with OVs model (Tarekuzzaman et al., 2025).

5.2.7 Photocatalytic degradation of AMX

The pH of the solution significantly influenced both the photocatalytic activity and the dark adsorption behavior of AMX. As observed from the non-irradiated period (-30 to 0 min) in Fig. 5.10a, the surface adsorption of AMX increased with increasing pH from 4 to 8. At pH 4, minimal adsorption occurred in the dark, indicating weak interaction between the catalyst surface and AMX molecules.

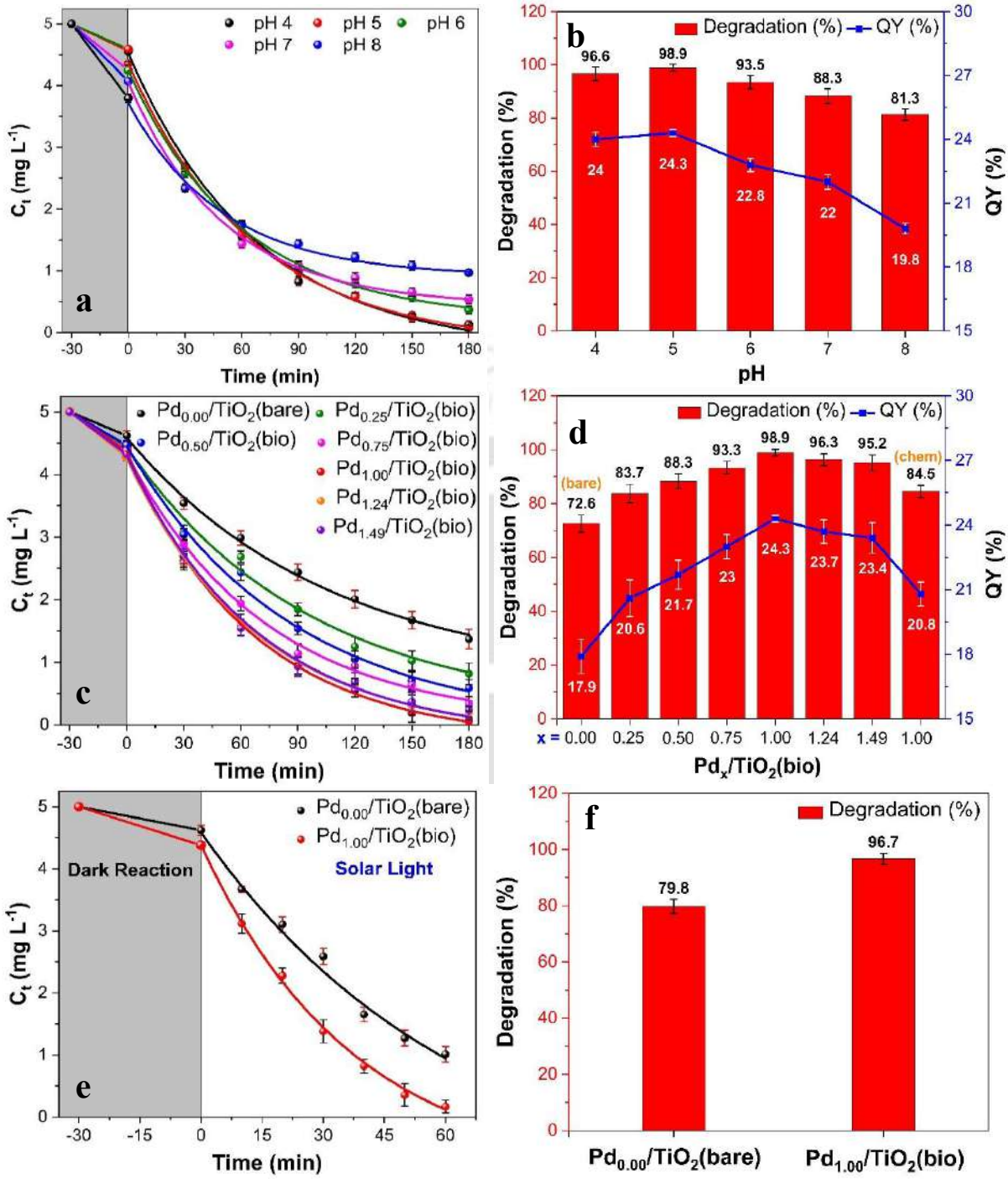

Figure 5.10: Artificial visible light: (a) First order kinetic model fitting and (b) Photocatalytic degradation (%) of AMX and QY (%) at various pH using $Pt_{1.00}/TiO_2$(bio); (c) First order kinetic model fitting and (d) Photocatalytic degradation (%) of AMX and QY (%) at pH5 using $Pd_{0.00}/TiO_2$(bare) and $Pd_{0.25\text{-}1.49}/TiO_2$(bio); (e) First order kinetic model fitting and (f) Photocatalytic degradation (%) of AMX and QY (%) at pH5 using $Pd_{0.00}/TiO_2$(bare) and $Pd_{1.00}/TiO_2$(bio) under direct solar light. The shaded part showed surface adsorption during dark reaction under artificial visible light.

Table 5.5: AMX degradation efficiency (%), rate constant (k_1, min^{-1}), and QY (%) of photocatalytic degradation of AMX at various pH (4-8) and at pH 5 using $Pd_{0.00}/TiO_2$(bare), $Pd_{0.25\text{-}1.49}/TiO_2$(bio), and $Pd_{1.00}/TiO_2$(chem) under visible light (reaction time: 180 min) and solar light (reaction time: 60 min).

Catalysts	pH	AMX degradation (%)	k_1 (min^{-1})	QY (%)
$Pd_{1.00}/TiO_2$(bio)	4	96.6 ± 2.7	1.48 x 10^{-2}	24.0 ± 0.3
	5	98.9 ± 1.3	1.51 x 10^{-2}	24.3 ± 0.2
	6	93.5 ± 2.6	1.67 x 10^{-2}	22.8 ± 0.3
	7	88.3 ± 2.8	1.97 x 10^{-2}	22.0 ± 0.3
	8	81.3 ± 2.1	2.01 x 10^{-2}	19.8 ± 0.3
$Pd_{0.00}/TiO_2$(bare)	5	72.6 ± 3.2	0.94 x 10^{-2}	17.9 ± 0.8
$Pd_{0.25}/TiO_2$(bio)		83.7 ± 3.5	1.04 x 10^{-2}	20.6 ± 0.9
$Pd_{0.50}/TiO_2$(bio)		88.3 ± 2.7	1.16 x 10^{-2}	21.7 ± 0.7
$Pd_{0.75}/TiO_2$(bio)		93.3 ± 2.3	1.36 x 10^{-2}	23.0 ± 0.6
$Pd_{1.24}/TiO_2$(bio)		96.3 ± 2.2	1.46 x 10^{-2}	23.7 ± 0.5
$Pd_{1.49}/TiO_2$(bio)		95.2 ± 2.9	1.44 x 10^{-2}	23.4 ± 0.7
$Pd_{1.00}/TiO_2$(chem)		84.5 ± 2.2	-	20.8 ± 0.6
$Pd_{0.00}/TiO_2$(bare)*	5	79.8 ± 2.5	1.57 x 10^{-2}	-
$Pd_{1.00}/TiO_2$(bio)*		96.7 ± 2.0	2.66 x 10^{-2}	-

*Photocatalytic degradation was performed under solar light.

In contrast, pH 7 and 8 exhibited greater dark adsorption, attributed to stronger electrostatic interactions between the AMX and catalyst surface under neutral and slightly basic conditions (Sheraz et al., 2024). Despite the increased adsorption at higher pH, the photocatalytic degradation efficiency decreased with increasing pH. The maximum degradation was observed at pH5, where 98.9±1.3% of AMX was degraded, with an apparent rate constant (k) of 0.0151 min^{-1} and a quantum yield (QY) of 24.3±0.2% (Fig. 5.10b and Table 5.5). The slightly acidic condition favors charge transfer and radical formation while maintaining sufficient surface interaction. At pH 8, although dark adsorption was highest, the degradation dropped to 81.3±2.1%, with k = 0.0201 min^{-1} and QY = 19.9±0.3%, likely due to reduced photogenerated radical efficiency (Fazilati, 2019). The dark adsorption of AMX slightly increased during dark reaction in Pd-doped TiO_2 photocatalysts, possibly due to increased surface defects and hydrophilicity (Cui et al., 2022).

Furthermore, degradation of AMX was performed with $Pd_{0.00}/TiO_2$(bare) and $Pd_{0.25\text{-}1.49}/TiO_2$(bio) at optimized pH 5. The surface adsorption of AMX was not affected with

different Pd concentrations (Fig. 5.10c). The primary impact of Pd was observed during the photocatalytic degradation under light irradiation. $Pd_{0.00}/TiO_2$(bare) showed limited photocatalytic activity with only 72.6±3.2% degradation, with k = 0.0094 min^{-1}, and QY = 17.9±0.8% (Fig. 10d). The increase in Pd doping increased the photocatalytic degradation to 98.9±1.3%, and QY(%) to 24.3±0.2% with $Pd_{1.00}/TiO_2$(bio). However, there was a slight decrease in the photodegradation to 96.3±2.2 and 95.2±2.9%. was observed in $Pd_{1.24}/TiO_2$(bio) and $Pd_{1.49}/TiO_2$(bio), respectively, which is in-line with bandgaps.

Additionally, the chemical-based photocatalyst ($Pd_{1.00}/TiO_2$(chem), exhibited inferior photocatalytic degradation efficiency of 84.5±2.2% with QY of 20.8±0.6% than its bio-based counterpart ($Pd_{1.00}/TiO_2$(bio)) (Fig. 5.10d). This enhancement through bio-based process attributed to more surface defects, narrow bandgap and surface functionalization by bio-analytes present in vegetal extract, facilitating better interaction with AMX and superior photoactivity. Furthermore, the photolysis process degraded only ~1.8% AMX under light irradiation, without photocatalyst, showing photo-stability of AMX.

5.2.8 Solar photodegradation

Based on the degradation efficiency of Pd-doped photocatalysts under artificial visible light, solar photocatalytic degradation of AMX was evaluated using $Pd_{0.00}/TiO_2$(bare) and most efficient $Pd_{1.00}/TiO_2$(bio) at optimum pH 5 to examine their practical efficiency and environmental relevance. The $Pd_{1.00}/TiO_2$(bio) exhibited a superior 96.7±2.0% degradation of AMX with a rate constant (k) of 0.0266 min^{-1}, substantially outperforming the bare TiO_2, which reached only 79.8±2.5% degradation (k = 0.0157 min^{-1}) under the solar conditions (Figs. 5.10e and 5.10f and Table 5.5). Almost equal AMX degradation was achieved under natural sunlight in just one-third of the time, highlighting the superior light-harvesting capability and photocatalytic efficiency of $Pd_{1.00}/TiO_2$(bio) in practical and sustainable conditions.

The photocatalytic performance of the synthesized Pd-doped TiO_2 was compared with previously reported studies on the degradation of AMX (Table 5.6). Notably, $Pd_{1.00}/TiO_2$(bio) exhibited significantly enhanced photocatalytic efficiency under artificial visible light and direct solar irradiation, outperforming many existing catalysts reported in the literature.

Table 5.6: Photocatalytic efficiency of Pd-doped TiO_2 (present study) and its comparison with chemical-based photocatalysts for AMX photodegradation.

Photocatalyst	Light Source	Initial Conc. (mg L^{-1})	Catalyst Dose (g L^{-1})	Reaction Time (min)	Degradation (%)	Ref.
TiO_2+H_2O_2	UV light (36×8 W)	10	0.25	150	~65	(Verma and Haritash, 2020)
Fe_3O_4	Solar light	100	0.12	240	~74.1	(Zulfiqar et al., 2023)
$Zn_xCo_{1-x}Fe_2O_4$	Visible light (250 W)	10	0.2	120	89	(Mmelesi et al., 2022)
CuI/$FePO_4$	Visible light (400 W)	10	1.0	120	~90	(Beshkar et al., 2022)
Na-doped HAp	Solar light	20	2.0	120	~60	(Tarannum et al., 2024)
GO-Fe_3O_4	UV light (18 W)	15	2.0	45	~87.1	(Fazilati, 2019)
Mn-doped Cu_2O	Solar light	5	1.0	180	~75	(Gaim et al., 2022)
Ni:TiO_2	Solar light	10	-	120	~96	(Ghorbani et al., 2022)
TiO_2/Bi_2MoO_6	Visible light (500 W)	20	0.4	100	94.1	(Wang et al., 2022)
GO/Ag-ZnO	Visible light	10	0.6	90	85.0	(Vu et al., 2025)
NiHCF/NSBC	Visible light (300 W)	10	0.5	90	92.0	(Kannadhasan et al., 2025)
$Pd_{0.00}$/TiO_2(bare)	Visible light (50 W)	5	0.5	180	72.6	**This Study**
$Pd_{1.00}$/TiO_2(chem)					84.5	
$Pd_{1.00}$/TiO_2(bio)					98.9	
$Pd_{0.00}$/TiO_2(bare)	Solar light			60	79.8	
$Pd_{1.00}$/TiO_2(bio)					96.7	

5.2.9 LC-MS and photodegradation mechanism

The LC-MS chromatograms and mass spectra of parent and photodegraded AMX are illustrated in Figs. 5.11a-5.11b and 5.11c-5.11d, respectively. The parent AMX spectrum (Fig. 5.11c) exhibited a characteristic peak at 365.1 m/z, corresponding to AMX, which diminished significantly after photocatalytic degradation with the appearance of several new peaks (Fig. 5.11d), indicating extensive mineralization through 17 intermediate compounds (C1-C17) by distinct radical-induced oxidative cleavage reactions (Ellepola and Rubasinghege, 2022).

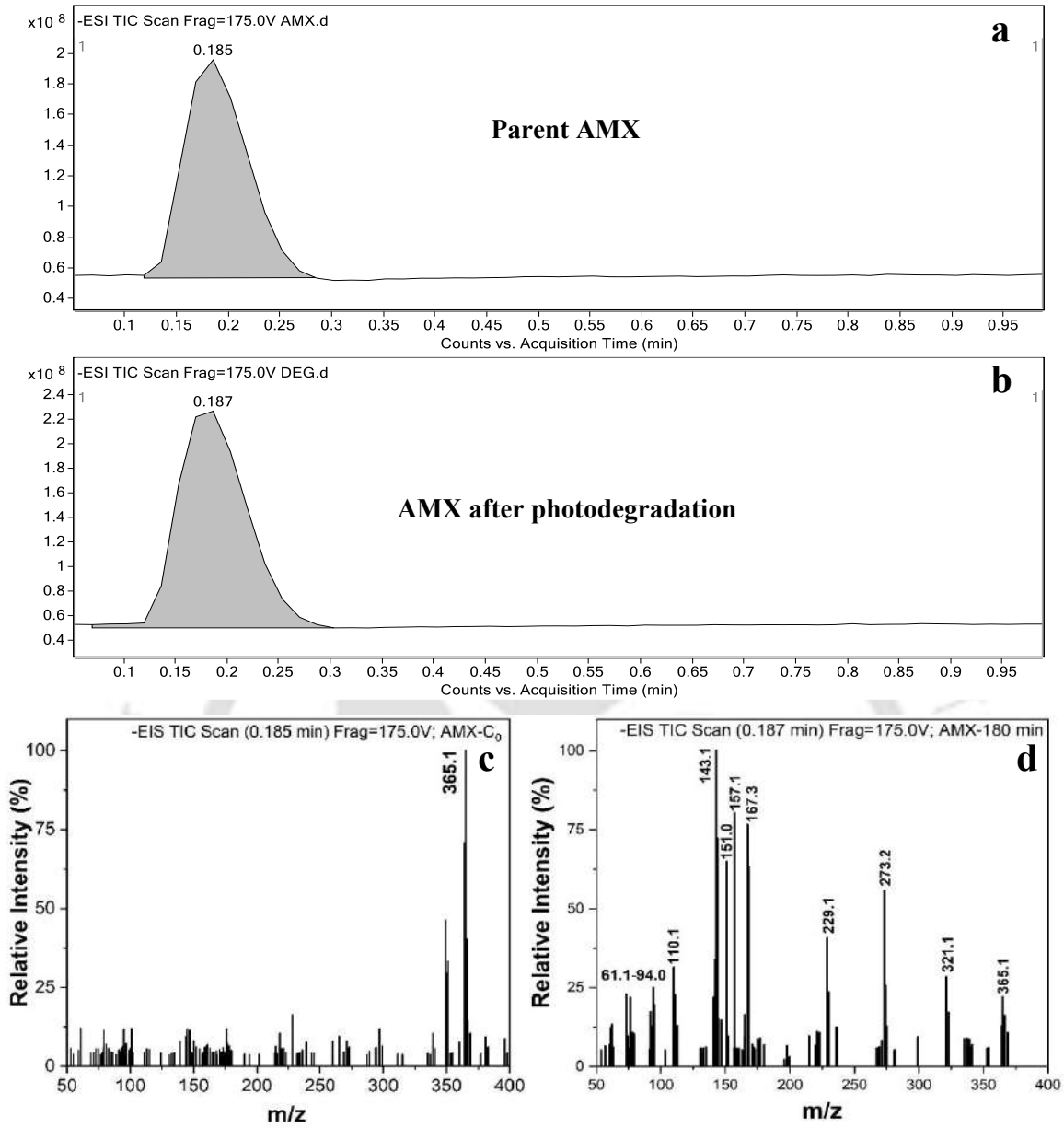

Figure 5.11: LC-MS analysis: Chromatograms of AMX (a) before and (b) after photocatalytic degradation using $Pd_{1.00}/TiO_2$(bio), captured via positive EIS mode $[M + H]^+$. MS spectra of AMX (c) before and (d) after photocatalytic degradation.

The photocatalytic degradation mechanism of AMX under oxidative conditions proceeds via two distinct transformation pathways (Pathway I and Pathway II), as shown in Fig. 5.12. Here, the formed intermediates are denoted as C (compounds) to avoid any confusion. In Pathway I (blue route), the transformation is initiated by the oxidative decarboxylation of AMX, leading to the formation of C1 (m/z = 321.1) via loss of a formaldehyde moiety ($-CH_2O_2$) under hydroxyl radical (•OH) attack. Compound C1 retains the thiazolidine core while exhibiting modification on the aromatic side chain. Subsequent

hydrolysis and cleavage of the amide bond yield C2 (m/z = 167.1), a catechol derivative, and C3 (thiazolidine-opened fragment, m/z = 157.1). C2 dehydration forms C4 (dehydrated phenol analog, m/z = 151.1), while the further hydroxylation and oxidative cleavage of C4 leads to the formation of C5 (phenol, m/z = 94.0) and C6 (amino alcohol fragment, m/z = 75.0). The dehydration of C5 results in the generation of C7 (m/z = 78.1), identified as benzene, which further oxidized to form dialdehyde, likely benzene-1,2-dicarboxaldehyde, highlighting aromatic ring scission. Concurrently, ring hydroxylation of AMX and successive oxidation of the β-lactam side chains yield small-molecule products, including C6 (m/z = 75.0) and C7 (m/z = 78.1). The C6 intermediate compound undergoes progressive transformation to generate C16 (m/z = 61.1), a short-chain amino alcohol, and C17 (m/z = 62.0), a diol formed via sequential N–C bond cleavage (Ellepola and Rubasinghege, 2022; Kanwar et al., 2024).

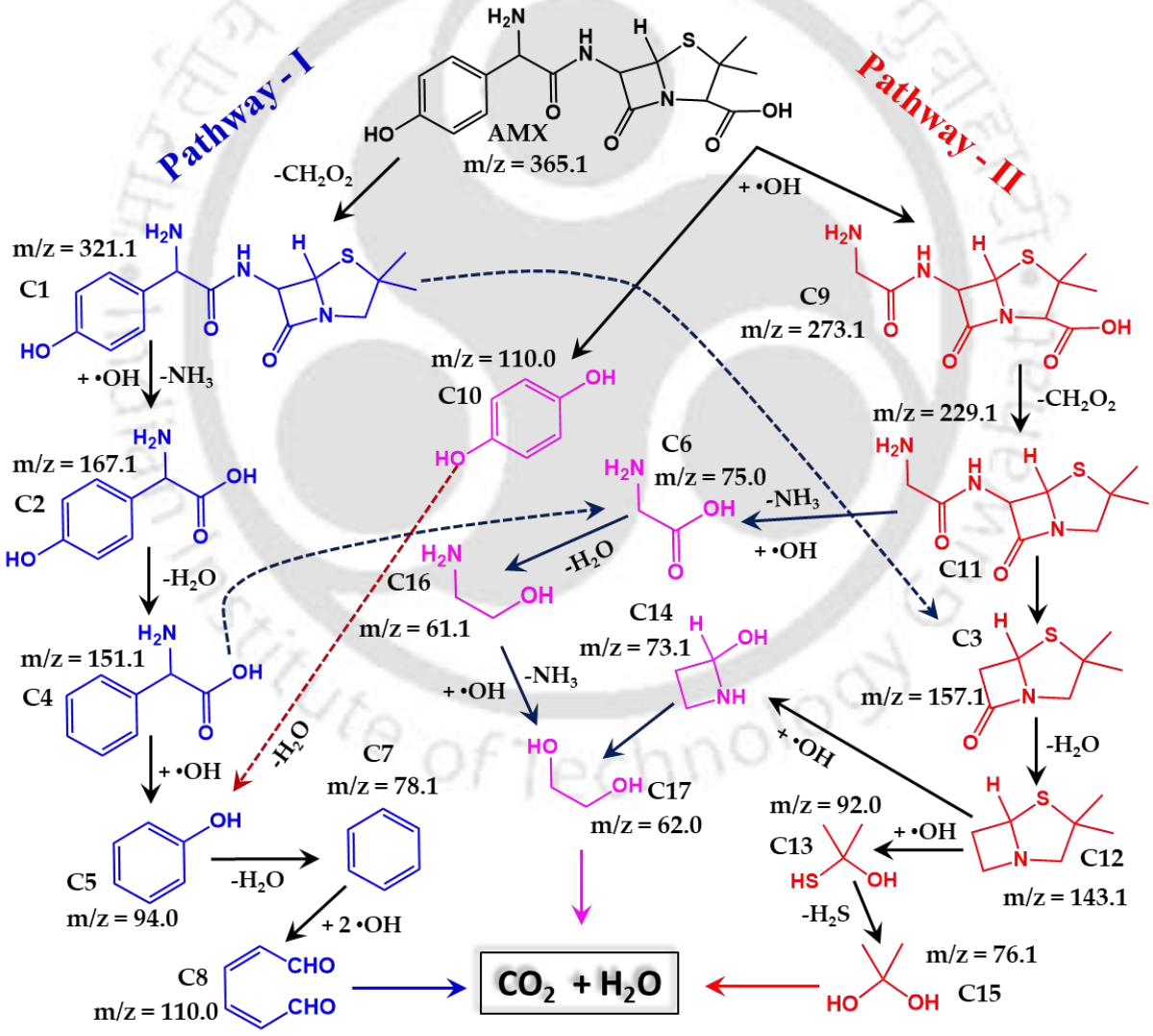

Figure 5.12: Photocatalytic degradation mechanism of AMX using $Pd_{1.00}/TiO_2$(bio) under visible light irradiation for 180 min.

Pathway II (red route) initiates with the •OH-induced oxidation of the thiazolidine ring of AMX, forming C9 (m/z = 273.1) and C10 (m/z = 110.0), followed by decarboxylation of C9 to produce C11 (m/z = 229.1). The generated C10 (m/z = 110.0), structurally resembling hydroquinone, served as a central branching point after dehydration to C5, linking pathways I and II through a shared oxidative intermediate. Successive oxidative cleavage of the amide and sulfur-containing moieties of C11 leads to the formation of C3 and C12 (m/z = 143.1), highlighting significant structural disruption of the core thiazolidine ring. Further hydroxylation of the thiol group in C12 forms C13 (m/z = 92.0), a low molecular weight thiol derivative, which further undergoes desulfurization (-H_2S) and •OH-mediated oxidation to yield C15 (m/z = 76.1), a thiol-containing diol. Additionally, C14 (m/z = 73.1), an oxazolidinone-like species, was formed via hydroxylation of C12 intermediate compound. The low molecular weight intermediate compounds such as C8, C15, and C17 were further oxidized to generate CO_2 and H_2O, confirming their mineralization (Sount harya et al., 2023; Kanwar et al., 2024).

Among 17 formed intermediate compounds, 5 intermediates displayed any mass error of only 0.1-0.2 mol/g between m/z values of proposed structures and obtained through mass spectra.

5.2.10 Reusability and stability

The reusability studies of the optimized $Pd_{1.00}/TiO_2$(bio) photocatalyst over five consecutive photocatalytic cycles revealed a gradual decline in surface adsorption and photocatalytic degradation efficiency, indicating slight deactivation with reuse. The initial surface adsorption decreased from 12.5±1.1% in the first cycle to 8.2±1.5% by the fifth cycle, suggesting a gradual saturation or passivation of active surface sites (Fig. 5.13a). Similarly, the photocatalytic degradation (under light) also declined progressively from 98.9±1.3% in the first cycle to 90.4±2.3% in the fifth cycle. This trend was further supported by the C/C_0 vs. time plot (Fig. 5.13b), which confirmed a consistent yet slightly diminishing photocatalytic performance over repeated use. Despite the reduction in efficiency, the catalyst retained over 90% degradation efficiency after five cycles, demonstrating good reusability potential for practical wastewater treatment applications.

The stability of the $Pd_{1.00}/TiO_2$(bio) photocatalyst after the first cycle of photocatalytic degradation was evaluated using XRD and XPS analyses. The XRD patterns (Fig. 5.13c) show that the crystalline structure of the used photocatalyst remains largely unchanged compared to the fresh sample, indicating no significant structural degradation after the photodegradation

reaction. Additionally, no new peaks appear in the used sample, confirming the phase stability of the catalyst. The XPS spectra (Fig. 5.13d) further support this by showing the consistency of characteristic peaks of O1s, Ti2p, Pd3d, and C1s in the used catalyst, implying that the chemical states of the elements remain stable post-reaction (Malolepszy et al., 2024). Overall, both structural and surface chemical analyses confirm that $Pd_{1.00}/TiO_2$(bio) demonstrates good stability after photocatalytic degradation.

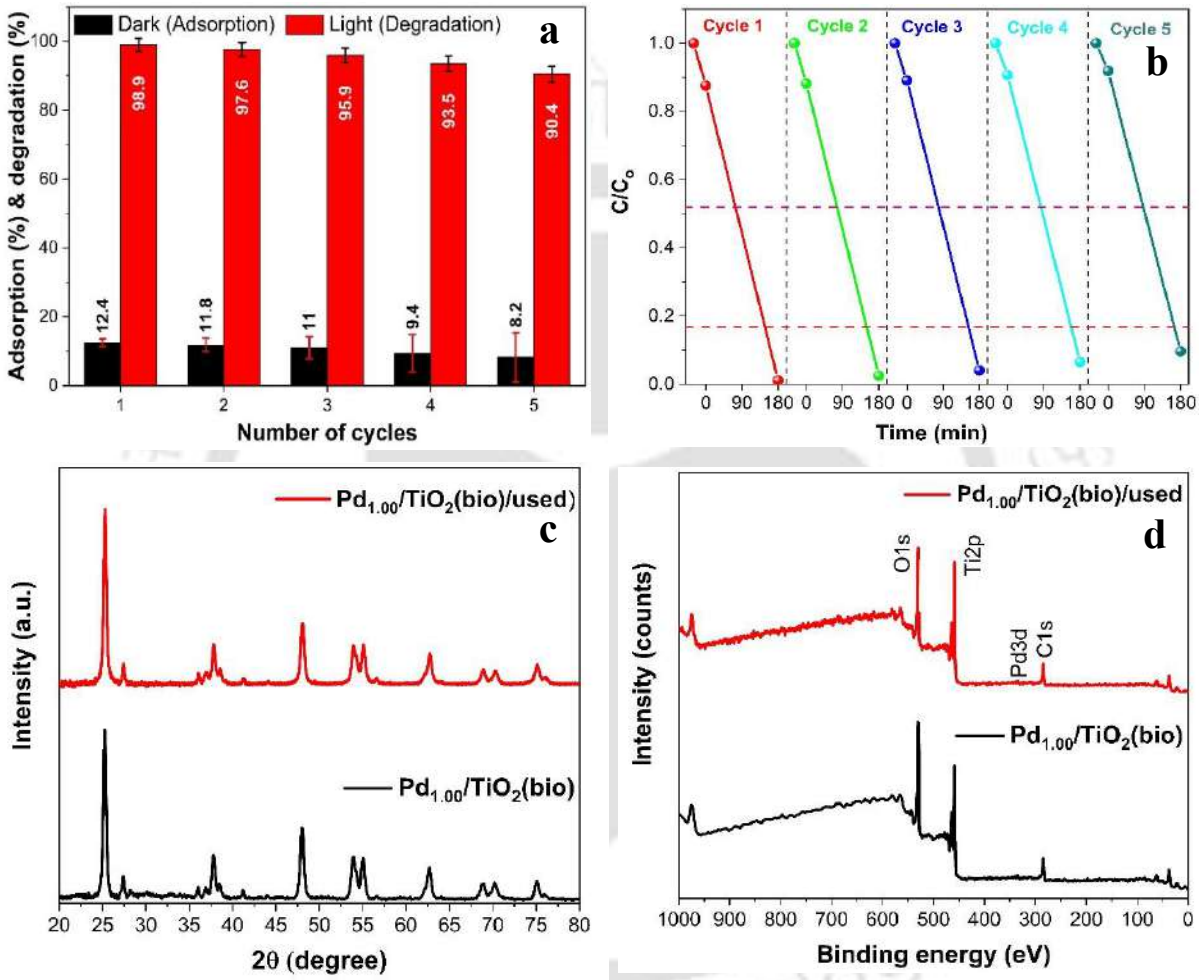

Figure 5.13: Reusability of $Pd_{1.00}/TiO_2$(bio) during AMX photodegradation for consecutive 5 cycles: (a) Surface adsorption in dark and AMX photodegradation and (b) C/C_0 plot; (c) XRD spectra and (d) XPS survey scan of $Pd_{1.00}/TiO_2$(bio) and $Pd_{1.00}/TiO_2$(bio)/used (after 1st cycle of photodegradation).

5.2.11 Toxicity assessment and antimicrobial activity

The toxicity profile of AMX and its photocatalytic degradation intermediates was assessed via QSAR-based in silico prediction. For Fathead minnow (*Pimephales promelas*), a freshwater fish, AMX exhibited high acute and chronic toxicity with an LC_{50} value of 2.3 mg

L^{-1} (Fig. 5.14a), positioning it as a significant ecological risk. Post-degradation intermediate compounds, particularly those with reduced aromaticity and lower molecular weight (e.g., C2-C7, C9-C18), demonstrated significantly decreased predicted toxicity levels with LC_{50} values of 38.7-8020.7 mg L^{-1}, indicating effective detoxification during photocatalysis. However, intermediate compounds, C1 and C9, exhibited slightly reduced toxicity with LC_{50} values of 3.4 and 8.7 mg L^{-1} (Wen et al., 2023).

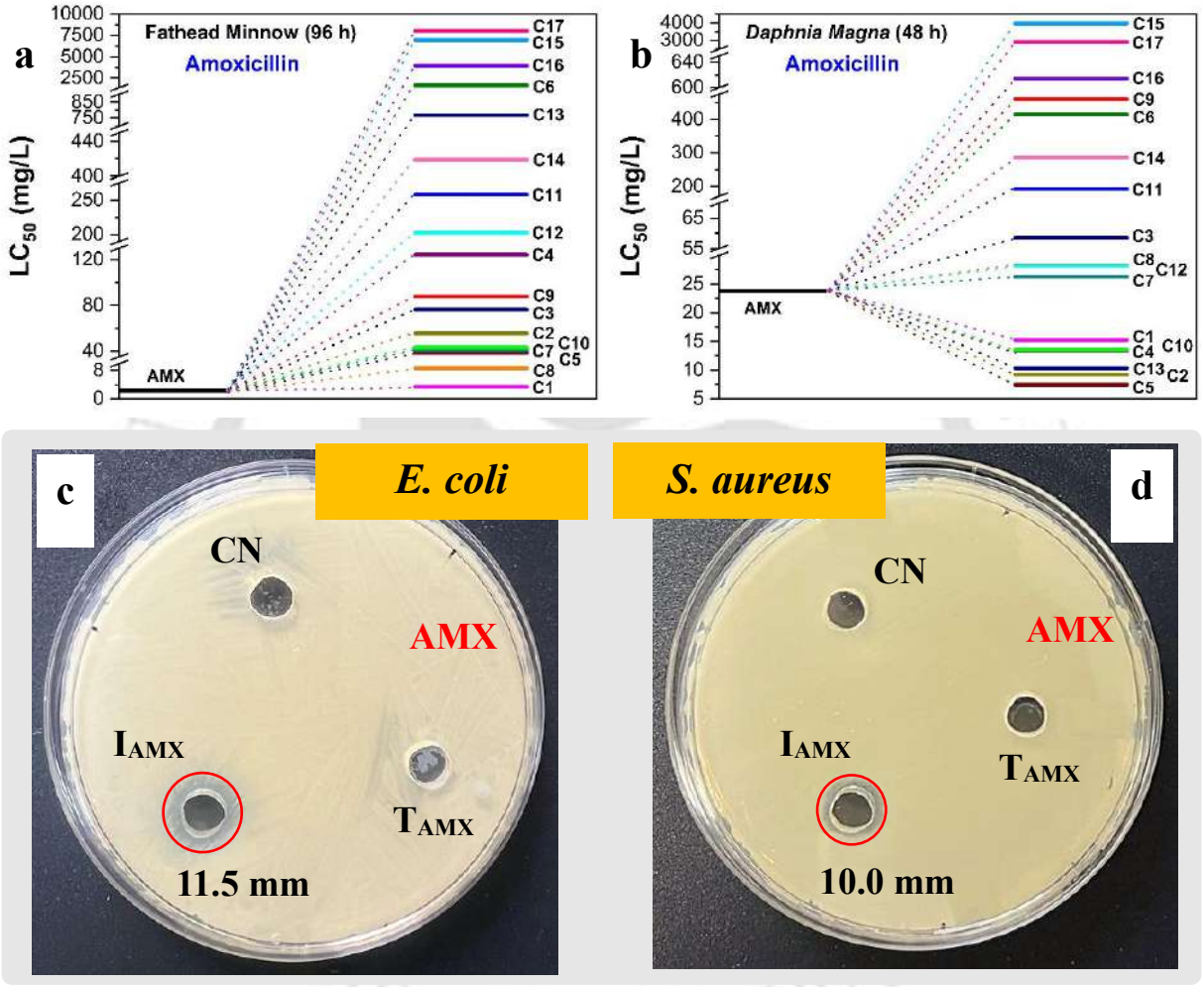

Figure 5.14: Toxicity assessment of AMX and intermediate compounds formed during photocatalytic degradation process: LC_{50} values for (a) Fathead Minnow (96 h) and (b) *Daphnia Magna* (48 h). Antimicrobial activity of AMX before and after photocatalytic degradation against (c) *E. coli* and (d) *S. aureus*. Here, I_{AMX}, and T_{AMX} are initial AMX and treated (photodegraded) AMX, while CN represents control containing DI water.

A similar trend was observed for *Daphnia magna* (Fig. 5.14b), where the predicted toxicity of AMX (LC_{50} = 23.8 mg L^{-1}) was substantially higher than that of its transformation products such as C3, C6-C9, C11, C12, C14-C17, with LC_{50} values lies in the range of 28.1-

3960.5 mg L^{-1}. However, intermediate compounds such as C1, C2, C4, C5, C10, and C13, exhibited a slightly reduced LC_{50} value could be due to exposure of aromatic ring (Han et al., 2024). The observed shift toward lower toxicity suggests reduced bioaccumulation potential and ecotoxicological impact. These results confirm that the photocatalytic process not only degrades AMX but also transforms it into environmentally benign intermediates, fulfilling the dual goal of pollutant removal and ecological safety.

The results of antimicrobial studies are shown in Figs. 5.14c and 5.14d. The parent AMX (5 mg L^{-1}) exhibited apparent antibacterial activity, showing a zone of inhibition of ~11.5 mm against *E. coli* (Fig. 5.14c) and ~10 mm against *S. aureus* (Fig. 5.14d), indicating its potent bactericidal effect. However, the photocatalytically degraded AMX solution showed no observable zone of inhibition for either bacterial strain, comparable to the negative control (Milli-Q water) (Das et al., 2018). This result confirms the effective degradation and detoxification of AMX by the $Pd_{1.00}/TiO_2$(bio), interpreting the byproducts as non-antibacterial and highlighting the potential of the process in reducing environmental and microbial resistance risks associated with pharmaceutical contaminants.

5.3 Major findings

This study successfully demonstrates the artificial visible- and solar light-assisted photocatalytic degradation of AMX using microwave-assisted bio-based Pd-doped TiO_2. The bio-based Pd-doping induced oxygen vacancies and Ti^{3+} defects, which collectively contributed to bandgap narrowing from 3.29 to 2.41 eV by shifting band edges, enhanced charge separation, high hydrophilicity, superior light absorption (from 377 to 515 nm) and improved photocurrent density (17 to 375 nA cm^{-2}). DFT studies showed mid-bands position between VB and CB, corresponding to Pd and OVs, with almost equal theoretical and experimental bandgaps. The photocatalyst exhibited significant AMX degradation efficiency under both artificial visible (98.9%) and solar irradiation (96.7%), outperforming bare and chemically synthesized Pd-TiO_2 counterparts. Furthermore, the catalyst displayed remarkable reusability over multiple cycles with minimal structural or functional deterioration, supported by XRD and XPS analyses. AMX photodegradation occurred through 17 different intermediates with a significant reduction in the aquatic toxicity and neutralization of antimicrobial activity against *E. coli* and *S. aureus*. In nutshell, this study offers a comprehensive experimental and computational insight into the development of defect-

engineered and bio-fabricated photocatalysts for sustainable antibiotic remediation with minimal environmental impact.

Compared to Pt- and Au-doping, Pd-doping resulted in a lower bandgap (2.41 eV) and >22-fold enhancement in photocurrent density, along with better reusability, maintaining >90% degradation efficiency even after the 5th cycle. Further, a transition metal such as nickel (Ni) as a dopant offers a highly economical and sustainable alternative (Chapter 6).

References

Alarab, F., Hricovini, K., Leikert, B., Nicolaï, L., Fanciulli, M., Heckmann, O., Richter, C., Prušakova, L., Jansa, Z., Šutta, P., Rault, J., Lefevre, P., Sing, M., Muntwiler, M., Claessen, R., Minár, J., 2021. Photoemission study of pristine and Ni-doped $SrTiO_3$ thin films. Phys. Rev. B 104. https://doi.org/10.1103/PhysRevB.104.165129

Ayaz, M., Alatawi, A.S., Hijji, M., Namazi, M.A., Ershath, M.I.M., 2024. Improving charge transfer properties and solar cell performance by In-doped TiO_2 as an efficient photoanode for dye-sensitized solar cells (DSSCs). J. Phys. Chem. Solids 188. https://doi.org/10.1016/j.jpcs.2024.111913

Baruah, M., Ezung, S.L., Sharma, S., Bora Sinha, U., Sinha, D., 2022. Synthesis and characterization of Ni-doped TiO_2 activated carbon nanocomposite for the photocatalytic degradation of anthracene. Inorg. Chem. Commun. 144. https://doi.org/10.1016/j.inoche.2022.109905

Beshkar, F., Al-Nayili, A., Amiri, O., Salavati-Niasari, M., Mousavi-Kamazani, M., 2022. Visible light-induced degradation of amoxicillin antibiotic by novel CuI/$FePO_4$ p-n heterojunction photocatalyst and photodegradation mechanism. J. Alloys Compd. 892. https://doi.org/10.1016/j.jallcom.2021.162176

Bhan, C., Golder, A.K., 2025. Nature-Inspired Vertically Oriented 1D Bi_2S_3 Surface Nanorods for Ultra-Selective Electrochemical Sensing of Mancozeb. https://doi.org/10.1021/acs.langmuir.5c00915

Bhan, C., Golder, A.K., 2023. Utilizing bioinspired AgNPs as an antibacterial agent to enhance ceramic membrane performance. J. Environ. Chem. Eng. 11, 110283. https://doi.org/10.1016/j.jece.2023.110283

Bhan, C., R, G.S., Golder, A.K., 2025a. Journal of Environmental Chemical Engineering A chemo-mimetic approach using bioanalytes for formation of $BiVO_4$ nanostructures for voltammetric detection of bisphenol A. J. Environ. Chem. Eng. 13, 117417.

https://doi.org/10.1016/j.jece.2025.117417

Bhan, C., Ravi, R., Golder, A.K., 2025b. Phyto-analytic formation of Ag nanostructures for targeted electrocatalytic sensing of ciprofloxacin. J. Environ. Chem. Eng. 13, 115140. https://doi.org/10.1016/j.jece.2024.115140

Chelli, V.R., Chakraborty, S., Golder, A.K., 2018. Ag-doping on TiO_2 using plant-based glycosidic compounds for high photonic efficiency degradative oxidation under visible light. J. Mol. Liq. 271. https://doi.org/10.1016/j.molliq.2018.08.140

Cheng, G., Liu, X., Song, X., Chen, X., Dai, W., Yuan, R., Fu, X., 2020. Visible-light-driven deep oxidation of NO over Fe doped TiO_2 catalyst: Synergic effect of Fe and oxygen vacancies. Appl. Catal. B Environ. 277. https://doi.org/10.1016/j.apcatb.2020.119196

Cui, T., Su, Y., Fu, X., Zhu, Y., Zhang, Y., 2022. The key role of surface hydroxyls on the activity and selectivity in photocatalytic degradation of organic pollutants and NO removal. J. Alloys Compd. 921. https://doi.org/10.1016/j.jallcom.2022.165931

Das, S., Ghosh, S., Misra, A.J., Tamhankar, A.J., Mishra, A., Lundborg, C.S., Tripathy, S.K., 2018. Sunlight assisted photocatalytic degradation of ciprofloxacin in water using Fe doped Zno nanoparticles for potential public health applications. Int. J. Environ. Res. Public Health 15. https://doi.org/10.3390/ijerph15112440

Dash, S.R., Bag, S.S., Golder, A.K., 2020. Synthesis of highly structured spherical Ag@Pt core-shell NPs using bio-analytes for electrocatalytic Pb(II) sensing. Sensors Actuators, B Chem. 314, 128062. https://doi.org/10.1016/j.snb.2020.128062

de Lima Marsiglia, W.I.M., Oliveira, L. de S.C., Lucas Jacinto Almeida, R., Santos, N.C., da Silva Neto, J.M., Santiago, Â.M., de Melo, B.C.A., Honorato da Silva, F.L., 2023. Thermal stability of total phenolic compounds and antioxidant activities of jaboticaba peel: Effect of solvents and extraction methods. J. Indian Chem. Soc. 100. https://doi.org/10.1016/j.jics.2023.100995

El-Sawaf, A.K., Nassar, A.A., Tolan, D.A., Ismael, M., Alhindawy, I., M. El-Desouky, E., El-Nahas, A., Shahien, M., Maize, M., 2024. A mesoporous Mo and N Co-doped TiO_2 nanocomposite with enhanced photocatalytic efficiency. RSC Adv. 14. https://doi.org/10.1039/d3ra07258d

Ellepola, N., Rubasinghege, G., 2022. Heterogeneous Photocatalysis of Amoxicillin under Natural Conditions and High-Intensity Light: Fate, Transformation, and Mineralogical Impacts. Environ. - MDPI 9. https://doi.org/10.3390/environments9070077

Fazilati, M., 2019. Photocatalytic degradation of amoxicillin, cephalexin, and tetracycline from aqueous solution: Comparison of efficiency in the usage of TiO_2, ZnO, or GO-Fe_3O_4

nanoparticles. Desalin. Water Treat. 169, 222–231. https://doi.org/10.5004/dwt.2019.24632

Gaim, Y.T., Yimanuh, S.M., Kidanu, Z.G., 2022. Enhanced Photocatalytic Degradation of Amoxicillin with Mn-Doped Cu_2O under Sunlight Irradiation. J. Compos. Sci. 6. https://doi.org/10.3390/jcs6100317

Gawal, P.M., Golder, A.K., 2024. Plant-Based Phytochemicals for Synthesis of Z-Scheme In_2O_3/CdS Heterostructures: DFT Analysis and Photocatalytic CO_2 Reduction to HCOOH and CO. Langmuir 40, 13538–13549. https://doi.org/10.1021/acs.langmuir.4c01015

Ghorbani, M., Faridan, M., Wantala, K., Shivaraju, H.P., Shahmoradi, B., Safari, M., Rezaee, R., Soltani, R.D.C., 2022. Solar photocatalytic degradation of amoxicillin using Ni:TiOstabilized on ceramic plates. Desalin. Water Treat. 270, 163–171. https://doi.org/10.5004/dwt.2022.28787

Gillies, M., Ranakusuma, A., Hoffmann, T., Thorning, S., McGuire, T., Glasziou, P., Del, C., 2015. Common harms from amoxicillin: A systematic review and meta-analysis of randomized placebo-controlled trials for any indication. CMAJ 187. https://doi.org/10.1503/cmaj.140848

Gogoi, D., Koyani, R., Golder, A.K., Peela, N.R., 2020. Enhanced photocatalytic hydrogen evolution using green carbon quantum dots modified 1-D CdS nanowires under visible light irradiation. Sol. Energy 208. https://doi.org/10.1016/j.solener.2020.08.061

Gonçalves, R.A., Kuznetsov, A., Ciapina, E.G., Quade, A., Teodoro, M.D., Baldan, M.R., Berengue, O.M., 2023. Insights into the origin of the enhanced electrical conductivity of Pd-Sb_2O_3 nanoparticles: A combined experimental and theoretical study. J. Alloys Compd. 933. https://doi.org/10.1016/j.jallcom.2022.167667

Guerrero-Ortega, L.P.A., Ramírez-Meneses, E., Cabrera-Sierra, R., Palacios-Romero, L.M., Philippot, K., Santiago-Ramírez, C.R., Lartundo-Rojas, L., Manzo-Robledo, A., 2019. Pd and Pd@PdO core–shell nanoparticles supported on Vulcan carbon XC-72R: comparison of electroactivity for methanol electro-oxidation reaction. J. Mater. Sci. 54. https://doi.org/10.1007/s10853-019-03843-8

Han, M., Wang, S., Yu, X., Zhang, Y., Li, M., Yi, Z., Gao, H., Yang, H., Fang, L., Syed, A., 2024. Enhanced Photocatalytic Activity of O-deficient Modified $CuAl_2O_4$/MoS_2 Composite Photocatalysts in Wastewater Treatment Applications. Adv. Sustain. Syst. 8, 1–19. https://doi.org/10.1002/adsu.202300478

Heryanto, H., Mutmainna, I., Rahmi, M.H., Tenri Ola, A.T., Tang, N.F.R., Mohamed, M.A.,

Tahir, D., 2024. Favourable peak diffraction shift moments as a function of Mg doping on ZnO matrix as a promising catalyst for methylene blue waste. Mater. Chem. Phys. 313. https://doi.org/10.1016/j.matchemphys.2023.128772

Hu, C., Chen, F., Lu, T., Lian, C., Zheng, S., Hu, Q., Duo, S., Zhang, R., 2014. Water-phase strategy for synthesis of TiO_2-graphene composites with tunable structure for high performance photocatalysts. Appl. Surf. Sci. 317, 648–656. https://doi.org/10.1016/j.apsusc.2014.08.161

Javaid, R., Kawasaki, S.I., Suzuki, A., Suzuki, T.M., 2013. Simple and rapid hydrogenation of p-nitrophenol with aqueous formic acid in catalytic flow reactors. Beilstein J. Org. Chem. 9. https://doi.org/10.3762/bjoc.9.129

Kannadhasan, V., Mahendran, K., Indhu, R., Manikannan, G., 2025. Strategic design of nitrogen and sulphur co-doped biocarbon/nickel hexacyanoferrate nanocomposite for efficient removal of ciprofloxacin and amoxicillin antibiotics from water. Diam. Relat. Mater. 156, 112420. https://doi.org/10.1016/j.diamond.2025.112420

Kanwar, B., Koli, M., Singh, S.P., 2024. Antibiotic amoxicillin degradation by electrochemical oxidation process: effects of process parameters and degradation pathway at environmentally relevant concentrations. Environ. Sci. Pollut. Res. 32, 575–586. https://doi.org/10.1007/s11356-024-35780-8

Kaur, H., Chadha, P., 2025. Assessment of untreated and vermifiltration treated pharmaceutical industrial effluent in fish Channa punctata using biochemical, histopathological, ultrastructural and ATR-FTIR analysis. Sci. Rep. 15, 1–13. https://doi.org/10.1038/s41598-025-98068-y

Kim, H. seok, Seo, Y.S., Kim, K., Han, J.W., Park, Y., Cho, S., 2016. Concentration effect of reducing agents on green synthesis of gold nanoparticles: size, morphology, and growth mechanism. Nanoscale Res. Lett. 11. https://doi.org/10.1186/s11671-016-1393-x

Komaraiah, D., Radha, E., Sivakumar, J., Ramana Reddy, M. V., Sayanna, R., 2020. Photoluminescence and photocatalytic activity of spin coated Ag^+ doped anatase TiO_2 thin films. Opt. Mater. (Amst). 108. https://doi.org/10.1016/j.optmat.2020.110401

Kumar, A., Das, C., 2023. A novel eco-friendly inhibitor of chayote fruit extract for mild steel corrosion in 1 M HCl: Electrochemical, weight loss studies, and the effect of temperature. Sustain. Chem. Pharm. 36, 101261. https://doi.org/10.1016/j.scp.2023.101261

Li, Q., Zhao, J., Shang, H., Ma, Z., Cao, H., Zhou, Y., Li, G., Zhang, D., Li, H., 2022. Singlet oxygen and mobile hydroxyl radicals co-operating on gas-solid catalytic reaction interfaces for deeply oxidizing NOx. Environ. Sci. Technol. 56.

https://doi.org/10.1021/acs.est.2c00622

Liza, T.Z., Tusher, M.M.H., Anwar, F., Monika, M.F., Amin, K.F., Asrafuzzaman, F.N.U., 2024. Effect of Ag-doping on morphology, structure, band gap and photocatalytic activity of bio-mediated TiO_2 nanoparticles. Results Mater. 22. https://doi.org/10.1016/j.rinma.2024.100559

Long, J., Chang, H., Gu, Q., Xu, J., Fan, L., Wang, S., Zhou, Y., Wei, W., Huang, L., Wang, X., Liu, P., Huang, W., 2014. Gold-plasmon enhanced solar-to-hydrogen conversion on the {001} facets of anatase TiO_2 nanosheets. Energy Environ. Sci. 7. https://doi.org/10.1039/c3ee43289k

Malolepszy, A., Mazurkiewicz-Pawlicka, M., Stobinski, L., Lesiak-Orłowska, B., Mierzwa, B., Kövér, L., Tóth, J., Chang, Y.C., 2024. Influence of TiO_2 coverage on activity and stability of Pd-TiO_2/MWCNT-supported catalysts used in direct formic acid fuel cells. J. Mater. Sci. 59, 6894–6915. https://doi.org/10.1007/s10853-024-09586-5

Mekhemer, I.M.A., Elewa, A.M., Elsenety, M.M., Samy, M.M., Mohamed, M.G., Musa, A.F., Huang, T.F., Wei, T.C., Kuo, S.W., Chen, B.H., Yang, S. Da, Chou, H.H., 2024. Self-condensation for enhancing the hydrophilicity of covalent organic polymers and photocatalytic hydrogen generation with unprecedented apparent quantum yield up to 500 nm. Chem. Eng. J. 497, 154280. https://doi.org/10.1016/j.cej.2024.154280

Mmelesi, O.K., Patala, R., Nkambule, T.T.I., Mamba, B.B., Kefeni, K.K., Kuvarega, A.T., 2022. Effect of Zn doping on physico-chemical properties of cobalt ferrite for the photodegradation of amoxicillin and deactivation of *E. coli.* Colloids Surfaces A Physicochem. Eng. Asp. 649. https://doi.org/10.1016/j.colsurfa.2022.129462

Nandi, S., Das, S., Singh, S., Verma, R., 2020. Phytotoxicity and Effect on Allium Cepa of the Permeate Obtained After the Physico-Biological Treatment of Congo Red By Physico-Biological Treatment 20, 3378–3384.

Nasrollahzadeh, M., Atarod, M., Sajjadi, M., Sajadi, S.M., Issaabadi, Z., 2019. Plant-mediated green synthesis of nanostructures: mechanisms, characterization, and applications, in: Interface science and technology. https://doi.org/10.1016/B978-0-12-813586-0.00006-7

Qahtan, T.F., Owolabi, T.O., Saleh, T.A., 2024. X-ray photoelectron spectroscopy of surface-treated TiO_2 mesoporous film by 500 eV argon ion beam. J. Mol. Liq. 393. https://doi.org/10.1016/j.molliq.2023.123556

Rega, R., Fioravanti, A., Hejazi, S.M.H., Shahrezaei, M., Kment, Š., Maddalena, P., Naldoni, A., Lettieri, S., 2024. Charge carrier recombination processes, intragap defect states, and photoluminescence mechanisms in stoichiometric and reduced TiO_2 brookite nanorods:

an interpretation scheme through in situ photoluminescence excitation spectroscopy in controlled environ. Nanoscale 16, 11296–11309. https://doi.org/10.1039/d4nr00593g

Report, C.C., 2024. Amoxicillin-associated hemorrhagic colitis 49, 1–4.

Saqib, M., Rahman, N., Safeen, K., Mekkey, S.D., Salem, M.A., Safeen, A., Husain, M., Zaman, S. u., Abdullaev, S., Kalsoom, A., El-Bahy, Z.M., Khan, R., 2023. Structure phase-induced photodegradation properties of cobalt-sulfur co-doped TiO_2 nanoparticles synthesized by hydrothermal route. J. Mater. Res. Technol. 26. https://doi.org/10.1016/j.jmrt.2023.09.151

Sheraz, N., Shah, A., Haleem, A., Iftikhar, F.J., 2024. Comprehensive assessment of carbon-, biomaterial- and inorganic-based adsorbents for the removal of the most hazardous heavy metal ions from wastewater. RSC Adv. 14, 11284–11310. https://doi.org/10.1039/d4ra00976b

Sount harya, S., Jones, B.M.F., Muthuraj, V., Swaminathan, K., 2023. Construction of Ternary Photocatalyst of Cu/ZnO/BN with Enrich the Photocatalytic Activity Driven by Visible Light Irradiation for Degradation of RhB-MO Mixture and Amoxicillin. J. Inorg. Organomet. Polym. Mater. 33. https://doi.org/10.1007/s10904-023-02621-z

Syeda, H.I., Muthukumaran, S., Baskaran, K., 2025. Dynamic adsorption of heavy metals on functionalized and regeneratable biopolymeric aerogels: Fixed-bed column reactor modelling and dual functionality elution technique. Sep. Purif. Technol. 363, 131861. https://doi.org/10.1016/j.seppur.2025.131861

Tarannum, S., Sahadat Hossain, M., Bashar, M.S., Bahadur, N.M., Ahmed, S., 2024. Amplification of photocatalytic degradation of antibiotics (amoxicillin, ciprofloxacin) by sodium doping in nano-crystallite hydroxyapatite. RSC Adv. 14, 12386–12396. https://doi.org/10.1039/d4ra00126e

Tarekuzzaman, M., Shahadath, N., Montasir, M., Alsalmi, O., Mia, M.H., Al-Dmour, H., Rasheduzzaman, M., Hasan, M.Z., 2025. DFT analysis of the physical properties of direct band gap semiconducting double perovskites A_2BIrCl_6 (A = Cs, Rb; B = Na, K) for solar cells and optoelectronic applications. RSC Adv. 15, 13643–13661. https://doi.org/10.1039/d5ra01748c

Valian, M., Soofivand, F., Khoobi, A., Yousif, Q.A., Salavati-Niasari, M., 2023. A green approach: Eco-friendly synthesis of $Gd_2Ti_2O_7$/N-GQD nanocomposite and photo-degradation and electrochemical measurement of hydroxychloroquine as a perdurable drug. Arab. J. Chem. 16. https://doi.org/10.1016/j.arabjc.2022.104401

Veerakumar, P., Sangili, A., Chen, S.M., Kumar, R.S., Arivalagan, G., Firdhouse, M.J.,

Hameed, K.S., Sivakumar, S., 2024. Photocatalytic degradation of phenolic pollutants over palladium-tungsten trioxide nanocomposite. Chem. Eng. J. 489, 151127. https://doi.org/10.1016/j.cej.2024.151127

Verma, M., Haritash, A.K., 2020. Photocatalytic degradation of Amoxicillin in pharmaceutical wastewater: A potential tool to manage residual antibiotics. Environ. Technol. Innov. 20. https://doi.org/10.1016/j.eti.2020.101072

Vu, V.P., Thi Le Na, N., Luong, M.T., Toan, N.D., Tran Thi, N.A., Nguyen, T.T., Hoang, M.H., Nguyen, L.D., Dao, K.L., Nguyen, T.B., Sai, C.D., 2025. Visible light-driven GO/Ag-ZnO ternary composites for enhanced photocatalytic degradation of amoxicillin and their antibacterial potential. Next Mater. 8, 100544. https://doi.org/10.1016/j.nxmate.2025.100544

Wang, Y., Zuo, G., Kong, J., Guo, Y., Xian, Z., Dai, Y., Wang, J., Gong, T., Sun, C., Xian, Q., 2022. Sheet-on-sheet TiO_2/Bi_2MoO_6 heterostructure for enhanced photocatalytic amoxicillin degradation. J. Hazard. Mater. 421. https://doi.org/10.1016/j.jhazmat.2021.126634

Wen, L., Liu, P., Zhou, Z., Wang, K., Zhou, Y., 2023. Biosafety Photooxidation Strategy of Levofloxacin Driven by Manganese-Doped Indium Zinc Sulfide. Chem. - An Asian J. 18, 2–8. https://doi.org/10.1002/asia.202300161

Yazdani, S., Daneshkhah, A., Diwate, A., Patel, H., Smith, J., Reul, O., Cheng, R., Izadian, A., Hajrasouliha, A.R., 2021. Model for Gold Nanoparticle Synthesis: Effect of pH and Reaction Time. ACS Omega 6. https://doi.org/10.1021/acsomega.1c01418

Zarhri, Z., Cano, A.D., Oubram, O., Ziat, Y., Bassam, A., 2022. Optical measurements and Burstein Moss effect in optical properties of Nb-doped $BaSnO_3$ perovskite. Micro and Nanostructures 166. https://doi.org/10.1016/j.micrna.2022.207223

Zhou, T., Shi, J., Li, G., Liu, B., Hu, B., Che, G., Liu, C., Wang, L., Yan, L., 2023. Advancing n-π* electron transition of carbon nitride via distorted structure and nitrogen heterocycle for efficient photodegradation: Performance, mechanism and toxicity insight. J. Colloid Interface Sci. 632. https://doi.org/10.1016/j.jcis.2022.11.073

Zulfiqar, N., Nadeem, R., Musaimi, O.A., 2023. Photocatalytic Degradation of Antibiotics via Exploitation of a Magnetic Nanocomposite: A Green Nanotechnology Approach toward Drug-Contaminated Wastewater Reclamation. ACS Omega. https://doi.org/10.1021/acsomega.3c08116

CHAPTER 6

Bio-based Synthesis of Oxygen-deficient Ni-doped TiO_2 for Photocatalytic Degradation of Furazolidone

In this chapter, a bio-based Ni-doped TiO_2 photocatalyst was synthesized using waste pineapple peel extract by focusing on reduced bandgap, increased hydrophilicity, and abundant surface defects of Ti^{3+} and oxygen vacancies. The band structures and density of Ti, O, and Ni states were analyzed using DFT studies, demonstrating comparable theoretical and experimental band gaps. Further, the synthesized photocatalyst demonstrated superior photocatalytic degradation of furazolidone (FZD) than that of bare and chemical counterparts. The photodegradation reduced the aquatic toxicity and neutralized the antimicrobial activity.

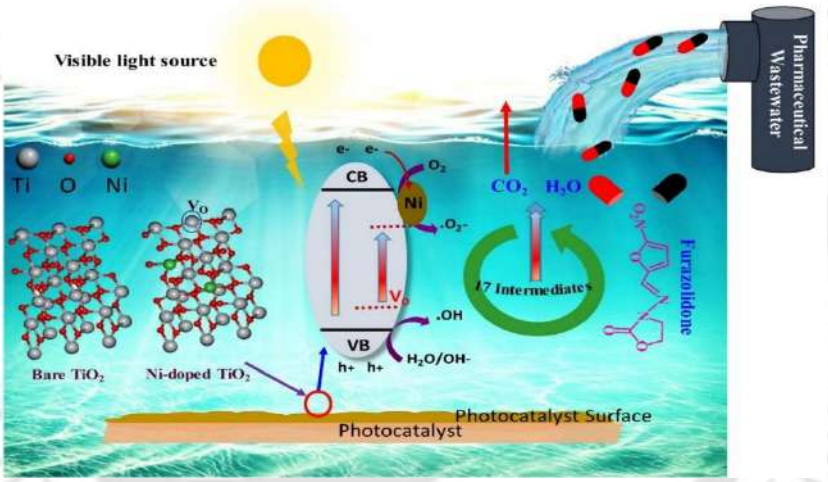

Chapter highlights

- Nature-inspired Ni-doping onto TiO_2 to increase oxygen vacancies and Ti^{3+} defects
- Density of state infers upper VB and lower CB potential mostly of O and Ti interactions
- DFT calculated bandgap well matches with UV-DRS and VB-XPS results
- Ni/TiO_2 achieves furazolidone degradation of 90.4% with 22.3 % quantum yield

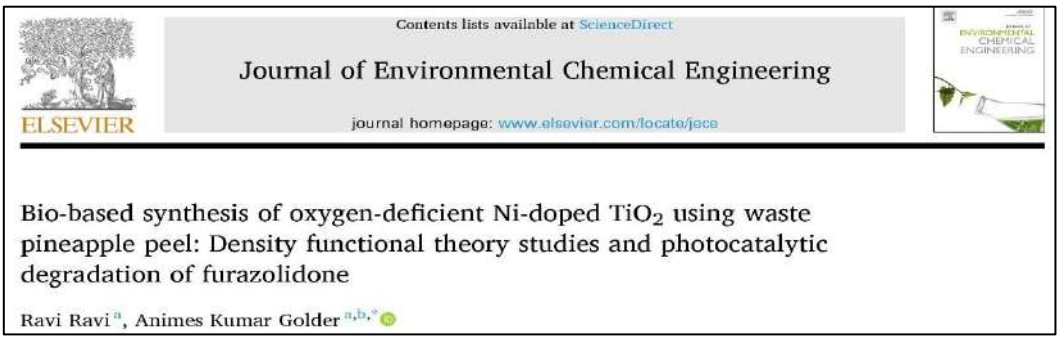

6.1 Background and executive motivation

In the last few decades, the consumption and production of pharmaceutically active compounds (PhACs) have significantly increased. This growth is attributed to factors such as global population boom, new drug development, and the recent pandemic. However, this surge in PhACs has led to groundwater and surface water contamination, posing a significant environmental threat. It could adversely affect the ecological balance and habitat conditions necessary for the optimum growth of flora and fauna (Devi et al., 2023). PhACs encompass a wide range of substances, including antibiotics, analgesics, tranquilizers, diuretics, hormones, etc. Furazolidone (FZD) is a broad-spectrum antibiotic that belongs to synthetic nitrofuran class, which is highly used for treating giardiasis (gastrointestinal infections) and diarrhea in human beings (Mohammadi et al., 2017).

FZD is also used to treat bacterial and protozoa infections in livestock animals such as pigs, cattle, fish, and poultry (McCracken et al., 2000; McCracken and Kennedy, 2013). Rapid execration in urine and high consumption of FZD result in the occurrence of FZD in surface waterbodies. A case study detected FZD in chicken liver and aviculture effluent collected from Isfahan, Iran (Mohammadi Toudeshki et al., 2018). Prolonged exposure to FZD could cause vomiting, allergic reactions, skin rash, drug fever, headache, and stomach pain and can be genotoxic carcinogenic in rare cases (Jiali Zhang et al., 2022). PhACs could easily survive the conventional treatment processes, leading to their presence in many water bodies. Therefore, it is crucial to implement effective treatment processes for PhACs containing effluents from various industrial and healthcare facilities to safeguard environmental health and prevent its widespread contamination of water.

Among various wastewater treatment methods, photocatalysis has gained massive attention for its effectiveness in degrading organic pollutants (Yan et al., 2023). This approach is valued for its high degradation efficiency, environmentally friendly characteristics, and non-selective reaction mechanism (Tao et al., 2023). Photocatalysis relies on activating photocatalysts with light energy to initiate oxidation reactions by generating free radicals that finally break down organic contaminants to CO_2 and H_2O (Cheng et al., 2020; Jahdi et al., 2020; Tao et al., 2023). This makes photocatalysis a promising and effective approach for treating water and wastewater. However, high bandgap, and rapid charge recombination, rate limited reactions process (adsorption and intra-particle diffusion), and low selectivity toward specific pollutants are some disadvantages of photocatalysis (Maarisetty et al., 2020).

Degussa P-25 TiO_2 is a promising photocatalyst for treating PhACs containing effluents and wastewater. However, its application is limited due to its relatively high bandgap energy (E_g = 3.29 eV), which restricts its ability to harness visible and solar light for photocatalytic reactions (Ghosh et al., 2018). The solar spectrum contains only 5% UV light and the exposure to UV light also can harm organisms. This limitation has confined TiO_2 to laboratory-scale experiments rather than practical applications in real-world scenarios. Indeed, developing visible-light-driven modified TiO_2 photocatalysts is crucial to harness the abundant sunlight at a larger scale for wastewater treatment (Gawal and Golder, 2024a). Lowering the bandgap energy, reducing the recombination rate, and high hydrophilicity of photocatalysts are key targets to enable effective visible light utilization (Gawal and Golder, 2024b). Various approaches and modifications, such as TiO_2 doping with other elements or materials and altering its surface characteristics, have been explored to achieve these objectives. By introducing metal dopants, the discrete energy levels of electrons within the TiO_2 structure is shifted, resulting in a reduction in the bandgap energy and delayed recombination (Cisneros et al., 2021). Recently, metals such as Fe, Mn, Pt, Au, Cu, Zn, etc., have been doped into TiO_2 to enhance their photocatalytic efficiency by targeting reduced bandgap and delayed recombination (Sukhadeve et al., 2022; Mingmongkol et al., 2023; Papitha et al., 2024; Sudha et al., 2024).

Sukhadev et al. (2022) reported an enhanced visible light-driven photodegradation of the indigo carmine dye by Fe-doped TiO_2 than bare TiO_2 with a reduction in bandgap from 3.17 to 2.82 eV (Sukhadeve et al., 2022). In another study, Mn-doped TiO_2 (E_g=2.67 eV) was highly efficient for salbutamol's photodegradation under visible light irradiation (Mingmongkol et al., 2023). Metal doping has traditionally been accomplished through various chemical routes, but these methods often result in producing harmful byproducts that can harm the environment (Bhan and Golder, 2023; Kumar and Das, 2023). In contrast, bio-based techniques utilizing plant extracts offer a promising alternative to chemical-based synthesis methods. These eco-friendly and readily available plant extracts serve dual roles as reducing and capping agents, enabling controlled synthesis of nanoparticles while minimizing unsafe environmental impact and could also increase the hydrophilicity of photocatalysts (Ramzan et al., 2021; Bhan and Golder, 2024; Kumar and Das, 2024; Bhan et al., 2025). Papitha et al. (2024) explored the reducing capabilities of *Parkia timoriana* bark, rich in ascorbic acid, in synthesizing CuO/TiO_2 and ZnO/TiO_2 nanocomposites (Papitha et al., 2024). Sudha et al. (2024) utilized *Morinda citrifolia* leaf extract to synthesize $ZnO:Mo/g\text{-}C_3N_4$ nanocomposites for photocatalytic applications (Sudha et al., 2024). Furthermore, utilizing plant waste is a

unique approach of controlling wastewater and solid waste management issues to safeguard the environment (Golder et al., 2021; Das et al., 2024).

The doping of Ni could introduce new energy levels between the valence and conduction band (CB) of TiO_2 by replacing Ti (atomic radius = 0.147 nm) with smaller Ni atoms of 0.124 nm radius, which could introduce its visible light-driven photocatalytic activity (Cheng et al., 2020; De Silva et al., 2024). Therefore, utilizing plant waste, such as pineapple peel (rich in gallic acid), for Ni doping onto TiO_2 represents a compelling pathway toward promoting environmental sustainability (Jatav et al., 2022). This study aims to functionalize TiO_2 by bio-based Ni doping using waste pineapple peel vegetal extract as the source of bio-analytes. A systematic investigation of the optical, physical, and chemical properties of TiO_2 upon Ni introduction was performed to understand the doping process. Density function theory (DFT) calculations were done for bare TiO_2 and Ni-doped TiO_2 with oxygen vacancies (OVs), both with and without Hubbard parameters. These calculations aimed to determine the theoretical geometric and band structures of both bare and Ni-doped TiO_2, which could provide valuable insights into understanding the doping mechanism. Photocatalytic degradation of FZD was conducted under various pH conditions (ranging from 3 to 8) and catalysts with different dopant concentrations under visible light irradiation. Moreover, a thorough examination of the mineralization of FZD and the intermediates that exhibit resistance to the degradation process was conducted to understand the degradation mechanism. The chemical stability and reusability of $Ni_{4.80}/TiO_2$(bio) were also investigated.

6.2 Results and discussion

6.2.1 Band structure and charge carrier separation

Fig. 6.1 illustrates the adsorbed amount and % adsorption of 5% (at%) Ni(II) onto TiO_2 surface at various pH (3 to 11) and various concentrations of Ni(II) ranging from 1 to 9% (at%) at optimized pH 7. The obtained results confirmed ~96% adsorption of Ni(II), equivalent to 4.80 % (at%) Ni(II), under the conditions of an initial Ni(II) concentration of 5% (atomic percentage) and a pH of 7.

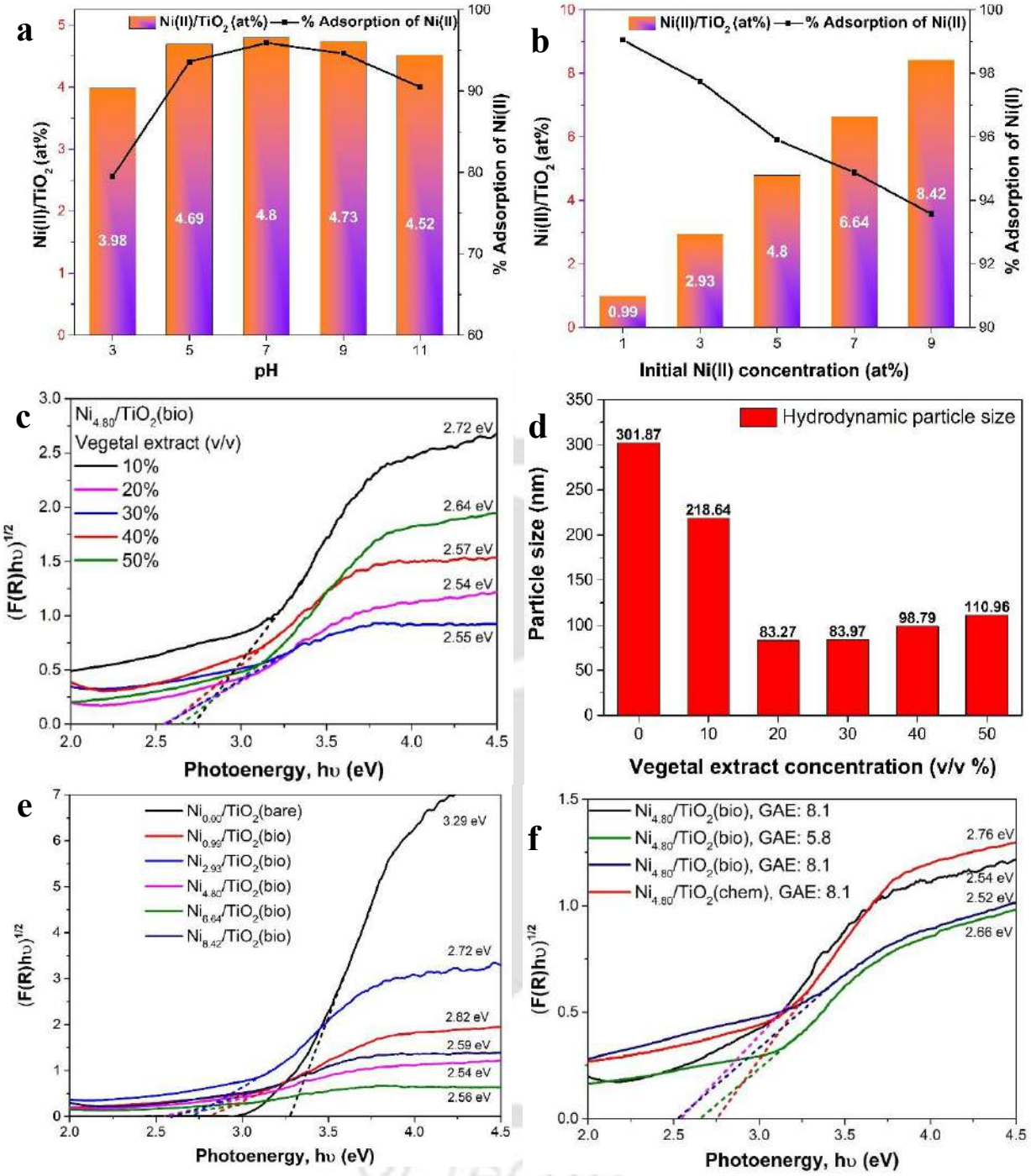

Figure 6.1: (a) Ni(II) adsorption (initial concentration 5.0% w/w Ni(II)) on TiO_2 at various pH (3-11), and (b) Ni(II) adsorption at various initial Ni(II) concentrations at optimized pH 7. (c) Optical bandgap (fitted Tau's plot) and (d) hydrodynamic particle size of $Ni_{4.80}/TiO_2$(bio) synthesized at different vegetal extract concentration (10 – 50% (v/v)); Optical bandgap (fitted Tau's plot) of (e) $Ni_{0.00}/TiO_2$(bare) and $Ni_{0.99\text{-}8.42}/TiO_2$(bio); and (f) $Ni_{4.80}/TiO_2$(bio) synthesized using different maturity waste pineapple peel vegetal extract.

Fig. 6.1c and Table 6.1 show the bandgap of $Ni_{4.80}/TiO_2$(bio) developed with various ranges of vegetal extract concentration (10-50%, v/v). The bandgap decreased from 3.29 to 2.54 eV at 20% vegetal extract, subsequently increasing to 2.64 eV at 50% vegetal extract. This change in bandgap is attributed to the formation of large Ni nanoparticles. Similarly, the hydrodynamic diameter of Ni-doped TiO_2 decreased from 301.87 to 83.27 nm with an increase in the vegetal extract concentration from 0 to 20%. However, it was gradually increased to 110.96 nm with further increase in the vegetal concentration to 50%, which indicated formation of larger Ni NPs over TiO_2 surface at higher vegetal extract concentration (Fig. 6.1d).

Additionally, the bandgap exhibited a reduction from 3.29 to 2.54 eV with the actual doping of 4.80% Ni, as observed in $Ni_{4.80}/TiO_2$(bio) (Fig. 6.1e). However, there was a slight increase in bandgap to 2.59 eV when the doped Ni concentration was raised to 8.42% (at%). This increase can be attributed to establishing a high electron density in the conduction band, a phenomenon well-supported by the Burstein-Moss effect (Gahlawat et al., 2019). The cut-off wavelength shifted from 377 to 489 nm with Ni doping, which indicates the improved efficacy of $Ni_{4.80}/TiO_2$(bio) in harnessing visible light for photocatalytic processes.

Fig. 6.1f show the Tauc's plot and bandgap of $Ni_{4.80}/TiO_2$(bio) synthesized using PP@DY (GAE, 8.1 mg L^{-1}) and PP@GY (GAE, 5.8 mg L^{-1}) vegetal extract. $Ni_{4.80}/TiO_2$(bio) synthesized using PP@DY (20% v/v) and PP@GY (28% v/v) with equal GAE showed nearly equal bandgap of 2.54 and 2.52 eV, respectively. However, PP@GY (20% v/v) based $Ni_{4.80}/TiO_2$(bio) demonstrated a higher bandgap of 2.66 eV. Additionally, $Ni_{4.80}/TiO_2$(chem) exhibited a bandgap of 2.76 eV higher than $Ni_{4.80}/TiO_2$(bio).

Table 6.1: Optical bandgap of $Ni_{0\text{-}8.42}/TiO_2$ synthesized using 20% vegetal extract and at various vegetal extract concentrations (10-50% v/v) in synthesizing $Ni_{4.80}/TiO_2$(bio).

Catalyst	Vegetal extract concentration (%) of 8.1 mg L^{-1} GAE*	Bandgap energy (eV)
$Ni_{4.80}/TiO_2$(bio)	10	2.72
	20	**2.54**
	30	2.55
	40	2.56
	50	2.64
$Ni_{0.00}/TiO_2$(bare)	20	3.29
$Ni_{0.99}/TiO_2$(bio)		2.82
$Ni_{2.93}/TiO_2$(bio)		2.72
$Ni_{6.64}/TiO_2$(bio)		2.56
$Ni_{8.42}/TiO_2$(bio)		2.59
$Ni_{4.80}/TiO_2$(chem)	20 (8.1 mg L^{-1} Gallic acid)	2.78

Fig. 6.2a provides insight into VB-XPS spectra and band structure (inset of Fig. 6.2a) of $Ni_{0.00}/TiO_2$(bare) and $Ni_{4.80}/TiO_2$(bio). The introduction of Ni caused the VB to rise from -0.75 to -0.52 eV, which could attributed to the abundance of oxygen vacancies above the VB (Yang et al., 2017). Additionally, the CB was shifted from 2.54 to 2.02 eV due to Ni impurities and Ti^{3+} defects. Consequently, OVs, Ti^{3+} defects, and Ni impurities collectively reduced the bandgap observed in Ni-doped TiO_2.

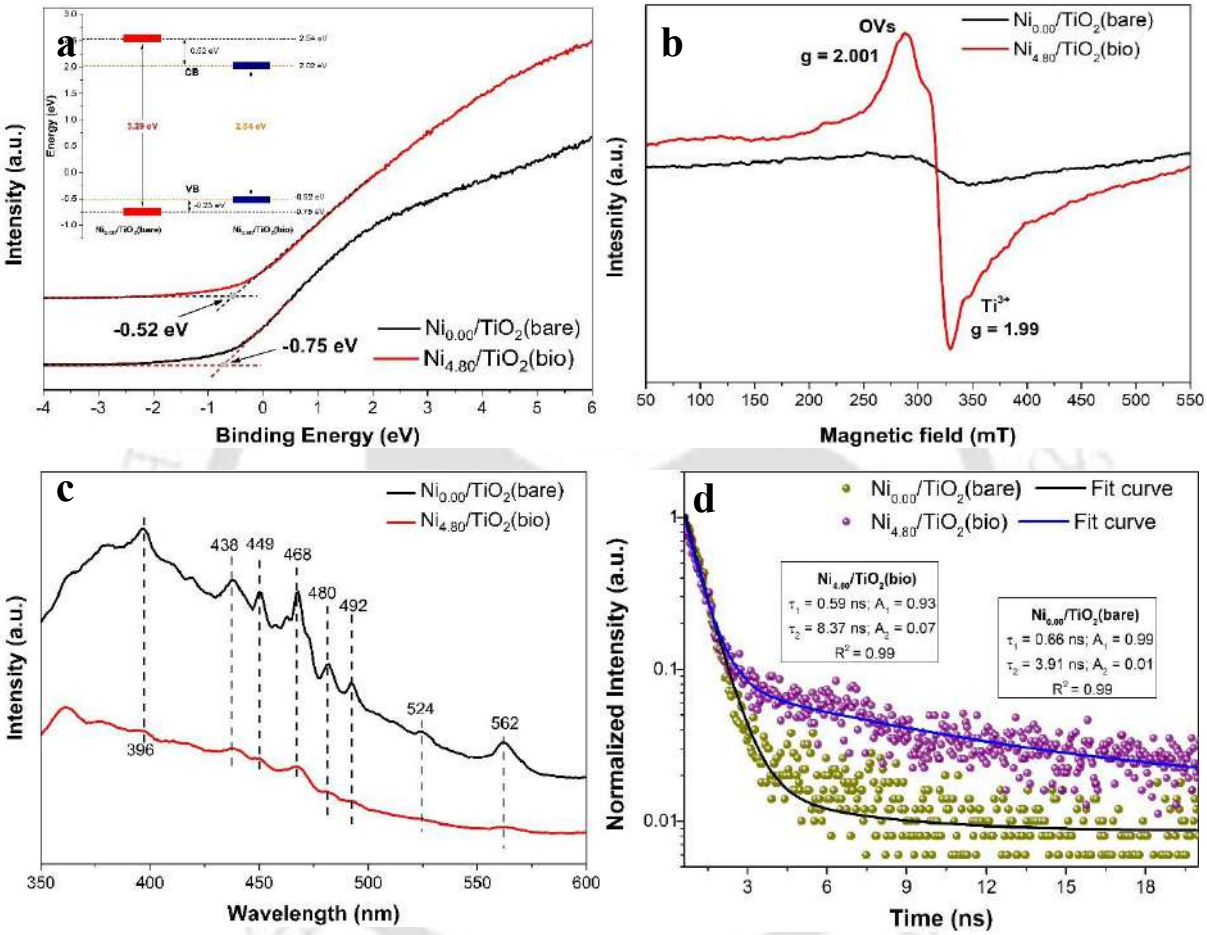

Figure 6.2: (a) Valence band - X-ray photoelectron spectroscopy (VP-XPS) spectra, and energy levels (CB and VB) diagram (inset), (b) Electron paramagnetic resonance (EPR) spectra (EPR spectra, showing Ti^{3+} defects and oxygen vacancies, (c) Photoluminescence (PL), and (d) Time-resolved photoluminescence (TRPL) spectra of $Ni_{0.00}/TiO_2$(bare) and $Ni_{4.80}/TiO_2$(bio).

EPR spectra of $Ni_{0.00}/TiO_2$(bare) and $Ni_{4.80}/TiO_2$(bio) are presented in Fig. 6.2b. The results reveal the presence of two distinct peaks at g-values of 1.99 and 2.001 in $Ni_{4.80}/TiO_2$(bio). EPR peak at 1.99 is attributed to Ti^{3+} defects, and the peak at a g-value of 2.001 indicates the abundance of OVs in $Ni_{4.80}/TiO_2$(bio) (Komaraiah et al., 2020). In contrast,

negligible EPR peaks were observed in $Ni_{0.00}/TiO_2$(bare), indicating the presence of insignificant OVs and Ti^{3+} defects. These defects could play a crucial role in enhancing charge separation and reducing the bandgap by introducing free electrons generated from oxygen vacancies and acting as charge carrier traps in the form of Ti^{3+} defects (Wang et al., 2024).

Photoluminescence (PL) and time-resolved photoluminescence (TRPL) analyses were performed to investigate the charge separation and recombination of free e^-/h^+ recombination in $Ni_{0.00}/TiO_2$(bare) and $Ni_{4.80}/TiO_2$(bio). A lower PL intensity was observed in $Ni_{4.80}/TiO_2$(bio) spectrum (Fig. 6.2c) compared to that of $Ni_{0.00}/TiO_2$(bare). This decrease in PL intensity indicates that the charge separation was improved with Ni doping. In particular, the charge carrier recombination (396 nm) was decreased with the involvement of free excitons due to OVs (449 nm) and shallow traps of Ti^{3+} (468 nm) (Baruah et al., 2022).

The TRPL spectra of $Ni_{0.00}/TiO_2$(bare) and $Ni_{4.80}/TiO_2$(bio) are presented in Fig. 6.2d, indicated high dispersion of the data points, which could be due to distinct recombination lifetime of anatase and rutile phases of TiO_2. It is observed that the Ni-doping led to an increase in the decay time (τ_2) of free charge carriers from 3.91 to 8.39 ns. This longer decay time determines the deferred Shockley-Read-Hall (SRH) recombination in $Ni_{4.80}/TiO_2$(bio) due to presence of charge traps as Ni metal along with Ti^{3+} defects and oxygen vacancies, indicating the improved capacity for charge carriers to remain separated and, therefore, contributes to the enhanced photocatalytic performance (Gogoi et al., 2021).

Overall, the abundance of OVs, Ti^{3+} defects, and Ni impurity synergistically reduced the bandgap and delayed the free e^-/h^+ recombination, which could potentially increase the visible light-driven photocatalytic efficacy of Ni-doped TiO_2.

6.2.2 Structural and morphological analysis

X-ray diffraction (XRD) patterns shown in Fig. 6.3a provide valuable insights into the crystal structures of $Ni_{0.00}/TiO_2$(bare) and $Ni_{0.99\text{-}8.42}/TiO_2$(bio). These patterns reveal that all the catalysts contain both the anatase phase (corresponding to JCPDS file No. 01-021-1272) and the rutile phase (corresponding to JCPDS file No. 01-21-1276) of TiO_2 (Baruah et al., 2022). However, two small peaks were observed in the $Ni_{4.80\text{-}8.42}/TiO_2$(bio) samples at 2θ values of 33.51 and 59.46°. These peaks correspond to oxidized form of Ni such as NiO, and NiOOH (as per JCPDS file No. 00-022-1189). However, these peaks were not detected in the samples with lower concentrations of Ni ($Ni_{0.99\text{-}2.93}/TiO_2$(bio)) (Kaiba et al., 2020).

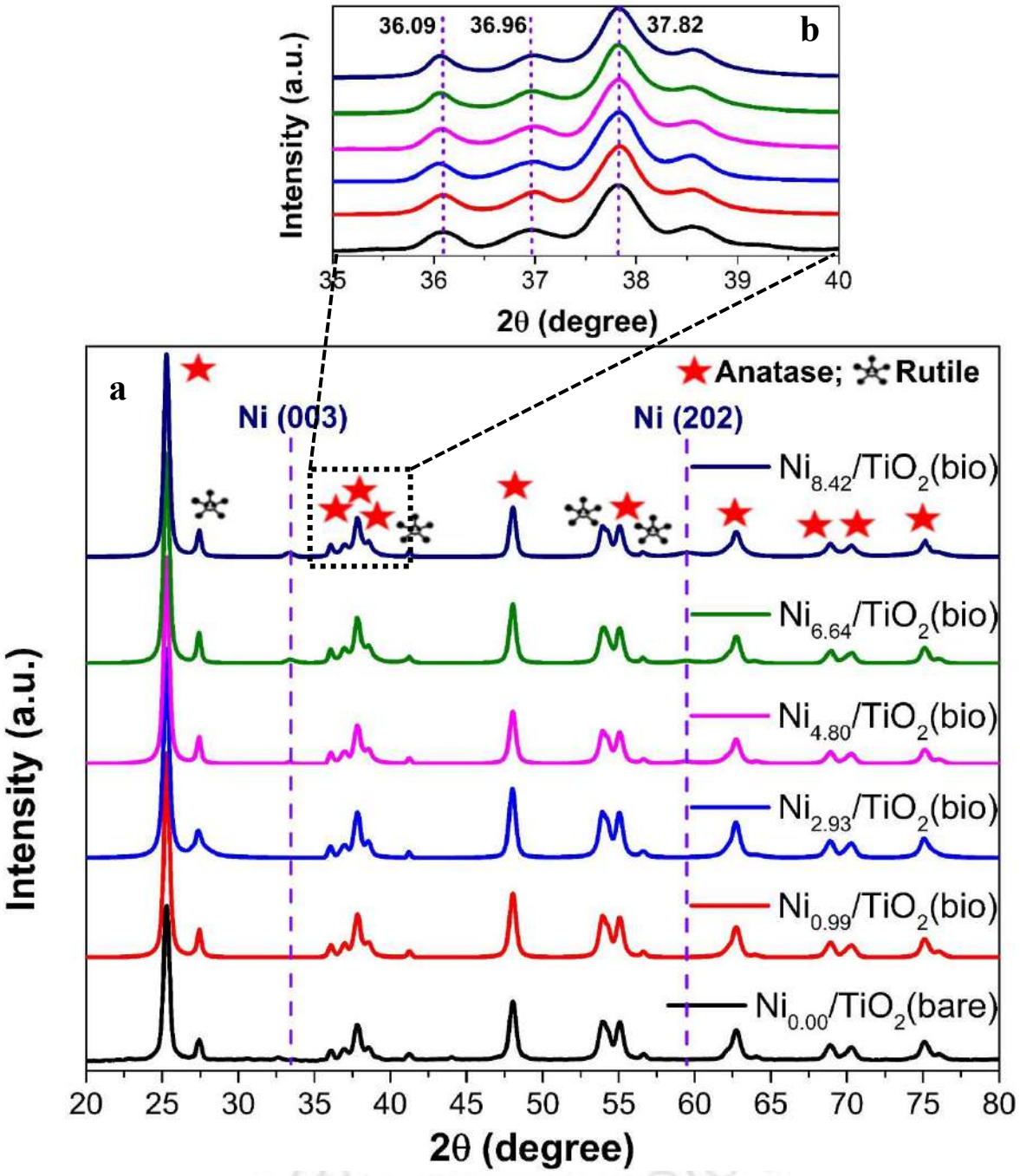

Figure 6.3: (a) X-ray diffraction (XRD) patterns, and (b) Magnified XRD patterns, showing peak shifting in $Ni_{0.00}/TiO_2$(bare) and $Ni_{0.99\text{-}8.42}/TiO_2$(bio). Here, "red star symbol" represents the anatase phase and "blue star symbol" represents the rutile phase of TiO_2.

Furthermore, there is an observable shift in the XRD peaks of TiO_2 at 2θ values of 36.09, 36.96, and 37.82° after Ni doping (Fig. 6.3b). This shift in the peak positions suggests that the incorporation of Ni into the TiO_2 lattice has occurred, altering the crystal structure (Bhan and Kumar Golder, 2023). The increase in the amount of Ni has led to noticeable variations in the crystallite size and lattice structure of the catalysts. The ratio of anatase/rutile

phases gradually decreased with increasing Ni concentration (Table 6.2). Moreover, the crystallite size of catalysts increased with higher Ni concentrations. This increase in crystallite size can be attributed to the filling of voids and the substitution of Ti with Ni within the TiO_2 lattice (Valian et al., 2023). Additionally, Ni doping appears to result in a decrease in lattice strain and dislocation density. This decrease could be due to relaxing of TiO_2 lattice through re-distribution of internal stress by introducing Ni dopant, and oxygen vacancies. A reduction in lattice strain and dislocations can enhance the diffusivity of free radicals within the catalyst, potentially increasing the overall catalytic activity (Li et al., 2019).

Table 6.2: XRD parameters of $Ni_{0.00}/TiO_2$(bare) and $Ni_{0.99\text{-}8.42}/TiO_2$(bio).

Sample	Crystallite size (nm)	Anatase (%)	Rutile (%)	Lattice strain (ε)	Dislocation densities (Lines/nm^2)
$Ni_{0.00}/TiO_2$(bare)	20.53	80	20	8.07×10^{-3}	2.37×10^{-3}
$Ni_{0.99}/TiO_2$(bio)	20.80	79.82	20.18	7.95×10^{-3}	2.31×10^{-3}
$Ni_{2.93}/TiO_2$(bio)	20.87	79.55	20.45	7.94×10^{-3}	2.30×10^{-3}
$Ni_{4.80}/TiO_2$(bio)	21.01	78.77	21.23	7.88×10^{-3}	2.27×10^{-3}
$Ni_{6.64}/TiO_2$(bio)	21.09	78.04	21.96	7.85×10^{-3}	2.25×10^{-3}
$Ni_{8.42}/TiO_2$(bio)	21.25	76.68	23.32	7.79×10^{-3}	2.21×10^{-3}
$Ni_{0.00}/TiO_2$(bare)	20.53	80	20	8.07×10^{-3}	2.37×10^{-3}

Figs. 6.4a and 6.4b illustrate the FETEM images of $Ni_{0.00}/TiO_2$(bare) and $Ni_{4.80}/TiO_2$(bio). In these images, the catalysts were observed as spherical, and the average particle size was increased from 21.07±2.51 to 22.16±2.77 nm with Ni doping. This increase in particle size could be attributed to the expansion of the lattice of TiO_2 and the adherence of Ni and its oxide nanoparticles on the surface of TiO_2. The d-spacing values of 0.352 (anatase) and 0.325 nm (rutile) in both catalysts indicate the presence of both anatase and rutile phases of TiO_2 (Fig. 6.4c). However, an additional fringe width with a d-spacing value of 0.268 (003) nm in $Ni_{4.80}/TiO_2$(bio) (Fig. 6.4d) corresponds to the presence of Ni nanoparticles, indicating the successful doping of Ni into the TiO_2 lattice. Figs. 6.4e and 6.4f show SAED patterns of both catalysts, confirming the polymorphic nature of the $Ni_{0.00}/TiO_2$(bare) and $Ni_{4.80}/TiO_2$(bio) (Gawal and Golder, 2024c).

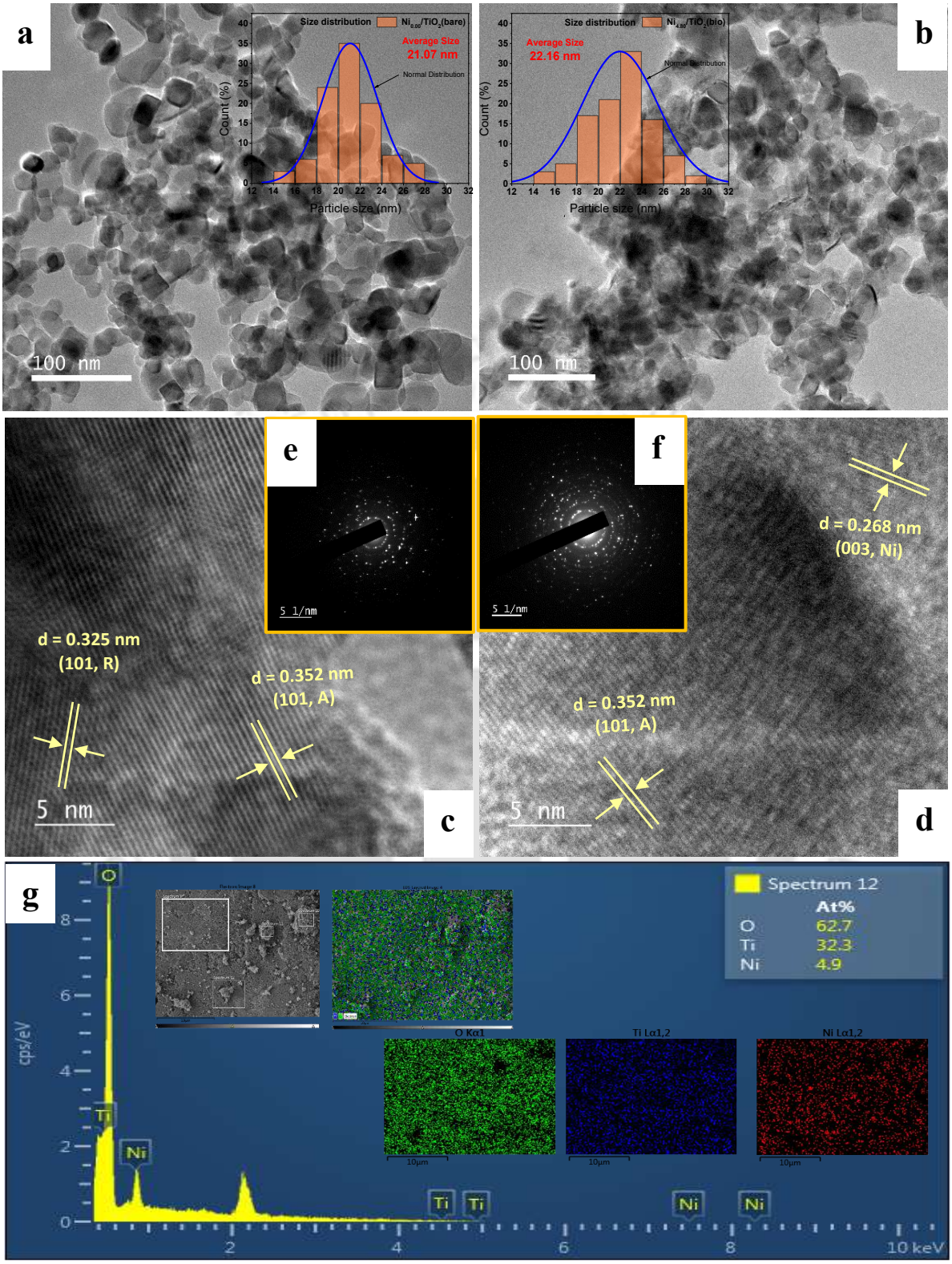

Figure 6.4: FETEM images showing morphology of (a) $Ni_{0.00}/TiO_2$(bare) and (b) $Ni_{4.80}/TiO_2$(bio) with insets illustrate the particle size distribution. (c and d) HRTEM images, and (e and f) SAED patterns of $Ni_{0.00}/TiO_2$(bare) and (d) $Ni_{4.80}/TiO_2$(bio). (g) EDX spectra and elemental mapping of $Ni_{4.80}/TiO_2$(bio).

6.2.3 Elemental and chemical states analysis

The EDX spectra and elemental mapping of $Ni_{4.80}/TiO_2$(bio) are illustrated in Fig. 6.4g. Notably, the elements Ti, O, and Ni were uniformly distributed, facilitating better photocatalytic activity due to the accessibility of active sites from all directions (Behnood and Sodeifian, 2022). The composition of Ni was found to be 4.9%, which is close to the Ni concentration (%) calculated by AAS analysis.

The XPS high resolution and survey spectra of chemical states of $Ni_{0.00}/TiO_2$(bare) and $Ni_{4.80}/TiO_2$(bio) are shown in Fig. 6.5a-6.5e and Fig. 6.5f, respectively. The composition of the chemical states is detailed in Table 6.3. The XPS survey spectra confirmed the presence of peaks correspond to Ti2p, O1s, and Ni2p states. Additionally, a peak represents C1s state was observed at 284.8 eV. Two peaks in the range of 0-100 eV are attributed to Ti3s and Ti3p states, appeared due to ejection of core-level electrons of Ti atoms due to high interaction with high energy photons during XPS analysis. An Auger peak of oxygen was also observed at 900-1000 eV, which could be generated due to releasing of energy during filling of the core holes with electrons from VB (Iatsunskyi et al., 2015; Appadurai et al., 2019; Velasquez-Tamayo et al., 2023). In the Ti2p spectra (Fig. 6.5a) of $Ni_{0.00}/TiO_2$(bare), two characteristic peaks at 460.4 and 466.2 eV, corresponding to Ti^{4+} were observed. However, these peaks were shifted to 458.8 and 464.5 eV after Ni-doping, respectively. Additionally, a small peak representing Ti^{3+} defects was observed in $Ni_{4.80}/TiO_2$(bio) (Fig. 6.5b) (Jianjun Zhang et al., 2022). Similarly, the O1s states, representing lattice oxygen (O_{lat}, at 531.7 eV) and surface adsorbed oxygen (O_{ads}, at 533.3 eV), of $Ni_{0.00}/TiO_2$(bare) shifted by -1.6 and 2.0 eV, respectively, with Ni doping (Figs. 6.5c and 6.5d). Two additional low-intensity peaks corresponding to C-O/N-O (at 532.3 eV) and NiOOH (at 533.4 eV) were also observed in $Ni_{4.80}/TiO_2$(bio) (Kotta et al., 2020; Wang et al., 2020). These changes in the Ti2p and O1s states and the appearance of Ti^{3+} defects suggest the presence of oxygen vacancies and the substitution of Ti^{4+} by Ni^{2+} in $Ni_{4.80}/TiO_2$(bio). These modifications enhance the free electron density in the Ni-doped catalyst, which is an important factor affecting its photocatalytic activity (Cheng et al., 2020).

Fig. 6.5e illustrates the high-resolution spectra of $Ni2p_{3/2}$, and the obtained spectra reveal the presence of three characteristic peaks corresponding to different nickel states: metallic Ni (Ni^0, 853.8 eV), lattice incorporated Ni^{2+}/Ni-O (Ni^{2+}, 855.8 eV), and NiOOH (Ni^{3+}, 857.5 eV) (Fan et al., 2016). These peaks indicate that approximately 74.2% of Ni^{2+} ions were either incorporated into the TiO_2 lattice by replacing $Ti^{4+}$and entering into interstitial sites or present in the form of NiO on TiO_2 surface, while the remaining Ni nanoparticles adhered to the TiO_2 surface.

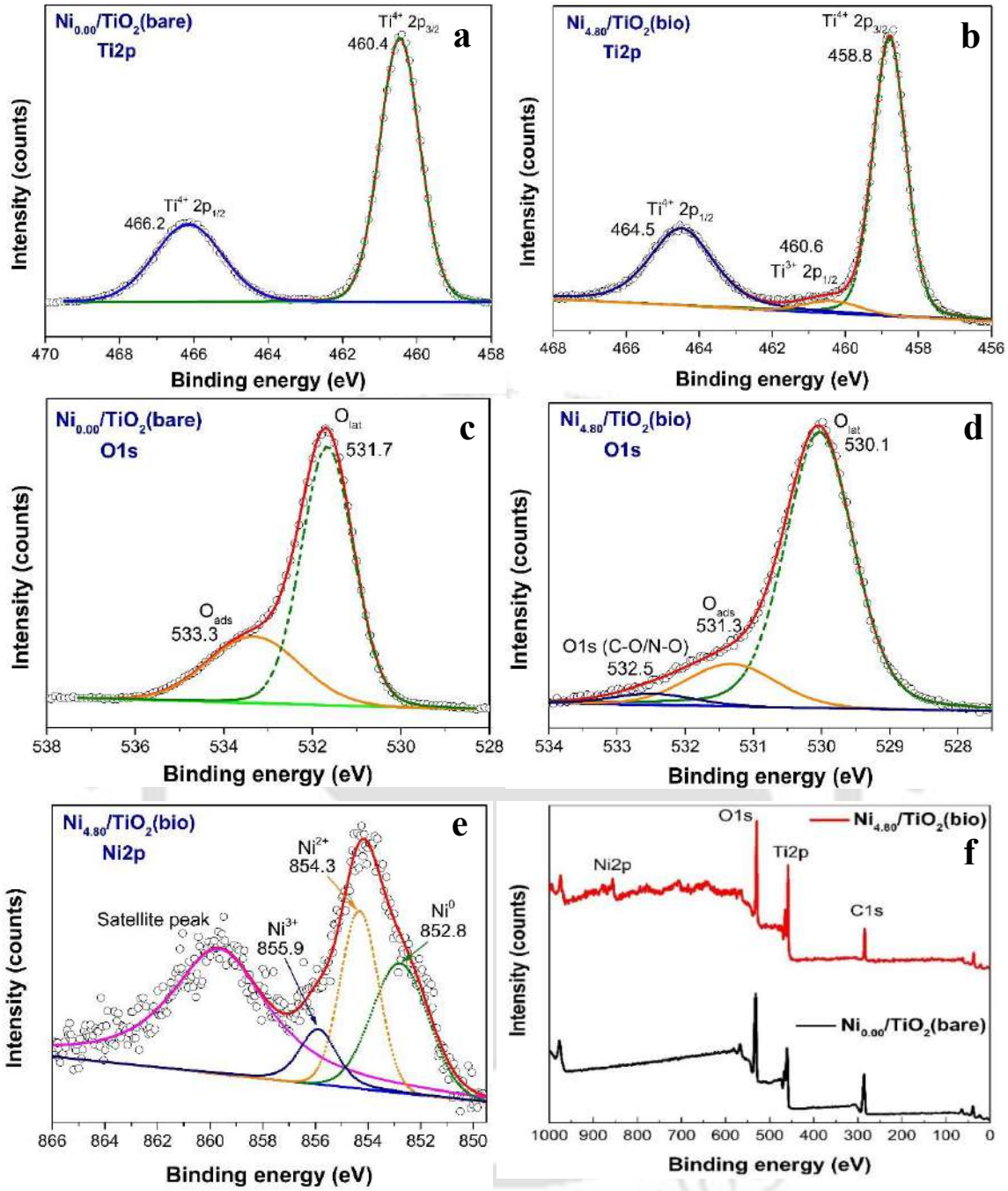

Figure 6.5: XPS spectra of Ti2p of (a) $Ni_{0.00}/TiO_2$(bare), and (b) $Ni_{4.80}/TiO_2$(bio); O1s of (c) $Ni_{0.00}/TiO_2$(bare), and (d) $Ni_{4.80}/TiO_2$(bio); and e) Ni2p of $Ni_{4.80}/TiO_2$(bio) and (f) XPS survey spectra of $Pd_{0.00}/TiO_2$(bare), and $Pd_{1.00}/TiO_2$(bio).

The Ni doping process involves the lattice insertion of Ni^{2+} into TiO_2 lattice with simultaneous reduction of Ni^{2+} to Ni^0 (~16.2%) over TiO_2 surface. It also undergoes a slow oxidation of the metallic Ni results in the transformation of surface Ni nanoparticles into NiO and NiOOH (~9.6%) nanoparticles through interaction with surface oxygen and H_2O molecules. The Ni oxides and hydroxides species acts as electron traps, reducing recombination

rate of charge carriers. They facilitate the photogeneration of superoxide radicals by accepting electrons and promote the formation of hydroxyl radicals via the hydroxyl groups of NiOOH. These properties, combined with enhanced pollutant-catalyst interactions due to hydroxyl groups and the direct oxidative activity of NiOOH, synergistically enhance the photocatalytic activity of Ni-doped TiO_2 (Guo et al., 2022). Additionally, a satellite peak was also observed in at 859.8 eV. Under X-ray exposure, the surface plasmons of free electrons excites, and their relaxation emits photoelectrons from the VB at higher binding energies, leading to the appearance of the satellite peak (Pauly et al., 2016; Stozharov, 2022).

Table 5.3: Relative elemental and configuration state composition of $Ni_{0.00}/TiO_2$(bare), and $Ni_{4.80}/TiO_2$(bio), analyzed through XPS.

Element	**State**	**Sample (% area)**	
		$Ni_{0.00}/TiO_2$(bare)	**$Ni_{4.80}/TiO_2$(bio)**
Ti	Ti^{4+} 2p	48.2	41.9
	Ti^{3+} 2p	-	3.7
	Ti 2p (Total)	48.2	45.6
O	O_L 1s	40.4	38.6
	O_a 1s	11.4	7.1
	O(C-O/N-O) 1s	-	3.6
	O(NiOOH) 1s	-	0.3
	O 1s (Total)	51.8	49.6
Ni	Ni(0) 2p	-	0.78
	Ni(II) 2p	-	3.56
	Ni(III) 2p		0.46
	Ni 2p (Total)	-	~4.8

6.2.4 Other physical characteristics

Fig. 6.6a illustrates the water contact angle of $Ni_{0.00}/TiO_2$(bare) and $Ni_{4.80}/TiO_2$(bio). The water contact angle of $Ni_{0.00}/TiO_2$(bare) was determined to be 120.8°. However, with Ni doping, this contact angle decreased significantly to 52.9°. The decrease in the water contact angle indicates a transition from a hydrophobic to a hydrophilic surface due to the modification of the TiO_2 surface by introducing Ni nanoparticles and adherence of functional groups from vegetal extract. Doping of Ni nanoparticles could alter the pore structure of TiO_2, and the surface functional groups can form hydrogen bonding with water molecules, resulting in formation of hydration layers over catalysts surface increasing its hydrophilicity (Zhao et al., 2021). Hydrophilic catalysts are known to exhibit enhanced photocatalytic efficiency

compared to hydrophobic catalysts. Hydrophilic catalysts generate more free radicals and provide better access to pollutants, resulting in improved photocatalytic activity (Mimouni et al., 2020).

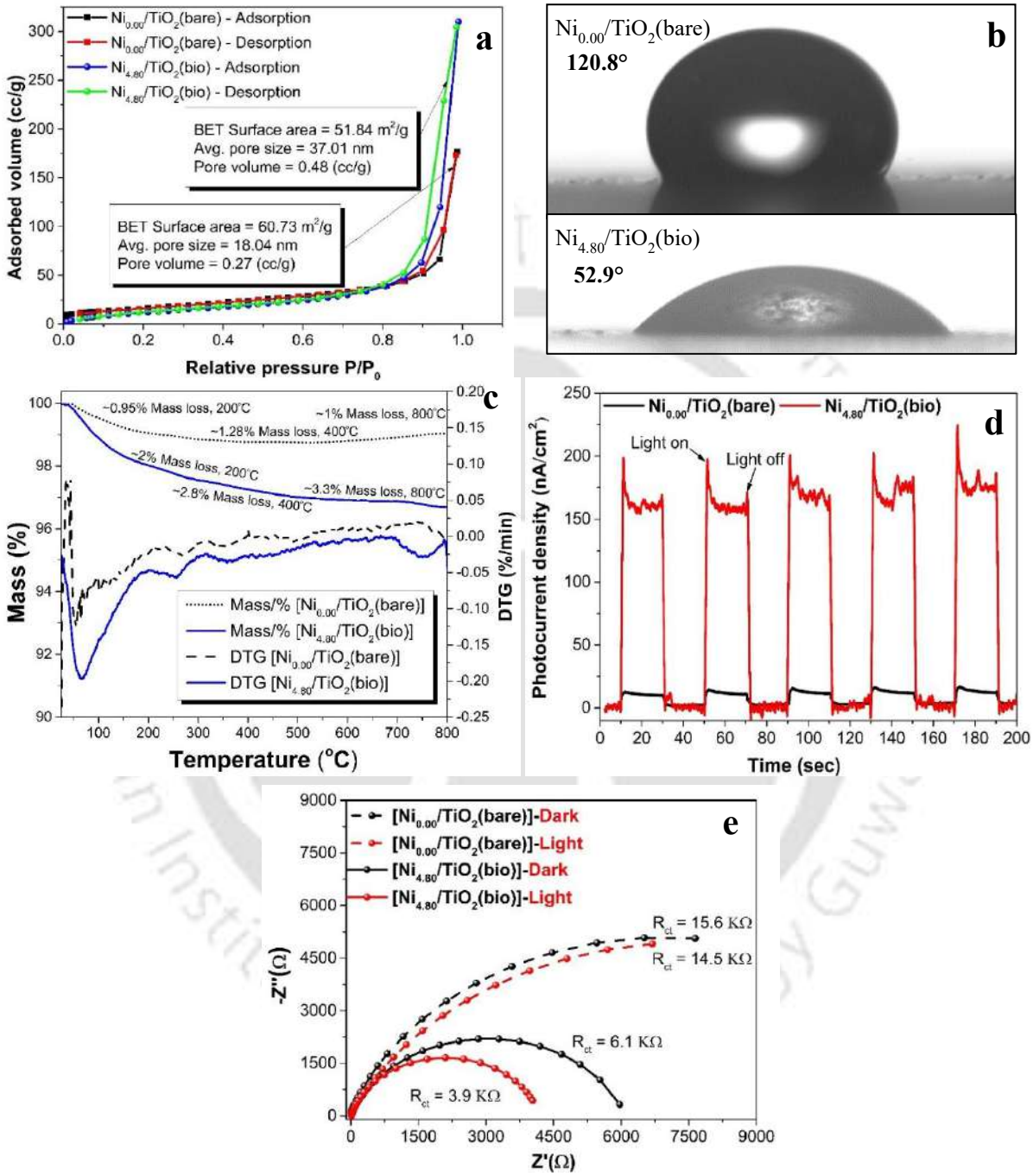

Figure 6.6: (a) Water contact angle, and (b) N_2 adsorption-desorption isotherm plots and BET parameters, and TGA profile (c) of $Ni_{0.00}/TiO_2$(bare) and $Ni_{4.80}/TiO_2$(bio); (d) Photocurrent at 20s intervals of light on/off cycles, and (e) Nyquist's plot (EIS) of $Ni_{0.00}/TiO_2$(bare) and $Ni_{4.80}/TiO_2$(bio) in presence/absence of light irradiation.

The pore size distribution and N_2 adsorption-desorption isotherms of $Ni_{0.00}/TiO_2$(bare) and $Ni_{4.80}/TiO_2$(bio) are shown in Fig. 6.6b. The obtained pattern follows type IV isotherm, indicating that both catalysts are mesoporous materials (Li et al., 2022). In comparison to $Ni_{0.00}/TiO_2$(bare), $Ni_{4.80}/TiO_2$(bio) exhibits an increase in both average pore size and pore volume, which rise from 0.27 cc g^{-1} and 18.04 nm to 0.47 cc g^{-1} and 37.01 nm, respectively. However, the BET surface area decreases from 60.73 m^2 g^{-1} for $Ni_{0.00}/TiO_2$(bare) to 51.84 m^2 g^{-1} for $Ni_{4.80}/TiO_2$(bio). This reduction in BET surface area in the Ni-doped sample may be attributed to the combined effects of pores filling by Ni nanoparticles and expansion of the crystal structure of TiO_2 upon Ni introduction.

Fig. 6.6c present the thermogravimetric profiles of $Ni_{0.00}/TiO_2$(bare) and $Ni_{4.80}/TiO_2$(bio). In $Ni_{4.80}/TiO_2$(bio), a mass loss of ~2% was observed at 200 °C, which gradually increased to 2.8% at 400 °C and 3.3% at 800 °C. This mass loss is likely attributed to the evaporation of water and deprivation of surface-adsorbed bio-analytes from the vegetable extract used in the synthesis process. On the other hand, $Ni_{0.00}/TiO_2$(bare) shows a lower mass loss of 0.95% at 200°C and 1.28% at 400°C. Interestingly, a slight mass gain was observed at temperatures exceeding 500°C, possibly due to buoyancy effects at higher temperatures (Nasrollahzadeh et al., 2019). The mass loss observed at temperatures below 200°C in both samples is likely due to the evaporation of water (Bhan and Golder, 2023). These results suggest that both catalysts possess excellent stability at higher temperatures.

6.2.5 Photoelectrochemical analysis

Chronoamperometric analysis was conducted to evaluate the photocurrent density of $Ni_{0.00}/TiO_2$(bare) and $Ni_{4.80}/TiO_2$(bio) with on/off light cycles at 20s intervals. $Ni_{4.80}/TiO_2$(bio) demonstrated an excellent photocurrent density of 197.75 nA cm^{-2} (Fig. 7c), which is 11.65 times higher than that of $Ni_{0.00}/TiO_2$(bare) (16.98 nA cm^{-2}). However, a slight decrease in photocurrent density of $Ni_{4.80}/TiO_2$(bio) was observed just after light irradiation. This decrease could be attributed to trapping generated electrons in traps formed from oxygen vacancies, Ti^{3+} defects, and Ni nanoparticles (Wang et al., 2016).

Electrochemical impedance spectra (EIS) were obtained using an integrated frequency response analyzer (FRA), and the EIS data was fitted in a Nyquist's plot (Fig. 7d) (Bhan and Kumar Golder, 2023). $Ni_{0.00}/TiO_2$(bare) exhibited a charge transfer resistance (R_{ct}) of 15.6 and 14.5 KΩ under dark and light irradiation, respectively. However, after Ni-doping, these R_{ct} values decreased to 6.1 and 3.9 KΩ, respectively. In $Ni_{4.80}/TiO_2$(bio), the R_{ct} value remarkably

decreased under light irradiation compared to dark conditions. This decrease in R_{ct} value could be due to increased electron density and conductivity of $Ni_{4.80}/TiO_2$(bio) than that of $Ni_{0.00}/TiO_2$(bare), resulting in in prevention of electron loss and uniform charge transfer channels (Ayaz et al., 2024). Conclusively, the improved photocurrent density and decreased R_{ct} in $Ni_{4.80}/TiO_2$(bio) indicate its excellent photo and electrochemical functionalities, which could enhance its photocatalytic activity under visible light (Senobari and Nezamzadeh-Ejhieh, 2020).

6.2.6 DFT analysis

The theoretical analysis using DFT calculations, both with and without Hubbard parameters, was conducted to understand the impact of Ni doping and OVs on the band structure of TiO_2. The self-consistent energy calculations performed to optimized the plane-wave energy cut-off and k-points mesh are shown in Fig. 6.7.

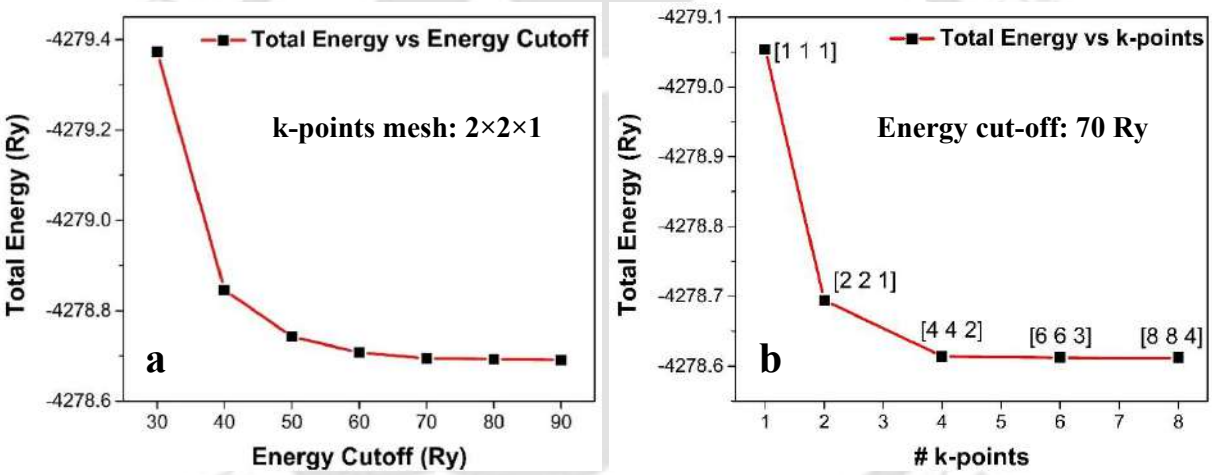

Figure 6.7: Self-consistent energy calculations: (a) Optimization of plane-wave energy cut-off (energy cutoff vs. total energy) and (b) k-points mesh (#k-point vs total energy).

Figs. 6.8a-6.8d illustrate the band structure and PDOS plot of both bare and Ni-doped TiO_2. The results are summarized in Table 5.4, including calculation method, Hubbard parameters, calculated bandgaps, and their difference with experimental bandgaps. The bandgap of bare TiO_2 was determined as 2.06 eV using the GGA-PBE method, as illustrated in Fig. 6.8a. When the GGA-PBE+U method, which incorporates Hubbard parameters, was employed, the bandgap increased to 3.25 eV (Fig. 6.8b). This value is close enough to the experimental bandgap of 3.29 eV. The introduction of the Hubbard parameters led to notable shifts in the VB and CB positions of bare TiO_2. Specifically, the VB shifted downward from -

0.15 to -0.73 eV, aligning closely with the VB position of TiO_2 (-0.75 eV) as determined by VB-XPS (Fig. 3d). Similarly, the CB shifted upward from 1.91 eV to 2.53 eV, nearly matching the experimental CB position at 2.54 eV. These adjustments likely contribute to the observed increase in the calculated bandgap and its closer agreement to the experimental results. Additionally, the PDOS plots stated that the upper VB and lower CB were primarily attributed to O and Ti, respectively. Similar results were also observed in reported studies (Ruiz Preciado et al., 2015; Salehi-Abar and Kazempour, 2017; Johari et al., 2022).

Following Ni doping and the introduction of VOs, the calculated bandgap of TiO_2 was initially determined to be 0.98 eV (Fig. 6.8c) using the GGA-PBE method. This value increased to 2.57 eV (Fig. 6.8d) when Hubbard parameters were incorporated (GGA-PBE + U). Upon Ni doping and OVs adoption, new states associated with Ni/OVs and Ni orbits appeared between the VB and CB of TiO_2 (Lin et al., 2012). This caused shifts in their positions to -0.05 eV and 0.93 eV, respectively, and increases in bands density at both VB and CB. With the application of the GGA-PBE+U method, these bands experienced further shifts, with the VB and CB moving to -0.54 eV (downward) and 2.02 eV (upward), respectively. These theoretical band positions closely matched the experimentally determined VB and CB positions, measured at -0.52 eV and 2.02 eV, respectively (Fig. 6.2a). Notably, the Ni/OVs and Ni bands merged with the VB and CB bands of TiO_2. In the PDOS plot depicted in Fig. 8c, two new peaks were observed between the VB and CB with Ni doping and OVs, without considering Hubbard parameters. However, these peaks were shifted and merged with the bands of TiO_2 when Hubbard parameters were included in the DFT calculation. The GGA-PBE+U method broadened the bands by shifting them away from the Fermi level. Consequently, the electronic structure and properties obtained through DFT calculations are in close proximity with UV-DRS and VB-XPS based experimental bandgaps and their arrangements as the maximum difference observed was only 1.2%. Additionally, the E_f of oxygen deficient Ni-doped TiO_2 model was found to be -21.68 eV. A negative E_f value supports thermodynamic feasibility, indicating stability of oxygen deficient Ni-doped TiO_2 (Zhang et al., 2014). The insertion of the Ni state and OVs could contribute in adsorption of visible light and better charge separation, which is also in alignment with experimental characteristics.

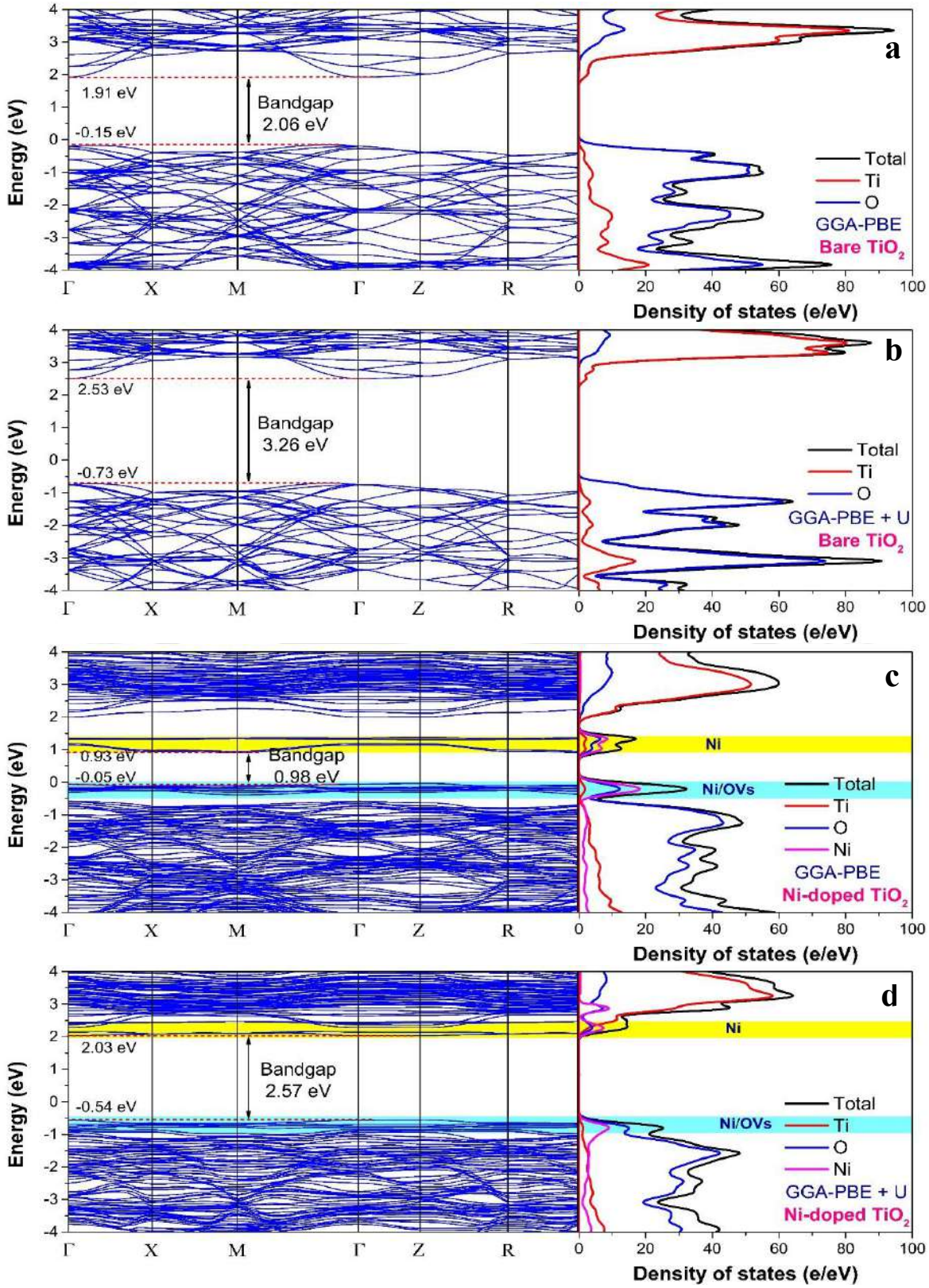

Figure 6.8: Band structure profile and PDOS plot of bare TiO_2 acquired using (a) GGA-PBE and (b) GGA-PBE+U method. Band structure profile and PDOS plot of Ni-doped TiO_2 with oxygen vacancies procured through (c) GGA-PBE and (d) GGA-PBE+U method.

Table 6.4: Comparison of calculated and experimental bandgaps of bare TiO_2 and Ni-doped TiO_2. The theoretical bandgaps were calculated with and without Hubbard parameters.

Photocatalyst	Method	Hubbard parameter (eV)	Cal. bandgap (eV)	Exp. bandgap (eV)	Difference (%)
Bare TiO_2	GGA-PBE	-	2.06	3.29	-37.4
	GGA-PBE+U	U (Ti) = 2.0	3.26		-0.9
		U (O) = 6.0			
Ni-doped TiO_2	GGA-PBE	-	0.98	2.54	-61.4
	GGA-PBE+U	U (Ti) = 2.0	2.57		+1.2
		U (O) = 6.0			
		U (Pd) = 4.7			

"-" sign indicates lower calculated bandgap; **"+"** sign indicates higher cal. bandgap than exp. data.

6.2.7 Photocatalytic degradation of FZD

Fig. 6.9 provides valuable insights into the photocatalytic degradation of FZD, with a focus on the non-linear first-order kinetic models (Figs. 6.9a and 6.9b), FZD photocatalytic degradation (%), and quantum yield (QY) across different pH levels (ranging from 3 to 7) and various Ni concentrations (ranging from 0 to 8.42 at%). The obtained parameters are tabulated in the Table 6.5. As pH of the solution increases from 3 to 7, both FZD photocatalytic degradation (%) and QY (%) experience a decrease, dropping from 90.44±2.73 to 57.03±2.57% and from 22.27±0.41 to 14.04±0.47%, respectively (Fig. 6.9c). Additionally, the rate constant (k_1) also decreased from 0.89×10^{-2} to 2.19×10^{-2} min^{-1}.

This trend can be attributed to the interaction of free H^+ ions with the loosely bound O^- ions of FZD, resulting in the formation of highly reactive $^{\bullet}OH$ free radicals. Studies have reported similar observations on the photocatalytic degradation of other compounds, such as furaltadone, methyl orange, and rhodamine B dyes (Kirankumar et al., 2019; Hanafi and Sapawe, 2020; Vasu et al., 2022a).

The FZD photocatalytic degradation showed a notable increase from 62.45±2.85 to 90.44±2.73% with Ni doping ($Ni_{4.80}/TiO_2$(bio)) (Fig. 6.9d). However, it was gradually decreased to 70.22±2.86% with further increase in Ni concentration ($Ni_{6.64\text{-}8.42}/TiO_2$(bio)). This decrease in FZD degradation could be attributed to a synergetic effect of higher bandgap and a high amount of surface adsorbed Ni and its oxide nanoparticles. Similarly, QY (%) and k_1 decreased at higher Ni concentrations. There was no significant influence of pH on surface adsorption of FZD in dark conditions. However, a slight increase in FZD adsorption was observed in dark conditions, rising from 6.72±0.60 to 10.66±0.73%, as the Ni concentration increased from 0 to 8.42%. $Ni_{4.80}/TiO_2$(bio) demonstrated superior photocatalytic degradation

than $Ni_{0.00}/TiO_2$(bare) and $Ni_{4.80}/TiO_2$(chem), which showed a photocatalytic degradation of 62.45±2.85 and 73.41±2.79%, respectively. About 4.36±0.34% photolysis of FZD was observed within 180 min of light exposure without a catalyst.

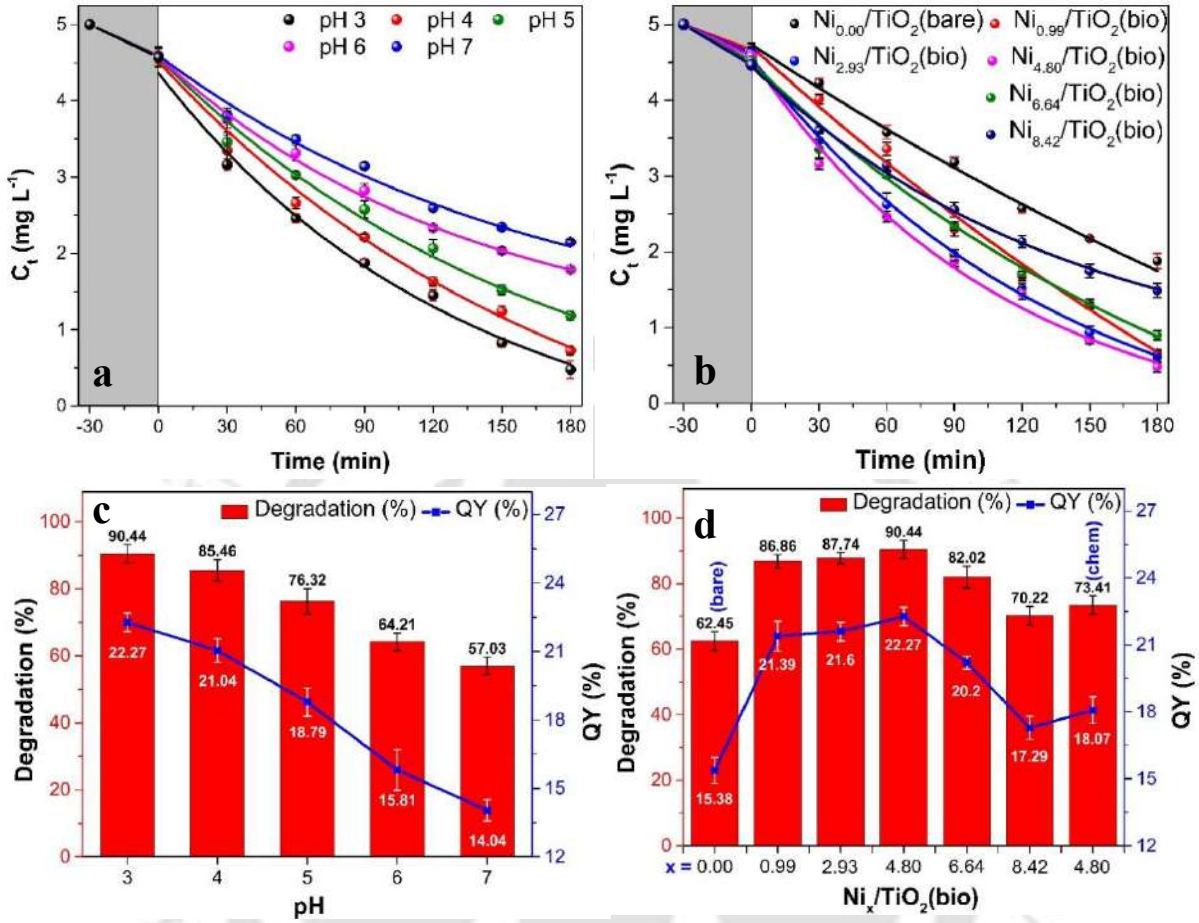

Figure 6.9: FZD photocatalytic degradation and first order kinetic model fitting at (a) various pH using $Ni_{4.80}/TiO_2$(bio) and (b) at pH 3 using variant photocatalysts. FZD photodegradation (%) and QY (%) at (c) various pH with $Ni_{4.80}/TiO_2$(bio) and (d) pH 3 with variant photocatalysts. Photocatalytic degradation of 100 mL of 5 mg L^{-1} FZD performed under visible light irradiation (50W LED light) with a fixed 0.5 g L^{-1} photocatalysts dosage for 180 min. *Shaded part in (a) and (b) shows FZD adsorption prior to light illumination.

$Ni_{4.80}/TiO_2$(bio) demonstrated superior photocatalytic performance compared to other reported studies for the photocatalytic degradation of nitrofuran drugs (Table 6.6). Recently, Vasu et al. (2022) employed a chemical-based N and S-doped TiO_2 photocatalyst to degrade FZD, achieving 95% photodegradation within 140 min under a 500 W tungsten-halogen lamp. The degradation efficiency is comparable to the current study (light source power: 50 W). However, a higher power light was used in the earlier work (Vasu et al., 2022b). In another

study, chemical-based g-C_3N_4 and $CoWO_4$/g-C_3N_4 achieved 19.8% and 56.3% photodegradation of FZD within 180 min under 300 W visible light, respectively. However, the degradation efficiency increased to 79.9% when molecularly imprinted $CoWO_4$/g-C_3N_4 was used (Zhang et al., 2025). Photocatalysts such as Cu/Ni/TiO_2/MWCNTs nanocomposite, g-C_3N_4/CdS photocathode, $NaGd(MoO_4)_2$:Dy^{3+}/Eu^{3+}, TiO_2, and Cu(II)-based MOF have been utilized for the photodegradation of other nitrofuran drugs, including nitrofurazone (NFZ), furaltadone (FLT), and nitrofurantoin (NFT) (Hou et al., 2020; Szabó-Bárdos et al., 2020; Vasu et al., 2022b, 2022a; Devi et al., 2023; Yan et al., 2023; Zhang et al., 2025). Notably, there have been very few studies on the photocatalytic degradation of FZD, underscoring the significance of this work as a valuable contribution to the field.

Table 6.5: FZD degradation efficiency (%), rate constant (k_1, min^{-1}), and QY (%) of photocatalytic degradation of FZD at various pH (3-7) and at pH 5 using $Ni_{0.00}$/TiO_2(bare), $Ni_{0.99\text{-}8.42}$/TiO_2(bio), and $Ni_{4.80}$/TiO_2(chem) under 50W visible light (450 nm) for 180 min with continuous stirring at 300 rpm.

Catalysts	pH	FZD degradation (%)	k_1 (min^{-1})	QY (%)
$Ni_{0.00}$/TiO_2(bare)	3	62.45 ± 2.85	0.20 x 10^{-2}	15.38 ± 0.58
$Ni_{0.99}$/TiO_2(bio)		86.86 ± 2.02	0.73 x 10^{-2}	21.39 ± 0.67
$Ni_{2.93}$/TiO_2(bio)		87.74 ± 1.72	0.78 x 10^{-2}	21.60 ± 0.43
$Ni_{4.80}$/TiO_2(bio)		90.44 ± 2.73	0.89 x 10^{-2}	22.27 ± 0.41
$Ni_{6.64}$/TiO_2(bio)		82.02 ± 3.36	0.70 x 10^{-2}	20.20 ± 0.29
$Ni_{8.42}$/TiO_2(bio)		70.22 ± 2.86	0.68 x 10^{-2}	17.29 ± 0.51
$Ni_{4.80}$/TiO_2(bio)	4	85.46 ± 3.22	0.72 x 10^{-2}	21.04 ± 0.52
	5	76.32 ± 3.73	0.60 x 10^{-2}	18.79 ± 0.62
	6	64.21 ± 2.59	0.58 x 10^{-2}	15.81 ± 0.89
	7	57.03 ± 2.57	0.55 x 10^{-2}	14.04 ± 0.47
$Ni_{4.80}$/TiO_2(chem)	3	73.41 ± 2.79	-	18.07 ± 0.59

Table 6.6: Photocatalytic efficiency of Ni-doped TiO_2 (present study) and its comparison with chemical-based photocatalysts for FZD photodegradation.

Drug	Photocatalyst	Light source	Initial conc. (mg L^{-1})	Catalyst dose (g L^{-1})	Reaction time (min)	Degradation (%)	Sources
FZD	$g\text{-}C_3N_4$	Visible light (300 W)	0.11	10	180	19.8	(Zhang et al., 2025)
	$CoWO_4/g\text{-}C_3N_4$					56.3	
	Molecularly imprinted $CoWO_4/g\text{-}C_3N_4$					79.9	
FZD	N and S-doped TiO_2	Visible light (500 W)	22.5	0.13	140	~95	(Vasu et al., 2022b)
FLT	Cu/Ni/TiO_2/MW CNTs nanocomposite	Visible light (500 W)	3.6	0.2	120	~50	(Vasu et al., 2022a)
NFZ	$g\text{-}C_3N_4$/CdS photocathode	Visible light (300 W)	50	-	600	~80	(Hou et al., 2020)
NFT	$NaGd(MoO_4)_2$:Dy^{3+}/Eu^{3+}	UVA light	20	0.45	45	~70	(Devi et al., 2023)
NFT	TiO_2	UV light	100	10	120	~99	(Szabó-Bárdos et al., 2020)
NFT	Cu(II)-based MOF	UV light	10	0.5	100	92.04	(Yan et al., 2023)
FZD	$Ni_{0.00}/TiO_2$(bare)	Visible light (50 W)	5	0.5	180	62.45	**Present study**
	$Ni_{1.00}/TiO_2$(chem)					73.41	
	$Ni_{1.00}/TiO_2$(bio)					90.44	

6.2.8 LC-MS and photodegradation mechanism

The liquid chromatograms and mass spectra of FZD solutions before and after photocatalytic degradation are shown in Fig. 6.10. A prominent spike (at m/z = 225.0) in mass spectra of untreated solution represents FZD (Fig. 6.10c). In the mass spectra of photocatalytically degraded solution, numerous spikes were observed, representing FZD and various intermediates formed during the photocatalytic process (Fig. 6.10d). The proposed FZD degradation mechanism, as illustrated in Fig. 6.11, suggests that the degradation process involves complex transformations and the generation of 17 intermediates in three different pathways. Here, the intermediates are denoted as I (intermediate) to avoid any confusion.

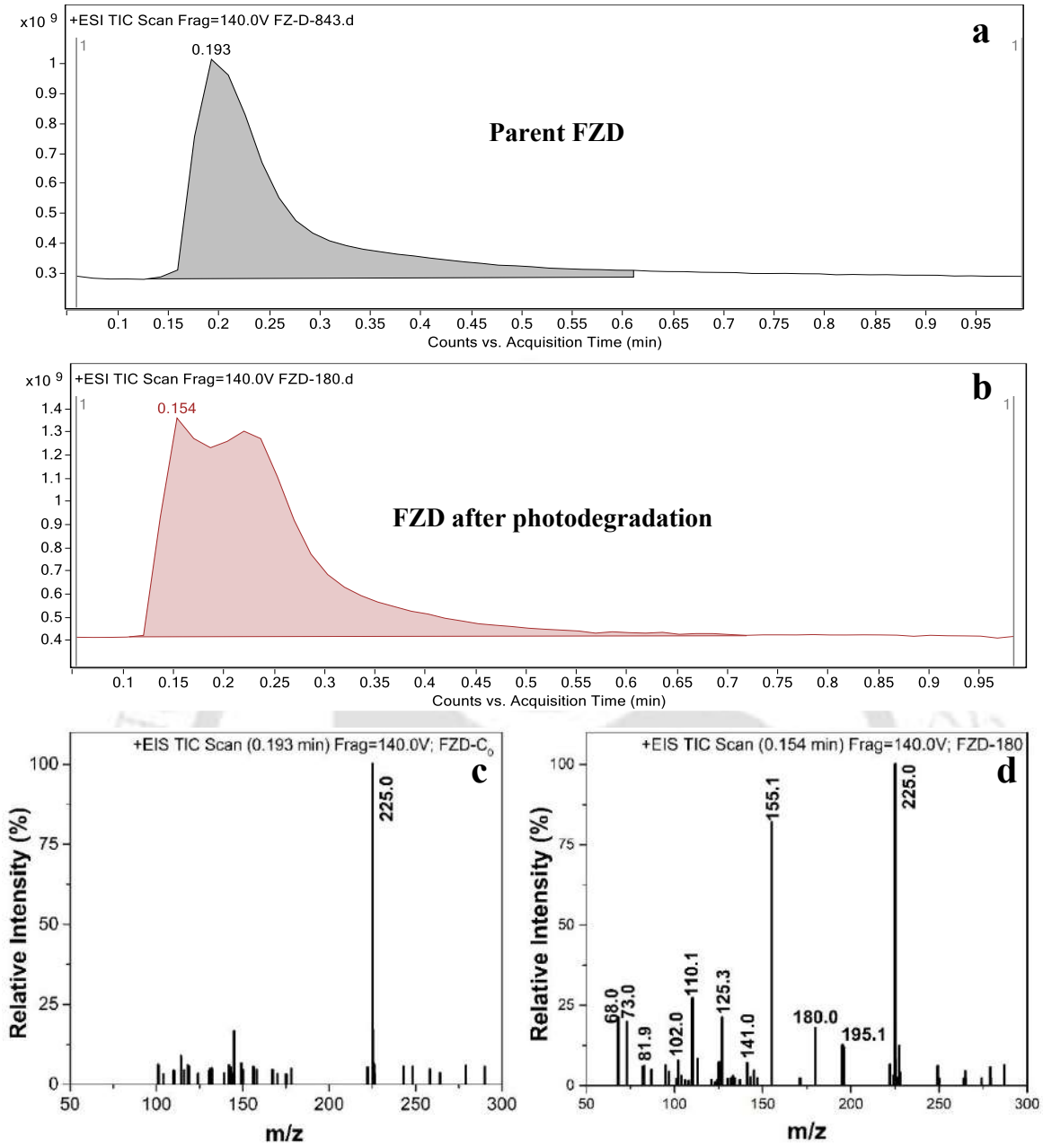

Figure 6.10: LC-MS analysis: Chromatograms of FZD (a) before and (b) after photocatalytic degradation using $Ni_{4.80}/TiO_2$(bio), captured via positive EIS mode $[M + H]^+$. MS spectra of FZD (c) before and (d) after photocatalytic degradation.

In pathway #1, the photocatalytic degradation process begins with reducing the NO_2 group of FZD to the NH_2 group in the I1 intermediate, which is subsequently converted to I2 through aromatic substitution with the release of NH_3. Dehydration of I2 resulted in the formation of I3, and the hydrogenous reaction cleaves the N-N bond in I3 to generate both I4 and I16. Further, I4 is then further transformed into the smallest detected intermediate, I14, by removing the CH_3N group from the furan ring. In pathway #2, I5 formed through a ring-

opening hydrolysis of the oxazolidine ring of I1. Dealkylation of I5, with the release of CH_3OH, leads to the formation of I6, which further undergoes a deamination process to become I7. I8 intermediate was formed through an aromatic substitution reaction, where a hydroxyl group replaced the NH_3 group of I7 (Hou et al., 2020; Szabó-Bárdos et al., 2020).

Pathway #3 comprises of two sub-pathways (Pathways #3a and #3b) with cleavage of the N-N bond between the furan and oxazolidine rings of FZD to form I9 (Pathway #3a) and I15 (Pathway #3b). I9 then undergoes hydrolysis to form I10. The nitro group in I10 was reduced to an amino group, resulting in the formation of I11. Additionally, I11 was also formed by hydrolysis of the P8 intermediate, which was further transformed into I12 and I13 through deamination and demethylation processes, respectively. I13 and I12 were converted into the smallest detected compound, the furan ring (I14), through demethylation and deamination, respectively. In pathway #3b, deamination of NH_3 from the I15 intermediate formed I16, which ultimately broke to the smallest detected intermediate, oxazolidine ring (I17), of pathway #3b. Further, I14 and I17, could be mineralized into CO_2 and H_2O (Hou et al., 2020; Szabó-Bárdos et al., 2020).

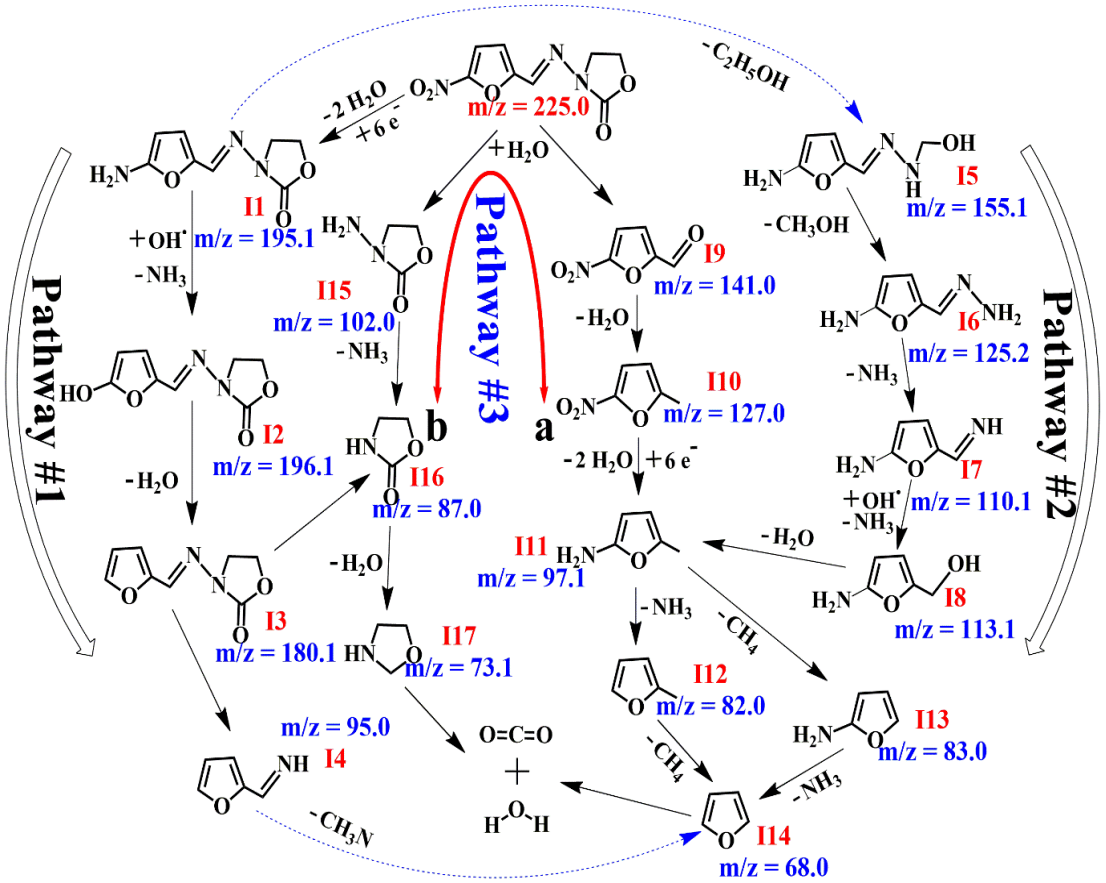

Figure 6.11: Photocatalytic degradation mechanism of FZD using $Ni_{4.80}/TiO_2$(bio) under visible light irradiation for 180 min.

Among 17 intermediates, only 5 exhibited a mass error in the 0.1-0.3% mol g^{-1} range. This suggests that the proposed compounds were closely aligned with the experimental mass spectra of the intermediates.

6.2.9 Reusability and stability

The surface adsorption in the dark (%) and photodegradation (%) in light for consecutive 4 cycles are shown in Fig. 6.12a. The photocatalytic degradation was gradually reduced by 7.68% (from 90.44±2.73 to 82.76±3.17%) during 3rd cycle of its reuse. However, it was further decreased to 72.80±2.87% during the 4th cycle. Additionally, the surface adsorption in the dark decreased from 8.46±0.41 to 5.75±0.49% as the reusability cycles progressed from the 1st to 4th. This decrease in surface adsorption and photocatalytic degradation could be attributed to the gradual masking of active sites with residual FZD and the intermediates formed during each cycle.

The washed $Ni_{4.80}/TiO_2$(bio)/used catalyst was further characterized using XRD and XPS analysis. Figs. 6.12b and 6.12c illustrate the XRD and XPS survey spectra of $Ni_{4.80}/TiO_2$(bio) and $Ni_{4.80}/TiO_2$(bio)/used, respectively. No significant changes were observed in the XRD and XPS survey spectra after photocatalytic degradation process. However, increased noise in both spectra was noted, which can be attributed to the adherence of FZD and its intermediate compounds on the catalyst surface. Such adherence may mask the active sites, leading to a gradual decrease in photocatalytic activity as the degradation cycles progress.

6.2.10 Toxicity assessment and antimicrobial activity

The photocatalytic degradation of FZD also followed three transformation routes, producing 17 different intermediates, as presented in Fig. 6.11. The LC_{50} values for fathead minnow (96 h) are shown in Fig. 6.12d. The parent FZD exhibited an LC_{50} of 0.64 mg L^{-1}, indicating severe toxicity toward aquatic organisms. All intermediates exhibited increased LC_{50} values ranging from 3.30-1744.35 mg L^{-1}, reflecting an extensive decline in the toxicity resulting of photocatalytic degradation. The intermediates such as I1-I3 and I6, posse moderate toxicity ($1 < LC_{50} < 10$). While I5 and I10 intermediates belong to harmful categories ($10 < LC_{50} < 100$), the remaining intermediates, except I4 (N/A) and I7 (N/A), were predicted as not harmful ($LC_{50} > 100$) (Cai et al., 2019).

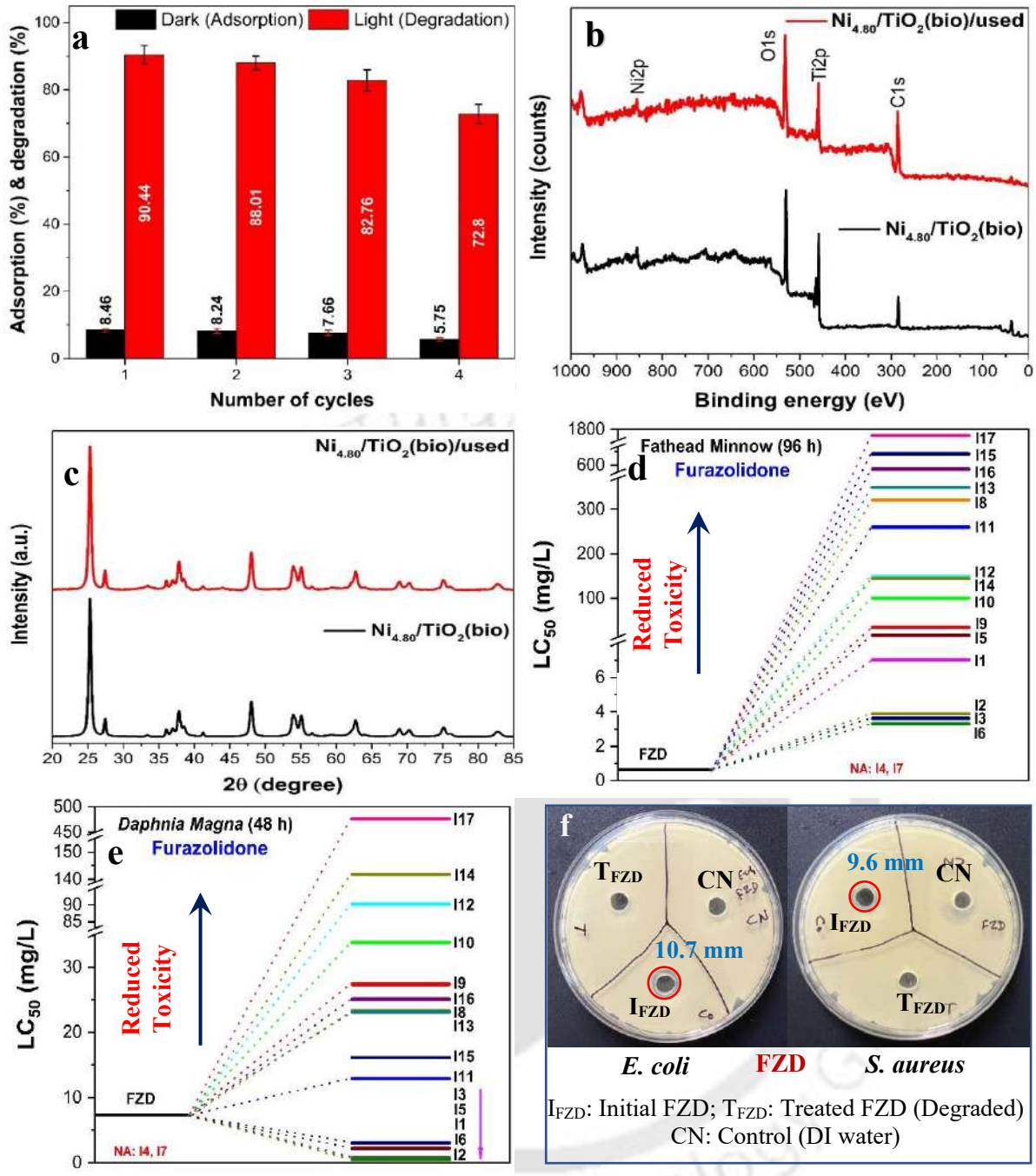

Figure 6.12: Reusability of $Ni_{1.00}/TiO_2$(bio) during FZD photodegradation for consecutive 4 cycles: (a) Surface adsorption in dark and FZD photodegradation and (b) XRD spectra and (d) XPS survey scan of $Ni_{4.80}/TiO_2$(bio) and $Ni_{4.80}/TiO_2$(bio)/used (after 1st cycle of photodegradation). Aquatic toxicity of FZD and formed intermediates against (d) Fathead minnow, and (e) *Daphnia magna*. (f) Antimicrobial activity of FZD before and after photocatalytic degradation against *E. coli* and *S. aureus*.

For *Daphnia magna*, FZD displayed an LC_{50} of 7.32 mg L^{-1}, denoting adequate toxicity toward aquatic invertebrates (Fig. 6.12e). Majority of intermediates, such as I8 to I17 exhibited

higher LC_{50} values ranging between 12.90 and 476.66 mg L^{-1}, suggesting that the photocatalytic process effectively reduces its toxicity. Among these, I14 and I17 were predicted as not harmful, while the remaining intermediates belong to harmful categories (Su et al., 2022). Nonetheless, intermediates like I1-I3, I5, and I6 exhibited marginally reduced LC_{50} values. Additionally, LC_{50} values of I4 and I7 intermediates were not assessed due to structural prediction limitations. These findings suggest that the post-degradation FZD solution presents a reduced environmental hazard for aquatic animals compared to the untreated form.

The antimicrobial activity of FZD was evaluated against *E. coli* and *S. aureus* bacterial strains. The untreated FZD exhibited significant antibacterial activity against both bacterial strains, with a zone of inhibition of 10.7 mm against *E. coli* and 9.6 mm against *S. aureus* (Fig. 6.12f) (Mosaleheh and Sarvi, 2020). In contrast, the degraded solutions (after photocatalytic degradation for 180 min) of FZD did not show any antimicrobial activity, indicating that the degradation process effectively neutralized its antibacterial properties. Similarly, the blank samples (sterile DI water) exhibited no inhibition. The absence of antimicrobial activity of treated solutions provides valuable insights into the effectiveness of post-photocatalytic integration of biological degradation for the complete degradation of remaining intermediate products.

6.3 Major findings

In this study, we present a pioneering approach for synthesizing Ni-doped TiO_2 using waste pineapple peel extract, achieving a significantly reduced bandgap (from 3.29 to 2.54 eV) through the introduction of Ni along with oxygen vacancies and Ti^{3+} defects, and improved hydrophilicity for photocatalytic applications. In Ni-doped TiO_2, Ni existed as Ni^0 (~16.2%), Ni^{2+} (~74.2%) and Ni^{3+} (~9.6%). With Ni doping, the photocurrent density of TiO_2 increased by 11.65 folds and charge transfer resistance decreased from 14.5 to 3.9 KΩ under illumination. The theoretical bandgap calculated using density functional theory incorporating oxygen vacancies closely matches the experimental bandgap, with a maximum deviation of 1.2%. This provides a deeper understanding of defect engineering in Ni-doped TiO_2 and marking a pivotal advancement in the development of environmentally benign photocatalysts. The highest 90.44±2.73% FZD degradation and 22.27±0.41% QY were achieved at optimized pH 3 using $Ni_{4.80}/TiO_2$(bio) under visible light. $Ni_{0.00}/TiO_2$(bare) and $Ni_{4.80}/TiO_2$(chem) showed a FZD degradation of 62.45±2.85 and 73.41±2.79%, respectively. $Ni_{4.80}/TiO_2$(bio) exhibited only 7.68% reduction in FZD degradation during the 3rd cycle of its reuse, which further decreased

by ~17.6% in the 4th cycle. The FZD degradation involved the formation of 17 intermediates in three different pathways. Additionally, the photocatalytic degradation process significantly reduced the aquatic toxicity and neutralized the antimicrobial activity of FZD. Therefore, the superiority in degrading antibiotic drugs using photocatalysts functionalized in an environmentally benign bio-based synthesis method offers valuable insights for potential photocatalytic applications. The proposed bio-based Ni-doped TiO_2 synthesis process further could be followed for scale-up studies targeting industrial applications.

The pilot plant and industrial-scale applications of photocatalysis in wastewater treatment are scanty. The catalysts must be recovered for their reuse to minimize the treatment cost and also to avoid secondary water pollution. A cross-flow ultrafiltration (CF-UF) membrane could be an efficient alternative for recovering photocatalytic nanomaterials, even at a larger scale (Chapter 7).

References

Appadurai, T., Subramaniyam, C.M., Kuppusamy, R., Karazhanov, S., Subramanian, B., 2019. Electrochemical performance of nitrogen-doped TiO_2 nanotubes as electrode material for supercapacitor and Li-ion battery. Molecules 24. https://doi.org/10.3390/molecules24162952

Ayaz, M., Alatawi, A.S., Hijji, M., Namazi, M.A., Ershath, M.I.M., 2024. Improving charge transfer properties and solar cell performance by In-doped TiO_2 as an efficient photoanode for dye-sensitized solar cells (DSSCs). J. Phys. Chem. Solids 188. https://doi.org/10.1016/j.jpcs.2024.111913

Baruah, M., Ezung, S.L., Sharma, S., Bora Sinha, U., Sinha, D., 2022. Synthesis and characterization of Ni-doped TiO_2 activated carbon nanocomposite for the photocatalytic degradation of anthracene. Inorg. Chem. Commun. 144. https://doi.org/10.1016/j.inoche.2022.109905

Behnood, R., Sodeifian, G., 2022. Synthesis of $Ag_4Bi_2O_5$ nanoparticles and evaluation of their photocatalytic activity. J. Photochem. Photobiol. A Chem. 427. https://doi.org/10.1016/j.jphotochem.2022.113776

Bhan, C., Golder, A.K., 2024. ZnO Nanorods Aligned in a Vertical Configuration for Targeted Electrochemical Detection of Aniline. ACS Appl. Bio Mater. https://doi.org/10.1021/acsabm.4c01050

Bhan, C., Golder, A.K., 2023. Utilizing bioinspired AgNPs as an antibacterial agent to enhance

ceramic membrane performance. J. Environ. Chem. Eng. 11, 110283. https://doi.org/10.1016/j.jece.2023.110283

Bhan, C., Kumar Golder, A., 2023. Bio-based hierarchical vertically aligned 2D ZnO nanostructures for ultra selective electrochemical sensing of p-Chloroaniline. Chem. Eng. J. 475. https://doi.org/10.1016/j.cej.2023.146122

Bhan, C., Ravi, R., Golder, A.K., 2025. Phyto-analytic formation of Ag nanostructures for targeted electrocatalytic sensing of ciprofloxacin. J. Environ. Chem. Eng. 13, 115140. https://doi.org/10.1016/j.jece.2024.115140

Cai, Z., Hao, X., Sun, X., Du, P., Liu, W., Fu, J., 2019. Highly active WO_3@anatase-SiO_2 aerogel for solar-light-driven phenanthrene degradation: Mechanism insight and toxicity assessment. Water Res. 162. https://doi.org/10.1016/j.watres.2019.06.017

Cheng, G., Liu, X., Song, X., Chen, X., Dai, W., Yuan, R., Fu, X., 2020. Visible-light-driven deep oxidation of NO over Fe doped TiO_2 catalyst: Synergic effect of Fe and oxygen vacancies. Appl. Catal. B Environ. 277. https://doi.org/10.1016/j.apcatb.2020.119196

Cisneros, S., Chen, S., Diemant, T., Bansmann, J., Abdel-Mageed, A.M., Goepel, M., Olesen, S.E., Welter, E.S., Parlinska-Wojtan, M., Gläser, R., Chorkendorff, I., Behm, R.J., 2021. Effects of SiO_2-doping on high-surface-area Ru/TiO_2 catalysts for the selective CO methanation. Appl. Catal. B Environ. 282. https://doi.org/10.1016/j.apcatb.2020.119483

Das, D., Bhan, C., Mukherjee, C., Golder, A.K., 2024. Improved selectivity of electrochemical aniline sensing using one-dimensional silver nanorods with high aspect ratio synthesized by ascorbic acid assisted method. Anal. Chim. Acta 1310, 342697. https://doi.org/10.1016/j.aca.2024.342697

De Silva, K.G.G.C., Helsel, N., Jeyashangararaj, H.S., Choudhury, P., Chowdhury, S., 2024. Plasmon assisted synthesis of TiN-supported single-atom nickel catalysts. Discov. Nano 19. https://doi.org/10.1186/s11671-024-03992-z

Devi, S., Singhaal, R., Sen, C., Sheikh, H.N., 2023. Luminescent and photocatalytic activity of $NaGd(MoO_4)_2$:Dy^{3+}/Eu^{3+} and $NaGd(WO_4)_2$:Dy^{3+}/Eu^{3+} nanorods for efficient sensing and degradation of the antibiotic drug, nitrofurantoin. New J. Chem. 47. https://doi.org/10.1039/d2nj05980k

Fan, L., Liu, P.F., Yan, X., Gu, L., Yang, Z.Z., Yang, H.G., Qiu, S., Yao, X., 2016. Atomically isolated nickel species anchored on graphitized carbon for efficient hydrogen evolution electrocatalysis. Nat. Commun. 7. https://doi.org/10.1038/ncomms10667

Gahlawat, S., Singh, J., Yadav, A.K., Ingole, P.P., 2019. Exploring Burstein-Moss type effects in nickel doped hematite dendrite nanostructures for enhanced photo-electrochemical

water splitting. Phys. Chem. Chem. Phys. 21. https://doi.org/10.1039/c9cp04132j

Gawal, P.M., Golder, A.K., 2024a. Plant-Based Phytochemicals for Synthesis of Z-Scheme In_2O_3/CdS Heterostructures: DFT Analysis and Photocatalytic CO_2 Reduction to HCOOH and CO. Langmuir 40, 13538–13549. https://doi.org/10.1021/acs.langmuir.4c01015

Gawal, P.M., Golder, A.K., 2024b. Vegetal route for synthesis of CQDs/CdS nanocomposites for photocatalytic reduction of CO_2 to methanol under visible light. Colloids Surfaces A Physicochem. Eng. Asp. 683. https://doi.org/10.1016/j.colsurfa.2023.133068

Ghosh, P., Chelli, V.R., Giri, A.S., Golder, A.K., 2018. Steroid glycosides as potential analytes for Cu-doping on TiO_2 for photocatalytic water treatment. Environ. Prog. Sustain. Energy 37. https://doi.org/10.1002/ep.12879

Gogoi, D., Shah, A.K., Rambabu, P., Qureshi, M., Golder, A.K., Peela, N.R., 2021. Step-Scheme Heterojunction between CdS Nanowires and Facet-Selective Assembly of MnOx-$BiVO_4$ for an Efficient Visible-Light-Driven Overall Water Splitting. ACS Appl. Mater. Interfaces 13, 45475–45487. https://doi.org/10.1021/acsami.1c11740

Golder, A.K., Chauhan, S., Ravi, R., 2021. Synthesis of low-cost bentonite/Duranta erecta's fruit powder imbedded alginate beads and its application in surfactant removal. Environ. Sci. Pollut. Res. 28, 58945–58957. https://doi.org/10.1007/s11356-021-14306-6

Guo, Z., Dai, F., Yin, H., Zhang, M., Xing, J., Wang, L., 2022. The dual role of Au nanoparticles in the surface plasmon resonance enhanced photocatalyst Au/g-C_3N_4. Colloids Interface Sci. Commun. 48. https://doi.org/10.1016/j.colcom.2022.100615

Hanafi, M.F., Sapawe, N., 2020. Influence of pH on the photocatalytic degradation of methyl orange using nickel catalyst, in: Materials Today: Proceedings. https://doi.org/10.1016/j.matpr.2020.06.094

Hou, Y., Yuan, G., Wang, S., Yu, Z., Qin, S., Tu, L., Yan, Y., Chen, X., Zhu, H., Tang, Y., 2020. Nitrofurazone degradation in the self-biased bio-photoelectrochemical system: g-C_3N_4/CdS photocathode characterization, degradation performance, mechanism and pathways. J. Hazard. Mater. 384. https://doi.org/10.1016/j.jhazmat.2019.121438

Iatsunskyi, I., Kempiński, M., Nowaczyk, G., Jancelewicz, M., Pavlenko, M., Załeski, K., Jurga, S., 2015. Structural and XPS studies of PSi/TiO_2 nanocomposites prepared by ALD and Ag-assisted chemical etching. Appl. Surf. Sci. 347. https://doi.org/10.1016/j.apsusc.2015.04.172

Jahdi, M., Mishra, S.B., Nxumalo, E.N., Mhlanga, S.D., Mishra, A.K., 2020. Smart pathways for the photocatalytic degradation of sulfamethoxazole drug using F-Pd co-doped TiO_2

nanocomposites. Appl. Catal. B Environ. 267. https://doi.org/10.1016/j.apcatb.2020.118716

Jatav, J., Tarafdar, A., Saravanan, C., Bhattacharya, B., 2022. Assessment of Antioxidant and Antimicrobial Property of Polyphenol-Rich Chitosan-Pineapple Peel Film. J. Food Qual. 2022. https://doi.org/10.1155/2022/8064114

Johari, N.A., Hamzah, N., Faizal, A.F.A., Samat, M.H., Hassan, O.H., Ali, A.M.M., Yahya, M.Z.A., Taib, M.F.M., 2022. Effects of Hubbard U correction on the structural and electronic properties of rutile, anatase and brookite TiO_2, in: Materials Today: Proceedings. https://doi.org/10.1016/j.matpr.2022.06.192

Kaiba, A., Ouerghi, O., Geesi, M.H., Elsanousi, A., Belkacem, A., Dehbi, O., Alharthi, A.I., Alotaibi, M.A., Riadi, Y., 2020. Characterization and catalytic performance of Ni-Doped TiO_2 as a potential heterogeneous nanocatalyst for the preparation of substituted pyridopyrimidines. J. Mol. Struct. 1203. https://doi.org/10.1016/j.molstruc.2019.127376

Kirankumar, V.S., Mayank, N., Sumathi, S., 2019. Photocatalytic performance of cerium doped copper aluminate nanoparticles under visible light irradiation. J. Taiwan Inst. Chem. Eng. 95. https://doi.org/10.1016/j.jtice.2018.09.020

Komaraiah, D., Radha, E., Sivakumar, J., Ramana Reddy, M. V., Sayanna, R., 2020. Photoluminescence and photocatalytic activity of spin coated Ag^+ doped anatase TiO_2 thin films. Opt. Mater. (Amst). 108. https://doi.org/10.1016/j.optmat.2020.110401

Kotta, A., Kim, E.-B., Ameen, S., Shin, H.-S., Seo, H.K., 2020. Communication—Ultra-Small NiO Nanoparticles Grown by Low-Temperature Process for Electrochemical Application. J. Electrochem. Soc. 167. https://doi.org/10.1149/1945-7111/abcf51

Kumar, A., Das, C., 2024. Corrosion inhibition of mild steel by Praecitrullus fistulosus (tinda fruit and peel) extracts. Sci. Total Environ. 929, 172569. https://doi.org/10.1016/j.scitotenv.2024.172569

Kumar, A., Das, C., 2023. A novel eco-friendly inhibitor of chayote fruit extract for mild steel corrosion in 1 M HCl: Electrochemical, weight loss studies, and the effect of temperature. Sustain. Chem. Pharm. 36, 101261. https://doi.org/10.1016/j.scp.2023.101261

Li, Q., Zhao, J., Shang, H., Ma, Z., Cao, H., Zhou, Y., Li, G., Zhang, D., Li, H., 2022. Singlet Oxygen and Mobile Hydroxyl Radicals Co-operating on Gas-Solid Catalytic Reaction Interfaces for Deeply Oxidizing NOx. Environ. Sci. Technol. 56. https://doi.org/10.1021/acs.est.2c00622

Li, R., Li, W., Liu, M., He, Q., Wang, Y., Zhan, Q., Wang, T., 2019. Structural, Morphological, Optical and Electrical Properties of Cu-Doped PbS Nanofilms. ES Mater. Manuf. 4.

https://doi.org/10.30919/esmm5f217

Lin, Y.M., Jiang, Z.Y., Zhu, C.Y., Hu, X.Y., Zhang, X.D., Fan, J., 2012. Visible-light photocatalytic activity of Ni-doped TiO_2 from ab initio calculations. Mater. Chem. Phys. 133, 746–750. https://doi.org/10.1016/j.matchemphys.2012.01.083

Maarisetty, D., Komandur, J., Sharma, S., Baral, S.S., Mohapatra, P., 2020. Unravelling the rate controlling step in degradation of phenol on a higher potential photocatalyst. J. Environ. Chem. Eng. 8. https://doi.org/10.1016/j.jece.2020.103938

McCracken, R.J., Kennedy, D.G., 2013. Furazolidone in chicken: Case study of an incident of widespread contamination. Br. Poult. Sci. 54. https://doi.org/10.1080/00071668.2013.850152

McCracken, R.J., McCoy, M.A., Kennedy, D.G., 2000. Furazolidone residues in pigs: Criteria to distinguish between treatment and contamination. Food Addit. Contam. 17. https://doi.org/10.1080/026520300283612

Mimouni, R., Askri, B., Larbi, T., Amlouk, M., Meftah, A., 2020. Photocatalytic degradation and photo-generated hydrophilicity of Methylene Blue over $ZnO/ZnCr_2O_4$ nanocomposite under stimulated UV light irradiation. Inorg. Chem. Commun. https://doi.org/10.1016/j.inoche.2020.107889

Mingmongkol, Y., Polnok, A., Phuinthiang, P., Channei, D., Ratananikom, K., Nakaruk, A., Khanitchaidecha, W., 2023. Photocatalytic Degradation Mechanism of the Pharmaceutical Agent Salbutamol Using the Mn-Doped TiO_2 Nanoparticles Under Visible Light Irradiation. ACS Omega 8. https://doi.org/10.1021/acsomega.3c01776

Mohammadi, M., Attaran, B., Malekzadeh, R., Graham, D.Y., 2017. Furazolidone, an Underutilized Drug for H. pylori Eradication: Lessons from Iran. Dig. Dis. Sci. https://doi.org/10.1007/s10620-017-4628-5

Mohammadi Toudeshki, R., Dadfarnia, S., Haji Shabani, A.M., 2018. Chemiluminescence determination of furazolidone in poultry tissues and water samples after selective solid phase microextraction using magnetic molecularly imprinted polymers. New J. Chem. 42. https://doi.org/10.1039/c8nj01670d

Mosaleheh, N., Sarvi, M.N., 2020. Minimizing the residual antimicrobial activity of tetracycline after adsorption into the montmorillonite: Effect of organic modification. Environ. Res. 182. https://doi.org/10.1016/j.envres.2019.109056

Nasrollahzadeh, M., Atarod, M., Sajjadi, M., Sajadi, S.M., Issaabadi, Z., 2019. Plant-Mediated Green Synthesis of Nanostructures: Mechanisms, Characterization, and Applications, in: Interface Science and Technology. https://doi.org/10.1016/B978-0-12-813586-0.00006-

7

Papitha, R., Hadkar, V., Sishu, N.K., Arunagiri, S., Roopan, S.M., Selvaraj, C.I., 2024. Green synthesis of CuO/TiO_2 and ZnO/TiO_2 nanocomposites using Parkia timoriana bark extract: Enhanced antioxidant and antidiabetic activities for biomedical applications. Ceram. Int. 50, 39109–39121. https://doi.org/10.1016/j.ceramint.2024.07.277

Pauly, N., Yubero, F., Tougaard, S., 2016. Quantitative analysis of satellite structures in XPS spectra of gold and silver. Appl. Surf. Sci. 383. https://doi.org/10.1016/j.apsusc.2016.03.185

Ramzan, M., Obodo, R.M., Shahzad, M.I., Mukhtar, S., Ilyas, S.Z., Mahmood, T., 2021. Green synthesis of Cu@TiO_2 via cedrus deodara leaf extract: A novel composite with high photocatalytic and antibacterial activity. Curr. Res. Green Sustain. Chem. 4. https://doi.org/10.1016/j.crgsc.2021.100137

Ravi, R., Bhan, C., Golder, A.K., 2025. Bio-analytic synthesis of Cu-doped TiO_2 for photocatalytic degradation of ciprofloxacin under visible light. Opt. Mater. (Amst). 159, 116577. https://doi.org/10.1016/j.optmat.2024.116577

Ruiz Preciado, M.A., Kassiba, A., Morales-Acevedo, A., Makowska-Janusik, M., 2015. Vibrational and electronic peculiarities of $NiTiO_3$ nanostructures inferred from first principle calculations. RSC Adv. 5. https://doi.org/10.1039/c4ra16400h

Salehi-Abar, P., Kazempour, A., 2017. Effect of N and F doping on the electronic properties of rutile TiO_2 quantum dot solar cells: A first principle study. Chem. Phys. Lett. 673. https://doi.org/10.1016/j.cplett.2017.02.001

Senobari, S., Nezamzadeh-Ejhieh, A., 2020. A novel ternary nano-composite with a high photocatalyitic activity: Characterization, effect of calcination temperature and designing the experiments. J. Photochem. Photobiol. A Chem. 394. https://doi.org/10.1016/j.jphotochem.2020.112455

Stozharov, V.M., 2022. Surface Plasmons Excited by X-rays in the Surface Layers of Solids. Solids. https://doi.org/10.3390/solids3010009

Su, Q., Li, J., Yuan, H., Wang, B., Wang, Y., Li, Y., Xing, Y., 2022. Visible-light-driven photocatalytic degradation of ofloxacin by g-C_3N_4/NH_2-MIL-88B(Fe) heterostructure: Mechanisms, DFT calculation, degradation pathway and toxicity evolution. Chem. Eng. J. 427. https://doi.org/10.1016/j.cej.2021.131594

Sudha, A., Manimehan, I., Shalini, R., Varshini, M., Ravichandran, K., Ayyanar, M., Praseetha, P.K., Saravanakkumar, D., 2024. Assessment of de-toxicity of treated dye solution via seed germination test: Photocatalytic treatment by Morinda citrifolia leaf extract

mediated ZnO:Mo/g-C_3N_4 nanocomposite. Mater. Sci. Semicond. Process. 178, 108437. https://doi.org/10.1016/j.mssp.2024.108437

Sukhadeve, G.K., Janbandhu, S.Y., Kumar, R., Lataye, D.H., Ramteke, D.D., Gedam, R.S., 2022. Visible light assisted photocatalytic degradation of Indigo Carmine dye and NO_2 removal by Fe doped TiO_2 nanoparticles. Ceram. Int. 48. https://doi.org/10.1016/j.ceramint.2022.05.053

Szabó-Bárdos, E., Cafuta, A., Hegedűs, P., Fónagy, O., Kiss, G., Babić, S., Škorić, I., Horváth, O., 2020. Photolytic and photocatalytic degradation of nitrofurantoin and its photohydrolytic products. J. Photochem. Photobiol. A Chem. 386. https://doi.org/10.1016/j.jphotochem.2019.112093

Tao, Y., Ma, Z., Wang, W., Zhang, C., Fu, L., Zhu, Q., Li, Y., Li, G., Zhang, D., 2023. Nickel Phosphide Clusters Sensitized TiO_2 Nanotube Arrays as Highly Efficient Photoanode for Photoelectrocatalytic Urea Oxidation. Adv. Funct. Mater. 33. https://doi.org/10.1002/adfm.202211169

Valian, M., Soofivand, F., Khoobi, A., Yousif, Q.A., Salavati-Niasari, M., 2023. A green approach: Eco-friendly synthesis of $Gd_2Ti_2O_7$/N-GQD nanocomposite and photo-degradation and electrochemical measurement of hydroxychloroquine as a perdurable drug. Arab. J. Chem. 16. https://doi.org/10.1016/j.arabjc.2022.104401

Vasu, D., Karthi Keyan, A., Sakthinathan, S., Chiu, T.W., 2022a. Investigation of electrocatalytic and photocatalytic ability of Cu/Ni/TiO_2/MWCNTs Nanocomposites for detection and degradation of antibiotic drug Furaltadone. Sci. Rep. 12. https://doi.org/10.1038/s41598-022-04890-z

Vasu, D., Keyan, A.K., Sakthinathan, S., Yu, C.L., Hsu, B.Z., Chiu, T.W., Wu, J., 2022b. Enhanced Electrocatalytic Activity of Non-metal-Doped Transition Metal Oxides for an Electrochemical Detection of Furazolidone. Electrocatalysis 13. https://doi.org/10.1007/s12678-022-00715-9

Velasquez-Tamayo, J.P., Torres-Ceron, D.A., Amaya-Roncancio, S., Santacruz, S.I., Acosta-Medina, C.D., Restrepo-Parra, E., 2023. Use of nickel-electroplating wastewater to synthesize Ni-doped TiO_2 and $NiTiO_3$ coatings by plasma electrolytic oxidation to treat hexavalent chromium in real electroplating wastewater. Chem. Eng. J. 477. https://doi.org/10.1016/j.cej.2023.147080

Wang, D.Y., Li, C.H., Li, S.S., Kuo, T.R., Tsai, C.M., Chen, T.R., Wang, Y.C., Chen, C.W., Chen, C.C., 2016. Iron Pyrite/Titanium Dioxide Photoanode for Extended Near Infrared Light Harvesting in a Photoelectrochemical Cell. Sci. Rep. 6.

https://doi.org/10.1038/srep20397

Wang, Q., Xie, D., Chen, J., Liu, G., Yu, M., 2020. Superhydrophobic paper fabricated via nanostructured titanium dioxide-functionalized wood cellulose fibers. J. Mater. Sci. 55. https://doi.org/10.1007/s10853-020-04489-7

Wang, Y., Qiu, C., Xie, Y., Wang, L., Ding, J., Zhang, J., Wan, H., Guan, G., 2024. Intentionally Introducing Oxygen Vacancies and Ti^{3+} Defects on the Surface of $Bi_4Ti_3O_{12}$ Nanosheets for Promoting the Photoreduction of CO_2 to CH_3OH. ACS Appl. Nano Mater. 7. https://doi.org/10.1021/acsanm.3c05346

Yan, M.H., Wang, J., Su, X.Y., Sakiyama, H., Qi, N., Afzal, M., Alarifi, A., Srivastava, D., Kumar, A., 2023. A 3D paddle-wheel type Cu(ii)-based MOF with pcu topology as an efficient photocatalyst for antibiotics photodegradation. New J. Chem. 47. https://doi.org/10.1039/d3nj01644g

Yang, Y., Wang, Y., Yin, S., 2017. Oxygen vacancies confined in SnO_2 nanoparticles for desirable electronic structure and enhanced visible light photocatalytic activity. Appl. Surf. Sci. 420, 399–406. https://doi.org/10.1016/j.apsusc.2017.05.176

Zhang, H., Yu, X., McLeod, J.A., Sun, X., 2014. First-principles study of Cu-doping and oxygen vacancy effects on TiO_2 for water splitting. Chem. Phys. Lett. 612, 106–110. https://doi.org/10.1016/j.cplett.2014.08.003

Zhang, Jiali, Rong, C., Yan, C., Chen, J., Yang, W., Yu, L., Dai, H., 2022. Risk factors of furazolidone-associated fever. PLoS One 17. https://doi.org/10.1371/journal.pone.0266763

Zhang, Jianjun, Zhang, L., Wang, W., Yu, J., 2022. In Situ Irradiated X-ray Photoelectron Spectroscopy Investigation on Electron Transfer Mechanism in S-Scheme Photocatalyst. J. Phys. Chem. Lett. https://doi.org/10.1021/acs.jpclett.2c02125

Zhang, X., Liu, Rui, Liu, Rijia, Han, X., Sun, Y., Ren, B., 2025. Target detection and simultaneous degradation of furazolidone by molecularly imprinted $CoWO_4$/g-C_3N_4. Colloids Surfaces A Physicochem. Eng. Asp. 705, 135694. https://doi.org/10.1016/j.colsurfa.2024.135694

Zhao, S., Liao, Z., Fane, A., Li, J., Tang, C., Zheng, C., Lin, J., Kong, L., 2021. Engineering antifouling reverse osmosis membranes: A review. Desalination. https://doi.org/10.1016/j.desal.2020.114857

CHAPTER 7

Efficient Recovery of Bare-TiO_2 and Metal-doped TiO_2 using a Pilot-scale Cross-flow Ultrafiltration System

In this chapter, the cross-flow ultrafiltration unit of the reactor was utilized for the recovery of bare-TiO_2 and metal-doped TiO_2 photocatalysts from their aqueous solution. The operational parameters, such as pH, catalyst concentration, transmembrane pressure, and flow rate, were optimized for optimum recovery of catalysts. The recovery process was performed through forward flow and back-flush. Further, the experimental and theoretical calculation of catalyst recovery were compared, and the recovered catalysts were characterized.

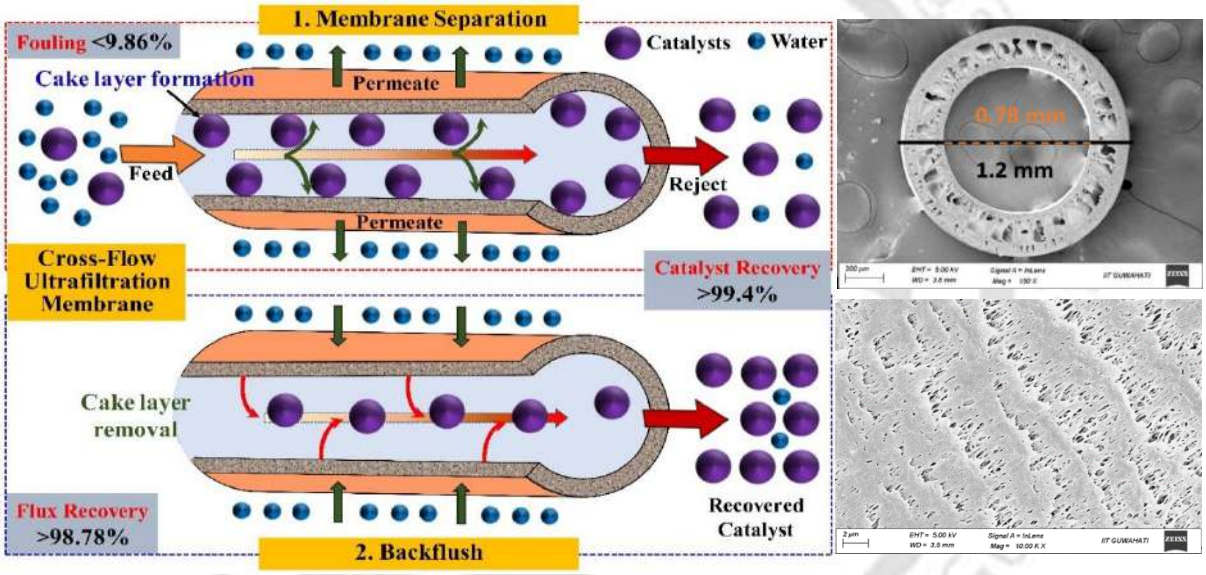

Chapter highlights

- Successful photocatalysts recovery by cross-flow ultra-filtration
- More than 99% catalysts recovery achieved for both bare-TiO_2 and metal-doped TiO_2
- Maximum ~10% reversible fouling and >98% flux recovery noted
- No significance difference was observed in fresh and recovered catalysts efficiencies

Contents lists available at ScienceDirect

Separation and Purification Technology

journal homepage: www.elsevier.com/locate/seppur

Efficient recovery of TiO_2 and Pt-doped TiO_2 photocatalysts in wastewater treatment using a pilot-scale cross-flow ultrafiltration membrane system

Ravi Ravi [a], Animes Kumar Golder [a,b,*]

Intentionally Left Blank
Intentionally Left Blank

7.1 Background and executive motivation

Recent advancements in nano-photocatalysts have led to a significant increase in their demand across a wide range of applications, from laboratory to industry. These applications include wastewater treatment, sensing, drug delivery, water splitting, CO_2 reduction, enhanced oil recovery, antimicrobial activity, and biomaterials (Safat et al., 2021; Chowdhury et al., 2022; Bhan and Golder, 2025). These catalysts are merited with their small size and high surface area, which synergistically boost their catalytic activity by facilitating better interactions with reactants and reducing mass transfer limitations (Wu et al., 2023). Among the various nano-catalysts, TiO_2 and noble metal-doped TiO_2 have emerged as versatile and environmentally friendly catalysts. Despite their numerous advantages and significant progress in catalyst development, the effective recovery and reuse of these catalysts for pilot and industrial-scale applications remain a challenging endeavour (Chelli et al., 2018). The recovery of catalysts is essential for their reuse to minimize treatment costs and prevent secondary water pollution arising from the existence of catalyst particles. It also is important to ensure that the treated water is free of catalysts for its potential reuse in various applications (Mishra and Sundaram, 2022). The presence of catalysts in water bodies can cause adverse effects on aquatic life and interfere with other treatment processes, such as biological degradation, coagulation-flocculation, membrane separation, chemical treatment, electrochemical treatment, and adsorption (Ravi and Pandey, 2019; Bhan and Golder, 2023; Ravi et al., 2025). Previous studies have reported the breakdown of ZnO into Zn^{2+}, which could potentially disrupt the biochemical pathways of organisms (Vimercati et al., 2020). Therefore, there is crucial to develop a highly efficient and robust recovery system to enable the widespread utilization of nano-photocatalysts at pilot and industrial scales.

Numerous efforts have been made to address the absence of a recovery system suitable for larger-scale applications. The substitution of noble metal-doped catalysts with more cost-effective earth-alkaline and base metal-doped catalysts has been investigated (Lv et al., 2019). However, their poor photocatalytic efficiency and limited stability impede their widespread adoption. Another significant challenge lies in immobilizing catalysts on resin or reactor tubes for larger-scale applications. This has been hindered by inefficient immobilization techniques and the obstruction of light transmission (Dijkstra et al., 2001). To overcome these issues, a slurry photoreactor has been identified as the most efficient method for pilot and industrial-scale applications. Several conventional separation techniques have been employed to recover the nanoparticles from aqueous solutions, including ultracentrifugation, fractional

precipitation, ion exchange and size exclusion chromatography, magnetic separation, electrophoresis, and membrane separation (Liriano-Jorge et al., 2014; Mehta et al., 2016; Patchaiyappan et al., 2016; Taylor et al., 2020; Bakhteeva et al., 2021; Bockenstedt et al., 2021). However, recovering used nano-catalysts at the pilot-scale faces many formidable challenges. Among these methods, membrane separation has emerged as a promising technique for recovering nano-catalysts from a homogeneous mixture due to several advantages such as high efficiency, easy handling, retention of photo- and electrochemical properties of catalysts, cost-effectiveness and can work with large volume (Qasem et al., 2021).

While the concept of membrane filters was initially proposed by R. Zsigmondy in 1922, it was not until 1963 that significant advancements were made in ultrafiltration and nanofiltration techniques (Wang et al., 2020). Membrane separation has since proven to be highly effective in separating heavy metals, ions, debris, and microbes from contaminated water. Recently, few studies have explored the combination of photocatalysis and membrane separation processes. However, the challenge of inefficient recovery has been a major setback to their practical application (Janssens et al., 2021). Dead-end membranes have been extensively used in laboratory applications, but they are more prone to fouling compared to cross-flow membranes. Pore blocking and the formation of cake layers have been identified as the leading causes of membrane fouling (Chen et al., 2023). To address this issue, the effect of membrane properties and operational parameters such as pore size, surface wettability, pH, transmembrane pressure drops, feed concentration, and CFV was investigated to better understand the fouling mechanisms (Suga et al., 2022). This exploration has also drawn attention to the potential of low-pressure micro and ultrafiltration polymeric membranes, such as polyacrylonitrile (PAN), cellulose acetate (CA), polytetrafluoroethylene (PTFE), polypropylene (PP) and polycarbonate (PC), for effective recovery (Sonawane et al., 2021). Cross-flow ultrafiltration (CF-UF) membranes exhibit substantial possibilities for pilot-scale implementation owing to their notably high flux at relatively low applied pressures (1-5 bar). These membranes facilitate efficient separation of particles encompassing a broad size spectrum, offer a high permeate-to-reject ratio, and can effectively mitigate fouling through backflushing techniques (Li et al., 2018).

CF-UF membranes have proven their effectiveness in recovering proteins, heavy metals, oils, and ZnO and TiO_2 nano-photocatalysts in laboratory-scale studies (Mehta et al., 2016; G.N. and M., 2021; Peng et al., 2022). In a study, ultrafine TiO_2 was recovered through a CF-UF membrane and exhibited the same photocatalytic activity as fresh TiO_2 (Xue et al., 2008). In another study, an ultrafiltration polyethersulfone (PES) membrane was utilized for

the separation of ZnO and achieved about 98% catalyst recovery (Mehta et al., 2016). However, when it comes to scaling up nano-catalyst-based applications to pilot scale, this remains a relatively unexplored area of research. Thus, the primary aim of this current study is to establish a system that prevents any loss of catalysts at the pilot scale, focusing on the recovery of bare-TiO_2 and Pt-doped TiO_2 (Pt/TiO_2) nano-photocatalysts using CF-UF membrane separation. The study delves into the impact of various factors, such as pH levels and catalyst concentrations on the flux, permeability, and recovery of these photocatalysts through a thorough examination. Furthermore, a thorough analysis was carried out to assess the stability of catalysts during the recovery process. This research is expected to advance the application of CF-UF membrane separation processes in the pilot-scale recovery of nano-photocatalysts.

7.2 Results and discussion

7.2.1 Membrane characterization

The surface wettability of the membrane was assessed by measuring the water contact angle on both the outer and inner sides of the flattened membrane sheet. To perform this analysis, a tubular section of the fresh membrane was unplugged and longitudinally sliced, then flattened by positioning it between two clean glass slides by applying 19.6 N weight force. Next, a drop of 2 μL DI water was placed, and the contact angle was measured. Figs. 7.1a and 7.1b illustrate the water drop formation and the corresponding contact angle of the inner and outer surfaces of the membrane. The water contact angle on the outer surface of the membrane was found to be 77.3°, while on the inner surface (filtration side), it was 54.1°. This indicates that the membrane is highly hydrophilic on the inside (filtration side) compared to the outer surface. In contrast, bare-TiO_2 and Pt/TiO_2 were reported as hydrophobic (water contact angle, $\theta = 120.8°$) and highly hydrophilic ($\theta = 23.9°$), respectively (Fig. 3.5d, Chapter 3). The hydrophilic membrane facilitates a better flux than the hydrophobic membrane due to its strong affinity for water molecules. Additionally, it possesses better antifouling properties (Kang et al., 2020). These characteristics make it particularly well-suited for applications where low flux and fouling are a concern.

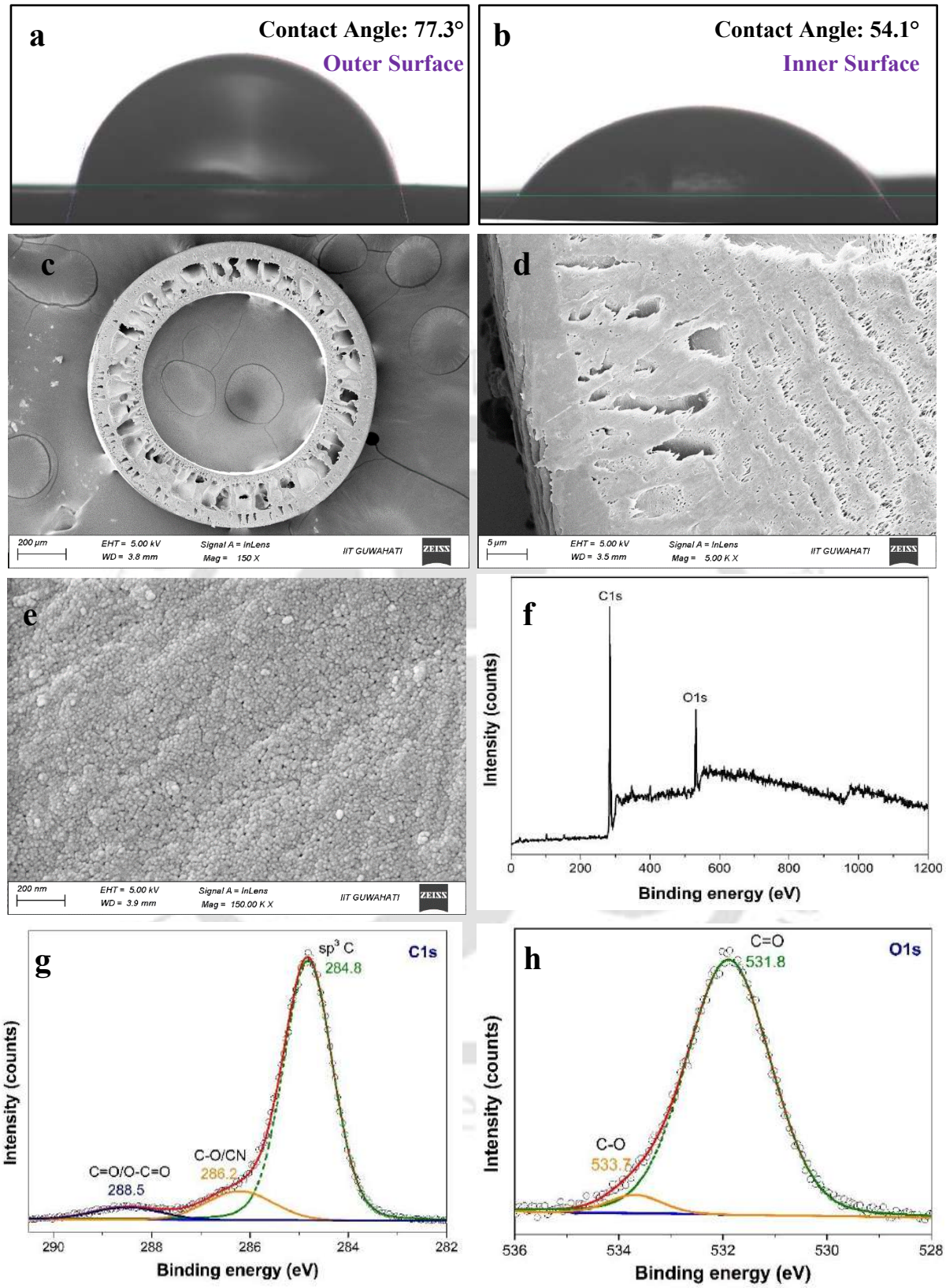

Figure 7.1: Water contact angle of (a) Outer surface and (b) Inner surface of flatted membrane spike; FESEM images of (c) Transverse cross-section, (d) Inner and (e) Outer surface of the flattened longitudinal cross-section of membrane spike. XPS analysis (f) XPS survey spectra, and high-resolution spectra of (g) C1s and (h) O1s.

Figs. 7.1c and 7.1d-7.1e illustrate the FESEM images of the transverse and longitudinal cross-sections of the membrane spike, respectively. As can be seen, the membrane spike exhibits a tubular geometry with an inner and outer diameter of 0.78 and 1.20 mm, respectively, and a thickness of 0.21 mm. Furthermore, Fig. 7.1d demonstrates the presence of cross-linked multilayers with uniformly distributed pores throughout the membrane. While, the outer surface of the membrane spike features small and uniformly distributed pores (Fig. 7.1e).

Figs. 7.1f, and 7.1g-7.1h illustrate the survey scan and the high-resolution spectra of the membrane, respectively, indicating the presence of major peaks of C1s and O1s with traces of N1s, Na1s, Al2p, and Cl2p. Peak positions were corrected according to C1s peak at 284.8 eV, and the obtained high-resolution spectra of C1s and O1s were fitted by using XPSPEAK 4.0 software with Shirley-Linear (S = 0) background subtraction. Fig. 7.1g represents the high-resolution XPS spectra of C1s, showing three peaks at 284.8, 286.2, and 288.5 eV corresponding to sp3 C, C-O/CN, and C=O/O- C=O, respectively. Further, Fig. 7.1h shows the O1s spectra of the membrane containing a set of two characteristic peaks, with a dominant peak at 531.8 eV (C-O) and a small peak at 533.7 eV (C=O) (Zhang et al., 2020).

The elements present in the membrane and their composition are given in Fig. 7.2a. The membrane comprises about 80% carbon and 11% oxygen, indicating that the polymeric membrane is made up of long carbon chains.

The X-ray diffraction pattern of the membrane is shown in Fig. 7.2b. The obtained XRD pattern confirmed the poor crystalline (~7.8%) nature of the membrane. A broad, amorphous peak at $2\theta = 24.91°$ (100) and a small crystalline peak at $2\theta = 17.07°$ (110) were observed (Zhang et al., 2010). The amorphous membrane usually experiences lower permeation resistance than crystalline membranes, consequently enhancing the flux of amorphous membranes (Chaudhari et al., 2021).

Fig. 7.2c illustrates the FTIR spectra of the membrane. The presence of peaks at 1078 and 3404 cm^{-1} corresponds to the C-O (carboxylic group) and O-H groups, respectively. Low-intensity peaks at 1438 and 2915 cm^{-1} represent -CH_2- and –CH_2 (cross-linker) groups of acrylonitrile and cross-linker, respectively. Furthermore, a stretching peak of the –CN group (nitrile) was observed at 2237 $cm^{-1,}$ and a peak at 1630 cm^{-1} shows the amide group of oxidized acrylonitrile. The presence of acrylonitrile and oxidized acrylonitrile suggests that the membrane is a modified PAN membrane (Siyanbola et al., 2016). The existence of an amide group on the membrane could increase the hydrophilicity, which subsequently improves the flux (Wagh et al., 2020).

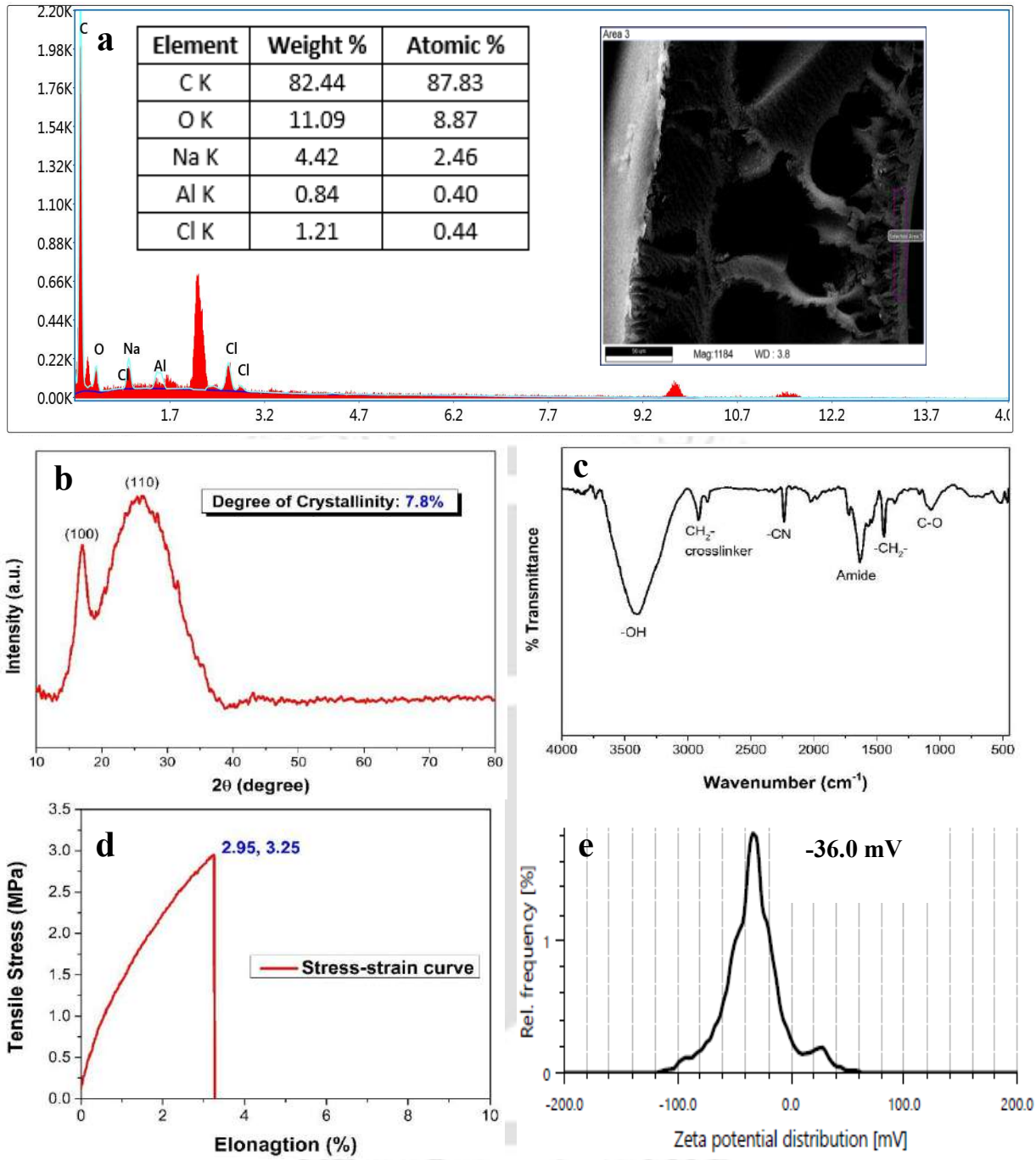

Figure 7.2: (a) EDX spectrum and elemental composition, (b) XRD pattern, (c) FTIR spectrum, (d) Stress-strain curve, and (e) Zeta potential of CF-UF membrane.

The stress-strain curve of the membrane spike is illustrated in Fig. 7.2d. The tensile strength measurement of an 8 cm long membrane spike was performed through a static tensile test. The membrane spike has a tensile strength of 2.95 MPa with 3.25% elongation, which indicates that the membrane could be operated at high pressure. The obtained tensile strength is comparable with reported tensile strength of pure PAN (0.55 MPa), carbonized PAN (1.34

MPa), polyvinylidene difluoride (PVDF, 3.38 MPa), and polyethersulfone (PES, 1.45 MPa) hollow fiber membrane (Kotsilkova et al., 2018).

Fig. 7.2e shows the zeta potential of the membrane. The surface charge of the membrane was found to be -36.0 mV. It is known that the negatively charged surface repels the negatively charged particles. Therefore, this membrane module could exhibit better recovery of negatively charged Pt/TiO_2 (-13.3 mV) than positively charged bare TiO_2 (6.7 mV) (Ravi and Golder, 2023).

7.2.2 Measurement of catalyst concentration

Fig. 7.3 presents the linearly fitted standard curve of both catalysts. The resulting equations, namely, y = 3.9212x and y = 4.2164x, were used to calculate the concentration of the bare-TiO_2 and Pt-doped TiO_2 (Pt/TiO_2), respectively, based on their turbidity measurements (Zhang et al., 2012). Here, x and y imply to catalyst concentration and the catalyst's solution turbidity, respectively.

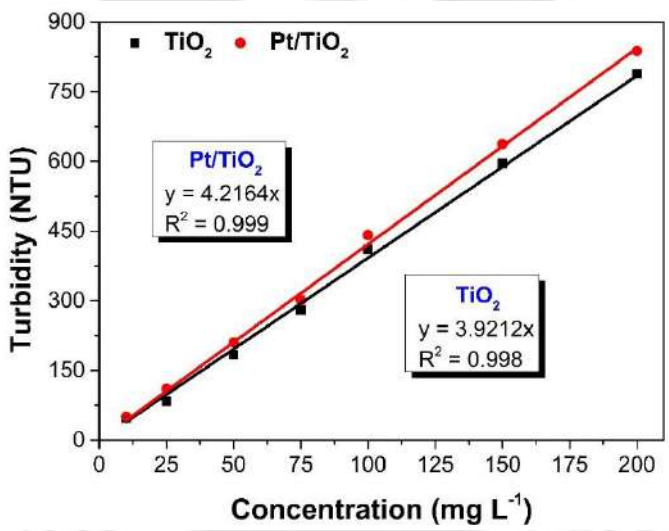

Figure 7.3: Standard curve of turbidity vs. concentration of bare-TiO_2 and Pt-doped TiO_2.

7.2.3 Recovery of bare-TiO_2

7.2.3.1 Effect of pH

The CF-UF membrane setup was employed to recover bare-TiO_2 (50 mg L^{-1}) at 25 °C with a constant CFV of 0.032 m s^{-1}, TMP of 0.75 kg cm^{-2}, and backflush TMFV of 0.14 m s^{-1}. The effect of pH on PWF, permeate flux, and recovery (%) of bare-TiO_2 was investigated across various pH conditions ranging from 4 to 9. As shown in Fig. 7.4a, the PWF exhibited a maximum value at pH 4, with a PWF of 11.19±0.13, gradually decreasing to 10.56±0.17 L m^{-}

^{2} h^{-1} at pH 9. Similarly, the bare-TiO_2 permeate flux and permeability (%) also exhibited a gradual decrease from 10.71±0.17 to 10.08±0.04 L m^{-2} h^{-1} and 95.71±0.22 to 92.31±0.39%, respectively, with an increase in pH from 4 to 9, as illustrated in Fig. 7.4a and Table 7.1. The recovery of bare-TiO_2 in the reject stream also demonstrated an increase with increasing pH. About 99.77±0.22 and 99.74±0.13% of bare-TiO_2 were recovered at pH 4 and 5, respectively, which further reduced to 86.57±2.82% at pH 8 (Fig. 7.4b). However, a slight increase in bare-TiO_2 recovery was observed at pH 9.

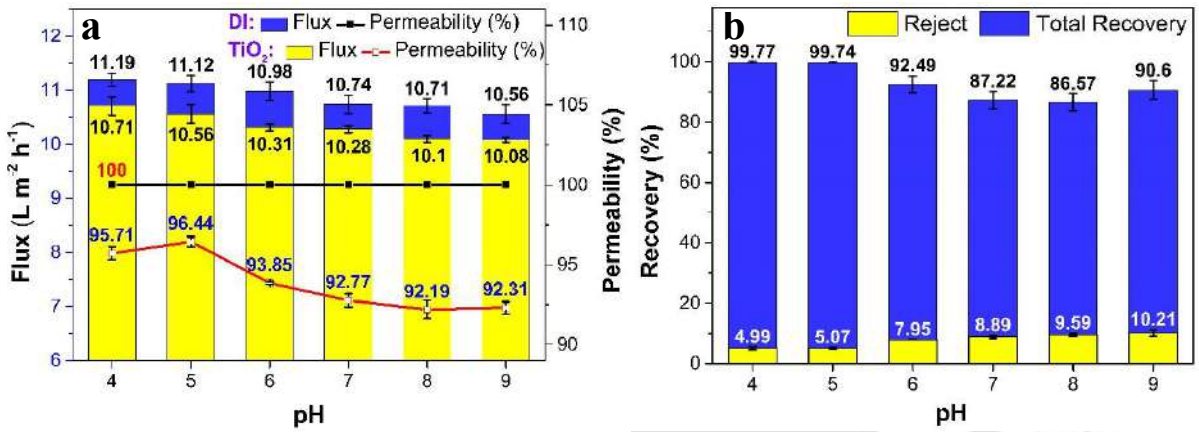

Figure 7.4: (a) Flux and permeability (%) of DI water and bare-TiO_2 solution and (b) bare-TiO_2 recovery in reject stream and overall recovery at different pH ranging from 4 to 9. Recovery of TiO_2 (50 mg L^{-1}) performed at 25 °C with a constant CFV of 0.032 m s^{-1} (flow rate of 22.5 L h^{-1}) and a backflush TMFV of 0.140 m s^{-1} (flow rate of 100 L h^{-1}).

Table 7.1: Obtained parameters at various pH ranging from 4 to 9 during recovery of 50 mg L^{-1} bare-TiO_2.

pH	Pure water flux (L/m².h)	Flux (TiO_2) (L m^{-2} h^{-1})	% Permeability	Recovery (%)		
				Reject	Backflush	Total
4	11.19 ± 0.13	10.71 ± 0.17	95.71 ± 0.43	4.99 ± 0.58	94.78 ± 0.80	99.77 ± 0.22
5	11.12 ± 0.15	10.56 ± 0.17	96.44 ± 0.32	5.07 ± 0.35	94.68 ± 0.48	99.74 ± 0.13
6	10.98 ± 0.17	10.31 ± 0.06	93.85 ± 0.07	7.95 ± 0.02	84.54 ± 2.82	92.49 ± 2.84
7	10.74 ± 0.17	10.28 ± 0.06	92.77 ± 0.42	8.89 ± 0.49	78.33 ± 2.45	87.22 ± 2.94
8	10.71 ± 0.13	10.10 ± 0.06	92.19 ± 0.58	9.59 ± 0.50	76.98 ± 2.32	86.57 ± 2.82
9	10.56 ± 0.17	10.08 ± 0.04	92.31 ± 0.39	10.21 ± 1.01	80.39 ± 2.11	90.60 ± 3.13

It is reported that the PAN fibres get swelled at high pH due to the formation of the carboxylate group through deprotonation of the carboxylic group, which further expands the PAN fibres (Choe et al., 2006). The swelling of membrane fibres at high pH resulting in the

alteration of membrane structure and compression of pores. The smaller pore size decreases the catalyst's recovery due to the trapping and accumulation of bare-TiO_2 inside the membrane (Sato et al., 2023). Additionally, positively charged bare-TiO_2 (6.7 mV) might experience less repulsion from the highly negatively charged membrane (-36.0 mV) at higher pH, which could have decreased the catalyst's recovery (Ravi and Golder, 2023).

Furthermore, the absence of any traces of bare-TiO_2 in the permeate indicates the complete rejection of catalyst particles by the membrane. This demonstrates the effective separation and retention of the catalyst within the membrane system, ensuring that the permeate remains free of catalyst particles. The permeate flux and bare-TiO_2 recovery at pH 4 and 5 demonstrated comparable results. Consequently, pH 5 was selected for further experiments as it provides practically more suitable conditions for the desired outcomes.

7.2.3.2 Effect of bare-TiO_2 concentration

The effect of various concentrations of bare-TiO_2 (ranging from 10 to 250 mg L^{-1}) on water flux, permeability (%), and recovery (%) was examined under optimized pH 5 and 25 °C with a constant CFV of 0.032 m s^{-1}, and backflush TMFV of 0.14 m s^{-1}. Fig. 7.5 illustrates the flux, permeability (%), and recovery of bare-TiO_2, and the obtained parameters are tabulated in Table 7.2.

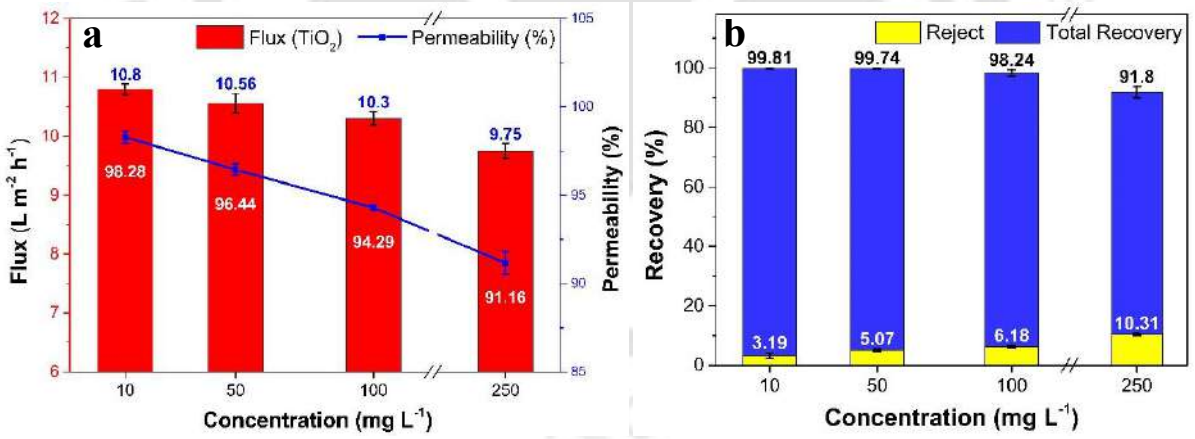

Figure 7.5: (a) Flux and permeability (%) and (b) Recovery of bare-TiO_2 in reject stream and overall recovery at different concentrations ranging from 10 to 250 mg L^{-1}. The recovery of bare-TiO_2 was performed at 25 °C and pH 5 with a constant CFV of 0.032 m s^{-1} (flow rate of 22.5 L h^{-1}) and a backflush TMFV of 0.140 m s^{-1} (flow rate of 100 L h^{-1}).

The permeate flux was gradually decreased from 11.19±0.13 to 9.75±0.13 L m^{-2} h^{-1} (~12.9% decrease) with the introduction of bare-TiO_2 at a concentration up to 250 mg L^{-1}.

Additionally, the bare-TiO_2 recovery in the reject stream increased from 3.19 ± 0.90 to 10.31±0.37, with an increase in the concentration of bare-TiO_2 from 0 to 250 mg L^{-1}. This observed behavior may be attributed to the clogging of a large number of pores and the cake layer formation. In a similar way, the bare-TiO_2 recovery was also decreased from 99.81±0.13 to 91.80±1.80% with an increase in bare-TiO_2 concentration from 10 to 250 mg L^{-1}. The dynamic viscosity of 0 to 250 mg L^{-1} bare-TiO_2 solution and filtration resistance are illustrated in Fig. 7.6.

Table 7.2: Obtained parameters during recovery of various concentrations of bare-TiO_2 (0 to 250 mg L^{-1}).

Bare-TiO_2 (mg L^{-1})	TMP (kg cm^{-2})	Flux, J (L m^{-2} h^{-1})	Permeability (%)	Recovery (%)		
				Reject	Backflushing	Total
0	0.6	11.19 ± 0.13	100	-	-	-
10	0.65	10.80 ± 0.08	98.28 ± 0.35	3.19 ± 0.90	96.62 ± 0.78	99.81 ± 0.12
50	0.75	10.56 ± 0.17	96.44 ± 0.32	5.07 ± 0.35	94.68 ± 0.48	99.74 ± 0.13
100	0.80	10.30 ± 0.12	91.16 ± 0.16	6.18 ± 0.36	92.06 ± 1.36	98.24 ± 1.01
250	0.90	9.75 ± 0.13	91.16 ± 0.65	10.31 ± 0.37	81.07 ± 2.03	91.80 ± 1.80

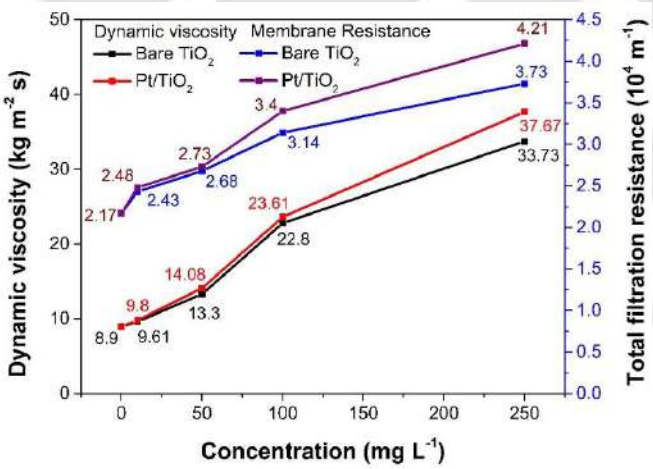

Figure 7.6: Dynamic viscosity of DI water and catalyst's solution (bare-TiO_2 and Pt-doped TiO_2) and membrane resistance at different concentrations ranging from 10 to 250 mg L^{-1}.

The dynamic viscosity of the bare-TiO_2 solution and filtration resistance gradually increased from 8.90 to 33.73 kg m^{-2} s and 2.17×10^4 to 3.73×10^4 m^{-1}, respectively, with an increase in the catalyst concentration from 0 to 250 mg L^{-1}. The dynamic viscosity of the catalyst's solution increased due to the presence of dispersed bare-TiO_2 particles. The clogging

of pores and formation of the cake layer increased the filtration resistance, which in turn, leads to reduced flux and hinders the recovery of catalysts (Berg and Ulbricht, 2020; Yan et al., 2021). Similar results were also observed in earlier studies. Ma et al. (2014) observed up to ~70% flux decline with an increase in the Fe/Al-alginate coagulant concentration (Ma et al., 2014).

7.2.3.3 Effect of CFV

The flux and recovery of bare-TiO_2 were studied across a range of CFV, ranging from 0.032 to 0.105 m s^{-1} (feed flow rates ranging from 22.5 to 75 L h^{-1}) while maintaining the constant TMP of 0.60 to 1.05 kg cm^{-2}. A constant backflush TMFV of 0.140 m s^{-1} (flow rate of 100 L h^{-1}) was utilized in all the experiments. The results of this investigation are shown in Figs. 7.7a-7.7c and Table 7.3.

PWF was increased from 11.19±0.13 to 30.69±0.55 L m^{-2} h^{-1} with an increase in CFV from 0.032 to 0.105 m s^{-1} when the permeability was 100%. The permeate flux exhibited an increase from 8.70±0.25 to 14.07±0.55 and 10.56±0.17 to 17.94±0.68 L m^{-2} h^{-1}, as the CFV was increased from 0.032 to 0.105 m s^{-1} at the constant TMP of 0.60 and 0.75 kg cm^{-2}, respectively (Fig. 7.7a). Similarly, the permeate flux was also increased with CFV at the constant TMP of 0.60 and 0.75 kg cm^{-2}. A rapid increase in the permeate flux was observed with an increase in the CFV from 0.032 to 0.063 m s^{-1}, which could be due to the removal of the cake layer and deformation of the membrane at high CFV (Ren et al., 2019). However, the permeate flux varied linearly at a slow rate with a further increase in the CFV from 0.063 to 0.105 m s^{-1}. Unlikely, the permeability (%) was decreased with an increase in the CFV due to an increase in the reject (%) at a constant TMP (Fig. 7.7b). The permeability exhibited a decrease from 83.88±2.35 to 39.64±1.94 and 99.30±0.08 to 66.67±1.52% with an increase in CFV of 0.032 and 0.105 m s^{-1} at TMP of 0.60 and 1.05 kg cm^{-2}, respectively.

Furthermore, almost complete recovery of bare-TiO_2 (99.21-99.74%) was observed at different CFV ranging from 0.032 to 0.105 m s^{-1}, when the TMP was fixed at 0.60 and 0.75 kg cm^{-2} (Fig. 7.7c). At higher TMP of 0.90 and 1.05 kg cm^{-2}, the bare-TiO_2 recovery increased from 96.49±1.74 to 99.03±0.47 and 92.33±3.02 to 97.16±2.04, when CFV was increased from 0.032 to 0.063 m s^{-1}, respectively. This increase in the bare-TiO_2 recovery could be due to the simultaneous removal of the cake layer at higher CFV (Ren et al., 2019). However, further increase in the CFV to 0.032 to 0.105 m s^{-1} slightly decreased the bare-TiO_2 recovery to 98.53±1.11 and 98.75±1.44% at TMP of 0.90 kg cm^{-2} and 96.08±2.34 and 94.17±3.19% at TMP of 1.05 kg cm^{-2}, respectively, which could be due to the clogging of the internal pores of

the membrane at a high CFV (Sioutopoulos et al., 2019). Furthermore, it was noted that the bare-TiO_2 recovery in the reject stream increased with an increase in the CFV due to the simultaneous removal of the cake layer and increased reject (%).

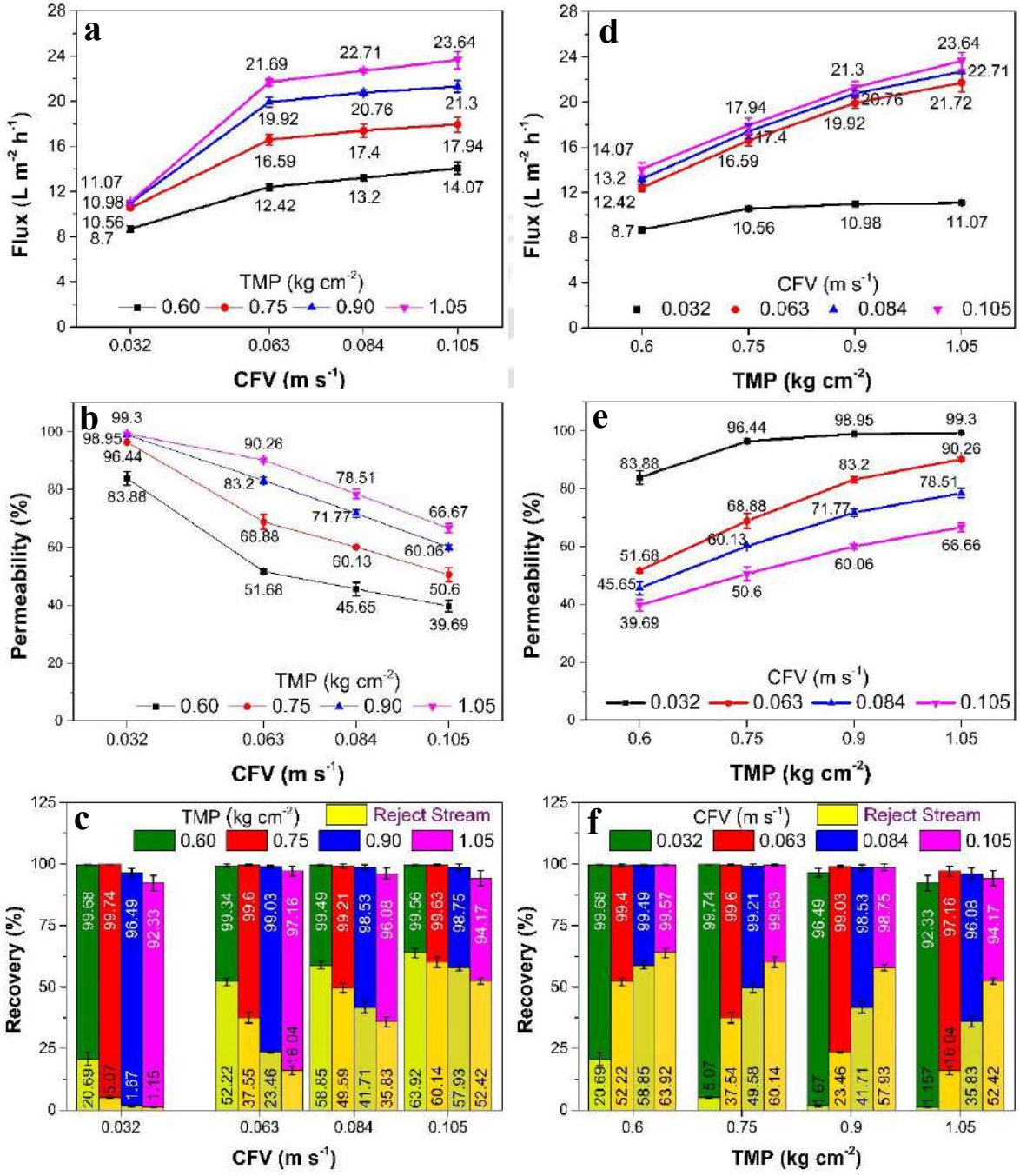

Figure 7.7: Effect of CFV on (a) Flux, (b) Permeability, and (c) TiO_2 recovery in reject stream and total recovery; Effect of TMP on (d) Flux, (e) Permeability, and (f) TiO_2 recovery in reject stream and total recovery. CFV ranging from 0.032 to 0.105 m s^{-1} (feed flow rates ranging from 22.5 to 75 L h^{-1}) and TMP ranging from 0.60 to 1.05 kg cm^{-2}. The yellow colour columns represent recovery through reject stream.

Table 7.3: Obtained parameters during recovery of bare-TiO_2 at different CFV ranging from 0.032 to 0.105 m s^{-1} (feed flow rates ranging from 22.5 to 75 L h^{-1}) and TMP ranging from 0.60 to 1.05 kg cm^{-2}.

CFV (m s^{-1})	TMP (kg cm^{-2})	Flux, J ($Lm^{-2}h^{-1}$)	Permeability (%)	Recovery (%)	
				Reject	Total
0.032	0.60	11.19 ± 0.13 (PWF)	100	-	-
	0.60	8.70 ± 0.25	83.88 ± 2.35	20.69 ± 2.67	99.68 ± 0.18
	0.75	10.56 ± 0.17	96.44 ± 0.32	5.07 ± 0.35	99.74 ± 0.13
	0.90	10.98 ± 0.08	98.95 ± 0.20	1.67 ± 0.25	96.49 ± 1.74
	1.05	11.07 ± 0.13	99.30 ± 0.08	1.15 ± 0.07	92.33 ± 3.02
0.063	0.60	22.29 ± 0.30 (PWF)	100	-	-
	0.60	12.42 ± 0.34	51.68 ± 0.59	52.22 ± 1.54	99.40 ± 0.59
	0.75	16.59 ± 0.47	68.88 ± 2.54	37.54 ± 2.15	99.60 ± 0.51
	0.90	19.92 ± 0.42	83.20 ± 1.18	23.46 ± 0.29	99.03 ± 0.47
	1.05	21.72 ± 0.85	90.26 ± 0.66	16.04 ± 1.62	97.16 ± 2.04
0.084	0.95	25.95 ± 0.21 (PWF)	100	-	-
	0.60	13.20 ± 0.25	45.65 ± 2.25	58.85 ± 1.62	99.49 ± 0.37
	0.75	17.40 ± 0.59	60.13 ± 0.25	49.58 ± 1.76	99.21 ± 0.75
	0.90	20.76 ± 0.25	71.77 ± 1.28	41.71 ± 2.32	98.53 ± 1.11
	1.05	22.71 ± 0.21	78.51 ± 1.63	35.83 ± 1.94	96.08 ± 2.34
0.105	1.30	30.69 ± 0.55 (PWF)	100	-	
	0.60	14.07 ± 0.55	39.64 ± 1.94	63.92 ± 1.85	99.56 ± 0.28
	0.75	17.94 ± 0.68	50.60 ± 2.40	60.14 ± 2.18	99.63 ± 0.41
	0.90	21.30 ± 0.51	60.06 ± 0.87	57.93 ± 1.36	98.75 ± 1.44
	1.05	23.64 ± 0.76	66.67 ± 1.52	52.42 ± 1.27	94.17 ± 3.19

7.2.3.4 Effect of TMP

The effect of various TMP, ranging from 0.60 to 1.05 kg cm^{-1} on permeate flux, permeability (%) and recovery of bare-TiO_2 (50 mg L^{-1}) at constant CFV ranging from 0.032 and 0.105 m s^{-1} (feed flow rates ranging from 22.5 and 75 L h^{-1}), respectively, was studied at the optimal pH of 5 and 25 °C with a constant backflush TMFV of 0.14 m s^{-1} (Figs. 7.7d-7.7f). Both permeate flux and permeability increased from 8.70±0.25 to 11.07±0.13 L m^{-2} h^{-1} and 83.88±2.35 to 99.30±0.08%, respectively, with an increase in TMP from 0.60 to 1.05 kg cm^{-2}

at a fixed CFV of 0.032 m s^{-1} (Figs. 7.7d and 7.7e). The permeate flux exhibited a linear increase from 12.42±0.34 to 21.72±0.85, 13.20±0.25 to 22.71±0.21, and 14.07±0.55 to 23.64±0.76 L m^{-2} h^{-1} with an increase in TMP from 0.60 to 1.05 kg cm^{-2} at a fixed CFV of 0.063, 0.084 and 0.105 m s^{-1}, respectively. Similarly, the permeability increased from 51.68±0.59 to 90.26±0.66, 45.65±2.25 to 78.51±1.63 and 39.61±1.94 to 66.67±1.52%. However, slowness in the increment of flux and permeability was observed at 1.05 kg cm^{-2} TMP, which could be due to an increase in the filtration and cake resistance at higher TMP.

Furthermore, almost a persistent bare-TiO_2 recovery of 99.74±0.13-99.21±0.75% was observed at TMP of 0.60 to 0.75 kg cm^{-2}, when operated at a fixed CFV of 0.032 to 0.105 m s^{-1} (Fig. 7.7f). At 0.032 and 0.063 m s^{-1} CFV, the bare-TiO_2 recovery decreased from 99.68±0.18 to 92.33±3.02 and 99.40±0.59 to 97.16±2.04% with an increase in TMP from 0.60 and 1.05 kg cm^{-2}, respectively. A similar trend was also observed at 0.084 and 0.105 m s^{-1} CFV, where bare-TiO_2 recovery decreased from 99.49±0.37 to 96.08±2.34 and 99.56±0.28 to 94.17±3.19%, respectively. Overall, a decrease in bare-TiO_2 recovery was observed at higher TMPs of 0.90 and 1.05 kg cm^{-2}. This decrease in the bare-TiO_2 recovery could be due to the cake layer formation and internal pore clogging (Ren et al., 2019). It is also reported that the recovery in the reject stream decreased from 20.69±2.67 to 1.15±0.07% and 63.92±1.85 to 52.42±1.27% with an increase in TMP at CFVs of 0.032 and 0.105 m s^{-1}, respectively. This decrease in bare-TiO_2 recovery in the reject stream is due to an increase in the permeability (%) associated with an increased TMP.

7.2.4 Resistance-in-series (RIS) model

The resistance-in-series (RIS) model (Chapter 2) was employed to calculate the theoretical flux of the bare-TiO_2 system at different CFV ranging from 0.032 to 0105 m s^{-1} and constant TMP ranging from 0.60 to 1.05 kg cm^{-2}. The calculated flux well matched with the experimental outcomes at different CFV and TMP, and the parity plot exhibited slopes of 0.995 to 0.957 (Fig. 7.8) with a spread of all experimental results within 95% confidence level.

The membrane resistance (R_m), total filtration resistance (R_t), cake resistance (R_c), and specific cake resistance (r_c) during bare-TiO_2 recovery (50 mg L^{-1}) at different CFV ranging from 0.032 to 0.105 m s^{-1} and TMP ranging from 0.60 to 1.05 kg cm^{-2} are presented in Table 7.4. The R_m was found to be 2.79×10^4 m^{-1} at a CFV of 0.032 m s^{-1}, which decreased to 1.27×10^4 m^{-1} at a CFV of 0.063 m s^{-1}. However, a further increase in the CFV to 0.90 and 0.105 m s^{-1} increased the R_m to 1.48×10^4 and 1.71×10^4 m^{-1}, respectively. These variations in R_m could be due to the deformation of the membrane with the change in CFV (Huisman et al., 1997).

In most CFV and TMP arrangements, both R_t and R_c gradually decreased with an increase in the CFV at a constant TMP. R_c gradually decreased from 0.62-1.41 ($\times 10^4$) to 0.01-0.08 ($\times 10^4$) m^{-1}, with an increase in CFV from 0.032 to 0.105 m s^{-1}. This decrease in R_c could be due to cake-layer formation on the outer surface of the membrane at a low CFV, which is simultaneously removed at a higher CFV during bare-TiO_2 recovery.

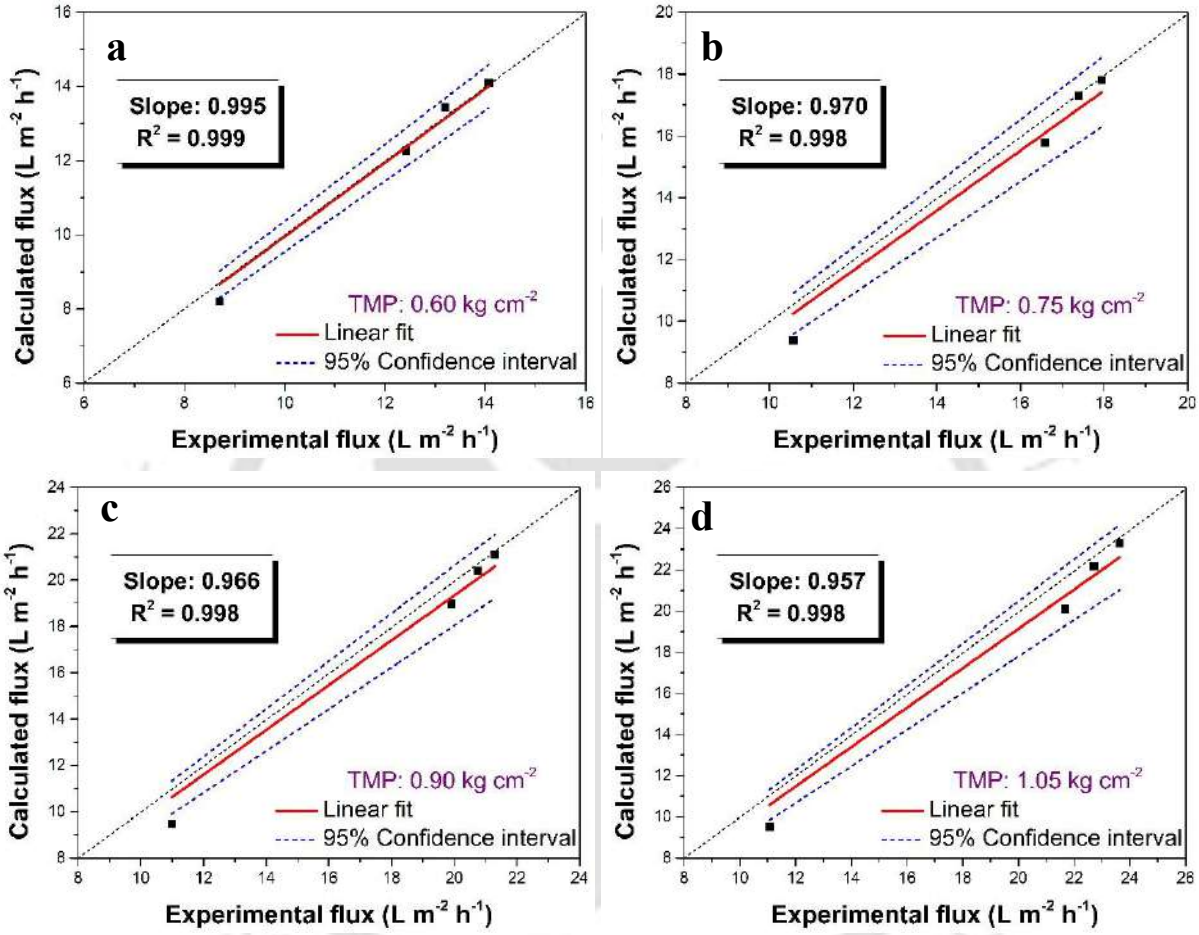

Figure 7.8: Comparison of calculated (using RIS model) and experimental flux at various CFV ranging from 0.032 to 0.105 m s^{-1} and a constant TMP of (a) 0.60, (b) 0.75, (c) 0.90 and (d) 1.05 kg cm^{-2}, during bare-TiO_2 recovery.

Table 7.4: Membrane resistance, total filtration resistance, cake resistance, and specific cake resistance during bare-TiO_2 recovery (50 mg L^{-1}) at different CFV ranging from 0.032 to 0.105 m s^{-1} (feed flow rates ranging from 22.5 to 75 L h^{-1}) and TMP (0.60 to 1.05 kg cm^{-2}).

CFV (m s^{-1})	TMP (kg cm^{-2})	Membrane resistance, R_m (m^{-1})	Total filtration resistance, R_t (m^{-1})	Cake resistance, R_c (m^{-1})	Specific cake resistance, r_c (m^{-2})

0.032	0.60	2.17×10^4	2.79×10^4	0.62×10^4	1.43×10^7
	0.75		2.76×10^4	0.59×10^4	1.13×10^7
	0.90		3.13×10^4	0.96×10^4	1.79×10^7
	1.05		3.58×10^4	1.41×10^4	2.61×10^7
0.063	0.60	1.27×10^4	1.95×10^4	0.68×10^4	1.26×10^7
	0.75		1.82×10^4	0.55×10^4	0.77×10^7
	0.90		1.73×10^4	0.46×10^4	0.52×10^7
	1.05		1.85×10^4	0.58×10^4	0.60×10^7
0.084	0.60	1.48×10^4	1.84×10^4	0.36×10^4	0.63×10^7
	0.75		1.74×10^4	0.26×10^4	0.38×10^7
	0.90		1.75×10^4	0.27×10^4	0.34×10^7
	1.05		1.82×10^4	0.34×10^4	0.38×10^7
0.105	0.60	1.71×10^4	1.72×10^4	0.01×10^4	0.02×10^7
	0.75		1.69×10^4	0.04×10^4	0.06×10^7
	0.90		1.80×10^4	0.08×10^4	0.12×10^7
	1.05		1.80×10^4	0.08×10^4	0.10×10^7

7.2.5 Membrane fouling and regeneration

The membrane fouling and regeneration studies were performed for 5 consecutive cycles of measuring PWF before and after bare-TiO_2 filtration, followed by backflushing. Fig. 7.9 and Tables 7.5 illustrate the PWFs, fouling (%), and flux recovery (%) at both 0.032 and 0.063 m s^{-1} CFV. As shown in Figs. 7.9a and 7.9c, the PWF decreased after filtration of bare-TiO_2 at both CFV. This reduction in the PWF is likely attributed to the clogging of the membrane pores and the formation of the bare-TiO_2 cake layer (Yan et al., 2021). However, the PWF of the fresh, used, and backflushed membranes showed a slight decrease as the flux cycles progressed, which could be due to the clogging of pores by trapped particles. It is also reported that high operating pressure and gradual plugging of pores could possibly damage the pore structures, which, in turn, decreased the PWF (You et al., 2021; Li et al., 2023). The antifouling properties of the membrane were investigated by describing the membrane fouling and flux recovery studies, as depicted in Figs. 7.9b and 7.9d. The obtained results revealed that there was about 9.56±0.24 to 9.86±0.04 and 7.29±0.45 to 9.63±0.14% reversible membrane fouling at 0.032 and 0.063 m s^{-1} CFV, respectively. Additionally, almost complete flux recovery, ranging from 99.33±0.18 to 99.53±0.11 and 98.78±0.20 to 99.33±0.57%, was observed at 0.032 and 0.063 m s^{-1} CFV, respectively. However, no extreme changes in the PWFs, reversible membrane fouling (%), and flux recovery (%) were observed with the progression of flux cycles. Excellent flux recovery after backflushing underscores outstanding antifouling properties of the UF-CF membrane.

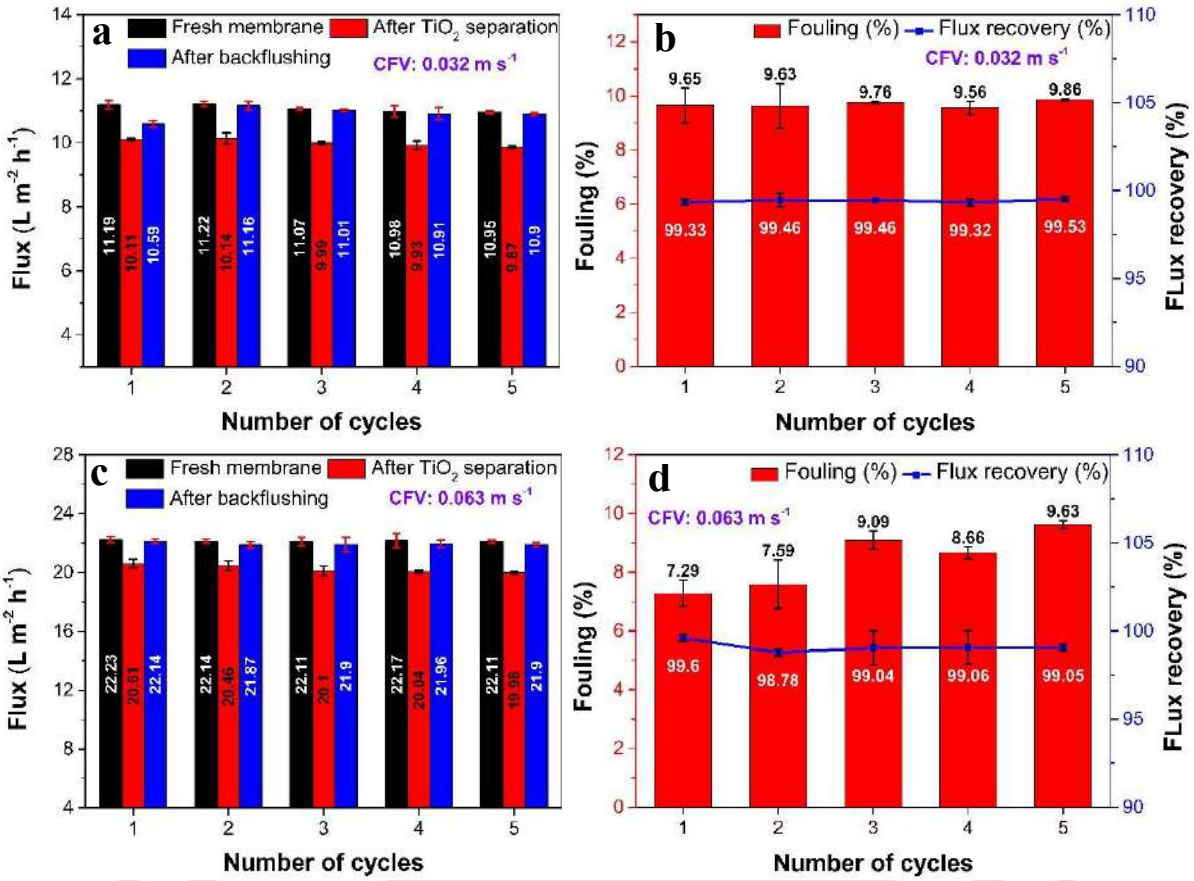

Figure 7.9: (a) PWF through fresh membrane, after bare-TiO_2 separation and backflushed membrane, and (b) Fouling (%) during TiO_2 separation at a constant CFV of 0.032 m s^{-1} (flow rate of 22.5 L h^{-1}) and flux recovery (%) after backflushing; (c) PWF through fresh membrane, after TiO_2 separation and backflushed membrane, and (d) Fouling (%) during TiO_2 separation a constant CFV of 0.063 m s^{-1} (flow rate of 45 L h^{-1}) and flux recovery (%) after for 5 consecutive cycles.

Table 7.5: Parameters of membrane fouling (%) and flux recovery (%) studies performed by measuring PWF of the fresh membrane after bare-TiO_2 separation at a constant CFV of 0.032 m s^{-1} (flow rate of 22.5 L h^{-1}) and backflushed membrane (after backflushing at a backflush TMFV of 0.140 m s^{-1} (flow rate of 100 L h^{-1}) for 5 consecutive cycles.

	PWF (L m^{-2} h^{-1})			Fouling (%)	Flux recovery (%)
Cycle	Fresh membrane	After TiO_2 filtration	Backflushed		
1	11.19 ± 0.13	10.11 ± 0.04	11.12 ± 0.11	9.65 ± 0.65	99.33 ± 0.18
2	11.22 ± 0.08	10.14± 0.17	11.16 ± 0.13	9.63 ± 0.83	99.46 ± 0.38
3	11.07 ± 0.04	9.99 ± 0.04	11.01 ± 0.04	9.76 ± 0.04	99.46 ± 0.00
4	10.98 ± 0.17	9.93 ± 0.13	10.91 ± 0.19	9.56 ± 0.24	99.33 ± 0.20
5	10.95 ± 0.04	9.87 ± 0.04	10.90 ± 0.03	9.86 ± 0.04	99.53 ± 0.11

7.2.6 Recovery of Pt-doped TiO_2

The recovery of 10-250 mg L^{-1} Pt-doped TiO_2 was performed at pH 5 and 25 °C with a constant CFV of 0.032 m s^{-1}, and backflush TMFV of 0.14 m s^{-1}. The obtained results are depicted in Fig. 7.10 and Table 7.6.

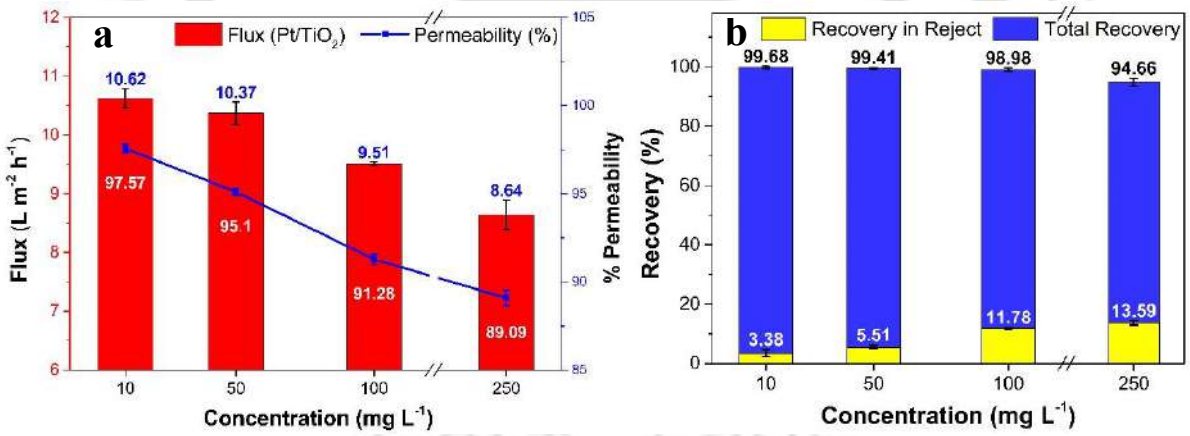

Figure 7.10: (a) Flux and permeability (%) and (b) Recovery of Pt-doped TiO_2 in reject stream and overall recovery at different concentrations ranging from 10 to 250 mg L^{-1}. The recovery of Pt-TiO_2 was performed at 25 °C and pH 5 with a constant CFV of 0.032 m s^{-1} (flow rate of 22.5 L h^{-1}) and a backflush TMFV of 0.140 m s^{-1} (flow rate of 100 L h^{-1}).

It is found that the permeate flux and permeability (%) decreased from 11.19±0.13 to 9.75±0.13 L m^{-2} h^{-1} and 100 to 91.16±0.65%, respectively, with an increase in Pt-doped TiO_2 concentration from 0 to 250 mg L^{-1}. About 99.68±0.39 and 99.41±0.29% Pt-doped TiO_2 were

recovered at 10 and 50 mg L^{-1} concentrations, which gradually decreased to 94.66±1.36% at 250 mg L^{-1}. However, the recovery in the reject stream increased with increasing Pt/TiO_2 concentration, caused due to lower permeability. This decrease in permeate flux and overall recovery with increasing Pt-doped TiO_2 concentration can be attributed to an increase in catalyst solution dynamic viscosity and filtration resistance caused by pore blockage and cake layer formation (Fig. 7.6). The dynamic viscosity of the Pt-doped TiO_2 solution and filtration resistance was increased from 8.90 to 37.67 kg m^{-2} s and 2.17×10^4 to 4.21×10^4 m^{-1}, respectively, with an increase in the catalyst concentration from 0 to 250 mg L^{-1}. Compared to bare-TiO_2 (Fig. 7.5), Pt-doped TiO_2 exhibited lower flux and permeability, which might be attributed to rapid blockage of the membrane pores by highly hydrophilic Pt-doped TiO_2 particles. The hydrophilic membrane surface facilitates the better transport of hydrophilic particles inside the membrane, leading to rapid pore plugging and, consequently, decreased flux and permeability (Kang et al., 2020; Yan et al., 2021).

Table 7.6: Obtained parameters during recovery of various concentrations of Pt-doped TiO_2 (0 to 250 mg L^{-1}).

Bare-TiO_2 (mg L^{-1})	TMP (kg cm^{-2})	Flux, J (L m^{-2} h^{-1})	Permeability (%)	Recovery (%)		
				Reject	Backflushing	Total
0	0.6	11.19 ± 0.13	100	-	-	-
10	0.65	10.62 ± 0.17	97.57 ± 0.27	3.38 ± 1.21	96.30 ± 0.81	99.68 ± 0.39
50	0.75	10.37 ± 0.19	95.10 ± 0.21	5.51 ± 0.58	93.90 ± 0.87	99.41 ± 0.29
100	0.80	9.51 ± 0.03	91.28 ± 0.29	11.78 ± 0.23	87.20 ± 0.68	98.98 ± 0.49
250	0.90	8.64 ± 0.25	89.09 ± 0.45	13.59 ± 0.67	81.07 ± 2.03	94.66 ± 1.36

The present study exhibited superior photocatalysts (bare-TiO_2 and Pt-doped TiO_2) recovery than reported studies. However, very few studies reported recovery of photocatalysts. Liriano-Jorge et al. (2014) achieved ~90% bare-TiO_2 recovery with a working volume of only 50 mL (Liriano-Jorge et al., 2014). A CF-UF membrane with a nominal area of 19.6 cm^2 exhibited >10^3 folds lower bare-TiO_2 recovery, in comparison to the present study (Xue et al., 2008). Mehta et al. (2016) performed ZnO separation through a membrane system and observed ~90% ZnO retention (Mehta et al., 2016). Additionally, Table 7.7 summarizes the performance of different potential techniques for catalyst particles recovery along with membrane separation.

Table 7.7: Photocatalysts recovery through different separation methods and their comparison with recovery of bare-TiO_2 and Pt-doped TiO_2 through membrane separation (present study).

Technique	Photocatalyst	Conc. (mg L^{-1})	Volume (L)	Recovery (%)	Source
Magnetic separation	TiO_2 with Fe-magnetic seeds	100	-	~99	(Bakhteeva et al., 2021)
Encapsulation and adsorption	TiO_2	50	0.05	24.3	(Taylor et al., 2020)
Coagulation and drying	TiO_2	50	0.1	64.4	(Patchaiyappan et al., 2016)
Settling, centrifugation and air plasma treatment	P25-TiO_2	70	7 (settling); 0.5 (centrifugation)	~77	(Bockenstedt et al., 2021)
	Porous TiO_2			~57	
Membrane separation	TiO_2	1000	0.05	~90	(Liriano-Jorge et al., 2014)
	ZnO			~90*	(Mehta et al., 2016)
	TiO_2	10-250	2-5	99.8-91.8	Present Study
	Pt-doped TiO_2			99.7-94.7	

*Retention (%)

7.2.7 Particle characterization after recovery

The hydrodynamic diameter (HDD) of fresh and recovered (in reject and backflush streams) catalysts was calculated to investigate any changes in their hydrodynamic particle size during catalysts recovery (50 mg L^{-1}, pH 5, and CFV of 0.032 m s^{-1}). For analysis, reject and backflush stream samples were diluted to maintain a final catalyst concentration of 50 mg $L^{-1,}$ and all samples were sonicated for 30 min. The obtained particle size distribution and corresponding HDDs are illustrated in Fig. 7.11.

The hydrophobic bare-TiO_2 particles exhibited a larger HDD of 301.87 nm (Fig. 7.11a) than highly hydrophilic Pt-doped TiO_2, which has an average HDD of 144.59 nm (Fig. 7.11d). This difference can be attributed to the tendency of hydrophobic particles to agglomerate in water, potentially increasing their HDD compared to hydrophilic particles. The HDD of recovered bare-TiO_2 and Pt-doped TiO_2 in the reject stream increased to 346.56 and 166.02 nm, respectively (Figs. 7.11b and 7.11e). Subsequently, it further increased to 395.22 and 193.65 nm, respectively (Figs. 7.11c and 7.11f) in the backflush stream due to the agglomeration of particles during the recovery process (Berg and Ulbricht, 2020).

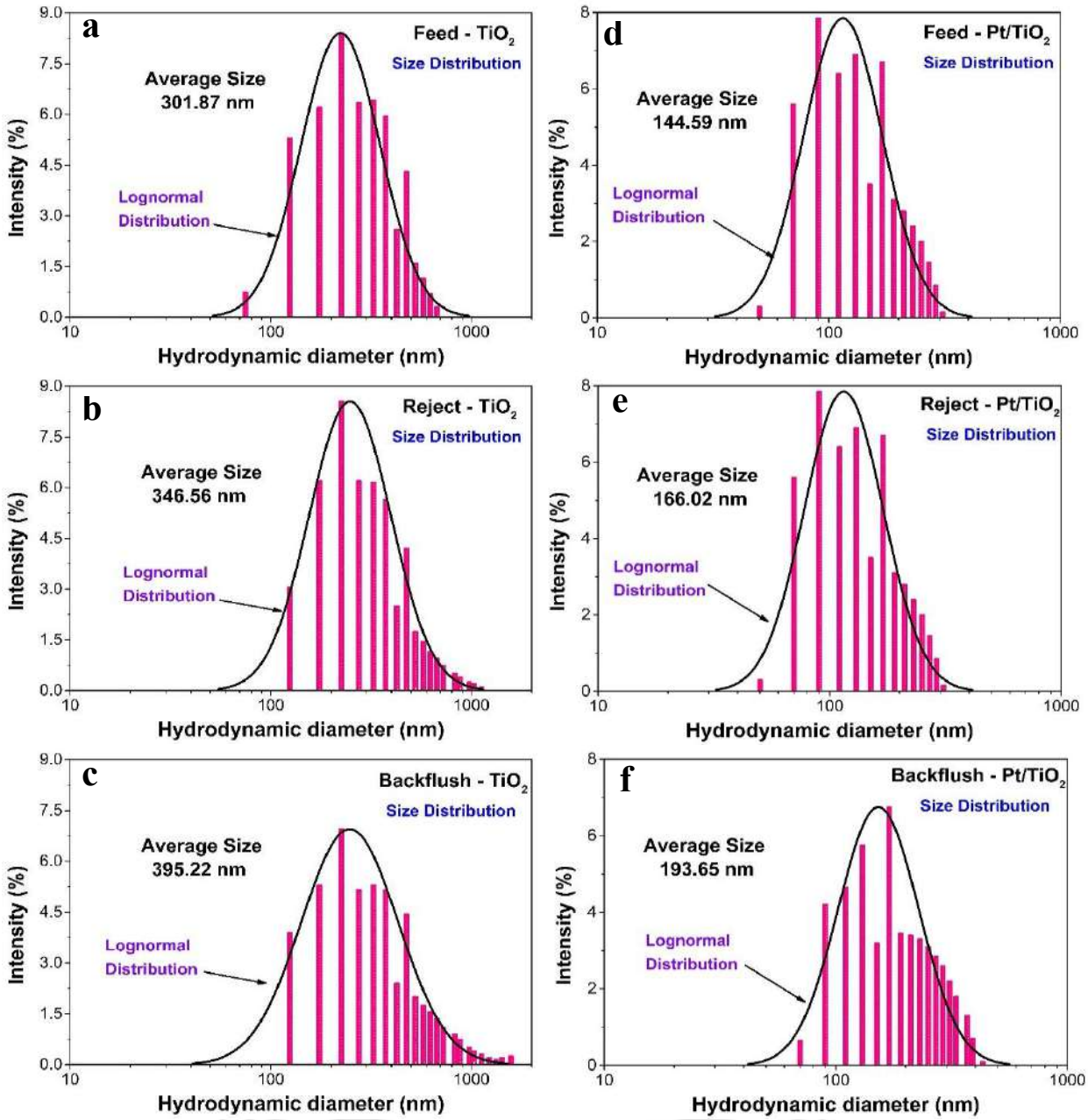

Figure 7.11: Hydrodynamic diameter and size distribution of TiO_2 particles in (a) Feed, (b) Reject and (c) Backflush stream; Hydrodynamic diameter and size distribution of Pt/TiO_2 particles in (d) Feed, (e) Reject and (f) Backflush stream.

The particle size lognormal distribution of both catalysts in the reject and backflush streams becomes right-tailed due to fewer large particles. This suggests that while some agglomeration of particles may occur during the recovery process, the size of the majority of catalyst particles remains relatively consistent. Although, a superior variation in the HDD was observed for fresh and recovered bare-TiO_2 compared to Pt-doped TiO_2. This difference could be due to the greater agglomeration of the bare-TiO_2 particles over the hydrophilic surface and

pores of the membrane, likely due to the hydrophobic effect (Loosli and Stoll, 2017). However, the HDDs of fresh and used catalysts remained relatively comparable and did not exhibit extreme differences.

7.2.8 Photocatalytic degradation of CIP using fresh and recovered photocatalysts

The photocatalytic performance of fresh and recovered bare-TiO_2 and Pt-doped TiO_2 was systematically evaluated in terms of surface adsorption in dark and photocatalytic degradation under visible light (Fig. 7.12). The dark adsorption was slightly decreased from 22.77±1.58 to 19.58±2.07% in the case of recovered bare-TiO_2 than fresh counterpart. Similarly, slight decrease from 49.71±2.21 to 45.56±3.65% was also observed for recovered Pt-doped TiO_2. However, no significance difference was observed in photocatalytic degradation of CIP by both photocatalysts. Recovered bare-TiO_2 and Pt-doped TiO_2 photocatalysts exhibited only 1.28 and 0.82% decreased, respectively, in CIP degradation than that of fresh counterparts. Importantly, both catalysts retained their performance after recovery, confirming excellent stability of photocatalysts and potential of recovery system in enabling their reusability.

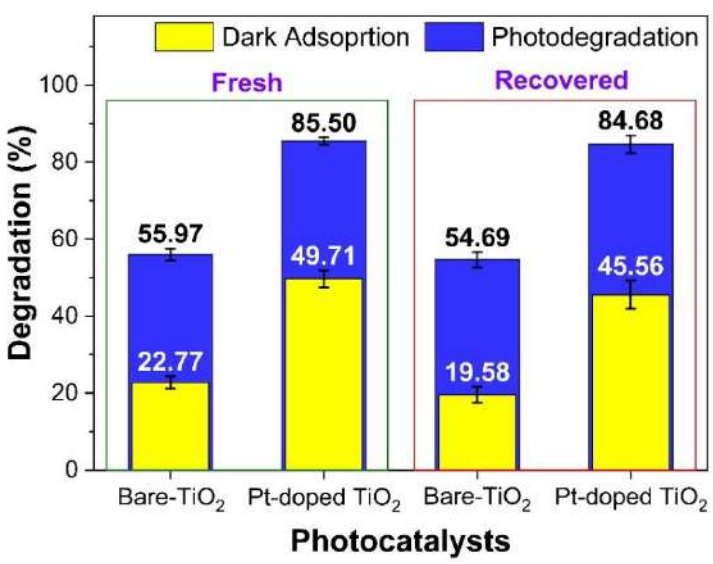

Figure 7.12: Surface adsorption in dark conditions and photocatalytic degradation under visible light using fresh and recovered bare-TiO_2 and Pt-doped TiO_2.

7.2.9 Recovery of other metal-doped TiO_2 photocatalysts

Fig. 7.13 demonstrates the flux, permeability, and recovery of bare-TiO_2 and various metal-doped TiO_2 photocatalysts under controlled operating conditions (50 mg L^{-1} concentration, 25 °C, pH 5, CFV = 0.032 m s^{-1}, and backflush TMFV = 0.140 m s^{-1}). The water

flux across all membranes remains nearly consistent, with values ranging from 10.31±0.06 to 10.56±0.17 L m^{-2} h^{-1} (Fig. 7.13a) with permeability of 94.80±0.10 to 96.44±0.32%, indicating that metal doping does not significantly affect the hydraulic performance.

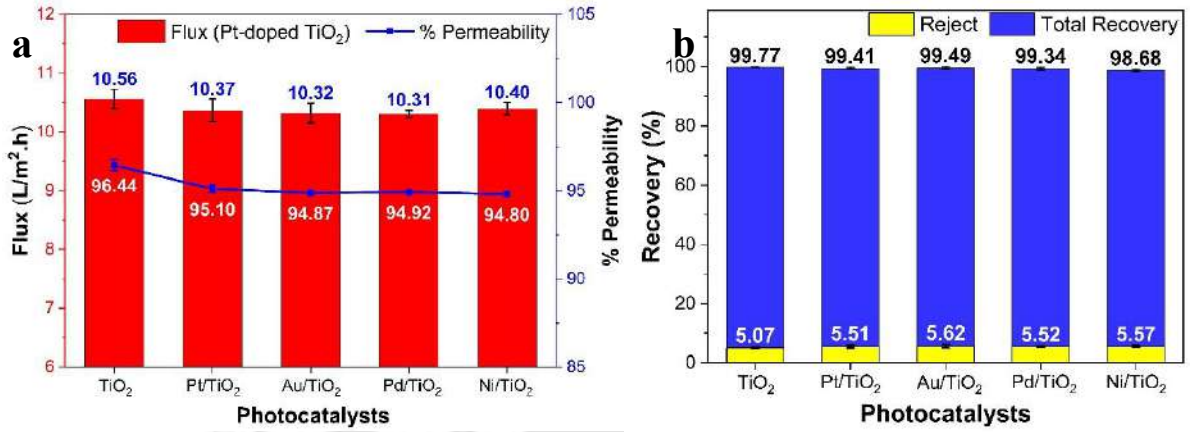

Figure 7.13: (a) Flux and permeability (%) and (b) Recovery of bare and metal-doped TiO_2 in reject stream and overall recovery at fixed concentration of 50 mg L^{-1}. The recovery was performed at 25 °C and pH 5 with a constant CFV of 0.032 m s^{-1} (flow rate of 22.5 L h^{-1}) and a backflush TMFV of 0.140 m s^{-1} (flow rate of 100 L h^{-1}).

Overall, the membrane separation process demonstrated >98.6% recovery of bare-TiO_2 and metal doped TiO_2. photocatalysts. Among them, bare-TiO_2 showed the highest recovery of 99.77±0.10%, while Ni-doped TiO_2 exhibited the lowest recovery of 98.68±0.34%. The contribution of the reject stream in catalysts recovery was minimal (~5%), indicating that the majority of the photocatalysts were successfully recovered via the backflushing. These results indicate that metal doping does not compromise flux, permeability, or recovery performance.

7.3 Major findings

The present has successfully demonstrated a pilot-scale cross-flow ultrafiltration (CF-UF) membrane system to recover bare-TiO_2 and Pt-doped TiO_2 nano-photocatalysts. This recovery system comprises a polymeric CF-UF membrane with a nominal pore size of 75 kDa (0.01 µm) and a surface area of 2 m^2. The membrane spikes were found to be more hydrophilic on the inside compared to the outer surface, with an inner and outer diameter of 0.78 and 1.20 mm, respectively, and a thickness of 0.21 mm. The membrane was made of modified PAN with 7.8% of crystallinity and 2.95 MPa tensile strength. The recovery of catalysts was performed through the reject and backflush streams, and the total recovery (%) was determined by measuring the turbidity of both the reject and backflush streams. PWF, permeate flux, and

catalysts recovery (%) exhibited a decrease with an increase in pH. Specifically, at pH 4 and 5, about 99.77±0.22 and 99.74±0.13% of TiO_2 were successfully recovered, respectively, with corresponding flux values of 10.71±0.17 and 10.56±0.17 L m^{-2} h^{-1}. The effect of various concentrations of bare-TiO_2 (ranging from 10 to 250 mg L^{-1}) on water flux, permeability (%), and catalyst recovery (%) was examined and showed almost complete recovery at 50 mg L^{-1} bare-TiO_2 concentration. Both the PWF and permeate flux were increased when operating at a high TMP, which is often associated with a higher CFV. Membrane fouling and flux recovery studies revealed excellent antifouling properties of CF-UF membrane with a maximum of 9.86±0.04% reversible fouling, and the flux recovery was substantial, reaching a minimum of 98.78±0.20%. About 99.41±0.29% Pt-doped TiO_2 (at a concentration of 50 mg L^{-1}) was recovered in conjunction with a flux and permeability of 10.37±0.19 L m^{-2} h^{-1} and 95.10±0.21%, respectively. The hydrodynamic diameters of bare-TiO_2 and Pt-doped TiO_2 particles gradually increased in the reject and backflush streams. However, despite this increase, the HDDs of fresh and used catalysts did not exhibit extreme differences. The recovered bare-TiO_2 and Pt-doped TiO_2 exhibited no significance difference in photocatalytic degradation of CIP. However, slight decrease in dark adsorption was observed. Additionally, >98.7% recovery of other metal-doped TiO_2 photocatalyst was achieved. Hence, the present study provides valuable insights into understanding the potential of CF-UF membrane as a pilot and industrial scale photocatalysts recovery system for their effective regeneration and reusability.

Almost complete recovery of the photocatalysts were achieved by membrane filtration. Therefore, the membrane system was further integrated with the pilot-scale photocatalytic and biological degradation process for the complete degradation of PhACs (Chapter 8).

References

Bakhteeva, I.A., Medvedeva, I. V., Zhakov, S. V., Byzov, I. V., Filinkova, M.S., Uimin, M.A., Murzakaev, A.M., 2021. Magnetic separation of water suspensions containing TiO_2 photocatalytic nanoparticles. Sep. Purif. Technol. 269. https://doi.org/10.1016/j.seppur.2021.118716

Berg, T. van den, Ulbricht, M., 2020. Polymer nanocomposite ultrafiltration membranes: The influence of polymeric additive, dispersion quality and particle modification on the integration of zinc oxide nanoparticles into polyvinylidene difluoride membranes. Membranes (Basel). 10. https://doi.org/10.3390/membranes10090197

Bhan, C., Golder, A.K., 2025. Nature-Inspired Vertically Oriented 1D Bi_2S_3 Surface Nanorods for Ultra-Selective Electrochemical Sensing of Mancozeb. https://doi.org/10.1021/acs.langmuir.5c00915

Bhan, C., Golder, A.K., 2023. Utilizing bioinspired AgNPs as an antibacterial agent to enhance ceramic membrane performance. J. Environ. Chem. Eng. 11, 110283. https://doi.org/10.1016/j.jece.2023.110283

Bockenstedt, J., Vidwans, N.A., Gentry, T., Vaddiraju, S., 2021. Catalyst recovery, regeneration and reuse during large-scale disinfection of water using photocatalysis. Water (Switzerland) 13. https://doi.org/10.3390/w13192623

Chaudhari, S., Shin, H.T., Choi, S.Y., Cho, K.Y., Shon, M.Y., Nam, S.E., Park, Y.I., 2021. Hydrophilic and organophilic pervaporation of industrially important α,β and α,ω-diols. RSC Adv. 11. https://doi.org/10.1039/d1ra00467k

Chelli, V.R., Chakraborty, S., Golder, A.K., 2018. Ag-doping on TiO_2 using plant-based glycosidic compounds for high photonic efficiency degradative oxidation under visible light. J. Mol. Liq. 271. https://doi.org/10.1016/j.molliq.2018.08.140

Chen, L., Li, R., Zhang, Y., Xu, Y., Chen, J., Wang, L., Zhu, H., Zhang, M., Zhang, H., 2023. In Situ Visualization of Membrane Fouling Evolution during Ultrafiltration Using Label-Free Hyperspectral Light Sheet Fluorescence Imaging. Environ. Sci. Technol. 57. https://doi.org/10.1021/acs.est.2c08731

Choe, K., Kim, K.J., Kim, D., Manford, C., Heo, S., Shahinpoor, M., 2006. Performance characteristics of electro-chemically driven polyacrylonitrile fiber bundle actuators. J. Intell. Mater. Syst. Struct. 17. https://doi.org/10.1177/1045389X06059074

Chowdhury, A., Bhan, C., Peela, N.R., Golder, A.K., 2022. A tunable bioinspired process of SnO_2 NPs synthesis for electrochemical CO_2-into-formate conversion. J. CO_2 Util. 66. https://doi.org/10.1016/j.jcou.2022.102263

Dijkstra, M.F.J., Michorius, A., Buwalda, H., Panneman, H.J., Winkelman, J.G.M., Beenackers, A.A.C.M., 2001. Comparison of the efficiency of immobilized and suspended systems in photocatalytic degradation. Catal. Today 66. https://doi.org/10.1016/S0920-5861(01)00257-7

G.N., M., M., H.K., 2021. Performance studies of GO/PF127 incorporated Polyetherimide Ultrafiltration membranes for the rejection of oil from oil wastewater. Chem. Eng. Res. Des. 168. https://doi.org/10.1016/j.cherd.2021.01.019

Huisman, I.H., Dutré, B., Persson, K.M., Trägårdh, G., 1997. Water permeability in ultrafiltration and microfiltration: Viscous and electroviscous effects. Desalination 113.

https://doi.org/10.1016/S0011-9164(97)00118-5

Janssens, R., Hainaut, R., Gillard, J., Dailly, H., Luis, P., 2021. Performance of a Slurry Photocatalytic Membrane Reactor for the Treatment of Real Secondary Wastewater Effluent Polluted by Anticancer Drugs. Ind. Eng. Chem. Res. 60. https://doi.org/10.1021/acs.iecr.0c04846

Kang, G.S., Baek, Y., Yoo, J.B., 2020. Relationship between surface hydrophobicity and flux for membrane separation. RSC Adv. 10. https://doi.org/10.1039/d0ra07262a

Kotsilkova, R., Borovanska, I., Todorov, P., Ivanov, E., Menseidov, D., Chakraborty, S., Bhattacharjee, C., 2018. Tensile and Surface Mechanical Properties of Polyethersulphone (PES) and Polyvinylidene Fluoride (PVDF) Membranes. J. Theor. Appl. Mech. 48. https://doi.org/10.2478/jtam-2018-0018

Li, J., Gao, J., Fang, J., Ling, T., Xia, M., Cao, X., Han, Z., Chen, Y., 2023. Environmental-friendly regenerated lignocellulose functionalized cotton fabric to prepare multi-functional degradable membrane for efficient oil–water separation and solar seawater desalination. Sci. Rep. 13. https://doi.org/10.1038/s41598-023-32566-9

Li, X., Jiang, L., Li, H., 2018. Application of Ultrafiltration Technology in Water Treatment. IOP Conf. Ser. Earth Environ. Sci. 186, 0–8. https://doi.org/10.1088/1755-1315/186/3/012009

Liriano-Jorge, C.F., Sohmen, U., Özkan, A., Gulyas, H., Otterpohl, R., 2014. TiO_2 photocatalyst nanoparticle separation: Flocculation in different matrices and use of powdered activated carbon as a precoat in low-cost fabric filtration. Adv. Mater. Sci. Eng. 2014. https://doi.org/10.1155/2014/602495

Loosli, F., Stoll, S., 2017. Effect of surfactants, pH and water hardness on the surface properties and agglomeration behavior of engineered TiO_2 nanoparticles. Environ. Sci. Nano 4. https://doi.org/10.1039/c6en00339g

Lv, C., Lan, X., Wang, L., Yu, Q., Zhang, M., Sun, H., Shi, J., 2019. Alkaline-earth-metal-doped TiO_2 for enhanced photodegradation and H_2 evolution: Insights into the mechanisms. Catal. Sci. Technol. 9. https://doi.org/10.1039/c9cy01687b

Ma, B., Yu, W., Liu, H., Qu, J., 2014. Comparison of iron (III) and alum salt on ultrafiltration membrane fouling by alginate. Desalination 354. https://doi.org/10.1016/j.desal.2014.10.003

Mehta, N., Basu, S., Kumar, A., 2016. Separation of zinc oxide nanoparticles in water stream by membrane filtration. J. Water Reuse Desalin. 6. https://doi.org/10.2166/wrd.2015.069

Mishra, S., Sundaram, B., 2022. A review of the photocatalysis process used for wastewater

treatment, in: Materials Today: Proceedings. https://doi.org/10.1016/j.matpr.2023.07.147

Patchaiyappan, A., Saran, S., Devipriya, S.P., 2016. Recovery and reuse of TiO_2 photocatalyst from aqueous suspension using plant based coagulant - A green approach. Korean J. Chem. Eng. 33. https://doi.org/10.1007/s11814-016-0059-9

Peng, G., Yaoqin, W., Changmei, S., Chunnuan, J., Ying, Z., Rongjun, Q., Ying, W., 2022. Preparation and properties of PVC-based ultrafiltration membrane reinforced by in-situ synthesized p-aramid nanoparticles. J. Memb. Sci. 642. https://doi.org/10.1016/j.memsci.2021.119993

Qasem, N.A.A., Mohammed, R.H., Lawal, D.U., 2021. Removal of heavy metal ions from wastewater: a comprehensive and critical review. npj Clean Water. https://doi.org/10.1038/s41545-021-00127-0

Ravi, Pandey, L.M., 2019. Enhanced adsorption capacity of designed bentonite and alginate beads for the effective removal of methylene blue. Appl. Clay Sci. 169. https://doi.org/10.1016/j.clay.2018.12.019

Ravi, R., Bhan, C., Golder, A.K., 2025. Bio-analytic synthesis of Cu-doped TiO_2 for photocatalytic degradation of ciprofloxacin under visible light. Opt. Mater. (Amst). 159, 116577. https://doi.org/10.1016/j.optmat.2024.116577

Ravi, R., Golder, A.K., 2023. A tuneable bioinspired process of Pt-doping in TiO_2 for improved photoelectrochemical and photocatalytic functionalities. Colloids Surfaces A Physicochem. Eng. Asp. 663, 131034. https://doi.org/10.1016/j.colsurfa.2023.131034

Ren, L., Yu, S., Li, J., Li, L., 2019. Pilot study on the effects of operating parameters on membrane fouling during ultrafiltration of alkali/surfactant/polymer flooding wastewater: optimization and modeling. RSC Adv. 9. https://doi.org/10.1039/C8RA10167A

Safat, S., Buazar, F., Albukhaty, S., Matroodi, S., 2021. Enhanced sunlight photocatalytic activity and biosafety of marine-driven synthesized cerium oxide nanoparticles. Sci. Rep. 11. https://doi.org/10.1038/s41598-021-94327-w

Sato, T., Makino, K., Tamesue, S., Ishiura, G., Itoh, N., 2023. Preparation and Permeation Properties of a pH-Responsive Polyacrylic Acid Coated Porous Alumina Membrane. Membranes (Basel). 13. https://doi.org/10.3390/membranes13010082

Sioutopoulos, D., Karabelas, A., Mappas, V., 2019. Membrane fouling due to protein—Polysaccharide mixtures in dead-end ultrafiltration; the effect of permeation flux on fouling resistance. Membranes (Basel). 9. https://doi.org/10.3390/membranes9020021

Siyanbola, T.O., Gurunathan, T., Akinsola, A.F., Adekoya, J.A., Akinsiku, A.A., Aladesuyi,

O., Rajiv, S., Mohanty, S., Natarajan, T.S., Nayak, S.K., 2016. Antibacterial and morphological studies of electrospun silver-impregnated polyacrylonitrile nanofibre. Orient. J. Chem. 32. https://doi.org/10.13005/ojc/320116

Sonawane, S., Thakur, P., Sonawane, S.H., Bhanvase, B.A., 2021. Nanomaterials for membrane synthesis: Introduction, mechanism, and challenges for wastewater treatment, in: Handbook of Nanomaterials for Wastewater Treatment: Fundamentals and Scale up Issues. https://doi.org/10.1016/B978-0-12-821496-1.00009-X

Suga, Y., Takagi, R., Matsuyama, H., 2022. Effect of hollow fiber membrane properties and operating conditions on preventing scale precipitation in seawater desalination with vacuum membrane distillation. Desalination 527. https://doi.org/10.1016/j.desal.2022.115578

Taylor, A.T., Iraganje, E., Lai, E.P.C., 2020. A method for the separation of TiO_2 nanoparticles from Water through encapsulation with lecithin liposomes followed by adsorption onto poly(L-lysine) coated glass surfaces. Colloids Surfaces B Biointerfaces 187. https://doi.org/10.1016/j.colsurfb.2019.110732

Vimercati, L., Cavone, D., Caputi, A., De Maria, L., Tria, M., Prato, E., Ferri, G.M., 2020. Nanoparticles: An Experimental Study of Zinc Nanoparticles Toxicity on Marine Crustaceans. General Overview on the Health Implications in Humans. Front. Public Heal. 8. https://doi.org/10.3389/fpubh.2020.00192

Wagh, P., Spencer, J., Steele, B., Escobar, I.C., 2020. Membrane functionalization using bisamide-based organic frameworks for molecular weight cutoff reduction. J. Appl. Polym. Sci. 137. https://doi.org/10.1002/app.48327

Wang, Q., Dai, F., Zhang, S., Chen, C., Yu, Y., 2020. Fabrication of ultrafiltration membranes by poly (aryl ether nitrile) with poly (ethylene glycol) as additives. Water Sci. Technol. 82. https://doi.org/10.2166/wst.2020.529

Wu, J., Ke, K., Qin, N., Lin, E., Kang, Z., Bao, D., 2023. Magnetically retrievable Fe_3O_4@SiO_2@ZnO piezo-photocatalyst: Synthesis and multiple catalytic properties. J. Colloid Interface Sci. 636. https://doi.org/10.1016/j.jcis.2023.01.009

Xue, X. dong, Fu, J. feng, Zhu, W. fang, Guo, X. chao, 2008. Separation of ultrafine TiO_2 from aqueous suspension and its reuse using cross-flow ultrafiltration (CFU). Desalination 225. https://doi.org/10.1016/j.desal.2007.04.089

Yan, X., Wang, G., Ma, C., Li, J., Cheng, S., Yang, C., Chen, L., 2021. Effects of pollutants in alkali/surfactant/polymer (ASP) flooding oilfield wastewater on membrane fouling in direct contact membrane distillation by response surface methodology. Chemosphere

282. https://doi.org/10.1016/j.chemosphere.2021.131130

You, M., Feng, G., Fei, P., Zhang, Y., Cao, Z., Xia, J., Lau, W.J., Meng, J., 2021. Probing and relating the morphology, structure and performance evolution of low pressure RO membranes under chlorine exposure. J. Environ. Chem. Eng. 9. https://doi.org/10.1016/j.jece.2021.106223

Zhang, G., Zhang, J., Wang, L., Meng, Q., Wang, J., 2012. Fouling mechanism of low-pressure hollow fiber membranes used in separating nanosized photocatalysts. J. Memb. Sci. 389. https://doi.org/10.1016/j.memsci.2011.11.027

Zhang, H., Xu, L., Yang, F., Geng, L., 2010. The synthesis of polyacrylonitrile/carbon nanotube microspheres by aqueous deposition polymerization under ultrasonication. Carbon N. Y. 48. https://doi.org/10.1016/j.carbon.2009.10.013

Zhang, J., Xue, C.H., Ma, H.R., Ding, Y.R., Jia, S.T., 2020. Fabrication of PAN electrospun nanofibers modified by tannin for effective removal of trace Cr(III) in organic complex from wastewater. Polymers (Basel). 12. https://doi.org/10.3390/polym12010210

CHAPTER 8

Development of a Pilot-scale Integrated PhACs Treatment System for Photocatalytic Degradation, Catalysts Recovery, and Biological Degradation

In this chapter, a pilot-scale integrated photocatalytic and biological degradation reactor with an ultrafiltration membrane system was designed, fabricated, and installed at the rooftop of the Department of Chemical Engineering, IIT Guwahati, India. The integrated process has three major units: (i) Photocatalytic degradation unit: For photocatalytic degradation of PhACs under solar light, (ii) Membrane separation unit: For recovery of used photocatalysts using cross-flow ultrafiltration membrane, and (iii) Biological degradation unit: For microbial degradation of PhACs surviving the photocatalytic process and reaction intermediates.

The pilot-scale reactor was utilized for the photodegradation of synthetic PhACs wastewater containing individual PhACs and mixtures of PhACs using bare-TiO_2, Pt-doped TiO_2, and Au-doped TiO_2 catalysts. Further, the hospital wastewater was collected and spiked with a mixture of five different PhACs. The spiked hospital wastewater was degraded in the integrated reactor with a reaction volume of 10 L. The degradation efficiency of all the photocatalysts was superior in the pilot-scale reactor than in the laboratory-scale reactor. The used photocatalysts were recovered by membrane filtration.

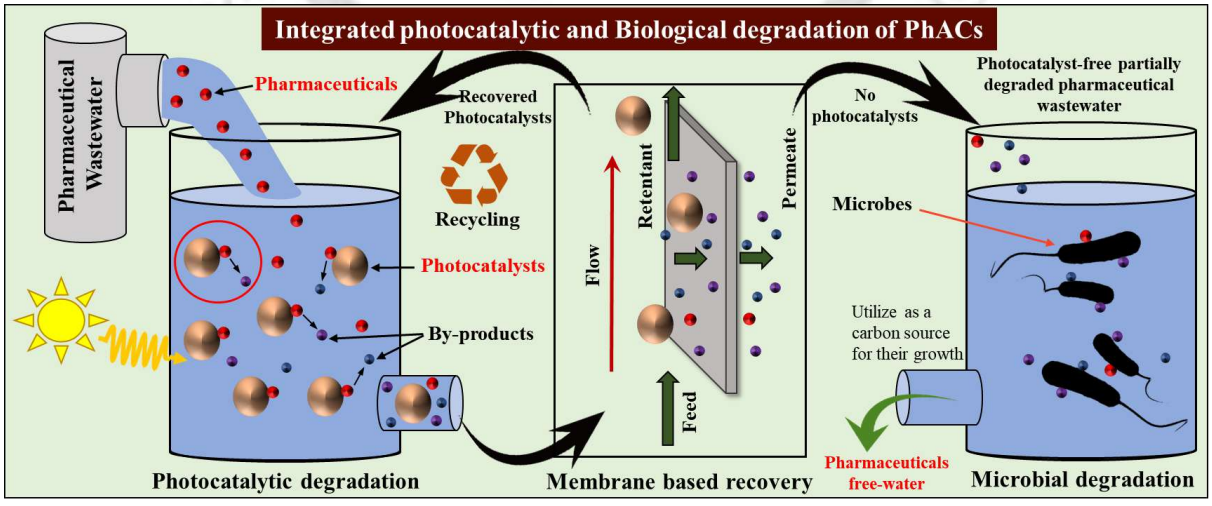

Intentionally Left Blank
Intentionally Left Blank

8.1 Background and executive motivation

Pharmaceutical active compounds (PhACs) are increasingly documented as emerging pollutants in aquatic systems due to their continuous unregulated discharge from hospitals, households, and pharmaceutical industries (Han et al., 2024). Their persistence, bioactivity, and resistance to conventional wastewater treatment processes result in long-term accumulation in surface water, groundwater, and even drinking water sources. The environmental risks associated with PhACs include endocrine disruption, the development of antibiotic resistance, and toxicity to aquatic organisms (Tamaddon et al., 2020). Furthermore, they can cause chronic ecological damage even at trace concentrations due to environmental persistence. Therefore, the treatment of pharmaceutical wastewater has become a critical global priority, requiring advanced strategies that ensure both effective removal and complete mineralization of PhACs.

Photocatalysis has emerged as a promising technology for PhACs degradation, as it utilizes solar or artificial light to generate reactive oxygen species, enabling breakdown of recalcitrant molecules (Wen et al., 2023). Extensive laboratory studies have reported efficient degradation of a wide range of antibiotics, anti-inflammatories, and other PhACs using TiO_2 and its doped variant photocatalysts. However, the majority of these studies remain confined to laboratory scale, with limited studies on real wastewater treatment. The primary challenges arise from the difficulty of catalyst recovery and reuse, as nanosized catalysts often remain dispersed in water, leading to secondary contamination and increase cost of operation (Truong et al., 2022). To address this limitation, membrane-based separation systems could be utilized, which allows efficient recovery of suspended catalysts and enabling continuous operation (Peng et al., 2022). Such hybrid photocatalysis and membrane systems are crucial towards pilot-scale deployment by ensuring reusability, stability, and cost-effectiveness of photocatalytic processes.

While photocatalysis initiates rapid degradation of PhACs, it may lead to incomplete mineralization, generating intermediate byproducts that may be more toxic than the parent compounds (Chen et al., 2024). This necessitates a complementary treatment strategy to ensure safe and complete degradation. Biological processes offer a sustainable and cost-effective solution, as microbial communities can utilize these intermediates as a carbon and energy source. Mechanistically, microorganisms metabolize partially oxidized organics through enzymatic pathways, converting them into simpler metabolites such as CO_2, H_2O, and biomass (Langenhoff et al., 2013). This synergy between advanced oxidation and biodegradation

ensures effective detoxification, overcoming the drawbacks of each standalone process. Therefore, coupling photocatalysis with biological treatment holds promise for achieving complete and environmentally benign mineralization of PhACs, which is a novel research area for PhACs pollution eradication.

Despite the potential of both photocatalytic and biological treatment, most studies remain limited to batch or bench-scale reactors. Scaling up to pilot scale is essential to assess process suitability under realistic operational conditions and variable wastewater compositions (Bahadur and Bhargava, 2019). The development of a pilot-scale integrated system for PhACs treatment, incorporating photocatalytic degradation, membrane-assisted catalyst recovery, and subsequent biological degradation, represents a crucial advancement towards practical application. In this system, the photocatalytic reactor ensures efficient breakdown of recalcitrant pharmaceuticals, while the membrane module allows continuous separation and recycling of catalysts. The biologically degradation unit subsequently mineralizes residual byproducts, ensuring complete detoxification. Moreover, pilot-scale operation provides critical insights into reactor hydrodynamics, scalability, energy demand, and operational stability, which are required to determine the transition to full-scale industrial application. Therefore, this pilot-scale integrated process offers a transformative platform for addressing pharmaceutical wastewater pollution, bridging the gap between laboratory innovation and real-world environmental remediation.

In this chapter, a pilot scale integrated photocatalytic and biological degradation process with membrane-based catalysts recovery system is designed, fabricated and installed. Further, the photocatalytic degradation of various PhACs was performed using bare-TiO_2 and metal-doped TiO_2 photocatalysts with simultaneous recovery of used photocatalysts. Moreover, the biological degradation of parent and partially degraded PhACs was also performed with bacterial strains. Additionally, the integrated process was utilized for degradation of mixture of PhACs in DI water and hospital wastewater targeting complete mineralization along with recovery of used photocatalysts.

8.2 Design, fabrication and installation of integrated process

A pilot scale integrated photocatalytic and biological treatment system was design and fabricated for photocatalytic PhACs degradation, catalysts recovery and biological degradation of PhACs surviving photocatalytic decomposition along with the intermediates formed. The purposed reactor consists of three main units, i.e., (i) ‘Photocatalytic degradation unit’ for

photocatalytic degradation of PhACs under solar light, (ii) 'Membrane separation unit' for recovery of used photocatalysts using cross-flow ultrafiltration membrane, and (iii) 'Biological degradation unit' for microbial degradation of PhACs and intermediates surviving the photocatalytic process. The design of the integrated process is provided in Fig. 8.1. The components of the reactor are listed in Table 8.1.

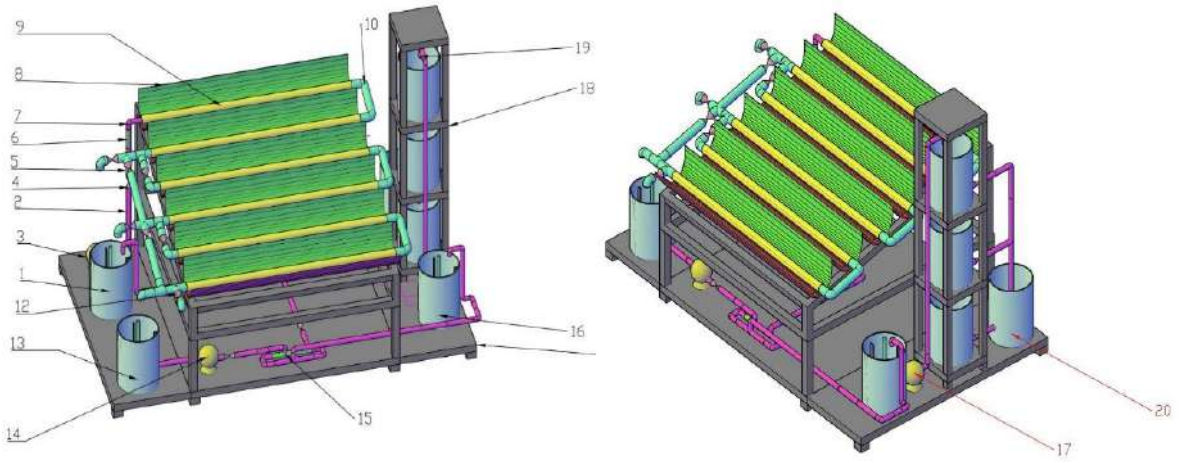

Figure 8.1: Design of integrated photocatalytic and biological degradation process with membrane-based recovery system.

Table 8.1: Components of the designed integrated photocatalytic and biological reactor with membrane system (Fig 8.1).

S. No.	Component Name	S. No.	Component Name
1	Catalyst and wastewater mixer tank	11	Support of reactor assembly
2	Flow pipes	12	Outlet valve
3	Peristaltic/Dosing pump	13	Outlet tank
4	Suitable flow-control valves	14	Peristaltic/Dosing pump
5	Non-return valve (NRV)	15	Membrane module (CF-UF)
6	Flow meter	16	Mixing tank
7	Flow pipe connectors	17	Peristaltic pump
8	CPC (Compound parabolic collector)	18	Bio-reactor stand
9	Photo reactor tubes	19	Bio-reactor tanks with air-diffuser
10	Reactor tube connector	20	Bioreactor outlet tank

Chemdist Membrane Systems Pvt. Ltd., Pune, Maharashtra, India, helped us to fabricate the integrated photocatalytic and biological reactor. The integrated process is installed on the rooftop of the Department of Chemical Engineering, Indian Institute of Technology Guwahati, Assam, India (Coordinates: 26°11′14″N 91°41′30″E). Figs. 8.2-8.4 illustrate the installed integrated photocatalytic and biological degradation process.

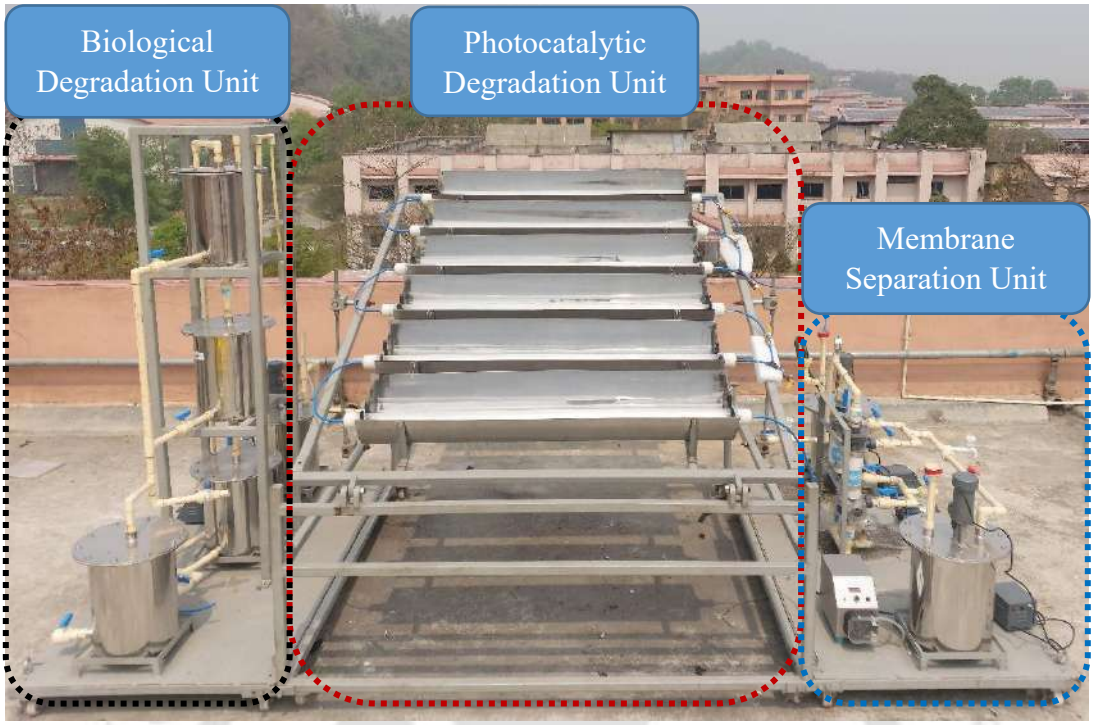

Figure 8.2: Integrated pilot-scale photocatalytic and biological degradation reactor coupled with membrane separation system for catalysts recovery.

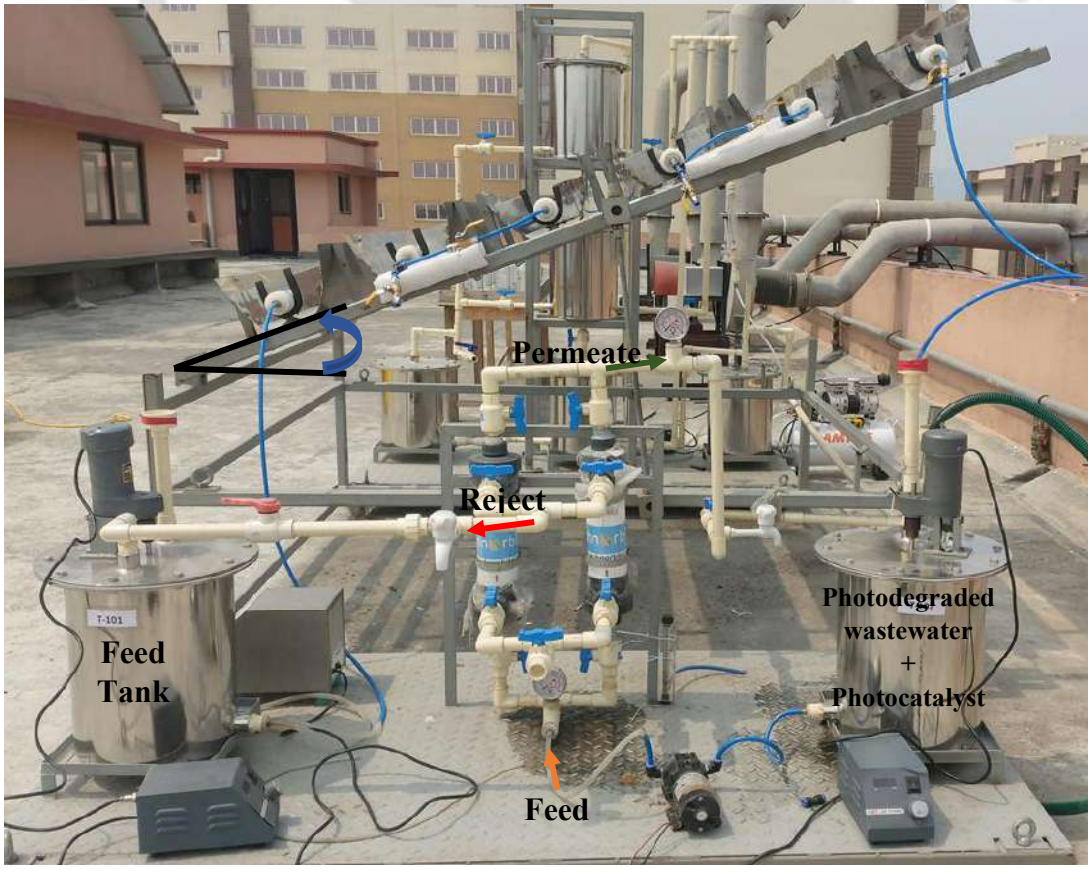

Figure 8.3: Membrane separation unit for photocatalysts recovery in the integrated system.

Figure 8.4: Biological degradation unit of integrated photocatalysis-biological reactor.

Even though the photocatalytic degradation of PhACs (Chapters 3-6) is efficient, however, the treatment process is left with the formation of various intermediates. Therefore, a biological degradation unit was incorporated for further treatment to achieve complete mineralization of residual PhACs and their by-products. Since the presence of photocatalyst particles may adversely interfere with microbial activity and biological oxidation processes, the catalyst recovery unit was introduced between the photocatalytic and biological reactors. This separation step enables the effective removal and reuse of the photocatalyst while ensuring that a catalyst-free effluent enters the biological unit for further degradation.

8.2.1 Photocatalytic degradation unit

The photocatalysis unit (Fig. 8.2) is used for photodegradation of the pharmaceutical wastewater degradation under direct sunlight with an effective volume of 10-25 L at a time. The slurry of pharmaceutical wastewater and photocatalysts flow through Pyrex glass tubes

under direct exposure of the sunlight. After photodegradation, the photodegraded wastewater and photocatalyst slurry solution separated using membrane separation unit for further studies. The photocatalytic degradation unit consist of various components as briefed below:

- ***Photocatalyst and wastewater mixer tank (1, 13, 16):*** A 316L stainless steel tank with 30L capacity used for mixing of the pharmaceutical wastewater and photocatalysts to perform dark reaction. The fabricated tank designed with four baffles to avoid the formation of the vertex during mixing. Fig. 8.5 shows the inner and outer views of fabricated photocatalyst and wastewater mixer tank. A four cross blade impeller operated with Remi- used for proper mixing at 100 - 900 rpm. Further, the pharmaceutical wastewater and photocatalysts flow to Pyrex tubes for photodegradation.

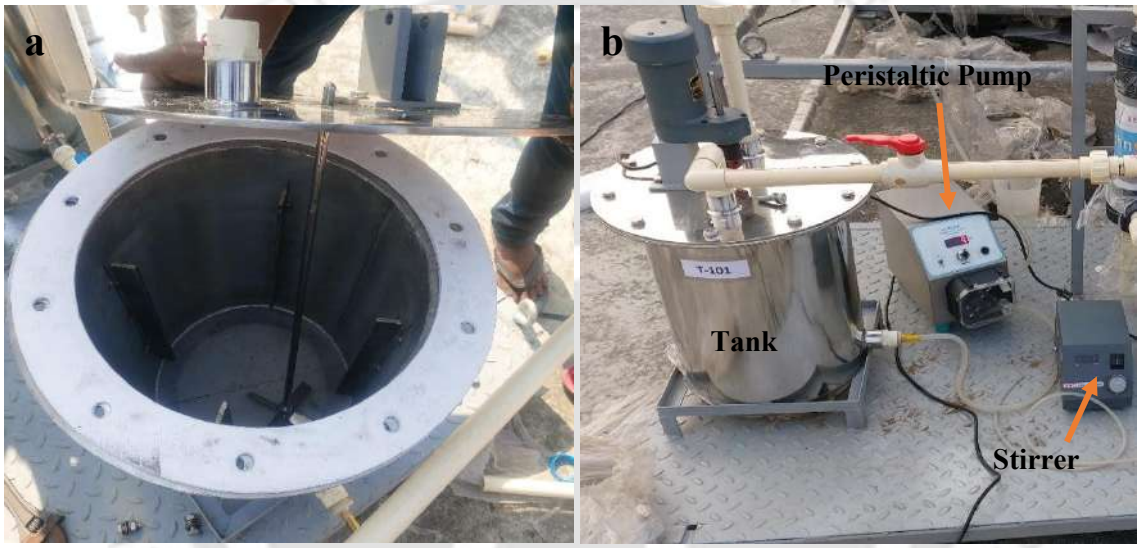

Figure 8.5: Photocatalyst and wastewater mixer tank (a) inner view and (b) outer view.

- ***Peristaltic pump (3, 14, 17):*** Peristaltic pumps with maximum flow rate of 280 to 3600 mL min^{-1} were used to flow the solution through the photocatalytic, membrane separation and biological degradation units. The peristaltic pumps (V series) were purchased from ELECTROLAB, Mumbai, India.
- ***Assembly of photo reactor tubes and compound parabolic collector (CPC) reflectors (8-10):*** Pyrex tubes with more than 95% light transmittance efficiency used as house for photodegradation of the pharmaceutical wastewater. Dimensions of a photoreactor tube is 1500 mm length, 50 mm internal diameter and 1.5 mm thickness which can hold about 2.95 L solution at its maximum capacity. Along with it, compound parabolic collector also used to concentrate the light on photoreactor tube to increase the photodegradation efficiency. The CPC reflector sheets are made up of polished stainless steel 304 with

dimension of 1500 nm length, 184.8 mm height, 283.9 mm width and 47° half-concentric angle. The photocatalytic degradation unit contains 6 numbers of photoreactor tube and compound parabolic collector assembly. A photoreactor tube is connected to next photoreactor tube via silicon tube and valve. Therefore, we can use any tubes separately for a photodegradation process. The connection of all the six-photoreactor tubes and their respective CPCs is illustrated in the photocatalytic degradation unit part of Fig. 8.2.

- ***Support of reactor assembly (11):*** The support of react assembly is made up of mild steel with corrosion resist polishing. The support of each unit is movable and can be horizontally move separately and altogether. The support of photoreactor tubes and CPCs assembly can be move vertically at required angle to the base to gain maximum light on photoreactor tubes and CPCs.

8.2.2 Membrane separation unit

The membrane separation unit targets to provide a zero photocatalyst loss system for recycling of used photocatalyst for multiple photodegradation cycles. The membrane separation unit is used for separation of the photocatalyst and photodegraded pharmaceutical wastewater after photodegradation. Fig. 8.3 shows the snap of membrane separation unit with briefed flow direction of feed, permeate and reject. The permeate represents the photodegraded pharmaceutical wastewater, while reject determine the concentrated photocatalyst. The partially degraded wastewater, if any, will flow to biological degradation unit and the concentrated photocatalyst solution will be used for next photodegradation cycle.

- ***Membrane module (15):*** The membrane module is equipped with a pair of cross-flow based ultrafiltration type polyNorbit polymer membranes with 75 KDa (~0.01 μm) cutoff value. The membranes were purchased from Technorbital Advance Material Pvt. Ltd. Kanpur, Uttar Pradesh (India). In the membrane separation unit, a pair of 75 KDa crossflow-ultrafiltration membrane is used for separation, which is operated by peristaltic pump. There is a provision to use only one membrane at a time or both membranes simultaneously. The membrane hosing is made up of high quality UPVC with a nominal (active) area of 9 m^2 (for large membrane) or 2 m^2 (for small membrane).

8.2.3 Biological degradation unit

The biological degradation unit is designed to degrade the partially degraded pharmaceutical wastewater or fresh pharmaceutical wastewater by microorganisms (bacteria).

Photocatalytic degradation not always completely degrade the organic pollutant (PhACs). Additionally, formation of few hazardous by-products during photocatalytic degradation can be engaged. Therefore, the complete degradation of pharmaceutically wastewater must be performed for complete mineralization. Some microbes, especially bacterial strains, can easily degrade the pharmaceutical wastewater by using PhACs as a carbon source without formation of large biomass. Although, maintenance of bacterial culture and aeration is quite challenging. Fig. 8.4 represent the biological degradation unit. The mixing tank (feeding tank) is similar to the previously explained mixing (feed tank, 1) and outlet tank (13).

- ***Bioreactor tanks with air diffuser (19):*** The pharmaceutical wastewater or permeate of membrane separation unit (partially degraded pharmaceutical wastewater) is transferred for further degradation by microbes. From mixing tank, the mixture of microbes and wastewater flows to bioreactor tanks. The dimensions of the bioreactor tanks are similar to the feed tank (1). However, the bioreactor tanks are different from feed/mixing tanks, which contain air diffuser (sparger) instead of impeller for proper mixing and aeriation. All the tanks are vertically connected in series. Although, there is provision to use each tank separately for different experiments. An air compressor with 0.2 μm filter used as a source of microbes free air for aeration and mixing. The outlet of air compressor is connected to all three bioreactor tanks through nozzle sparger. A rotameter also equipped to control the airflow rate. A safety value is also provided in the bioreactor tank to eject the extra pressure from the tank. All the three-bioreactor tanks are propped on a corrosion resistant polished mild steel base support. After biological degradation process, the completely degraded wastewater could be transfer to the bioreactor outlet tank (20) and discard with proper safety measures.

8.3 Working of integrated process

8.3.1 Photocatalytic degradation of PhACs

The photocatalytic degradation of PhACs was carried out using TiO_2 and metal-doped TiO_2 under solar irradiation in the photocatalytic degradation unit of the integrated reactor. The photodegradation process in the integrated setup followed a similar procedure to the batch-scale process described in ‘Section 2.7.1 of Chapter 2’, with some modifications customized for continuous operation.

For photocatalytic treatment, the photocatalyst (0.010-0.025 g L^{-1}) was dispersed in DI water through sonication for 30 min to ensure homogeneous suspension. Subsequently, the

target PhACs (5 mg L^{-1}) were added, and the mixture was kept in the dark for 30 min under continuous stirring at 500 rpm in the mixing tank to establish adsorption-desorption equilibrium. The prepared slurry was then circulated through Pyrex glass tubes at a fixed flow rate of 190 L h^{-1} under direct solar irradiation to facilitate photocatalytic degradation. The aliquots of photodegraded samples were collected at different time intervals for analysis. The residual concentration of PhACs was quantified by UV–Vis spectrophotometry and HPLC analysis. Further, chemical oxygen demand (COD) and total organic carbon (TOC), were determined as outlined in 'Section 2.7.2 of Chapter 2'. In addition, dissolved CO_2 originated during mineralization was measured at regular intervals using CO_2 probe (Orion star A214, Thermo scientific, Massachusetts, United States).

The effect of key process parameters was systematically investigated, including photocatalyst dosage (0.010-0.025 g L^{-1}) and the role of compound parabolic concentrator (CPC) reflectors in enhancing solar light utilization. Furthermore, the photocatalytic degradation studies were performed using both bare TiO_2 and metal-doped TiO_2 for (i) individual PhACs, (ii) mixed PhACs in DI water, and (iii) hospital wastewater spiked with PhACs to evaluate catalyst performance under real conditions.

8.3.2 Photocatalyst recovery

Following the photocatalytic degradation process, the used photocatalytic material was separated and recovered using the membrane-based separation unit. The separation was performed at a constant feed flow rate of 22.5 L h^{-1}, while a backflow rate of 100 L h^{-1} was applied to minimize membrane fouling and recovery of residual photocatalytic material. The recovery protocol followed the methodology described in 'Section 2.9.3 of Chapter 2'.

8.3.3 Biological degradation

The biological degradation of fresh and partially degraded PhACs was carried out at both laboratory (reaction volume: 100 mL) and pilot (reaction volume: 7.5 L) scales using bacterial strains obtained from NIT Rourkela, India. Following the photocatalytic treatment, the photocatalyst-free partially degraded PhAC solution was transferred to the biological degradation unit for further degradation of residual PhACs and intermediates.

For biological degradation, PhAC-degrading bacterial strains were first revived in minimal salt medium (MSM) supplemented with glucose (1 g L^{-1}) as a carbon source for 24 h. The cultures were then centrifuged, and the resulting cells were resuspended in phosphate-buffered saline (PBS) to remove residual glucose. Subsequently, 5% bacterial inoculum

(optical density = 1.0) was added to MSM broth containing PhACs. Laboratory-scale experiments were conducted in an incubator at 30 °C and 120 rpm (Poddar et al., 2024). At pilot scale, the inoculated PhACs containing MSM broth was added into a biological degradation tank with continuous aeration at 375 mL min^{-1} via a sparger to ensure proper mixing. The bacterial growth profile was monitored by measuring optical density at 600 nm (OD_{600}) at different intervals using a UV-Vis spectrophotometer. Degradation efficiency was evaluated using UV-Vis and HPLC analysis, while COD and TOC removal were measured to assess the extent of degradation and mineralization (Bhan and Golder, 2023).

8.4 Results and discussion

8.4.1 Photocatalytic degradation of PhACs

8.4.1.1 Effect of photocatalyst dosage

The photocatalytic degradation of 5 mg L^{-1} ciprofloxacin (CIP) was performed using bare-TiO_2 with different photocatalysts dosage ranging from 0.025 to 0.1 g L^{-1} under solar light irradiation for 120 min with exposed CPC reflectors. The dark adsorption and photocatalytic degradation profile at different time intervals is illustrated in Fig. 8.6a.

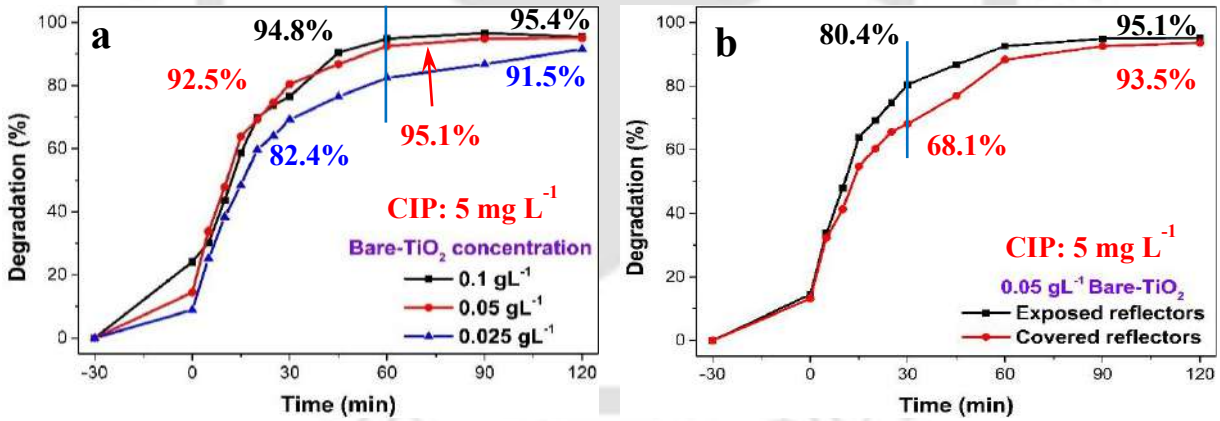

Figure 8.6: Dark adsorption (-30 to 0 min) and photocatalytic degradation at different time interval at (a) different bare-TiO_2 dosage (0.025 to 0.1 g L^{-1}) with exposed reflectors, and (b) at 0.05 g L^{-1} bare-TiO_2 with exposed and covered reflectors.

The negative time scale (x-axis) shows pre-adsorption (or dark adsorption) time prior to initiate photocatalytic reaction. The dark adsorption of CIP was increased from 8.89 to 24.10% with an increase in the bare-TiO_2 concentration from 0.025 to 0.1 g L^{-1}, which could be due to availability of a higher number of adsorption sites at higher concentration (Ravi and Pandey, 2019). Under solar light, at 0.025 g L^{-1} bare-TiO_2, degradation reached 56.2% at 60

min and 91.5% at 120 min. Increasing the dosage to 0.05 g L^{-1} resulted in faster kinetics, with 72.4 and 94.7% degradation at 60 and 120 min, respectively. A further increase in catalyst dose to 0.1 g L^{-1} produced nearly comparable results (74.8% within 60 min and 95.3% within 120 min), indicating that beyond an optimum dosage (0.05 g L^{-1}), the light scattering, catalysts settlement and reduced light penetration limited the further improvement in photocatalytic activity (Anuradha et al., 2025). Therefore, 0.05 g L^{-1} catalyst dose was used for further experiments.

8.4.1.2 Effect of CPC reflectors

The effect of CPC reflectors on photocatalytic degradation process was investigated by photocatalytic degradation of 5 mg L^{-1} CIP using 0.05 g L^{-1} bare-TiO_2 under solar light irradiation with exposed and covered CPC reflectors. Fig. 8.6b illustrates the dark adsorption and photocatalytic degradation profile at different time intervals with exposed and covered CPC reflectors. No significance difference in the dark adsorption was observed. With exposed CPC reflectors, degradation was significantly enhanced due to improved photon capture over the Pyrex tubes (Jaaz et al., 2017). At 30 min, 80.43% degradation was achieved with exposed reflectors compared to 68.13% with covered reflectors, while the final degradation efficiencies were reached to 95.06 and 93.54%, respectively, after 120 min. Therefore, the photocatalytic degradation process was performed with exposed CPC reflector in further experiments.

8.4.1.3 Photocatalytic degradation coupled with catalysts recovery

The photocatalytic degradation of 5 mg L^{-1} CIP, chloroquine (CLQ), paracetamol (PM), diclofenac (DIC), and sulfamethoxazole (SULF) was performed using 0.05 g L^{-1} bare-TiO_2 under solar light irradiation with exposed CPC reflectors. Furthermore, 0.05 g L^{-1} Pt-doped TiO_2 and Au-doped TiO_2 photocatalysts were employed for photocatalytic degradation of CIP and CLQ, respectively at optimized pH 5 and pH 7 (batch scale studies, Fig. 3.6c of Chapter 3 and Fig. 4.7 of Chapter 4).

Fig. 8.7 illustrates the degradation and CO_2 profiles, TOC removal, COD removal and photocatalysts recovery during photodegradation of PM, DIC and SULF by bare-TiO_2. During the dark adsorption phase (–30 to 0 min), ~9% surface adsorption was observed for PM and DIC, while negligible adsorption (<1%) was observed for SULF, confirming that subsequent pollutant removal was primarily governed by photocatalytic oxidation rather than physical sorption. Upon solar illumination, rapid degradation was recorded, with DIC exhibiting the

highest degradation efficiency (85.60%), followed by PM (80.76%) and SULF (69.23%) within 60 min (Fig. 8.7a). At the extended irradiation period (120 min), degradation efficiencies reached 94.93%, 92.43%, and 85.47% for DIC, PM, and SULF, respectively.

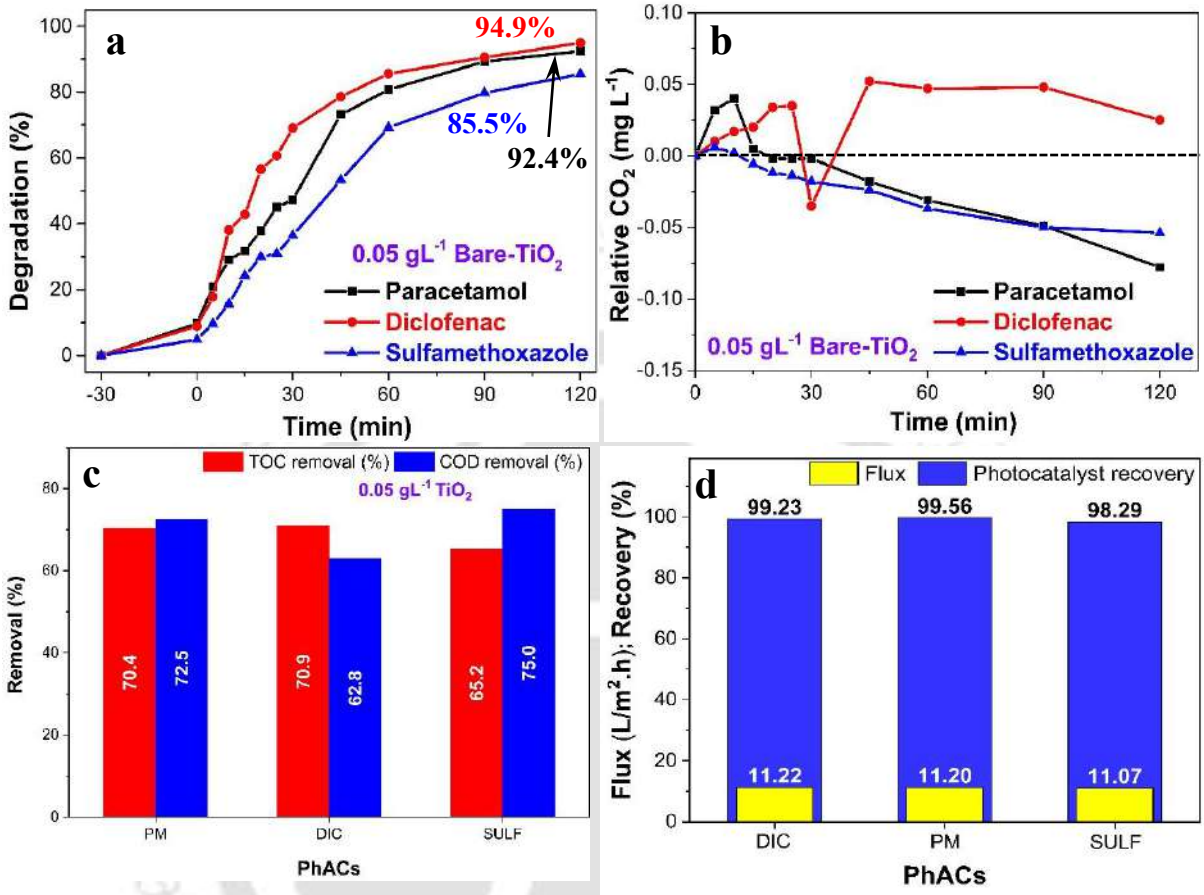

Figure 8.7: (a) Dark adsorption (-30 to 0 min) and photocatalytic degradation of PM, DIC and SULF, (b) CO_2 profiles at different time intervals, (c) TOC and COD removal (%) during photocatalytic degradation, and (d) Flux and photocatalyst recovery (%) after photodegradation through membrane system.

The mineralization was assessed through CO_2 profiles (Fig. 8.7b). A gradual increase in relative CO_2 levels for PM and SULF indicated progressive mineralization of organic intermediates during first 15 min, while DIC showed higher CO_2 concentration, suggesting higher mineralization among three PhACs (Barquín et al., 2024). However, the dissolved CO_2 was further decreased for PM and SULF, which could be due to releasing of CO_2 in outer environment due to vigorous mixing. The TOC and COD analyses (Fig. 8.7c) further confirmed partial mineralization, with TOC removal efficiencies of 70.4% (PM), 70.9% (DIC), and 65.2% (SULF). COD removal was 72.5 to 75.0%, reflecting oxidative transformation of PhACs into oxygenated intermediates that are less chemically demanding but not fully mineralized.

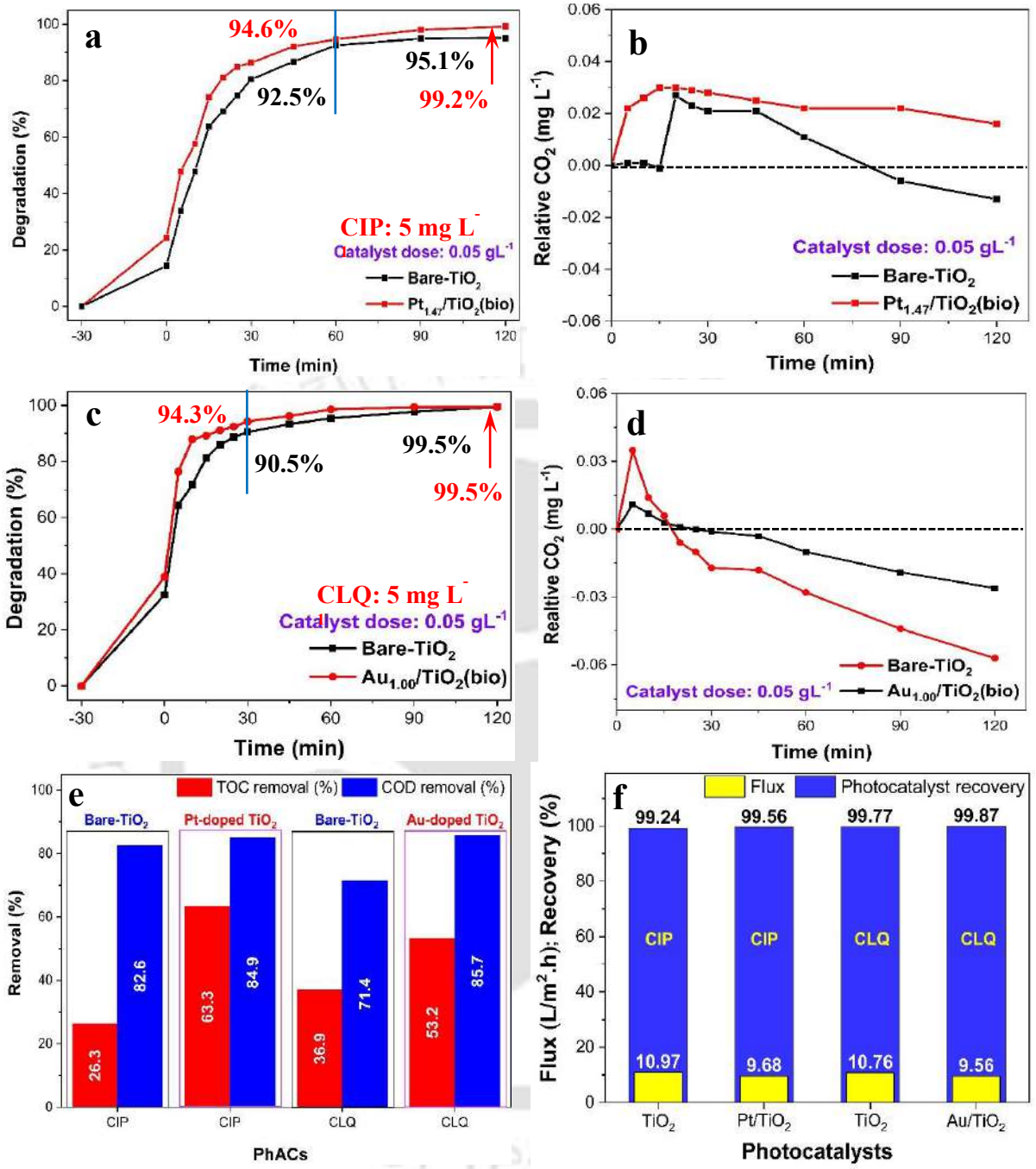

Figure 8.8: (a) Dark adsorption and photocatalytic degradation, and (b) CO_2 profiles during CIP degradation using bare-TiO_2 and Pt-doped TiO_2; (c) Dark adsorption and photocatalytic degradation, and (d) CO_2 profiles during CLQ degradation using bare-TiO_2 and Au-doped TiO_2; (e) TOC and COD removal (%) during photocatalytic degradation, and (f) Flux and photocatalyst recovery (%) after photodegradation through membrane system.

Furthermore, the used bare-TiO_2 was recovered through membrane filtration system. About 99.23%, 99.56%, and 98.29% catalysts recoveries were achieved for DIC, PM, and SULF, respectively, with a stable flux in the range of 11.07-11.22 L m^{-2} h^{-1}.

Fig. 8.8 presents the performance of bare TiO_2, Pt-doped TiO_2, and Au-doped TiO_2 during photocatalytic degradation of CIP and CLQ under solar irradiation. As shown in Fig. 8.8a, the degradation of CIP followed a rapid increase after the irradiation period, with bare-TiO_2 achieving 92.5, and 95.1% removal within 60, and 120 min, respectively. In contrast, Pt-doped TiO_2 exhibited significantly enhanced performance, achieving ~94.6% degradation within 60 min and 99.2% within 120 min. A similar trend was observed for CLQ degradation (Fig. 8.8c), where bare-TiO_2 and Au-doped TiO_2 reached 90.5, and 94.3% degradation within 120 min, respectively, whereas almost similar degradation of 99.5% was achieved by both photocatalysts at 120 min.

CO_2 concentration (Figs. 8.8b and 8.8d) further corroborates these findings by highlighting differences in mineralization. For CIP, Pt-doped TiO_2 exhibited relatively higher and steady CO_2 release compared to bare-TiO_2, suggesting more efficient breakdown of intermediates and mineralization (Barquín et al., 2024). Similarly, in the case of CLQ, Au-doped TiO_2 demonstrated improved mineralization compared to bare-TiO_2, though the dissolved CO_2 was higher for bare-TiO_2 during initial 15 min.

The fluctuation in CO_2 concentration is indicative of stepwise degradation pathways with partial mineralization and accumulation of intermediates (Zhou et al., 2024). The gradual reduction in CO_2 could be due to release of dissolve CO_2 due to rapid mixing during beyond 30 min degradation phase. Mineralization of CIP and CLQ was quantitatively assessed through TOC and COD removal (Fig. 8.8e). Bare-TiO_2 showed moderate mineralization efficiency with 26.3% TOC and 82.6% COD removal for CIP along with 36.9% TOC and 71.4% COD removal for CLQ. While noble-metal doping significantly improved TOC removal, reaching 63.3% for Pt-doped TiO_2 (CIP) and 53.2% for Au-doped TiO_2 (CLQ). The enhanced COD removal (>85% for both systems) indicates effective oxidation of organic intermediates. These results confirm the role of noble-metal doping in enhancing charge separation and light absorption, thereby accelerating photocatalytic degradation kinetics.

The integration of a membrane-assisted recovery system (Fig. 8.8f) demonstrated almost complete recovery (>99%) of used photocatalysts with steady permeate fluxes of 9.56-10.97 $Lm^{-2}h^{-1}$ across all systems. This highlights the potential of photocatalytic degradation process coupled with membrane separation for efficient degradation for PhACs with almost complete recovery for economic feasibility.

Overall, noble-metal doping (Pt and Au) substantially enhances the photocatalytic degradation and mineralization of CIP and CLQ, while the membrane-assisted recovery unit ensures high recyclability of photocatalysts, paving the way for practical application of this

integrated system in pharmaceutical wastewater treatment. However, the lower TOC and COD removal compared to degradation efficiency reveals that the mineralization lagged behind primary pollutant degradation, highlighting the persistence of partially oxidized by-products. This underlines the necessity of integrating the photocatalytic process with biological treatment to ensure complete mineralization of residual PhACs and intermediates.

8.4.2 Biological degradation of PhACs

8.4.2.1 Bacterial strains screening for PhACs degradation

The screening of bacterial strains received from NIT Rourkela was conducted to evaluate their potential for degrading CIP, PM) and DIC under laboratory-scale conditions. The strains were cultured on agar plates supplemented with (i) MSM + glucose (1 g L^{-1}), (ii) MSM + glucose + PhACs (3 mg L^{-1}), and (iii) MSM + PhACs without glucose. The bacterial cultures were inoculated onto the agar plates using the streaking method and incubated at 30 °C for 48 h (Poddar et al., 2024). The growth patterns of the strains under these conditions are summarized in Table 8.2.

All bacterial strains exhibited vigorous growth on MSM + glucose, confirming their viability. In the presence of CIP (3 mg L^{-1}) along with glucose, four strains (DY7, DY10, DY11, and DY18) demonstrated moderate growth, while PB5 and PB9 exhibited comparatively weaker growth. Notably, no strain showed growth on MSM supplemented with CIP in the absence of glucose, suggesting that although these strains were resistant to CIP, they could not utilize it as a sole carbon source (Zhang et al., 2022). The remaining strains did not exhibit any considerable growth in presence of CIP.

For PM and DIC, most strains demonstrated moderate to high growth on MSM + glucose + PhACs agar plates, indicating tolerance and potential metabolic activity. Among these, PDC10 and PDC11 exhibited moderate growth in MSM + PM and MSM + DIC even in the absence of glucose, highlighting their ability to utilize these PhACs as carbon sources (Poddar et al., 2024). In contrast, PDC14 showed weak growth in MSM + DIC and negligible growth in MSM + PM without glucose supplementation.

Based on these observations, *Pseudomonas spp.* strains PDC10 and PDC11 were selected for further degradation studies of PM and DIC under laboratory-scale conditions prior to scale-up in the integrated reactor. Additionally, strain PDC14 was employed specifically for DIC degradation in MSM broth media at the laboratory scale.

Table 8.2: Growth of bacterial strains in different nutrient media, i.e., MSM + glucose, MSM + glucose + PhACs, and MSM + PhACs without glucose.

S. no.	Strain	Growth in agar plate of						
		M-G	M-G-C	M-C	M-G-P	M-P	M-G-D	M-D
1.	DY7	+++++	+++	-	++++	-	+++++	-
2.	DY10	+++++	+++	-	++++	-	+++++	-
3.	DY11	+++++	+++	-	++++	-	++++	-
4.	DY18	+++++	+++	-	++++	-	+++++	-
5.	PB5	++++	+	-	+++	-	++++	-
6.	PB9	++++	+	-	++++	-	++++	-
7.	PDC3	+++++	-	-	+++++	-*	+++++	+
8.	PDC10	+++++	-	-	+++++	++	+++++	++
9.	PDC11	+++++	-	-	+++++	++	+++++	++
10.	PDC14	+++++	-	-	+++++	-*	+++++	+
11.	Control	-	-	-	-	-	-	-

[M: MSM; G: Glucose; C: Ciprofloxacin; P: Paracetamol; D: diclofenac]
[-: No growth, -*: Negligible growth, + to +++++: Increase in growth (+: Very less growth; +++++: Very high growth); Concentration of PhACs: 3 mg L^{-1}]

8.4.2.2 Degradation of PM and DIC at laboratory and pilot-scale

The biological degradation of PM and DIC was performed using PDC10, PDC11, and PDC14 (only for DIC) bacterial strains under laboratory conditions, with additional evaluation in an integrated reactor system. The bacterial growth profiles presented in Fig. 8.9a show that all strains exhibited an initial lag phase followed by exponential growth, reaching peak optical density around 24-36 h before declining due to substrate depletion and accumulation of by-products (Amorim et al., 2024). Among the tested conditions, the PDC11 strain grown with DIC in the reactor (D-M@PDC11/R) demonstrated the highest growth, indicating effective utilization of the pollutant as a carbon source under scaled-up conditions. In contrast, laboratory-scale cultures showed comparatively lower biomass formation, with moderate growth in PDC11 and PDC14 for DIC, while PM supported limited growth, particularly in PDC10.

Fig. 8.9b illustrates the biological degradation efficiencies. At the laboratory scale, PDC11 achieved the highest degradation of DIC (56.98%), followed by PDC14 (51.66%) and PDC10 (43.22%). For PM, degradation efficiencies were comparatively lower, with 36.04% for PDC10 and only 21.64% for PDC11, suggesting strain-specific limitations in metabolizing PM. Importantly, under reactor conditions, PDC11 achieved 47.46% degradation of DIC,

which, although slightly lower than laboratory performance, highlights the potential of scale-up for practical applications.

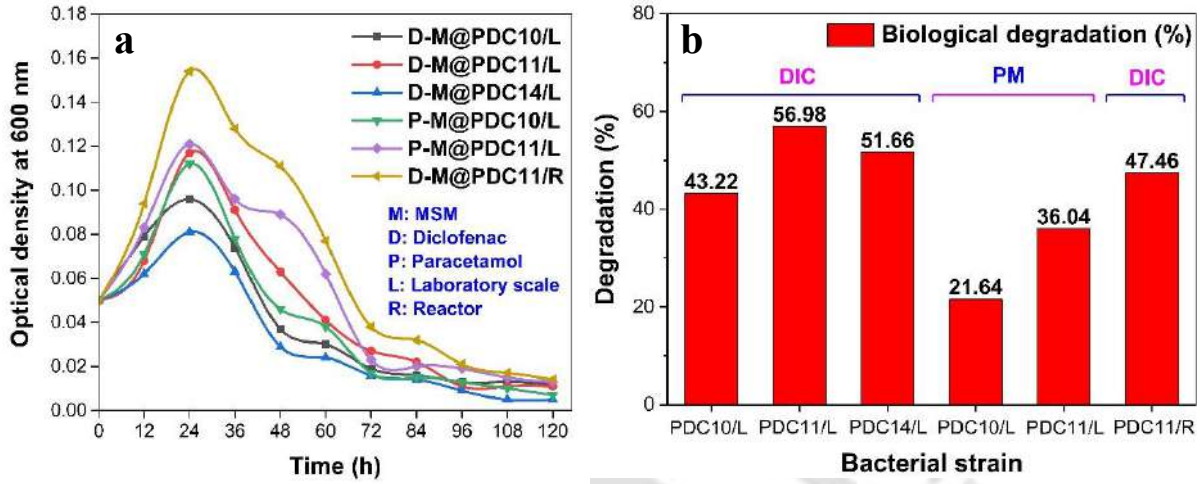

Figure 8.9: (a) Growth profiles of bacterial strains, and (b) Degradation of DIC and PM by *Pseudomonas spp.* PDC10, PDC11, and PDC14 strains. L denotes degradation carried out at laboratory scale, while R denotes degradation performed in the integrated reactor.

8.4.3 Integrated degradation of mixture of PhACs spiked in DI water (PDW)

8.4.3.1 Photocatalytic degradation and catalysts recovery

The photocatalytic degradation of synthetic pharmaceutical wastewater, prepared by spiking a mixture of CIP, CLQ, DIC, PM, and SULF (1 mg L^{-1} each) in deionized water (PDW), was investigated using bare-TiO_2 and Au-doped TiO_2 photocatalysts. Experiments were conducted with a photocatalyst loading of 0.05 g L^{-1} under continuous solar irradiation for 3 h at pH 6.5, simulating the pH conditions of hospital wastewater, with a working volume of 10 L.

Fig. 8.10a illustrates that the initial dark adsorption was 5.68 and 2.42% for bare-TiO_2 and Au-doped TiO_2, respectively. Upon solar illumination, bare-TiO_2 achieved 76.69% degradation of PDW within 60 min, which further increased to 89.65% after 180 min. The corresponding TOC and COD removal was 65.17 and 76.25%, respectively (Fig. 8.10c). In comparison, Au-doped TiO_2 exhibited superior photocatalytic activity, achieving 91.14 and 96.09% degradation within 60 and 180 min, respectively, with significantly higher TOC (87.67%) and COD (87.78%) removal. The slower degradation rate after 60 min is attributed to the breakdown and subsequent mineralization of intermediate products, as confirmed by the increase in relative CO_2 concentration beyond 45 min (Fig. 8.10b).

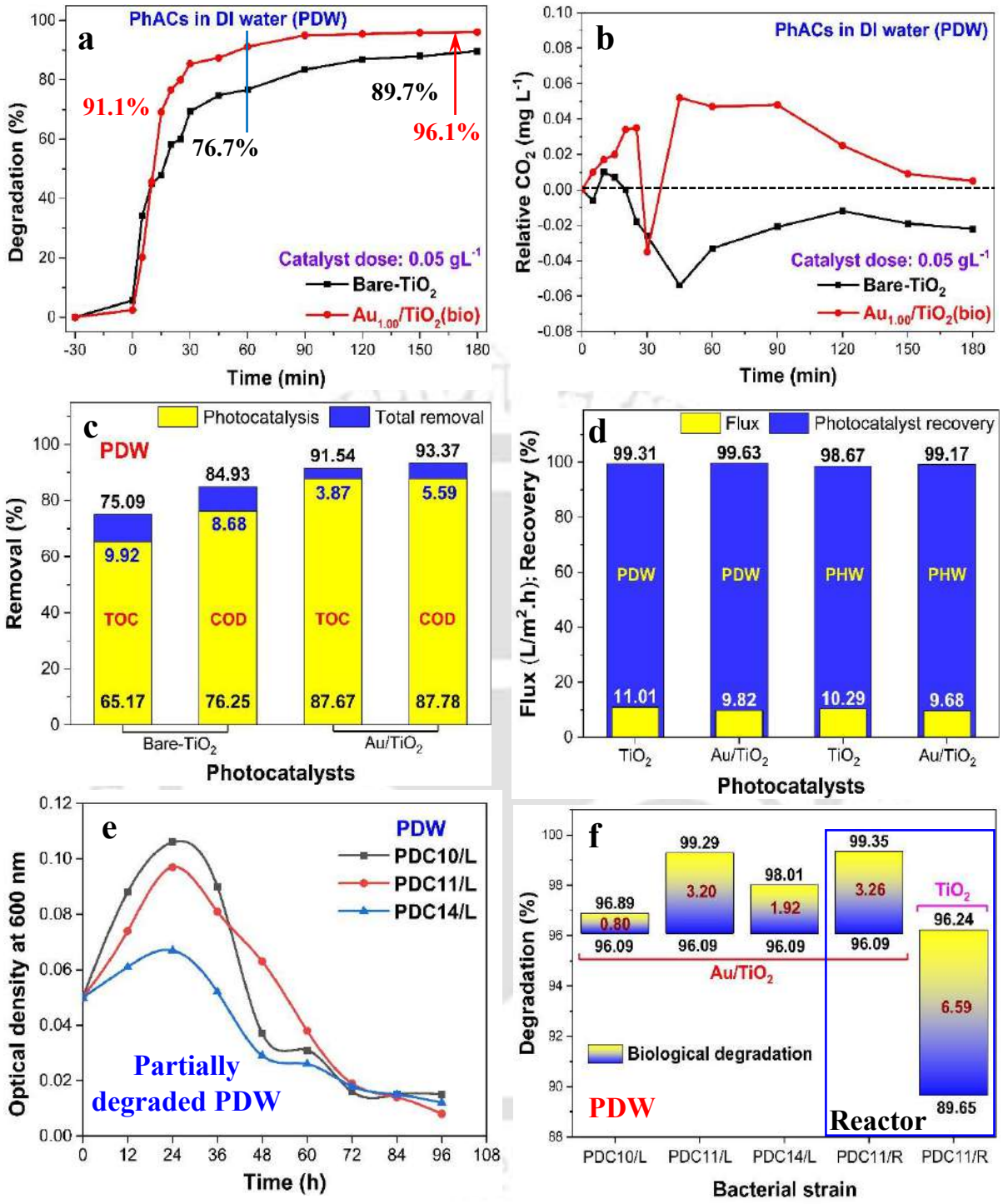

Figure 8.10: (a) Dark adsorption and photocatalytic degradation of mixture of PhACs spiked DI water (PDW), and (b) CO_2 concentration profiles, (c) TOC and COD removal (%) during photocatalytic degradation, (d) Photocatalysts recovery after the degradation process, (e) Growth profiles of bacterial strains at the laboratory scale, and (f) Biological degradation of partially degraded PDW by bacterial strains at both laboratory and pilot-scale.

Post-photodegradation, the photocatalysts were recovered using a membrane separation unit. Recovery efficiencies of 99.31 and 99.63% were achieved for bare-TiO_2 and Au-doped TiO_2, respectively, with permeate fluxes of 11.01 and 9.82 L m^{-2} h^{-1} (Fig. 8.10d).

8.4.3.2 Biological degradation of partially degraded PDW

The catalyst-free, partially degraded PDW was subsequently treated in the biological degradation unit to further eliminate residual PhACs and by-products formed during photocatalysis. Prior to pilot scale degradation, laboratory-scale batch experiments were performed with Au-doped TiO_2 degraded PDW in MSM medium using *Pseudomonas spp.* strains PDC10, PDC11, and PDC14 at 30 °C and 120 rpm. As shown in Figs. 8.10e-8.10f, bacterial growth increased steadily up to 24 h, followed by a decline due to depletion of available carbon substrates. Owing to the low residual concentration of PhACs and intermediates, biomass generation was limited (Boshoff et al., 2004). Among the tested strains, PDC11 demonstrated the highest degradation efficiency of 3.2% within 24 h, enhancing the total PDW degradation to 99.29% at laboratory scale.

The integrated reactor studies confirmed the contribution of the biological unit to overall degradation. For bare-TiO_2 degraded PDW, total degradation increased to 96.24% with an additional 6.59% degradation achieved biologically. Corresponding TOC and COD removals reached 75.09 and 84.93%, respectively, with 9.92 and 8.68% contributions from the biological stage. Similarly, for Au-doped TiO_2 degraded PDW, an additional 3.26% degradation was observed, raising the overall removal efficiency to 99.35%. TOC and COD removal improved from 87.67 to 91.54% and 87.78 to 93.37%, respectively.

In summary, the integrated photocatalytic (96.09% degradation) and biological process (3.26% degradation) demonstrated remarkable efficiency, achieving the highest 99.35% degradation of PDW with 99.63% recovery of used Au-doped TiO_2.

8.4.4 Integrated degradation of mixture of PhACs spiked in hospital wastewater (PHW)

8.4.4.1 Collection and characterization of hospital wastewater

The hospital wastewater was collected from GNRC Hospital, North Guwahati, Assam, India, by following proper safety protocols. Further, the collected water was kept for gravity-based settlement of the sand and large particles. The supernatant was filtered through Whatman filter paper (Grade 591) and stored at 4 °C. Further, the filtrate hospital wastewater was

characterized for its physiochemical characteristics. pH and conductivity of wastewater were measured as 6.5 and 711 µS, respectively, at 25 °C. Further, TOC and total carbon were measured using a TOC analyzer after filtration through 0.2 µm filter paper. TOC was found to be quite less (1.08±0.11 mg L^{-1}), even with repeated analysis. While the total carbon was found 8.44±0.1 mg L^{-1}. Additionally, TDS and turbidity of wastewater were found to be 291 mg L^{-1} and 68 NTU.

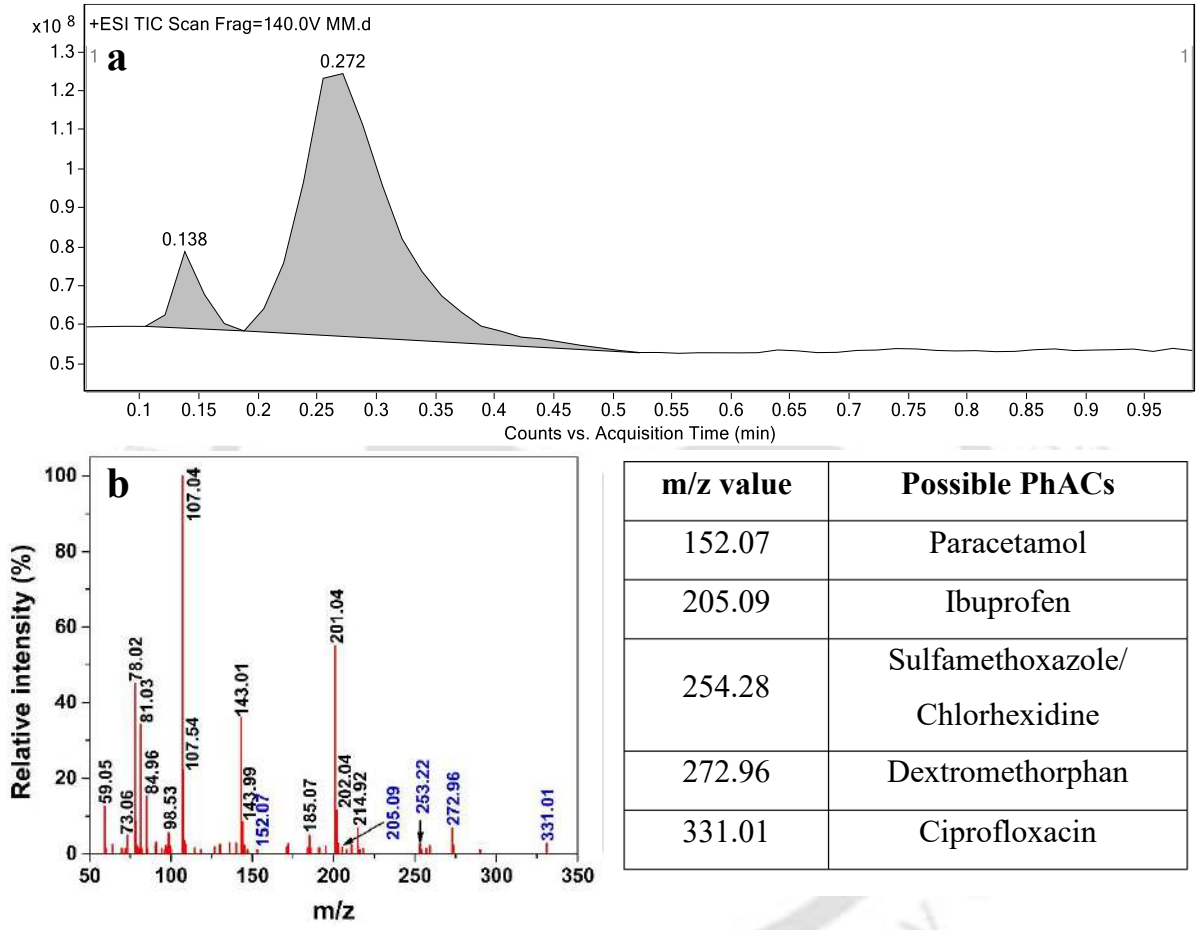

m/z value	Possible PhACs
152.07	Paracetamol
205.09	Ibuprofen
254.28	Sulfamethoxazole/ Chlorhexidine
272.96	Dextromethorphan
331.01	Ciprofloxacin

Figure 8.11: LC-MS analysis: (a) Chromatogram and (b) Mass spectra of hospital wastewater, and possible PhACs with their m/z values presence in hospital wastewater.

The HRMS analysis of hospital wastewater was performed, and the obtained chromatogram and mass spectra are illustrated in Fig. 8.11. Two peaks were observed in the chromatogram of hospital wastewater, indicating presence of vast variety of organic compounds. The most of peaks in the mass spectra (Fig. 8.11b) suggest presence of diverse range of small organic pollutants and disinfection by-products in hospital wastewater, with m/z 59.05 to 143.01, 201.04 corresponding to benzene-like fragments, allyl alcohol, chlorinated ions, phosphocholine fragments, polyaromatic hydrocarbons, which are mainly

originated from detergents, and personal care products (Lores et al., 2016). However, some small peaks were observed at m/z = 152.07, 205.09, 254.028, 272.96, and 331.01, which could be related to paracetamol, ibuprofen, sulfamethoxazole or chlorhexidine dimer, dextromethorphan and ciprofloxacin, respectively (Fig. 8.11c) (Amaratunga et al., 2016; Omotola and Olatunji, 2020). Although, these PhACs are presence in very concentration.

8.4.4.2 Photocatalytic degradation and catalysts recovery

For photodegradation studies, the filtered hospital wastewater was directly spiked with various PhACs (1 mg L^{-1} each), i.e., CIP, CLQ, DIC, PM and SULF (PHW) for degradation in integrated process. The photocatalytic degradation of PHW was carried out using bare-TiO_2 and Au-doped TiO_2, followed by catalyst recovery and subsequent biological treatment of the partially degraded PHW and formed intermediates, as described in Section 8.4.4.1.

Figs. 8.12a and 8.12b present the degradation efficiency and corresponding CO_2 concentration profiles at different time intervals, respectively. Compared with PDW, the surface adsorption of PHW by bare-TiO_2 and Au-doped TiO_2 increased significantly, from 5.68 to 16.1% and from 2.42 to 17.1%, respectively. This enhancement could be attributed to the presence of organic moieties in hospital wastewater, which promoted stronger adsorption of PhACs onto the photocatalyst surface (Ozcan et al., 2024).

Bare-TiO_2 achieved 57.61% degradation of PHW within the first 60 min, which further increased to 90.23% after 180 min, along with TOC and COD removal of 58.58 and 66.67%, respectively (Fig. 8.12c). These values were lower than those obtained during PDW degradation, likely due to the complex organic matrix of PHW. In contrast, Au-doped TiO_2 exhibited superior performance, achieving 64.08 and 94.21% degradation within 60 and 180 min, respectively. Furthermore, TOC (64.61%) and COD (85.56%) removal were significantly higher than those of bare-TiO_2, which is line with the elevated CO_2 concentrations observed in the mineralization profiles (Fig. 8.12b), indicating more effective mineralization with Au-doped TiO_2.

Post-treatment catalyst recovery through the membrane separation unit revealed 98.67% recovery of bare-TiO_2 with a permeate flux of 10.29 L m^{-2} h^{-1}, while Au-doped TiO_2 showed 99.17% recovery with a flux of 9.68 L m^{-2} h^{-1} (Fig. 8.12d). The slight reduction in catalyst recovery and flux compared with PDW experiments could be ascribed to interference from impurities and suspended matter present in PHW, which may have partially interacted with the membrane surface and photocatalytic material.

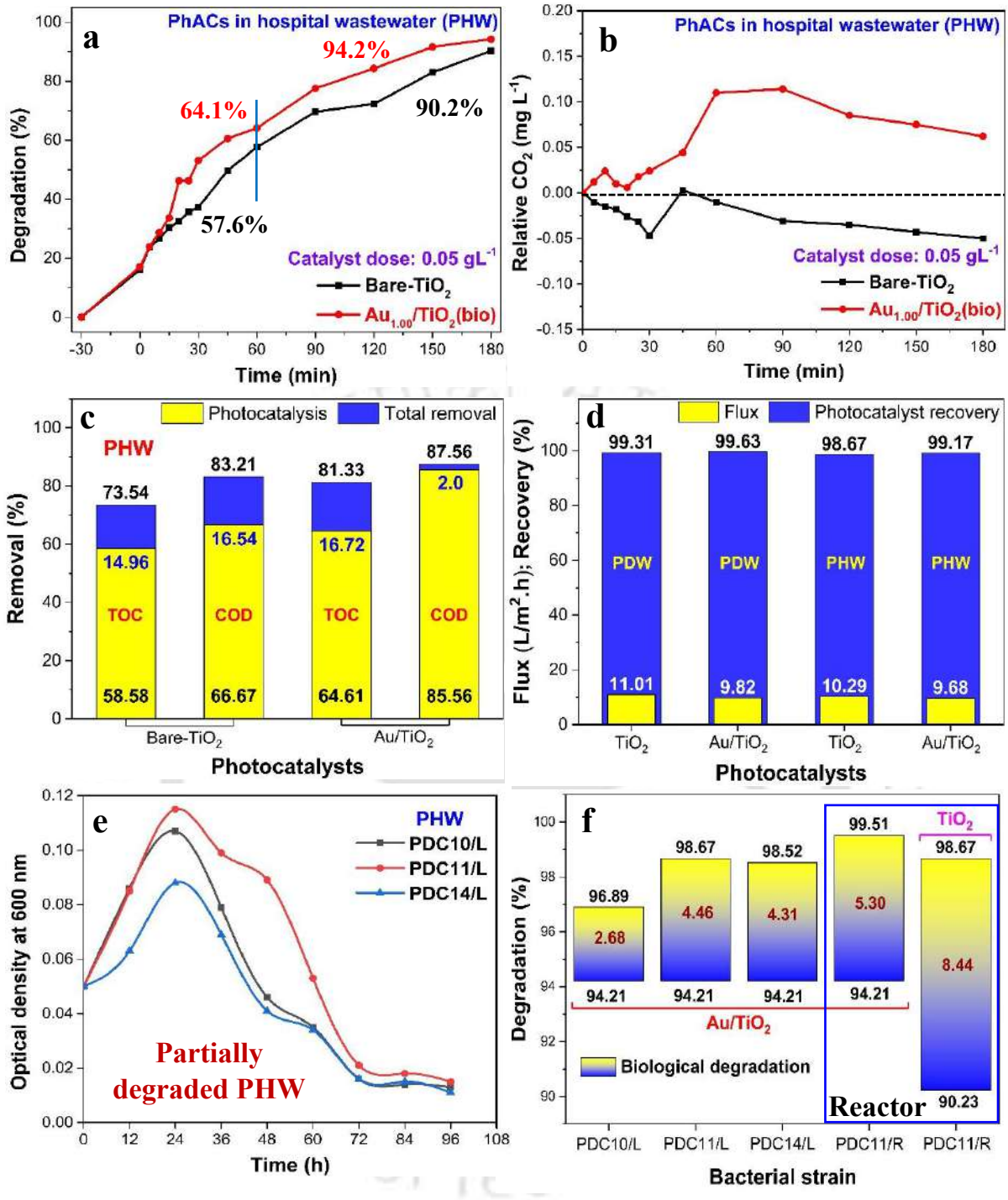

Figure 8.12: (a) Dark adsorption and photocatalytic degradation of mixture of PhACs spiked hospital wastewater (PHW), and (b) CO_2 concentration profiles, (c) TOC and COD removal (%) during photocatalytic degradation, (d) Photocatalysts recovery after the degradation process, (e) Growth profiles of bacterial strains at the laboratory scale, and (f) Biological degradation of partially degraded PDW by bacterial strains at both laboratory and pilot-scale.

8.4.4.3 Biological degradation of partially degraded PHW

The biological treatment of partially degraded PHW was performed at both laboratory and pilot scale, following a similar approach as for PDW. The bacterial growth profiles are shown in Fig. 8.12e. A slightly higher bacterial growth was observed compared to PDW, which can be attributed to the availability of additional biodegradable organic compounds in PHW that served as supplementary carbon sources (Chahal et al., 2016). Among the tested strains, *Pseudomonas spp. PDC11* demonstrated the highest degradation, achieving 4.46% additional degradation at laboratory scale, which increased the total PHW degradation to 98.67% within 24 h (Fig. 8.12f). At pilot scale, PDC11 further enhanced the degradation efficiency of bare-TiO_2 treated PHW from 90.23 to 98.67%, while TOC and COD removal were increased from 58.58 to 73.54% and from 64.61 to 83.21%, respectively (Fig. 8.12c). For Au-doped TiO_2 treated PHW, PDC11 contributed an additional 5.30% degradation, elevating the overall degradation to 99.51%, with TOC and COD removal reaching 81.33 and 87.56%, respectively. The biological degradation of PHW was higher than PDW, which could be due to the presence of easily consumable compounds in hospital wastewater, supporting microbial growth.

Overall, the integrated photocatalytic and biological process achieved a maximum degradation of 99.51% for PHW, with contributions of 94.21% from Au-doped TiO_2 photocatalysis and 5.30% from subsequent biological degradation. Catalyst recovery was maintained at 99.17% for Au-doped TiO_2. These findings highlight the potential of the integrated process for efficient degradation of complex industrial pharmaceutical wastewater.

8.5 Major findings

This study demonstrated a pilot-scale integrated treatment system for the degradation of PhACs, combining photocatalytic degradation, catalyst recovery, and biological degradation. The system successfully addressed three critical challenges of scalability, photocatalyst recovery, and detoxification of residual intermediates, thereby offering a sustainable and practical approach for pharmaceutical wastewater management.

Solar-assisted photocatalysis using bare TiO_2 and bio-based noble metal-doped TiO_2 exhibited efficient performance under optimized conditions. The catalyst dosage was optimized at 0.05 g L^{-1} with exposed CPC reflectors, which yielded the highest photocatalytic efficiency. Individual PhAC degradation using bare TiO_2 showed variable removal efficiencies of 94.93% for DIC, 92.43% for PM, and 85.47% for SULF. Noble-metal doping significantly enhanced photocatalytic activity, with Pt-doped TiO_2 and Au-doped TiO_2 achieving >99%

degradation of CIP and CLQ, respectively. CO_2 profiles confirmed progressive mineralization, and corresponding TOC and COD removal followed similar patterns. In PhAC-spiked distilled water (PDW), Au-doped TiO_2 achieved 96.09% degradation with 87.67% TOC removal, which was further enhanced through biological degradation. In contrast, PhAC-spiked hospital wastewater (PHW) exhibited 94.21% degradation with 64.61% TOC removal, slightly reduced due to the interference of organic impurities. The cross-flow ultrafiltration membrane system achieved almost complete recovery of photocatalysts (>99%) after photodegradation of both PDW and PHW, ensuring catalyst reusability and operational cost-effectiveness. Biological degradation by *Pseudomonas spp.* PDC11 contributed an additional 5.30% degradation of residual PhACs in Au-doped TiO_2 treated PHW, increasing overall degradation to 99.51%. TOC and COD removal also improved significantly during biological degradation, confirming enhanced mineralization.

In conclusion, the integrated pilot-scale reactor demonstrated highly efficient degradation of both individual and mixed PhACs, almost complete photocatalyst recovery, and effective detoxification of intermediates. The synergy of solar photocatalysis, membrane-based catalyst recovery, and microbial degradation establishes this process as a scalable, economical, and sustainable strategy for the treatment of complex pharmaceutical wastewaters.

References

Amaratunga, P., Clothier, M., Lemberg, B.L., Lemberg, D., 2016. Determination of dextromethorphan in oral fluid by LC-MS-MS. J. Anal. Toxicol. 40. https://doi.org/10.1093/jat/bkw033

Amorim, J., Liao, K., Mandal, A., Costa, A.F. de S., Roumeli, E., Sarubbo, L.A., 2024. Impact of Carbon Source on Bacterial Cellulose Network Architecture and Prolonged Lidocaine Release. Polymers (Basel). 16, 3021. https://doi.org/10.3390/polym16213021

Anuradha, Singh, A., Seth, R.K., Kumar, P., Kumar, S., 2025. Optimizing operational parameters for improved photocatalytic activity of hematite–rGO nanocomposites in methylene blue dye degradation. Eur. Phys. J. B 98, 4. https://doi.org/10.1140/epjb/s10051-024-00849-3

Bahadur, N., Bhargava, N., 2019. Novel pilot scale photocatalytic treatment of textile & dyeing industry wastewater to achieve process water quality and enabling zero liquid discharge. J. Water Process Eng. 32. https://doi.org/10.1016/j.jwpe.2019.100934

Barquín, C., Rivero, M.J., Ortiz, I., 2024. Revealing the role of individual components in the

high performance photocatalytic mineralization of mixtures of organohalogen pollutants. J. Environ. Chem. Eng. 12, 114572. https://doi.org/10.1016/j.jece.2024.114572

Bhan, C., Golder, A.K., 2023. Utilizing bioinspired AgNPs as an antibacterial agent to enhance ceramic membrane performance. J. Environ. Chem. Eng. 11, 110283. https://doi.org/10.1016/j.jece.2023.110283

Boshoff, G., Duncan, J., Rose, P.D., 2004. The use of micro-algal biomass as a carbon source for biological sulphate reducing systems. Water Res. 38. https://doi.org/10.1016/j.watres.2004.03.031

Chahal, C., van den Akker, B., Young, F., Franco, C., Blackbeard, J., Monis, P., 2016. Pathogen and Particle Associations in Wastewater: Significance and Implications for Treatment and Disinfection Processes. Adv. Appl. Microbiol. 97. https://doi.org/10.1016/bs.aambs.2016.08.001

Chen, S., Zhang, L., Melhi, S., Alshammari, D.A., Amin, M.A., Dai, L., Li, S., Yu, W., Cui, L., 2024. Photocatalytic degradation of Toluene by three-dimensional monolithic Titanium Dioxide / Cuprous Oxide foams with Z-schemed Heterojunction. Adv. Compos. Hybrid Mater. 7, 1–14. https://doi.org/10.1007/s42114-024-01032-z

Han, M., Wang, S., Yu, X., Zhang, Y., Li, M., Yi, Z., Gao, H., Yang, H., Fang, L., Syed, A., 2024. Enhanced Photocatalytic Activity of O-deficient Modified $CuAl_2O_4/MoS_2$ Composite Photocatalysts in Wastewater Treatment Applications. Adv. Sustain. Syst. 8, 1–19. https://doi.org/10.1002/adsu.202300478

Jaaz, A.H., Hasan, H.A., Sopian, K., Haji Ruslan, M.H. Bin, Zaidi, S.H., 2017. Design and development of compound parabolic concentrating for photovoltaic solar collector: Review. Renew. Sustain. Energy Rev. https://doi.org/10.1016/j.rser.2017.03.127

Langenhoff, A., Inderfurth, N., Veuskens, T., Schraa, G., Blokland, M., Kujawa-Roeleveld, K., Rijnaarts, H., 2013. Microbial removal of the pharmaceutical compounds ibuprofen and diclofenac from wastewater. Biomed Res. Int. 2013. https://doi.org/10.1155/2013/325806

Lores, M., Llompart, M., Alvarez-Rivera, G., Guerra, E., Vila, M., Celeiro, M., Lamas, J.P., Garcia-Jares, C., 2016. Positive lists of cosmetic ingredients: Analytical methodology for regulatory and safety controls - A review. Anal. Chim. Acta. https://doi.org/10.1016/j.aca.2016.02.033

Omotola, E.O., Olatunji, O.S., 2020. Quantification of selected pharmaceutical compounds in water using liquid chromatography-electrospray ionisation mass spectrometry (LC-ESI-MS). Heliyon 6. https://doi.org/10.1016/j.heliyon.2020.e05787

Ozcan, D.O., Hendekci, M.C., Ovez, B., 2024. Enhancing the adsorption capacity of organic

and inorganic pollutants onto impregnated olive stone derived activated carbon. Heliyon 10. https://doi.org/10.1016/j.heliyon.2024.e32792

Peng, G., Yaoqin, W., Changmei, S., Chunnuan, J., Ying, Z., Rongjun, Q., Ying, W., 2022. Preparation and properties of PVC-based ultrafiltration membrane reinforced by in-situ synthesized p-aramid nanoparticles. J. Memb. Sci. 642. https://doi.org/10.1016/j.memsci.2021.119993

Poddar, K., Sarkar, D., Bhoi, R., Sarkar, A., 2024. Biotransformation of diclofenac by isolated super-degrader *Pseudomonas sp.* DCα4: Postulated pathways, and attenuated ecotoxicological effects. Environ. Pollut. 344. https://doi.org/10.1016/j.envpol.2024.123388

Ravi, Pandey, L.M., 2019. Enhanced adsorption capacity of designed bentonite and alginate beads for the effective removal of methylene blue. Appl. Clay Sci. 169. https://doi.org/10.1016/j.clay.2018.12.019

Ravi, R., Singh, A., Golder, A.K., 2025. Electrifying CQDs-doped PANI-embedded membrane for enhanced self-cleaning targeting wastewater treatment. J. Chem. Technol. Biotechnol. https://doi.org/10.1002/jctb.70017

Tamaddon, F., Nasiri, A., Yazdanpanah, G., 2020. Photocatalytic degradation of ciprofloxacin using $CuFe_2O_4$@methyl cellulose based magnetic nanobiocomposite. MethodsX 7. https://doi.org/10.1016/j.mex.2019.12.005

Truong, H.B., Huy, B.T., Ray, S.K., Gyawali, G., Lee, Y.I., Cho, J., Hur, J., 2022. Magnetic visible-light activated photocatalyst $ZnFe_2O_4/BiVO_4/g\text{-}C_3N_4$ for decomposition of antibiotic lomefloxacin: Photocatalytic mechanism, degradation pathway, and toxicity assessment. Chemosphere 299. https://doi.org/10.1016/j.chemosphere.2022.134320

Wen, L., Liu, P., Zhou, Z., Wang, K., Zhou, Y., 2023. Biosafety Photooxidation Strategy of Levofloxacin Driven by Manganese-doped Indium Zinc Sulfide. Chem. - An Asian J. 18, 2–8. https://doi.org/10.1002/asia.202300161

Zhang, J., Li, X., Klümper, U., Lei, H., Berendonk, T.U., Guo, F., Yu, K., Yang, C., Li, B., 2022. Deciphering chloramphenicol biotransformation mechanisms and microbial interactions via integrated multi-omics and cultivation-dependent approaches. Microbiome 10. https://doi.org/10.1186/s40168-022-01361-5

Zhou, H., Wang, H., Yue, C., He, L., Li, H., Zhang, H., Yang, S., Ma, T., 2024. Photocatalytic degradation by TiO_2-conjugated/coordination polymer heterojunction: Preparation, mechanisms, and prospects. Appl. Catal. B Environ. https://doi.org/10.1016/j.apcatb.2023.123605

CHAPTER 9

Conclusions and Scopes for Future Studies

This chapter presents the key conclusions drawn from the entire study. The chapter also outlines limitations and proposes future research directions.

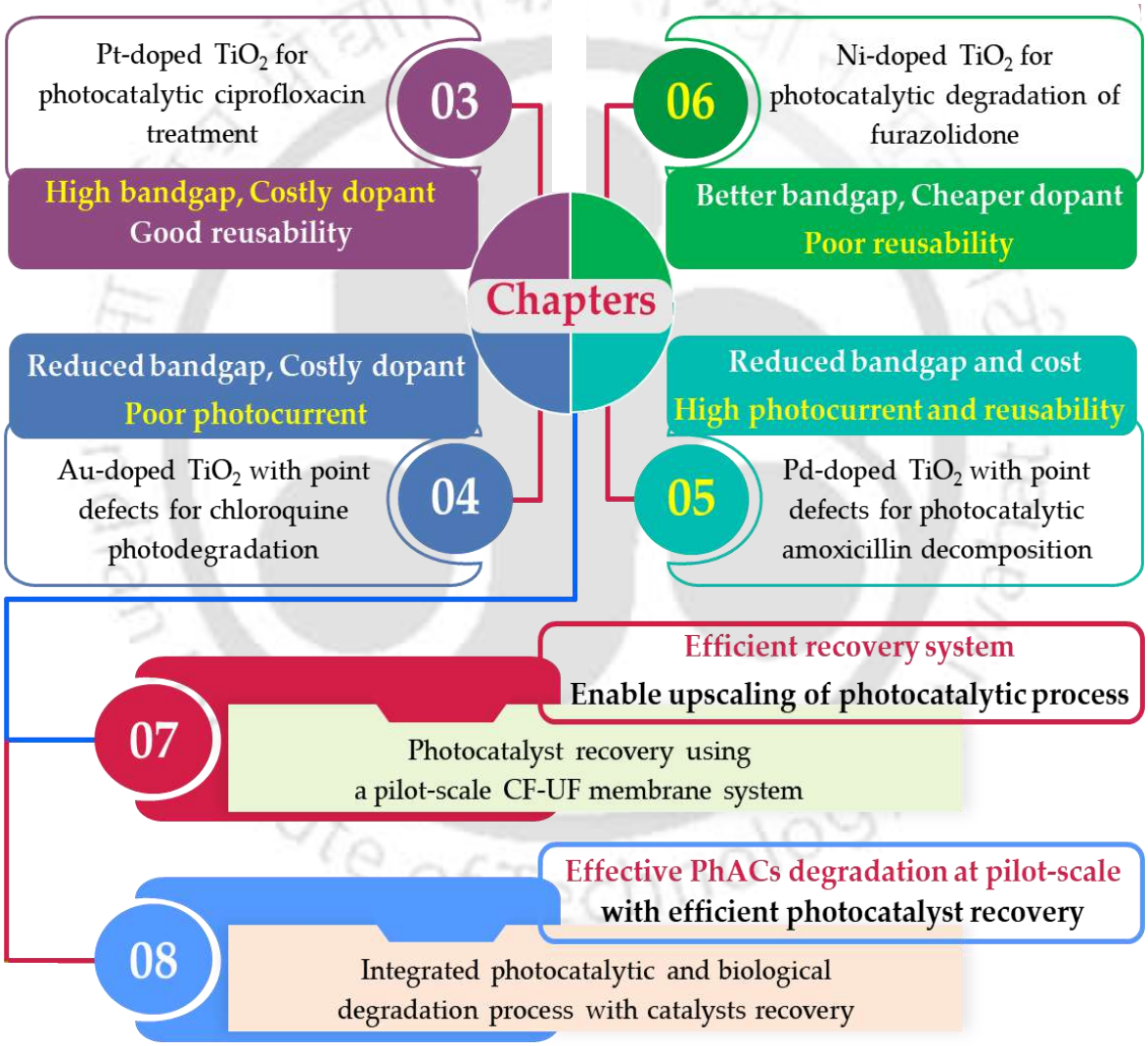

Intentionally Left Blank
Intentionally Left Blank

9.1 Overall conclusions

This thesis presented the development of bio-based metal-doped TiO_2 photocatalysts using plant bioanalytes and their application in degradation of pharmaceutically active compounds (PhACs), with an emphasis on bandgap engineering, charge carrier separation, point defects, and surface hydrophilicity, collectively enhanced photocatalytic activity. Further, the bio-based catalysts employed for degradation of PhACs in a pilot-scale integrated system coupled with catalyst recovery, and biological degradation for complete mineralization of residual PhACs and formed intermediates. The major outcomes are summarized below in accordance with the thesis chapters.

Using bio-analytes as sustainable reducing and stabilizing agents, Pt-, Au-, Pd-, and Ni-doped TiO_2 were synthesized, each showing significant structural and electronic modifications compared to bare TiO_2. Metal doping led to lower bandgap, delayed charge-carrier recombination, and increased oxygen vacancies, Ti^{3+} defect density, and surface hydrophilicity, which led to enhanced visible-light-driven photocatalytic activity. Pt-doping reduced the bandgap to 3.02 eV and achieved an 8-fold increase in photocurrent, resulting in nearly two-fold higher degradation and quantum yield of ciprofloxacin (CIP) with good recyclability and reduced aquatic toxicity. Similarly, Au-doping narrowed the bandgap to 2.45 eV, introduced electron traps and oxygen vacancies, and produced ~4-fold higher current density, enabling over 94% degradation of chloroquine (CLQ) with superior mineralization efficiency compared to bare and chemically synthesized counterparts. Pd-doped TiO_2, derived from banana peel extract, further lowered the bandgap to 2.41 eV, improved charge separation by ~22-fold higher photocurrent density, and achieved almost complete degradation of amoxicillin (AMX) under both visible and solar irradiation, supported by density functional theory predictions that aligned well with experiments. Likewise, Ni-doped TiO_2 synthesized from pineapple peel extract exhibited a bandgap reduction to 2.54 eV, an 11-fold increase in photocurrent density, and the highest degradation efficiency of furazolidone (FZD), with consistent performance across multiple reuse cycles. In all cases, bio-based doping effectively neutralized the antimicrobial activity of residual pollutants and reduced aquatic toxicity, confirming the environmental relevance of the methodology. The bio-based doped photocatalysts demonstrated superior performance compared to their chemically doped counterparts, exhibiting a reduced bandgap, enhanced surface hydrophilicity, and significantly improved photocatalytic degradation efficiency toward PhACs.

To address the challenge of photocatalyst recovery, a pilot-scale cross-flow ultrafiltration (CF-UF) membrane system was demonstrated, achieving >98.7% recovery of both bare and metal-doped TiO_2 with minimal fouling and nearly complete flux recovery. The hydrodynamic diameters of TiO_2 and Pt-doped TiO_2 particles gradually increased in the reject and backflush streams. However, despite this increase, the recovered catalysts retained their photocatalytic activity, confirming the suitability of membrane-assisted recovery for large-scale processes. Building on this, a pilot-scale integrated treatment system was established, combining photocatalysis, catalyst recovery, and biological degradation. Bare TiO_2 achieved >85% degradation of diclofenac (DIC), paracetamol (PM), and sulfamethoxazole (SULF), while noble-metal doping further enhanced efficiencies to >99% for CIP and CLQ with almost complete recovery of used photocatalysts. Au-doped TiO_2 was particularly effective for mixed pharmaceutical wastewater, reaching >96% degradation with ~88% total organic carbon (TOC) removal, which was further improved by biological degradation using *Pseudomonas spp.* PDC11, ultimately achieving >99.5% overall removal with significant mineralization gains.

Collectively, the findings demonstrate that bio-based metal doping substantially enhances the photocatalytic performance of TiO_2 by reducing its bandgap, enriching defect states, and improving surface properties, while the CF-UF system ensures nearly complete recovery of catalysts for reuse. The integration of photocatalysis, recovery, and biodegradation at pilot scale bridges the gap between laboratory studies and industrial implementation, establishing a scalable, sustainable, and environmentally benign strategy for pharmaceutical wastewater treatment.

9.2 Scopes for future studies

This doctoral work opens multiple paths for further advancement of the integrated photocatalytic and biological treatment system for treatment of pharmaceutical wastewater:

- **Pilot-scale validation of Pd-doped TiO_2 and Ni-doped TiO_2 photocatalysts:** Future work may focus on scaling Pd-doped TiO_2 and Ni-doped TiO_2 catalysts in the photocatalytic degradation unit to validate their superior photocatalytic efficacy under real wastewater conditions, ensuring reproducibility beyond laboratory experiments.
- **Long-term stability and reusability:** Extended reusability studies across multiple degradation cycles are necessary to assess structural stability, resistance to deactivation, and sustained photocatalytic efficiency over prolonged operation, which is crucial for industrial adaptation.

- **Techno-economic analysis:** A comprehensive cost-benefit analysis, including energy consumption, catalyst regeneration, and operational expenditure, should be performed to evaluate the feasibility of transitioning the process from pilot-scale demonstration to industrial-scale wastewater treatment plants.
- **Enhanced biological degradation:** Isolation and utilization of high-efficiency bacterial strains, either engineered or naturally robust, can complement photocatalysis by mineralizing residual PhACs and toxic intermediates, thereby achieving almost complete detoxification.
- **Industrial effluent trials:** Future research must extend the integrated system to real-time pharmaceutical industry effluents, which are more complex than spiked wastewater, to test performance under variable pollutant concentration, fluctuating pH, and mixed contaminants.
- **Advanced catalyst recovery systems:** Development of a magnetic-sonication-based recovery system instead of membrane system, may reduce operation costs and processing time. Electromagnetic separation enables rapid catalyst recovery, while sonication-assisted dispersion of recovered photocatalysts can restore surface activity and minimize agglomeration for subsequent reuse.
- **Illumination optimization:** Hybridization of solar and artificial visible-light sources could mitigate weather and diurnal limitations, ensuring continuous operation. Coupling of integrated system with automated tracking systems for dynamic alignment of CPC reflectors for maximum photon flux could be implemented, which will enhance the degradation efficiency.
- **Energy sustainability:** Integration of solar panels as a renewable power input for pumping, aeration, and illumination could substantially reduce energy dependence and operational costs, promoting a sustainable and self-sufficient treatment system.
- **Photocatalytic efficiency regeneration:** Photocatalyst regeneration strategies could be explored to restore photocatalytic activity by removing surface-adsorbed intermediates and residual PhACs. Techniques such as mild thermal treatment, solvent washing, or in-situ oxidative regeneration could be investigated to recover active sites and prolong catalyst lifetime.

Research Outcomes

Journal papers (thesis)

1. **R. Ravi** and A.K. Golder, Pd-doped TiO_2 with Induced Ti^{3+} Defects and Oxygen Vacancies for Photocatalytic Amoxicillin Decomposition: DFT Studies and Ecotoxicity Assessment – ***Chem. Eng. Sci. 122802*** (2025). https://doi.org/10.1016/j.ces.2025.122802.
2. **R. Ravi** and A.K. Golder, Oxygen Deficient Ni-doped TiO_2 by Nature-inspired Process: Density Functional Theory and Photocatalytic Studies, ***J. Environ. Chem. Eng***. 13(3), 116198 (2025). https://doi.org/10.1016/j.jece.2025.116198.
3. **R. Ravi** and A.K. Golder, Photocatalytic and Biological Degradation Processes to Mineralize Pharmaceutically Active Compounds and Catalyst Recovery: A review, ***Coord. Chem. Rev.*** 523(1), 216267 (2025). https://doi.org/10.1016/j.ccr.2024.216267.
4. **R. Ravi** and A.K. Golder, Efficient Recovery of TiO_2 and Pt-doped TiO_2 Photocatalysts in Wastewater Treatment Using a Pilot-Scale Cross-Flow Ultrafiltration Membrane System, ***Sep. Purif. Technol.*** 339, 126710 (2024). https://doi.org/10.1016/j.seppur.2024.126710.
5. **R. Ravi** and A.K. Golder, Bio-based Au Doping with Dominant Oxygen Vacancies and Ti^{3+} Defects on Photocatalytic Functionalities of TiO_2, ***Ind. Eng. Chem. Res.*** 62(48), 20702-20715 (2023). https://doi.org/10.1021/acs.iecr.3c02850.
6. **R. Ravi** and A.K. Golder, A Tuneable Bioinspired Process of Pt-Doping in TiO_2 for Improved Photoelectrochemical and Photocatalytic Functionalities, ***Colloids Surf. A: Physicochem. Eng. Asp.*** 663, 131034 (2023). https://doi.org/10.1016/j.colsurfa.2023.131034.
7. **R. Ravi** and A.K. Golder, Toxicity and Antimicrobial Assessment of Ciprofloxacin, Chloroquine, and Furazolidone: Insights into Reaction By-products Formed during Photocatalysis – **Under Review.**

Journal papers (others)

1. **R. Ravi,** A. Singh and A.K. Golder, Electrifying CQDs-doped PANI-embedded Membrane for Enhanced Self-cleaning Targeting Wastewater Treatment, ***J. Chem. Technol. Biotechnol.*** (2025). https://doi.org/10.1002/jctb.70017.
2. **R. Ravi**, C. Bhan, A.K. Golder, Bio-analytic Synthesis of Cu-doped TiO_2 for Photocatalytic Degradation of Ciprofloxacin under Visible Light, ***Opt. Mater.*** 159, 2025, 116577. https://doi.org/10.1016/j.optmat.2024.116577.

3. C. Bhan, **R. Ravi**, A.K. Golder, Phyto-analytic Formation of Ag Nanostructures for Targeted Electrocatalytic Sensing of Ciprofloxacin, ***J. Environ. Chem. Eng.*** 13, 2025, 115140. https://doi.org/10.1016/j.jece.2024.115140.
4. **R. Ravi,** S.K. Yadav, C. Bhan and A.K. Golder, Defect Engineering in Amla-derived Zn-doped TiO_2 for Enhanced Norfloxacin Photodegradation and Ecotoxicological Assessment – **Communicated**.

Book chapters

1. **R. Ravi** and A.K. Golder, Pharmaceutically Active Compounds' (PhACs) Threat: An Environmental Prospective, Conference proceeding, NERC, IIT Guwahati – 2022 (Springer). https://doi.org/10.1007/978-981-19-8464-8_3.
2. **R. Ravi**, C. Bhan, A.K. Golder, Recent advances in bio-based synthesis of nanomaterials for photocatalytic applications*, RIC, IIT Guwahati, Springer* (2024) – **Accepted**.
3. C. Bhan, **R. Ravi**, A.K. Golder, Recent advancement in monitoring of environmental pollutants using structured nano-catalyst integrated electrochemical sensing technique: A review, *RIC, IIT Guwahati, Springer* (2024) – **Accepted**.

Patent

1. A.K. Golder, and **R. Ravi**. Integrated System for Solar-photocatalytic and Biological Degradation of Wastewater Pollutants with Membrane-based Catalyst Recovery. Indian patent application no. 202431072569, temporary reference no. TEMP/E-1/78417/2024-KOL, date of filing 25 Oct 2024.

Conferences/Symposium/Workshop attended

1. **R. Ravi** and A.K. Golder, Visible Light Driven Ni/TiO_2 Photocatalyst Synthesis via Bioinspired Route using Waste Pineapple Peel, Research & Industrial Conclave (RIC) - 2022, 20-23th Jan 2022 held at IIT Guwahati, Guwahati, Assam, India (**Oral Presentation**).
2. **R. Ravi** and A.K. Golder, Pharmaceutically Active Compounds' (PhACs) Threat: An Environmental Prospective, North East Research Conclave (NERC) - 2022, 20-23th Jan 2022 held at IIT Guwahati, Guwahati, Assam, India (**Poster Presentation**).
3. **R. Ravi** and A.K. Golder, Photocatalytic Degradation of CIP by Waste Pineapple Peel based Ni/TiO_2 Photocatalyst under Visible Light, North East Research Conclave (NERC) - 2022, 20-23th Jan 2022 held at IIT Guwahati, Guwahati, Assam, India (**Oral Presentation**).

4. **R. Ravi** and A.K. Golder, Visible Light-Driven Photodegradation of Chloroquine Using Green Synthesized Au-doped TiO_2, International Chemical Engineering Conference (IChEC) 2022, 12-13th Nov 2022 held at IIT Patna, Patna, Bihar, India (**Oral Presentation**).
5. **R. Ravi** and A.K. Golder, Microwave-assisted Bio-based Pd-doping onto TiO_2 using *S. edule* Vegetal-extract for Photocatalytic Degradation of Ciprofloxacin, Research & Industrial Conclave (RIC) - 2023, 14-16th May 2023 held at IIT Guwahati, Guwahati, Assam, India (**Oral Presentation**).
6. **R. Ravi** and A.K. Golder, Pilot-scale Recovery of Photocatalysts using Ultrafiltration Membrane, IIChE-CHEMCON - 2023, 27-30th Dec 2023 held at Heritage Institute of Technology, Kolkata, West Bangal, India (**Oral Presentation**).
7. **R. Ravi** and A.K. Golder, Nature-inspired Metal Doping onto Semiconductor Photocatalysts for Enhanced Photocatalytic Degradation of PhACs, India-Dalhousie Student Research Symposium: Addressing Common Challenges via Research & Innovation - 2024, Dalhousie University, Nova Scotia, Canada, (**Online Oral Presentation**).
8. **R. Ravi**, A. Singh, A.K. Golder, Development of Electrical Stimuli Self-cleaning Membrane using Carbon Nanostructures for Wastewater Treatment, Symposium on Environmental Challenges, Opportunities and Sustainable Solutions - 2024, 5th June 2024 held at Centre for the Environment, IIT Guwahati, Guwahati, Assam, India (**Poster Presentation**).
9. **Ravi** and A.K. Golder, Bio-analytes for Synthesizing Cu-doped TiO_2 for Photocatalytic Degradation of Ciprofloxacin under Visible Light, Research & Industrial Conclave (RIC) - 2024, held at IIT Guwahati, Guwahati, Assam, India (**Oral Presentation**).
10. **R. Ravi**, C. Bhan and A.K. Golder, Recent Advances in Bio-based Synthesis of Nanomaterials for Photocatalytic Applications, Research & Industrial Conclave (RIC) - 2024, held at IIT Guwahati, Guwahati, Assam, India (**Oral Presentation**).
11. C. Bhan, **R. Ravi**, and A.K. Golder, Recent Advancement in Monitoring of Environmental Pollutants using Structured Nano-catalyst Integrated Electrochemical Sensing Technique: A review, Research & Industrial Conclave (RIC) - 2024, held at IIT Guwahati, Guwahati, Assam, India (**Oral Presentation**).
12. **R. Ravi**, A. Singh, A.K. Golder, Electrifying CQDs-Doped PANI Embedded Membrane for Enhanced Self-Cleaning Targeting Wastewater Treatment, An International Conference on Environmental Challenges, Opportunities and Sustainable Solution (ENVIRONMENT

2024) 2024, 09-11th Dec 2024 held at IIT Guwahati, Guwahati, Assam, India (**Oral Presentation**).

13. **R. Ravi**, and A.K. Golder, Toxicity Assessment of Intermediates Formed during Photocatalytic Degradation of Pharmaceuticals using Bio-based Metal-doped TiO_2, Symposium on ending plastic pollution, 5th June 2025, organized by Centre for the Environment, IIT Guwahati, Assam, India (**Poster Presentation**).
14. S. Halder, **R. Ravi**, and A.K. Golder, Bio-Based Metal-doped Photocatalysts: A Sustainable Approach for Enhanced Photocatalytic Degradation of Organic Pollutants, Symposium on ending plastic pollution, 5th June 2025, organized by Centre for the Environment, IIT Guwahati, Assam, India (**Poster Presentation**).
15. **Ravi** and A.K. Golder, Integrated Photocatalytic and Biological Process with Membrane Separation for Pilot-scale Pharmaceutical Wastewater Treatment, Research & Industrial Conclave (RIC) - 2025, held at IIT Guwahati, Guwahati, Assam, India (**Oral Presentation**).
16. **Ravi** and A.K. Golder, Integrated Photocatalytic Treatment of Pharmaceutical Wastewater and Catalyst Recovery, Research & Industrial Conclave (RIC) - 2025, held at IIT Guwahati, Guwahati, Assam, India (**Oral Presentation – Thesis Presentation**).
17. **Ravi** and A.K. Golder, Photocatalytic and Biological Degradation of PhACs with Catalyst Recovery, Global Conference for Decarbonization of Energy and Materials (GCDEM 2025), held at Nanyang Technological University (NTU), Singapore (**Oral Presentation**).

Awards

1. **Best Paper Award** for "**Ravi** and A.K. Golder, Photocatalytic Degradation of CIP by Waste Pineapple Peel based Ni/TiO_2 Photocatalyst under Visible Light, North East Research Conclave (NERC) - 2022, 20-23th Jan 2022 held at IIT Guwahati, Guwahati, Assam, India (**Oral Presentation**)".
2. **First Place in SCIENTIFIQUE: ORAL PRESENTATION,** "**Ravi** and A.K. Golder, Microwave-assisted Bio-based Pd-doping onto TiO_2 using *S. edule* Vegetal-extract for Photocatalytic Degradation of Ciprofloxacin, Research & Industrial Conclave (RIC) - 2023, 14-16th May 2023 held at IIT Guwahati, Guwahati, Assam, India (**Oral Presentation**)".
3. **Best Poster Presentation Award,** "**Ravi**, A. Singh, A.K. Golder, Development of Electrical Stimuli Self-cleaning Membrane using Carbon Nanostructures for Wastewater Treatment, Symposium on Environmental Challenges, Opportunities and Sustainable

Solutions - 2024, 5th June 2024 held at Centre for the Environment, IIT Guwahati, Guwahati, Assam, India **(Poster Presentation)**".

4. **First Place in SCIENTIFIQUE: ORAL PRESENTATION** (Centre for the Environment), "**Ravi** and A.K. Golder, Bio-analytes for Synthesizing of Cu-doped TiO_2 for Photocatalytic Degradation of Ciprofloxacin under Visible Light, Research & Industrial Conclave (RIC) - 2024, 09-11th Aug 2024 held at IIT Guwahati, Guwahati, Assam, India (**Oral Presentation**)".
5. **2nd Best Poster Presentation Award** for "**R. Ravi**, and A.K. Golder, Toxicity Assessment of Intermediates Formed during Photocatalytic Degradation of Pharmaceuticals using Bio-based Metal-doped TiO_2, Symposium on ending plastic pollution, 5th June 2025, organized by Centre for the Environment, IIT Guwahati, Assam, India (**Poster Presentation**)".
6. **Best Departmental Innovation Award (Theiss Presentation)** for "**R. Ravi**, and A.K. Golder, Integrated Photocatalytic Treatment of Pharmaceutical Wastewater and Catalyst Recovery, Research & Industrial Conclave (RIC) - 2025, 10-12th Oct 2025 held at IIT Guwahati, Guwahati, Assam, India (**Oral Presentation**)".
7. **Best Oral Presentation Award, "R. Ravi,** and A.K. Golder, Photocatalytic and Biological Degradation of PhACs with Catalyst Recovery, Global Conference for Decarbonization of Energy and Materials (GCDEM 2025), held at Nanyang Technological University (NTU), Singapore (**Oral Presentation**).

Ravi

Roll Number: 206152102
PhD – Environment
Indian Institute of Technology Guwahati

+91-7404240003
vashistrs76@gmail.com
https://www.researchgate.net/profile/Ravi-Ravi?ev=hdr_xprf
http://www.linkedin.com/in/ravi-vashist-8977b6169/

Education

Year	Degree / Certificate	Institute / Board	CGPA/Percentage
2020 - 2025	PhD	Indian Institute of Technology, Guwahati	-
2017 - 2019	M.Tech	Indian Institute of Technology, Guwahati	9.16
2013 - 2017	B.Tech	Kurukshetra University - Kurukshetra	72.8%
2012	Senior secondary	HBSE Board	77.2%
2010	Secondary	HBSE Board	84.0%

Publications

- Pd-doped TiO_2 with Induced Ti^{3+} Defects and Oxygen Vacancies for Photocatalytic Amoxicillin Decomposition: DFT Studies and Ecotoxicity Assessment – ***Chem. Eng. Sci.*** 321, 122802 (2025)
  ***R. Ravi**, and A.K. Golder* *https://doi.org/10.1016/j.ces.2025.122802*
- Electrifying CQDs-doped PANI-embedded Membrane for Enhanced Self-cleaning Targeting Wastewater Treatment, ***J. Chem. Technol. Biotechnol.*** 100(10), 2078-2093 (2025)
  ***R. Ravi**, A. Singh and A.K. Golder* *https://doi.org/10.1002/jctb.70017*
- Oxygen Deficient Ni-doped TiO_2 by Nature-inspired Process: Density Functional Theory and Photocatalytic Studies, ***J. Environ. Chem. Eng.*** 13(3), 116198 (2025)
  ***R. Ravi**, and A.K. Golder* *https://doi.org/10.1016/j.jece.2025.116198*
- Phyto-analytic Formation of Ag Nanostructures for Targeted Electrocatalytic Sensing of Ciprofloxacin, ***J. Environ. Chem. Eng.*** 13(1), 115140 (2025)
  *C. Bhan, **R. Ravi**, and A.K. Golder* *https://doi.org/10.1016/j.jece.2024.115140*
- Bio-analytic Synthesis of Cu-doped TiO_2 for Photocatalytic Degradation of Ciprofloxacin under Visible Light, ***Opt. Mater.*** 159, 116577 (2025)
  ***R. Ravi,** C. Bhan, and A.K. Golder* *https://doi.org/10.1016/j.optmat.2024.116577*
- Photocatalytic and Biological Degradation Processes to Mineralize Pharmaceutically Active Compounds and Catalyst Recovery: A review, ***Coord. Chem. Rev.*** 523(1), 216267 (2025)
  ***R. Ravi**, and A.K. Golder* *https://doi.org/10.1016/j.ccr.2024.216267*
- Efficient Recovery of TiO_2 and Pt-doped TiO_2 Photocatalysts in Wastewater Treatment Using a Pilot-scale Cross-flow Ultrafiltration Membrane System, ***Sep. Purif. Technol.*** 339, 126710 (2024)
  ***R. Ravi**, and A.K. Golder* *https://doi.org/10.1016/j.seppur.2024.126710*
- Bio-based Au Doping with Dominant Oxygen Vacancies and Ti^{3+} Defects on Photocatalytic Functionalities of TiO_2, ***Ind. Eng. Chem. Res.*** 62(48), 20702-20715 (2023)
  ***R. Ravi**, and A.K. Golder* *https://doi.org/10.1021/acs.iecr.3c02850*
- A Tuneable Bioinspired Process of Pt-Doping in TiO_2 for Improved Photoelectrochemical and Photocatalytic Functionalities, ***Colloids Surf. A: Physicochem. Eng. Asp.*** 663, 131034 (2023)
  ***R. Ravi**, and A.K. Golder* *https://doi.org/10.1016/j.colsurfa.2023.131034*
- Synthesis of low-cost bentonite/Duranta erecta's fruit powder imbedded alginate beads and its application in surfactant removal, ***Environ. Sci. Pollut. Res.*** 28, 58945-58957 (2021)
  *A.K. Golder, S. Chauhan, and **R. Ravi*** *https://doi.org/10.1007/s11356-021-14306-6*

- Enhanced adsorption capacity of designed bentonite and alginate beads for the effective removal of methylene blue, ***Appl. Clay Sci.*** 169, 102-111 (2019)
  ***R. Ravi**, and L.M. Pandey* *https://doi.org/10.1016/j.clay.2018.12.019*
- Toxicity and Antimicrobial Assessment of Ciprofloxacin, Chloroquine, and Furazolidone: Insights into Reaction By-products Formed during Photocatalysis (2025)
  ***R. Ravi**, and A.K. Golder* *Under Review*
- Defect Engineering in Amla-derived Zn-doped TiO_2 for Enhanced Norfloxacin Photodegradation and Ecotoxicological Assessmen (2025)
  ***R. Ravi**, S.K. Yadav, C. Bhan and A.K. Golder* *Submitted*
- Pharmaceutically Active Compounds' (PhACs) Threat: An Environmental Prospective, Conference proceeding, NERC, IIT Guwahati – 2022 (***Springer***) (2023) – Book Chapter
  ***R. Ravi**, and A.K. Golder* *https://doi.org/10.1007/978-981-19-8464-8_3*
- Recent Advances in Bio-based Synthesis of Nanomaterials for Photocatalytic Applications, RIC, IIT Guwahati (***Springer***) (2023) – Book Chapter
  ***R. Ravi**, C. Bhan and A.K. Golder* *Accepted*
- Recent Advancement in Monitoring of Environmental Pollutants using Structured Nanocatalyst Integrated Electrochemical Sensing Technique: A review (***Springer***) (2023) – Book Chapter
  *C. Bhan, **R. Ravi**, and A.K. Golder* *Accepted*

Patent

- Integrated System for Solar-photocatalytic and Biological Degradation of Wastewater Pollutants with Membrane-based Catalyst Recovery. Indian patent application no. 202431072569, temporary reference no. TEMP/E-1/78417/2024-KOL
  *A.K. Golder, and **R. Ravi*** *Filled on 25th Oct 2024*

Conferences/Symposium/Workshop Participation

Conference/Symposium Participation (Oral/Poster Presentation): **23**

Workshop/FDP/Webinar Attended: **7**

Some of Conference/Symposium (Oral Presentation):

- Enhancement of Adsorption Capacity of Designed Bentonite/Alginate Beads for Effective Removal of Methylene Blue Dye, Sustainable energy and environmental challenges (SEEC) - 2018, IIT Roorkee, India
- Visible Light-Driven Photodegradation of Chloroquine using Green Synthesized Au-doped TiO_2, International Chemical Engineering Conference 2022, IIT Patna, India
- Nature-inspired Metal Doping onto Semiconductor Photocatalysts for Enhanced Photocatalytic Degradation of PhACs, India-Dalhousie Student Research Symposium - 2024, Dalhousie University, Canada (online)
- Electrifying CQDs-doped PANI Embedded Membrane for Enhanced Self-Cleaning Targeting Wastewater Treatment, An International Conference, ENVIRONMENT 2024, IIT Guwahati, India
- Photocatalytic and Biological Degradation of PhACs with Catalyst Recovery, Global Conference for Decarbonization of Energy and Materials (GCDEM 2025), Nanyang Technological University (NTU), Singapore

Experience

- **Junior Research Fellow (Project Staff)** at Indian Institute of Technology Guwahati, India [*Jul 2019 - Dec 2020]*
- **FESEM Operator** at Indian Institute of Technology Guwahati, India [*Mar 2021 - June 2025]*
- **HPLC Operator** at Indian Institute of Technology Guwahati, India [*Mar 2022 - Nov 2025]*

Projects

- **Integrated Photocatalytic-Biological Treatment of Pharmaceutical Wastewater & Catalyst Recovery**
  Prof. Animes Kumar Golder, Centre for the Environment, IIT Guwahati, Assam, India *Dec 2025*
- **Isolation, Characterization & Optimization of Biosurfactant Production by Inherent Microbes and its Applications**
  Dr. Lalit Mohan Pandey, Dept. of Bioscience and bioengineering, IIT Guwahati, Assam, India *July 2019*
- **Isolation & Characterization of PGPR & Their Effect on Seedling Growt of Maize, & Antifungal Activity**
  Dr. Deepak Malik, UIET, KUK, Haryana, India *May 2017*

Technical Skill

- **Writing:** Academic Publications, Scientific Writing, Project Proposal
- **Instruments:** FESEM, FETEM, EDX, TGA, AFM, XRD, XPS, UV-Vis, Spin Coater, BET, LCMS, FTIR, HPLC, NMR, TGA, Raman, Microwave reactor, Potentiostat, Membrane Separation Unit
- **Electrochemical techniques:** EIS, CV, SWV, DPV, Chronoamperometry
- **Software:** Microsoft Office, Origin, ImageJ, ChemDraw, XPS peak fit, Mendeley, Nova, Mass Hunter, Quantum espresso
- **Miscellaneous:** Nanomaterial Synthesis, Wastewater Treatment, Photocatalysis, Surface Functionalization, Ceramic Membrane Fabrication, CO_2 Reduction, Adsorption, Biosurfactant Production, Biodegradation

Positions of Responsibility

- **Department Placement Representative**, Centre for Career Development (CCD), IIT Guwahati, 2024-2025
- **Key Member of Organizing Committee**, WED2025 Symposium, Centre for the Environment, IIT Guwahati (2025)
- **Student Coordinator**, Plastic Collection Drive, IIT Guwahati (World Environment Day 2025)
- **Key Member of Organizing Committee**, ENVIRONMENT 2024 - An International Conference on Environmental Challenges, Opportunities and Sustainable Solutions, Dec 2024
- **Volunteer**, Workshop-cum Symposium on Bio-inspired Nanomaterials for Environmental Applications, IIT Guwahati, Feb 2020
- **Core Member and Event Coordinator,** Across Multiple Events, Red Ribbon Club, IIT Guwahati (2018-2019)

Achievements

- **JEE Mains 2013:** Qualified (Rank: 182893)
- **Gate (Biotechnology):** Qualified 2017 (Rank: 399) and 2020 (Rank: 579)
- **CSIR NET 2018 (Life Science):** Qualified (Rank: 85)
- **Department of Biotechnology (DBT) NET 2019:** Qualified
- **Best Poster Presentation Award**, Internation Conference SEEC 2018, IIT Roorkee, India (2018)
- **Best Paper Award** (Oral Presentation), NERC 2022, IIT Guwahati, India (2022)
- **First Place in SCIENTIFIQUE** (Oral Presentation), RIC 2023, IIT Guwahati, India (2023)
- **Best Poster Presentation Award**, Symposium 2024, IIT Guwahati, India (2023)
- **First Place in SCIENTIFIQUE** (Oral Presentation), RIC 2024, IIT Guwahati, India (2024)
- **2nd Best Poster Presentation Award**, WED2025 Symposium, IIT Guwahati, India (2025)
- **Best Departmental Innovation Award** for PhD Thesis Presentation, RIC 2025, IIT Guwahati, India (2025)
- **Best Oral Presenter Award**, International Conference "GCDEM 2025", NTU Singapore (2025)
- **MHRD Doctoral Fellowship**, Government of India, 2020

Key courses taken

- Analytical Biotechnology Lab
- Industrial Microbiology Lab
- Food & Environment Biotech. Lab
- Biotechniques
- Environmental Studies
- Enzymology
- Environmental Biotechnology
- Genetics
- Bioprocessing Engineering
- Thermodynamics of Bioprocesses
- Quantitative Biology
- Microbiology
- Molecular and cell biology
- Immunology

Extracurriculars

- 1st in Arm Wrestling, 2nd in Medley Relay and 3rd in Water Polo, SPARDHA'18, IIT Guwahati (Inter-Hostel)
- Winner (Team Captain), Badminton Tournament 2025, Environment, IIT Guwahati
- Participation in “Blood Donation”, Plastic Collection, and Plantation Drives”